THE HONG KONG
POLYTECHNIC UNIVERSITY
香港理工大學
Pao Yue-kong Library
包玉剛圖書館

Copyright Undertaking

This thesis is protected by copyright, with all rights reserved.

By reading and using the thesis, the reader understands and agrees to the following terms:

1. The reader will abide by the rules and legal ordinances governing copyright regarding the use of the thesis.
2. The reader will use the thesis for the purpose of research or private study only and not for distribution or further reproduction or any other purpose.
3. The reader agrees to indemnify and hold the University harmless from and against any loss, damage, cost, liability or expenses arising from copyright infringement or unauthorized usage.

If you have reasons to believe that any materials in this thesis are deemed not suitable to be distributed in this form, or a copyright owner having difficulty with the material being included in our database, please contact lbsys@polyu.edu.hk providing details. The Library will look into your claim and consider taking remedial action upon receipt of the written requests.

Pao Yue-kong Library, The Hong Kong Polytechnic University, Hung Hom, Kowloon, Hong Kong

http://www.lib.polyu.edu.hk

BUFFETING RESPONSE OF LONG SPAN CABLE-SUPPORTED BRIDGES UNDER SKEW WINDS: FIELD MEASUREMENT AND ANALYSIS

by

LE-DONG ZHU

BE.(Civil), MEngSc. (Civil)

A Dissertation for the Degree of Doctor of Philosophy

Department of Civil and Structural Engineering

The Hong Kong Polytechnic University

2002

Pao Yue-kong Library
PolyU • Hong Kong

To my family

DECLARATION

I hereby declare that this dissertation entitled *"Buffeting Response of Long Span Cable-supported Bridges under Skew Winds: Field Measurement and Analysis"* has not been, either in whole or in part, previously submitted for a degree in this or any other institution, and the work presented in this dissertation is original unless otherwise acknowledged in the text.

SINGED

Le-Dong ZHU

ACKNOWLEDGMENTS

I wish to express my eternally sincere appreciation to my supervisor, Professor Y.L. Xu, and my co-supervisor, Professor H.F. Xiang, for their generous support, excellent guidance, invaluable suggestions and discussions throughout the course of this work. I have been deeply impressed by their insights to the problems and their conscientious and meticulous attitudes to research and enterprise, which benefit me inexhaustibly.

I am grateful to the Hong Kong Polytechnic University for giving me the opportunity of being the PhD candidate of this university and providing me with the financial support. The work is also partially supported by the National Natural Science Foundation of China (Grant 59895410).

Sincere thanks should go to Tsing Ma Control Area Division, Highways Department of the Government of the Hong Kong Special Administrative Region, for providing me with the field measurement data of wind and structural response of the Tsing Ma Bridge.

The three wind tunnel experiments described in this dissertation were carried out in the TJ-2 Wind Tunnel of the State Key Laboratory for Disaster Reduction in Civil Engineering at Tongji University, Shanghai, China, for which I am appreciated to the State Key Laboratory.

I would like to extend my special thanks to Mr. F. Zhang who gave me many valuable suggestions to my wind tunnel experiment, put great efforts to develop the elaborate six-component balance system for the experiment, and also took part in the experiment as an indispensable member.

I would also like to thank all the other kind persons in the State Key Laboratory who gave me great assistance and support in my wind tunnel experiment. They are Dr. Q.S. Ding, Ms. J.Y. Xu, Mr. L. Zhao, Mr. Y.P. Yao, Mr. Z.D. Liu, Prof. Z.X. Lin, Prof. J.Z. Song, Dr. W. Chen, Prof. Y.J. Ge, Prof. A.R. Chen and Prof. Z.C. Shi. I also wish to thank Dr. J. Chen of The Hong Kong Polytechnic University for providing me with his results on the modal damping ratios of the Tsing Ma Bridge

during Typhoon Sam. I am grateful to Mr. M.C.H. Hui and Dr. K.Y. Wong of Highways Department of the Government of the Hong Kong Special Administrative Region for their constructive discussions on the amendments of the dissertation.

Special thanks are due to my friends and colleagues in the Department of Civil and Structural Engineering of The Hong Kong Polytechnic University. In particularly, I am thankful to Dr. X.F. Yuan and Y.F. Fu for their great help in the printing and binding of the dissertation.

Finally, I am particularly indebted to my wife, Ying Lu, and son, Yi-Min Zhu, for their understanding and continuous encouragement. It would be impossible to finish this dissertation without their great supports and sacrifices that they have made during the whole period of my study.

Abstract of Thesis Entitled

BUFFETING RESPONSE OF LONG SPAN CABLE-SUPPORTED BRIDGES UNDER SKEW WINDS: FIELD MEASUREMENT AND ANALYSIS

Submitted by

Le-Dong ZHU

for

the Degree of Doctor of Philosophy in Civil & Structural Engineering

at The Hong Kong Polytechnic University in January 2002

This thesis mainly focuses on the development and verification of a modified method in frequency-domain for the analysis of buffeting response and the understanding of buffeting behavior of long span cable-supported bridges under skew winds, supported by a series of wind tunnel tests and field measurements.

First, the Tsing Ma suspension Bridge in Hong Kong and the Wind And Structural Health Monitoring System (WASHMS) installed by the Hong Kong Highways Department in the Bridge are introduced. The field measurement data of the Tsing Ma Bridge during Typhoon Victor recorded by the WASHMS are analyzed for both wind structure and bridge response. It is demonstrated that for a long span cable-supported bridge located in a complicated topography, typhoon-induced winds seldom attack the bridge at a right angle. Important wind characteristics such as mean wind speed and turbulence intensity vary along the bridge longitudinal axis. The measured response of main cables by the WASHMS also cannot be utilized to facilitate the comparison between field measurement and analysis if the conventional frequency-domain buffeting analysis method is used. A modified frequency-domain method for long span bridges under skew winds is thus required for a reasonable comparison between field measurement and analysis and a better understanding of bridge behavior under skew winds.

The modified buffeting analysis method of long span bridges is then developed in this study based on the quasi-steady linear theory and the oblique strip theory in conjunction with the pseudo excitation method and the finite element method. It is capable of performing fully coupled 3D buffeting analysis of long span bridges under skew winds and naturally including the effects of inter-modes, multi-modes, and spatial modes as well as the interaction between bridge deck, towers and main cables. In the modified method, a concept of oblique strip along the mean wind direction is introduced and a set of universal expressions of six component buffeting forces associated with the oblique strip is derived. The general expression of cross-spectral matrix of buffeting forces is then presented after considering turbulence spatial correlation and aerodynamic admittance. Self-excited aeroelastic forces are also taken into consideration in the modified method by including 18 flutter derivatives of oblique strip under skew winds. A comprehensive computer program is then developed in accordance with the proposed modified method.

To implement the modified method for buffeting analysis of a long span bridge, it is essential to obtain six component aerodynamic coefficients for oblique strips of a bridge deck. To this end, a wind tunnel test technique for measuring such aerodynamic coefficients is developed in this study, which includes the design of sectional model, the development of test rig and measurement system, and the analysis of test results. A typical oblique sectional model of the Tsing Ma Bridge deck is manufactured and tested in a wind tunnel under a series of combination of mean wind inclination and yaw angle. The measured data are fitted to obtain the six aerodynamic coefficient curves as functions of wind inclination and yaw angle for the late comparison between field measurement and analysis. The obtained six aerodynamic coefficient curves are also used to examine the cosine rule currently used in the buffeting analysis of long span bridges under yaw winds. It is found that the traditional cosine rule may significantly underestimate buffeting forces, in particular at large yaw angles.

Self-excited aeroelastic forces, often coming on the scene in the form of aeroelastic damping and stiffness, have been recognized as not only the key factors for bridge stability but also one of the important parameters for bridge buffeting response. To include this effect in the buffeting analysis of long span bridges under skew winds, a

wind tunnel test technique is developed, which includes the design of oblique sectional model, the development of a dynamic test rig, and the application of unifying least-square (ULS) method for identification. The flutter derivatives of a typical oblique strip of the Tsing Ma Bridge deck under skew winds are measured. The measured data are fitted and analyzed to find the relationship between flutter derivatives, reduced frequency, wind inclination, and wind yaw angle. The results are also used to examine the approximate formulae derived from the skew wind theory proposed by Scanlan. In general, significant discrepancies exist except for lower reduced velocities, where the approximate formulae may give an acceptable estimation of flutter derivatives of a bridge deck under skew winds. Furthermore, the effects of wind yaw angle on the critical wind speed of the Tsing Ma Bridge are also investigated based on the SDOF torsional flutter theory. It is found that critical wind speed may not increase with increasing wind yaw angle.

To perform a more reasonable comparison of buffeting response of the Tsing Ma Bridge between field measurement and analysis, the aerodynamic coefficients of the bridge towers should be measured under yaw winds consistent with the measurements of aerodynamic coefficients and flutter derivatives of the bridge deck. For this purpose, a 3D stiff model comprised of a whole tower and a segment of bridge deck is designed and tested. The averaged aerodynamic coefficients of the upper and lower segments of both upwind and leeward tower legs and those of tower transverse beams under yaw winds are obtained. With additional comparative tests, the interference effects between the tower legs, the tower transverse beams, and the bridge deck are also discussed.

The comparison of buffeting response of the Tsing Ma Bridge during Typhoon Sam is then conducted. The field measurement data of wind structures surrounding the Bridge during Typhoon Sam are first analyzed and used as input data to the computer program. These data include the mean wind speed, wind inclination, wind yaw angle, auto and cross spectra of wind turbulence, friction velocity, and others. The aerodynamic coefficients and flutter derivatives of the bridge deck and the aerodynamic coefficients of the bridge tower under the identified skew wind are then determined from the measured curves which are inputted into the computer program. Meanwhile, some empirical formulae are adopted for determining the drag and lift

coefficients of the main cables for the identified skew wind. Finally, the computed buffeting acceleration responses of both bridge deck and cables are compared with those measured by the WASHMS, and the comparison is found to be satisfactory in general. The discrepancies of RMS response are, respectively, less than 24%, 17% and 17% in the lateral, vertical and torsional acceleration responses of the main span of the bridge deck. The differences of RMS acceleration response of the main span cables are not more than 20%, 5% and 6% in the lateral, vertical and longitudinal directions, respectively.

Finally, this thesis takes the Tsing Ma Bridge as an example to carry out a parametric study. The parameter study focuses on the effects of wind inclination and yaw angle on the buffeting response of the Bridge. The results reveal that the variation of buffeting response of the Bridge is not monotonous with wind yaw angle and inclination. The maximum bridge response may not occur at zero wind yaw angle, as indicated by the traditional cosine rule. For the Tsing Ma Bridge within a range of wind yaw angles (±30°) and wind inclinations (±5°), the maximum displacement response of bridge deck occurs at about ±12° (yaw angle) and 4° (inclination) in the vertical direction, about 5° (yaw angle) and –2.5° (inclination) in the lateral direction, and about 0° (yaw angle) and -2° (inclination) in the torsional direction. In particular, the lateral RMS displacement response of the bridge deck is not sensitive to wind yaw angle within a range of ±15° for all wind inclination concerned. Furthermore, the influences of aerodynamic crosswind force, yawing and rolling moments on bridge responses are rather small whereas the effects of flutter derivatives may be significant on bridge responses.

LIST OF PUBLICATIONS

Zhu, L.D., Xiang, H.F., Xu, Y.L., Triple-girder Model for Modal Analysis of Cable-Stayed Bridges with Warping Effect, *Engineering Structures*, **22**, 2000, 1313-1323.

Xu Y.L., Zhu L.D., Wong K.Y., Chan K.W.Y., Field Measurement Results of Tsing Ma Suspension Bridge during Typhoon Victor, *Structural Engineering and Mechanics-An International Journal*, **10:6**, 2000, 545-559.

Zhu, L.D., Xu, Y.L., Zhang, F., and Xiang, H.F., Tsing Ma Bridge Deck under Skew Winds. I: Aerodynamic Coefficients, *Journal of Wind Engineering and Industrial Aerodynamics*, in printing.

Zhu, L.D., Xu, Y.L., and Xiang, H.F., Tsing Ma Bridge Deck under Skew Winds. II: Flutter Derivatives, *Journal of Wind Engineering and Industrial Aerodynamics*, in printing.

Zhu, L.D., Xu, Y.L., Zhang, F. and Xiang, H.F., Measurement of Aerodynamic Coefficients of Tower Components of Tsing Ma Bridge under Yaw Wind, *Wind and Structures*, tentatively accepted and under revision.

Xu, Y.L., Zhu, L.D., Field Measurement Results of a Long Suspension Bridge during Typhoon and their Implications, *Proceedings of US-Korea Workshop on New Frontier in INFRASTRUCTURAL/SEISMIC ENGINEERING*, 24-25 August 1999, Soul, Korea, 319-330.

Zhu, L.D., Xu, Y.L., Wong, K.Y., and Chan K.W.Y., Wind characteristics and response of Tsing Ma Bridge during Typhoon Victor, *Advances in Steel Structures*: *Proceedings of the 2nd International Conference on Advances in Steel Structures*, 15-17 December 1999, Hong Kong, China, S.L., Chan and J.G., Teng (eds), Amsterdam, Elsevier Science Ltd., Netherlands, **Vol. I**, 497-504.

Zhu, L.D., Xu. Y.L., and Xiang, H.F., Buffeting analysis of a long suspension bridge under inclined wind, *Advances in Structural Dynamics: Proceedings of International Conference on Advances in Structural Dynamics*, 13-15 December 2000, Hong Kong, China, J.M., Ko and Y.L., Xu (eds.), Amsterdam, Elsevier Science Ltd., Netherlands, **Vol. II**, 1535-1542.

Xu, Y.L., Xia, H., Zhu, L.D. and Sun, D.K., Response of long suspension bridges to typhoon and running trains, *Proceedings of Structural Symposium 2000: Highway and Railway Structures*, 5 May 2000, Hong Kong, 67-107.

Zhu L.D., Xu Y.L., Zhang F., Xiang H.F., Buffeting of a long suspension bridge: analysis and field measurement, *Proceedings of SPIE 6th Annual International Symposium on NDE for Health Monitoring and Diagnostics*, 4-8 March 2001, Newport Beach, California, USA, 323-334.

Zhu L.D., Xiang H.F., Xu Y.L., Wind tunnel study on flutter derivatives of Tsing Ma Bridge deck under skew wind, *Proceedings of The Fifth Asia-Pacific Conference on Wind Engineering*, 21-24 October, 2001, Kyoto, Japan, 465-468.

Xu, Y.L., and Zhu, L.D., Field Measurement and Health Monitoring of Large Civil Engineering Structures during Strong Winds, *Proceedings of The 10th National Academic Conference on Structural Wind Engineering*, 5-10 Nov. 2001, Guilin, China, China Civil Engineering Society and China Aerodynamics Society, 22-30.

CONTENTS

DECLARATION v
ACKNOWLEGMENTS vii
ABSTRACT ix
LIST OF PUBLICATIONS xiii
CONTENTS xv
NOTATIONS xxiii
LIST OF FIGURES xlv
LIST OF TABLES liii

CHAPTER 1 INTRODUCTION 1-1

1.1 RESEARCH MOTIVATIONS 1-1
1.2 OBJECTIVES 1-4
1.3 ASSUMPTIONS AND LIMITATIONS 1-6
1.4 LAYOUT OF THE THESIS 1-7

CHAPTER 2 LITERATURE REVIEW 2-1

2.1 BUFFETING ANALYSIS OF LONG SPAN BRIDGES 2-1
2.1.1 Background 2-1
2.1.2 Buffeting Analysis of Bridges under Normal Wind 2-1
2.1.2.1 Davenport's Theory *2-1*
2.1.2.2 Scanlan's Theory *2-3*
2.1.2.3 Lin's Theory *2-5*
2.1.2.4 Effects of Multi-modes, Inter-mode Coupling and Bridge Component Interaction *2-7*
2.1.2.5 Nonlinear Effects *2-7*
2.1.3 Buffeting Analysis of Bridges under Yaw Wind 2-10
2.2 IDENTIFICATION OF AEROELASTIC COEFFICIENTS 2-17
2.2.1 Models for Self-excited Forces 2-17
2.2.2 Identification of Aeroelastic Coefficients (Flutter Derivatives) 2-23
2.2.2.1 Vertical and Torsional Aeroelastic Coefficients *2-23*

2.2.2.2 Lateral Aeroelastic Coefficients *2-28*
2.2.2.3 Turbulence Effects *2-30*
2.2.3 Unifying Least Square Method for Flutter Derivative Identification .. 2-34
2.2.3.1 Relation between Flutter Derivatives and System Parameters *2-34*
2.2.3.2 Relation between System Parameters and Modal Properties *2-36*
2.2.3.3 Identification of Modal Parameters *2-37*
2.2.3.3.1 MITD method 2-38
2.2.3.3.2 ULS method 2-39
2.3 CHARACTERISTICS OF NATURAL WIND 2-42
2.3.1 Atmospheric Boundary Layer 2-42
2.3.2 Profile of Mean Wind 2-45
2.3.3 Shear Stress and Friction Velocity 2-46
2.3.4 Turbulence Intensity 2-48
2.3.5 Integral Scales of Wind Turbulence 2-49
2.3.6 Auto Spectra of Wind Turbulence 2-52
2.3.7 Cross Spectra of Wind Turbulence 2-59
2.3.7.1 Cross Spectra between Two Same Components of Wind Turbulence at Two Different Spatial Points *2-59*
2.3.7.2 Root-coherence Functions *2-61*
2.3.7.3 Cross Spectra between Two Different Components of Wind Turbulence at One Spatial Point *2-63*

CHAPTER 3 FIELD MEASUREMENT RESULTS OF TSING MA BRIDGE DURING TYPHOON VICTOR 3-1

3.1 INTRODUCTION 3-1
3.2 MAIN FEATURES AND MODAL PROPERTIES OF TSING MA BRIDGE 3-2
3.3 WIND AND STRUCTURAL HEALTH MONITORING SYSTEM 3-3
3.4 BRIEF DESCRIPTION OF LOCAL TERRAIN 3-5
3.5 TYPHOON VICTOR 3-7
3.6 DATA PROCESSING 3-7
3.6.1 Data Processing 3-7
3.6.2 Determination of Wind Speed Components 3-8
3.7 MAIN RESULTS OF MEASURED WIND CHARACTERISTICS 3-11
3.7.1 Mean Wind 3-11

3.7.2 Friction Velocity 3-14
3.7.3 Standard Deviations and Turbulence Intensities 3-15
3.7.4 Integral Scales of Wind Turbulence 3-19
3.7.5 Wind Spectra 3-21
3.7.6 Curve Fitting of Auto Spectra 3-23
3.7.7 Curve Fitting of Cross Spectra 3-25
3.8 MAIN RESULTS OF MEASURED ACCELERATION RESPONSES 3-26
3.8.1 Standard Deviations of Acceleration Responses 3-26
3.8.2 Peak Factors of Acceleration Responses 3-28
3.8.3 Response Spectra and Natural Frequencies 3-29
3.9 IMPLICATIONS TO BUFFETING ANALYSIS 3-30
3.10 SUMMARY 3-31

CHAPTER 4 FORMULATION FOR BUFFETING ANALYSIS OF LONG SPAN BRIDGES UNDER SKEW WINDS 4-1

4.1 INTRODUCTION 4-1
4.2 GOVERNING EQUATION FOR BRIDGE BUFFETING 4-3
4.3 COORDINATES SYSTEMS 4-4
4.3.1 Global Structural and Wind Coordinate Systems 4-4
4.3.2 Local Structural Coordinate Systems 4-5
4.3.3 Local Reference Coordinate System 4-6
4.3.4 Local Mean and Instantaneous Wind Coordinate Systems 4-7
4.4 TRANSFORMATION BETWEEN COORDINATE SYSTEMS 4-8
4.4.1 Global Structural and Wind Coordinate Systems 4-8
4.4.2 Global and Local Structural Coordinate Systems 4-9
4.4.3 Local Structural and Reference Coordinate Systems 4-11
4.4.4 Global Structural Coordinate System and Local Reference Coordinate System 4-12
4.4.5 Global Wind Coordinate System and Local Reference Coordinate System 4-12
4.4.6 Local Reference and Mean Wind Coordinate Systems 4-13
4.4.7 Local Reference and Instantaneous Wind Coordinate Systems 4-14
4.5 DETERMINATION OF LOCAL WIND YAW ANGLE AND INCLINATION 4-15
4.5.1 Wind Components in *qph*-system 4-15

4.5.2 Local Mean Wind Yaw Angle and Inclination 4-16
4.5.3 Local Instantaneous Wind Yaw Angle and Inclination 4-16
4.5.4 Increments of Local Wind Yaw and Inclination 4-18
4.6 DETERMINATION OF BUFFETING FORCES AND SPECTRA 4-18
4.6.1 Buffeting Forces on Element per Unit Length 4-18
4.6.1.1 With Respect to Local Mean Wind Coordinate System 4-19
4.6.1.2 With Respect to Local Structural Coordinate System 4-24
4.6.2 Buffeting Forces at Element Nodes 4-25
4.6.2.1 With Respect to Local Structural Coordinate System 4-25
4.6.2.2 With Respect to Global Structural Coordinate System 4-27
4.6.3 Global Buffeting Force Vector 4-28
4.6.4 Spectral Density Function Matrix of Global Buffeting Forces 4-29
4.7 DETERMINATION OF AEROELASTIC STIFFNESS AND DAMPING MATRICES ... 4-30
4.7.1 Aeroelastic Forces on Element per Unit Length 4-30
4.7.2 Aeroelastic Stiffness and Damping Matrices for Elements 4-32
4.7.2.1 With Respect to Local Structural Coordinate System 4-32
4.7.2.2 With Respect to Global Structural Coordinate System 4-35
4.7.3 Global Aeroelastic Stiffness and Damping Matrices 4-36
4.8 SOLUTIONS OF BUFFETING GOVERNING EQUATION 4-36
4.8.1 Traditional CQC Method and SRSS Method 4-36
4.8.2 Pseudo Excitation Method 4-39
4.8.3 Solution for Bridge Buffeting Response 4-39
4.9 SUMMARY 4-43

CHAPTER 5 IMPLEMENTATION IN COMPUTER PROGRAM 5-1

5.1 INTRODUCTION 5-1
5.2 COMPUTER PROGRAM 5-2
5.2.1 Introduction 5-2
5.2.2 Combinations of Global Coordinates Systems 5-3
5.2.3 Combinations of Local Coordinates Systems 5-4
5.3 DRAG AND CROSSWIND COEFFICIENTS OF BRIDGE CABLES 5-5
5.4 FLUTTER DERIVATIVES OF BRIDGE DECK 5-7
5.4.1 Empirical Formulae Based on Scanlan's Skew Wind Theory 5-7
5.4.2 Empirical Formulae Based on Flat Plate Theory 5-10

5.4.3 Empirical Formulae Based on Quasi-steady Theory 5-11
5.5 AERODYNAMIC ADMITTANCE FUNCTIONS 5-14
5.6 CROSS SPECTRA OF WIND TURBULENCE 5-18
5.7 TOPOGRAPHIC IMPROVEMENT OF CROSS-SPECTRAL MATRIX 5-20
5.8 SUMMARY 5-21

CHAPTER 6 WIND TUNNEL TEST FOR DECK AERODYNAMIC COEFFICIENTS UNDER SKEW WINDS 6-1

6.1 INTRODUCTION 6-1
6.2 DESIGN OF OBLIQUE SECTIONAL MODEL 6-2
6.2.1 Tsing Ma Suspension Bridge Deck 6-2
6.2.2 Design of Deck Sectional Model 6-3
6.3 TEST RIG AND MEASUREMENT SYSTEM 6-6
6.3.1 Installation of Sectional Model and Force Balance 6-6
6.3.2 Force/ Moment Measurement System 6-7
6.4 WIND TUNNEL TESTS 6-10
6.4.1 Wind Tunnel 6-10
6.4.2 Tests Cases 6-11
6.4.3 Data Acquisition and Test Wind Speed 6-13
6.5 CALCULATION OF AERODYNAMIC COEFFICIENTS 6-13
6.6 MEASUREMENT RESULTS 6-15
6.6.1 Effects of Model End Angle Distortion 6-16
6.6.2 Data Interpolation and Fitting 6-17
6.6.3 Main Features of Aerodynamic Coefficients 6-17
6.7 DISCUSSION ON COSINE RULE 6-19
6.8 SUMMARY 6-20

CHAPTER 7 WIND TUNNEL TEST FOR DECK FLUTTER DERIVATIVES UNDER SKEW WINDS 7-1

7.1 INTRODUCTION 7-1
7.2 MODEL DESIGN AND TEST TECHNIQUE 7-2
7.2.1 Prototype Parameters 7-2
7.2.2 Model Design 7-3
7.2.3 Model Installation and Position Adjustment 7-5

7.2.4 Model Parameters 7-7
7.3 WIND TUNNEL TEST 7-9
7.4 MEASUREMENT RESULTS 7-11
7.5 COMPARISON WITH SCANLAN'S SKEW WIND THEORY 7-15
7.6 SUMMARY 7-18

CHAPTER 8 WIND TUNNEL TEST FOR TOWER AERODYNAMIC COEFFICIENTS UNDER YAW WINDS 8-1

8.1 INTRODUCTION 8-1
8.2 DESIGN OF TOWER MODEL 8-2
8.2.1 Tsing Ma bridge tower 8-2
8.2.2 Design of tower model 8-3
8.2.3 Test Cases and Model Installation 8-4
8.3 MEASUREMENT SYSTEM 8-6
8.4 WIND TUNNEL TEST 8-9
8.5 CALCULATION OF AERODYNAMIC COEFFICIENTS 8-11
8.5.1 Drag and Lift Coefficients of Tower Leg 8-11
8.5.2 Coefficients of Drag and Crosswind Force of Tower Transverse Beam 8-13
8.6 MEASUREMENT RESULTS 8-14
8.6.1 Drag and Lift Coefficients of Tower Legs 8-15
8.6.1.1 Drag and Lift Coefficients of Isolated Single Tower Leg 8-15
8.6.1.2 Drag and Lift Coefficients of Windward Tower Leg 8-15
8.6.1.3 Drag and Lift Coefficients of Leeward Tower Leg 8-16
8.6.2 Drag and Lift Coefficients of Upper and Lower Tower Leg Segments 8-18
8.6.2.1 Drag Coefficients of Upper and Lower Tower Leg Segments 8-18
8.6.2.2 Lift Coefficients of Upper and Lower Tower Leg Segments 8-19
8.6.3 Drag and Crosswind force Coefficients of Transverse Beams 8-20
8.7 SUMMARY 8-20

CHAPTER 9 COMPARISON BTWEEN COMPUTED AND MEASURED BUFFETING RESPONSES 9-1

9.1 INTRODUCTION 9-1

9.2 FIELD MEASUREMENT OF TSING MA BRIDGE DURING TYPHOON SAM 9-2
9.2.1 Typhoon Sam 9-2
9.2.2 Wind Characteristics 9-3
9.2.3 Acceleration responses 9-4
9.2.3.1 RMS Responses *9-5*
9.2.3.2 Response spectra *9-9*
9.2.3.3 Modal Damping Ratios *9-13*
9.3 COMPARISON BETWEEN COMPUTED AND MEASURED BUFFETING RESPONSES 9-15
9.3.1 Input Data 9-15
9.3.2 Computed Acceleration Responses and Comparison 9-18
9.3.2.1 Acceleration Responses of Bridge Deck *9-18*
9.3.2.2 Acceleration Responses of Bridge Cables *9-21*
9.4 SUMMARY 9-23

CHAPTER 10 PARAMETRIC STUDIES 10-1

10.1 INTRODUCTION 10-1
10.2 EFFECT OF AERODYNAMIC ADMITTANCE FUNCTION 10-2
10.3 EFFECTS OF WIND YAW ANGLE AND INCLINATION 10-4
10.4 INFLUENCE MECHANISM OF WIND YAW ANGLE AND INCLINATION 10-7
10.5 EFFECTS OF SELF-EXCITED FORCES 10-11
10.6 EFFECTS OF CROSSWIND FORCE, ROLLING AND YAWING MOMENTS 10-12
10.7 SUMMARY 10-13

CHAPTER 11 CONCLUSIONS AND RECOMMENDATIONS 11-1

11.1 CONCLUSIONS 11-1
11.2 RECOMMENDATIONS 11-6

APPENDIX A COMPUTED NATURAL MODES OF TSING MA BRIDGE A-1

APPENDIX B ELEMENTAL AEROELASTIC STIFFNESS AND DAMPING MATRICES B-1

REFERENCES.....**R-1**

NOTATIONS

$\mathbf{0}$ = zero matrix

$\overline{\mathbf{A}}^{b}$ = 6×3 aerodynamic coefficient matrix of buffeting forces per unit length of an element with respect to $\overline{qph}$-system due to fluctuating wind components

$\overline{\mathbf{A}}^{se}$ = 6×3 coefficient matrix of quasi-steady self-excited forces per unit length of an element with respect to $\overline{qph}$-system

$\mathbf{A}_D$ = 6×6 matrix of quasi-steady aerodynamic damping per unit length

$\mathbf{A}_{D,k}$ = 3×3 matrix of aerodynamic damping per unit length of the kth element under skew wind

A_i^* = flutter derivatives for self-excited pitching moment on bridge deck due to deck motion

$\overline{\mathbf{A}}_r^b$ = 6×3 aerodynamic coefficient matrix of buffeting forces per unit length of an element with respect to *qph*-system due to fluctuating wind components

$\mathbf{A}_S$ = 6×6 matrix of quasi-steady aerodynamic stiffness per unit length

$\mathbf{A}_{S,k}$ = 3×3 matrix of aerodynamic stiffness per unit length of the kth element under skew wind

$\mathbf{a}$ = $3m$×1 fluctuating wind component vector of bridge

a = subscript representing turbulence components u,v,w

= one of three parameters determined by curve fitting of the normalized auto spectrum

$\overline{\mathbf{a}}$ = 3×1 fluctuating wind component vector of a segment

$\widehat{\mathbf{a}}$ = Fourier transformation of fluctuating wind vector $\mathbf{a}(t)$

$\mathbf{a}_{p,j}$ = j^{th} harmonic pseudo excitation

$\mathbf{B}$ = Beta function or B function

= 6×6 diagonal matrix of bridge component width

B = bridge component width

B' = width of oblique cross section along mean wind direction

B_m = model width

b = half width of bridge deck

= one of three parameters determined by curve fitting of the normalized auto spectrum

$\mathbf{C}$ = $N \times N$ total damping matrix of bridge

C = Theodorsen's function

$\tilde{\mathbf{C}}$ = $M_\Phi \times M_\Phi$ total generalized damping matrix of bridge

$\overline{\mathbf{C}}$ = aerodynamic coefficient vector at $\overline{\beta}$ and $\overline{\theta}$

$\tilde{\mathbf{C}}$ = aerodynamic coefficient vector at $\tilde{\beta}$ and $\tilde{\theta}$

$\mathbf{C}^e$ = 2×2 effective total damping matrix of 2D sectional model

$\tilde{\mathbf{C}}^e$ = 2×2 normalised effective total damping matrix of 2D sectional model

$\mathbf{C}^s$ = 2×2 structural damping matrix of 2D sectional model

= $N \times N$ structural matrix damping of bridge

$\tilde{\mathbf{C}}^s$ = $M_\Phi \times M_\Phi$ generalized structural damping matrix of bridge

$\mathbf{C}^{se}$ = $N \times N$ aerodynamic damping matrix of bridge

$\tilde{\mathbf{C}}^{se}$ = $M_\Phi \times M_\Phi$ generalized aerodynamic damping matrix of bridge

C_a = auto-covariance function of turbulence component a

$C_{a_1 a_2}$ = cross-covariance function between turbulence components a_1 and a_2

= co-spectrum between turbulence components a_1 at point P_1 and a_2 at point P_2

$C_{a_1 a_2 j}$ = co-spectrum between two different turbulence components a_1 and a_2 at a spatial point P_j

C_{C_q} = aerodynamic coefficient of crosswind force along axis q

$C_{C_{\overline{q}}}$ = aerodynamic coefficient of crosswind force along axis $\overline{q}$

C_D = aerodynamic drag coefficient

C_{D_p} = aerodynamic coefficient of drag along axis p

$C^e_{D_p}$ = effective coefficient of buffeting drag along axis p

$C_{D_{\overline{p}}}$ = aerodynamic coefficient of drag along axis $\overline{p}$

C_{D0} = mean drag coefficient of bridge cable at zero yaw angle

$\mathbf{C}_{e,k}^{se}$ = 12×12 aerodynamic damping matrix of kth element with respect to *XYZ*-system

$\mathbf{C}_{e,k}^{rse}$ = 12×12 aerodynamic damping matrix of kth element with respect to *xyz*-system

$C_{f_r a}$ = coefficient of buffeting force f_r due to the fluctuating wind component a

$\tilde{C}_{ij}^{e}$ = element of matrix $\tilde{\mathbf{C}}^{e}$

C_L = aerodynamic lift coefficient

C_{L_h} = aerodynamic coefficient of lift along axis h

$C_{L_h}^{e}$ = effective coefficients of buffeting lift along axis h

$C_{L_{\bar{h}}}$ = aerodynamic coefficient of lift along axis $\bar{h}$

C_M = aerodynamic pitching moment coefficient

C_{M_α} = aerodynamic coefficient of pitching moment around axis q

$C_{M_\alpha}^{e}$ = effective coefficient of buffeting pitching moment around axis q

$C_{M_{\bar{\alpha}}}$ = aerodynamic coefficient of pitching moment around axis $\bar{q}$

C_{M_ϕ} = aerodynamic coefficient of yawing moment around axis h

$C_{M_{\bar{\phi}}}$ = aerodynamic coefficient of yawing moment around axis $\bar{h}$

C_{M_γ} = aerodynamic coefficient of rolling moment around axis p

$C_{M_{\bar{\gamma}}}$ = aerodynamic coefficient of rolling moment around axis $\bar{p}$

C_q^b = buffeting crosswind force per unit length along axis q

$C_{\bar{q}}$ = aerodynamic crosswind force per unit length along axis $\bar{q}$

$C_{\bar{q}}^{b}$ = buffeting crosswind force per unit length along axis $\bar{q}$

$C_{X_u}^{a}$ = turbulence coherence decay coefficient of component a in X_u direction

$C_{Y_v}^{a}$ = turbulence coherence decay coefficient of component a in Y_v direction

$C_{Z_w}^{a}$ = turbulence coherence decay coefficient of component a in Z_w direction

c_a = normalized auto-covariance function of turbulence component a

$\mathbf{c}_{IR}$ = directional cosine vector of reference vector IR in *XYZ*-system

$\mathbf{c}_{x'}$ = directional cosine vector of axis x' in XYZ-system

$\mathbf{c}_{y'}$ = directional cosine vector of axis y' in XYZ-system

$\mathbf{c}_{z'}$ = directional cosine vector of axis z' in XYZ-system

$\mathbf{D}$ = $M_\Phi \times M_\Phi$ diagonal matrix of $\mathbf{L}^*\mathbf{D}\mathbf{L}^T$ decomposition of generalized buffeting force spectral matrix

D = height of bridge component

D_p^b = buffeting drag per unit length along axis p

D_p^{se} = self-excited drag per unit length along axis p

$D_{\bar{p}}$ = aerodynamic drag along axis $\bar{p}$

$D_{\bar{p}}^b$ = buffeting drag per unit length along axis $\bar{p}$

$D_{p'}^{se}$ = self-excited drag along axis p'

D_r = r^{th} non-zero diagonal element of matrix $\mathbf{D}$

D_{se} = self-excited drag per unit length

$\mathbf{d}$ = $3m \times 3m$ real diagonal matrix of $\mathbf{l}^*\mathbf{d}\mathbf{l}^T$ decomposition of wind turbulence spectral matrix

d_j = j^{th} non-zero diagonal element of matrix $\mathbf{d}(\omega)$

e_m = a half of the distance between two suspending springs onto a same support arm

$\mathbf{e}_h$ = error vector of vertical response of 2D sectional model

e_x = coordinate of the qph-system origin along axis $\bar{x}$

e_y = coordinate of the qph-system origin along axis $\bar{y}$

e_z = coordinate of the qph-system origin along axis $\bar{z}$

$\mathbf{e}_\alpha$ = error vector of torsional response of 2D sectional model

F = real part of Theodorsen's function

$\mathbf{F}^b$ = N-dimensional vector of buffeting forces in XYZ-system

$\widehat{\mathbf{F}}^b$ = Fourier transformation of buffeting force vector $\mathbf{F}^b(t)$

$\widetilde{\mathbf{F}}^b$ = M_Φ-dimensional vector of generalized buffeting forces

$\mathbf{F}^{se}$ = N-dimensional vector of aeroelastic forces in XYZ-system.

$\mathbf{F}_{e,k}^{b}$ = 12-dimensional vector of nodal buffeting forces of kth element in *XYZ*-system

$\mathbf{F}_{e,k}^{se}$ = 12-dimensional vector of nodal aeroelastic forces of kth element in *XYZ*-system

$\mathbf{F}_{se}$ = aeroelastic force vector of 2D sectional model

$F_{\bar{x}}$ = measured balance force along axis $\bar{x}$

$F_{\bar{y}}$ = measured balance force balance along axis $\bar{y}$

$F_{\bar{z}}$ = measured balance force along axis $\bar{z}$

f = frequency of structural vibration in Hz

$\hat{f}$ = decay exponent of root-coherence function

$\tilde{\mathbf{f}}^{ad}$ = vector of total wind forces per unit length in $\tilde{q}\tilde{p}\tilde{h}$ -system

$\mathbf{f}^{b}$ = vector of buffeting forces per unit length in *xyz*-system

$\bar{\mathbf{f}}^{b}$ = vector of buffeting forces per unit length in $\bar{q}\bar{p}\bar{h}$ -system

$\bar{\mathbf{f}}^{se}$ = vector of quasi-steady self-excited forces per unit length in $\bar{q}\bar{p}\bar{h}$ -system

$\hat{f}_{a_1a_2}$ = exponent of root coherence function between two different turbulent components a_1 at point P_1 and a_2 at point P_2

$\hat{f}_{aa}$ = exponent of root coherence function between turbulent components a at points P_1 and P_2

f_c = Coriolis parameter

$\mathbf{f}_{e,k}^{b}$ = 12-dimensional nodal buffeting force vector of kth element in *xyz*-system

$\mathbf{f}_{e,k}^{se}$ = 12-dimensional nodal aeroelastic force vector of kth element in *xyz*-system

f_m = reduced frequency of wind turbulence at a normalized spectral peak

f_{m1} = vertical-dominant natural frequency of 2D sectional model under wind

f_{m2} = torsional-dominant natural frequency of 2D sectional model under wind

$\mathbf{f}_r^{b}$ = 6-dimensional buffeting force vector per unit length in *qph*-system

$\mathbf{f}_r^{se}$ = 6-dimensional vector of quasi-steady self-excited forces per unit length in *qph*-system

$\mathbf{f}_{r,k}^{se}$ = 3-dimensional self-excited force vector per unit length of kth element in *qph*-system

f_s = sampling frequency

= lower limit of inertial subrange of wind turbulence

f_t = natural frequency of deck torsional vibration

f_{tm} = torsional vibration natural frequency of 2D deck model in still air

f_v = natural frequency of deck vertical bending vibration

f_{vm} = vertical vibration natural frequency of 2D deck model in still air

f_z = reduced frequency of wind turbulence

G = imaginary part of Theodorsen's function

H = height of bridge component

$\overline{H}$ = mean height of the buildings

$\tilde{\mathbf{H}}$ = $M_\Phi \times M_\Phi$ matrix of generalized frequency response function of the bridge

H_i^* = flutter derivative for deck self-excited lift

H_r = r^{th} modal frequency response function of bridge

$\mathbf{h}$ = recorded vertical response sample of 2D sectional model

h_n = n^{th} datum in recorded vertical response sample $\mathbf{h}$

$\hat{h}_n$ = an estimate of h_n

$\mathbf{I}$ = identity matrix

I = left node of an element

$\mathbf{I}_6$ = 6×6 identity matrix

I_a = turbulence intensity of component a

I_m = mass moment of inertia per unit length

I_m^e = effective deck mass moment of inertia per unit length

I_{mm} = mass moment of inertia per unit length of 2D deck

J = unifying error function defined in ULS method

= right node of an element

J_i = second kind Bessel function of order i.

$\mathbf{K}$ = $N \times N$ total stiffness matrix of bridge

K = reduced frequency

$\tilde{\mathbf{K}}$ = $M_\Phi \times M_\Phi$ matrix of total generalized stiffness of bridge

K' = reduced frequency associated with oblique cross section

$\mathbf{K}^e$ = 2×2 effective stiffness matrix of 2D sectional model

$\tilde{\mathbf{K}}^e$ = 2×2 generalized effective stiffness of 2D sectional model

$\mathbf{K}^s$ = 2×2 structural stiffness matrix of 2D sectional model

= $N \times N$ structural stiffness matrix of bridge

$\mathbf{K}^{se}$ = $N \times N$ aerodynamic stiffness matrix of bridge

$\tilde{\mathbf{K}}^s$ = $M_\Phi \times M_\Phi$ generalized structural stiffness matrix of bridge

$\tilde{\mathbf{K}}^{se}$ = $M_\Phi \times M_\Phi$ generalized aerodynamic stiffness matrix of bridge

$\mathbf{K}^{se}_{e,k}$ = 12×12 aerodynamic stiffness matrix of kth element in *XYZ*-system

$\mathbf{K}^{rse}_{e,k}$ = 12×12 aerodynamic stiffness matrix of kth element in *xyz*-system

K_i = modified second kind Bessel function of order i

$\tilde{K}^e_{ij}$ = elements of matrix $\tilde{\mathbf{K}}^e$

K_{tm} = torsional stiffness of deck model

K_{vm} = vertical stiffness of deck model

k = reduced frequency with respect to half width

= 0.4, von Karman's constant

$\mathbf{L}$ = $M_\Phi \times M_\Phi$ lower triangular matrix of $\mathbf{L}^*\mathbf{D}\mathbf{L}^T$ decomposition of generalized buffeting force spectral matrix

L = Monin-Obukhov length

L^r_a = integral scale of turbulence component a in direction r

L_b = buffeting lift per unit length

L_d = total length of bridge deck

L^b_h = buffeting lift per unit length along axis h

L^{se}_h = aeroelastic lift per unit length along axis h

$L_{\bar{h}}$ = aerodynamic lift per unit length along axis $\bar{h}$

$L^b_{\bar{h}}$ = buffeting lift per unit length along axis $\bar{h}$

$L^{se}_{h'}$ = self-excited lift per unit length along axis h'

$L_{i,k}$ = length of ith segment of kth element

L_{IR} = length of reference vector $\boldsymbol{IR}$

L_k = length of kth element

L_m = measured segment length of section model

$\mathbf{L}_r$ = r^{th} column of lower triangular complex matrix $\mathbf{L}$

$\mathbf{l}$ = $3m \times 3m$ lower triangular complex matrix of $\mathbf{l}^*\mathbf{d}\mathbf{l}^T$ decomposition of wind turbulence spectral matrix

$\mathbf{l}_j$ = j^{th} column of lower triangular complex matrix $\mathbf{l}$

$\mathbf{M}$ = $N \times N$ bridge mass matrix

M = number of elements of bridge FE model

= the number of discrete datum in a sample

$\tilde{\mathbf{M}}$ = $M_\Phi \times M_\Phi$ generalized mass matrix

$\mathbf{M}^s$ = 2×2 structural mass matrix of 2D sectional model

= $N \times N$ structural mass matrix of bridge

M_b = buffeting pitching moment per unit length

M_P = a sufficiently large positive number for calculating priority numbers of elements

M_p = rank of generalized buffeting force spectral matrix

= number of generalized pseudo harmonic excitations

$\tilde{M}_t$ = generalized mass moment of inertia of first symmetric torsional mode

$\tilde{M}_v$ = generalized mass of first symmetric vertical bending mode

$M_{\bar{x}}$ = measured balance moment around axis $\bar{x}$

$M_{\bar{y}}$ = measured balance moment around axis $\bar{y}$

$M_{\bar{z}}$ = measured balance moment around axis $\bar{z}$

M_α^b = buffeting pitching moment per unit length around axis q

M_α^{se} = self-excited pitching moment per unit length around axis q

$M_{\bar{\alpha}}$ = aerodynamic pitching moment per unit length around axis $\bar{q}$

$M_{\bar{\alpha}}^b$ = buffeting pitching moment per unit length around axis $\bar{q}$

$M_{\alpha'}^{se}$ = self-excited pitching moment per unit length around axis q'

M_Φ = number of modes used in buffeting analysis

M_ϕ^b = buffeting yawing moment per unit length around axis h

$M_{\bar{\phi}}$ = aerodynamic yawing moment per unit length around the axis $\bar{h}$

$M_{\bar{\phi}}^b$ = buffeting yawing moment per unit length around axis $\bar{h}$

M_γ^b = buffeting rolling moment per unit length around axis p

$M_{\bar{\gamma}}$ = aerodynamic rolling moment per unit length around the axis $\bar{p}$

$M_{\bar{\gamma}}^b$ = buffeting rolling moment per unit length around axis $\bar{p}$

m = mass per unit length

= one of three parameters determined by curve fitting of the normalized auto spectrum

= total number of segments in bridge FE model

m^e = effective mass of bridge deck per unit length

m_m = mass per unit length of 2D deck model

m_p = rank of wind turbulence spectral matrix

= number of pseudo harmonic excitations

N = total number of nodes in bridge FE model

= length of the response sample

N_i = elements of matrix $\mathbf{N}_{se,k}$

$\tilde{\mathbf{N}}_{i,k}$ = 6×12 transformation matrix used to constitute $\mathbf{Q}_{i,k}^b$ from $\overline{\mathbf{A}}_{i,k}^b$

$\tilde{N}_{j,i,k}$ = elements of the transformation matrix $\tilde{\mathbf{N}}_{i,k}$

$N_{j,k}$ = elements of displacement interpolation matrix $\mathbf{N}_{\delta,k}(\xi)$

N_s = primary frequency of vortex shedding transversely to mean wind direction

$\mathbf{N}_{se,k}$ = 3×12 displacement interpolation matrix of the kth element in xyz-system

$\overline{\mathbf{N}}_{se,k}$ = 3×12 displacement interpolation matrix $\boldsymbol{\delta}_{Lr,k}$ from $\boldsymbol{\delta}_{e,k}$ of kth element

$\mathbf{N}_{\delta,k}$ = 6×12 displacement interpolation matrix of kth element in xyz-system

n = frequency of turbulence in Hz

n_k = total number of segments of kth element

n_x = modified turbulence frequency with integral scale effect; in Hz

n_{xa} = modified turbulence frequency with turbulence scale effect; in Hz

$\mathbf{P}^b$ = $6N\times3m$ nodal buffeting force coefficient matrix of bridge

P_i^* = flutter derivatives for self-excited drag on bridge deck

$\mathbf{P}_{i,k}^b$ = 12×3 nodal buffeting force coefficient matrix of kth element in *XYZ*-system due to wind turbulence on the ith segment

$p_{i,k}$ = priority number of ith segment of kth element for topography optimization of wind turbulence spectral matrix

$Q_{a_1a_2}$ = quadrature spectrum between turbulence components a_1 at point P_1 and a_2 at point P_2

$Q_{a_1a_2j}$ = quadrature spectrum between two different turbulence components a_1 and a_2 at a spatial point P_j

$\mathbf{Q}_{i,k}^b$ = 12×3 nodal buffeting force coefficient matrix of kth element in *xyz*-system due to wind turbulence on i^{th} segment

$q'p'h'$ = a coordinate system used in Scanlan's skew wind theory; attained by rotating the local reference *qph*-system around the axis *h* with an angle of $\overline{\beta}$

qph = local reference coordinate system of an element

$\overline{qph}$ = local mean wind coordinate system of an element

$\widetilde{qph}$ = local instantaneous wind coordinate system of an element

R = reference node of an element

$R_{a_1a_2}$ = root-coherence function between the two turbulence components a_1 at point P_1 and a_2 at P_2

R_{D_p} = ratio between measured and estimated drag coefficients at $\overline{\beta}$ and $\overline{\theta}$

Re = Reynolds number

$\mathbf{R}_j$ = j^{th} pseudo response vector of bridge caused by the jth pseudo excitation; $j=1,\cdots,m_p$

R_{L_h} = ratio between measured and estimated lift coefficients at $\overline{\beta}$ and $\overline{\theta}$

R_{M_a} = ratio between measured and estimated pitching moment coefficients at $\overline{\beta}$ and $\overline{\theta}$

r^e = effective radius of deck gyration

S_a = auto-spectrum of wind turbulence component a

$\mathbf{S}_{aa}$ = wind turbulence spectral matrix

$S_{a_1 a_2}$ = cross spectrum between the turbulent component a_1 at point P_1 and the turbulent component a_2 at point P_2 and ; $a_1 = u, v, w$; $a_2 = u, v, w$

$S_{a_1 a_2 j}$ = cross spectrum between two different turbulence components a_1 and a_2 at a spatial point P_j

S_{aj} = auto spectrum of turbulent component a at point P_j

$S_{a_{i,k} a_{j,l}}$ = auto/cross spectrum between two fluctuating wind components $a_{i,k}$ at i^{th} segment center of kth element and $a_{j,l}$ at j^{th} segment center of lth element

$\mathbf{S}_{\tilde{a}_{i,k}\tilde{a}_{j,l}}$ = 3×3 matrix of auto/cross spectra between two of the six fluctuating wind components at i^{th} segment center of kth element and at j^{th} segment center of lth element

$\mathbf{S}_{aa,j}$ = j^{th} sub-spectral matrix corresponding to the jth pseudo excitation

$\mathbf{S}_b$ = calibration matrix of balance

$\mathbf{S}_{FF}^b$ = spectral matrix of nodal buffeting force $\mathbf{F}^b(t)$

$\mathbf{S}_{\tilde{F}\tilde{F}}^b$ = $M_\Phi \times M_\Phi$ spectral matrix of generalized buffeting force $\tilde{\mathbf{F}}^b(t)$

S_t = Strouhal number

$\mathbf{S}_{\Delta_i}$ = auto-spectral vector of displacement responses at i^{th} node

$\mathbf{S}_{\dot{\Delta}_i}$ = auto-spectral vector of velocity responses at i^{th} node

$\mathbf{S}_{\ddot{\Delta}_i}$ = auto-spectral vector of acceleration responses at i^{th} node

$\mathbf{S}_{\Delta\Delta}$ = N×N response spectral matrix of bridge nodal displacements

$\mathbf{S}_{\dot{\Delta}\dot{\Delta}}$ = N×N response spectral matrix of bridge nodal velocities

$\mathbf{S}_{\ddot{\Delta}\ddot{\Delta}}$ = N×N response spectral matrix of bridge nodal accelerations

$\mathbf{S}_{\eta\eta}$ = $M_\Phi \times M_\Phi$ response spectral matrix of generalized displacements

$s_1 \sim s_6$ = coefficients used to constitute the transformation matrices the and coefficient matrix of buffeting forces $\overline{\mathbf{A}}^b$;

T = time length of recorded sample

T_a^x = time scales of turbulence component a

$\mathbf{T}_{GsGw}$ = 3×3 transformation matrix from $X_uY_vZ_w$-system to XYZ-system

$\mathbf{T}_{GsLr}$ = 3×3 transformation matrix from qph-system to XYZ-system

$\mathbf{T}_{GsLs}$ = 3×3 transformation matrix from xyz-system to XYZ–system

$\overline{\mathbf{T}}_{GsLs,k}$ = 12×12 transformation matrix of kth element from xyz-system to XYZ-system

$\mathbf{T}_{GsLs'}$ = 3×3 transformation matrix from $x'y'z'$-system to XYZ–system

$\mathbf{T}_{GwGs}$ = 3×3 transformation matrix from XYZ-system to $X_uY_vZ_w$–system

$\mathbf{T}_{GwLr}$ = 3×3 transformation matrix from qph-system to $X_uY_vZ_w$-system

$\mathbf{T}_k$ = $6N$×12 transformation matrix for assembling nodal buffeting force vector

$\mathbf{T}_{LrGw}$ = 3×3 transformation matrix from $X_uY_vZ_w$-system to qph-system

$\mathbf{T}_{LrLs}$ = 3×3 transformation matrix from the xyz-system to the qph-system

$\mathbf{T}_{Lr\bar{L}\bar{w}}$ = 3×3 transformation matrix from $\bar{q}\bar{p}\bar{h}$ -system to qph –system

$\overline{\mathbf{T}}_{Lr\bar{L}\bar{w}}$ = 6×6 transformation matrix from $\bar{q}\bar{p}\bar{h}$ -system to qph-system

$\mathbf{T}_{Lr\tilde{L}\tilde{w}}$ = 3×3 transformation matrix from $\tilde{q}\tilde{p}\tilde{h}$ -system to qph –system

$\overline{\mathbf{T}}_{Lr\tilde{L}\tilde{w}}$ = 6×6 transformation matrix from $\tilde{q}\tilde{p}\tilde{h}$ -system to qph-system

$\mathbf{T}_{LsGs}$ = 3×3 transformation matrix from XYZ-system to xyz–system

$\mathbf{T}_{Ls'Gs}$ = 3×3 transformation matrix from XYZ-system to $x'y'z'$–system

$\mathbf{T}_{LsLr}$ = 3×3 transformation matrix from the qph-system to the xyz-system

$\overline{\mathbf{T}}_{LsLr}$ = 6×6 transformation matrix from qph-system to xyz-system

$\mathbf{T}_{LsLs'}$ = 3×3 transformation matrix from $x'y'z'$-system to xyz–system

$\mathbf{T}_{Ls'Ls}$ = 3×3 transformation matrix from xyz-system to $x'y'z'$–system

$\mathbf{T}_{L\bar{w}Bl}$ = 6×6 transformation matrix from $\overline{xyz}$ -system to $\bar{q}\bar{p}\bar{h}$ -system

$\mathbf{T}^0_{L\bar{w}Bl}$ = 3×3 transformation matrix from $\overline{xyz}$ -system to $\bar{q}\bar{p}\bar{h}$ -system

$\mathbf{T}_{L\bar{w}Lr}$ = 3×3 transformation matrix from qph-system to $\bar{q}\bar{p}\bar{h}$ -system

$\overline{\mathbf{T}}_{L\bar{w}Lr}$ = 6×6 transformation matrix from qph-system to $\bar{q}\bar{p}\bar{h}$ -system

$\mathbf{T}_{L\tilde{w}Lr}$ = 3×3 transformation matrix from qph -system to $\tilde{q}\tilde{p}\tilde{h}$ –system

$\overline{\mathbf{T}}_{L\tilde{w}Lr}$ = 6×6 transformation matrix from qph-system to $\tilde{q}\tilde{p}\tilde{h}$ -system

$\overline{\mathbf{T}}_{L\tilde{w}L\tilde{w}}$ = 6×6 transformation matrix from $\tilde{q}\tilde{p}\tilde{h}$ -system to $\overline{qph}$ –system

$\mathbf{T}_v$ = 3×3 matrix for constituting $\overline{\mathbf{T}}_{L\tilde{w}L\tilde{w}}$

$\overline{\mathbf{T}}_v$ = 6×6 matrix for constituting $\overline{\mathbf{T}}_{L\tilde{w}L\tilde{w}}$

$\mathbf{T}_w$ = 3×3 matrix used to constitute $\overline{\mathbf{T}}_{L\tilde{w}L\tilde{w}}$

$\overline{\mathbf{T}}_w$ = 6×6 matrix used to constitute $\overline{\mathbf{T}}_{L\tilde{w}L\tilde{w}}$

t = time

t_{ij} = element at i^{th} raw and j^{th} column of matrix $\mathbf{T}_{LrGw}$

U = total wind speed

$\overline{U}$ = mean wind speed

U_E = eastward component of instantaneous wind speed

$\overline{U}_E$ = mean value of $U_E(t)$

$\mathbf{U}_{Gw}$ = mean wind vector in $X_uY_vZ_w$-system

U_{geo} = geostrophic wind speed

U_{gra} = gradient wind speed

U_H = horizontal component of instantaneous wind speed

$\overline{U}_h$ = mean wind speed component along axis h

U_{hr} = real part of vertical component of rth mode shape of 2D sectional model under wind

$\mathbf{U}_{Lr}$ = mean wind vector in qph –system

$\overline{U}_m$ = test mean wind speed in wind tunnel

$\overline{U}_{P_j}$ = mean wind speed at point P_j

$\overline{U}_p$ = mean wind speed component along axis p

$\overline{U}_q$ = mean wind speed component along axis q

$\overline{U}_{qp}$ = mean wind speed component in the qp-plane

$\overline{U}_r$ = reference mean wind speed at the reference height

U_S = southward component of instantaneous wind speed

$\overline{U}_S$ = mean value of U_S

U_U = upward component of instantaneous wind speed

$\overline{U_U}$ = mean value of U_U

U_{vs} = critical wind speed of vortex-induced resonance

$\overline{U_{\bar{z}}}$ = average value of mean wind speeds at heights of z_1 and z_2

$U_{\alpha r}$ = real part of torsional component of rth mode shape of 2D sectional model under wind

$\overline{U_\delta}$ = mean wind speed at the gradient height

U/fB = reduced wind speed

u = fluctuating wind speed along mean wind

$\tilde{u}$ = equivalent alongwind fluctuating wind speeding due to structural motion

u_S = fluctuating wind speed along axis X_S

u_E = fluctuating wind speed along axis Y_E

u_U = fluctuating wind speed along axis Z_U

u_* = friction velocity or shear velocity

V = instantaneous wind speed

V_b = voltage applied onto the electric balance bridge; in V

$\mathbf{V}_{Gw}$ = instantaneous wind vector in $X_u Y_v Z_w$-system

V_h = instantaneous wind speed component along axis q

V_{hr} = imaginary part of vertical component of rth mode shape of 2D sectional model under wind

$\mathbf{V}_{Lr}$ = instantaneous wind vector in qph -system

V_p = instantaneous wind speed component along axis q

V_q = instantaneous wind speed components along axis q

V_{qp} = instantaneous wind speed component in the qp-plane

$V_{\alpha r}$ = imaginary part of torsional component of rth mode shape of 2D sectional model under wind

v = lateral fluctuating wind speed in horizontal direction

$\tilde{v}$ = equivalent lateral fluctuating wind speed due to structural motion

w = upward fluctuating wind speed

$\tilde{w}$ = equivalent upward wind fluctuating wind speed due to structural motion

X_S = southward horizontal axis of reference wind co-ordinate $X_S Y_E Z_U$ -system

X_u = alongwind axis of $X_u Y_v Z_w$-system

$X_u Y_v Z_w$ = global wind coordinate system

XYZ = global structural coordinate system

$X_{ui,k}$ = coordinate of the ith segment center of kth element along axis X_u

$Y_{vi,k}$ = coordinate of the ith segment center of kth element along axis Y_v

$Z_{wi,k}$ = coordinate of the ith segment center of kth element along axis Z_w

X_{uj} = coordinate of point P_j along axis X_u

Y_{vj} = coordinate of point P_j along axis Y_v

X_{uj} = coordinate of point P_j along axis Z_w

$x_{i,k}$ = longitudinal coordinate of the right end of ith segment in xyz-system of kth element

xyz = local structural coordinate system of an element considering initial torsional angle of α_0

$x'y'z'$ = local structural coordinate system of an element

$\overline{xyz}$ = balance coordinate system

Y_E = eastward horizontal axis of reference wind co-ordinate $X_S Y_E Z_U$ -system

Y_i = second kind Bessel function of order i.

Y_v = horizontal axis of $X_u Y_v Z_w$-system along the positive direction of turbulence component v

Z_w = upward axis of $X_u Y_v Z_w$-system along the positive direction of turbulence component w

z = height of a spatial point concerned

z_0 = roughness length

z_d = zero plane displacement of mean wind profile

z_r = reference height

Z_U = upward vertical axis of reference wind co-ordinate $X_S Y_E Z_U$ –system

z_δ = gradient height of boundary layer

α = torsional response sample of 2D sectional model

α = angle around axis q

= exponent of mean wind power law

$\bar{\alpha}$ = angle around axis $\bar{q}$

$\tilde{\alpha}$ = angle around axis $\tilde{q}$

α_0 = initial torsional angle of element due to static wind load

α_n = n^{th} datum in torsional response sample

$\hat{\alpha}_n$ = an estimate of α_n

α_u = directional angle between positive directions of $u(t)$ and axis X_S

= directional angle between mean wind $\bar{U}$ and axis X_S

α_v = directional angle between positive directions of $v(t)$ and axis X_S

α_w = directional angle between positive directions of $w(t)$ and axis X_S

β = yaw angle of wind;

$\bar{\beta}$ = local yaw angle of mean wind relative to an element

$\tilde{\beta}$ = local yaw angle of instantaneous wind relative to an element

β_0 = global yaw angle of mean wind relative to bridge

β_a = turbulence ratio of component a

β_H = azimuth angle of $U_H(t)$; zero for winds from the due north and 90° for winds from the due east

β_m = model end angle of sectional model for the measurement of deck aerodynamic admittance

β_T = rotation angle of turning table in clockwise direction in tower model test

β_u = directional angle between positive directions of $u(t)$ and axis Y_E

β_v = directional angle between positive directions of $v(t)$ and axis Y_E

β_w = directional angle between positive directions of $w(t)$ and axis Y_E

χ = aerodynamic admittance function

$|\chi|^2$ = module of aerodynamic admittance function

χ_r = real part of aerodynamic admittance function

χ_i = imaginary part of aerodynamic admittance function

$\chi_{f_b a}$ = aerodynamic admittance function between the buffeting force f_b and turbulence component a

$\chi_{\tilde{f}a}$ = aerodynamic admittance functions between the buffeting force $\tilde{f}$ and turbulence component a of skew wind

Δ = N-dimensional vector of bridge nodal displacements in XYZ-system

$\Delta_{e,k}$ = nodal displacement response vector of kth element in XYZ-system

Δ_i = displacement response vector of ith node

$\Delta_{p,j}$ = j^{th} pseudo displacement response vector

Δt = time interval of the sampling

$\Delta\beta$ = increment of local wind yaw due to fluctuating wind speed

$\Delta\tilde{\beta}$ = additional increment of local wind yaw due to structural motion

$\Delta\theta$ = increment of local wind inclination due to fluctuating wind speed

$\Delta\tilde{\theta}$ = additional increment of local wind inclination due to structural motion

$\boldsymbol{\delta}$ = vector of dynamic displacement

$\boldsymbol{\delta}_{e,k}$ = 12-dimensional vector of nodal displacement responses of kth element in xyz-system

$\bar{\boldsymbol{\delta}}_{e,k}$ = virtual nodal displacements of kth element with respect to xyz-system

δ_h = dynamic translational displacement at a position within an element along axis h

$\delta_{h'}$ = dynamic translational displacement at a position within an element along axis h'

$\boldsymbol{\delta}_{Lr,k}$ = dynamic displacement vector at a position within k^{th} element with respect to qph-system

$\bar{\boldsymbol{\delta}}_{Lr,k}$ = virtual displacements at a position within k^{th} element with respect to qph-system

$\boldsymbol{\delta}_{Ls,k}$ = dynamic displacement vector at a position within k^{th} element with respect to xyz-system

δ_p = dynamic translational displacement at a position within an element along axis p

$\delta_{p'}$ = dynamic translational displacement at a position within an element along axis p'

δ_r = real part (damping) of rth eigenvalue λ_r of 2D sectional model

$\delta_r^{(0)}$ = real part (damping) of rth initial eigenvalue $\lambda_r^{(0)}$ of 2D sectional model

$\dot{\delta}_{X_w}$ = structural velocity along axis X_w

$\dot{\delta}_{Y_w}$ = structural velocity along axis Y_w

$\dot{\delta}_{Z_w}$ = structural velocity along axis Z_w

δ_y = dynamic translational displacement at a position within an element along axis y

δ_z = dynamic translational displacement at a position within an element along axis z

δ_α = dynamic angular displacement at a position within an element around axis q

$\delta_{\alpha'}$ = dynamic angular displacement at a position within an element around axis q'

$\delta_{\bar{\alpha}}$ = dynamic angular displacement at a position within an element around axis $\bar{q}$

δ_ϕ = dynamic angular displacement at a position within an element around axis h

$\boldsymbol{\varepsilon}$ = error vector

ε = ratio of torsional eigen frequency to vertical bending eigen frequency of bridge

ε_m = ratio of torsional eigen frequency to vertical eigen frequency of 2D deck model

$\boldsymbol{\Phi}$ = instrumental variable constituted from sampled response data in ITD method

= $N \times M_\Phi$ mode shape matrix of bridge

$\overline{\boldsymbol{\Phi}}$ = instrumental variable constituted from response data simulated using the identified system parameters in MITD method

$\hat{\boldsymbol{\Phi}}$ = instrumental variable constituted from sampled response data in ITD method

$\Phi_{a_1 a_2}$ = phase function between two turbulence components a_1 at point P_1 and a_2 at point P_2

ϕ = latitude of the location concerned

= angle around the axis h

$\bar{\phi}$ = angle around axis $\bar{h}$

$\tilde{\phi}$ = angle coordinate around axis $\tilde{h}$

ϕ_ε = dimensionless dissipation rate for turbulent energy

Γ = Gamma function

γ = angle around the axis p

$\bar{\gamma}$ = angle coordinate around the axis $\bar{p}$

$\tilde{\gamma}$ = angle coordinate around the axis $\tilde{p}$

γ_u = directional angle between positive directions of $u(t)$ and axis Z_U

γ_v = directional angle between positive directions of $v(t)$ and axis Z_U

γ_w = directional angle between positive directions of $w(t)$ and axis Z_U

η = dynamic response state vector of 2D sectional model

= M_Φ -dimensional vector of generalized displacement coordinates

$\eta_{p,j}$ = j^{th} harmonic generalized pseudo displacement response vector

φ_{aa} = phase spectra between the turbulent components of a at points P_1 and P_2

$\varphi_{a_1a_2}$ = phase spectra between the different turbulent component a_1 at point P_1 and a_2 at point P_2

φ_r = r^{th} complex mode shape vector of 2D sectional model

= r^{th} mode shape vector of bridge

φ_t = torsional mode shape component of bridge deck in selected torsional mode

φ_v = vertical bending mode shape component of bridge deck in selected vertical mode

Λ = diagonal matrix of eigenvalues

λ = complex eigenvalue

= wavelengths of turbulence

= decay exponent of an exponential function determined by normalized auto-covariance fitting

λ_f = frequency scale of model

λ_L = length scale of model

$\lambda_r^{(0)}$ = r^{th} initial complex eigenvalue in ULS method obtained with MITD method

λ_r = r^{th} complex eigenvalue of 2D sectional model

λ_V = velocity scale of model

μ_{vu} = ratio of turbulence spectrum of component v to that of component u

μ_{wu} = ratio of turbulence spectrum of component w to that of component u

$\bar{\theta}$ = local inclination of mean wind relative to an element

$\tilde{\theta}$ = local inclination of instantaneous wind relative to an element

θ_0 = global inclination of mean wind relative to bridge

θ_m = rotational angle of 2D dynamic deck model around its longitudinal axis

θ_X = angle around the axis X

θ_x = angle around the axis x

$\theta_{x'}$ = angle around the axis x

θ_Y = angle around the axis Y

θ_y = angle around the axis y

$\theta_{y'}$ = angle around the axis y

θ_Z = angle around the axis Z

θ_z = angle around the axis z

$\theta_{z'}$ = angle around the axis z

ρ = air density (1.225kg/m^3)

σ_a = standard deviation of fluctuating wind speed component a

$\sigma_{a_1a_2}$ = co-variance between two turbulence components a_1 at point P_1 and a_2 at P_2

$\boldsymbol{\sigma}_{\Delta_i}$ = RMS displacement response vector of ith node

$\boldsymbol{\sigma}_{\dot{\Delta}_i}$ = RMS velocity response vector of ith node

$\boldsymbol{\sigma}_{\ddot{\Delta}_i}$ = RMS acceleration response vector of ith node

τ = time delay

= stress

τ_0 = surface shear stress of wind flow near the ground

τ_H = horizontal turbulent shear stress

τ_R = Reynolds stress

Ω = 72.92×10^{-6} rad/s, angular velocity of the Earth

ω = circular frequency of structural vibration or wind turbulence

ω_h = circular frequency of vertical vibration (along axis h)

ω_r = imaginary part (circular frequency) of rth eigenvalue λ_r of 2D dynamic sectional model

= circular eigen frequency of rth natural mode of bridge vibration in static air

$\omega_r^{(0)}$ = imaginary part (damping) of $\lambda_r^{(0)}$

ω_α = circular frequency of torsional vibration (around axis q)

ξ = reduced coordinate

= damping ratio

$\xi_{i,k}$ = longitudinal reduced coordinate of the right end of ith segment in xyz-system of kth element

ξ_h = modal damping ratio of vertical vibration (along axis h)

ξ_{tm} = damping ratio of torsional vibration of 2D dynamic deck model in still air

ξ_{vm} = damping ratio of vertical vibration of 2D dynamic deck model in still air

ξ_α = modal damping of vertical vibration (around axis q)

Ψ = complex eigenvector of 2D sectional model state equation

ζ_r = damping ratio of rth mode of bridge vibration in static air

$()'$ = $d()/d\theta$; first order derivative with respect to wind inclination

$()'^{\theta}$ = $\partial()/\partial\theta$; first order partial derivative with respect to wind inclination

$()'^{\beta}$ = $\partial()/\partial\beta$; first order partial derivative with respect to wind yaw angle

$\dot{()}$ = first order derivative with respect to time

= velocity of motion

$\ddot{()}$ = second order derivative with respect to time

= acceleration of motion

LIST OF FIGURES

Figure 2-1 Aeroelastic self-excited forces on 2D motion section 2-64

Figure 2-2 Typical Curves of Normalized Auto-covariance of Wind Turbulence Measured at Mid-maispan of Tsing Ma Bridge deck during Typhoon Victor 2-64

Figure 3-1 Elevation of Tsing Ma Bridge 3-33

Figure 3-2 Locations of Anemometers and Accelerometers 3-33

Figure 3-3 Positions of Sensors on Cross Section of Bridge Deck 3-34

Figure 3-4 Local Topography of Tsing Ma Bridge 3-34

Figure 3-5 Track of Typhoon Victor 3-35

Figure 3-6 Definition of Positive Directions of Mean Wind and Fluctuating Wind 3-35

Figure 3-7 Variations of Azimuth of 10min Mean Wind 3-36

Figure 3-8 Variations of Inclination of 10min Mean Wind 3-36

Figure 3-9 Variations of 10min Mean Wind Speed 3-37

Figure 3-10 Typical Time Histories of Fluctuating Wind Components 3-38

Figure 3-11 Variations of Friction Velocity 3-38

Figure 3-12 Variations of Standard Deviations of Wind Fluctuations 3-39

Figure 3-13 Variations of Turbulence Intensities 3-40

Figure 3-14 Variations of Turbulence Intensities with Wind Speed 3-41

Figure 3-15 Variations of Integral Scales of Turbulence 3-42

Figure 3-16 Normalized Auto Spectra of Wind Turbulence at Mid-mainspan .. 3-43

Figure 3-17 Normalized Co-spectra of Wind Turbulence at Mid-mainspan 3-44

Figure 3-18 Normalized Quadrature Spectra of Wind Turbulence at Mid-mainspan 3-45

Figure 3-19 Time Histories of Lateral, Vertical and Torsional Accelerations of Deck at ATTJD (cm/s^2) 3-46

Figure 3-20 Time Histories of Lateral, Vertical and Torsional Accelerations of Cables at ABTLC (cm/s^2) 3-46

Figure 3-21 Standard Deviations of Acceleration at ATTJD vs. Time (10-minute Duration) 3-47

Figure 3-22 Standard Deviations of Acceleration at ABTLC vs. Time (10-minute Duration) 3-47
Figure 3-23 Standard Deviations of Acceleration at ATTJD vs. Mean Wind Speed (10-minute Duration) 3-48
Figure 3-24 Standard Deviations of Acceleration at ABTLC vs. Mean Wind Speed (10-minute Duration) 3-48
Figure 3-25 Spectra of Acceleration Responses of Bridge Deck at ATTID (21:00 to 22:00) 3-49

Figure 4-1 Global Structural and Wind Coordinate Systems 4-45
Figure 4-2 Local Structural Coordinate Systems 4-45
Figure 4-3 Local Reference Coordinate System 4-46
Figure 4-4 Local Mean Wind Coordinate System 4-46
Figure 4-5 Local Instantaneous Wind Coordinate System 4-47
Figure 4-6 Aerodynamic Forces and Moments on Oblique Segment in Local instantaneous Coordinate system 4-47
Figure 4-7 Buffeting Forces and Moments on Oblique Segment in Local Mean Wind Coordinate System 4-48
Figure 4-8 Aeroelastic Forces and Moment on Oblique Segment in Local Reference Coordinate System 4-48
Figure 4-9 Aeroelastic Forces and Moments at Element Nodes 4-49

Figure 5-1 Main Flowchart of Computer Program 5-23
Figure 5-2 Flowchart of the Computing Algorithm 5-24
Figure 5-3 Combinations of Global Coordinate Systems 5-25
Figure 5-4 Combinations of Local Coordinate Systems 5-28
Figure 5-5 Aerodynamic Coefficients of Drag and Crosswind Force on Circular Section ($Re < 3.5 \times 10^5$) 5-29
Figure 5-6 Positive Directions of Aeroelastic Forces/Moment 5-29
Figure 5-7 Comparison of Real and Imaginary Parts of Sears Function 5-30
Figure 5-8 Comparison of Module of Sears Function 5-31

Figure 6-1 Schematic Diagram of Tsing Ma Bridge Deck 6-23
Figure 6-2 Definition of Mean Wind Inclination and Yaw Angle 6-23
Figure 6-3 Positive Directions of Aerodynamic Forces/Moments 6-23

Figure 6-4 Static Sectional Model of Tsing Ma Bridge Deck ($\bar{\beta}=31°, \bar{\theta}=-10°$) 6-24
Figure 6-5 Configuration and Constitution of Static Deck Sectional Model.... 6-25
Figure 6-6 Details of Static Deck Sectional Model 6-26
Figure 6-7 Cross Sections of Static Deck Sectional Model 6-29
Figure 6-8 Force Balance and Steel-pipes in Model 6-30
Figure 6-9 Balance Coordinates and Model Coordinates 6-30
Figure 6-10 Force/Moment Measurement System 6-31
Figure 6-11 Calibration Curves of Six-component Force Balance 6-32
Figure 6-12 Layout of TJ-2 Boundary Layer Wind Tunnel 6-33
Figure 6-13 Comparison of Aerodynamic Coefficients ($\bar{\beta}=5°$, $\beta_m=5°$ vs. $\bar{\beta}=5°$, $\beta_m=0°$) 6-34
Figure 6-14 Comparison of Aerodynamic Coefficients ($\bar{\beta}=13°$, $\beta_m=13°$ vs. $\bar{\beta}=13°$, $\beta_m=0°$) 6-37
Figure 6-15 Comparison of Aerodynamic Coefficients ($\bar{\beta}=20°$, $\beta_m=20°$ vs. $\bar{\beta}=20°$, $\beta_m=0°$) 6-40
Figure 6-16 Comparison of Aerodynamic Coefficients ($\bar{\beta}=31°$, $\beta_m=31°$ vs. $\bar{\beta}=31°$, $\beta_m=0°$) 6-43
Figure 6-17 Comparison of Aerodynamic Coefficients ($\bar{\beta}=8°$, $\beta_m=13°$ vs. $\bar{\beta}=8°$, $\beta_m=5°$) 6-46
Figure 6-18 Comparison of Aerodynamic Coefficients ($\bar{\beta}=10°$, $\beta_m=13°$ vs. $\bar{\beta}=10°$, $\beta_m=5°$) 6-49
Figure 6-19 Comparison of Aerodynamic Coefficients ($\bar{\beta}=16°$, $\beta_m=20°$ vs. $\bar{\beta}=16°$, $\beta_m=13°$) 6-52
Figure 6-20 Comparison of Aerodynamic Coefficients ($\bar{\beta}=17°$, $\beta_m=20°$ vs. $\bar{\beta}=17°$, $\beta_m=13°$) 6-55
Figure 6-21 Comparison of Aerodynamic Coefficients ($\bar{\beta}=25°$, $\beta_m=31°$ vs. $\bar{\beta}=25°$, $\beta_m=20°$) 6-58

Figure 6-22 Aerodynamic Coefficients of Tsing Ma Bridge Deck 6-61
Figure 6-23 Variations of Aerodynamic Coefficients with Yaw Angle 6-64
Figure 6-24 Variations of Aerodynamic Coefficients with Angle of Inclination 6-67
Figure 6-25 Variations of Aerodynamic Coefficients with Yaw Angle (Model Coordinates) 6-70
Figure 6-26 Aerodynamic Coefficient Ratios (Model Coordinates) 6-73

Figure 7-1 Dynamic Sectional Model of Bridge Deck under Yaw Wind 7-21
Figure 7-2 Top and Bottom Views of Dynamic Sectional Model ($\bar{\beta} = 31°$) .. 7-22
Figure 7-3 Cross Section of Middle Part of Dynamic Model 7-23
Figure 7-4 Aluminium End Plate of Middle Part of Dynamic Model 7-24
Figure 7-5 Installation of Dynamic Sectional Model in TJ-2 Wind Tunnel ($\bar{\beta} = 31°$) 7-25
Figure 7-6 Aluminium Support Arms 7-26
Figure 7-7 Data Acquisition and Analysis System Used Tests 7-27
Figure 7-8 Definition of Local Reference Coordinates and Self-excited Forces 7-28
Figure 7-9 Flutter Derivative Curves: H_1^* vs. $\bar{U}/fB$ 7-29
Figure 7-10 Flutter Derivative Curves: H_2^* vs. $\bar{U}/fB$ 7-31
Figure 7-11 Flutter Derivative Curves: H_3^* vs. $\bar{U}/fB$ 7-33
Figure 7-12 Flutter Derivative Curves: H_4^* vs. $\bar{U}/fB$ 7-35
Figure 7-13 Flutter Derivative Curves: A_1^* vs. $\bar{U}/fB$ 7-37
Figure 7-14 Flutter Derivative Curves: A_2^* vs. $\bar{U}/fB$ 7-39
Figure 7-15 Flutter Derivative Curves: A_3^* vs. $\bar{U}/fB$ 7-41
Figure 7-16 Flutter Derivative Curves: A_4^* vs. $\bar{U}/fB$ 7-43
Figure 7-17 Curves of A_2^* for Critical Wind Speeds 7-45
Figure 7-18 Measured and estimated A_2^* at $\bar{\theta} = -5°$ 7-46
Figure 7-19 Measured and estimated A_2^* at $\bar{\theta} = -3°$ 7-47
Figure 7-20 Measured and estimated A_2^* at $\bar{\theta} = 0°$ 7-48

Figure 7-21 Measured and estimated A_2^* at $\bar{\theta} = 3°$ 7-49
Figure 7-22 Measured and estimated A_2^* at $\bar{\theta} = 5°$ 7-50
Figure 7-23 Measured and estimated A_3^* at $\bar{\theta} = -5°$ 7-51
Figure 7-24 Measured and estimated A_3^* at $\bar{\theta} = -3°$ 7-52
Figure 7-25 Measured and estimated A_3^* at $\bar{\theta} = 0°$ 7-53
Figure 7-26 Measured and estimated A_3^* at $\bar{\theta} = 3°$ 7-54
Figure 7-27 Measured and estimated A_3^* at $\bar{\theta} = 5°$ 7-55
Figure 7-28 Measured and estimated H_1^* at $\bar{\theta} = -5°$ 7-56
Figure 7-29 Measured and estimated H_1^* at $\bar{\theta} = -3°$ 7-57
Figure 7-30 Measured and estimated H_1^* at $\bar{\theta} = 0°$ 7-58
Figure 7-31 Measured and estimated H_1^* at $\bar{\theta} = 3°$ 7-59
Figure 7-32 Measured and estimated H_1^* at $\bar{\theta} = 5°$ 7-60

Figure 8-1 Ma Wan Tower of Tsing Ma Bridge 8-23
Figure 8-2 Schematic Diagram of Tower Model Installation 8-24
Figure 8-3 Configuration of Dummy Deck Segment Model 8-25
Figure 8-4 Connection of Tower Leg to Force Balance 8-26
Figure 8-5 Installation of Force Balance on Turning Table 8-26
Figure 8-6 Single Leg Measurement with Bridge Deck 8-27
Figure 8-7 Single Leg Measurement without Bridge Deck 8-28
Figure 8-8 Lower Leg Segment Measurement with Bridge Deck 8-29
Figure 8-9 Five Component Force Balance 8-30
Figure 8-10 Calibration Curves of Five-component Force Balance 8-31
Figure 8-11 Positive Directions of Aerodynamic Forces on Tower Legs 8-32
Figure 8-12 Positive Directions of Aerodynamic Forces on Tower Transverse Beams 8-33
Figure 8-13 Drag Coefficients of Tower Legs 8-34
Figure 8-14 Lift Coefficients of Tower Leg 8-34
Figure 8-15 Drag Coefficients of Upper Segment of Tower Leg 8-35
Figure 8-16 Drag Coefficients of Lower Segment of Tower Leg 8-35

Figure 8-17 Lift Coefficients of Upper Segment of Tower Leg 8-36
Figure 8-18 Lift Coefficients of Lower Segment of Tower Leg 8-36
Figure 8-19 Coefficients of Drag and Crosswind Force of Lower Transverse Beam 8-37
Figure 8-20 Coefficients of Drag and Crosswind Force of Lower-middle Transverse Beam 8-37
Figure 8-21 Coefficients of Drag and Crosswind Force of Upper-middle Transverse Beam 8-38
Figure 8-22 Coefficients of Drag and Crosswind Force of Upper Transverse Beam 8-38

Figure 9-1 Moving Track of Typhoon Sam 9-25
Figure 9-2 Three Components of Wind Velocity Recorded by Anemometer WITJN01 9-25
Figure 9-3 Three Components of Fluctuating Wind Velocity at Anemometer WITJN01 9-26
Figure 9-4 Auto Spectra of Fluctuating Wind Speeds 9-27
Figure 9-5 Co-spectra of Fluctuating Wind Speeds 9-28
Figure 9-6 Quadrature Spectra of Fluctuating Wind Speeds 9-29
Figure 9-7 Time Histories of Measured Deck Acceleration Responses to Typhoon Sam 9-30
Figure 9-8 Time Histories of Measured Cable Acceleration Responses to Typhoon Sam 9-32
Figure 9-9 Measured Deck Acceleration Spectra at ATTJD 9-33
Figure 9-10 Measured Deck Acceleration Spectra at ATTID 9-34
Figure 9-11 Measured Deck Acceleration Spectra at ATTFD 9-35
Figure 9-12 Measured Deck Acceleration Spectra at ATTBD 9-36
Figure 9-13 Measured Cable Acceleration Spectra at ABTQC 9-37
Figure 9-14 Measured Cable Acceleration Spectra at ABTLC 9-38
Figure 9-15 Measured Cable Acceleration Spectra at ATTGC 9-39
Figure 9-16 Measured Cable Acceleration Spectra at ABTCC 9-40
Figure 9-17 Comparison between Measured and Computed Spectra of Deck Lateral Acceleration 9-41

Figure 9-18 Comparison between Measured and Computed Spectra of Deck Vertical Acceleration 9-42
Figure 9-19 Comparison between Measured and Computed Spectra of Deck Torsinal Acceleration 9-43
Figure 9-20 Comparison between Measured and Computed Deck RMS Acceleration Responses 9-44
Figure 9-21 Comparison between Measured and Computed Spectra of Cable Lateral Acceleration 9-45
Figure 9-22 Comparison between Measured and Computed Spectra of Cable Vertical Acceleration 9-46
Figure 9-23 Comparison between Measured and Computed Spectra of Cable Longitudinal Acceleration 9-47
Figure 9-24 Comparison between Measured and Computed Cable RMS Acceleration Responses 9-48

Figure 10-1 Response Spectra of Deck Accelerations at Mid-mainspan with Different Aerodynamic Admittance Functions 10-17
Figure 10-2 Contour Plots of RMS Responses of Deck Displacements at Mid-mainspan 10-18
Figure 10-3 Variations of RMS Responses of Deck Displacements at Mid-mainspan with θ_0 10-19
Figure 10-4 Variations of RMS Responses of Deck Displacements at Mid-mainspan with β_0 10-20
Figure 10-5 Contour Plots of RMS Responses of Cable Displacements at Quarter-mainspan 10-21
Figure 10-6 Contour Plots of RMS Displacement Responses at the Top of Ma Wan Tower 10-22
Figure 10-7 Ratios of Auto Spectra as Functions of Reduced Frequency 10-23
Figure 10-8 Contour Plots of Effective Coefficients of Buffeting Forces/Moment on Bridge Deck 10-24
Figure 10-9 Variations of Effective Coefficients of Buffeting Forces/ Moment on Bridge Deck with θ_0 10-25

Figure 10-10 Variations of Effective Coefficients of Buffeting Forces/ Moment on Bridge Deck with β_0 10-26

Figure 10-11 Effects of Self-excited Forces, Crosswind Force, Rolling and Yawing Moments on Buffeting Responses of Bridge Deck ($\theta_0 = -2°, \beta_0 = 12°$) 10-27

Figure 10-12 Effects of Self-excited Forces, Crosswind Force, Rolling and Yawing Moments on Buffeting Responses of Bridge Cables ($\theta_0 = -2°, \beta_0 = 12°$) 10-28

Figure 10-13 Effects of Self-excited Forces, Crosswind Force, Rolling and Yawing Moments on Buffeting Responses of Bridge Deck ($\theta_0 = 4°, \beta_0 = 12°$) 10-29

Figure 10-14 Effects of Self-excited Forces, Crosswind Force, Rolling and Yawing Moments on Buffeting Responses of Bridge Cables ($\theta_0 = 4°, \beta_0 = 12°$) 10-30

LIST OF TABLES

Table 2-1 The First Seventeen Longest Suspension Bridges in the World 2-2

Table 2-2 The First Evelen Longest Cable-stayed Bridges in the World 2-3

Table 3-1 Average Values of Standard Deviations of Wind Fluctuations 3-15

Table 3-2 Average Values of Turbulence Intensities 3-17

Table 3-3 Average Values of Ratios between Turbulence Intensities 3-18

Table 3-4 Average Values of Integral Scales of Turbulence 3-20

Table 3-5 Lateral Natural Frequencies 3-29

Table 3-6 Vertical Natural Frequencies 3-29

Table 3-7 Torsional Natural Frequencies 3-29

Table 6-1 Test Cases for Six Aerodynamic Coefficients of Tsing Ma Bridge Deck 6-11

Table 7-1 Model Parameters 7-8

Table 7-2 Range of Wind Speed Used in Tests 7-9

Table 7-3 Flutter Critical Wind Speed of Tsing Ma Bridge Based on Measured A_2^* Curves 7-14

Table 7-4 Flutter Critical Wind Speed of Tsing Ma Bridge Based on the Estimated A_2^* Curves 7-16

Table 8-1 Test Cases for Aerodynamic Coefficients of Tsing Ma Bridge Tower 8-8

Table 9-1 RMS Acceleration Responses of the Tsing Ma Bridge Deck (without any Filter) 9-5

Table 9-2 RMS Acceleration Responses of the Tsing Ma Bridge Deck (with Bandpass Filter) 9-6

Table 9-3 RMS Acceleration Responses of the Tsing Ma Bridge Deck (with Lowpass Filter) 9-6

Table 9-4 RMS Acceleration Responses of the Tsing Ma Bridge Cable (without any Filter) 9-8

Table 9-5 RMS Acceleration Responses of the Tsing Ma Bridge Cable (with Bandpass Filter)..... 9-8
Table 9-6 RMS Acceleration Responses of the Tsing Ma Bridge Cable (with Lowpass Filter)..... 9-8
Table 9-7 Computed and Measured Lateral Natural Frequencies..... 9-9
Table 9-8 Computed and Measured Vertical Natural Frequencies..... 9-11
Table 9-9 Computed and Measured Torsional Natural Frequencies..... 9-12
Table 9-10 Computed Bridge Deck RMS Acceleration Responses and Relative Differences (with Bandpass Filter)..... 9-21
Table 9-11 Computed Cable RMS Acceleration Responses and Relative Differences (with Bandpass Filter)..... 9-22

Chapter 1

INTRODUCTION

1.1 RESEARCH MOTIVATIONS

To meet the economic, social and recreational needs of the community for efficient and convenient transportation systems, more and more long span cable-supported bridges have been built throughout the world since 1980s, among which 10 suspension bridges were built with main span length beyond 1000m, and 11 cable-stayed bridges were constructed with main span length over 500m. The super long span suspension bridges with main span length beyond 3000m, such as Messina Narrow Bridge (3300m, Italy), and the super long span cable-stayed bridges with main span length beyond 1000m, such as Sutong Bridge (1088m, Jiangsu, China) and Stonecutters Bridge (1018m, Hong Kong, China) are also under design.

In China, to promote further the rapid economic development, a new state highway network has been planned by the Chinese Government and will be completed within the 21st Century (Xiang and Chen, 1998). One of the lines in the new state highway network will start from Tongjiang of Helongjiang Province, Northeast China, and end at Sanya of Hainan Province, South China. This coastal line will pass through many mega-cities and cross over Bohai Strait, Yangtze River Estuary near Shanghai, Hangzhou Bay, Lingtingyang at Pearl River Estuary, and Qiongzhou Sea Strait. These strait crossing projects will involve the construction of a number of super long span cable-supported bridges but most of these super long span bridges will be situated in typhoon-prone regions along the eastern coast of China. The design mean wind speed at deck level may be over 60m/s and the critical wind speed for avoiding aeroelastic instability of the bridge may have to be more than 90m/s (Xiang and Chen, 1998). Therefore, wind-induced vibrations become a very serious problem and are dominant factors for both serviceability and safety of super long span cable-supported bridges.

Wind-induced vibrations of super long span cable-supported bridges can be classified mainly into self-excited vibration and buffeting vibration. Self-excited vibration depends on structural motion whilst buffeting vibration is due to wind turbulence. Flutter, vortex shedding resonance and galloping are three main kinds of self-excited vibration, where flutter and galloping belong to unstable vibration while vortex shedding resonance is limit-amplitude vibration. Any unstable vibration is not permitted for any long span bridge. Vortex shedding resonance may happen to a long span bridge at a relative low wind speed when the vortex shedding frequency is close to the natural frequency of the bridge. In the last two decades, many efforts have been made to prevent the bridge from flutter and galloping instability and to mitigate vortex-shedding response by means of aerodynamic measures, such as optimizing deck cross-sections and installing aerodynamic devices. Buffeting, however, is inevitable to happen to any bridge exposing to natural turbulent wind because this phenomenon is caused not much by the way the bridge is designed but by the atmospheric turbulence existing inherently. The increase of span length of modern cable-supported bridges will significantly increase their buffeting response, which may cause serious fatigue damage to structural components and connections, instability of the vehicles travelling on the deck and discomfort to the pedestrians. Therefore, the realistic prediction of buffeting responses becomes more and more important for super long span cable-supported bridges in typhoon-prone regions.

To achieve the satisfactory prediction of buffeting response of long span bridges, great efforts have been made to refine the existing analytical methods, such as Davenport's theory (Davenport, 1962b), Scanlan's theory (Scanlan and Gade, 1977; Scanlan, 1978b), and Lin's theory (Lin & Arianratnam, 1978; Lin, 1979a; Lin, 1979b; Lin and Yang, 1983). At present, the multi-mode effects, aerodynamic and inter-mode coupling effects are often considered in buffeting analysis of long span bridge either in time-domain (Diana et al., 1998; Diana et al., 1999a, Boonyapinyo et al., 1999; Chen et al., 2000a), or in frequency-domain (Jain et al., 1996; Xu el al., 1998; Chen et al., 1999; Katsuchi et al., 1999; Chen et al., 2000b; Chen et al., 2001). A fully-coupled 3D buffeting analysis in frequency-domain has also been proposed to consider varying wind properties along the bridge deck and interaction between the bridge deck, cables and towers (Xu et al., 1998; Xu, 1999; Xu et al., 2000a). However, most of the previous investigations take incident mean wind at a right

angle to the longitudinal axis of bridge deck with the assumption that this is the worse case. Very little investigation has been carried out on the behaviour of long span bridges under skew winds and the effects of skew winds on bridge buffeting response.

The most common approach to handle the effects of yaw wind on buffeting response is the decomposition approach or cosine rule (Xie and Tanaka, 1991; Kimura and Tanaka, 1992; Kimura et al., 1994; Scalan; 1993; Kimura and Ohara; 1999). In this approach, the yaw wind is decomposed into a cosine component normal to the bridge longitudinal axis and a sine component along the bridge longitudinal axis. The buffeting responses to the two wind components may then be analyzed separately, but in most cases only the normal component is taken into account and the longitudinal components is ignored. However, some wind tunnel tests of aeroelastic models under yaw winds have revealed that the employment of the traditional decomposition method or cosine rule may lead to an unsafe estimation of buffeting response of bridge under yaw wind (Tanaka and Davenport; 1982; Irwin and Gamble; 1985; Zan, 1987; Diana et al., 1995, 1999b; etc.), and the most unfavourable buffeting response of the bridge may not occur in the normal wind case.

Furthermore, the monitoring of wind and structural health of long span bridges has been paid great attention in recent years. Various wind and structural health monitoring systems have been and will be installed in several long span cable-supported bridges in the world to carry out field measurements with one of the objectives being the verification of analytical processes used in wind-resistant design. For instance, the "Wind And Structural Health Monitoring System" (WASHMS) has been installed on the Tsing Ma Bridge by the Highways Department of Hong Kong Special Administrative Region of China (Lau et al., 1998). From the recent field measurements on the Tsing Ma Bridge during Typhoon Victor (Zhu et al., 1999; Xu et al., 2000b) and others, one can find that strong winds seldom attack the bridge at a right angle to the bridge longitudinal axis. These observations, however, have not been properly considered in the previous buffeting response predictions. Therefore, it will be difficult to have a direct comparison of buffeting response between the field measurement results and the theoretical results obtained

using existing analysis methods. It is thus needed to develop a new analysis method of buffeting response of long span bridges capable of handling yaw winds.

In fact, bridge alignment is often determined to avoid the dominant wind direction as much as possible based on the local climate information. Thus, risk or probability evaluation may be required to relate buffeting response of long span bridges to the local wind climate, such as an expected annual peak response for a given return period, as done by Davenport (Davenport et al. 1969, 1979; Davenport, 1977). In such an evaluation of wind-resistant performance of long span bridges, the wind azimuth needs to consider in buffeting analysis. This also leads to the demand for a new analytical method with the yaw wind included.

1.2 OBJECTIVES

This thesis thus focuses on buffeting response of long span cable-supported bridges under skew winds with the following major objectives:

(1) To carry out comprehensive investigations of natural wind characteristics and bridge responses using the field measurement data recorded on the Tsing Ma Bridge in Hong Kong by the WASHMS. For this purpose, the programs for analyzing field measurement data of wind characteristics and buffeting responses of bridges will be written using MATLAB as a platform incorporated with traditional signal processing techniques. The wind characteristics, such as mean wind speed, mean wind direction, friction velocity, turbulence intensity, integral scale of turbulence, and auto and cross spectra will be analyzed using wind data recorded on the Tsing Ma Bridge during the passages of Typhoon Victor and Typhoon Sam. The buffeting responses of the Tsing Ma Bridge to Typhoon Victor and Typhoon Sam will be also analyzed in terms of the standard deviation and spectra of acceleration response.

(2) To develop a modified frequency-domain method and the associated computer program for predicting buffeting response of long span cable-supported bridges under natural skew wind based on the quasi-steady linear theory and the oblique strip theory. The concept of an oblique strip along the mean wind direction will

be introduced to establish a set of universal expressions of six-component aerodynamic buffeting forces on a arbitrary bridge component, such as bridge deck, tower, and cable, caused by all the three orthogonal turbulence components of the skew wind. Aeroelastic damping and stiffness, and aerodynamic coupling effect will be considered by introducing 18 flutter derivatives associated with the same oblique strip along the mean wind direction. The effects of unsteadiness and chordwise partial coherence of wind turbulence will be taken into consideration by introducing 18 complex aerodynamic admittance functions. A finite element (FE) method will be employed to establish the equations of motion of a fully-coupled three-dimensional bridge naturally including the effects of multi-modes and spatial modes, inter-mode coupling, as well as the interaction among bridge components. The equations of motion will be solved using the pseudo excitation method (Lin, 1985; Lin, 1992; Lin, et al., 1993; Lin et al., 1994; Xu el al., 1998) to efficiently obtain the response spectra and RMS response of the bridge with acceptable computation efforts.

(3) To develop adequate wind tunnel test techniques for measuring the six-component aerodynamic coefficients, flutter derivatives of an oblique bridge deck strip as the functions of mean wind yaw angle and inclination in order to implement the proposed modified buffeting analysis method and the computer program. To present a practical wind tunnel technique for measuring aerodynamic coefficients of bridge tower members under yaw winds to get more realistic results of buffeting response of the bridge under the frame of the modified analysis method in conjunction with the FE method.

(4) To compute the buffeting response of the Tsing Ma Bridge to skew winds during Typhoon Sam using the developed modified analysis method. To carry out a detailed comparison between the computed and field-measured results of acceleration responses of the Tsing Ma Bridge to Typhoon Sam and to verify the modified frequency-domain method proposed in this study. In such a comparison, the measured wind characteristics surrounding the Tsing Ma Bridge during Typhoon Sam and the measured aerodynamic coefficients and flutter derivatives of the bridge deck and tower under skew wind in the wind tunnel will be used as input data to the computer program.

(5) To carry out an extensive parametric study of the buffeting response of the Tsing Ma Bridge to assess the effects of wind yaw angle and inclination on the bridge response; to find out the most unfavorable wind direction; to understand the influence mechanism of wind yaw and inclination on the bridge buffeting responses; to investigate the roles of the aeroelastic self-excited forces and the aerodynamic coefficients of the crosswind force, yawing and rolling moments acting on the bridge.

1.3 ASSUMPTIONS AND LIMITATIONS

The modified buffeting analysis method proposed in this thesis is a frequency-domain method and is developed based on the quasi-steady linear theory and the oblique strip theory with the following assumptions and limitations.

1. To ensure the validity of the quasi-steady theory in frequency-domain, it is assumed that fluctuating wind is a weakly stationary random process. The average scales of turbulence are sufficiently larger than the chordwise dimensions of bridge members, say 10 times, so that the fluctuating flow can be regarded to be spatially smooth as viewed by the bridge at any given moment.

2. To ensure the validity of the aerodynamic strip theory, the mean wind is assumed to be unidirectional along bridge span. The skew wind flow is supposed to cross the oblique cross section in the mean wind direction, and the spanwise wind flow generated due to the interference of brig deck is secondary and can be ignored.

3. It is assumed that the mean wind speed is sufficiently larger than the fluctuating wind components so that the non-linear effects of turbulence components on the aerodynamic coefficients and flutter derivatives can be ignored and linearization can be performed.

4. Wind-induced dynamic response is assumed small and linear around the static equilibrium position of the bridge so that the non-linear effects of the bridge motion on the aerodynamic coefficients and flutter derivatives can be ignored. Correspondingly, the mean wind speed used in the buffeting analysis should not

be in the vicinity of any aerodynamic and aeroelastic instability. This method is also not applicable to the case when the mean wind speed approaches any distinct velocity for vortex shedding, because the vortex-induced forces are not included in this method.

1.4 LAYOUT OF THE THESIS

This thesis contains a variety of research topics to achieve the aforementioned objectives. It is divided into eleven chapters and is organized in the following way.

- Chapter 1 gives a brief introduction of the research motivations, the objectives, the assumptions and limitations, and the layout of the thesis.

- Chapter 2 presents an extensive literature review on three relevant topics. The first section reviews the existing analytical methods, including both the frequency-domain and time-domain methods and both the linear and non-linear approaches, for predicting buffeting response of long span bridges to gusty winds. The second section gives a review on the various models of aeroelastic self-excited forces and the different approaches for the identification of flutter derivatives or aeroelastic coefficients. The third section presents a brief introduction of the basic knowledge with respect to the atmospheric boundary layer and natural wind characteristics.

- Chapter 3 first introduces the main features and modal properties of the Tsing Ma Bridge. The Wind And Structural Health Monitoring System (WASHMS) installed on the Tsing Ma Bridge, the local terrain surrounding the bridge and Typhoon Victor are then concisely described. Finally, a detail analysis of wind characteristics and structural responses of the Tsing Ma Bridge under Typhoon Victor is conducted using the field measurement data recorded by the WASHMS.

- Chapter 4 derives the relevant formulae of the new modified method for buffeting analysis of long span bridges under natural skew winds. Some coordinate systems employed in this modified frequency-domain method and the corresponding transformation matrices among these systems are first

introduced. Then, the local wind yaw angle and inclination of mean wind and transient wind relative to an arbitrary element are defined, and the corresponding formulae are presented for determining the local yaw angle and inclination and their increments due to wind turbulence. Subsequently, the formulae of buffeting forces on an oblique strip of an arbitrary bridge component due to the three fluctuating components of skew wind turbulence are derived based on the quasi-steady linear theory and the oblique strip theory. The ensemble force vector and spectral matrix of the nodal buffeting forces are also established. To take the contribution of self-excited forces into account, the elemental matrices and ensemble matrices of aerodynamic stiffness and damping for skew wind cases are also presented. Finally, the equations of motion of the whole bridge established under the frame of FEM are generalized and an efficient solution procedure is provided based on the pseudo excitation method using the double $\mathbf{L}^*\mathbf{D}\mathbf{L}^T$ decomposition.

- Chapter 5 briefly introduces the computer program for buffeting analysis of long span bridges under skew winds following the modified frequency-domain method developed in Chapter 4. Some empirical or approximate formulae for aerodynamic coefficients, flutter derivatives, and aerodynamic admittance functions embedded in the computer program are then presented and extended to skew wind cases. This chapter also gives the general expressions of cross spectra between two turbulence components at two different spatial points required in the modified method and the associated computer program, taking into account the turbulent coherence in all the three orthogonal directions simultaneously.

- Chapter 6 presents a wind tunnel test technique for measuring the six-component aerodynamic coefficients of bridge deck under skew winds using an oblique sectional model and an internally-placed six-component balance to implement a more realistic buffeting analysis of long span bridges to skew winds using the proposed modified method. Typical oblique strips of the Tsing Ma bridge deck are selected and tested using this wind tunnel test technique to obtain the aerodynamic coefficients of the bridge deck as the functions of mean wind yaw angle and inclination. The measured results are then analyzed to find

the relationship between the aerodynamic coefficients and the mean wind yaw angle and inclination. The measured results are also used to examine the cosine rule currently used for buffeting analysis of a bridge under yaw winds.

- Chapter 7 first presents a wind tunnel test technique for measuring the flutter derivatives of bridge deck under skew winds. Flutter derivatives of the Tsing Ma bridge deck under skew winds are then measured using an oblique sectional model suspended with 8 springs. The measured results are then analyzed to find the relationship between the flutter derivatives, the reduced frequency, and the wind yaw angle and inclination. Finally, the measured flutter derivatives are used to examine the approximate formula suggested by Scanlan for estimating the flutter derivatives of a bridge deck under yaw winds.

- Chapter 8 provides a wind tunnel investigation for determining aerodynamic coefficients of the tower legs and tower transverse beams of the Tsing Ma Bridge under yaw winds. The measured aerodynamic coefficient of tower components are then used in the buffeting analysis of the Tsing Ma Bridge under skew winds in conjunction with the aerodynamic coefficients and flutter derivatives of the bridge deck measured under skew wind as described in Chapters 6 and 7.

- Chapter 9 first carries out the field measurement data analysis to obtain the wind characteristics and buffeting responses of the Tsing Ma Bridge during Typhoon Sam. The buffeting response of the bridge to Typhoon Sam is then computed using the developed modified frequency-domain method. The field-measured wind characteristics, such as mean wind yaw angle and inclination, friction velocity, auto and cross spectra of wind turbulence, and the measured modal damping ratios are taken as input data in the computation of buffeting response. The aerodynamic coefficients and flutter derivatives of the bridge components measured in the wind tunnel under skew winds as presented in Chapters 6, 7, and 8 are also used in the computation as input data. The verification of the modified buffeting analysis method is finally conducted by comparing the computed acceleration responses of the bridge deck and cables with those measured on the bridge during Typhoon Sam.

- Chapter 10 presents an extensive parametric study on the buffeting response of the Tsing Ma Bridge. The influence of different aerodynamic admittance functions on buffeting response of the Tsing Ma Bridge is investigated first. The effect of wind yaw angle and inclination on buffeting response of the Ting Ma Bridge is then studied in detail and the unfavorable wind directions are identified. The influence of aeroelastic self-excited forces acting on the bridge deck on the buffeting response is also examined. Finally, the effects of the aerodynamic crosswind forces and yawing and rolling moments acting on the bridge deck are also discussed in this chapter.

- Chapter 11 summarizes the main conclusions obtained from this study and provides some recommendations for further studies.

Chapter 2

LITERATURE REVIEW

2.1 BUFFETING ANALYSIS OF LONG SPAN BRIDGES

2.1.1 Background

To meet the economic, social and recreational needs of the community for efficient and convenient transportation systems, more and more long span bridges have been built throughout the world. Listed in Table 2-1 and Table 2-2 are 17 large suspension bridges with main span length beyond 1000m, and 11 large cable-stayed bridges with main span length over 500m. Further, super long span suspension bridges with main span length beyond 3000m, such as Messina Narrow Bridge (3300m, Italy), and super long span cable-stayed bridges with main span length beyond 1000m, such as Sutong Bridge (1088m, Jiangsu, China) and Stonecutters Bridge (1018m, Hong Kong, China) are under design.

With increasing span length, modern long span cable-supported bridges become more and more flexible and susceptible to strong wind than ever. This leads to significantly increasing buffeting response of the bridge, which may result in excess of ultimate stress or serious fatigue damage to structural components and connections, instability of the vehicles travelling on the deck, and discomfort to the pedestrians. Therefore, the prediction of buffeting response of super long span cable-supported bridges to strong winds becomes more and more important for the bridges constructed in wind-prone regions.

2.1.2 Buffeting Analysis of Bridges under Normal Wind

2.1.2.1 Davenport's Theory

Research on bridge buffeting analysis was initiated by Davenport in the early sixties last century. Owing to the stochastic nature of wind, Davenport pioneered the application of the statistical concepts of the stationary time series and stochastic

Table 2-1 The First Seventeen Longest Suspension Bridges in the World

Bridge Name	Main span (m)	Location	Country	Year of completion
Akashi Kaikyo Bridge	1991	Kobe-Naruto	Japan	1998
Great Belt Bridge	1624	Halsskov-Sprogoe	Denmark	1998
Humber Bridge	1410	Hull	UK	1981
Jiangyin Bridge over Yangtze River	1385	Jiangyin, Jiangsu	China	1998
Tsing Ma Bridge	1377	Hong Kong	China	1997
Verrazano-Narrows Bridge	*1298*	*New York, NY*	*USA*	*1964*
Golden Gate Bridge	*1280*	*San Francisco, CA*	*USA*	*1937*
Höga Kusten Bridge	1210	Veda	Sweden	1997
Mackinac Bridge	*1158*	*Mackinaw City, MI*	*USA*	*1957*
Minami Bisan-Seto Bridge	1100	Kojima-Sakaide	Japan	1988
Fatih Sultan Mehmet Bridge	1090	Istanbul	Turkey	1988
Bospours I Bridge	*1074*	*Istanbul*	*Turkey*	*1973*
George Washington Bridge	*1067*	*New York, NY*	*USA*	*1931*
Kurushima-3 Bridge	1030	Onomichi-Imabari	Japan	1999
Kurushima-2 Bridge	1020	Onomichi-Imabari	Japan	1999
Ponte 25 de Abril Bridge	*1013*	*Tejo, Lisbon*	*Portugal*	*1966*
Forth Road Bridge	*1006*	*Edinburgh*	*UK*	*1964*

Note: bridges built before 1980 are listed in italics.

vibration theory to the buffeting analysis of long span bridges in frequency-domain (Davenport, 1961a, 1961b, 1962a, 1962b). The quasi-static linear theory was employed in the Davenport's theory to establish the buffeting forces and aeroelastic damping, and the buffeting response was analyzed mode by mode based on the strip theory of aerodynamics. The concept of joint acceptance function was introduced to consider the effectiveness of the temporal and spanwise cross correlation of buffeting loading, which was assumed to be the same as that of wind turbulence. Meanwhile, the concept of aerodynamic admittance was adopted to take into account the effects of unsteadiness and spatial variation of wind turbulence surrounding the cross section. However, the aerodynamic stiffness and aerodynamic coupling effect were

Table 2-2 The First Evelen Longest Cable-stayed Bridges in the World

Bridge Name	Main span (m)	Location	Country	Year of completion
Tatara Bridge	890	Onomichi-Imabari	Japan	1999
Pont de Normandie Bridge	856	Le Havre	France	1995
2nd Nanjing Bridge over Yangtze River	628	Nanjing, Jiangsu	China	2001
3rd Wuhan Bridge over Yangtze River	618	Wuhan, Hubei	China	2001
Qingzhou Minjiang Bridge	605	Fuzhou, Fujian	China	2002
Yangpu Bridge	602	Shanghai	China	1993
Xupu Bridge	590	Shanghai	China	1997
Meiko-Chuo Bridge	590	Nagoya	Japan	1997
Skarnsundet Bridge	530	Trondheim Fjord	Norway	1991
2nd Shantou Bay Bridge	518	Shantou, Guangdong	China	1999
Tsurumi Tsubasa Bridge	510	Yokohama	Japan	1994

ignored in this theory. The theory was further improved by himself in the next few years (Davenport, 1963, 1964, 1966, 1969; Davenport et al., 1971). Following his step, significant achievements were accomplished by various investigators, both in buffeting analysis and in wind tunnel experiments of real bridges (Miyata and Ito, 1972; Davenport & Tanaka, 1974; Holmes, 1975; Melbourne, 1979; Irwin, 1977a, 1977b, 1978).

2.1.2.2 Scanlan's Theory

Based on the research experience on flutter instability of long span bridges (Scanlan and Tomko, 1971; Scanlan, 1978a), Scanlan and his co-workers believed that the self-excited aeroelastic forces would exert an important influence on the buffeting response of bridges. Thus, in the seventies of the last century, they proposed their buffeting response analysis method in light of time-invariant linear system and aerodynamic strip theories (Scanlan and Gade, 1977; Scanlan, 1978b). By simultaneously considering both self-excited (aeroelastic) forces due to bridge deck motion and quasi-static linearized aerodynamic forces caused by wind turbulence,

the effects of both the aeroelastic stiffness and aeroelastic damping, and the aeroelastic coupling among translational and torsional vibrations can be taken into account in buffeting analysis. The effect of wind turbulence on the self-excited forces can be considered, to some extent, in such a way that the flutter derivatives are identified under flow with a certain turbulence level (Scanlan and Lin, 1978), but afterwards, keep the same for different levels of turbulent intensity in analysis. The buffeting forces are assumed to be linear to the fluctuations of wind speed, i.e., the aerodynamic coefficients are independent of wind turbulence. The self-excited forces may be expressed in terms of some frequency-dependent flutter derivatives or time-dependent aerodynamic indicial functions. The analysis results with this theory (Beliveau et al., 1977) showed the notable effects of self-excited forces on buffeting response.

Scanlan has made great efforts to investigate the self-excited forces. By expressing the self-excited forces with time-dependent aerodynamic indicial functions, his theory can be used in time domain (Scanlan et al., 1974; Scanlan, 1984). The indicial functions can be either measured directly through wind tunnel test, or derived from the flutter derivatives obtained often by section model wind tunnel test (Scanlan and Budlong, 1972; Scanlan et al., 1974; Scanlan, 1993b; Scanlan, 1996). However, because both the flutter derivatives and wind spectra are the functions of frequency, it is convenient to carry out the analysis of buffeting response in the frequency domain. To this end, the self-excited forces are usually expressed with the frequency-dependent flutter derivatives (Scanlan, 1978b, 1987a; Scanlan and Jones, 1990).

The effect of the unsteadiness of aerodynamic forces is not included in the earlier Scanlan's theory. Hence, to overcome this weakness, Gu and his colleagues, and also Scanlan himself, introduced the admittance functions, as in the Davenport's theory, into the mode-by-mode buffeting analysis with Scanlan's earlier theory (Gu and Xiang, 1992; Chen, 1993; Scanlan, 1993b;). Nowadays, the buffeting forces of lift (L_b), drag (D_b) and pitching moment (M_b) per unit deck length are commonly expressed as follows (Chen et al., 2001):

$$D_b(t) = \frac{1}{2}\rho U^2 B\left(2C_D\chi_{D_bu}(K)\frac{u(t)}{U} + (C_D' - C_L)\chi_{D_bw}(K)\frac{w(t)}{U}\right) \qquad (2\text{-}1a)$$

$$L_b(t) = \frac{1}{2}\rho U^2 B\left(2C_L\chi_{L_bu}(K)\frac{u(t)}{U} + (C_L' + C_D)\chi_{L_bw}(K)\frac{w(t)}{U}\right) \quad (2\text{-}1b)$$

$$M_b(t) = \frac{1}{2}\rho U^2 B\left(2C_M\chi_{M_bu}(K)\frac{u(t)}{U} + C_M'\chi_{M_bw}(K)\frac{w(t)}{U}\right) \quad (2\text{-}1c)$$

where ρ is the air density; B is the deck width and U is the mean wind speed; u and w are, respectively, the alongwind and vertical fluctuations of wind velocity; C_D, C_L and C_M are the coefficients of lift, drag and pitching moment of the bridge deck while C_D', C_L' and C_M' are, respectively, the derivatives of C_D, C_L and C_M with respect to wind inclination; χ_{D_bu}, χ_{D_bw}, χ_{L_bu}, χ_{L_bw}, χ_{M_bu} and χ_{M_bw} are the frequency-dependent aerodynamic admittance functions or transfer function between velocity fluctuations and buffeting forces; $K = B\omega/U$ is the reduced frequency; and ω is the circular frequency of wind turbulence.

For the convenience of engineering application, Chen (1993) also proposed a buffeting response spectrum for design use as done in earthquake engineering. The complicated formula of joint acceptance function was reduced to a very simple one using sinusoidal mode shape with equivalent span length. Thus, buffeting response of each mode is expressed as a product of eight coefficients, which can easily be determined with very simple formulas or from pre-settled figures and tables according to the corresponding structural and wind parameters.

2.1.2.3 Lin's Theory

While the frequency domain method was applied to buffeting analysis, Y. K. Lin and his co-workers presented the time-domain method for predicting bridge response to turbulent winds, using Ito's stochastic differential equations (Lin & Arianratnam, 1978; Lin, 1979a; Lin, 1979b; Lin and Arianratnam, 1980). The effects of turbulence on stability of the bridge motion were included in their theory by regarding the self-excited aeroelastic forces as random time-varying unknowns. The aerodynamic strip theory was also employed in this theory, and the following assumptions were adopted. (1) Base on the fact that typical scale of turbulence in a natural wind is in the order of 10 times lager than the lateral dimensions of a bridge, the wind flow is spatially smooth as viewed by the bridge at any given moment, and the flow pattern around the bridge is supposed to be similar to that associated with a non-turbulent

flow. (2) The aerodynamic coefficients and indicial functions obtained under non-turbulent flow are still applicable to spatially smooth turbulent flow. (3) The effects of turbulence on the random time-varying aeroelastic forces can be adequately accounted for in the random variation to the dynamic pressure of transient velocity consisting of mean and random perturbations. (4) The wind velocity fluctuations are weakly stationary wide-band random processes, and the correlation time of the excitation field is short compare with the relaxation time of the dynamic system; thus, the bridge response is approximately a component of a Markov vector, and the Ito's calculus can be used. The above method was initially used to investigate the aeroelastic stability of bridge in turbulent wind. Therefore, only the basic torsional mode was employed in the theory. The example analysis conducted by Lin et al. (Lin, 1979a; Lin, 1979b; Lin and Arianratnam, 1980) shows that the existence of wind turbulence may strikingly reduce the stability of a bridge motion. However, if the motion is not in the vicinity of being unstable, the fluctuations of wind speed in the self-excited forces may be neglected in computing the bridge response to the random buffeting loads. Thus, base on the foregone single-torsional-mode flutter-buffeting theory, Lin and Yang (1983) proposed a general framework to handle multi-mode buffeting analysis of time-invariant linear dynamic system, discarding the wind fluctuations in self-exited forces. In this method, the governing equations of bridge motion, containing the effects of the disaccord between elastic and mass centers of bridge deck and the effects of aerodynamic coupling, are established at first in the time-domain. The time-domain equations are then transformed into the counterparts in the frequency domain by means of Fourier-Stieltjes integrals. Meanwhile, the relationships are found between the time-domain indicial functions and the frequency-domain Scanlan's flutter derivatives. Finally, a framework was established for calculating the cross-spectral density of buffeting responses taking the turbulent cross-spectra as input. Uncoupled undamped ortho-normal modes are used in this theory. Scanlan's flutter derivatives are employed to describe the self-excited forces without the effect of turbulence. Buffeting loads are also represented with the forms adopted by Scanlan (1978b) based on the aerodynamic strip theory and quasi-steady linear theory.

2.1.2.4 *Effects of Multi-modes, Inter-mode Coupling and Bridge Component Interaction*

Although some frameworks of multi-mode buffeting analysis methods had already been proposed in eighties of last century (Lin and Yang, 1983; Scanlan, 1988), analysis of buffeting response was always carried out mode by mode before the middle of the nineties. The final resultant value of response was then estimated by SRRS (Square Root Sum of Square) method usually, which excluded the effects of aerodynamic inter-mode coupling. The main reason is the lack of efficient means in dealing with the enormous time-consuming calculation work encountered in multi-mode buffeting analysis. The mode-by-mode method may be adequate for bridges with small span length but, of course, should be discarded in buffeting analysis of long cable-supported bridges, because the closely distributed natural frequencies are this case and the aerodynamic inter-mode coupling may play a significant role. Therefore, to raise the reliability of long span bridges against wind, more realistic prediction of buffeting response has been demanded, and this has led to continuous refinement of buffeting analysis method. Nowadays, with the rapid and continuous rising of computer efficiency, the multi-mode effects and aerodynamic inter-mode coupling effects are often considered in buffeting analysis either in the time-domain (Diana et al., 1998; Diana et al., 1999a, Boonyapinyo et al., 1999; Chen et al., 2000a), or in the frequency domain (Jain et al., 1996; Xu el al., 1998; Chen et al., 1999; Katsuchi et al., 1999; Chen et al., 2000b; Chen et al., 2001). A fully-coupled 3D buffeting analysis method in the frequency domain has also been proposed based on FEM (finite element nethod) and PEM (pseudo excitation method) which make the computing efficiency conspicuously enhanced. With this method, not only the effects of multi-modes and the aerodynamic inter-mode coupling, but also the varying wind properties along bridge deck and the interaction among the bridge deck, cables and towers can be automatically taken into consideration (Xu et al., 1998; Xu, 1999; Xu et al., 2000a). In addition, with FEM, the 3D spatial modes can naturally be processed in buffeting analysis.

2.1.2.5 *Nonlinear Effects*

As mentioned above, in the Lin's time-domain flutter-buffeting theory, the effect of alongwind turbulence on self-excited aeroelastic forces is taken into account by

expressing the aeroelastic forces as a random variation associated with the dynamic pressure of mean wind speed plus random fluctuations. However, non-linear effects of turbulence, both alongwind and vertical components, on self-excited and buffeting forces due to the transient inclination angle of wind to bridge deck plane are generally neglected in the Lin's time-domain flutter-buffeting theory and the other frequency-domain buffeting theories mentioned foregoing based on the assumption of linearity. However, the results of the field measurements carried on the Humber Bridge (Bocciolone et al., 1990) show that the variation of instantaneous inclination angle between wind to bridge deck due to the fluctuation components of wind velocity can reach ±10° with the usual turbulence intensity of around 10%. Moreover, as well known, flutter derivatives are highly sensitive to the inclination angle variation (Zasso and Curami,1993). Thus, by using artificially simulated space-time history of turbulent wind, several time-domain methods have been presented to consider this kind of the non-linear effects and the similar effects of variation of the inclination angle between wind and bridge deck due to the deck motion.

Wall and Bucher (1992a, 1992b) utilised an "corrected quasi-static linearized theory" to model the aerodynamic forces associate with wind turbulence, and counted separately for the forces dependent on deck motion by means of the convolution integral with deck translations, rotation and velocities of motion as inputs. Similar to the identification of flutter derivatives using wind tunnel test, the response of wind deck-motion-depended forces to an impulsive variation of each the single input is extracted from measured information by wind tunnel test. By introducing indicial functions for the portion of turbulence-related forces, the Wall's method could be further improved to consider the effect of unsteady flow, as proposed by Li and Dexin (1997). Nevertheless, non-linearity cannot be taken into consideration in this method, for it separately treats the turbulence-induced and deck-motion-induced wind forces.

To take this sort of non-linearity into account, Miyata et al. (1995) established the wind forces using the quasi-static theory. Both portions of the variation of the transient inclination angle between the wind and deck due to the wind turbulence components and the deck motion velocity were accounted for in these formulas. And, the aerodynamic coefficients are used as the functions of the total inclination angle

including the initial static portion and the variant portion mentioned above. However, this approach does not consider the dependency of the aerodynamic coefficients on the reduced wind speed or reduced frequency, and therefore, in principle, is not adequate for the cases of unsteady wind. In fact, the conventional quasi-steady linear theory is effective only for the cases of sufficiently low reduced frequencies, of which the turbulence scale of wind should be in the order of 10 times larger than the width of bridge deck, and hence the wind flow around the bridge deck can be regarded as spatially smooth in any given instant of time. One may try to solve this problem by introducing indicial functions, but the determination of the indicial functions varying with inclination angle is very difficult at the present stage.

To include the non-linear effects due to the inclination angle variation and the contributions of high frequency components of wind turbulence in buffeting response analysis, Diana proposed a "corrected quasi-static linear theory" to establish the non-linear aerodynamic forces dependent on wind turbulence, deck motion and the reduced velocity (Diana et al., 1995; Diana et al., 1998; Diana et al., 1999a; Diana, et al. 1999b). The spectra of wind turbulence are divided, at first, into a low frequency range (labelled "0") with the reduced frequency less than 0.1, for which the aerodynamic coefficients can adequately be regarded as reduced-frequency-independent, and a number of small high frequency ranges labelled "1","2", etc. A series of artificial space-time histories of wind, $u_0(t)$, $w_0(t)$, $\Delta u_1(t)$, $\Delta w_1(t)$, $\Delta u_2(t)$, $\Delta w_2(t)$, etc. can then be generated, representing the contributions of wind turbulence within different frequency ranges previously introduced. The total buffeting response, $\mathbf{X}(t)$, can be expressed with the superposition of the sub-responses, $\mathbf{X}_0(t)$, $\mathbf{X}_1(t)$, $\mathbf{X}_2(t)$, etc. contributed by wind turbulence within different frequency range.

Initially disregarding the contributions of high frequency wind turbulence, the low frequency response, $\mathbf{X}_0(t)$, can thus be obtained with the method similar to that employed by Miyata et al. (1995), based on the conventional quasi-steady linearized theory. In this way, the non-linear effects of the resultant relative inclination angle of transient wind on the aerodynamic forces are kept into consideration, whilst the aerodynamic unsteadiness is regarded as negligible in the low frequency region.

Based upon the fact that the main portion of the inclination angle variation is associated with the range of low frequency, the high frequency wind turbulence components, $\Delta u_1(t)$, $\Delta w_1(t)$, $\Delta u_2(t)$, $\Delta w_2(t)$, etc. and the corresponding high frequency responses, $\mathbf{X}_1(t)$, $\mathbf{X}_2(t)$, etc. are small compared with $u_0(t)$, $w_0(t)$ and $\mathbf{X}_0(t)$. Thus, the equation of motion can be linearised around the low frequency response, $\mathbf{X}_0(t)$, when calculating the high frequency portion of responses $\mathbf{X}_1(t)$, $\mathbf{X}_2(t)$, etc. A separate set of motion equations can be derived for each high frequency range, ignoring the coupling terms between the different frequency ranges.

To solve the high frequency portions of response from these linearised equations of motion, a modal approach is then introduced to consider the unsteadiness of aerodynamic coefficients in high frequency regions through multiplying the aerodynamic coefficients by several reduced-velocity or reduced-frequency dependent corrective coefficients. This corrective coefficients are expressed as the ratio between the Scanlan's flutter derivatives and the corresponding terms in wind forces formulas based on the linearized quasi-static theory (Diana et al., 1998) and can be determined through wind tunnel test. The corrective coefficients also depend on the inclination angle of wind, and are modulated by the variation of inclination angle corresponding to the already gained low frequency response, $\mathbf{X}_0(t)$.

2.1.3 Buffeting Analysis of Bridges under Yaw Wind

Various buffeting analysis theories, either in the time domain or in the frequency domain, have been introduced in the foregoing context. However, most of the previous investigations take mean wind at a right angle to the longitudinal bridge axis. This may not be true when compared with field observations (Bietry 1994; Zhu et al., 1999; Xu et al., 2000b). As pointed out in Chapter 3, both the inclination of the mean wind from the deck plane, and the yaw of the mean wind deviating from the normal of the bridge span were significant during the passage of Typhoon Victor over the Tsing Ma suspension Bridge in Hong Kong. The mean wind was seldom perpendicular to the bridge deck. In fact, for a long span bridge, the bridge alignment is always chosen under the guidance of wind rose plot in such a way that its normal can, as far as possible, evade from the dominant direction of the prevailing winds.

Hence, for long span bridges, strong winds always attack the bridge with a certain yaw angle. On the other hand, a so-called cosine rule has been traditionally used to handle the yaw wind. In this rule, the yaw wind is decomposed into two components, respectively, normal to and along the bridge longitudinal axis, and only the normal component is taken into account and the longitudinal components is ignored. However, some wind tunnel tests carried out for studying the effect of yaw angle of wind on the bridge buffeting response have revealed that the employment of the traditional cosine rule method may lead to an unsafe estimation of buffeting response of bridges under yaw wind.

A full aeroelastic model test of a suspension bridge was performed by Davenport et al. (1969) in turbulent wind with yaw angle at several levels of mean wind speed. The aim of this test was to get data for predicting, in the sense of probability, the bridge response level vs. return period by jointly integrating experimental response data and wind climate statistics. It was found that, for the completed bridge, the lateral RMS (root mean square) responses under different yaw angles up to 40° were generally at similar level for all four levels of mean wind speed (40, 60, 80, 100 mph in full scale). The vertical and torsional RMS responses under 40mph mean wind speed were almost independent of yaw angle when the yaw angle was less than 40°. For the other three levels of mean wind speed, the vertical and torsional RMS responses decreased with the increase of yaw angle, but obviously were inconsistent with the traditional cosine rule. For the erection phases, the results clearly showed that the relation between the RMS responses and yaw angle did not comply with the traditional cosine rule.

Furthermore, Tanaka and Davenport (1982) studied the yaw angle effects on the buffeting response through taut strip model wind tunnel tests in turbulent boundary layer. They found that, under the condition of low turbulence, the yaw wind effect could be fairly well reflected by the cosine rule, i.e., the major portion of the response was mainly contributed by the wind component normal to the bridge longitudinal axis. However, for winds with high turbulence, the cosine rule resulted in an underestimated result of model response. Irwin and Gamble (1985) also observed similar phenomena during the wind tunnel test of Annacis Island Bridge.

The results of the full aeroelastic model tests of Quincy Bridge, a cable stayed bridge, in Quincy, Illinois (Zan, 1987), also showed the high level vertical and torsional responses under a yaw wind of 30°, both for the full and half bridge status, compared to the same model under normal wind. The results of the full aeroelastic model test of Messina suspension bridge with a main span of 3300m (Diana et al., 1995; Diana, et al., 1999b) revealed that the dynamic response did not follow a cosine law for 30° yaw angle and was at the same level as for 0° yaw angle. This issue could also be found in the wind tunnel test results of the Pont de Normandie Bridge and the Kao Ping His Bridge (Kimura and Ohara, 1999), where the bridge response under yaw wind was observed to be larger than that of normal wind.

Thus, to gain more realistic prediction of buffeting response of long span bridges, it is necessary to develop a new buffeting analysis method, which is able to deal with skew winds. In addition, if risk or probability evaluation is required for buffeting response of long span bridges related to local wind climate, such as an expected annual peak response for a given return period as done by Davenport (Davenport et al., 1969, 1979; Davenport, 1977), the wind azimuth needs to considered in the buffeting analysis. This also leads to the demand for a new capable analytical method.

Another motivation for the development of the new buffeting analysis method suitable to the skew wind condition is the demands of verifying analytical results of buffeting response by comparing with field measurement results. This kind of comparison has been paid more and more attentions, and great efforts have been made (Okubo et al., 1979; Bietry 1994). However, due to the lack of adequate analytical methods for buffeting response of bridges under skew wind, the discrepancies between the computed and field measured responses were significant. Therefore, the foregoing analytical methods should be improved in order to perform reasonable comparisons. Nonetheless, to the best of the writer's recollection, only a few theoretical work has been done on this topic.

Xie and Tanaka (1991) proposed a method to deal with the yaw wind in buffeting analysis of long span bridges without free deck end. In their method, mean wind and along-/across-wind fluctuations were first resolved into normal and longitudinal components. The co-spectra between the resultant normal fluctuation and vertical

fluctuation at two points along the central line of bridge deck were then established by one of three models of horizontal space-time correlation of turbulence, i.e., the homogeneous isotropic model, the "frozen" model based on Taylor's hypothesis, and the so-called ellipse model proposed. Finally, by ignoring the wind component along the bridge deck and utilising the aerodynamic coefficients of true cross section, the buffeting responses of bridges were calculated mode by mode and the SRSS method was employed for the final resultant RMS responses. In addition, the buffeting response associated with lateral-torsional coupled modes, which often existed for cable-stayed bridges, was also treated in this method. According to the Xie's method, it seems that the yaw angle (β) affects the buffeting response by decreasing the effective mean wind by $\cos\beta$, decreasing the aerodynamic admittance due to the increase of reduced frequency by $1/\cos\beta$, and slightly increasing the integral magnitude of coherence.

Kimura and Tanaka (1992) also proposed a mode-by-mode method for vertical buffeting analysis of a cantilever beam based on a decomposition of wind and later, the method was applied to the vertical buffeting response analysis of a cable-stayed bridge at its erection stage (Kimura et al., 1994). In this theory, the mean speed of yaw wind is decomposed first by the cosine rule or sine rule into two orthogonal components, respectively, normal to and along the bridge longitudinal axis. Then, they are studied separately as a cosine case (for normal component) and a sine case (for longitudinal component). The strip theory and quasi-steady linearized theory are adopted for the both cases, and the strips are taken in the mean flow direction. The alongwind turbulence is neglected provided that the lift coefficient of bridge deck is small when the mean wind is horizontal. The contribution from the drag coefficient for the sine case is also ignored because the drag coefficient is difficult to be estimated and its effect is supposed to be small in this method. The slope of lift coefficient for the sine case is also difficult to measure in the wind tunnel. However, it is important for the sine case response and thus it is estimated with an approximate means. For yaw angles in the small vicinity about 0°, the response may be estimated with only the cosine case. For yaw angles in the close proximity of 90°, the response may be obtained approximately with only the sine case. However, for yaw angles in between, it is uncertain to assign the turbulence fluctuation to the cosine and sine cases. Furthermore, how to combine the results of two cases is also a complicated

problem. Wind tunnel test was carried out with three cantilever beam models of flat plate sections to check the method (Kimura and Tanaka 1992). Although the responses of cosine case are generally lower than the measured model responses, they seem quite close to each other when yaw angle is less than 60°. However, the results of sine case are very different from the measured even if the wind approaches the model with near 90° from it free end. This means that the sine rule proposed in this method, as well as the corresponding approximate model of the lift coefficient slope, may be unsuitable. The calculated results of a cable-stayed bridge in its construction stage are also quite different from the wind tunnel test results under the yaw wind of 0°, 10° and 90° (Kimura et al., 1994).

Scalan (1993) also developed a buffeting analysis method for cable-stayed bridges in erection stages. Similar to the Kimura's method, the skew wind, including mean and turbulent components, is decomposed into two components, respectively, normal and parallel to the bridge longitudinal axis. Based on the strip theory and quasi-steady linear theory, the buffeting forces and self-excited forces are then formulated separately for normal wind component and parallel wind component, considering the vertical static deflection and dynamic deflection of one single mode and its slope along deck axis. Different from the Kimura's method, the strips along true cross section are adopted in this method, instead of the oblique strips along the mean wind direction. And the wind loads for the above two cases are combined when forming the generalized wind force. Some new aerodynamic coefficients and flutter derivatives, which are very difficult to be determined at present for a long span bridge, are introduced into this method to describe the wind force of parallel case. Thus, there is still a long way to apply this method into engineering practice.

Furthermore, based upon a cantilever beam model, Kimura and Ohara (1999) presented a method for single mode analysis of lateral sway buffeting of bridge at its erection stage in yaw wind, using the strip theory and quasi-steady linear theory. In this method, the longitudinal component of wind load was ignored and the strip along true the cross section was adopted, as done by Xie and Tanaka (1991) , but the wind remains in yaw. The formula of normal wind load was established by introducing a static normal force coefficient, which was expressed as a function of yaw angle and longitudinal location of strip. The effect of the horizontal lateral

turbulence fluctuation on the normal wind force was also taken into account by considering the yaw angle variation due to the velocity fluctuation. Because of the limited length of the cantilever beam model, the normal force coefficient should vary along the model longitudinal axis. A linear model and a non-linear model of power law were thus used to simulate the coefficient distribution. The shape of the coefficient distribution was found to affect the response considerably. The calculated results were generally less than the measured results for the corresponding wind tunnel tests of several bridges. Especially, the discrepancies were conspicuous not only for the bridges concerned in the cases of the yaw angle larger than 40°, but also for the Pont de Normandie Bridge even in the cases of small yaw angle.

Based on a conventional quasi-steady linear theory, Strømmen and Hjorth-Hasen (1995) proposed a set of formulae of buffeting forces acting on a structural element with an arbitrary attitude in the wind flow using FEM. Again, the method of the simple decomposition of wind speed was used, and only the normal component was considered for lift, drag and pitching moment, and only the parallel component was included for the crosswind force along the elemental axis. The rolling moment and yawing moment were neglected. Besides, the influence of wind yaw on the aerodynamic coefficients of lift, drag and pitching moment was supposed to be insignificant. Thus, it was assumed that these coefficients were only functions of wind inclination and took the values associated with the true section. However, the coefficient of the crosswind force along the elemental axis was supposed to be only a function of wind yaw.

To cater to the demands for more realistic prediction of buffeting response of long span bridges under skew turbulent wind and to carry out reasonable comparison between computed and field measured buffeting responses, a new frequency-domain analysis method and the associated computer program will be developed in this thesis based on the strip theory and the quasi-steady linear theory. The concept of oblique strip along mean wind direction will be employed in this method. Buffeting forces of six components acting on the oblique strip will be described first in the local coordinate system of the yawed mean wind with the corresponding six aerodynamic coefficients, which are related to the oblique strip. Then they will be transformed to the structural coordinates system. Thus, it is not necessary to have any

decomposition on the mean wind and the corresponding turbulence perturbations. All three turbulence components will be taken into account when formulating the buffeting force. However, to commence a real buffeting analysis, the above-mentioned aerodynamic coefficients associated with oblique cross section should be determined beforehand.

Because bridge deck is generally a bluff-body and has its own exterior appearance, its aerodynamic coefficients are usually obtained through wind tunnel static tests or dynamic tests, using either force/moment balances, dynamometers or pressure-measurement method (Ferraro and Irwin, 1990; Damsgaard and Jensen, 1990; Falco et al., 1992). Nevertheless, most of the tests have been carried out for the measurements of the coefficients of three component aerodynamic forces of the true cross section of bridge deck, few for measuring all coefficients of six component forces. Thus, the knowledge about six-component aerodynamic coefficients of bridge deck is still very poor for the case of skew wind.

Vicent (1953) carried out a series full model wind tunnel tests to investigate the wind forces on highway bridges with short span. The results were also cited in Sachs 1978. For the case of multi-plate girder bridges, skew winds tend to increase the lift force and reduce the lateral force, and the longitudinal force is small even in lager yaw angle of 40°. However, for the case of truss girder bridges, skew winds cause relatively little change of lateral force up to 20° yaw angle, and result in significant longitudinal force at larger yaw angle. In spite of this information, the values of six component aerodynamic coefficients under skew wind condition are still unclear for the special case of the Tsing Ma bridge deck, which has a very complicated exterior appearance. Thus, a particular wind tunnel test with special test rigs and model will be conducted in this study as introduced in Chapter 6 to obtain the six components of aerodynamic coefficients of the Tsing Ma Bridge deck under the skew wind condition. Apart from the six-component aerodynamic coefficients of the bridge deck, aeroelastic coefficients (flutter derivatives) associated with oblique cross section are also necessary for a modified buffeting analysis to take the aeroelastic self-excited forces into account. Therefore, various approaches for determination of aeroelastic coefficients are reviewed in the next section.

2.2 IDENTIFICATION OF AEROELASTIC COEFFICIENTS

2.2.1 Models for Self-excited Forces

As it is well known, self-excited (aeroelastic) forces on bridge deck play a major role in aeroelastic instability analysis and a large role in buffeting response prediction of long span bridges in natural strong wind. Investigation on aeroelastic instability or flutter of bridges commenced only after the collapse of the original Tacoma Narrows Bridge in November 1940 due to wind-excited torsional unstable vibration although many wind-induced failures of bridges had already been observed before this collapse. The earlier aerodynamic instability analysis of bridge was based on the Theodorsen's flat plate theory for flutter of aircraft wings (Bleich, 1949), in which the unsteady motion-dependent self-excited lift and pitching moment on unit length deck segment were derived using potential flow theory as follows (Theodorsen, 1935):

$$L_{se} = -\pi\rho bU^2\left\{2C(k)\frac{\dot{h}}{U}+[1+(1-2a)C(k)]\frac{b\dot{\alpha}}{U}+2C(k)\alpha-\frac{ab^2\ddot{\alpha}}{U^2}+\frac{b\ddot{h}}{U^2}\right\} \tag{2-2a}$$

$$M_{se} = \pi\rho b^2U^2\left\{(1+2a)C(k)\frac{\dot{h}}{U}+\frac{1}{2}[(1+2a)C(k)-1](1-2a)\frac{b\dot{\alpha}}{U}\right.$$
$$\left.+(1+2a)C(k)\alpha-\frac{1}{8}(1+8a^2)\frac{b^2\ddot{\alpha}}{U^2}+\frac{ba\ddot{h}}{U^2}\right\} \tag{2-2b}$$

where ρ is the air density; b is the half width of the flat plate; $a\times b$ is the coordinate of the rotation axis in p direction, and generally is zero for bridge deck. U is the wind speed; h and α are, respectively, the vertical displacement and torsional angle of vibration (see Figure 2-1); $k=\omega b/U$ is the non-dimensional reduced frequency of vibration; ω is the circular frequency; and $C(k)=F(k)+iG(k)$ is called Theodorsen's function expressed as follows

$$F(k)=\frac{J_1(k)[J_1(k)+Y_0(k)]+Y_1(k)[Y_1(k)-J_0(k)]}{[J_1(k)+Y_0(k)]^2+[Y_1(k)-J_0(k)]^2} \tag{2-3a}$$

$$G(k)=-\frac{J_1(k)J_0(k)+Y_1(k)Y_0(k)}{[J_1(k)+Y_0(k)]^2+[Y_1(k)-J_0(k)]^2} \tag{2-3b}$$

where J_i and Y_i are the Bessel functions of the first and second kind, respectively, of order i.

The above Thoedorsen's formulas may be applicable to describe the aeroelastic forces acting on a bridge deck with flat streamline cross section. However, it is obviously inadequate to be directly applied to much more aerodynamically bluff deck sections such as that of the Tacoma Narrow Bridge, because the potential flow theory employed is no longer applicable to these cases due to the effect of flow separations. In the absence of any pure theoretical means to determine aeroelastic motion-dependent self-excited forces acting on aerodynamically bluff deck sections, great efforts have then been put into the experimental approaches through wind tunnel tests and identification of system parameters. Taking the form similar to the Theodorsen's formulas, the aeroelastic forces are commonly expressed as the linearised functions of translational and torsional displacements and velocities of bridge deck with various representation conventions of aeroelastic coefficients to be determined experimentally.

Based on the assumptions of linearity and small amplitude vibration, Scanlan and Tomko (1971) expressed the self-excited lift force and pitching moment acting on a bluff deck as the linear functions of displacements and velocity of deck motion by introducing some coefficients, the so called flutter derivatives. Generally speaking, the flutter derivatives introduced can only be evaluated experimentally for the particular bluff shape of bridge deck in question. The Scanlan's representation convention for the aeroelastic self-excited forces has been widely used in the practice of wind-induced instability analysis and buffeting prediction of long span bridges (Gade et al.,1976; Beliveau and Vaicaitis, 1977; Scanlan and Gade, 1977; Scanlan, 1978a; Scanlan, 1978b; Scanlan and Lin, 1978c; Scanlan, 1981; Scanlan, 1987b; Huston, 1987; Huston et al., 1988; Agar, 1989; Dowell et al., 1989; Scanlan and Jones, 1990; Scanlan, 1992; Namini et al., 1992; Singh et al, 1995; Pfeil and Batista, 1995; Simiu and Scanlan, 1996; Jain et al., 1996a; Jain et al., 1996b; Scanlan, R.H., 1997; Cai et al., 1997; Scanlan et al., 1997; Xu et al., 1998; Thorbek and Hansen, 1998; Astiz, 1998; Jones and Scanlan, 1998; Katsuchi et al., 1999; Scanlan, 1999; Cobo del Arco and Aparicio, 1999; Lau et al., 2000; Ge and Tanaka, 2000a; Ge and Tanaka, 2000b). Among these applications, the most general expressions of self-excited forces on unit length deck segment with Scanlan's representation convention are as follows

$$L_{se}=\frac{1}{2}\rho U^2 B\left[KH_1^*\frac{\dot{h}}{U}+KH_2^*\frac{B\dot{\alpha}}{U}+K^2H_3^*\alpha+K^2H_4^*\frac{h}{B}+KH_5^*\frac{\dot{p}}{U}+K^2H_6^*\frac{p}{B}\right] \quad (2\text{-}4a)$$

$$D_{se}=\frac{1}{2}\rho U^2 B\left[KP_1^*\frac{\dot{p}}{U}+KP_2^*\frac{B\dot{\alpha}}{U}+K^2P_3^*\alpha+K^2P_4^*\frac{p}{B}+KP_5^*\frac{\dot{h}}{U}+K^2P_6^*\frac{h}{B}\right] \quad (2\text{-}4b)$$

$$M_{se}=\frac{1}{2}\rho U^2 B^2\left[KA_1^*\frac{\dot{h}}{U}+KA_2^*\frac{B\dot{\alpha}}{U}+K^2A_3^*\alpha+K^2A_4^*\frac{h}{B}+KA_5^*\frac{\dot{p}}{U}+K^2A_6^*\frac{p}{B}\right] \quad (2\text{-}4c)$$

where $B=2b$ is the deck width; $K=B\omega/U$ is the reduced frequency and it is noted to be 2 times of k in Eqs.(2-2) and (2-3); 18 non-dimensional coefficients H_i^*, P_i^* and A_i^* (i=1, 2, ..., 6) are called flutter derivatives and are functions of reduced frequency K. H_1^*, H_4^*, P_1^*, P_4^*, A_2^* and A_3^* are called direct flutter derivatives, representing the contributions of vertical translational motion (h, $\dot{h}$) to lift force (L_{se}), of lateral translational motion (p, $\dot{p}$) to drag force (D_{se}), and of torsional motion (α, $\dot{\alpha}$) to the pitching moment (M_{se}). Meanwhile, the others are called coupling or cross flutter derivatives measuring self-excited forces or moments in the direction of one DOF contributed by the deck motion in one of the other two DOFs.

Besides the Scanalan's representation convention, there have been various conventions. In French, the flutter derivatives are known as 8 Küssner coefficients: k_{1a}, k_{2a}, k_{1b}, k_{2b} and m_{1a}, m_{2a}, m_{1b}, m_{2b} as in the application of the Normandy Bridge (Virgoleux, 1992). The self-excited lift and moment on unit length deck segment are expressed as follows

$$L_{se}=\frac{1}{2}\rho U^2 B\left[2\pi\left(k_{1a}\frac{h}{B}+k_{2a}\frac{\dot{h}}{B\omega}\right)+\pi\left(k_{1b}\alpha+k_{2b}\frac{\dot{\alpha}}{\omega}\right)\right] \quad (2\text{-}5a)$$

$$M_{se}=\frac{1}{2}\rho U^2 B^2\left[\pi\left(m_{1a}\frac{h}{B}+m_{2a}\frac{\dot{h}}{B\omega}\right)+\frac{\pi}{2}\left(m_{1b}\alpha+m_{2b}\frac{\dot{\alpha}}{\omega}\right)\right] \quad (2\text{-}5b)$$

In Japan, the self-excited forces and moment on unit length deck segment are frequently expressed in the following form (Shiraishi and Ogawa, 1979; Miyata et al., 1995; Miyata and Yamada, 1998; Yamada et al., 1999; Miyata, 1999)

$$D_{se}=\pi\rho b^2\omega^2\left[D_{pR}\tilde{p}+D_{pI}\frac{\dot{\tilde{p}}}{\omega}+D_{hR}\tilde{h}+D_{hI}\frac{\dot{\tilde{h}}}{\omega}+D_{\alpha R}\alpha+D_{\alpha I}\frac{\dot{\alpha}}{\omega}\right] \quad (2\text{-}6a)$$

$$L_{se} = \pi\rho b^2\omega^2\left[L_{pR}\tilde{p} + L_{pI}\frac{\dot{\tilde{p}}}{\omega} + L_{hR}\tilde{h} + L_{hI}\frac{\dot{\tilde{h}}}{\omega} + L_{\alpha R}\alpha + L_{\alpha I}\frac{\dot{\alpha}}{\omega}\right] \quad (2\text{-}6b)$$

$$M_{se} = \pi\rho b^4\omega^2\left[M_{pR}\tilde{p} + M_{pI}\frac{\dot{\tilde{p}}}{\omega} + M_{hR}\tilde{h} + M_{hI}\frac{\dot{\tilde{h}}}{\omega} + M_{\alpha R}\alpha + M_{\alpha I}\frac{\dot{\alpha}}{\omega}\right] \quad (2\text{-}6c)$$

where $\tilde{p}$ and $\tilde{h}$ are the lateral and vertical translation displacement of deck motion normalised by the half width b. α is, as foregoing, the twisting angle of the deck. D_{pR}, D_{pI}, D_{hR}, D_{hI}, $D_{\alpha R}$, $D_{\alpha I}$, L_{pR}, L_{pI}, L_{hR}, L_{hI}, $L_{\alpha R}$, $L_{\alpha I}$, and M_{pR}, M_{pI}, M_{hR}, M_{hI}, $M_{\alpha R}$, $M_{\alpha I}$ are 18 frequency-dependent aeroelastic coefficients. Obviously, the models of self-excited forces shown in Eqs.(2-5) and (2-6) are equivalent to those of Scanlan's, and thus the aeroelastic coefficients here and Scanlan's flutter derivatives can be converted to each other.

As reviewed foregoing, during the research works concerning the design of the Messina Bridge in Italy, Diana et al. developed a "corrected quasi-static linearized theory" to calculate the wind-induced forces due to the combined effect of deck motion and turbulent wind action (Diana et al, 1992; Falco et al, 1992; Diana et al., 1993; Diana et al., 1998; Diana et al., 1999a; Diana, et al. 1999b). The corrected quasi-static linearized theory provides the possibility of taking into consideration the non-linear effect of the effective inclination angle of wind flow on the aeroelastic coefficients or flutter derivatives. As the dependency of the aeroelastic coefficients on the reduced frequency (K) or the reduced velocity (V^*) cannot be reflected in the traditional quasi-steady linearized formulas, the application of the traditional quasi-steady linearized theory should be confined to those cases where V^* is sufficiently high, say greater than 10, in principle. In these cases, the time taken by the flow to cross the deck section is much shorter than the period of deck vibration so that the flow around bridge deck can be approximately regarded as steady. To make the self-excited model applicable to the cases with lower V^*, some so-called "corrective coefficients", h_i, g_i, a_i, $i=1,2,3,4$, which are the functions of reduced frequency and effective inclination angle, are introduced to correct the "quasi-steady linearized aeroelastic forces". These corrective coefficients are expressed as the ratio between the Scanlan's flutter derivatives and their corresponding terms in the linearized

quasi-steady formulas, and they should be determined experimentally. As a result, the aeroelastic self-excited forces are represented as follows.

$$\begin{Bmatrix} F_y \\ F_z \\ M_x \end{Bmatrix}_{se} = \mathbf{K}_{F0} \begin{Bmatrix} y \\ z \\ \theta \end{Bmatrix} + \mathbf{R}_{F0} \begin{Bmatrix} \dot{y} \\ \dot{z} \\ \dot{\theta} \end{Bmatrix} \tag{2-7}$$

$$\mathbf{K}_{F0} = \frac{1}{2}\rho b U^2 \begin{bmatrix} 0 & 0 & g_3 K_{D0} \\ 0 & 0 & h_3 K_{L0} \\ 0 & 0 & a_3 b K_{M0} \end{bmatrix} \tag{2-8a}$$

$$\mathbf{R}_{F0} = \frac{1}{2}\rho b U \begin{bmatrix} -2g_4 C_{D0} & g_1(K_{D0}+C_{L0}) & -g_2 b_{1y}(K_{D0}+C_{L0}) \\ -2h_4 C_{L0} & h_1(K_{L0}-C_{D0}) & -h_2 b_{1z}(K_{L0}-C_{D0}) \\ -2a_4 b C_{M0} & a_1 b K_{M0} & -a_2 b_{1\theta} b K_{M0} \end{bmatrix} \tag{2-8b}$$

where y, z and θ are, respectively, the lateral and vertical translation displacements, and the twist angle of oscillation of bridge deck. C_{D0}, C_{L0} and C_{M0} are the mean drag, lift and pitching moment coefficients at zero inclination angle, respectively. K_{D0}, K_{L0} and K_{M0} are the derivatives of drag, lift and pitching moment coefficients with respect to inclination angle at the zero inclination angle. B is half width of bridge deck. b_{1y}, b_{1z} and $b_{1\theta}$ are characteristic parameters of the deck. The details about the meaning of the symbols used can be referred to Diana, et al. (1999b).

In China, Xie developed a state-space method based on linear and small amplitude oscillation assumption, to carry out flutter analysis of long span bridges in the Laplace domain (Xie, 1984; Xie and Xiang, 1985). In this method, the aeroelastic self-excited forces are described in the Laplace domain using Roger's series form of rational fraction as follows

$$\begin{Bmatrix} D_{se} \\ L_{se} \\ M_{se} \end{Bmatrix} = \rho U^2 \begin{bmatrix} 1 & 0 & 0 \\ 0 & 1 & 0 \\ 0 & 0 & B \end{bmatrix} \mathbf{A}(\bar{s}) \begin{bmatrix} 1 & 0 & 0 \\ 0 & 1 & 0 \\ 0 & 0 & B \end{bmatrix} \begin{Bmatrix} \delta_x \\ \delta_y \\ \delta_\theta \end{Bmatrix} \tag{2-9}$$

where δ_x, δ_y and δ_θ are, respectively, the lateral, vertical and torsional displacements of deck motion; B is the deck width; $\bar{s} = \beta + iK = B/U(-\xi\omega + i\omega)$; $i = \sqrt{-1}$; β and K are, respectively, the reduced damping coefficients and frequency; and $\mathbf{A}(\bar{s})$ is a 3×3 matrix of aeroelastic coefficients expressed with the following Roger's series form of rational fraction.

$$\mathbf{A}(\bar{s}) = \mathbf{P}_1 + \mathbf{P}_2 \bar{s} + \mathbf{P}_3 \bar{s}^2 + \sum_{j=1}^{N_\gamma} \frac{\bar{s}}{\bar{s} + \gamma_j} \mathbf{Q}_j \tag{2-10}$$

where γ_j is the jth positive model parameter; $\mathbf{P}_1$, $\mathbf{P}_2$, $\mathbf{P}_3$ and $\mathbf{Q}_j$ ($j = 1,...,N_\gamma$) are 3×3 coefficient matrices which are independent of vibration frequency of deck and should also be obtained experimentally. The first term represents the contribution of aerodynamic stiffness while the second term denotes the contribution of aerodynamic damping. The third term indicates the contribution of aerodynamic inertia, which is conventionally ignored, such as, in the Scalan's model. The terms of rational fraction represent the unsteady components that lag the contribution of aerodynamic stiffness, namely, the self-excited forces depend upon not only the current structural motion state but also the past structural motion state. In this model, different model parameters reflect different time lags. Thus, more terms of the rational parts, more past state contributions of structural motion are counted for the self-excited forces. On the other hand, the current self-excited forces certainly affect the future structural motion. Actually, this model reflects the interaction between air flow and structural motion to some extent, which is not included in the conventional models. Another important advantage of the rational fraction model consists in the independence of the coefficient matrices from the oscillatory frequency, which facilitates the solution of flutter to great extent when using the state-space method without any iterative calculation.

In recent years, the rational fraction model of self-excited forces and the corresponding state-space method have drawn the attentions of some investigators and have been applied to flutter and buffeting analyses in either the frequency domain or the time domain (Boonyapinyo et al., 1999; Chen and Kareem, 1999; Chen et al., 2000a; Chen et al., 2000b;). Agar (1989, 1991) and Katsuchi et al. (1998) also used the state-space method to solve flutter problem of suspension bridges, but the iterative calculation is still inevitable in their approaches because of the adoption of the Scanlan's or Theodorsen's self-excited force models, both of which are of functions of oscillatory frequency.

Apart from the frequency domain method, flutter and buffeting analysis of bridges can also be carried out in the time domain (Lin & Arianratnam, 1978; Lin, 1979a; Lin, 1979b; Lin and Arianratnam, 1980, Chen et al., 2000a). In those approaches,

aeroelastic forces are often expressed with time-dependent aerodynamic indicial functions. The indicial functions are rather difficult to directly determine the indicial functions for aerodynamic bluff sections. However, they can be obtained by inverse Fourier translation from the experimentally-determined Scanlan's flutter derivatives (Scanlan and Budlong, 1972; Scanlan et al., 1974; Scanlan, 1978b; Scanlan, 1984; Scanlan, 1993b; Scanlan, 1996), or by the inverse Laplace transform from the coefficients of aeroelastic forces in Roger's rational fraction form (Chen et al., 2000a).

2.2.2 Identification of Aeroelastic Coefficients (Flutter Derivatives)

As aforementioned, aeroelastic motion-dependent self-excited forces acting on aerodynamically bluff deck sections can, generally speaking, only be determined through experimental approaches. Thus, various methods of experiments and corresponding identification of parameters have been developed. In light of vibration type, they can basically be classified into two major categories: forced vibration method and free decayed vibration method. According to the test object, they can also be categorised into four major types: sectional model test, taut strip model test, full model test, and full-scale measurement of ambient vibration.

2.2.2.1 Vertical and Torsional Aeroelastic Coefficients

Ukeguchi et al. (1966) was probably the first to apply the forced vibration method to measure the aeroelastic forces on bridge deck. The method was further extended and developed in Japan and elsewhere in the world to cover various aerodynamic bluff sections (Tanaka, 1971; Otsuki et al., 1974; Matsumoto et al., 1993; Curami and Zasso, 1993; Matsumoto, 1994; Zasso, 1996) and to investigate the non-linear effects of deck motion on wind-induced forces (Falco et al., 1992). In this approach, rigid sectional models were mechanically driven into simple harmonic motion of one or two DOFs in two dimensional wind flow with a series of specified oscillatory amplitudes and frequencies and, if necessary, amplitude ratios and phase lags between the motions of two DOFs. The total external forces acting on the deck models, including the aerodynamic, aeroelastic motion-dependent and motion-induced inertia forces, are measured using dynamometers. Meanwhile, the acceleration information is recorded to eliminate inertial forces from the measured overall forces. And the aeroelastic coefficients can be then extracted from measured

data based on the corresponding force model employed. The unsteady wind-induced forces on the force-driven models can also be evaluated by direct real-time integration of the distribution of instantaneous dynamic pressure signals synchronously measured by means of pressure taps installed on the model surface and the high speed pressure scanning technique (Matsumoto et al., 1993; King et al., 1991). Clearly, the pressure measurement approach is only applicable to air-sealed box sections, not for any open sections. The forced vibration method is sometimes implemented in water tunnel to promote the measurement accuracy of the flow-induced forces on the model by making use of the higher density of water (Li, 1995).

Beside wide application of forced vibration method, free decay oscillation method has also been a popular experimental approach in the world. Scanlan and his co-workers (Scanlan and Sabzevari, 1967; Scanlan and Tomko, 1971) initiated the application of this approach to the bridge aeroelastics using a spring-suspended sectional model of 2DOFs which can be tuned for a coupled vertical and torsional motion. In the practice of this method, the torsional and vertical motions have to be restrained respectively to extract the so-called direct flutter derivatives by means of the logarithm decrement method, from recorded signals of free decay oscillation of single DOF with a certain initial displacement. Then, to obtain the coupled flutter derivatives, the model should be tuned for every grades of applied wind speed so that the resulting vertical and torsional motions $h(t)$ and $\alpha(t)$ of the model, given a certain initial displacement condition, have the same damped frequency and decay rate. Meanwhile, the direct derivatives, already obtained from the single DOF vibration tests, are supposed to be valid in the case of coupled vibration irrespective of the inconsistency in the vibration states.

The Scanlan's method has been widely practised over the world (Huston, 1987, etc.). However, it was found extremely difficult to attain the same frequency and decay rate even though all the initial displacement and mechanical conditions of the model were satisfied. Therefore, a method of "coupled model" with a certain eccentricity between its mass and elastic centres was devised by Kumarasena (1989) to facilitate the test procedure. In this method, the coupled flutter derivatives are identified from the curve of the cross-covariance $R_{h\alpha}(\tau)$ between the resulting $h(t)$ and $\alpha(t)$, which are found to have the same decay rate and damped frequency as $h(t)$ if the model is

given a certain initial vertical displacement and allowed to couple with the torsional motion mechanically as well as aerodynamically. The direct flutter derivatives, obtained in advance through single DOF vibration test, also have to be employed while extracting the coupled flutter derivatives.

In the last two decades, many efforts have been made to reduce the requirements for techniques in the test and measurement, and to avoid the inconsistency in the vibration states of model when identifying the direct and coupled flutter derivatives in Scalan's and Kumarasena's methods. Developments of sophisticated system identification (SI) techniques have made it possible to simultaneously extract the direct and coupled derivatives using fully coupled vibration test of spring-suspended sectional model (Sarkar et al., 1991; Poulsen et al., 1991; Yamada et al., 1991; Jakobsen and Hjorth-Hasen, 1993). Earliest work in SI may date back from the earlier 1970s. Various SI methods, such as the Ordinary Least Squares (OLS), Instrumental Variable (IV), Kalman Filtering, Maximum Likelihood (ML), Limited Information Maximum Likelihood (LIML) and Generalised Least Squares (GLS), Auto Regressive Moving Average with Measured Input (ARMAX) model, have been applied to structural dynamics problems in the past (Imai et al., 1989), taking the noisy signals of either displacement or velocity or accelerations or a combination of the multi-DOF sectional model motion as inputs to these methods. All these methods have certain limitations.

As aforementioned, Scanlan and Tomko (1971) used the logarithmic decrement method to extract the damped frequency and the decay rate of free oscillation of single DOF. Beliveau, J.G. (1973) adopted a non-linear least square method to identify the flutter derivatives of bridge decks both in laminar and turbulent wind flow. This method is based on a Taylor series expansion of the parameter matrix about some initial estimates of this matrix and its convergence rate of iteration is of second order. However, the final estimates are largely dependent of the quality of the initial estimates of the parameters.

More recently, Shinozuka et al. (1982) applied the ARMA model to identify the flutter derivatives. Linear multi-DOF structural dynamic system was represented with ARMA model based on the observed discrete samples of excitation and response. The system parameters, further the flutter derivatives, were then extracted

with various identification methods, such as IV method and LIML method. Yamada et al. (1991) introduced the Extended Kalman Filter (EKF) method into the identification of aeroelastic coefficients using the recorded displacement and velocity signals and the corresponding initial conditions of coupled free decay oscillation. By introducing weighted global iterations into the EKF method (EKWGI), the convergence of the identification procedure can be further accelerated (Hoshiya and Saito, 1984; Iwamoto and Fujino, 1993). Yamada and Miyata (1997) further proposed a modal decomposition and reassembly (MDRA) method. All observed responses over a wide range of wind speed are firstly decomposed into the modal information by means of the EKWGI method. The obtained modal information is then reassembled and substituted into the equation of motion to get the aeroelastic forces. Poulsen et al.(1991) proposed a method combining control theory and system identification techniques to extract flutter derivatives from sectional model tests for the Great Belt East Bridge.

A so-called Ibrahim Time Domain (ITD) Method was developed in 1970s based upon the philosophy of the IV method, to directly extract properties of a dynamic system from harmonic decay signals of free coupled vibration (Ibrahim and Mikulcik, 1973, 1976, 1977). In this time-domain method, a system eigen matrix is first established using IV based upon all the sampled data of the decay response history of free coupled oscillation. The complex frequencies and modes of the vibration system are then inferred from the complex eigenvalues and vectors of the established system eigenmatrix. Two parameters of time shift are introduced to constitute the system eigenmatrix. In practice, an average positive and negative time shift techniques are often used to remove the positive bias in the real part of the estimated eigenvalues of the vibration system, which does occurs when only the positive time shift is used in ITD method (Pappa, 1983). However, the values of the two time shifts will still significantly affect the identified parameters, and the errors will be high if the number of measurements used to constitute the instrumental variables is the same as the number of system DOFs.

In practice, the errors in the estimated system parameters with the ITD method, especially the eigenvectors, were found rather high in the cases of high level noise. Thus, Sarkar et al. (1992; 1991, 1993, 1994) proposed a modified ITD (MITD)

method by introducing the iterative concept. The initial estimates of the system dynamic parameter are obtained from measured data using the average positive and negative time shift techniques of the ITD method. Then, a new group of emulated data of free response is generated using the first estimated parameters. Furthermore, a new instrumental variable and a corresponding new system eigenmatrix can be constituted using the same time shifts. The second estimates of system dynamic parameters thus can be obtained. The above steps will be repeated until the converged values of all dynamic parameters are attained. Numerical imitative calculation shows the higher accuracy of the MITD method than the ITD method, but how to take the proper time shifts for a unique system is still an open problem in the MITD method.

Recently, Zhang et al. proposed an Unifying Least Square (ULS) method to identify 8 Scanlan's flutter derivatives from the time histories of coupled free decay vibrations of a 2DOF spring-suspended sectional model in smooth or turbulent wind flow (Zhang, 1998; Gu et al., 2000). In this method, the initial values of complex dynamic properties of the vibration model system are first estimated using the MITD method. An unified error function composed of two error components of vertical and torsional motions was then defined as the objective function to optimize the complex dynamic properties starting from the estimated initial values. The optimization is carried out in turn for the linear parameters of complex mode and the non-linear parameters of complex frequency, respectively, with linear and non-linear least square method. Finally, the flutter derivatives were identified from the optimal complex dynamic properties. This method will be further introduced later in detail in this chapter, because it will be employed to identify the flutter derivatives of the Tsing Ma Bridge deck in Chapter 7.

As a complement to the state-space flutter analysis method, Xie (1984, 1986, 1988) presented a so-called the Coupled Vibration Records (CVR) method to extract the frequency-independent aeroelastic coefficient matrices in the self-excited force formula with the form of Roger's rational fraction. A simple spring-suspended sectional model is used in this method. The first step of CVR method is to establish the state equation and the system eigenmatrix based upon the CVR method under initial impulse. As is well known, for a bluff deck section, severe flow detachment

generally will happen under high wind speed, and this will initiate high level signature turbulences around the deck model, which do not comply with white noise assumption. Thus, to promote the identification accuracy, a concept of noise mode is introduced into the state equation and the system eigenmatrix is enlarged by m+1 times if m is the number of introduced noise modes. This means that the number of measurements is much larger than the number of the system DOFs. Furthermore, Kalman Filter methods is employed while generating the system eigenmatrix in the CVR method to diminish the noise disturbance and thus to promote the identification accuracy. The second step is to extract the structural modes as well as the noise modes from the enlarged system eigenmatrix. Afterwards, the structural modes can be picked out with tracing technique based on the corresponding initial values at zero wind speed, or with Ibrahim MCF method (Ibrahim, 1978). After obtaining the system dynamic parameters, the third step is then to identify the rational fraction model of the self-excited forces using the least square method based on the equation of motion in the Laplace domain. There are three time shifts used in the CVR method to constitute the system eigenmatrix. The choice of these time shifts is also a subtle problem. In addition, there is a relationship between these frequency-independent coefficients and the Scanlan's flutter derivatives, and thus can be transferred from/to each other (Xie, 1984; Zhu, 1991; Boonyapinyo et al., 1999; Chen and Kareem, 1999; Chen et al., 2000a; Chen et al., 2000b;).

2.2.2.2 Lateral Aeroelastic Coefficients

With the continuous increase of span length of modern long span bridges, the lateral response of bridges to wind becomes more significant than ever, and the flutter derivatives associated with lateral motion of bridge deck may exert considerable influence on wind-induced response of long span bridges. Theoretically, the aforementioned methods for identification aeroelastic coefficients are applicable to or can be expanded to the 3 DOF motion. However, this will lead to a much higher demand on test rigs and technique. Thus, the experimental data pertaining to the lateral motion-related flutter derivatives have been, heretofore, very poor. The quasi-steady linearized formula (Scanlan, 1987b) have often been used to estimate the lateral motion-related flutter derivatives in analysis.

Chen measured the direct lateral flutter derivative, P_1^*, of the Yangpu bridge deck through free decay lateral vibration test of a single DOF sectional model (Chen 1993; Chen and Xiang , 1993). The deck has a semi-open section with two small separated boxes and a width-over-height ratio of about 9.2. The oscillatory frequency was obtained by spectral analysis, and the logarithmic decay rate was extracted through the least square fitting of the envelope line of the decay vibration time history. P_1^* was, then, calculated from the identified frequency and damping ratio. The result showed that for the erection stage, the P_1^* curve of the sections without parapet was almost linear, but was only about 60% of that obtained with the quasi-steady linearized formula. For the case of the operation stage in which the parapets had been installed on deck, the curve pattern of P_1^* was far away from linearity. The curve was nearly linear within the range of reduced velocity (U/fB) lower than 2.0, and then became very flat and kept increasing very slowly until U/fB reached 8.0. After this, P_1^* increased rapidly with U/fB almost in second order. The experimental values of P_1^* were generally smaller than the quasi-steady estimates when the reduced velocity (U/fB) was less than 11.0.

A 3 DOF suspension rigs was developed in the Corrsin Wind Tunnel at the Johns Hopkins University for section modeling application (Jones et al., 1995). Using this rigs, Singh et al. (1996) measured the lateral direct flutter derivatives of the decks of the Tsurumi Fairway Bride (Japan) and the Deer Isle Bridge (USA). The former has a box section with width-over-height ratio of 10.4 whilst the latter has a H-type section with the aspect ratio of 3.6. The tests were conducted under smooth flow condition. The sectional model was suspended from a high-frequency force balance, and was restrained in vertical and torsional directions. A fixed initial displacement in lateral direction was given to the model using an electromagnetic release system operated outside the wind tunnel. Then, the time histories of total lift, moment and drag forces transferred to the balance through the aeroelastic suspension system were recorded, and the flutter derivatives were extracted from the recorded signals. The result shows a good agreement between quasi-steady and experimental values of P_1^* for the Tsurumi Bridge. In the case of the Deer Isle Bridge, the trend of measured P_1^* is similar to the quasi-steady one, although the values are conspicuously different

from each other. Additionally, the value of P_4^* for the Tsurumi Bridge has clear negative tendency at higher wind speed, leading to the increase in the lateral frequency of the bridge.

2.2.2.3 Turbulence Effects

Conventionally, the identification of aeroelastic coefficients is often conducted under smooth flow condition. However, turbulence may affect the aeroelastic coefficients in some subtle ways. One obvious reason is the variation of instantaneous wind direction due to the turbulence. Actually, the aeroelastic coefficients of bluff bridge deck are, generally, highly sensitive to the flow inclination angle (Zasso and Curami, 1993). On the other hand, the usual turbulence intensity of around 10% may lead to a change of the instantaneous wind inclination angle of ±10° (Bocciolone et al., 1990). Furthermore, turbulence will certainly affect the flow pattern around bridge deck, especially that with a streamline section, and the flow correlation along the deck chord. However, the degree of the turbulence effects on aeroelastic coefficient is largely dependent of the aerodynamic appearance of bridge deck and the ratio of the integral scales of turbulence to deck width. Thus, it is, of course, different from case to case.

Scanlan and Lin (1978) studied effects of turbulence on flutter derivatives through the test of a spring-suspended sectional model in both the laminar flow and turbulent flow. The tests were conducted state by state following the Scanlan's traditional method. Under laminar flow the model oscillated, from given initial positions, mainly in sinusoid with positive or negative damping. Under turbulent flow, the model was buffeted constantly, responding in a narrow-band random manner to turbulence. The flutter derivatives under turbulence flow were distinguished using response spectra and cross-spectra of buffeting forces and those of displacement responses. The turbulence was initiated with a grid of slats. The intensities was about 11% and the alongwind and lateral scales were about 93mm and 47mm, respectively. The model had a 76mm×38mm standard aluminum channel section with 19mm holes on its fringes regularly spaced at 38mm central intervals, which were used to suppress vortex-induced response. The results show that the presence of turbulence raise the flutter derivatives by an increment of no more than 15%. However, in the test, the ratio of the along wind turbulence scales to deck width is in the vicinity of

1.0, which is significantly smaller than in reality, six or more. Thus, the effects of turbulence may be overemphasised. The test results obtained by Huston et al. (1988) shows, on the other hand, that the flutter derivative A_2^* of the Tacoma Narrows Bridge deck or a similar H-section with the ratio of width-to-height being 3.6 or 4.6, is almost not affected by turbulence, even if the intensity is up to 20%.

Sarkar (1994) also carried out the measurement of the 8 flutter derivatives, associated with vertical and torsional motion, in turbulence wind flow using the same free coupled vibration approach and the MITD identification method as for the tests in smooth laminar flow. The test results suggest no definitive trend in the turbulence effects on flutter derivatives. For most of the 8 flutter derivatives, the turbulent-flow values differ only slightly from their smooth-flow counterparts. It seems that the smooth-flow values could represent the averages about which the turbulent-flow values fluctuate. However, the longitudinal turbulent intensity of the wind flow was no more than 3.5% in these tests. Hence, the drawn comments on the turbulence effects on flutter derivatives may not be suitable for the cases of high turbulence.

Zhang (1998) measured the flutter derivatives of flat plate section and the deck of Jiangying Bridge over Yangtse River, both in smooth and turbulence flows, using the Unifying Least Square method combining with free coupled vibration of sectional model. The deck of Jiangying Bridge has a streamline box section with a width of 36.9m and a width-to-height ratio of 12.3. The tests were carried out in the TJ-1 wind tunnel with a working segment of 18m long, 1.2m wide and 1.8m high, at Tongji University, China. The model widths of the flat plate and the Jiangying bridge deck model were 45cm and 52.7cm, respectively. The 10.5% turbulence with the integral scales of 42.5cm and 16.7cm, respectively, in alongwind and vertical directions, was generated with a grid of slats. The ratio of alongwind turbulence scale to model width is 0.94 for the flat plate model and 0.81 for the Jiangying Bridge model. Both of them were conspicuously lower than in reality. In spite of the possible overemphasised turbulence effects, the results still show that the turbulence effects on flutter derivatives may be ignored for bridge decks with streamline cross sections.

Jakobsen presented a flutter derivative identification method by directly utilising buffeting response data of sectional model to turbulent wind (Jakobsen, 1995;

Jakobsen and Hjorth-Hansen, 1995). The buffeting response data were first converted to the response covariance function estimate inheriting all the essential information of the dynamic system concerned. Then, the covariance block Hankel matrix (CBHM) method was employed for determining the dynamic matrix, consisting of the stiffness, damping and mass matrices of the motion system, from the covariance estimate. Finally, the flutter derivatives were identified from the obtained matrices of dynamic parameters combining those under still air. In this method, both the excitation and noise were assumed to be white noise process to decompose the response covariance estimate into a simple form. This may be the main reason why the identified H_2^* and H_4^* are dispersed rather widely.

Since 1990s, taut strip model tests, full model tests, and even full scale measurements have been employed for the identification of aeroelastic coefficients of bridge deck under turbulence flow. Davenport et al. (1992) conducted a forced vibration test of taut strip model in turbulent boundary layer flow to identify the flutter derivatives of the Storebaælt Bridge from the measured data of normalised cross-correlation of the input model acceleration and the output aerodynamic forces. The time-varying aerodynamic forces were also obtained by means of simultaneous measurement of pressures from distributed taps on box cross section, and the flutter derivatives were extracted.

Diana et al. (1995; 1999b) used a force-driven vibration test of aeroelastic full model in both smooth and turbulent flows to extract the aerodynamic parameters of the Massina Bridge deck. The time histories of exciting vertical force and torque were measured with two dynamometers, and the response time histories were simultaneously measured with optical displacement sensors. The dynamic parameters of the vibration system were identified, respectively, by analysing the decay response signals using a Hilbert transform for the smooth flow case and by extracting the transfer function between the exciting forces and displacement responses for the turbulent flow case. The result suggested no strong influence of turbulence on aeroelastic behavior.

Diana et al.(1992) made use of the responses of the Humber Bridge in U.K. obtained through full scale measurement to correct the aeroelastic coefficients gained by the

sectional model test. The complex modal eigenvalues of the bridge as the functions of mean wind speed were firstly identified from the measured acceleration and displacement responses to natural turbulent winds by means of spectral analysis. Then, the aeroelastic coefficients concerned were corrected step by step with an iterative procedure taking the corresponding values gained with wind tunnel test as the starting values until a convergence on the aeroelastic coefficients was reached. The initial values of the theoretical modal eigenvalues of each step were calculated utilising the aeroelastic coefficients corrected in the last step, through a complex eigenvalue analysis based on a state-space equation of motion. The corrected portions of the aeroelastic coefficients for the current step were then obtained with the least square (LS) method. The minimised objective function consisted of a double summation of the deviations between calculated and measured complex modal eigenvalues for all wind speeds and all modes concerned. In fact, the modal eigenvalues were the non-linear functions of the aeroelastic coefficients concerned. However, in each step, they were linearised around the initial values of the current step, through the Taylor expansion by neglecting all the non-linear terms. Thus, only one linear LS calculation was performed. The non-linear effects of the aeroelastic coefficients on the modal eigenvalues were taken into account in the procedure of iteration.

The above least square iterative strategy was also adopted by Zasso et al. (1996), while finishing the flutter derivatives through forced vibration test of the aeroelastic full model of the Messina Straits Bridge. However, in this approach, the optimal objective was set to the minimisation of the difference between the experimental and numerical transfer functions from input forces to the output responses. The flutter derivatives, which had been obtained in advance through a forced vibration test of sectional mode, also served as the starting values of the iteration and were utilised to calculate the initial transfer functions.

Based on the experience gained during the identification of flutter derivatives from buffeting response data of a sectional model to turbulence wind, Jakobsen expanded the CBHM method to the flutter derivative identification from the ambient vibration data obtained through full aeroelastic model test and full scale measurement of a 1210m suspension bridge (Jakobsen and Larose, 1999). However, significant

differences can be observed among the results gained, respectively, from the sectional model test, the full model test and the full-scale measurement. Furthermore, the dispersion degree of identified flutter derivatives is generally high when using the ambient vibration data.

2.2.3 Unifying Least Square Method for Flutter Derivative Identification

As aforementioned, the Unifying Least Square (ULS) method (Zhang, 1998; Gu et al., 2000) will be utilised in this study to identify 8 Scanlan's flutter derivatives through a series coupled free vibration tests of a 2DOF spring-suspended sectional model in smooth skew wind flow. Therefore, it is necessary to give a brief introduction to this identification method.

2.2.3.1 Relation between Flutter Derivatives and System Parameters

As it is well known, the equations of motion of the 2DOF sectional model can be written in a matrix style as follows:

$$\mathbf{M}^s\ddot{\boldsymbol{\delta}}+\mathbf{C}^s\dot{\boldsymbol{\delta}}+\mathbf{K}^s\boldsymbol{\delta}=\mathbf{F}_{se} \tag{2-11}$$

where $\boldsymbol{\delta}^{\mathrm{T}}=(h,\alpha)^{\mathrm{T}}$ is the displacement vector of model motion; h and α are, respectively, the vertical translational displacement and torsional angle of the sectional model motion, as shown in Figure 2-1; $\mathbf{M}^s$, $\mathbf{C}^s$ and $\mathbf{K}^s$ are, respectively, the 2×2 matrices of structural mass, damping and stiffness of the model system in still air; $\mathbf{F}_{se}^{\mathrm{T}}=(L_{se},M_{se})^{\mathrm{T}}$ is the vector of aeroelastic self-excited forces; and L_{se} and M_{se} are the aeroelastic self-excited force and moment acting on the per unit length segment of the sectional model, respectively. These structural parameter matrices and the self-excited force and moment are given as follows.

$$\mathbf{M}^s=\begin{bmatrix} m & 0 \\ 0 & I_m \end{bmatrix} \tag{2-12a}$$

$$\mathbf{C}^s=\begin{bmatrix} 2m\xi_h\omega_h & 0 \\ 0 & 2I_m\xi_\alpha\omega_\alpha \end{bmatrix} \tag{2-12b}$$

$$\mathbf{K}^s=\begin{bmatrix} m\omega_h^2 & 0 \\ 0 & I_m\omega_\alpha^2 \end{bmatrix} \tag{2-12c}$$

$$L_{se}=\rho U^2B\left[K_1H_1^*(K_1)\frac{\dot{h}}{U}+K_2H_2^*(K_2)\frac{B\dot{\alpha}}{U}+K_2^2H_3^*(K_2)\alpha+K_1^2H_4^*(K_1)\frac{h}{B}\right] \tag{2-13a}$$

$$M_{se}=\rho U^2B^2\left[K_1A_1^*(K_1)\frac{\dot{h}}{U}+K_2A_2^*(K_2)\frac{B\dot{\alpha}}{U}+K_2^2A_3^*(K_2)\alpha+K_2^2A_4^*(K_1)\frac{h}{B}\right] \quad (2\text{-}13b)$$

where m and I_m are the model mass and the inertia moment of mass per unit length, respectively; ω_h and ω_α are the natural circular frequencies of the model oscillations in still air in h and α directions, respectively; ξ_h and ξ_α are the corresponding structural damping ratios; ρ is the air density; B is deck width; U is the mean wind speed; $K_i=B\omega_i/U$ (i=1,2,) are the reduced frequencies; ω_1 and ω_2 are two natural circular frequencies of the model system under the wind action; and H_i^* and A_i^* (i=1,2,3,4) are the 8 Scanlan's flutter derivatives. It should be noted that the values of H_i^* and A_i^* (i=1,2,3,4) in the above two equations are only half of those in Eq.(2-3) because the factor of ½, which is present in the right side of Eq.(2-4), is removed here. Additionally, Eq.(2-13) implies that the main portion of the vertical response is contributed to by the first mode while the second mode is dominant in the torsional response. This assumption is based on the ground that, otherwise, the number of unknown flutter derivatives will be doubled and thus the available independent conditions will be insufficient for determining all the flutter derivatives in doubled number.

Further, the equation of motion, Eq. (2-11), can be rewritten by moving the self-excited forces to the left side as

$$\mathbf{M}^s\ddot{\boldsymbol{\delta}}+\mathbf{C}^e\dot{\boldsymbol{\delta}}+\mathbf{K}^e\boldsymbol{\delta}=\mathbf{0} \quad (2\text{-}14)$$

where the wind-induced inertia is ignored; $\mathbf{C}^e$ and $\mathbf{K}^e$ are the matrices of effective system damping and stiffness of the unit length segment of the sectional model, including the wind-induced damping and stiffness, namely,

$$\mathbf{C}^e=\mathbf{C}^s-\begin{bmatrix}\rho B^2\omega_1H_1^*(K_1) & \rho B^3\omega_2H_2^*(K_2)\\ \rho B^3\omega_1A_1^*(K_1) & -\rho B^4\omega_2A_2^*(K_2)\end{bmatrix} \quad (2\text{-}15a)$$

$$\mathbf{K}^e=\mathbf{K}^s-\begin{bmatrix}\rho B^2\omega_1^2H_4^*(K_1) & \rho B^3\omega_2^2H_3^*(K_2)\\ \rho B^3\omega_1^2A_4^*(K_1) & \rho B^4\omega_2^2A_3^*(K_2)\end{bmatrix} \quad (2\text{-}15b)$$

Thus, the relation between flutter derivatives and system parameters can be expressed with the following equations.

$$H_1^*(K_1) = \frac{m}{\rho B^2 \omega_1}\left(\tilde{C}_{11}^s - \tilde{C}_{11}^e\right) \tag{2-16a}$$

$$H_2^*(K_2) = \frac{m}{\rho B^3 \omega_2}\left(\tilde{C}_{12}^s - \tilde{C}_{12}^e\right) \tag{2-16b}$$

$$H_3^*(K_2) = \frac{m}{\rho B^3 \omega_2^2}\left(\tilde{K}_{12}^s - \tilde{K}_{12}^e\right) \tag{2-16c}$$

$$H_4^*(K_1) = \frac{m}{\rho B^2 \omega_1^2}\left(\tilde{K}_{11}^s - \tilde{K}_{11}^e\right) \tag{2-16d}$$

$$A_1^*(K_1) = \frac{I_m}{\rho B^3 \omega_1}\left(\tilde{C}_{21}^s - \tilde{C}_{21}^e\right) \tag{2-16e}$$

$$A_2^*(K_2) = \frac{I_m}{\rho B^4 \omega_2}\left(\tilde{C}_{22}^s - \tilde{C}_{22}^e\right) \tag{2-16f}$$

$$A_3^*(K_2) = \frac{I_m}{\rho B^4 \omega_2^2}\left(\tilde{K}_{22}^s - \tilde{K}_{22}^e\right) \tag{2-16g}$$

$$A_4^*(K_1) = \frac{I_m}{\rho B^3 \omega_1^2}\left(\tilde{K}_{21}^s - \tilde{K}_{21}^e\right) \tag{2-16h}$$

where $\tilde{C}_{ij}^e$ and $\tilde{K}_{ij}^e$ $(i,j = 1,2)$ are, respectively, the elements of the matrices, $\tilde{\mathbf{C}}^e (= \mathbf{M}^{s^{-1}}\mathbf{C}^e)$ and $\tilde{\mathbf{K}}^e (= \mathbf{M}^{s^{-1}}\mathbf{K}^e)$. Clearly, the flutter derivatives can be easily determined with Eq.(2-16), if the system parameter matrices has been identified for all the wind speeds including zero speed. Thus, the problem of the flutter derivative identification has been converted to that of the system parameter identification of the free oscillatory model.

2.2.3.2 Relation between System Parameters and Modal Properties

The identification of the system parameter of the free oscillatory model can be fulfilled through the extraction of the vibration frequency, damping and modes from recorded free vibration data. Actually, the system described by Eq.(2-14) is a non-proportional damping system due to the aerodynamic damping. Therefore, the analysis of its eigen properties should be performed in state-space. By introducing the state vector $\boldsymbol{\eta}^{\mathrm{T}} = \left(\boldsymbol{\delta}, \dot{\boldsymbol{\delta}}\right)^{\mathrm{T}}$, Eq.(2-14) then can be converted to the following state equation.

$$\dot{\boldsymbol{\eta}} = \mathbf{A}\boldsymbol{\eta} \tag{2-17}$$

where,

$$\mathbf{A}=\begin{bmatrix} \mathbf{0} & \mathbf{I} \\ -\tilde{\mathbf{K}}^{e} & -\tilde{\mathbf{C}}^{e} \end{bmatrix} \tag{2-18}$$

The solution of the homogeneous form of Eq.(2-17) can be taken as

$$\eta = \psi e^{\lambda t} \tag{2-19}$$

And the associated complex eigenvalue problem becomes

$$\mathbf{A}\psi = \lambda \psi \tag{2-20}$$

where λ is the complex eigenvalue and ψ is the associated complex eigenvector of 4 elements. For a underdamped system, the solution of Eq.(2-20) consists of four eigenvalues and four associated eigenvectors existing in complex conjugate pairs, i.e., λ_r and λ_r^*, ψ_r and ψ_r^* (r=1,2). Furthermore ψ_r has the form as

$$\psi_r = \begin{Bmatrix} \varphi_r \\ \lambda_r \varphi_r \end{Bmatrix}, \quad \varphi_r = \begin{Bmatrix} \phi_{hr} \\ \phi_{ar} \end{Bmatrix} \tag{2-21}$$

Then, the solution of Eq.(2-14) can be expressed with these eigenvalues and eigenvectors as follows.

$$\delta = \sum_{r=1}^{2} \left(a_r \varphi_r e^{\lambda_r t} + a_r^* \varphi_r^* e^{\lambda_r^* t} \right) \tag{2-22}$$

where a_1 and a_2 are two constants determined by the initial condition of the free vibration of the sectional model.

By putting Eq.(2-22) into Eq.(2-17), the relation between the system parameters and the eigen properties can be established as follows.

$$\begin{bmatrix} \tilde{\mathbf{K}}^{e} & \tilde{\mathbf{C}}^{e} \end{bmatrix} = -\begin{bmatrix} \varphi\Lambda^{2} & \varphi^{*}\Lambda^{*2} \end{bmatrix} \begin{bmatrix} \varphi & \varphi^{*} \\ \varphi\Lambda & \varphi^{*}\Lambda^{*} \end{bmatrix}^{-1} \tag{2-23}$$

where,

$$\varphi = [a_1\varphi_1, a_2\varphi_2] \tag{2-24}$$

$$\Lambda = \begin{bmatrix} \lambda_1 & \\ & \lambda_2 \end{bmatrix} \tag{2-25}$$

2.2.3.3 Identification of Modal Parameters

Up to now, the problem of the flutter derivative identification has been converted to the problem of determination of modal parameters of a sectional model in wind flow. In the ULS method, a least square iterative strategy is adopted to optimize the modal

parameters initially obtained with the MITD method. For this reason, the MITD method is introduced below.

2.2.3.3.1 MITD method

Suppose $\mathbf{Y}(t)$ is the actually observed response vector of the model vibration. It can be expressed as the real response, $\delta(t)$, plus the noise disturbance, $\varepsilon(t)$, which include the measurement error and those due to the incident wind turbulence and characteristic turbulence.

$$\mathbf{Y}(t) = \left(\tilde{h}(t) \;\; \tilde{\alpha}(t)\right)^{\mathrm{T}} = \delta(t) + \varepsilon(t) \tag{2-26}$$

According to the ITD method (Ibrahim and Mikulcik, 1973, 1976, 1977), two instrumental variables $\mathbf{\Phi}$ and $\hat{\mathbf{\Phi}}$ can be constituted from the sampled response data as follows

$$\mathbf{\Phi} = \begin{bmatrix} \mathbf{Y}(0) & \mathbf{Y}(\Delta t) & \cdots & \mathbf{Y}([N-N_1-N_2-1]\Delta t) \\ \mathbf{Y}(N_2\Delta t) & \mathbf{Y}([N_2+1]\Delta t) & \cdots & \mathbf{Y}([N-N_1-1]\Delta t) \end{bmatrix} \tag{2-27}$$

$$\hat{\mathbf{\Phi}} = \begin{bmatrix} \mathbf{Y}(N_1) & \mathbf{Y}([N_1+1]\Delta t) & \cdots & \mathbf{Y}([N-N_2-1]\Delta t) \\ \mathbf{Y}([N_1+N_2]\Delta t) & \mathbf{Y}([N_1+N_2+1]\Delta t) & \cdots & \mathbf{Y}([N-1]\Delta t) \end{bmatrix} \tag{2-28}$$

where both $\mathbf{\Phi}$ and $\hat{\mathbf{\Phi}}$ are $4\times(N-N_1-N_2)$ matrices; N is the length of the response sample; Δt is the time interval of the sampling; N_1 and N_2 are two time shifts of natural number ($N_1 << N, N_2 << N$). The following eigen equation can then be established based on the least squares principle.

$$\left[\hat{\Phi} \;\; \Phi^{\mathrm{T}}\right]\left[\Phi \;\; \Phi^{\mathrm{T}}\right]^{-1}\begin{Bmatrix} \varphi_r \\ \lambda_r\varphi_r \end{Bmatrix} = e^{\lambda_r N_1 \Delta t}\begin{Bmatrix} \varphi_r \\ \lambda_r\varphi_r \end{Bmatrix} \tag{2-29}$$

where, as before, λ_r, φ_r (r=1,2) are the complex frequencies and the complex modes of the sectional model system, to be identified by solving the eigenvalues and eigenvectors of the matrix, $\left[\hat{\Phi} \;\; \Phi^{\mathrm{T}}\right]\left[\Phi \;\; \Phi^{\mathrm{T}}\right]^{-1}$.

The accuracy of the results, especially for the modes obtained with the above ITD method, was proved unsatisfactory in the case of higher noise, which does often happen in tests. An iterative strategy was therefore introduced into the Sarkar's MITD method to improve the identification accuracy (Sarkar et al., 1992; 1991, 1993, 1994). The modal parameters gained with the ITD method as introduced above serves as the initial estimates and are used to simulated, in light of Eq.(2-22), a new

discrete sample of model vertical and torsional responses, $\bar{\boldsymbol{\delta}}^{\mathrm{T}}(i\Delta t)=\left(\bar{h}(i\Delta t)\ \ \bar{\alpha}(i\Delta t)\right)^{\mathrm{T}}$, i=1,2,...,N, at the same time interval. A new instrumental variable $\bar{\boldsymbol{\Phi}}$ is then generated with the same time shifts as

$$\bar{\boldsymbol{\Phi}}=\begin{bmatrix} \bar{\boldsymbol{\delta}}(0) & \bar{\boldsymbol{\delta}}(\Delta t) & \cdots & \bar{\boldsymbol{\delta}}([N-N_1-N_2-1]\Delta t) \\ \bar{\boldsymbol{\delta}}(N_2\Delta t) & \bar{\boldsymbol{\delta}}([N_2+1]\Delta t) & \cdots & \bar{\boldsymbol{\delta}}([N-N_1-1]\Delta t) \end{bmatrix} \tag{2-30}$$

The new estimates of modal parameters can be obtained by solving the eigenvalues and eigenvectors of the new eigen matrix, $\left[\hat{\Phi}\ \ \bar{\Phi}^{\mathrm{T}}\right]\left[\bar{\Phi}\ \ \bar{\Phi}^{\mathrm{T}}\right]^{-1}$. The above iteration is repeated until reaching a convergence on the modal parameters.

2.2.3.3.2 ULS method

It has been found in the practice of the ITD or MITD method that the different choice of N_1 and N_2 affects, to some extent, the final values of the extracted modal parameters, and thus becomes a source of error. Therefore, a strategy of least square iteration is employed in the ULS method to improve further the estimation accuracy of the modal parameters. The eigenvalues estimated with the MITD method is taken as the starting eigenvalues of the iteration in the ULS method, for the reason that the request of the Gauss-Newton non-linear least square method for the initial values of objective parameters is generally rather high.

Let $\mathbf{h}=(h_1,h_2,\cdots,h_n,\cdots,h_N)$ and $\boldsymbol{\alpha}=(\alpha_1,\alpha_2,\cdots,\alpha_n,\cdots,\alpha_N)$ denote, respectively, the recorded series of the vertical and torsional responses of the sectional model under a certain wind speed, where n=1,2, ..., N and N is the number of points of each sample. Then, according to Eq.(2-22), the estimates of h_n and α_n can be given as

$$\hat{h}_n=2\sum_{r=1}^{2}e^{\delta_r n\Delta t}\left[U_{hr}\cos(\omega_r n\Delta t)-V_{hr}\sin(\omega_r n\Delta t)\right] \tag{2-31a}$$

$$\hat{\alpha}_n=2\sum_{r=1}^{2}e^{\delta_r n\Delta t}\left[U_{\alpha r}\cos(\omega_r n\Delta t)-V_{\alpha r}\sin(\omega_r n\Delta t)\right] \tag{2-31b}$$

where δ_r and ω_r are, respectively, the real part and imaginary part of the rth eigenvalue, i.e., $\lambda_r=\delta_r+i\omega_r$; $(U_{hr}+iV_{hr},U_{\alpha r}+iV_{\alpha r})$ is the rth mode of the model system. A unifying error function, simultaneously considering the errors between the estimated and measured responses both for the vertical and torsional motions, is defined as

$$J = \mathbf{e}_h^{\mathrm{T}}\mathbf{e}_h + \mathbf{e}_\alpha^{\mathrm{T}}\mathbf{e}_\alpha \tag{2-32a}$$

$$\mathbf{e}_h = \left(h_1 - \hat{h}_1, h_2 - \hat{h}_2, \cdots, h_n - \hat{h}_n, \cdots, h_N - \hat{h}_N\right)^{\mathrm{T}} \tag{2-32b}$$

$$\mathbf{e}_\alpha = \left(\alpha_1 - \hat{\alpha}_1, \alpha_2 - \hat{\alpha}_2, \cdots, \alpha_n - \hat{\alpha}_n, \cdots, \alpha_N - \hat{\alpha}_N\right)^{\mathrm{T}} \tag{2-32b}$$

Now, the problem is to determine the optimal values of 12 parameters, δ_r, ω_r, U_{hr}, V_{hr}, $U_{\alpha r}$, $V_{\alpha r}$ (r=1, 2) in Eq.(2-31) by minimizing the above unifying error function. Obviously, this is a linear-non-linear hybrid least square problem, where the 8 mode parameters are linear parameters whilst the 4 eigenvalue parameters are non-linear parameters. Therefore, a corresponding hybrid iterative strategy, introduced below, is adopted in the ULS method.

(1) Take the estimate of the complex natural frequency of the model system obtained with MITD method as the starting value, $\lambda_r^{(0)} = \delta_r^{(0)} + i\omega_r^{(0)}$ (r=1,2) of the hybrid least square iteration. Then, with the linear least square method, the corresponding mode parameters, U_{hr}, V_{hr}, $U_{\alpha r}$, $V_{\alpha r}$ (r=1, 2), can be determined with the following equations.

$$\begin{bmatrix} \mathbf{C}^{\mathrm{T}}\mathbf{C} & -\mathbf{C}^{\mathrm{T}}\mathbf{S} \\ -\mathbf{S}^{\mathrm{T}}\mathbf{C} & \mathbf{S}^{\mathrm{T}}\mathbf{S} \end{bmatrix} \begin{Bmatrix} U_{h1} \\ U_{h2} \\ V_{h1} \\ V_{h2} \end{Bmatrix} = \begin{bmatrix} \mathbf{C}^{\mathrm{T}}\mathbf{h} \\ -\mathbf{S}^{\mathrm{T}}\mathbf{h} \end{bmatrix} \tag{2-33a}$$

$$\begin{bmatrix} \mathbf{C}^{\mathrm{T}}\mathbf{C} & -\mathbf{C}^{\mathrm{T}}\mathbf{S} \\ -\mathbf{S}^{\mathrm{T}}\mathbf{C} & \mathbf{S}^{\mathrm{T}}\mathbf{S} \end{bmatrix} \begin{Bmatrix} U_{\alpha 1} \\ U_{\alpha 2} \\ V_{\alpha 1} \\ V_{\alpha 2} \end{Bmatrix} = \begin{bmatrix} \mathbf{C}^{\mathrm{T}}\boldsymbol{\alpha} \\ -\mathbf{S}^{\mathrm{T}}\boldsymbol{\alpha} \end{bmatrix} \tag{2-33b}$$

where **C** and **S** are the two N×2 matrices with their elements, C_{nr} and S_{nr} (n=1,2, ..., N, r=1, 2), as follows

$$C_{nr} = 2e^{\delta_r^{(0)} n\Delta t}\cos(\omega_r n\Delta t) \tag{2-34a}$$

$$S_{nr} = 2e^{\delta_r^{(0)} n\Delta t}\sin(\omega_r n\Delta t) \tag{2-34b}$$

Inserting the solution of Eq.(2-33) and $\delta_r^{(0)}, \omega_r^{(0)}$ into Eqs.(2-31) and (2-32), the unifying error function for this step can then be evaluated.

(2) Determine the new values of δ_r and ω_r (r=1,2). Thus, the non-linear least square problem of solving δ_r and ω_r is first converted into the linear least square problem of determining their increments, Δ_j (j=1,2,3,4), by applying the linearised Taylor's expansion on Eq.(2-31) around $\delta_r^{(0)}, \omega_r^{(0)}$ (r=1,2) using the following approximation.

$$\delta_1 \approx \delta_1^{(0)} + \Delta_1; \quad \delta_2 \approx \delta_2^{(0)} + \Delta_2; \quad \omega_1 \approx \omega_1^{(0)} + \Delta_3; \quad \omega_2 \approx \omega_2^{(0)} + \Delta_4 \tag{2-35}$$

Then, by employing the linear least square method again, the approximate increments can be obtained by solving the following linear equations.

$$\sum_{j=1}^{4}(a_{ij} + b_{ij})\Delta_j = a_{ik} + b_{i\alpha} \tag{2-36}$$

where i=1,2,3,4; and

$$a_{ij} = \sum_{n=1}^{N} h_{ni} h_{nj} \tag{2-37a}$$

$$b_{ij} = \sum_{n=1}^{N} \alpha_{ni} \alpha_{nj} \tag{2-37b}$$

$$a_{ik} = \sum_{n=1}^{N} h_{ni}(h_n - h_{n0}) \tag{2-37c}$$

$$b_{i\alpha} = \sum_{n=1}^{N} \alpha_{ni}(\alpha_n - \alpha_{n0}) \tag{2-37d}$$

$$h_{n0} = \sum_{j=1}^{2}(U_{hj}C_{nj} - V_{hj}S_{nj}) \tag{2-38a}$$

$$\alpha_{n0} = \sum_{j=1}^{2}(U_{\alpha j}C_{nj} - V_{\alpha j}S_{nj}) \tag{2-38b}$$

$$h_{nj} = \begin{cases} n\Delta t(U_{hj}C_{nj} - V_{hj}S_{nj}), & j = 1,2 \\ -n\Delta t(U_{h(j-2)}S_{n(j-2)} + V_{h(j-2)}C_{n(j-2)}), & j = 3,4 \end{cases} \tag{2-38c}$$

$$\alpha_{nj} = \begin{cases} n\Delta t(U_{\alpha j}C_{nj} - V_{\alpha j}S_{nj}), & j = 1,2 \\ -n\Delta t(U_{\alpha(j-2)}S_{n(j-2)} + V_{\alpha(j-2)}C_{n(j-2)}), & j = 3,4 \end{cases} \tag{2-38d}$$

(3) With the determined Δ_j (j=1,2,3,4), the new estimated values of δ_r and ω_r, (r = 1, 2), can be obtained in light of Eq.(2-35). Taking the new estimates as the new initial values of the complex frequencies, i.e., $\delta_r^{(0)}, \omega_r^{(0)}$, the above step (2) is repeated until all the four $|\Delta_j|$ are sufficient small.

(4) The above three iterative steps are circulated until the change of the unifying error is small enough.

Having obtained the modal parameters, the system parameters can then be determined according to Eq.(2-23), where,

$$\Psi = \begin{bmatrix} U_{h1} + iV_{h1} & U_{h2} + iV_{h2} \\ U_{\alpha 1} + iV_{\alpha 1} & U_{\alpha 2} + iV_{\alpha 2} \end{bmatrix} \tag{2-39}$$

$$\Lambda = \begin{bmatrix} \delta_1 + i\omega_1 & 0 \\ 0 & \lambda\delta_2 + i\omega_2 \end{bmatrix} \tag{2-40}$$

2.3 CHARACTERISTICS OF NATURAL WIND

2.3.1 Atmospheric Boundary Layer

It is well known (Simiu and Scanlan, 1996; Dyrbye and Hansen, 1996) that the speed of wind in atmosphere varies with the height due to the retardance of the rough surface of the Earth. Besides, the direction of the wind also veers as a result of the combined effect of the Coriolis force originating from the Earth's rotation and the friction force due to the roughness of the Earth's surface. The angle between the mean wind and the isobars will be zero at the gradient height and will reach its maximum value near the ground. The retardant effect of the rough Earth's surface spread upwards and wears off at a height called geostrophic or gradient height, which is typically approximately 1km. Therefore, above this signature height, the wind speed and direction depend only on the horizontal pressure gradient, the Coriolis force and the centrifugal force due to the curvature of the isobars, and thus is independent of the height. In the areas far from high-pressure and lower-pressure zones in the weather system concerned, the radii of the isobars are so large that the centrifugal forces can be ignored, and the wind above the geostrophic height moves along almost straight line. This wind speed is then called geostophic wind speed. However, in other areas where the radii of the isobars are relatively small, say less than a few thousand kilometers, the centrifugal force must be taken into account, and the height-independent speed of the wind above the gradient height is then called the gradient wind speed. If $f_c = 2\Omega \sin\phi$ denotes the Coriolis parameter, where Ω is the

angular velocity of the Earth and ϕ is the latitude of the location concerned, the geostrophic wind speed, U_{geo}, can be determined as follows

$$U_{geo} = \frac{1}{\rho f_c}\frac{dp}{dn} \tag{2-41}$$

and the gradient wind speed, U_{gra}, is as Eq.(2-42a) for cyclonic winds around a low pressure:

$$U_{gra} = -\frac{f_c r}{2} + \sqrt{\left(\frac{f_c r}{2}\right)^2 + \frac{r}{\rho}\frac{dp}{dn}} \tag{2-42a}$$

and Eq.(2-42b) for anticyclonic winds around a high pressure:

$$U_{gra} = \frac{f_c r}{2} - \sqrt{\left(\frac{f_c r}{2}\right)^2 + \frac{r}{\rho}\frac{dp}{dn}} \tag{2-42b}$$

where ρ is the air density; and r is the radius of the isobar; and dp/dn is the pressure gradient at the gradient or geostrophic height. Clearly, the upper limit gradient wind speed for the anticyclonic wind is $U_{gra} = f_c r/2$ whilst there is no limits for the most common cyclonic winds. However, the gradient wind speed of a cyclonic wind is less than the corresponding geostrophic wind speed, and

$$U_{geo} = U_{gra}[1 + U_{gra}/f_c r] \tag{2-43}$$

The region below the gradient height is called the atmospheric boundary layer. The atmospheric boundary layer has three states: stable, unstable and neutral states, which depend on the temperature distribution along the height in the atmosphere. In a stable atmosphere, the air temperature remains constant or increases with the increasing height, and there is no any unstable motion of air mass between the layers at different elevations. Stable conditions prevent any mixing of air in different vertical layers, thus, result in very small vertical wind turbulence. The stable conditions are typically found when an inversion phenomenon takes place, such as when the ground surface and thus also the air at the lower level are cooled down by the radiation in a cloudless sky at night.

An atmosphere is unstable when the air temperature in the atmosphere decreases significantly with the increasing height, which happens when the ground surface and the lower layer air are heated by the sunlight. In this case, the vertical motion of air

mass is unstable, namely, an air mass moving upwards will find itself surrounded by cold heavier air and will probably move even higher. This leads to a convection phenomenon and gives rise to significant air mixing and then the larger vertical wind turbulence.

Obviously, there will be a neutral state of the atmosphere between the stable and unstable states aforementioned. In this state, the equilibrium of an air mass always holds wherever it is positioned so long as there is no heat exchange with the surroundings. This state occurs when the air temperature decreases with the increasing height in a moderate rate. It is the case for a dry atmosphere when the decreasing rate of the air temperature is about 1°C per 100m upwards.

It is known that mechanically generated wind conditions normally dominate the heat convection by far in the strong winds. Thus, in most cases in engineering practices where the effect of strong winds are primarily concerned, the atmosphere is often assumed to be neutral, therefore the thermal contributions to wind condition can be neglected. However, the thermal effects must be considered when the wind speed is less than approximately 10m/s (Dyrbye and Hansen, 1996). Therefore, the thermal conditions may be important to the vortex-shedding induced vibrations of slender structures such as towers, chimneys, etc., because the vortex-shedding induced vibrations often take place at moderated wind speed and may lead to the greatest wind loads on these kinds of structures. In addition, measurements indicate that up to a height of 180m, direction of mean wind changes only few degrees (Harris, 1970). Therefore, apart from very high structures and those unusually sensitive to wind direction, the change of mean wind direction along the height is often ignored in engineering practices.

Wind in the atmospheric boundary layer may be characterized by a mean wind profiles and some important turbulence parameters such as intensity, integral scales, friction velocity, roughness length and auto/cross spectra etc. These wind characteristics are also necessary to the buffeting prediction of long span bridges. Thus, a brief review on these wind characteristics is given below, where, if not indicated specially, the assumption of the neutral atmospheric boundary layer is employed.

2.3.2 Profile of Mean Wind

There are two characteristic length scales related to the atmospheric boundary layer. The roughness length (z_0) measuring the surface roughness of ground is the dominant length scale in the lower part of the boundary layer whilst the gradient height of the boundary layer (z_δ) is the most important length scale in the upper part of the boundary layer close to the free flow regime. Historically, the power law has been the first representation of mean wind profile in horizontally homogeneous terrain and is assumed to hold with constant exponent α up to gradient height (Simiu and Scanlan, 1996), namely,

$$\overline{U}(z) = \overline{U}_r (z/z_r)^\alpha = \overline{U}_\delta (z/z_\delta)^\alpha \tag{2-44}$$

where z_r is a reference height; $\overline{U}_r$ is the wind velocity at reference height; and $\overline{U}_\delta$ is the gradient wind speed. The power law is frequently adopted by the wind codes of many countries and regions including China (Xiang et al., 1996) and Hong Kong (Code of practice on wind effects Hong Kong-1983) because of its simplicity. The gradient height and the exponent of power law depend on the local terrain categories, and are specified with different values in various codes. The empirical values for some typical terrain categories can be found in the literature (Simiu and Scanlan, 1996). In the Code of Practice on Wind Effects, Hong Kong-1983, the local terrain of Hong Kong is simply classified into two types, general terrain and built-up terrain. For the general terrain, α and z_δ are assumed as 0.19 and 250m, respectively. For the built-up terrain, they are set to be 0.33 and 300m, respectively. Above the specified z_δ, the variation of the mean wind is not significant and thus regarded as constant.

Another expression of mean wind profile is the logarithmic law as follows,

$$\overline{U}(z) = \frac{1}{k} u_* \ln \frac{z - z_d}{z_0} \tag{2-45}$$

where k is the well-known von Karman's constant and is generally assumed to be 0.4; u_* is called the shear velocity or friction velocity which will be explained later; z is the height above ground and z_d is a length known as the zero plane displacement (Jackson, 1981), and they are determined empirically and are functions of the nature, height and distribution of the roughness elements (Chamberlain, 1983); and the quantity z-z_d is referred to as the effective height. The roughness length can be

interpreted as the size of a characteristic vortex, which is formed as a result of friction between the air and the ground surface. As indicated by Eq.(2-42), if the zero plane displacement is ignored, z_0 is the height above the ground at which the mean wind speed is equal to zero. Empirical values of z_0 of some typical terrain categories, based on various measurements taken at many locations around the world, can be found in some relevant literatures (Simiu and Scanlan, 1996; Dyrbye and Hansen, 1996). Reasonable values of z_d in cities may be estimated with the following formula (Helliwell, 1972).

$$z_d = \overline{H} - z_0/k \tag{2-46}$$

where $\overline{H}$ is the mean height of the buildings. The logarithmic law is currently regarded as a superior representation of strong wind profiles in the lower atmosphere. However, it only applies to the atmospheric surface layer close to the ground (the lowest 100m of the atmospheric boundary layer) because only the surface roughness is considered in the derivation (Simiu and Scanlan, 1996; Dyrbye and Hansen, 1996). Thus, a so-called corrected logarithmic profile taking the gradient height into consideration was proposed by Harris and Deaves as follows (Harris and Deaves, 1980; Dyrbye and Hansen, 1996)

$$\overline{U}(z) = \frac{u_*}{k}\left[\ln\frac{z-z_d}{z_0} + 5.75\frac{z-z_d}{z_\delta} - 1.88\left(\frac{z-z_d}{z_\delta}\right)^2 - 1.33\left(\frac{z-z_d}{z_\delta}\right)^3 + 0.25\left(\frac{z-z_d}{z_\delta}\right)^4\right] \tag{2-47}$$

where the gradient height z_δ is given by

$$z_\delta = u_*/(6f_c) \tag{2-48}$$

For high wind velocity, say more than 20m/s, this corrected logarithmic profile gives accurate results up to 300m above ground. However, it is relatively complicated. Besides, another logarithm formulae were suggested by some investigators to consider the effect of thermal convection, which were summarized by Simu and Scanlan (1996).

2.3.3 Shear Stress and Friction Velocity

As aforementioned, the wind near the ground is retarded by a horizontal drag force exerted by the Earth's surface on the moving air. This retarding effect is diffused

upwards by turbulent mixing existing between neighbor strata of the moving air, until the gradient height. This kind of turbulent mixing comprises the major source of shear stress between the strata of moving air. One distinguished feature of the atmospheric surface layer for thermally neutral and unstable flow is that the turbulent shear stress varies by only 5%~10% across the layer (Panofsky and Dutton, 1984; Cermak and Cochran, 1992). Surface shear velocity, also called friction velocity, which is associated with the shear stress near the ground, is a very important characteristic of the atmospheric boundary layer. It is defined by

$$u_* = \sqrt{\tau_0/\rho} \tag{2-49}$$

where τ_0 is the surface shear stress of wind flow near the ground. Friction velocity may be (1) evaluated through measuring the Reynolds stress; (2) measured directly by means of a skin-friction balance; (3) inferred from the momentum integral equation; (4) deduced by fitting the profile of mean wind speed. The first and fourth methods are frequently used to estimated the friction velocity in fields or in wind tunnels, and the results obtained by the two methods are rather close to each other (Farell and Iyengar, 1999; Duchene-Marullaz, 1980; Hoxey and Richards, 1992; Richards et al., 1997; Bowen 1980). The Reynolds stress is defined as the momentum fluxes of horizontal velocity transferred by eddies (Panofsky and Dutton, 1984). It can be obtained from the co-variances of $\overline{uw}$, $\overline{vw}$ and $\overline{uv}$, and are zero for isotropic turbulence (ESDU 8520). However, turbulence in atmospheric boundary layer is non-isotropic due to the effect of ground surface friction. Therefore, the Reynolds stress in atmospheric boundary layer is not zero and, in practice, is often determined as follows

$$\tau_R = -\rho\overline{uw} \tag{2-50}$$

where the co-variances of $\overline{vw}$ and $\overline{uv}$ are normally small compared to $\overline{uw}$ and ignored frequently; and the u and w represent the longitudinal and vertical velocity fluctuations, respectively; and bar means the mean value. By replacing surface shear stress (τ_0) in Eq.(2-43) with τ_R of Eq.(2-50), the friction velocity can be estimated as follows

$$u_* = \sqrt{\tau_R/\rho} = \sqrt{-\overline{uw}} \tag{2-51}$$

In principle, the application of Eq.(2-51) requires the measurement of wind turbulence to be carried out at lower elevations near ground surface, where the co-

variance $\overline{uw}$ is dominant. The results obtained by Farell and Iyengar (1999) and Duchene-Marullaz (1980) show that the Reynolds stress may vary only slightly up to a rather high elevation (e.g. 60m). Therefore, the Reynolds stress measured at a relatively higher level may be used to estimate the friction velocity.

Instead of Eq.(2-51), Tieleman and Mullins (1980) used the following horizontal turbulent shear stress (τ_H) to estimate the friction velocity to consider the lateral component of shear stress, i.e.

$$\tau_H = \rho\sqrt{\left(\overline{uw}\right)^2 + \left(\overline{vw}\right)^2} \tag{2-52}$$

$$u_* = \sqrt[4]{\left(\overline{uw}\right)^2 + \left(\overline{vw}\right)^2} \tag{2-53}$$

The results showed that the horizontal shear stress was nearly constant within the height of about 50m above the ground although the magnitude of the individual components $\overline{uw}$ and $\overline{vw}$ might vary considerably with height. Additionally, there was a good agreement between the friction velocity based on the horizontal shear stress and the method of mean wind profile fitting. The latter is sometimes called profile friction velocity.

2.3.4 Turbulence Intensity

Turbulence intensities at the height z above the terrain are the simplest descriptors of the atmospheric turbulence. They are defined by

$$I_a(z) = \frac{\sigma_a(z)}{\overline{U}(z)} \tag{2-54}$$

where $\overline{U}(z)$ is the mean wind speed at the height of z; the subscript a can be one of the three turbulence components: longitudinal component u which is along the mean wind direction, lateral component v which is horizontal and perpendicular to the mean wind direction, upward component w which is also perpendicular to the mean wind direction and vertical when mean wind is horizontal; and $\sigma_a(z)$ is the standard deviation of velocity fluctuations of the corresponding turbulence component at the height z. All the three turbulence stand deviations, σ_u, σ_v and σ_w wear off close to zero when reaching the gradient height. However, some experimental results show that they usually decrease very slowly with increasing height up to the heights of the

ordinary structures (Davenport, 1967; Harris, 1970). Define three turbulence ratios as follows

$$\beta_u = \sigma_u / u_* ; \quad \beta_v = \sigma_v / u_* ; \quad \beta_w = \sigma_w / u_* \tag{2-55}$$

which are commonly assumed to be independent of height. Then, considering Eq.(2-45) , it can be obtained that

$$I_u(z) = \frac{k\beta_u}{\ln[(z - z_d)/z_0]} \tag{2-56a}$$

$$I_v(z) = \frac{k\beta_v}{\ln[(z - z_d)/z_0]} \tag{2-56b}$$

$$I_w(z) = \frac{k\beta_w}{\ln[(z - z_d)/z_0]} \tag{2-56c}$$

For a homogeneous terrain, Dyrbye and Hansen (1996) suggest that $\beta_u \approx 2.5$, $\beta_v \approx 1.88$, $\beta_w \approx 1.25$ when z_0=0.05m and $\beta_u \approx 1.8$, $\beta_v \approx 1.35$, $\beta_w \approx 0.9$ when z_0=0.3m, for heights up to about 100m~200m. The empirical values of turbulence ratios for flat smooth uniform terrain are $\beta_u = \sigma_u / u_* = 2.5$, $\beta_v = \sigma_v / u_* = 2.0$ and $\beta_w = \sigma_w / u_* = 1.25$ (Tieleman, 1992), which are close to that given by Dyrbye and Hansen. The values of β_u suggested by Bietry et al. (1978) for structural design purpose are 2.55, 2.45, 2.29, 2.20 and 2.0, respectively, for z_0=0.005m, 0.07m, 0.30m, 1.00m and 2.50m. It is then seen from these empirical values that the ratios β_u, β_v and β_w decrease with the increasing roughness length. As pointed out by Panofsky et al. (1980), the large scale eddies primarily generated by upwind heterogeneous terrain have significant contribution to the variance of the horizontal turbulence but not to the variance of vertical turbulence, because they are oriented in a horizontal plane. Thus, the observed values of β_u and β_v over a heterogeneous are often larger than those observed over a flat smooth uniform terrain, whilst the observed value of β_w is relatively independent of the nature of the upwind terrain. For complex heterogeneous terrain with mountains, the observed average turbulence ratios β_u and β_v may reach 4.5 and 3.2, respectively, which are significantly larger than that for flat smooth uniform terrain (Tieleman, 1992).

2.3.5 Integral Scales of Wind Turbulence

Integral scales of turbulence represent the average size of the turbulent eddies in the flow. Totally, there are nine integral scales of turbulence, L_u^x, L_u^y, L_u^z, L_v^x, L_v^y, L_v^z, L_w^x, L_w^y, L_w^z, at a certain point (x_1, y_1, z_1) corresponding to the three dimensions of the eddies related to three components of velocity fluctuations, u, v and w (Dyrbye and Hansen, 1996). Mathematically, the integral scales are defined as

$$L_a^r = \int_0^\infty C_{a_1a_2}(r)dr \Big/ \sigma_a^2 \tag{2-57}$$

where $a = u, v, w$, and $r = x, y, z$; σ_a^2 is the variance of velocity fluctuations; $C_{a_1a_2}(r)$ is the corresponding cross-covariance function, i.e., $C_{a_1a_2}(x)$ is the cross-covariance function between the velocity components, $a(x_1, y_1, z_1, t)$ and $a(x_1 + x, y_1, z_1, t)$; $C_{a_1a_2}(y)$ is the cross-covariance function between the velocity components, $a(x_1, y_1, z_1, t)$ and $a(x_1, y_1 + y, z_1, t)$; and $C_{a_1a_2}(z)$ is the cross-covariance function between the velocity components, $a(x_1, y_1, z_1, t)$ and $a(x_1, y_1, z_1 + z, t)$, where t is time.

Generally, it is hard to estimate the integral scales with Eq.(2-57) because measurement of wind turbulence needs to be carried out simultaneously at many positions scattered in the space. In practicel, the three integral length scales in longitudinal direction, L_u^x, L_v^x and L_w^x, are often estimated with the corresponding integral time scales based on Taylor's hypothesis of convected "frozen turbulence"(Batchelor, 1953), namely, it is assumed that the flow disturbance travels at the mean wind speed $\overline{U}$ without any decay (Duchene-Marullaz, 1980; Simiu and Scanlan, 1996). Therefore, $a(x_1 + x, y_1, z_1, t)$ can be replaced with $a(x_1, y_1, z_1, t - x/\overline{U})$, and

$$C_{a_1a_2}(x) = C_{a_1}(x/\overline{U}) \tag{2-58}$$

Substituting τ for $x/\overline{U}$, and $\overline{U}d\tau$ for dr and inserting Eq.(2-58) into Eq.(2-57) then yield

$$L_a^x = \overline{U}\int_0^\infty C_a(\tau)d\tau \Big/ \sigma_a^2 = \overline{U}\int_0^\infty c_a(\tau)d\tau = \overline{U}\, T_a^x \tag{2-59}$$

where $C_a(\tau)$ is the auto-covariance function; and $c_a(\tau)$ is the normalized auto-covariance function; and T_a^x is the time scales of turbulenc.

$$c_a(\tau) = C_a(\tau)/C_a(0) = C_a(\tau)/\sigma_a^2 \tag{2-60a}$$

$$T_a^x = \int_0^\infty c_a(\tau)d\tau \tag{2-60b}$$

As shown in Figure 2-2, the normalised auto-covariance function is equal to unity at zero time-lag, and generally oscillates about the τ axis after the first zero point τ_0, because of the periodical signals contained in the signal of velocity fluctuations. The less the contained periodical signals, the smaller oscillation of the auto-covariance is. Obviously, the total area between the time axis and auto-covariance curve after τ_0 approaches zero. Therefore L_u^x, L_v^x and L_w^x may be approximated by the following equation, based on the field measurement data of wind turbulence.

$$L_a^x = \overline{U}\int_0^{\tau_0} c_a(\tau)d\tau \tag{2-61}$$

As noted in ESDU 85020 for a region relatively close to the ground, wind speed and turbulence properties are more closely related to z/z_0. Therefore, length scales at a given height should decrease with the increasing terrain roughness, and there will be little or no dependence on wind speed. In contrary, for larger heights, length scales will increase with increasing wind speed and are larger over a rougher terrain. In this context, a complicated model has been proposed in ESDU 85020 to consider these trends. However, for the structures which are not very high, some simple empirical formulae can be used for estimating the integral scales when lacking for the measurement data. Counihan (1975) suggested the following purely empirical formula for the turbulence length scales (in meter) as functions of height z (in meter) and roughness z_0.

$$L_u^x = Cz^m; \qquad L_u^y = L_u^x/3; \qquad L_u^z = L_u^x/2 \tag{2-62}$$

where both the coefficient C and m are the functions of z_0. In the figure with the bi-logarithmic coordinates, C almost linearly decreases with increasing z_0 whilst m increases with increasing z_0 in an order less than 1. The results of L_u^x estimated with Eq.(2-62) may be twice as high as the measured values (Simiu and Scanlan, 1996).

For L_u^y the following relationship suggested by Duch ne-Marullaz (1980) may lead to a better estimate.

$$L_u^y \approx 0.2 L_u^x \tag{2-63}$$

The formula for L_u^z proposed by Bietry (Simiu and Scanlan, 1996) is as follows

$$L_u^z \approx 6\sqrt{z} \tag{2-64}$$

where the effect of terrain roughness is ignored. Furthermore, the following Eq.(2-65) and Eq.(2-66), and Eq.(2-67) are given by Teunissen (Teunissen, 1970; Irwin, 1977b), Dyrbye and Hansen (1996) and in ESDU 74031, respectively.

$$L_u^x = 11.04\sqrt{z}\,; \quad L_w^x = 0.8z \tag{2-65}$$

$$L_u^x = \begin{cases} 100\,(0.1z)^{0.3}, & 10\text{m} \le z \le 200\text{m} \\ 100, & z \le 10\text{m} \end{cases}; \; L_u^y \approx L_u^x/3; \; L_u^z \approx L_u^x/4 \tag{2-66}$$

$$L_u^x = 280\left(\frac{z - z_d}{z_\delta}\right)^{0.35}; \; L_v^x = 140\left(\frac{z - z_d}{z_\delta}\right)^{0.48}; \; L_w^x = 0.35(z - z_d) \tag{2-67}$$

All the above expressions of turbulence integral scales take meter as the unit of length or height. In summary, the values of turbulence integral scales scattee in a wide range. Estimates of integral scales of turbulence largely depend on the length and the degree of stationarity of the analysed samples, the height above ground, the roughness of terrain and maybe the wind speed, and thus they usually vary widly from experiment to experiment. This gives rise to a variety of the empirical expressions.

2.3.6 Auto Spectra of Wind Turbulence

Modern wind engineering practice requires the response spectral density to be determined in order to examine the variance and energy distribution of response with respect to the frequency. Knowledge of the wind turbulence spectra is thus demanded. Spectra of wind turbulence are often presented in the normalized form ($nS(n)/u_*^2$ or $nS(n)/\sigma^2$), for the curve of each normalized spectrum always has at least one peak and such peaks are representative of the typical scales of the turbulence (Panofsky and Dutton, 1984). As proposed by Kolmogorov, all spectra of wind turbulence (not just those of the velocity fluctuations) can be divided into three portions: energy-containing subrange, inertial subrange, and dissipation subrange.

Most of the turbulence energy are input in the energy-containing subrange, in which length scales are typically tens of meters to several kilometers and local time scales vary between tens of seconds and tens of minutes. The spectra of wind turbulence in the energy-containing subrange then depend on the wind itself, the roughness of surface, the height of the atmospheric boundary layer, and so on. Energy input into the energy-containing subrange from the outside of the turbulence system is then transferred to the inertial subrange, where wavelengths of turbulence ($\lambda = \overline{U}(z)/n$) are between the Kolmogorov microscale and the height (z) above the surface. There is supposed to be no energy input from the outside, nor any energy dissipated in this inertial subrange. The eddy motion is independent of viscosity and is determined solely by the rate of energy transfer (known as Kolmogorov second hypothesis). Thus, in the inertial range, the turbulence is isotropic and no longer depends on the original geometry. The dissipation subrange is comprised of turbulence with wavelengths less than the Kolmogorov microscale. In this subrange, the energy fed from the inertial subrange is balanced by the energy dissipated due to viscosity effects, otherwise, the turbulence will be decay. The motion of eddies in the dissipation subrange is then determined solely by two factors: the energy transfer rate, or equivalently, by the energy dissipation rate, and the viscosity (Kolmogorov first hypothesis).

The isotropic formulae derived based on the Kolmogorov Hypotheses are generally valid for the range region of $\lambda < z/10$, even for $\lambda < z/3$ (Wester and Burling, 1981). Furthermore, for the alongwind velocity fluctuation, the isotropic formula is valid for even more lager wavelengths, essentially when $\lambda < z$, in light of some empirical results (Panofsky and Dutton, 1984). According to Kolmogorov's hypotheses and Taylor's hypothesis, the following expressions, describing the spectrum of alongwind velocity fluctuation of wind turbulence, can be obtained from dimensional consideration and some experimentally determined coefficients as Eq.(2-68a) (Kaimal et al., 1972) or Eq.(2-68b) (Simiu and Scanlan, 1996),

$$\frac{nS_u(z,n)}{u_*^2} = \frac{\alpha_1}{(2\pi k)^{2/3}} \phi_\varepsilon^{2/3} f_z^{-2/3} \approx 0.27 \phi_\varepsilon^{2/3} f_z^{-2/3} \tag{2-68a}$$

$$\frac{nS_u(z,n)}{u_*^2} = 0.26 f_z^{-2/3} \tag{2-68b}$$

where $k \approx 0.4$ is the von Karman constant; $\alpha_1 \approx 0.5$ (Tennekes and Lumley, 1972); ϕ_ε is the dimensionless dissipation rate for turbulent energy and it is a function of a dimensionless height z/L, and it can be determined using an interpolation formula proposed by Kansas (Kaimal et al., 1972; Panofsky and Dutton, 1984) and will be unity if z/L=0; the Monin-Obukhov length L is an index of the air stability, and $L = \infty$ under the neutral atmospheric condition, $L < 0$ under the unstable condition, $L > 0$ under the stable condition; and non-dimensional reduced frequency

$$f_z = nz/\overline{U}(z) \tag{2-69}$$

Eqs.(2-68a) and (2-68b) are often referred to as Kolmogorov's spectral law. The measurement results given by Kaimal et al. (1972) show that, based on the criteria of $S_w(n)/S_u(n) = 4/3$, the lower limiting value of f_z for the local isotropy of turbulence is about 1.2 under unstable condition and about $10.0z/L$ under the stable condition. Kolmogorov's spectral law is sometimes also applied to the lateral (horizontal crosswind) component, v and upward crosswind (vertical when mean wind is horizontal), w, as follows

$$\frac{nS_a(z,n)}{u_*^2} = A_a f_z^{-2/3} \tag{2-68c}$$

where A_a approximates 0.27, 0.36, and 0.36 for a = u, v, w, respectively (Tieleman 1992). According to the measurement reported by Tieleman (1992), the measured normalized spectrum, $nS_u(z,n)/u_*^2$, reaches a peak value at $f_z = f_m \approx 0.03$, and Kolmogorov's spectral law can be, on average, a good representation of wind turbulence spectra over flat smooth uniform terrain in the high frequency range of, conservatively, $f_z \geq 0.2$. However, for frequency range of $0<f_z<0.01$, the normalized spectral values vary generally in a linear pattern with f_z. Therefore, the Kolmogorov's spectral law is no more suitable in this range.

Summarily, the lower limit of the reduced frequency f_z of the inertial subrange is, in practice, often supposed to be 1.0 for unstable air, 3.0 for stable air (Panofsky and Dutton, 1984), and between 1.0 and 3.0 for neutral air, say 1.6 according to Kaimal et al. (1972). Further, as noted in some measurement reports (Bush and Panofsky, 1968; Pasquill, 1972), in energy-containing subrange (i.e. lower frequency range) similarity of spectral no longer exists and the spectra cannot be described with a

universal expression. However, simplified empirical formulae, that are very useful in engineering practice where the atmosphere is often supposed to be neutral, may be obtained if the following principles are satisfied (Simiu and Scanlan, 1996).

1. $S_a(0) = 4\sigma_a^2 L_a^x / \overline{U}$ (2-70)
2. $dS_a(n)/dn\big|_{n=0} = 0$ (2-71)
3. $S_a(n)$ is monotonically decreasing.
4. $S_a(n)$ is continuous at the lower end of initial subrange with the curve $S_a(n)$ given by Eqs.(2-68)
5. For single-side spectra , $\int_0^\infty S_a(n)dn = \sigma_a^2$ (2-72)

Based on wind tunnel test data, Von Karman (1948) suggested the following spectrum before the development of Eq.(2-68), with which his name is associated

$$\frac{nS_u(n)}{u_*^2} = 4\beta_u^2 \frac{nL_u^x}{\overline{U}} \Bigg/ \left[1 + 70.78\left(\frac{nL_u^x}{\overline{U}}\right)^2\right]^{5/6} = 4\beta_u^2 f_{Lu} / \left[1 + 70.78 f_{Lu}^2\right]^{5/6} \quad (2\text{-}73)$$

where $\beta_u = \sigma_u / u_*$, $f_{Lu} = nL_u^x / \overline{U}$. The above Von Karman spectrum satisfies the aforementioned first three and the 5th principles. Compared with Eq.(2-68b), it would be necessary to have $L_u^x \approx 0.3\beta_u^3 z$, which is evidently not the real case in the atmosphere. Therefore it is regarded to be unsuitable for the case that the magnitude of higher-frequency components of along-wind velocity fluctuations is of interest, and on the other hand, it can be applied to where the low-frequency component is important. However, the results of turbulence field measurement conducted by Morfiadakis et al (1996) reveals that the von Karman's spectrum is suitable for the structure of the turbulence measured at some location in free stream conditions. The turbulence length was determined in light of Eqs.(2-65) by Irwin (1977b) when applying the von Karman's Spectrum.

Davenport evaluated the results of many wind spectra at various sites in Canada, USA, UK, and others over different terrains and at various elevations, and suggested the following formula (Danvenport, 1961b, 1961c)

$$\frac{nS_u(n)}{u_*^2} = 4.0x^2 / \left(1 + x^2\right)^{4/3} \quad (2\text{-}74)$$

where $x=1200n/\overline{U}(10)$. The formula does not reflect the dependence of spectra on height. In addition, $S_u(0)=0$ and $dS_u/dn|_{n=0}\neq 0$, not satisfying the Eq.(2-70) and Eq.(2-71). Obviously, the Danvenport Spectrum of Eq.(2-74) implies that $L_u^x=0$, which is not right. Thus, Harris modified the Danvenport Spectrum based on more experimental data as follows (Harris 1971):

$$\frac{nS_u(n)}{u_*^2}=4.0x/\left(2+x^2\right)^{5/6} \tag{2-75}$$

where $x=1800n/\overline{U}(10)$. Harris's formula is very similar to von Karmen spectrum. It overcomes the shortcoming of $L_u^x=0$ which Danvenport's Spectrum has, but it does not reflect the variation of spectrum with elevation. Furthermore, to improve the performance of von Karman spectrum in high-frequency region, Harris (1990) modifies the von Karman spectrum with a functional series as follows

$$\begin{aligned}\frac{nS_u(n)}{\sigma_u^2}=&4n\frac{L_u^x}{\overline{U}}\frac{\sqrt{\pi}\Gamma(5/6)}{\Gamma(1/3)}\alpha^{2/3}\left[\alpha^2+4\pi^2n^2\left(L_u^x/\overline{U}\right)^2\right]^{-5/6}\cdot\beta_1\\&+4n\frac{L_u^x}{\overline{U}}\frac{\sqrt{\pi}\Gamma(5/6)}{\Gamma(1/3)}\alpha^{2/3}\frac{\sqrt{3}}{4}\,{}_2F_1\left(\frac{5}{6},\frac{1}{6},\frac{4}{3};\frac{\pi^2n^2\left(L_u^x/\overline{U}\right)^2}{\alpha^2+\pi^2n^2\left(L_u^x/\overline{U}\right)^2}\right)\cdot\beta_2\\&+\frac{12}{(2\pi)^{5/3}}\frac{\sqrt{\pi}\Gamma(5/6)}{\Gamma(1/3)}\alpha^{2/3}\left(n\frac{L_u^x}{\overline{U}}\right)^{-2/3}\cdot\beta_3+\cdots\end{aligned} \tag{2-76}$$

where ${}_2F_1(a,b,c;z)$ is the Gauss hypergeometric function with parameters a, b and c and argument z. Parameters α and β_1, β_2, β_3, $\cdots$ are to satisfy the following equations,

$$\beta_1+\beta_2+\beta_3+\cdots=1 \tag{2-77a}$$

$$\alpha=0.746834\beta_1+0.323389\beta_2+0.194116\beta_3+\cdots \tag{2-77b}$$

$$\alpha^{2/3}(0.0.139632\beta_1+0.279264\beta_2+0.418895\beta_3+\cdots)=A \tag{2-77c}$$

where A is a measured coefficient determined by the folowing constraint equation for spectra in high frequency region.

$$[nS_u(n)/\sigma_u^2]_{h.f.}=A(nL_u^x/\overline{U})^{-2/3} \tag{2-77d}$$

The formula suggested by Kaimal et al. (1972) for the spectrum of alongwind turbulence component is

$$\frac{nS_u(n,z)}{u_*^2}=105f_z/(1+33f_z)^{5/3} \tag{2-78}$$

It proved to be a good approximation of the observed curves in range of $0.01<f_z<4.0$, and is modified by Simiu and Scanlan (1996) into the following form for the purpose of structural design.

$$\frac{nS_u(n,z)}{u_*^2}=200f_z/(1+50f_z)^{5/3} \tag{2-79}$$

The above Simiu's Spectrum of Eq.(2-79) approximates very closely the Kolmogorov's spectral law in the initial subrange. Both Kaimal spectrum and Simiu's Spectrum do not conform the 2nd principle of Eq.(2-71). From the 5th principle of Eq.2-72, it can be inferred that the ratio $\beta_u^2=\sigma_u^2/u_*^2$ is equal to 4.77 for Eq.(2-78) and 6.0 for for Eq.(2-79). Simiu also proposed the following piecewise function for the spectrum of the alongwind velocity fluctuation, which depends on the ratio β_u and length scale L_u^x, and an additional parameter f_m used to modulate the spectral shape in the energy-containing subrange (Simiu, 1974; Simiu and Leigh, 1983).

$$\frac{nS_u(z,n)}{u_*^2}=\begin{cases}a_1f_z+b_1f_z^2+d_1f_z^3 & f_z\le f_m\\ c_2+a_2f_z+b_2f_z^2 & f_m<f_z<f_s\\ 0.26f_z^{-2/3} & f_z\ge f_s\end{cases} \tag{2-80a}$$

where the Kolmogorov law is adopted for the inertial subrange with the lower limit f_s being supposed to be 0.2; and

$$a_1=4L_u^x(z)\beta_u^2/z \tag{2-80b}$$

$$a_2=-2b_2f_m \tag{2-80c}$$

$$b_1=-a_1/(2f_m)-1.5f_md_1 \tag{2-80d}$$

$$b_2=\frac{\frac{a_1f_m}{3}+\left(\frac{7}{3}+\ln\frac{f_s}{f_m}\right)\beta_1-\beta_u^2}{\frac{5}{6}(f_m-f_s)^2+\frac{1}{2}(f_m^2-f_m^2)-2f_m(f_m-f_s)-f_s(2f_m-f_s)\ln\frac{f_s}{f_m}} \tag{2-80e}$$

$$c_2=\beta_1-a_2f_s-b_2f_s^2 \tag{2-80f}$$

$$d_1=\frac{2}{f_m^3}\left[\frac{a_1f_m}{2}-\beta_1+b_2(f_m-f_s)^2\right] \tag{2-80g}$$

$$\beta_1 = 0.26 f_s^{-2/3} \tag{2-80h}$$

For spectrum of the upward component of turbulence, *w(t)*, the following formulas were, respectively, suggested by Panofsky & McCormick (1959), and Lumley & Panofsky (1962):

$$\frac{nS_w(n,z)}{u_*^2} = 6f_z/(1+4f_z)^2 \tag{2-81}$$

$$\frac{nS_w(n,z)}{u_*^2} = 3.36f_z/(1+10f_z^{5/3}) \tag{2-82}$$

The expression given by Kaimal et al. (1972) for the spectrum of upward turbulence component $w(t)$ is similar to Eq.(2-82) with different coefficients and expressed as follows

$$\frac{nS_w(n,z)}{u_*^2} = 2f_z/(1+5.3f_z^{5/3}) \tag{2-83}$$

Irwin (1977b) used the expression in Eq.(2-84) for the spectrum of velocity fluctuation $w(t)$

$$\frac{nS_w(n,z)}{u_*^2} = 2\beta_w^2 \frac{L_2}{\overline{U}} \cdot [1+188.8(nL_2/\overline{U})^2]/\left[1+70.78(nL_2/\overline{U})^2\right]^{11/6} \tag{2-84}$$

where $L_2 = 0.8z$ is the integral scale of *w(t)*. The von Karman's spectrum of upward velocity fluctuation $w(t)$ (Morfiadakis et al., 1996) is

$$\frac{nS_w(n)}{u_*^2} = 4\beta_w^2 f_{Lw}\left(1+755.2f_{Lw}^2\right)/\left(1+283.2f_{Lw}^2\right)^{11/6} \tag{2-85}$$

where $f_{Lw} = nL_w^x/\overline{U}$.

For spectrum of the horizontal lateral component of wind turbulence, *v(t)*, the following Eq.(2-86) was suggested by Kaimal et al. (1972) and then modified a little by Simiu and Scanlan (1996) into Eq.(2-87).

$$\frac{nS_v(n,z)}{u_*^2} = 17f_z/(1+9.5f_z)^{5/3} \tag{2-86}$$

$$\frac{nS_v(n,z)}{u_*^2} = 15f_z/(1+9.5f_z)^{5/3} \tag{2-87}$$

And the von Karman's spectrum of horizontal lateral velocity fluctuation $v(t)$ (Morfiadakis et al., 1996) is

$$\frac{nS_v(n)}{u_*^2}=4\beta_v^2 f_{Lv}\left(1+755.2f_{Lv}^2\right)/\left(1+283.2f_{Lv}^2\right)^{11/6} \tag{2-88}$$

where $f_{Lv}=nL_v^x/\overline{U}$.

Similar to Eq.(2-76), Harris (1990) also suggested the formulae of spectra for the turbulence components $v(t)$ and $w(t)$ with the form of functional series as follows,

$$\frac{nS_a(n)}{\sigma_a^2}=\beta_1 4n\frac{L_a^x}{\overline{U}}\frac{\sqrt{\pi}\Gamma(5/6)}{\Gamma(1/3)}\frac{\alpha^{2/3}}{2}\frac{\left[\alpha^2+(8/3)4\pi^2n^2\left(L_a^x/\overline{U}\right)^2\right]}{\left[\alpha^2+4\pi^2n^2\left(L_a^x/\overline{U}\right)^2\right]^{11/6}}$$

$$+\beta_2 4n\frac{L_a^x}{\overline{U}}\frac{\sqrt{\pi}\Gamma(5/6)}{\Gamma(1/3)}\frac{\sqrt{3}}{8}\frac{\alpha^{2/3}}{\left[\alpha^2+\pi^2n^2\left(L_a^x/\overline{U}\right)^2\right]^{5/6}}$$

$$\times\left[{}_2F_1\left(\frac{5}{6},\frac{1}{6},\frac{4}{3};\frac{\pi^2n^2\left(L_a^x/\overline{U}\right)^2}{\alpha^2+\pi^2n^2\left(L_a^x/\overline{U}\right)^2}\right)+\frac{35}{24}\left(\frac{\pi^2n^2\left(L_a^x/\overline{U}\right)^2}{\alpha^2+\pi^2n^2\left(L_a^x/\overline{U}\right)^2}\right)\right.$$

$$\left.\times{}_2F_1\left(\frac{11}{6},\frac{1}{6},\frac{7}{3};\frac{\pi^2n^2\left(L_a^x/\overline{U}\right)^2}{\alpha^2+\pi^2n^2\left(L_a^x/\overline{U}\right)^2}\right)\right]+\cdots \tag{2-89}$$

where a = v, w; and the coefficients β_i (i=1,2,...) are determined in similar way as that for the alongwind components.

It should be noted that all the aforementioned empirical expressions of auto spectra of wind turbulence are presented in the form of single-side spectrum to be consistent with Eq.(2-72).

2.3.7 Cross Spectra of Wind Turbulence

2.3.7.1 Cross Spectra between Two Same Components of Wind Turbulence at Two Different Spatial Points

Suppose that $a_1(t)$ is one of the velocity components, $u(t)$, $v(t)$ and $w(t)$ of wind turbulence at a spatial point $P_1(x_1, y_1, z_1)$ and $a_2(t)$ is another one of the same kind at a second spatial point $P_2(x_2, y_2, z_2)$. (x_i, y_i, z_i) are the coordinates of the point P_i in the wind coordinate system, and generally the axes x, y and z are respectively consistent with three velocity components of turbulence, $u(t)$, $v(t)$ and $w(t)$. Then, the two-side cross spectrum of between $a_1(t)$ and $a_2(t)$, $S_{a_1a_2}(P_1,P_2,n)$, is complex in general.

$$S_{a_1a_2}(P_1,P_2,n) = C_{a_1a_2}(P_1,P_2,n) + jQ_{a_1a_2}(P_1,P_2,n) \tag{2-90}$$

where $j=\sqrt{-1}$; n is the frequency in Hertz ; and the real part, $C_{a_1a_2}(P_1,P_2,n)$, is called co-spectrum and it is a even function of n; the imaginary part, $Q_{a_1a_2}(P_1,P_2,n)$, is named as quadrature spectrum and it is an odd function of n. For these spectra, the following relations hold

$$S_{a_1a_2}(P_1,P_2,n) = S^*_{a_2a_1}(P_1,P_2,n) \tag{2-91a}$$

$$S_{a_1a_2}(P_1,P_2,-n) = S_{a_2a_1}(P_1,P_2,n) = S^*_{a_1a_2}(P_1,P_2,n) \tag{2-91b}$$

$$C_{a_1a_2}(P_1,P_2,-n) = C_{a_1a_2}(P_1,P_2,n) = C_{a_2a_1}(P_1,P_2,n) \tag{2-91c}$$

$$Q_{a_1a_2}(P_1,P_2,-n) = -Q_{a_1a_2}(P_1,P_2,n) = Q_{a_2a_1}(P_1,P_2,n) \tag{2-91d}$$

where the superscript * indicates a conjugate operation. The co-variance between a_1 and a_2 can be calculated as follows

$$\sigma_{a_1a_2}(P_1,P_2) = \int_{-\infty}^{+\infty} S_{a_1a_2}(P_1,P_2,n)\,dn = 2\int_{-\infty}^{+\infty} C_{a_1a_2}(P_1,P_2,n)\,dn \tag{2-91d}$$

Cross spectrum Eq. (2-90) is often expressed with the following form.

$$S_{a_1a_2}(P_1,P_2,n) = \sqrt{S_{a_1}(P_1,n)S_{a_2}(P_2,n)}\,R_{a_1a_2}(P_1,P_2,n)e^{j\Phi_{a_1a_2}(P_1,P_2,n)} \tag{2-92}$$

where $S_{a_i}(P_i,n)$ is the auto spectrum of turbulence component a_i at point P_i (i=1,2); $R_{a_1a_2}(P_1,P_2,n)$ and $\Phi_{a_1a_2}(P_1,P_2,n)$ are, respectively the root-coherence function and the phase function between the two turbulence components a_1 at point P_1 and a_2 at P_2, and defined as

$$R_{a_1a_2}(P_1,P_2,n) = \frac{\left|S_{a_1a_2}(P_1,P_2,n)\right|}{\sqrt{S_{a_1}(P_1,n)S_{a_2}(P_2,n)}} = \sqrt{\frac{C^2_{a_1a_2}(P_1,P_2,n)+Q^2_{a_1a_2}(P_1,P_2,n)}{S_{a_1}(P_1,n)S_{a_2}(P_2,n)}} \tag{2-93a}$$

$$\Phi_{a_1a_2}(P_1,P_2,n) = \tan^{-1}\frac{Q_{a_1a_2}(P_1,P_2,n)}{C_{a_1a_2}(P_1,P_2,n)} \tag{2-93a}$$

In homogeneous turbulence, the quadrature spectrum vanished (Teunissen, 1970). The reports on the quadrature spectrum or the phase spectrum of the wind turbulence in the atmospheric boundary layer are very scanty. In fact, it is generally regarded that in the atmosphere the ratio of quadrature spectrum to co-spectrum is small so that the quadrature spectrum or the phase spectrum is often ignored in engineering practice.

2.3.7.2 Root-coherence Functions

The coherence function reflects the variation of correlation between two turbulence components with the spatial distance between two points and the turbulence frequency. It largely depends on the turbulence scales and the mean wind speed, and it decreases with the increasing distance or with the decreasing wavelength of turbulence. The idea of describing the root-coherence function with an exponential function was suggested by Davenport (1961c) in an analysis of wind data from vertically displaced cup anemometers. Afterwards, this exponential form of root-coherence function was adopted by various investigators and also applied to those in alongwind and horizontal lateral directions (Davenport, 1962a; Ropelewski et al., 1972; Panofsky and Mizuno, 1975; Kristensen, 1978; Kristensen and Jensen, 1979; Kristensen et al., 1981). For two transverse points on a plane perpendicular to the mean wind direction, the original expression was extended to allow for difference decays of turbulence correlation in the horizontal and vertical directions as follows (Davenport, 1968).

$$R(P_1,P_2,n)=e^{-\hat{f}(P_1,P_2,n)} \tag{2-94a}$$

$$\hat{f}(P_1,P_2,n)=n\sqrt{[C_z(z_1-z_2)]^2+[C_y(y_1-y_2)]^2}\Big/\overline{U}_{\bar{z}} \tag{2-94b}$$

$$\overline{U}_{\bar{z}}=[\overline{U}(z_1)+\overline{U}(z_2)]/2 \tag{2-94c}$$

where x_1=x_2; C_y and C_z are the two non-dimensional exponential decay coefficients which are determined experimentally. An modified format of Eq.(2-94) was proposed as follows to ensure the co-spectral integral over the plane perpendicular to the mean wind to be zero and the coherence function at zero frequency to approach a value less than 1 for a non-zero separation, which don't satisfied by Eqs.(2-94) (Krenk, 1995; Dyrbye and Hansen, 1996).

$$R(P_1,P_2,n)=\left(1-\hat{f}(P_1,P_2,n)/2\right)e^{-\hat{f}(P_1,P_2,n)} \tag{2-95a}$$

$$\hat{f}(P_1,P_2,n)=n_x\sqrt{[C_z(z_1-z_2)]^2+[C_y(y_1-y_2)]^2}\Big/\overline{U}_{\bar{z}} \tag{2-95b}$$

$$n_x=\sqrt{n^2+\frac{1}{78.78}\left(\frac{\overline{U}_{\bar{z}}}{L_u^x}\right)^2} \tag{2-95c}$$

A similar formula for the root-coherence in horizontal lateral direction can be also referred to Roberts and Surry (1973) and Katsuchi et al. (1999), which is expressed by Eq.(2-94b) incorporated with the following expression of the exponent.

$$\hat{f}(\Delta y, z, n) = n_x C_y |\Delta y| / \overline{U}(z) \tag{2-96a}$$

$$n_x = \frac{\Gamma(5/6)}{2\sqrt{\pi}\Gamma(1/3)} \sqrt{1 + 70.78\left(\frac{nL_a^x}{\overline{U}(z)}\right)^2} \frac{\overline{U}(z)}{L_a^x} \approx 1.06 \sqrt{n^2 + \frac{1}{70.78}\left(\frac{\overline{U}(z)}{L_a^x}\right)^2} \tag{2-96b}$$

where Γ is the gamma function; the subscript a can be u or w, and the effective frequency n_x is almost the same as defined in Eq.(2-95c).

The values of the exponential decay coefficients C_y and C_z may be set, respectively, to 16 and 10 for longitudinal velocity fluctuations, u, according to some experimental results. However, they are dependent of terrain roughness, wind speed and height above the surface. Generally, the decay coefficients are larger for rough surface conditions such as urban areas than for smooth surfaces, and decreases with the increasing height above ground or with the decreasing wind speed (Simiu and Scanlan, 1996). In addition, it is noted that surface pressures on a structure are better correlated than the longitudinal turbulence in the undisturbed, oncoming wind flow. This may lead to a choice of relatively lower decay coefficients for engineering purposes, such as $C_y = C_z = 10$ (Dyrbye and Hansen, 1996). The values of both the two decay coefficients are set to 11.5 in the Eurocode based on the measurement results provided by Solari (1993a, b). In addition, the value of C_y is set to 8 in the Eq.(2-96a).

As for the alongwind coherence of alongwind velocity fluctuations at two points $P_1(x_1,y,z)$ and $P_2(x_2,y,z)$, Eq.(2-94a) is also frequently used in practice in conjunction with the following expression of the exponent (Simiu and Scanlan, 1996).

$$\hat{f} = \frac{nC_x|(x_1 - x_2)|}{\overline{U}(z)} \tag{2-97}$$

with $C_x \approx 3.0$ over water and $C_x \approx 6.0$ over land according to Panofsky (1974).

For lateral and upward velocity fluctuations, v and w, Eq.(2-94) can tentatively be used for engineering purposes. The exponential decay coefficients for the lateral component v are lower by about 33% than those for the alongwind component u, namely, C_y is typically 7 to 11 and C_z is typically about 7 (Blackadar et al., 1974;

Kristensen and Jensen, 1979). For upward component, w, C_y was suggested to be 8 which is in the scope of C_y for the lateral component v (Kristensen and Jensen, 1979), but less suggestion is available for C_z. Nevertheless, it seems rational to set the value of C_z to 7 for the upward component w as same as that for the lateral component v.

As aforementioned, the exponential decay coefficients are dependent on the height above ground surface, and may decrease rather rapidly with increasing height. This means that the turbulence is correlated better in higher level than in lower level. To consider this effect of height on the exponential decay coefficients, an improved formula was then presented by Kanda and Royles (1978) for evaluating the height-dependent root-coherence function of the alongwind turbulence component both in lateral and vertical directions. This formula was derived based on a more general expression of spectrum. A modified frequency similar to Eq.(2-95c), but without the factor of 1/70.78, was also introduced. The improved formula was supported by some measurement data, but is relatively complicated.

2.3.7.3 Cross Spectra between Two Different Components of Wind Turbulence at One Spatial Point

Compared with the information on the auto spectra and chorence functions of wind turbulece, there has been no information on the cross spectra between two different components of wind turbulence, except for the co-spectrum between the alongwind and upward components of wind turbulence ($C_{uw}(n)$). Measurement results demonstrated a –7/3 to –8/3 power law of $C_{uw}(n)$ in the inertial subrange (Panofsky and Mares, 1968; Kukharets and Tsvang, 1969; McBean, 1970; Wyngaard and Coté, 1972; Kaimal et al., 1972). The empirical expression of two-side cospectrum $C_{uw}(n)$ suggested by Kaimal et al.(1972) for the positive frequency region is as follows

$$\frac{nC_{uw}(n)}{u_*^2} = -\frac{7f_z}{(1+9.6f_z)^{2.4}} \tag{2-98}$$

The empirical expression has been widely used in engineering practice, and generally it fits the measurement results quite well. On the other hand, other co-spectra and quadrature spectra are often ignored in the engineering practice.

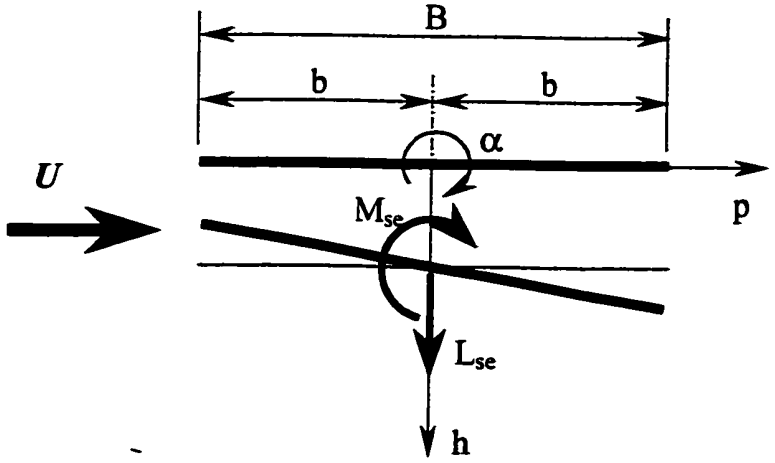

Figure 2-1 Aeroelastic self-excited forces on 2D motion section

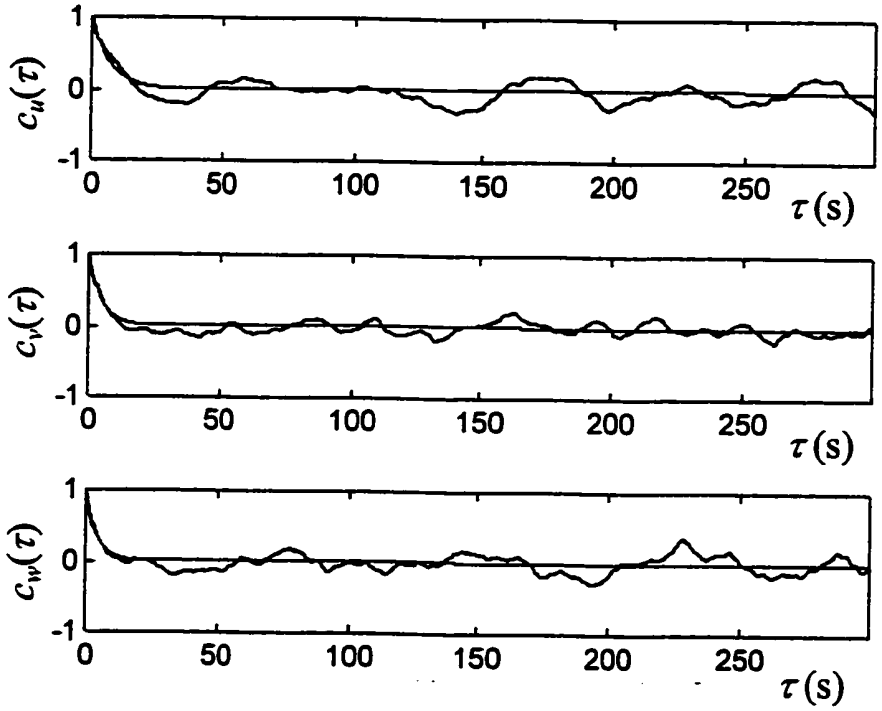

Figure 2-2 Typical Curves of Normalized Auto-covariance of Wind Turbulence Measured at Mid-maispan of Tsing Ma Bridge deck during Typhoon Victor

Chapter 3

FIELD MEASUREMENT RESULTS OF TSING MA BRIDGE DURING TYPHOON VICTOR

3.1 INTRODUCTION

Increasing of span length of modern cable-supported bridges makes the prediction of bridge responses to strong winds more and more important for bridges constructed within a wind-prone area. To meet this task, various analytical methods have been developed in the past three decades as reviewed in Chapter 2. In most of the existing analytical methods, the mean wind is often assumed to be normal to the longitudinal axis of a bridge. The wind characteristics, such as mean wind speed, mean wind inclination, turbulence intensity, integral scale, and auto-spectrum, are assumed to remain constant along the longitudinal axis of a bridge. The wind forces on the bridge towers and cables and the full interaction between the bridge deck, towers and cables are not included for simplification.

The rationality of these assumptions involved in buffeting analysis of long span cable-supported bridges, however, was unable to be examined in detail before. Only recently, comprehensive wind and structural health monitoring systems installed in several long span cable-supported bridges provide a good opportunity of having an overall examination of the currently used analytical methods. Among those bridges with wind and structural health monitoring systems, the system installed in the Tsing Ma Bridge in Hong Kong by the Highways Department of Hong Kong Special Administrative Region is the most comprehensive one in the world. The Wind And Structural Health Monitoring System (WASHMS) of the Tsing Ma Bridge has recorded more than 20 typhoons and tropical cyclones since it opening in 1997.

This chapter performs a detailed analysis of field measurement data recorded by the WASHMS when Tsing Ma Bridge was hit by Typhoon Victor on 2 August 1997, three months after the opening of the Bridge. The selection of Typhoon Victor rather

than other typhoons is because the Typhoon Victor's eye just crossed over the Bridge and the wind speeds and bridge responses were successfully recorded by the WASHMS. Therefore, after a brief description of Typhoon Victor, the Bridge and its surroundings, and the measurement instrumentation, the recorded wind and structural response data are analyzed in this chapter to evaluate the mean wind speed, mean wind direction, friction velocity, turbulence intensity, integral scale, auto and cross wind spectra, bridge acceleration responses, and others. Implications of the field measurement results to the currently used methods for buffeting analysis are finally highlighted.

3.2 Main Features and Modal Properties of Tsing Ma Bridge

The Hong Kong new international airport is located on Lantau Island. The key section of the transportation between the new airport and the existing commercial centers of Kowloon and Hong Kong Island is the Lantau Fixed Crossing with the Tsing Ma Bridge as its key structure. The Tsing Ma Bridge, stretching from Tsing Yi Island to Ma Wan Island, is a suspension bridge with an overall length of 2,160m, carrying a dual three-lane highway on the upper level of the bridge deck and two railway tracks and two carriageways on the lower level within the bridge deck (Beard and Young, 1995). As shown in Figures 3-1 to 3-3, the Tsing Ma Bridge has a main span of 1,377m between the Tsing Yi tower in the east and the Ma Wan Tower in the west. The height of the two pre-stressed concrete towers is 206m measured from the base level to the tower saddle. The Tsing Yi tower sits on the northwest seashore of Tsing Yi Island whilst the Ma Wan tower is located about 400m from the original shoreline of Ma Wan Island and founded on a reef approximately 12m under water. The two main cables with diameter of 1.1m and of 36m apart in the north and south are accommodated by the four saddles located at the tops of the tower legs in the main span. On the Tsing Yi side, the main cables are extended from the tower saddles to the main anchorage through the splay saddles, forming a 300m Tsing Yi side span. On the Ma Wan side, the main cables extended from the Ma Wan tower are held first by the saddles on the pier at a horizontal distance of 355.5 m from the Ma Wan tower and then by the main anchorage through splay saddles at the Ma Wan abutment. The two main anchorages are gravity structures resting on the underlying

rock. The bridge deck is a hybrid steel structure continuing between the two main anchorages. It has a width of 41 m and a height of 7.643m (see Figure 3-3). The deck is suspended by the suspenders from the main cables in the main span to allow a sufficient large navigation channel of 62m high and 1110m wide and in the Ma Wan side span to minimize the number of the substructures founded in the sea. On the Tsing Yi side, the deck is supported by three piers rather than suspenders. This arrangement and the difference of span between the Ma Wan side and Tsing Yi side introduce some asymmetries with respect to the mid-span of the Bridge.

The eigenvalue analysis of the Tsing Ma Bridge was carried out by Xu et al (1997), using a finite element (FE) computer program called DDJ-W, jointly developed by Dalian University of Technology and the Hong Kong Polytechnic University. The details of the FE models of the bridge deck, towers, piers, cables and suspenders can be found in Xu et al (1997), in which a comprehensive comparison between the computed modal properties and those obtained by ambient vibration measurement was provided. The computed modal properties are in a good agreement with the measured ones. The established FE model of the Bridge and the computed modal properties are used in this study for buffeting analysis. The first 45 natural frequencies, ranging from 0.0681Hz to 0.7062 Hz, and the corresponding mode shapes are shown in the figures in Appendix A. It is seen that the natural frequencies of the Bridge are spaced very closely and some modes of vibration are observed with a significant coupling between the deck lateral and torsional motions or the deck vertical and longitudinal motions. The strong interactions between the bridge deck, towers, cables and piers are also observed. In particular, the lateral vibration of the deck always appeared in phase and out of phase with the lateral vibration of the cables. The results also unveil the interaction between the main span and side span; the higher wave number vibrations of the main span are often associated with the lower wave number vibration of the side span.

3.3 WIND AND STRUCTURAL HEALTH MONITORING SYSTEM

The Wind And Structural Health Monitoring System (WASHMS) is a comprehensive monitoring system mounted on the three neighboring cable-supported bridges, namely, Tsing Ma Bridge, Kap Shui Mun Bridge and Ting Kau Bridge by

the Highway Department of HKSAR Government. The WASHMS is used to evaluate the health status of the three bridges through monitoring various working environments including wind environment, temperature distribution, traffic load distribution, and others. The WASHMS is comprised of four subsystems: Sensory System, Data Acquisition System (DAS), Data Processing and Analysis System (DPAS), and Computer for System Operation and Control. DAS is composed of 9 Data Acquisition Outstation Units (DAOU), which are mounted in the bridges. Each DAOU has more than 64 channels and a buffer, which can store data of 12 hours. The digitized signals are conveyed into DPAS via optical fiber cables and then processed and analyzed. There are altogether seven different type sensors in the WASHMS, including, amongst others, six anemometers and 24 uni-axial servo-type accelerometers on the Tsing Ma Bridge only (Lau et al., 1998). As demonstrated in Figures 3-2 and 3-3, two digital ultrasonic anemometers (AneU), called Gill Wind Master Ultrasonic Anemometer, were installed on the north side and south side, respectively, of the bridge deck at the mid-mainspan at a level of 75.314m. They are specified as WITJN01 and WITJS01, respectively. Each ultrasonic anemometer has three channels to simultaneously measure the westward, southward and downward components of wind velocity. In addition, two analogue mechanical anemometers (AneM) were located at two sides of the bridge deck near the mid-sidespan on the Ma Wan side and at the elevation of 62.944m.They are designated as WITBN01 for the north one and as WITBS01 for the south one. Each analogue mechanical anemometer consists of a horizontal component called RM YOUNG 05106 Horizontal Anemometer with two channels, giving the horizontal resultant wind speed and its azimuth, and a vertical component named as RM YOUNG 27106 Vertical Anemometer to measure the downward wind component. The output azimuth angle will be zero when the wind blows from the due north and 90° when the wind is from the due east. Moreover, two analogue mechanical anemometers (AneM) of horizontal component only were arranged on the top of each bridge tower at the elevation of 217.084m; they are denoted as WITPT01 for the Tsing Yi tower and WITET01 for the Ma Wan tower. The sample frequencies of all anemometers are set to 2.56Hz for recording wind speeds and the time interval is about 0.3906s.

The servo-type accelerometers used are of the brand Allied Signal Aerospace Q-Flex QA700. Three different types of arrangement for acceleration measurement were

used in the system, namely AccT, AccB and AccU as indicated in Figure 3-2. They represent, respectively, Tri-axial measurement (three uni-axial accelerometers assembled orthogonally to each other), Bi-axial measurement (two uni-axial accelerometers assembled perpendicularly to each other) and Uni-axial measurement (only one accelerometer in one prescribed direction). As shown in Figure3-2, all 12 uni-axial accelerometers are located at the four sections of the bridge deck (ATTJD, ATTID, ATTFD, ATTBD). At each section, there are two accelerometers measuring the accelerations in the vertical direction and one accelerometer for the acceleration in the lateral direction, as shown in Figur3-3. The position of the lateral accelerometer is close to the horizontal neutral axis of the corresponding cross section. The two vertical accelerometers are symmetrically arranged about the vertical central axis of the cross section with a horizontal central space of 26m. Thus, the vertical acceleration of the deck section can be obtained by averaging the accelerations measured by the two vertical accelerometers, and the torsional one is equal to the difference between the two vertical accelerations divided by the distance of the separation (26m). Accelerometers are also mounted at the location of ATTAA on Ma Wan Anchorage for measurement of the ground motion, and at the locations on the south cables, ATTGC, ABTCC, ABTLC and ABTQC to measure the cable acceleration responses (see Figure 3-2). At each location of ATTAA and ATTGC, three uni-axial accelerometers are assembled orthogonally to each other at one point to measure the longitudinal, lateral and vertical acceleration responses. At each location of ABTCC, ABTLC and ABTQC, two uni-axial accelerometers are assembled perpendicularly to each other at one point to measure the lateral and vertical acceleration responses. The sample frequencies of all the accelerometers are set to 25.6Hz and the time interval is about 0.03906s.

3.4 BRIEF DESCRIPTION OF LOCAL TERRAIN

Hong Kong is situated in the coastal area of South China. Not only there are many islands in Hong Kong, but also there are many mountains covering most areas of the territory. The topography of Hong Kong thus varies from place to place (see Figure. 3-4). The local topography surrounding the Tsing Ma Bridge within the dashed circle of 5km in radius is a typical example. The bridge is embraced by sea, islands, and

mountains of 200 to 500m high. The alignment of bridge deck deviates from the east-west axis by about 17° in anti-clockwise (Beard et al., 1995; Lau et al., 1999). If taking the bridge as a center, the whole surrounding area may be roughly classified into seven types of regions (I to VII), bounded by seven lines R1, R2, R3, R4, R5, R6 and R7 as shown in Figure 3-4. The Tsing Yi Island adjacent to the Bridge is in Region I and VII. The top levels of Tsing Yi Island are 218m in the north (Region I) and 334m in the south (Region VII). Next to the southeast of Tsing Yi Island in Region VII is seawaters of 5~6km wide, and then is the Hong Kong Island with mountains of height up to 552m. To the east of Tsing Yi Island in Region I is the narrow channel of Tsuen Wan, a broad mountainous country parks at height up to 702m and downtown areas of Kowloon and Sha Tin.

To the north and northwest of the Bridge is Region II which contains the west part of the mountainous New Territories of Hong Kong. Ta Mo Shan of 957m high, the highest peak in Hong Kong, is also located in this region and is about 8.4km from the center of Tsing Ma Bridge. In the dashed circle, the nearest part of this region to the Bridge is seawaters about 1.5 to 3km wide, then are several hills of 200~500m high just standing on seashore. Obviously, the terrain of this region is strongly inhomogeneous. Because the Bridge is lower than these mountains on the seashore and the transitional waters is not very wide, it becomes difficult to predict the wind characteristics at the Bridge site, such as mean wind profile and roughness length, when wind blows from this region. These wind characteristics surely depend on the wind speed itself.

The Ma Wan Island due west to the Bridge is in Regions III and IV. The top level of Ma Wan Island is only 69m, close to the deck level of the Bridge. Apart from the north part of Ma Wan Island, Region III to the west of the Bridge is dominated by seawaters. To the southwest of the Bridge is Lantau Island, the largest island in Hong Kong. The highest peak of Lantau Island is 934m high and is located in the southwest part. Fa Peng Teng Hill of 273m is the highest peak in the northeast of Lantau Island and about 3.5km away from the center of Tsing Ma Bridge.

Scattered with small islands of low height, Region VI is also dominated by seawaters and is to the south of the Bridge. The nearest one of these small islands is more than 6.5km away south to Tsing Ma Bridge. Therefore, the terrain of this region may be

approximated with that of seawaters. A small transitional region may be necessary to set between Regions IV and VI and denoted as Region V. Seawaters are also dominant in this region. However, some peninsulas of Lantau Island with relative lower height is situated in this region, including one in the dashed circle, which makes the terrain condition of this region somewhat different from that of pure seawater region. Therefore the terrain condition of this region will be between Regions IV and VI.

3.5 TYPHOON VICTOR

Victor originated, as a tropical depression, in the middle of the South China Sea on 31 July 1997 and its intensity continuously increased afterwards (Hong Kong Observatory, 1998; Li et al., 1998). Tropical depression Victor first moved northwesterly for 12 hours and then had a sudden turn to near north and remained in almost the same direction during its passage over Hong Kong (see Figure 3-5). The tropical depression Victor became a real typhoon when it entered the region 250km south of Hong Kong at 8:00 on 2 August 1997 HKT (Hong Kong Time). At 19:00 HKT on 2 August, the center of Typhoon Victor moved into the region about 8km east of Cheung Chau Island (see Figure 3-4). The lowest air pressure measured on Cheung Chau Island at sea level was 972hPa. Typhoon Victor then crossed over the Tsing Ma Bridge at 20:05 and made landfall over the western part of the New Territories. Victor crossed over the whole Hong Kong within 2 hours at the average translational speed about 25km per hour. After leaving Hong Kong, Typhoon Victor continued moving north until it decayed on 3 August in the southeast of China. The measured highest 10 minute mean wind speed in the wall area of the Typhoon during its passage over Hong Kong was about 110km per hour (30.6m/s) at 500 m height above the ground, just 2 hours after its landfall (Li et al, 1998).

3.6 DATA PROCESSING

3.6.1 Data Processing

Time histories of wind speed components of 7 hour duration were recorded at the aforementioned 6 locations by the anemometers of WASHMS at a sampling rate of

2.56Hz during the passage of Typhoon Victor over Hong Kong from 17:00 to 24:00 on 2 Aug. 1997. However, the vertical wind component at WITBS01 was not available because of malfunction of the vertical channel of the anemometer. Each time history contained 64512 data. By using MATLAB as a platform, computer programs were developed to analyze the measured data to obtain mean wind speed, friction velocity, turbulent intensity, integral scale of turbulence, auto and cross wind spectra. The variations of these parameters during the passage of Typhoon Victor were also studied. Each sample (time history) of seven hours duration is evenly divided into seven segments. According to the principles of statistics and random procedure, the spectrum (S_X) of a random viable (X), obtained from M samples using FFT and piecewise smoothing technique, is also a random variable and complies with χ_n^2 distribution with degree of freedom being n=2M if X complies with standard normal distribution. The mean value (μ) and standard deviation (σ) of S_X are, respectively, μ=n and $\sigma = \sqrt{2n}$. The random error is $\varepsilon = \sigma/\mu = \sqrt{2/n} = \sqrt{1/M}$. If S_X is computed from only one sample, the random error will be 100% which is the major source of error of spectral estimate, although there may be some other measurement error such as error of measurement system. Thus, to reduce the random error, the piecewise smooth method is then applied to the spectral analysis of each one hour segment, which is further divided into 11 sub-segments of 10-minute duration, with an overlapped length of 5 minutes between two neighboring sub-segments. The 1536 data points in the 10-minute sub-segment are zero-padded to 2048 points to meet the requirement of Fast Fourier Transformation (FFT). To decrease the leakage of signal in frequency domain because of the limited sample length in time domain, Hamming Window is used in spectral analysis of each sub-segment. In considering the effect of hamming window, the actual frequency resolution of wind spectra is equal to 0.00175Hz.

3.6.2 Determination of Wind Speed Components

Before being able to analyze wind characteristics in detail, the mean wind and the three orthogonal turbulence components of fluctuating wind should be extracted from the recorded data. For this purpose, the reference wind co-ordinate system $X_S Y_E Z_U$ is selected as shown in Figure 3-6. The axis X_S points to the due south horizontally; the axis Y_E points to the due east horizontally; and the axis Z_U is

vertically upward. Further, let $U_S(t)$, $U_E(t)$ and $U_U(t)$, respectively, denote the horizontally southward and eastward components of the transient wind velocity and the vertically upward component. In consideration of the specifications of the anemometers, for the ultrasonic anemometers $U_S(t)$ is equal to the southward component from the anemometer whilst $U_E(t)$ and $U_U(t)$, respectively, take the minus values of the westward and downward components from the anemometer. For the mechanical anemometers, $U_U(t)$ also takes the minus values of the downward component from the anemometer while $U_S(t)$ and $U_E(t)$, however, should be determined from the simultaneously recorded horizontal transient wind speed and azimuth.

$$U_S(t) = U_H(t) \times \cos\beta_H(t) \tag{3-1a}$$

$$U_E(t) = -U_H(t) \times \sin\beta_H(t) \tag{3-1b}$$

where $U_H(t)$ is the horizontal resultant wind speed measured by the anemometer; and β_H indicates the azimuth of $U_H(t)$: the azimuth angle will be zero when the wind blows from the due north and 90° when wind is from the due east.

By assuming the recorded wind velocity is an ergodic stochastic process, the mean values of $U_S(t)$, $U_E(t)$ and $U_U(t)$ can be obtained by the following formulas:

$$\overline{U}_S = \frac{1}{T}\int_0^T U_S(t)dt = \frac{1}{M}\sum_{i=1}^{M} U_{Si} \tag{3-2a}$$

$$\overline{U}_E = \frac{1}{T}\int_0^T U_E(t)dt = \frac{1}{M}\sum_{i=1}^{M} U_{Ei} \tag{3-2b}$$

$$\overline{U}_U = \frac{1}{T}\int_0^T U_U(t)dt = \frac{1}{M}\sum_{i=1}^{M} U_{Ui} \tag{3-2c}$$

where T is the time-length of sample of wind velocity; $M = T/\Delta t = Tf_s$ is the discrete data number of each sample; Δt is the time interval of sampling; and f_s is the sampling frequency. The three turbulence components of fluctuating wind along the axes X_S, Y_E and Z_U can be determined as follows:

$$u_S(t) = U_S(t) - \overline{U}_S \tag{3-3a}$$

$$u_E(t) = U_E(t) - \overline{U}_E \tag{3-3b}$$

$$u_U(t) = U_U(t) - \overline{U}_U \tag{3-3c}$$

The resultant mean speed and its directional cosine vector in the $X_S Y_E Z_U$ co-ordinate system (see Figure 3-6a) can be determined by the following equations

$$\overline{U} = \sqrt{\left(\overline{U}_S^2 + \overline{U}_E^2 + \overline{U}_U^2\right)} \tag{3-4}$$

$$\left(\cos\alpha_u, \cos\beta_u, \cos\gamma_u\right) = \left(\overline{U}_S, \overline{U}_E, \overline{U}_U\right)/\overline{U} \tag{3-5a}$$

As the positive direction of longitudinal turbulence component $u(t)$ is normally defined to be in the same direction as the resultant mean wind, the positive direction of $u(t)$ is indicated by the unit victor of $\left(\cos\alpha_u, \cos\beta_u, \cos\gamma_u\right)$ (see Figure 3-6b). Furthermore, it is stipulated that the lateral turbulence component $v(t)$ is horizontal and normal to the mean wind. The vertical turbulence component $w(t)$ is upward and perpendicular to both $u(t)$ and $v(t)$. As a result, the unit vector $\left(\cos\alpha_v, \cos\beta_v, \cos\gamma_v\right)$ indicating the positive direction of $v(t)$ and the unit vector $\left(\cos\alpha_w, \cos\beta_w, \cos\gamma_w\right)$ indicating the positive direction of $w(t)$ can be determined as follows:

$$\begin{aligned}\left(\cos\alpha_v, \cos\beta_v, \cos\gamma_v\right) &= \frac{(0,0,1)\times\left(\cos\alpha_u, \cos\beta_u, \cos\gamma_u\right)}{\left|(0,0,1)\times\left(\cos\alpha_u, \cos\beta_u, \cos\gamma_u\right)\right|} \\ &= \frac{\left(-\cos\beta_u, \cos\alpha_u, 0\right)}{\sqrt{\cos^2\alpha_u + \cos^2\beta_u}}\end{aligned} \tag{3-5b}$$

$$\begin{aligned}\left(\cos\alpha_w, \cos\beta_w, \cos\gamma_w\right) &= \frac{\left(\cos\alpha_u, \cos\beta_u, \cos\gamma_u\right)\times\left(\cos\alpha_v, \cos\beta_v, \cos\gamma_v\right)}{\left|\left(\cos\alpha_u, \cos\beta_u, \cos\gamma_u\right)\times\left(\cos\alpha_v, \cos\beta_v, \cos\gamma_v\right)\right|} \\ &= \frac{\left(-\cos\alpha_u\cos\gamma_u, -\cos\beta_u\cos\gamma_u, \cos^2\alpha_u + \cos^2\beta_u\right)}{\sqrt{\cos^2\alpha_u + \cos^2\beta_u}}\end{aligned} \tag{3-5c}$$

After having determined the above directional cosine vectors, the alongwind, lateral and upward components of wind turbulence can then be obtained with the following formulae.

$$\begin{aligned}u(t) &= u_S(t)\cos\alpha_u + u_E(t)\cos\beta_u + u_U(t)\cos\gamma_u \\ &= U_S(t)\cos\alpha_u + U_E(t)\cos\beta_u + U_U(t)\cos\gamma_u - \overline{U}\end{aligned} \tag{3-6a}$$

$$\begin{aligned}v(t) &= u_S(t)\cos\alpha_v + u_E(t)\cos\beta_v + u_U(t)\cos\gamma_v \\ &= U_S(t)\cos\alpha_v + U_E(t)\cos\beta_v + U_U(t)\cos\gamma_v\end{aligned} \tag{3-6b}$$

$$\begin{aligned}w(t) &= u_S(t)\cos\alpha_w + u_E(t)\cos\beta_w + u_U(t)\cos\gamma_w \\ &= U_S(t)\cos\alpha_w + U_E(t)\cos\beta_w + U_U(t)\cos\gamma_w\end{aligned} \tag{3-6c}$$

It should be noted that the positive direction of $w(t)$ is upward but it may not be in the vertical direction if the upward component of mean wind speed $\overline{U}_U$ is not zero.

3.7 Main Results of Measured Wind Characteristics

3.7.1 Mean Wind

The 10-minute-averaged mean wind speed, the azimuth and inclination of the mean wind are analyzed using the MATLAB computer program based on the foregoing formulation and presented in this section. Displayed in Figure 3-7 are the time-varying azimuths of the mean winds measured at the six locations on the Bridge. It is seen that the wind azimuths measured at the tops of the two towers and the south side of the mid-sidespan are generally consistent with each other. However, they were somewhat different from those measured at the mid-mainspan and the north side of the mid-sidespan. This may be caused by the complicated local terrain condition. As the deck level of the Bridge is significantly lower than the heights of the hills surrounding the Bridge, it may be reasonable to describe the general azimuth of the approaching mean wind using those measured at the tower tops. With this understanding, it is seen that the mean wind blew from Region I (the northeast) and it was almost along the longitudinal axis of the Bridge between 17:00 and 19:50, and from Region V (the southwest) between 21:00 and 22:00, and from Region VI (the southwest) between 22:00 and 24:00. In addition, there was a sudden change of wind direction from the northeast to the southwest between 19:50 and 20:10. The reason for such a sudden change is that during this period, Typhoon Victor's eye just crossed over the Bridge. Furthermore, the mean wind yaw angle is defined as the horizontal angle between the direction of mean wind and the normal to the bridge alignment. Then, the average yaw angle of hourly mean wind measured at the tops of two towers were 75°, 65°, 69°, 56°, 38°, 38° for the first three hours and the last three hours, respectively. Between 20:00 and 21:00 the center of Victor crossed over the Bridge and made landfall on and moved through over the mountainous area of New Territories of Hong Kong, leading variable and unstable wind characteristics. The measured wind azimuths also indicate that the wind data recorded by the south anemometers (WITJS01 and WITBS01) between 17:00 and 19:50 and by the north

anemometers (WITJN01 and WITBN01) between 20:10 and 24:00 might be contaminated by the sheltering effect of the bridge deck on the leeward wind flow.

The wind inclination is defined in this study as the angle between the mean wind and the horizontal plane, and it is positive when wind blows upwards. Figure 3-8 shows the time-varying inclination of 10-minute-averaged mean wind measured at the deck level during the passage of Victor. It is seen that the measured wind inclinations varied within about ±6°. The wind inclinations measured by the north anemometer at mid-mainspan (WITJN01) were much more scattered. The reason may be the disturbing effect of the bridge deck on the wind flow because the wind direction during the period from 17:00 to 20:00 was too close to the longitudinal direction of the Bridge. In addition, because the mean wind speed was very small within the Typhoon eye, wind inclination larger than 10° was observed during the short crossing period of Victor over the Bridge, namely from 19:50 and 20:10. Nevertheless, this larger wind inclination should not lead to severe wind-induced vibration and instability due to the low wind speed. The inclinations of hourly-mean wind during the first three hours measured by the anemometer of WITBN01 and during the last four hours measured by WITJS01 were 3.6°, 2.9°, 2.8°, 3.1°, 3.2°, 2.0° and 2.5°, respectively.

Figures 3-9 show the variations of the 10-minute mean wind speeds with time measured by the six anemometers. The maximum 10-minute mean wind speeds were measured as 12.9m/s at the deck level and 16m/s at the tower-top level before Typhoon Victor crossed the Bridge. After the crossing, they became, respectively, 18.5m/s and 21.1m/s between 21:00 and 22:00, and 17.4m/s and 23.3m/s between 22:00 and 24:00. Clearly, the maximum 10-minute mean wind speed was larger after Typhoon Victor crossed the Bridge than before the crossing. Namely, it was larger when wind blew from the sea than wind blew from the mountainous region. For the horizontal distribution of mean wind speed, one may compare the mean wind speed measured by the anemometer WITJS01 with that by the anemometer WITBS01 (see Figure 3-9a) because they were arranged on the same side of the bridge deck with a horizontal distance about 860m. Although the patterns of variation of the 10-minute mean wind speed with time are similar to each other, there are some differences in the values of mean wind speed, particularly after the crossing of Typhoon Victor.

The same feature can also be found via the comparison between the mean wind speeds measured at the tops of Tsing Yi and Ma Wan towers (see Figure 3-8a) with a horizontal separation of 1377m and between the mean speeds measured by the two north anemometers on the bridge deck, WITJN01 and WITBN01 (see Figure 3-9b).

The winds at WITJS01 and WITBS01 before the crossing of Typhoon Victor and the winds at WITJN01 and WITBN01 after the crossing were weakened to some extent by the shelter of the upwind bridge deck. Obviously, this effect of the upwind bridge deck was small before the crossing of Typhoon Victor because the wind direction was very close to the bridge alignment. Therefore, the mean winds measured on two sides of the bridge deck before the crossing were very close to each other (Figure 3-9). However, after the crossing the sheltering effect increased significantly due to the increase of the angle between the mean wind direction and the bridge alignment. This change can be clearly observed by comparing the mean wind speeds measured at south side of the bridge deck with that measured at north side of the bridge deck (Figure 3-9).

The maximum hourly mean wind speeds at the deck level and the tower-top level were 8.5m/s and 13.4m/s, 9.8m/s and 13.9m/s, 10.1m/s and 12.7m/s for each of the three hours before Victor crossed over the Bridge. During each of the four hours after the crossing, they became, respectively, 7.9m/s and 9.3m/s, 14.9m/s and 17.8m/s, 15.7m/s and 21.2m/s, and 13.6m/s and 19.0m/s. The mean wind profile during a typhoon is not well known yet. It also cannot be exactly explored this time, for only three level wind speeds are available. However, by fitting the measured two levels mean wind speeds to the power law mean wind profile expressed by Eq.(2-44),

$$\overline{U}(z) = \overline{U}_r(z/z_r)^{\alpha}$$

one may obtain the estimated value of the exponent α. The measured data indicate that the exponent value varied with time and along the bridge longitudinal axis and scattered to quite large extent. However, the mean value of α was about 0.324 (scattered from 0.189 to 0.461) when wind blew from the northeast in Region I and 0.199 (scattered from 0.155 to 0.271) when wind blew from the southwest in Region V, and 0.212 (scattered from 0.039 to 0.316) when wind blew in Region VI. The first measured mean value is very close to that specified for the build-up terrain (0.33) in

the Code of Practice on Wind Effects, Hong Kong-1983, whilst the second and third are very close to that specified in the Code for the general terrain (0.19).

3.7.2 Friction Velocity

Friction velocity is one of the important parameters describing the turbulence of natural wind. It is defined by Eq.(2-49) and can be estimated in various ways as introduced in Chapter 2. It may be evaluated through directly measured Reynolds stress by means of a skin-friction balance, inferred from the momentum integral equation, deduced by fitting the profile of mean wind speed, or derived from the shear stress estimated through measurement of wind turbulence. In this study, the last method based on Eq.(2-53) was adopted to estimate the friction velocity because of the limitations of measurement instruments and the number of anemometers. The vertical component of wind turbulence was measured during Typhoon Victor only at three deck positions of WITJS01, WITJN01 and WITBN01, which were mounted at heights of 75.314m and 62.944m respectively. Although the velocity fluctuations were measured at rather high level, they can still be used to approximate the surface shear stress because the shear stress is generally not sensitive to the variation of height layer (Panofsky and Dutton, 1984; Cermak and Cochran, 1992; Farell and Iyengar, 1999; Duchene-Marullaz, 1980; Tieleman and Mullins, 1980).

10-minute-averaged $\overline{uw}$ and $\overline{vw}$ are calculated using the time-varying velocity fluctuations obtained from the transient wind on the Bridge deck during Typhoon Victor based on the aforementioned formulae. Figure 3-10 shows typical time histories of three fluctuating wind components measured at the mid-mianspan. The results indicate that most of values $\overline{uw}$ are negative while the values of $\overline{vw}$ are either positive or negative which are similar to the results observed by Tieleman and Mullins (1980). The friction velocity was computed using Eq.(2-53) for every 10-minute duration and the results are shown in Figures 3-11. It is seen that in the period 17:00~20:00 the friction velocity measured at the mid-sidespan (WITBN01) is smaller than that measured at the mid-mainspan (WITJN01). The reason may be that during this period wind blew from the northeast and it was almost along the longitudinal axis of the bridge. Thus, the wind crossed over additional seawaters of about 800m wide to arrive at the mid-sidespan after reaching the mid-mainspan. Hence the upwind mountainous region (Region I) exerted less influence on the wind

flow at the mid-sidespan than on the mid-mainpsan. This led the turbulence at the mid-sidespan to be weaker than at the mid-mainspan. Because the vertical channel of the anemometer WITBS01 failed to work during Typhoon Victor, the friction velocity at the mid-sidespan could not be evaluated after the crossing of Victor over the Bridge. Therefore, in this study the values of friction velocity were simply estimated using the wind fluctuations obtained at the mid-mainspan. The average values of the measured friction velocity are about 1.23, 1.09 and 0.86m/s, respectively, for Region I, Region V and Region VI corresponding to the hourly mean wind speed about 8.2~9.5m/s, 15m/s and 13.5~15.7m/s.

3.7.3 Standard Deviations and Turbulence Intensities

The intensities of three turbulence components are defined by Eq.(2-54), i.e.

$$I_a(z) = \frac{\sigma_a(z)}{\overline{U}(z)}$$

where $\overline{U}(z)$ is the mean wind speed at the height of z; the subscript a can be any of u, v and w; $\sigma_a(z)$ is the standard deviation of the corresponding turbulence component at the height z, which should wear off and be close to zero at the gradient height. However, it was found to decrease very slowly with increasing height up to the heights of the ordinary structures (Davenport, 1967; Harris, 1970).

Table 3-1 Average Values of Standard Deviations of Wind Fluctuations

Location	σ_u (m/s)			σ_v (m/s)			σ_w (m/s)		
	Region			Region			Region		
	I	V	VI	I	V	VI	I	V	VI
Tsing Yi tower	3.092	2.492	1.744	2.755	2.612	1.604	—	—	—
Mid-mainspan	2.536	2.368	1.745	2.171	2.189	1.696	1.919	2.096	1.241
Ma Wan tower	2.535	2.358	2.145	2.453	2.458	2.127	—	—	—
Mid-sidespan	2.209	2.750	2.286	1.860	2.511	2.010	1.302	—	—

Figures 3-12 show $\sigma_u(z)$, $\sigma_v(z)$ and $\sigma_w(z)$ based on 10-minute averaging duration measured at difference positions on the Tsing Ma Bridge during the passage of

Typhoon Victor. The corresponding mean values for three different upwind regions are listed in Table 3-1. It is seen that before Victor crossed over the Bridge, when wind blew from Tsing Yi Island in a direction close to the bridge alignment, the turbulence of wind around the Bridge was fairly stable. The measured $\sigma_u(z)$, $\sigma_v(z)$ and $\sigma_w(z)$ in this period decreased with the increasing distance between the measurement location and Tsing Yi Island in spite of the significant difference of height. Particularly, σ_u and σ_v on the top of the Tsing Yi tower were on average about 1.4 and 1.5 times of those at the mid-sidespan near Ma Wan Island, respectively, although the tower rises more than 130m above the deck. The standard deviation σ_w at the mid-mainspan was about 1.5 times of that at the mid-sidespan. This is because the wind flows around the Bridge were severely affected by the wind turbulence generated in the upwind mountainous region (particularly by Tsing Yi Island) which decayed evidently with the increasing distance of the measurement location from the Tsing Yi Island. During the first hour after the crossing of Victor, the Bridge was located within or close to the typhoon eye, the wind turbulence around the Bridge was governed by the turbulent behavior of typhoon itself rather than by the surface roughness. The standard deviations measured at different locations were thus close to each other with relatively small values. In addition, during this period the center of Victor made landfall and moved northwards over the mountainous region (Region II), the wind turbulence was thus very unstable. In the next hour, the standard deviations increased with time and reached the extreme values at about 21:35, and dropped again afterwards. Then, the turbulence of wind around the Bridge returned to be relatively stable again during the last two hours concerned. In the last two hours, the wind blew towards the Bridge from southwest seawaters near Lantau Island (Region VI). The measured standard deviations on the top of Ma Wan Tower and at the mid-sidespan near Ma Wan Island became larger than those at other two positions because of the influences of the Lantau Island and Ma Wan Island. The above measurement results indicate that for the complicated local terrain, such as that around Tsing Ma Bridge, the standard deviations of velocity fluctuations may vary significantly along the bridge span in the case of large wind yaw because of the influence of the mountains on upwind. The effect of the height increase on the standard deviations, on the other hand, is insignificant.

Figure 3-13 shows the turbulence intensities measured at various locations on the Bridge during the passage of Victor based on 10-minute averaging duration. The corresponding mean values for three different upwind regions are listed in Table 3-2. One may find that the turbulence intensities are much larger under typhoon condition than under seasonal wind. Particularly, more than 20% alongwind and lateral turbulence intensities were measured at tower top level (about 217m), and more than 20% lateral and upward turbulence intensities and nearly 30% alongwind turbulence intensity were measured at deck level (60m to 75m). It can also be found clearly that the turbulence intensities vary with the change of wind azimuth, i.e., the variation of the upwind terrain. By comparing the turbulence intensities on the top of Tsing Yi tower with those on the top of Ma Wan tower, or those at mid-mainspan with the same quantities at the mid-sidespan, one may find that turbulence intensities may not distribute uniformly along the longitudinal axis of the bridge surrounded by a complicated heterogeneous local terrain with mountains, islands and waters. Furthermore, compared with the same quantities at the tower top level, the turbulence intensities at the deck level are larger at most time, but occasionally smaller because of the influence of the upwind obstacles.

Table 3-2 Average Values of Turbulence Intensities

Location	I_u (%)			I_v (%)			I_w (%)		
	Region			Region			Region		
	I	V	VI	I	V	VI	I	V	VI
Tsing Yi tower	23.8	14.3	8.9	21.0	15.9	8.1	—	—	—
Mid-mainspan	28.3	15.8	12.1	24.2	14.6	11.7	21.5	11.6	8.6
Ma Wan tower	19.5	12.9	13.5	19.0	13.3	13.3	—	—	—
Mid-sidespan	23.9	21.6	19.7	20.0	20.0	17.2	13.9	—	—

As pointed out in ESDU 8520, for neutral atmospheric conditions the ratios of I_v/I_u and I_w/I_u are essentially constant irrespective of the nature of the terrain and can be represented by

$$I_v/I_u = 1 - 0.22\cos^4(\pi z/2z_\delta) \tag{3-7a}$$

$$I_w/I_u = 1 - 0.45\cos^4(\pi z/2z_\delta) \qquad (3\text{-}7b)$$

where the gradient height $z_\delta = u_*/(6f_c)$; f_c is the Coriolis parameter and is equal to $2\times 72.92\times 10^{-6}\sin 22^\circ = 5.4633\times 10^{-5}$ in Hong Kong. The estimated values of I_v/I_u and I_w/I_u using Eqs.(3-7a) and (3-7b) are, respectively, about 0.79 and 0.56 at the tower top level of Tsing Ma bridge, and 0.78 and 0.55 at the deck level of the Bridge, in which friction velocities are taken as 0.8 to 1.3m/s as measured during Typhoon Victor. The empirical values of I_v/I_u and I_w/I_u up to a height of 200m above homogenous terrain are suggested by Dyrbye and Hansen (1996) as 0.75 and 0.5 respectively, which are close to those obtained by Eqs.(3-7a) and (3-7b). However, these ratios over a heterogeneous terrain and under Typhoon condition may be much higher than the usual ones as demonstrated by the data, shown in Table 3-3, measured at four locations on Tsing Ma bridge during Typhoon Victor. Furthermore, the ratios also largely depend upon the upwind terrain condition, hence may vary significantly along the longitudinal axis of the Bridge.

Table 3-3 Average Values of Ratios between Turbulence Intensities

Location	I_u / I_v			I_u / I_w		
	Region			Region		
	I	V	VI	I	V	VI
Tsing Yi tower	0.88	1.11	0.91	—	—	—
Mid-mainspan	0.86	0.92	0.97	0.76	0.73	0.71
Ma Wan tower	0.97	1.03	0.99	—	—	—
Mid-sidespan	0.84	0.93	0.87	0.58	—	—

Figure 3-14 shows the variations of turbulence intensities with 10-minute mean wind speed under different terrain conditions. One may find from these figures that the turbulence intensities scatter much more within lower wind speed range than within higher wind speed range. However, the turbulence intensities tend to decrease with the increasing wind speed, and they seem to converge to certain values. It can also be seen that the turbulence intensities are much larger and more dispersed when wind blows from Region I (mountainous region) than those when wind blows from Region

VI (seawaters). Comparatively, the turbulence intensities are moderate both in value and in dispersion when wind blows from Region V (seawaters near Lantau Island with scattered small islands).

3.7.4 Integral Scales of Wind Turbulence

Integral scales of turbulence are a measure of the average dimensions of turbulence eddies in the flow. Some empirical formulae for estimating the integral scales were introduced in Chapter 2. This section focuses on the results of the integral scales of turbulence measured on Tsing Ma Bridge during Typhoon Victor. Under the Taylor's hypothesis of convicted "frozen turbulence" (Batchelor, 1953), they can be expressed with time integral scales (T_u^x, T_v^x and T_w^x) of turbulence or normalized auto-covariance functions ($c_u(\tau)$, $c_v(\tau)$ and $c_w(\tau)$) by Eq.(2-59), i.e.,

$$L_a^x = \overline{U}\int_0^\infty c_a(\tau)d\tau = \overline{U}\,T_a^x$$

Figure 2-2 shows typical curves of the normalized auto-covariance functions of three velocity components of wind turbulence measure on Tsing Ma Bridge during Typhoon Victor. It is then noticed that, before the first zero point, each of the measured curves of $c_a(\tau)$ (a=u,v,w) can be well approximated with an exponential function as

$$c_a(\tau) = e^{-\lambda\tau}, \quad a = u, v, w \tag{3-8}$$

Eq.(2-59) yields $\lambda = \overline{U}/L_a^x$ and further the length scales can be obtained by least square curve fitting of the logarithm of the measured normalized auto-covariance data using the following objective function

$$\ln c_a(\tau) = -\left(\overline{U}/L_a^x\right)\tau, \quad a = u, v, w \tag{3-9}$$

The integral scales during Typhoon Victor were then obtained using the above fitting method based on 10-minut duration. Figure 3-15 shows the variations of the measured integral scales of three turbulence velocity components u, v, w with time, and the corresponding average values are listed in Table 3-4. It is seen that the measured integral scales generally scattered to a great degree, and they also varied with the change of the upwind terrain. The average integral scale of alongwind turbulence component u was between 207m to 294m at the tower top level and

between 111m to 195m at the deck level. The average integral scale of lateral turbulence component v was between 130m to 189m at the tower top level and between 65m to 121m at the deck level. The integral scale of the upward turbulence component w was measured only at the deck level and the average value was between 62m to 72m.

Table 3-4 Average Values of Integral Scales of Turbulence

Location	L_u^x (m)			L_v^x (m)			L_w^x (m)		
	Region			Region			Region		
	I	V	VI	I	V	VI	I	V	VI
Tsing Yi tower	210	243	294	114	189	135	—	—	—
Mid-mainspan	135	188	195	83	120	121	58	72	65
Ma Wan tower	207	232	223	130	130	158	—	—	—
Mid-sidespan	163	164	111	109	67	65	62	—	—

One can then find from the measured results that the integral scale of the upward turbulence component w was the smallest and, on average, it was only about 40% of that of the alongwind turbulence component u. Comparatively, the integral scale of the horizontally lateral turbulence component v was moderate and about 60% of that of the alongwind turbulence component u. However, except for that measured at the mid-mainspan, the ratios between the measured integral scales varied with the change of the wind direction rather significantly. This was because the synthetic effects of upwind terrain change was more significant on the flow around other three locations than on the mid-mainspan, which is relatively farther from the surrounding mountains and island. Furthermore, the average integral scales of the alongwind and lateral components measured on the two tower tops might be significantly different from each other irrespective of the same level of the two measurement locations. In the same way, the average integral scales measured at two deck locations might also be evidently different from each other. It is also found that the average integral scales at the deck level were always smaller than at the level of tower top.

The integral scales of wind turbulence were also analyzed using the above least square fitting approach based on 1-hour time duration to investigate the effect of the statistic duration of time. It is found that when the statistic duration is increased from 10 minutes to 1 hour, the obtained integral scales will increase in general by about 15% to 35% for the component u, 10% to 25% for the component v, respectively. On the other hand, the change of the statistic time duration exerts almost no effect on the integral scale of the component w.

3.7.5 Wind Spectra

Auto spectrum of wind turbulence describes wind energy distribution over frequency n, and it is a real quantity. Cross spectrum reflects the statistical dependence between two different turbulence components at a given frequency, and it is a complex quantity. As usual, the auto spectrum is analyzed and presented in this study in the form of one-side spectrum. However, the real part of cross spectrum, called co-spectrum, is an even function of frequency n whilst the imaginary part of cross spectrum, called quadrature spectrum, is an odd function of frequency n. The cross spectrum is thus analyzed in the form of two-side spectrum, and only the half part in the positive frequency region is presented in this study. Auto and cross spectra of wind turbulence components are indispensable input information in the buffeting analysis of bridges when the frequency-domain method is employed. Some empirical formulae were proposed by various investigators based on many measurements and experiments and were reviewed in Chapter 2. These empirical formulae have been frequently applied to engineering practice for several decades. However, these empirical formulae may not be adequate for wind flows over a complicated and heterogeneous local terrain, such as that around the Tsing Ma Bridge. Thus, field measurement is necessary for determining more accurately the spectra of wind turbulence over a complicated and heterogeneous terrain, particularly when carrying out a comparison between the analyzed and field measurement buffeting responses of long span bridges.

The auto and cross spectra of three fluctuating wind components during Typhoon Victor are thus analyzed in detail in this study using the turbulence components measured at all the anemometer locations on Tsing Ma Bridge and in different time periods using the FFT technique. Because the magnitudes of the cross spectra

between two turbulence components at any two locations of anemometers will be very small due to the large separation between them, only the co-spectra and quadrature spectra between two different components of wind turbulence at the same location are analyzed in this study. Figure 3-16 displays typical one-side auto spectra of the alongwind, lateral and upward vertical components of wind turbulence measured at the mid-mainspan by WITJS01 during the period of 21:00 to 22:00. Typical two-side co-spectra and quadrature spectra, measured at the same location and in the same period, are plotted respectively in Figures 3-17 and 3-18 for the half part of the positive frequency only.

It is found from these results that the normalized auto spectra of three velocity fluctuations of wind turbulence (nS_u/u_*^2, nS_v/u_*^2, nS_w/u_*^2) varied strongly with the time due to the change of wind direction and upwind terrain and also with the height of the anemometer position. However, in most cases, the slopes of all auto spectra were approximately equal to –5/3 in the reduced frequency range $f_z \geq 0.3$ for nS_u/u_*^2 and nS_w/u_*^2, and $f_z \geq 0.6$ for nS_v/u_*^2. The obtained auto-spectra are then compared with those expressed by Eqs.(2-73), (2-88) and (2-85) (Von Karman spectra), Eqs.(2-78), (2-86) and (2-83) (Kaimal spectra), Eqs.(2-79) and (2-87) (Simiu Spectra) and Eq.(2-82) (Lumley spectrum). It is found that the von Karman spectra, using measured integral scales and turbulence ratios ($\beta_u, \beta_v, \beta_w$), fit the measured spectral much better than Kaimal and Simiu and Lumley spectra in most cases, especially in the low frequency region. However, the values of von Karman spectra may sometimes be smaller than those measured in the higher frequency region.

The measured cross spectra also varied strongly with time due to the variations of the wind direction and the upwind terrain. It is also found from the measured results that under the typhoon condition the magnitude of the quadrature spectra had the same order as that of the corresponding co-spectra. Therefore, it may be better to take the quadrature spectra in the buffeting analysis of long span bridges. The measured co-spectrum between the alongwind and upward turbulence components (C_{uw}) are also compared with that expressed by Eq.(2-98) which was suggested by Kaimal et al. (1972), and good agreements are found in most cases.

3.7.6 Curve Fitting of Auto Spectra

The magnitudes of wind spectra and their shapes depend upon wind and terrain conditions, and thus often vary from place to place and from time to time. In spite of this variation, auto spectral curve may be well fitted with a proper objective function using non-linear least square method. Tieleman (1992) used the following formula to fit the normalized auto spectrum

$$\frac{nS_a(n)}{u_*^2} = \frac{Af_z^\gamma}{(C+Bf_z^\alpha)^\beta} \tag{3-10}$$

where $a = u, v, w$; A, B, C, and α, β, γ are six parameters to be determined; and γ represents the slope on logarithmic frequency scale in the low frequency region. Obviously, this expression causes the spectral magnitude at zero frequency to be either zero when $\gamma > 1$ or infinite when $\gamma < 1$, which seriously breaks the condition of Eq.(2-70). Facchini (1996) and Garg (1997) used the following Fichtl-McVehil spectrum in conjunction with the constraint conditions of Eqs.(2-70) and (2-72) to fit the measurement data of spectrum and obtained good fitted curves agreeing with measured data both in high and low frequency ranges.

$$\frac{nS(n)}{\sigma^2} = \frac{a\, n/n_p}{\left(1+1.5\left(n/n_p\right)^r\right)^{5/3r}} \tag{3-11}$$

where a, r, n_p are positive; r controls the magnitude of the peak; and n_p determines the position of the peak.

Based on the above two objective functions and noticing the expressions of the well-known empirical spectral formulas as introduced in Chapter 2, the following expression is employed in this study to fit the measured normalized auto spectra of wind turbulence.

$$h(a,b,m;f) = \frac{nS_a}{u_*^2} = \frac{a\, f_z}{\left(1+b\, f_z^{1/m}\right)^{cm}} \tag{3-12}$$

where the subscript a can be one of three velocity fluctuations u, v, w; $f_z = nz/\overline{U}(z)$ is the reduced dimensionless frequency of wind turbulence; the value of c is set to $5/3$, to ensure the fitted auto spectra to have the same net exponent of f_z as Kolmogorov's law (see Eq.(2-68)); and a, b and m are three parameters to be determined. Obviously, some prevailing empirical formula of auto spectral

mentioned in Chapter 2, such as Kailmal spectrum, Simu spectrum and Harris spectrum, Panofsky spectrum, Lumley spectrum, etc., can be attained as special cases of Eq.(3-12) by setting a, b and m to the corresponding values. However, the three parameters, a, b and m, are dependent on the measured spectral data and are determined by minimizing the residue function $E(a,b,m)$ given by Eq.(3-13), via non-linear least square fitting.

$$E(a,b,m)=\sum_{i=1}^{M}\left[h(a,b,m;f_i)-\hat{h}(f_i)\right]^2 \tag{3-13}$$

where, $\hat{h}(f_i)$ is the measured value of normalized spectrum; M is the data number of the measured spectrum. In addition, according to the principle given by Eq.(2-72), the three parameter should satisfy the following constraint condition

$$\int_0^{\infty}\frac{a\,df}{\left(1+bf^{1/m}\right)^{cm}}=\beta_a^2 \tag{3-14}$$

namely,

$$a=\frac{\beta_a^2 b^m}{m\,\mathbf{B}\left((c-1)m,m\right)}=\frac{\beta_a^2 b^m\Gamma(cm)}{m\,\Gamma\left((c-1)m\right)\Gamma(m)} \tag{3-15}$$

where, $\beta_a=\sigma_a/u_*$; $\mathbf{B}$ and Γ are, respectively, Beta function and Gamma Function. Furthermore, the principle given by Eq.(2-71) yields the following constraints condition on m

$$\lim_{n\to 0}(n^{1/m-1})=0\,;\quad \text{i.e.,}\quad 0<m<1.0 \tag{3-16}$$

Finally, from the principle given by Eq.(2-70) for zero turbulence frequency, the objective function of Eq. (3-12) implies the following assumption about integral scales of turbulence if the parameter a is regarded as independent of height.

$$L_a^x=\frac{az}{4\beta_a^2} \tag{3-17}$$

Eq.(3-17) may not be satisfied by measured data of turbulence scales and turbulence ratios. Fortunately, the disagreement between the parameter a and the measured turbulence scales and turbulence ratios on Eq.(3-17) will only affect the spectral values in very low frequency region, thus will lead little influence on the predicted structural response to wind.

The discrete turbulence spectral data measured at the six locations on the Tsing Ma Bridge during Typhoon Victor are fitted using the above non-linear least square

fitting method. The results demonstrate that the curves fit the measured spectral data very well both in the higher and lower frequency region. However, the three parameters may vary from location to location because of the nonuniform wind field due to the complicated and heterogeneous local terrain, and may vary from time to time because of the change of the upwind terrain. Typically, the fitted spectra of alongwind, lateral and upward turbulence components measured at the mid-mainspan between 21:00 to 22:00 during Typhoon Victor are plotted in Figures 3-16.

3.7.7 Curve Fitting of Cross Spectra

As mentioned in Chapter 2, the measurement results demonstrated a –7/3 to –8/3 power law of the co-spectrum between the alongwind and upward turbulence components (C_{uw}) in the inertial sub-range. The field measurement carried out during Typhoon Victor also shows that the empirical expression of Eq.(2-98) given by Kaimal fits the measured co-spectral data of C_{uw} fairly well in most cases. Further, it is noticed that Eq.(2-98) is also a special case of Eq.(3-12) by set a= -7, b= 9.6, m= 1 and c=2.4. Thus, Eq.(3-12) with c=2.4 is also used in this study to fit the C_{uw} curves from discrete co-spectral data measured during Typhoon Victor. In general, the fitted curves of C_{uw} can well represent the measured data. A typical fitted curve of C_{uw} is plotted in Figure 3-17b corresponding to the period from 21:00 to 22:00.

It is found that the measured quadrature spectra Q_{uw} and co-spectra C_{vw} have similar variation pattern with frequency to that of the measured co-spectra C_{uw} in most cases. Thus, they may also be fitted using Eq.(3-12) with c=2.4. The co-spectra C_{uv} and the quadrature spectra Q_{uv} and Q_{vw} measured during Typhoon Victor seem to vary rather arbitrarily with frequency. However, the variation pattern of these three quantities is found to be similar to that of C_{uw}. Therefore, the curve fitting based on Eq. (3-12) is also carried out on the co-spectra C_{uv} and the quadrature spectra Q_{uv} and Q_{vw} measured during Typhoon Victor. Typical fitted curves of the co-spectra and quadrature spectra can also be found in Figure 3-17 and Figure 3-18. It can be

found that the fitting results of C_{uw}, C_{vw} and Q_{uw} are much better than those of C_{uv}, Q_{uv} and Q_{vw}.

3.8 Main Results of Measured Acceleration Responses

Time histories of acceleration responses of 6 hour duration were recorded by the WASHMS at the four sections of the bridge deck and the four locations of the south cable and one reference location on Ma Wan anchorage, as shown in Figure 3-2, during the passage of Typhoon Victor over Hong Kong from 18:00 to 24:00 on 2 August 1997. The sampling rates of all the accelerometers were set to 25.6Hz. Each time history contains 552960 data. All these recorded data are then analyzed in this section using a computer programs developed on MATLAB platform to obtain the standards deviations, peak factors and auto spectra of the acceleration responses of the Tsing Ma bridge deck and cables to Typhoon Victor. Each time history of six-hour duration is evenly divided into six segments of one-hour duration. The piecewise smooth method is then applied in the spectral analysis of each one-hour segment, which is further divided into 21 sub-segments with an overlapped length of 2.6 minutes between two neighboring sub-segments. The data point number for FFT is thus equal to 8192. Hamming Window is also used in spectral analysis of each sub-segment to decrease the leakage of signal in frequency domain. Then, taking the effect of Hamming Window into account, the actual frequency resolution of spectrum is 0.004375 Hz.

3.8.1 Standard Deviations of Acceleration Responses

Figure 3-19 illustrates the time histories of the lateral, vertical and torsional acceleration responses of the bridge deck at the mid-mainspan (ATTJD) during the period from 18:00 to 24:00. The lateral response of bridge deck is directly taken from the lateral accelerometer. The vertical response is obtained by averaging the signals from the two vertical accelerometers. The torsional acceleration response is expressed as a half of the difference between the two vertical signals. Figure 3-20 shows the time histories of the lateral and vertical acceleration responses of the bridge cable at the quarter-mainspan near the Tsing Yi tower (ABTLC) during the same period. It is found that responses of the bridge deck between 18:00 and 20:00

(before the crossing of Victor over the Bridge) were considerably smaller than those between 20:40 and 24:00 (after the crossing). During the period from 20:00 to 20:40, the center of Victor crossed over the Bridge, and immediately made landfall on the seashore opposite to the Bridge, then moved across the mountainous region of New Territories (see Figure 3-4). As shown in Figures 3-9 and Figures 3-11 to 3-13, the mean wind speed and wind turbulence were very low during this period, hence, the corresponding acceleration responses of the Bridge were much smaller than those within other periods.

Figure 3-21 shows the variations of standard deviations of lateral, vertical and torsional accelerations of the bridge deck at the mid-mainspan (ATTJD) with time in 10-minute interval. The maximum standard deviations of the deck lateral, vertical and torsional acceleration responses at ATTJD were $0.588\,cm/s^2$, $3.082\,cm/s^2$ and $0.0010\,rad/s^2$, occurring at about 21:35, 23:35 and 22:45, respectively. Clearly, the vertical response was much larger than the lateral and torsional responses. In addition, it is also found that standard deviations of the vertical and torsional acceleration responses at ATTJD (mid-mainspan) were close to those at ATTID, and were somewhat larger than those at the ATTFD (see Figure 3-2 for locations in detail). The standard deviations of the vertical and torsional acceleration responses at ATTBD (mid-sidespan) were much smaller than those at other locations. However, the standard deviations of the lateral acceleration responses at the four deck sections were rather close to each other.

Figure 3-22 displays the variations of standard deviations of lateral and vertical accelerations of the bridge cable at the quarter-mainspan (ABTLC) with time in 10-minute interval. The maximum standard deviations of the cable lateral and vertical acceleration responses at ABTLC were $0.157cm/s^2$ and $2.965cm/s^2$, occurring about 21:35 and 22:45, respectively. For the cable in the Tsing Yi side span, the maximum standard deviations of the lateral and vertical acceleration responses at ABTQC were $4.296cm/s^2$ and $3.131cm/s^2$, respectively, at 23:55. Clearly, the standard deviation of the lateral acceleration response of the "free" cable without suspenders in the Tsing side span was much larger than that of the bridge deck. However, the standard deviation of the lateral acceleration response of the cable in the main span was much smaller than that of the bridge deck. The standard deviations of the vertical

acceleration responses of the bridge deck and cables were, on the other hand, close to each other.

Furthermore, Figure 3-23 and Figure 3-24 illustrate, respectively, the standard deviations of the lateral, vertical, and torsional (for the deck only) acceleration responses of the bridge deck and cable against 10 minutes mean wind speed. It is seen that the vertical responses of the bridge deck and cable and the torsional response of the bridge deck increased almost proportionally to the cube of mean wind speed. The lateral acceleration response of the bridge deck increased almost proportionally to the square of mean wind speed whilst that of the bridge cables in the main span increased almost linearly with mean wind speed. It is thus demonstrated that the patterns of the vertical and torsional vibrations were different from the pattern of lateral vibration, and the pattern of the lateral vibration of deck was also slightly different from that of the cable.

3.8.2 Peak Factors of Acceleration Responses

Probability analysis of transient acceleration (in the sense of 0.039s time interval) is also carried out in this study based on the 10-minute averaging duration. It is found that the lateral, vertical and torsional transient acceleration responses of the bridge deck and cables to Typhoon Victor approximately complied with the Gaussian distribution. The peak factor of acceleration response is defined as the ratio of the maximum acceleration response within a given duration over the response standard deviation during the same time duration. The peak factor is then analyzed based on both 10-minute duration and 1-hour duration using the acceleration responses of the Tsing Ma Bridge to Typhoon Victor during the period from 20:40 to 24:00 on 2 August 1997, for the responses were comparatively larger during this period. The analyzed results show that when 10-minute time duration is used the average values of peak factor are, respectively, 4.04, 3.76 and 4.33 for the deck lateral, vertical and torsional accelerations and are, respectively, 4.49, 4.30 and 4.53 for the lateral, vertical and longitudinal accelerations of the cables. Furthermore, when 1-hour time duration is considered, the average values of peak factor become 5.05, 4.61 and 5.70 respectively for the deck lateral, vertical and torsional accelerations and 5.73, 5.44 and 5.27 respectively for the lateral, vertical and longitudinal accelerations of cables. By averaging the above values, the peak factor of acceleration response of the Bridge

to Typhoon Victor is about 4.3 for 10-minute time duration and 5.3 for 1-hour time duration. Clearly, the elongation of time duration from 10 minutes to 1 hour amplifies the peak factor of acceleration response by about 23%.

Table 3-5 Lateral Natural Frequencies (Hz)

No.	1	2	3	4	5	6	7
Measured	0.0688	0.1594	0.2406	0.2875	0.3469	0.3875	0.4094
Computed	0.0681	0.1578	0.2401	0.2851	0.3651	0.3800	0.3960
Discrepancy (%)	1.0	1.0	0.2	0.8	-5.0	2.0	3.4

Table 3-6 Vertical Natural Frequencies (Hz)

No.	1	2	3	4	5	6	7
Measured	0.1125	0.1375	0.1844	0.2375	0.2812	0.3250	0.4062
Computed	0.1166	0.1367	0.1890	0.2448	0.2945	0.3246	0.4060
Discrepancy (%)	-3.5	0.6	-2.4	-3.0	-4.5	0.1	0.0

Table 3-7 Torsional Natural Frequencies (Hz)

No.	1	2	3	4
Measured	0.2656	0.3219	0.4844	0.6133
Computed	0.2173	0.3106	0.4755	0.6162
Discrepancy (%)	-2.1	3.6	1.9	-0.5

3.8.3 Response Spectra and Natural Frequencies

The auto spectra of the deck and cable acceleration responses to Typhoon Victor are also analyzed in this study. The natural frequencies of the Bridge under typhoon wind can then be identified from the analyzed spectra. As an example, Figures 3-25 illustrate the auto spectra of the lateral, vertical and torsional acceleration responses of the deck at ATTID for the period of 21:00 to 22:00. The frequencies of some

lower natural modes of the lateral, vertical and torsional motions of the Bridge identified from the given response spectra are listed in Tables 3-5 to 3-7. The computed frequencies from eigenvalue analysis (see Appendix A) are also given in these tables for comparison. One can then see that measured natural frequencies are very close to those computed. The relative difference is less than 5% for all of the lateral, vertical and torsional natural frequencies. Furthermore, strong coupling between the lateral and torsional motions of the bridge deck is found from the analyzed spectra. For instance, significant peaks can be seen on the curves of lateral spectrum at the frequencies of 0.2656Hz, 0.3219Hz, 0.4844Hz, etc. (see Figure 3-25a), of which the modes are dominated by the torsional motion of the deck. Similarly, peaks also occur on the curve of torsional spectrum at the frequencies of 0.2406Hz, 0.2875Hz, 0.3469Hz, etc. (see Figure 3-25c), of which the modes are dominated by the lateral motion of the deck. Finally, these frequencies are found to remain almost constant during the passage of Typhoon Victor in spite of the variation of the wind speed, wind direction, and upwind terrain.

3.9 Implications To Buffeting Analysis

The currently used buffeting analysis of long suspension bridges is mainly based on the Scanlan's theory (Scanlan and Jones, 1990; Jain et al., 1996). Such an analytical process is basically a combination of numerical, experimental, and analytical approaches. Finite element technique is usually used to determine the natural frequencies and mode shapes of a bridge. The wind tunnel tests of bridge section models provide flutter derivatives and aerodynamic coefficients. The buffeting response of bridge deck is then determined using the mode superposition method under the frame of random vibration theory. In general, it is assumed that mean wind is perpendicular to the longitudinal axis of bridge deck. The wind characteristics, such as mean wind profile, friction velocity, roughness length, turbulence intensity, integral scale, and auto-spectrum, do not vary with the longitudinal axis of the bridge. The wind forces on the bridge towers and cables are also not considered so that the wind-induced response of the bridge cables and towers and their interaction can not be predicted and estimated.

From the measured wind structures and bridge responses of the Tsing Ma Bridge during Typhoon Victor, it is clearly seen that for a long suspension bridge located in a complex and heterogeneous topography and attacked by a typhoon, wind direction may not be perpendicular to the longitudinal axis of the bridge. The mean wind speed, roughness length, friction velocity, turbulence intensity, auto-spectrum, and others also vary with the longitudinal axis. The turbulence intensity and integral scale under the typhoon condition are usually higher than those used for the seasonal trade wind case. Thus, it will be difficult to have a reasonable comparison between the field measurement results and the prediction results. Furthermore, the responses of bridge cables are usually measured by a WASHMS. However, these results can not be used to facilitate the comparison. All these indicate the need of improvement of the currently used analytical process for predicting buffeting response of long suspension bridges in typhoon prone regions.

3.10 SUMMARY

The wind and structural response data recorded by the Wind And Structural Health Monitoring System during Typhoon Victor were analyzed in this chapter for evaluating wind characteristics and acceleration responses of the Tsing Ma Bridge. The results show that during Typhoon Victor, both mean and turbulent characteristics varied considerably due to the change of wind direction and the heterogeneous upwind terrain. Turbulence intensities measured during Typhoon Victor were higher than those due to seasonal trade winds. The decreasing rate of turbulence intensities with height under the complex and heterogeneous terrain and Typhoon conditions might be significantly lower than that under the smooth terrain and seasonal trade winds conditions. The wind excitation mechanism of the Bridge in the lateral direction was obviously different from that in the vertical direction or in the rotation. The wind excitation mechanism of the bridge cable was also slightly different from that of the bridge deck. The implications of these measurement results to the currently used analytical process for predicting buffeting response of long suspension bridges were also given. It is necessary to modify existing analytical process for predicting the buffeting response of long suspension bridges located in complicated terrain and typhoon prone regions.

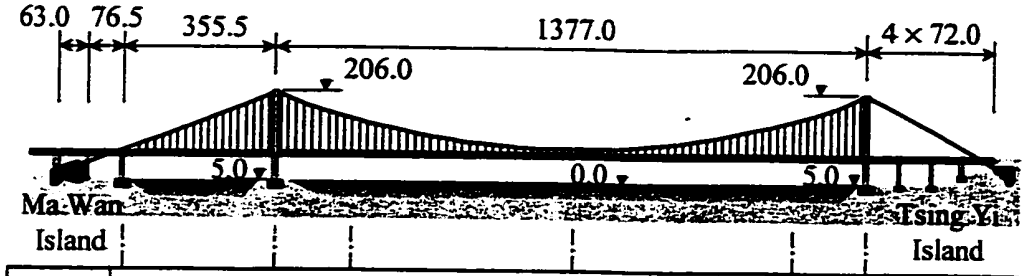

Chainage	23267.5	23623.0	23811.5	24311.5	24811.5	25000.0
Route Profile	62.759	69.869	73.639	78.639	73.639	69.869
Vertical Curve	2%	↔ Circular arc with R=25000m			↔ 2%	

Figure 3-1 Elevation of Tsing Ma Bridge

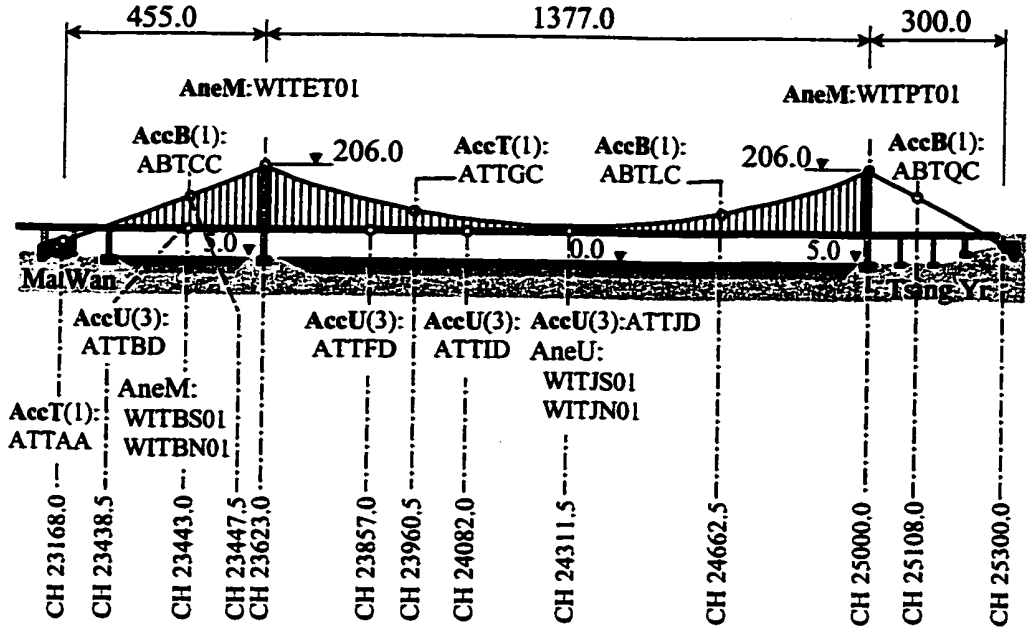

Figure 3-2 Locations of Anemometers and Accelerometers

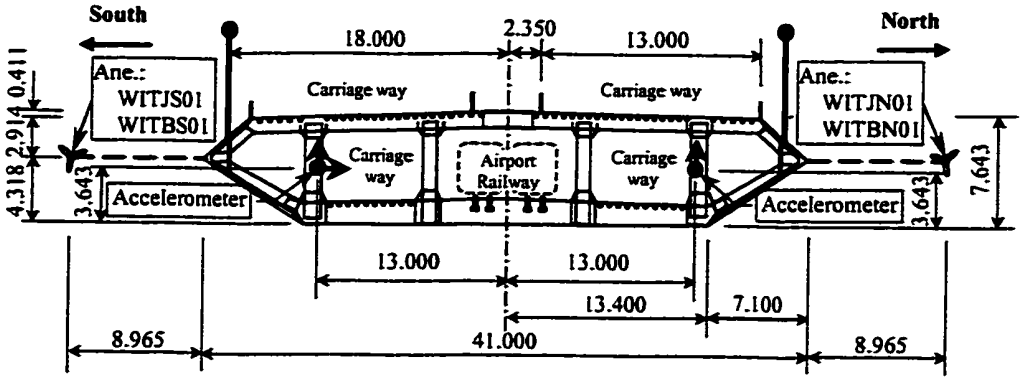

Figure 3-3 Positions of Sensors on Cross Section of Bridge Deck

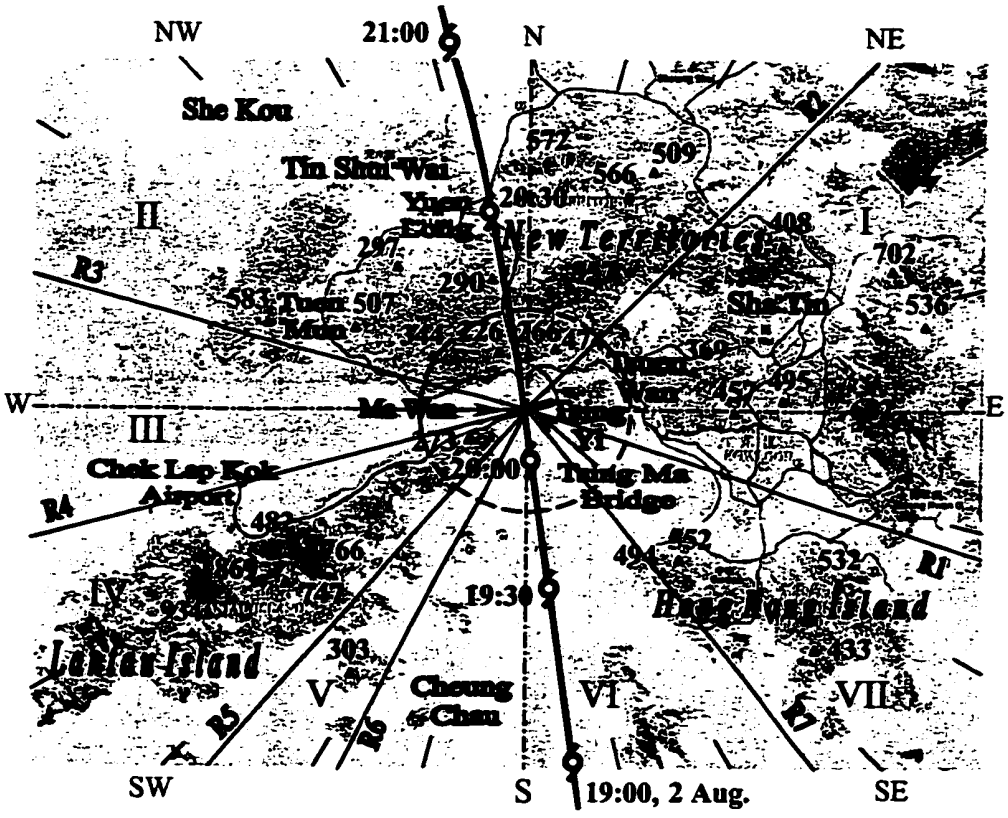

Figure 3-4 Local Topography of Tsing Ma Bridge

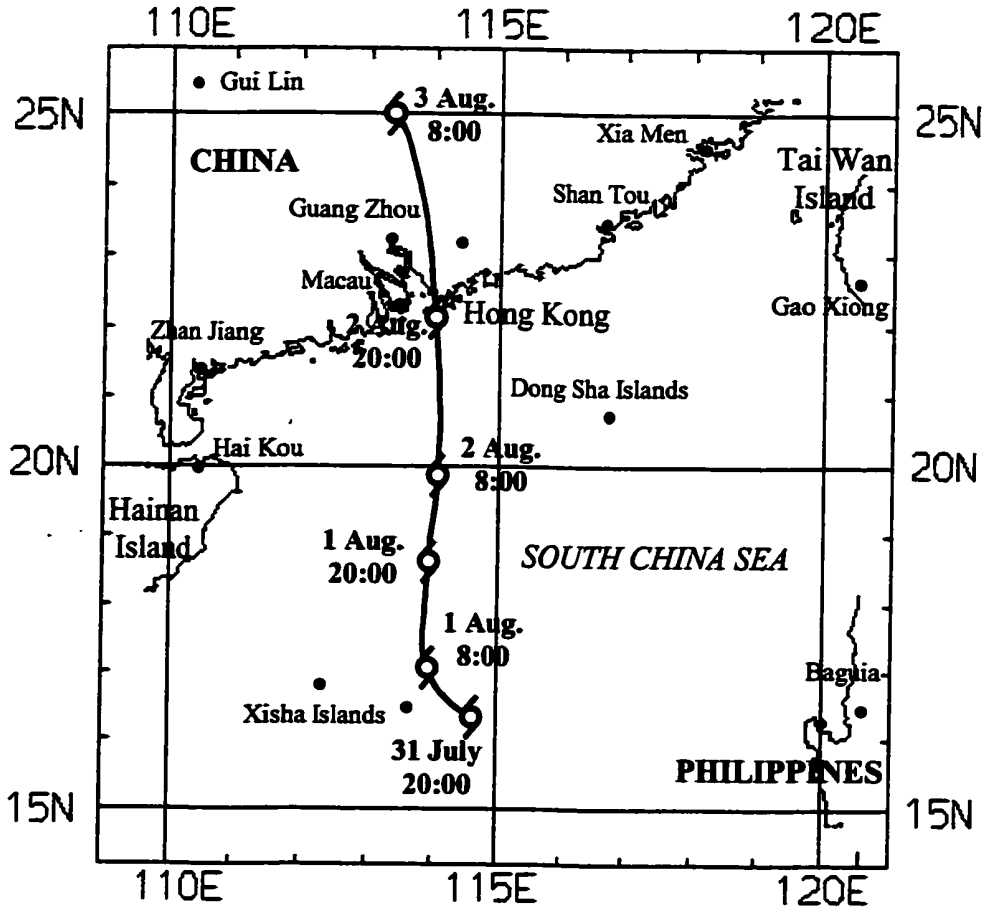

Figure 3-5 Track of Typhoon Victor

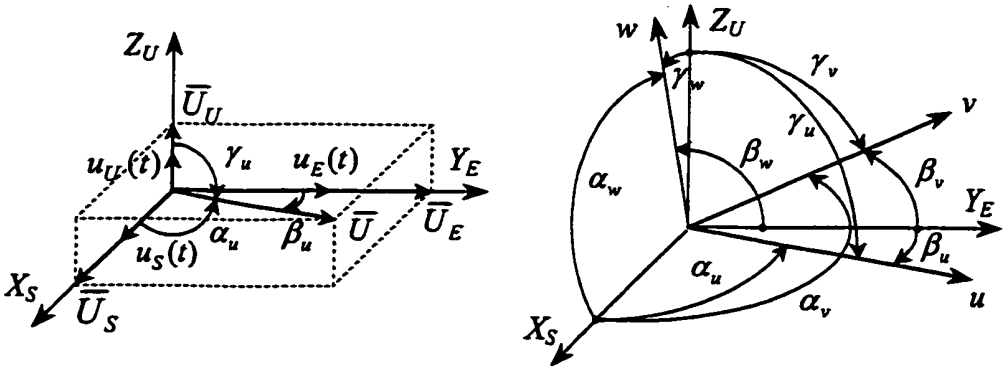

(a) Reference wind coordinate system

(b) Directional angels of fluctuating wind

Figure 3-6 Definition of Positive Directions of Mean Wind and Fluctuating Wind

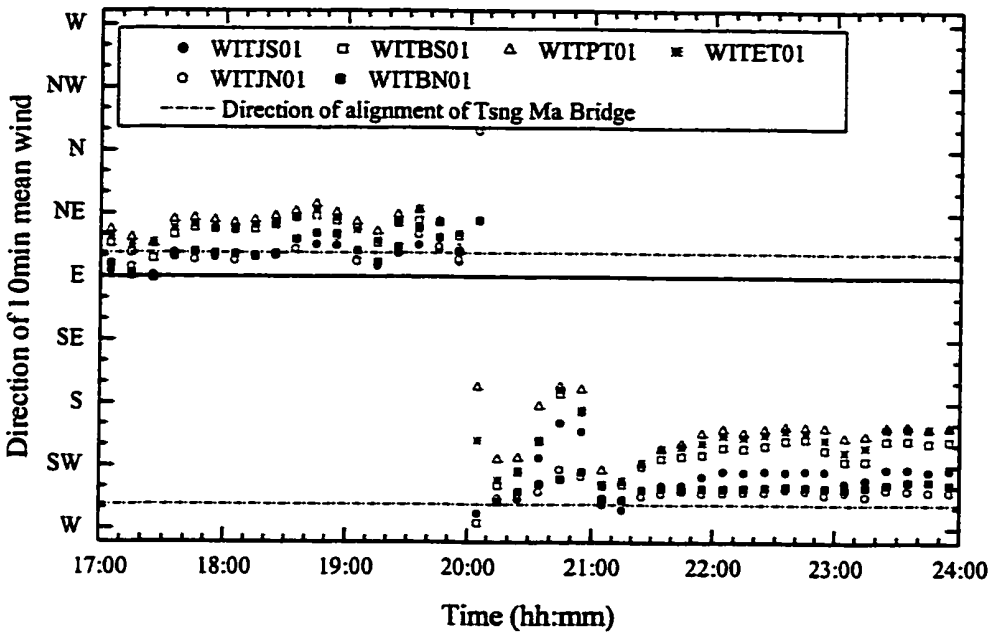

Figure 3-7 Variations of Azimuth of 10min Mean Wind

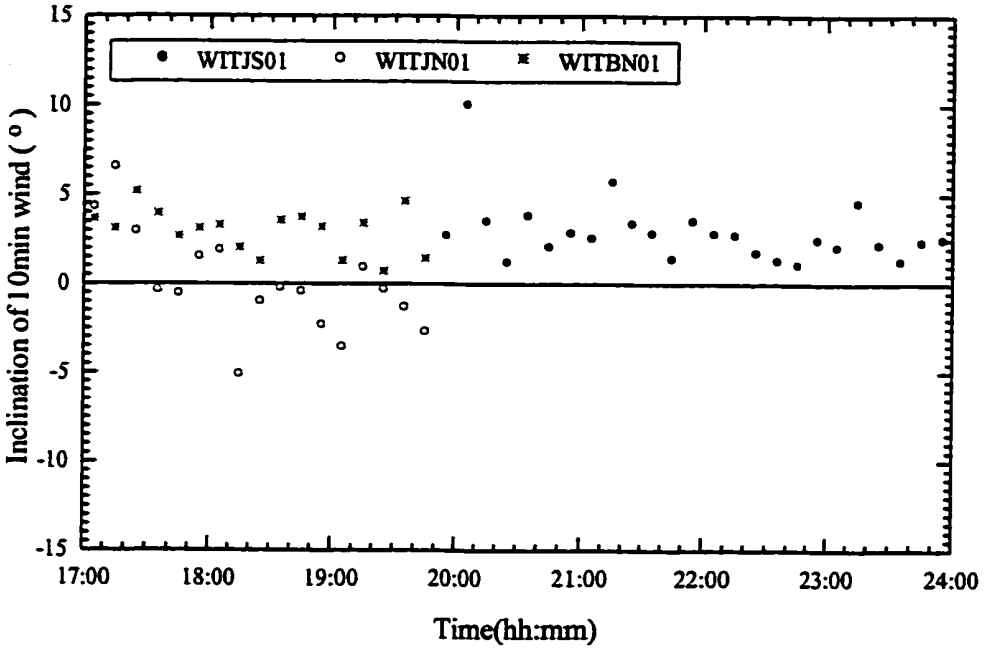

Figure 3-8 Variations of Inclination of 10min Mean Wind

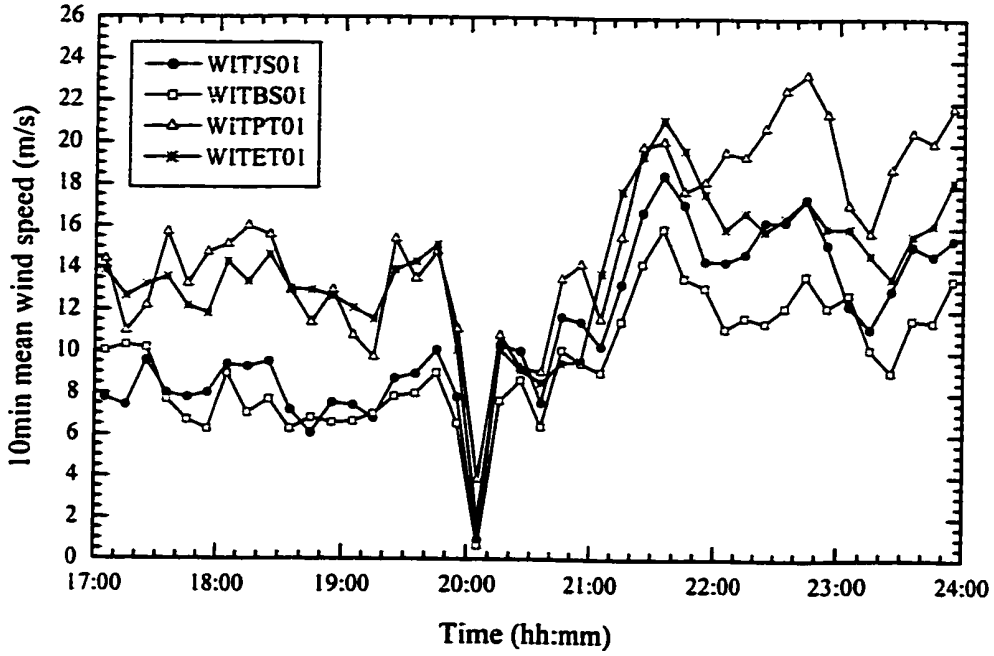

(a) South side

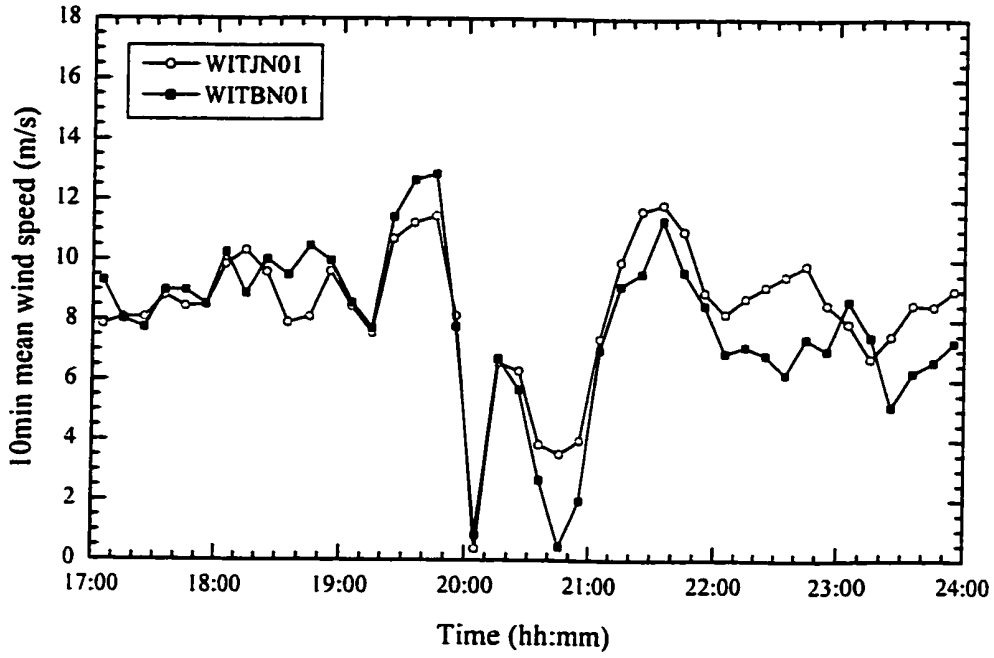

(b) North side

Figure 3-9 Variations of 10min Mean Wind Speed

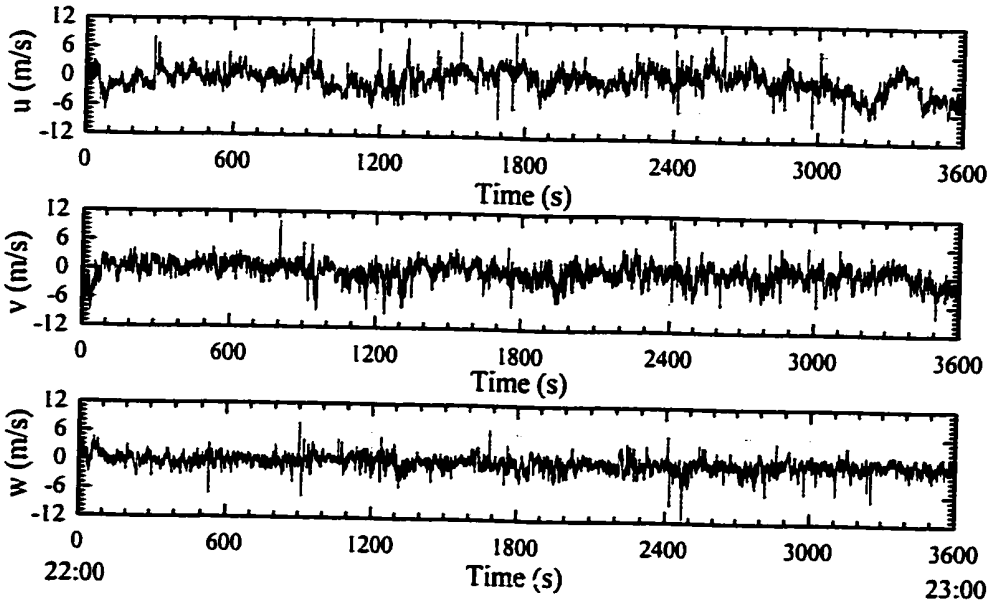

Figure 3-10 Typical Time Histories of Fluctuating Wind Components

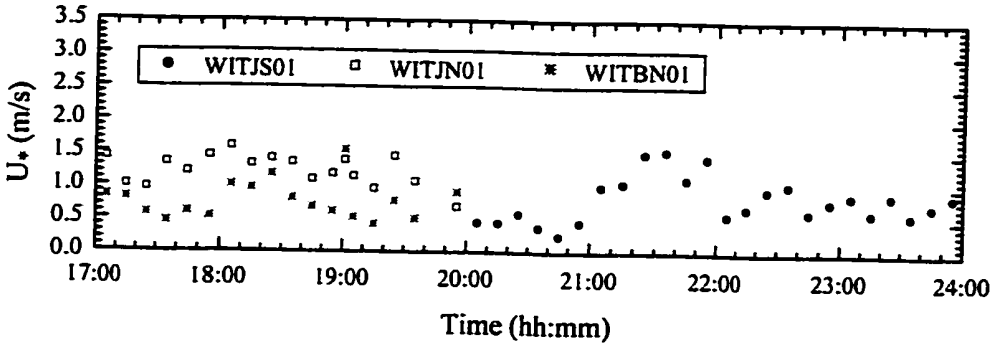

Figure 3-11 Variations of Friction Velocity

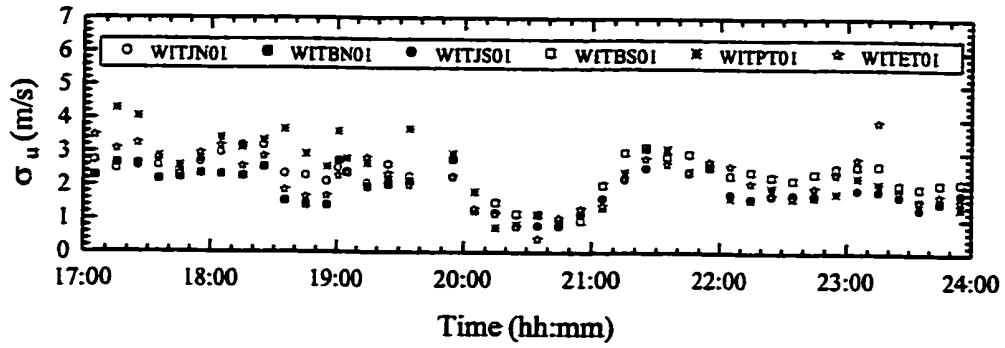

(a) Alongwind turbulence component

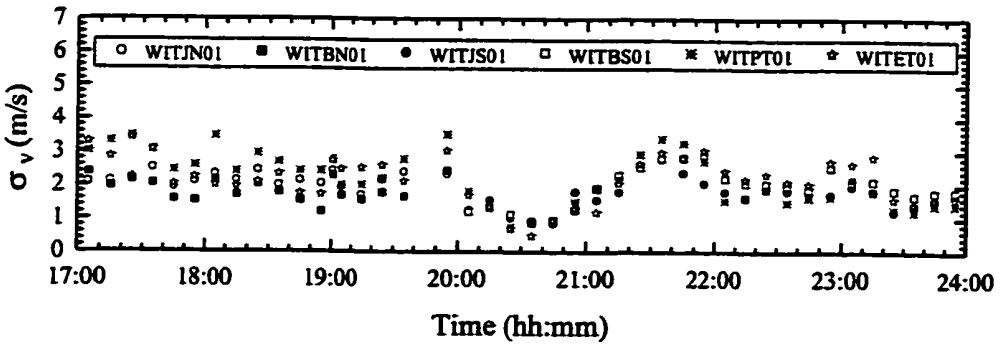

(b) Lateral turbulence component

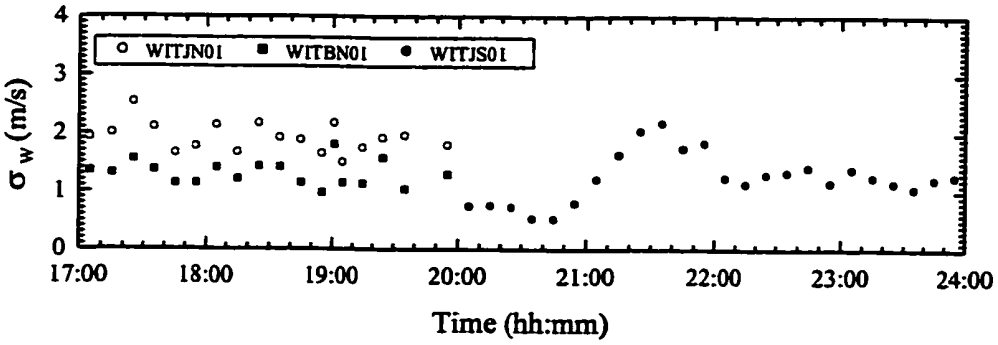

(c) Upward turbulence component

Figure 3-12 Variations of Standard Deviations of Wind Fluctuations

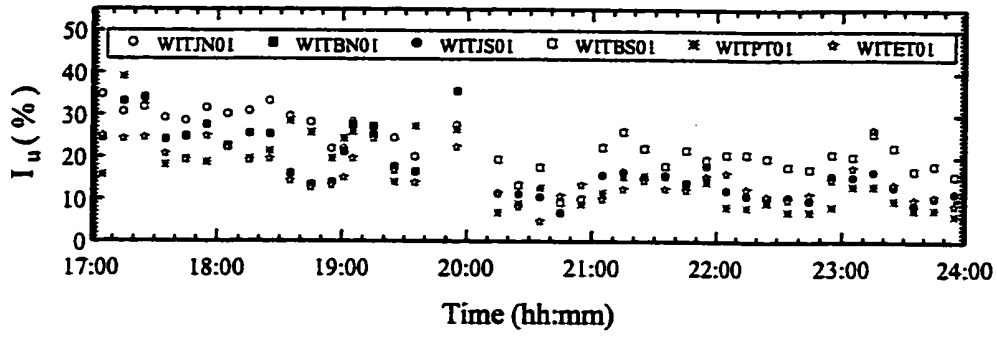

(a) Alongwind turbulence component

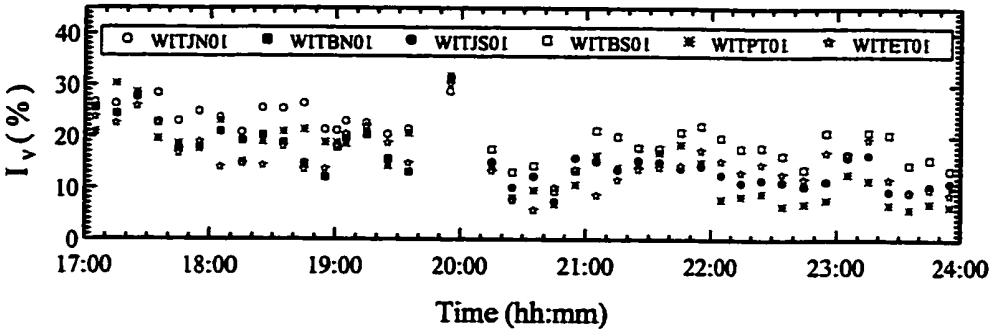

(b) Lateral turbulence component

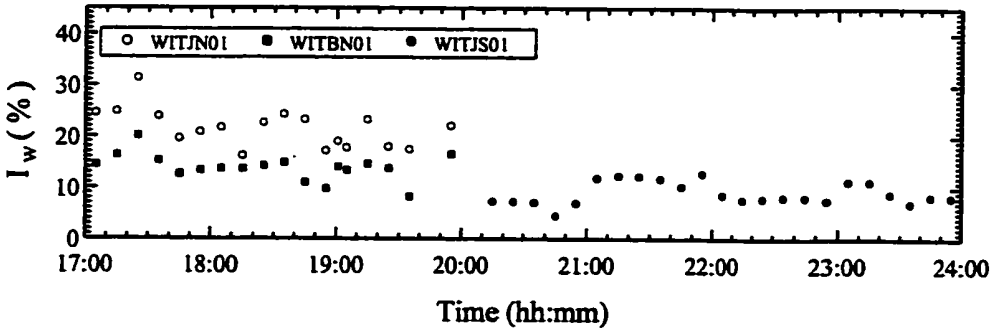

(c) Upward turbulence component

Figure 3-13 Variations of Turbulence Intensities

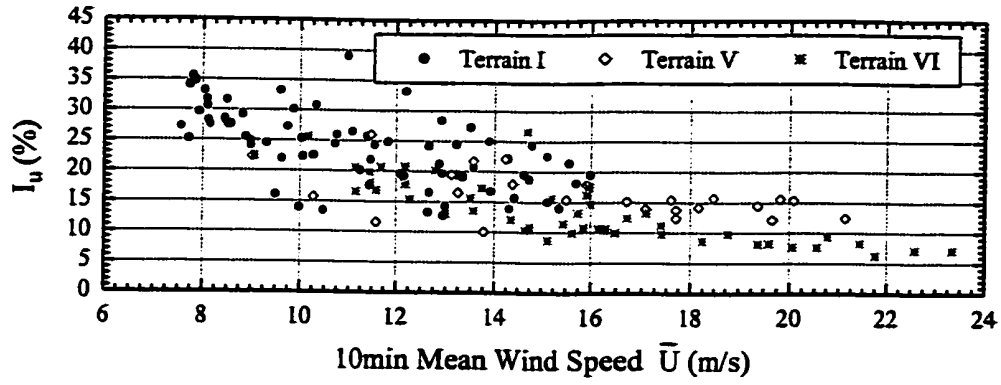

(a) Alongwind turbulence component

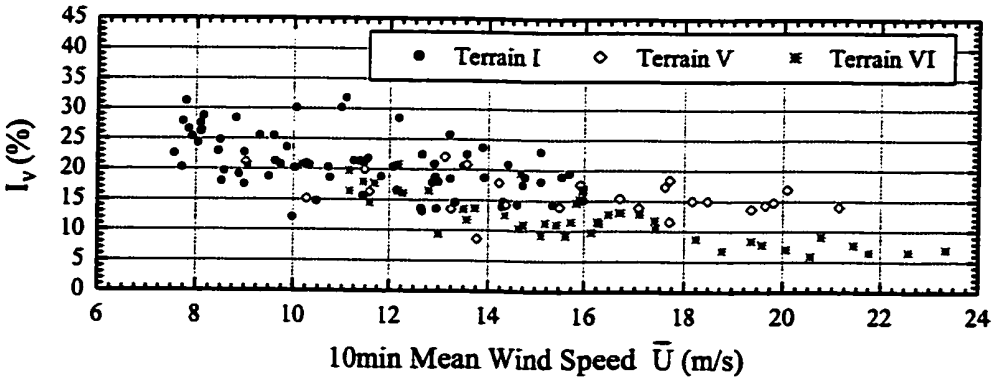

(b) Lateral turbulence component

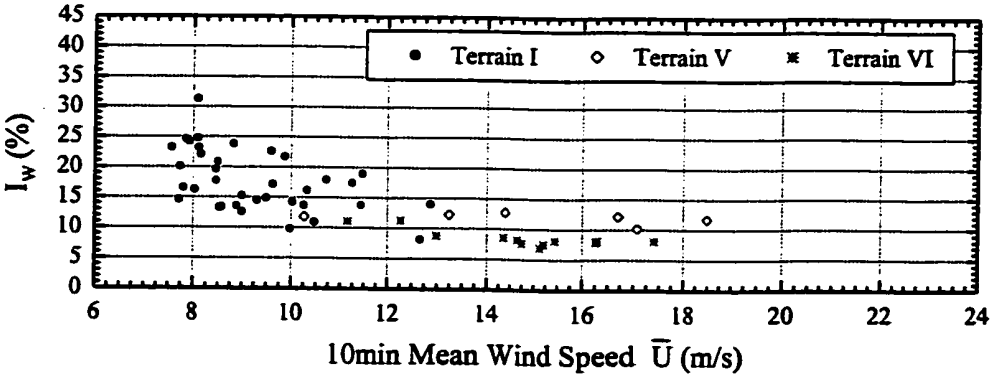

(c) Upward turbulence component

Figure 3-14 Variations of Turbulence Intensities with Wind Speed

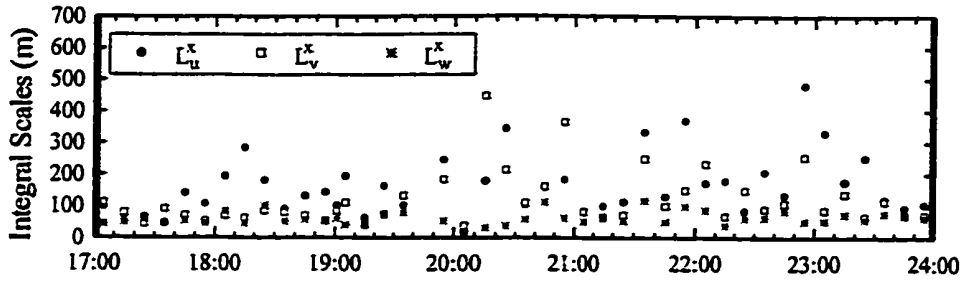

(a) At mid-mainspan

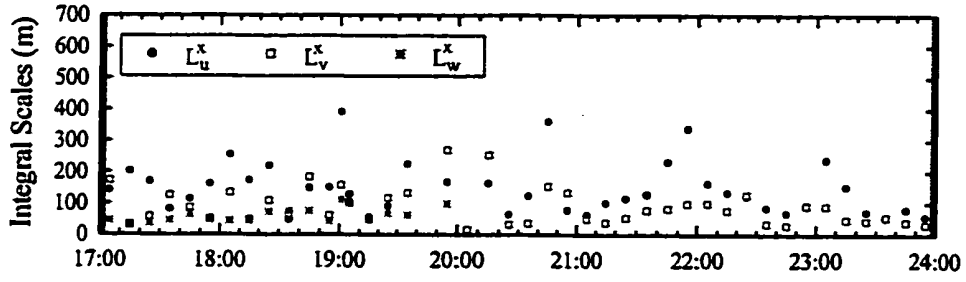

(b) At mid-sidespan

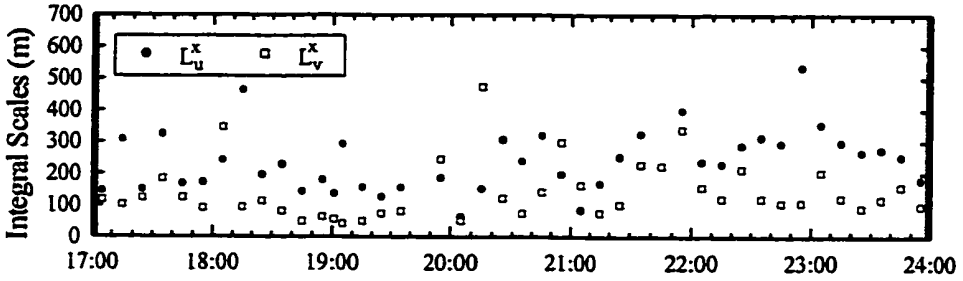

(c) On the top of Tsing Yi tower

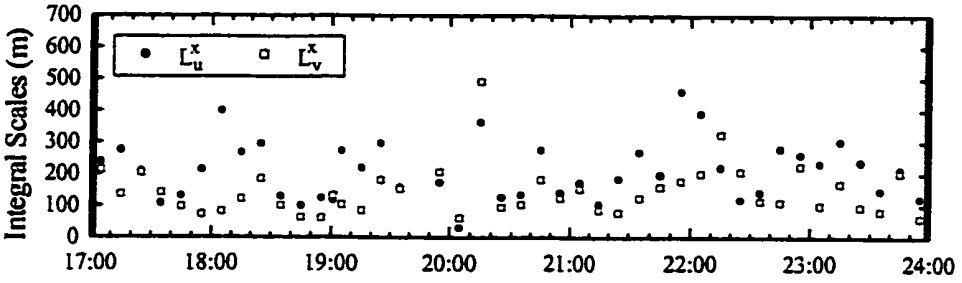

(d) On the top of Ma Wan tower

Figure 3-15 Variations of Integral Scales of Turbulence

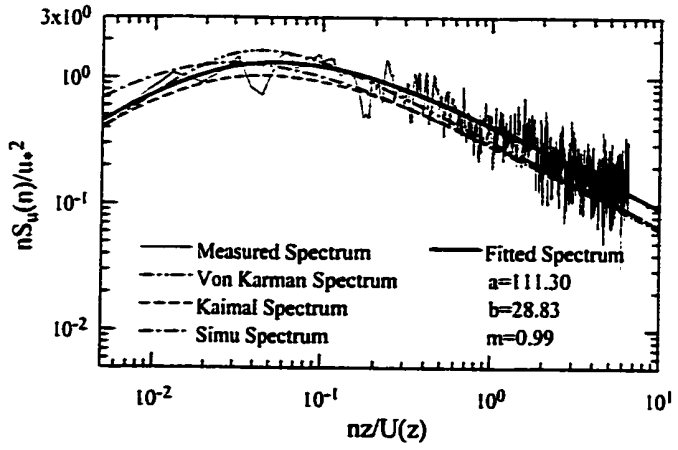

(a) Alongwind component

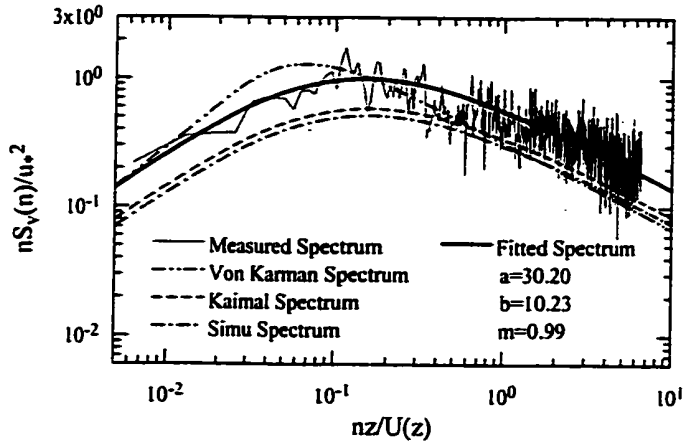

(b) Lateral component

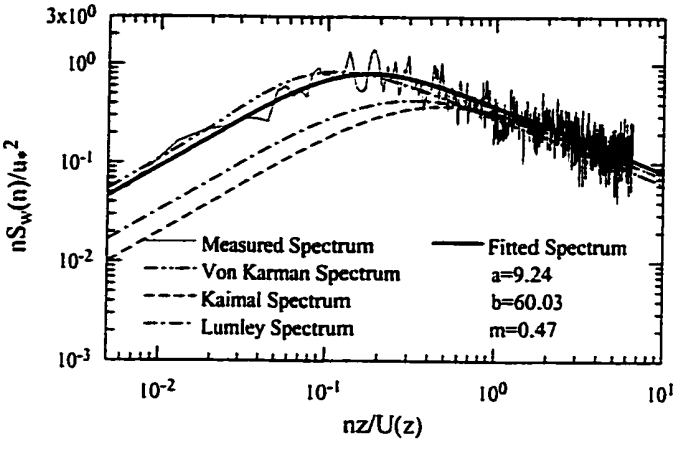

(c) Upward component

Figure 3-16 Normalized Auto Spectra of Wind Turbulence at Mid-mainspan

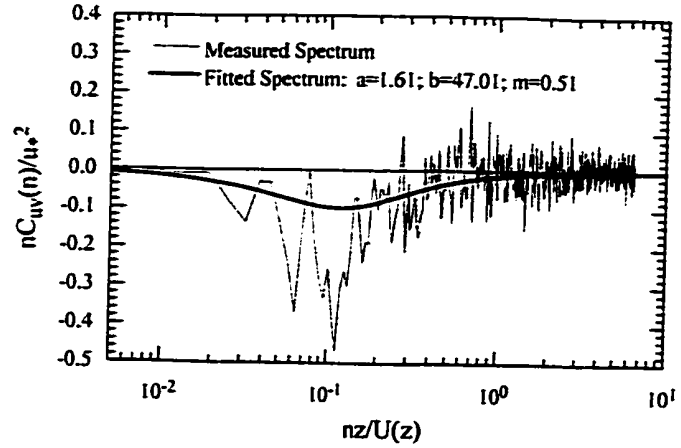

(a) Between alongwind and lateral components

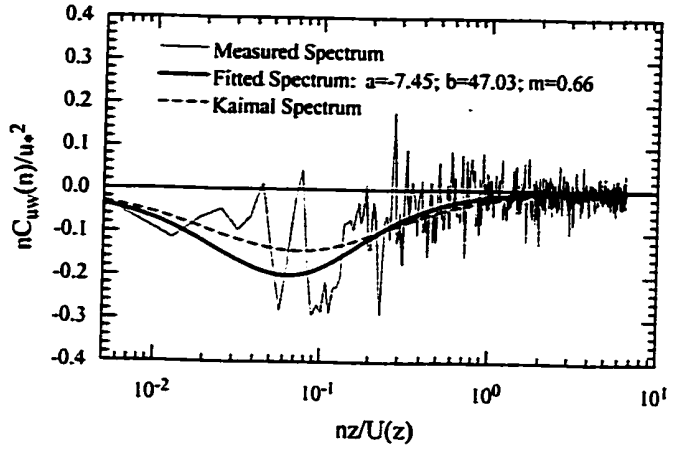

(b) Between alongwind and upward components

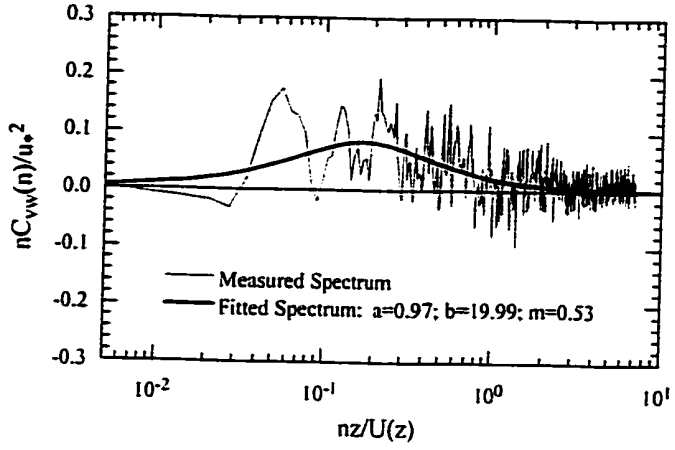

(c) Between lateral and upward components

Figure 3-17 Normalized Co-spectra of Wind Turbulence at Mid-mainspan

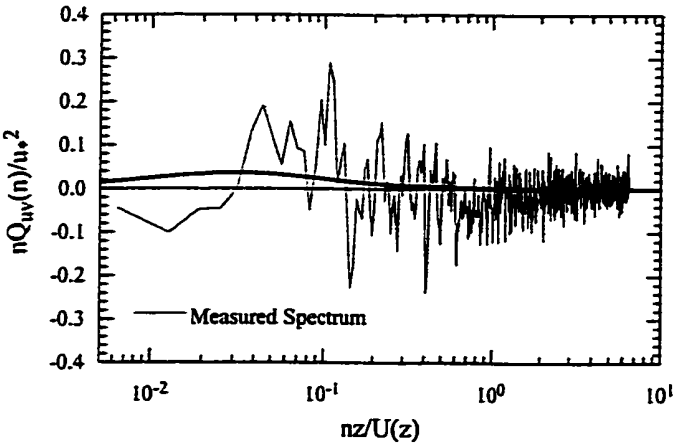

(a) Between alongwind and lateral components

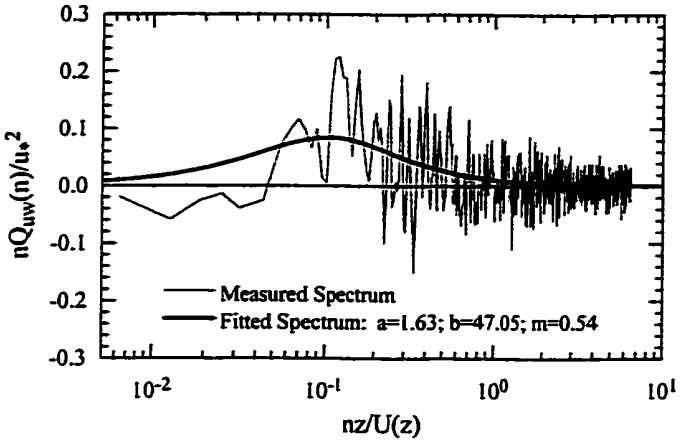

(b) Between alongwind and upward components

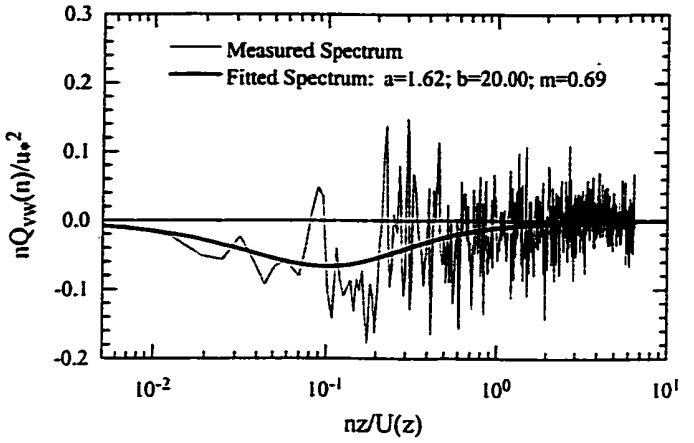

(c) Between lateral and upward components

Figure 3-18 Normalized Quadrature Spectra of Wind Turbulence at Mid-mainspan

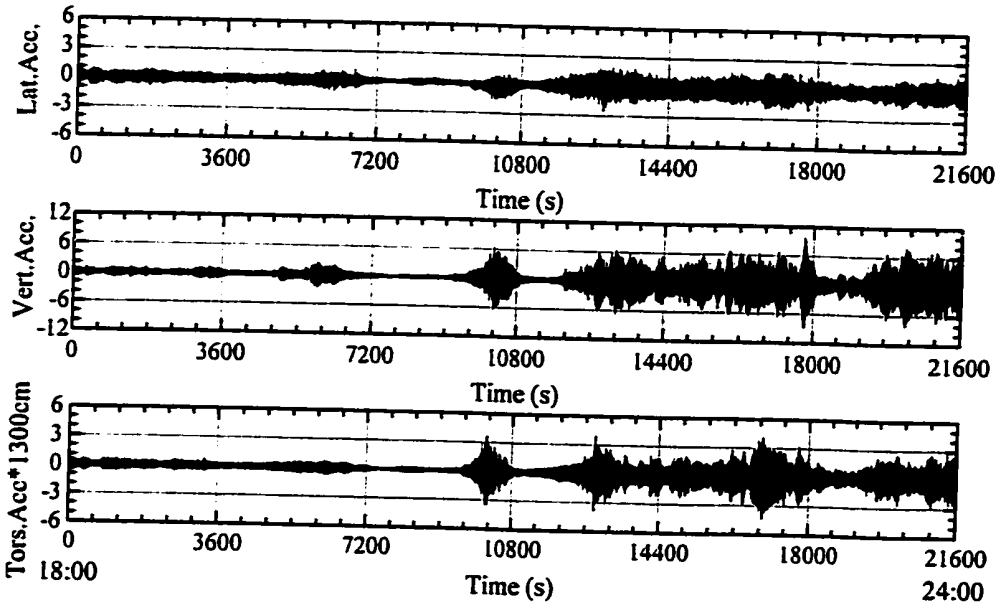

Figure 3-19 Time Histories of Lateral, Vertical and Torsional Accelerations of Deck at ATTJD (cm/s^2)

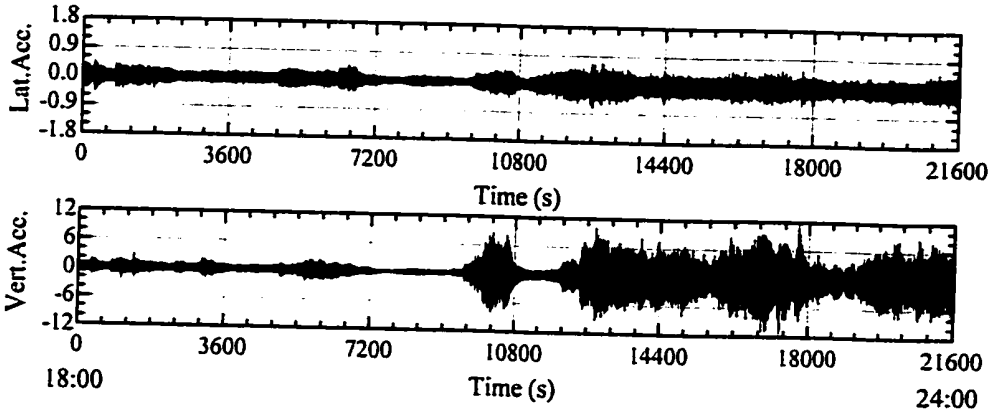

Figure 3-20 Time Histories of Lateral, Vertical and Torsional Accelerations of Cables at ABTLC (cm/s^2)

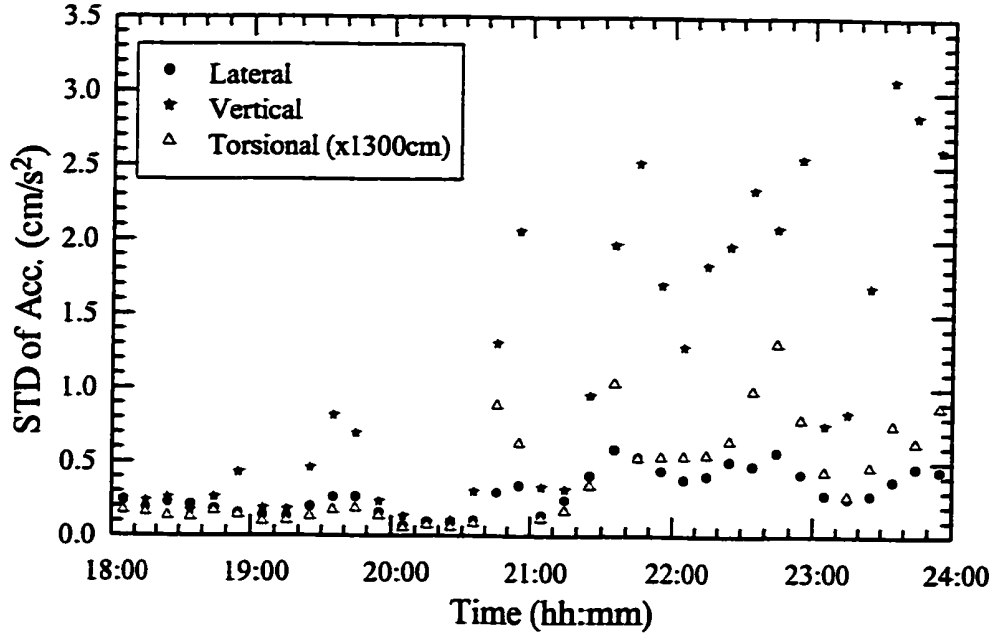

Figure 3-21 Standard Deviations of Acceleration at ATTJD vs. Time (10-minute Duration)

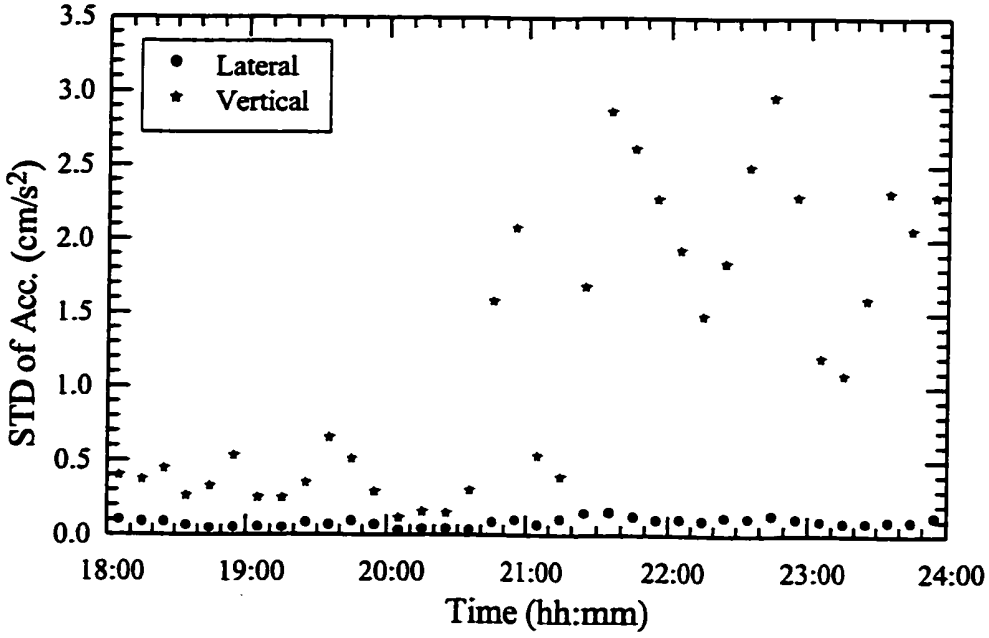

Figure 3-22 Standard Deviations of Acceleration at ABTLC vs. Time (10-minute Duration)

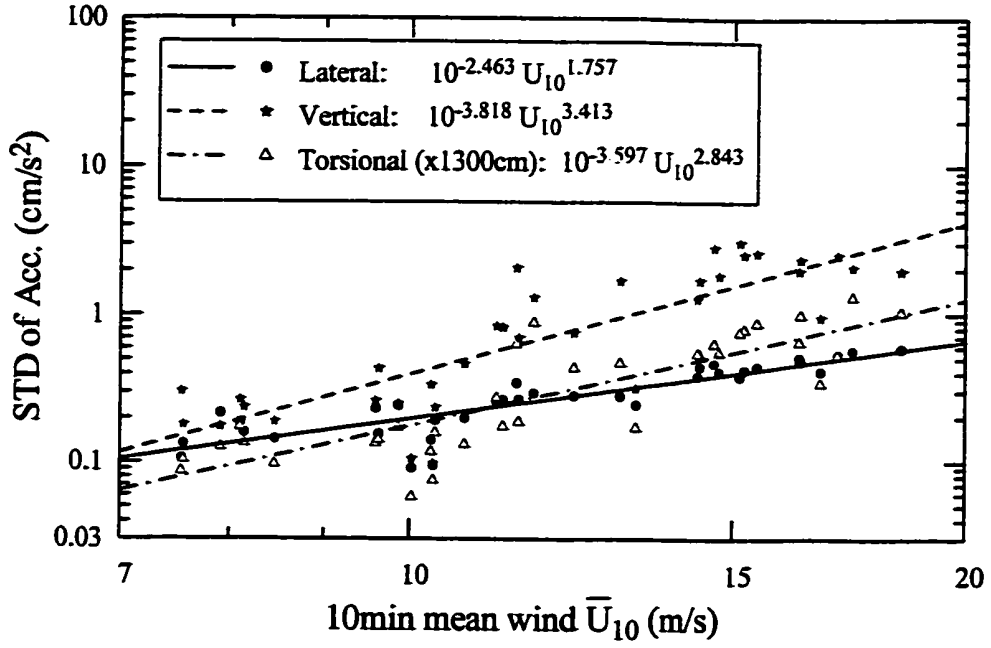

Figure 3-23 Standard Deviations of Acceleration at ATTJD vs. Mean Wind Speed (10-minute Duration)

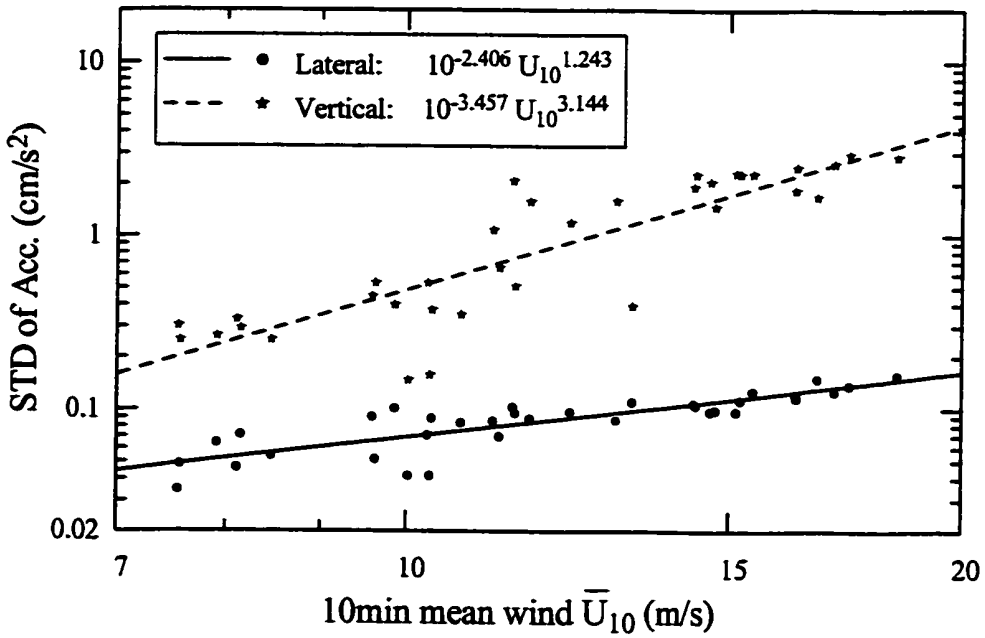

Figure 3-24 Standard Deviations of Acceleration at ABTLC vs. Mean Wind Speed (10-minute Duration)

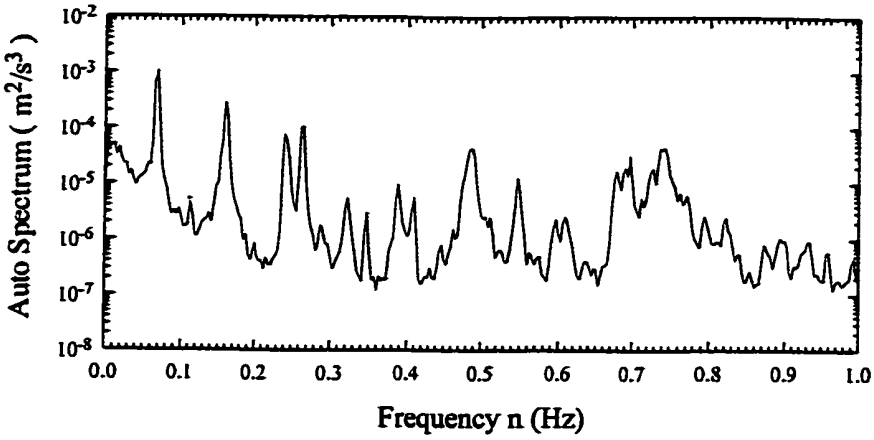

(a) Lateral acceleration

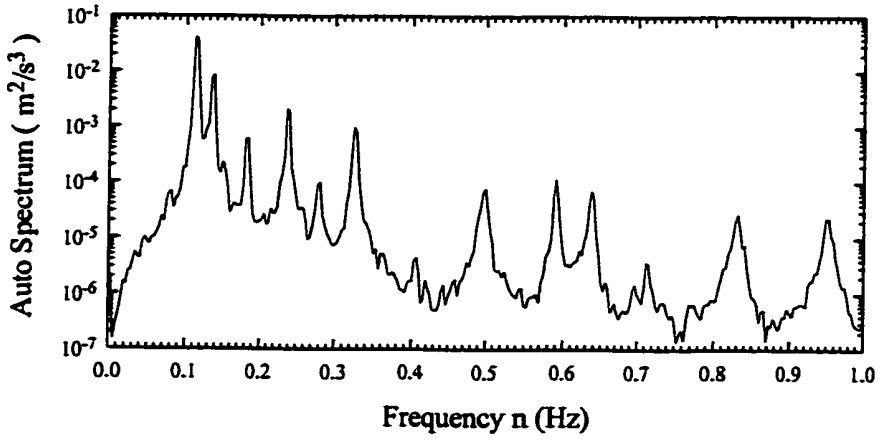

(b) Vertical acceleration

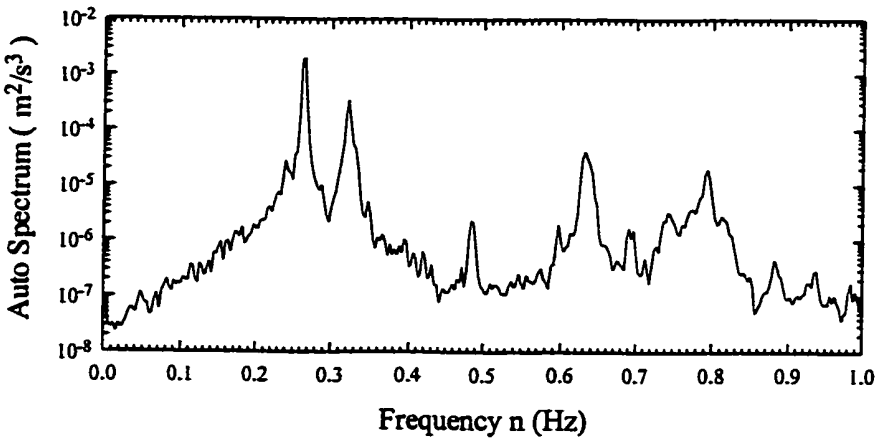

(c) Torsional acceleration (×13m)

Figure 3-25 Spectra of Acceleration Responses of Bridge Deck at ATTID (21:00 to 22:00)

Chapter 4

FORMULATION FOR BUFFETING ANALYSIS OF LONG SPAN BRIDGES UNDER SKEW WINDS

4.1 INTRODUCTION

As span lengths increase significantly, buffeting analysis of modern long-span cable-supported bridges becomes more and more important. The existing methods for buffeting analysis of long span bridges have been reviewed in Chapter 2 in detail. The multi-mode and inter-mode effects on bridge response can be now included in the buffeting prediction in either the time domain (Diana et al., 1998; Diana et al., 1999a; Boonyapinyo et al., 1999; Chen et al., 2000a) or the frequency domain (Jain et al., 1996; Xu el al., 1998; Chen et al., 1999; Katsuchi et al., 1999; Chen et al., 2000b; Chen et al., 2001). Fully-coupled 3D buffeting analyses, including not only the effects of inter-modes and multi-modes but also the interaction among major bridge components, can be also performed using a combination of the pseudo-excitation method and the conventional finite element method (FEM) (Xu et al., 1998; Xu, 1999; Sun et al, 2000; Xu et al., 2000a).

However, most of the previous investigations take incident mean wind at a right angle to the longitudinal axis of the bridge. This may not be true when the bridge is located in a complex and heterogeneous topography and attacked by a typhoon. The recent field measurements on the Tsing Ma suspension Bridge during Typhoon Victor (see Chapter 3) and Typhoon Sam (see Chapter 9) clearly demonstrate that strong winds seldom attack the bridge at a right angle to the bridge longitudinal axis. Though some efforts have been made to take into consideration of skew winds in buffeting analysis of bridges (Xie and Tanaka, 1991; Kimura and Tanaka, 1992; Kimura et al., 1994; Scalan, 1993; Kimura and Ohara, 1999), they are all based on the decomposition approach (cosine and sine rules). That is, the mean yaw wind is decomposed into two components: one is normal and the other parallel to the bridge deck. The contributions of the parallel mean wind component is then either ignored

or separately analyzed from that of the normal mean wind component. More difficult issue in the decomposition approach is how to decompose fluctuating winds with respect to the bridge axis.

According to the decomposition approach, the buffeting response of a long span cable-supported bridge to the yaw wind should be smaller than that to the normal wind of the same speed. However, some wind tunnel tests revealed that the buffeting response to the yaw wind would reach the same level as that to the normal wind (Davenport et al., 1969; Tanaka and Davenport, 1982; Irwin and Gamble, 1985; Zan, 1987; Diana et al., 1995; Diana, et al., 1999b; Kimura and Ohara, 1999). This indicates that the decomposition approach underestimates the buffeting response of bridges under yaw wind and this approach may not truly reflect the effects of skew or yaw wind on bridge buffeting response.

Also as mentioned in Chapter 2, more and more attentions are nowadays paid to the comparison of bridge buffeting response between field measurements and analyses (Okubo et al., 1979;Bietry 1994) aiming to verify various assumptions involved in the analytical methods. However, it is a quite difficult and challenging task because buffeting behaviour of long span bridges under skew winds is not so clear and the appropriate analytical methods for predicting the buffeting response of the bridges to skew winds are not available. Further mentioned in Chapter 2 is the requirement of buffeting response of a long span cable-supported bridge to skew winds for a better probability evaluation or risk analysis of the bridge exposed to local wind climate.

To cater for the demands aforementioned, a modified buffeting analysis method of long span cable-supported bridges under skew winds is developed in this chapter based on the quasi-steady linear theory and the oblique strip theory in conjunction with the pseudo excitation method (PEM) and the finite element method (FEM). Several coordinate systems and the transformation matrices among these coordinate systems are established first. A set of universal expressions for six component buffeting forces associated with the oblique cross section is then derived using the quasi-steady linear theory. These buffeting forces are formed with respect to the wind coordinate systems and then converted to the structural coordinate systems. Thus, the three orthogonal fluctuating wind components can be easily handled without artificial decomposition. This set of universal expressions is applicable to all

the structural members including the bridge deck, cables and towers. The coherence of wind turbulence between any two arbitrary spatial points is considered in the global wind coordinate system rather than the global structural coordinate system. Aeroelastic stiffness and damping matrices due to self-excited forces are taken into consideration in the modified method by introducing 18 flutter derivatives with respect to the oblique cross section. Finally, the buffeting response and response spectra of a bridge under skew winds are efficiently computed using the pseudo excitation method. The modified method developed in this chapter is capable of performing a fully coupled 3D buffeting analysis of the bridge to skew winds including the effects of inter-modes, multi-modes and spatial modes and the interaction among major bridge components. The variations of mean wind speed, turbulence intensity, and auto-spectrum along the bridge longitudinal axis can also be easily included in the prediction.

Nevertheless, the modified method still requires some basic assumptions. Firstly, the incident wind is assumed to be stationary and its mean wind speed $\overline{U}$ is sufficiently larger than any one of three fluctuating wind components $u(t)$, $v(t)$, and $w(t)$. Secondly, the mean wind speed used in buffeting analysis is away from the range that may cause either aeroelastic instability or vortex shedding of the bridge. Thirdly, the average scales of the turbulence are assumed to be sufficiently larger than the chord-wise dimension of the bridge members so that the quasi-steady theory is applicable. Finally, wind-induced bridge motion is small so that the linear approach can be accepted.

4.2 GOVERNING EQUATION FOR BRIDGE BUFFETING

Under the framework of finite element approach, the governing equation for buffeting analysis of long span cable-supported bridges under skew winds can be expressed as

$$\mathbf{M}^s\ddot{\Delta}(t)+\mathbf{C}^s\dot{\Delta}(t)+\mathbf{K}^s\Delta(t)=\mathbf{F}^{se}(t)+\mathbf{F}^b(t) \tag{4-1}$$

where $\mathbf{M}^s$, $\mathbf{C}^s$ and $\mathbf{K}^s$ are, respectively, the $N\times N$ mass, damping and stiffness matrices of the whole bridge, in which N is the total number of degree of freedom; $\Delta(t)$ is the N-dimensional vector of the nodal displacement of the whole bridge

referring to the global structural coordinate system while $\dot{\Delta}(t)$ and $\ddot{\Delta}(t)$ are the corresponding N-dimensional vectors of velocity and acceleration, respectively; $\mathbf{F}^b(t)$ is the N-dimensional vector of buffeting forces in the global coordinate system; $\mathbf{F}^{se}(t)$ is the N-dimensional vector of aeroelastic forces in the global coordinate system. The superscript *se* or *b* indicates the corresponding term associated with self-excited vibration or buffeting. Conventionally, $\mathbf{F}^{se}(t)$ can be represented by the following linear function of bridge velocity and displacement responses.

$$\mathbf{F}^{se}(t) = -\mathbf{K}^{se}\Delta(t) - \mathbf{C}^{se}\dot{\Delta}(t) \tag{4-2}$$

where $\mathbf{K}^{se}$ and $\mathbf{C}^{se}$ are, respectively, the $N \times N$ aeroelastic stiffness and damping matrices. By moving the aeroelastic force vector to the left side of Eq.(4-1), the governing equation can then be rewritten as

$$\mathbf{M}\ddot{\Delta}(t) + \mathbf{C}\dot{\Delta}(t) + \mathbf{K}\Delta(t) = \mathbf{F}^b(t) \tag{4-3}$$

where

$$\mathbf{M} = \mathbf{M}^s \tag{4-4}$$

$$\mathbf{K} = \mathbf{K}^s + \mathbf{K}^{se} \tag{4-5}$$

$$\mathbf{C} = \mathbf{C}^s + \mathbf{C}^{se} \tag{4-6}$$

Though Eqs. (4-3) to (4-6) are similar to the traditional equations of motion for bridge buffeting, the buffeting force vector $\mathbf{F}^b(t)$, the aeroelastic stiffness matrix $\mathbf{K}^{se}$, and the aeroelastic damping matrix $\mathbf{C}^{se}$ refer to the bridge under skew winds. Clearly, before solving the above governing equation using the pseudo excitation method, the buffeting force vector $\mathbf{F}^b(t)$, the aeroelastic stiffness matrix $\mathbf{K}^{se}$, and the aeroelastic damping matrix $\mathbf{C}^{se}$ should be determined. This requires the introduction of several coordinate systems.

4.3 COORDINATES SYSTEMS

4.3.1 Global Structural and Wind Coordinate Systems

It is well known that when employing the finite element method (FEM) to describe the vibration problem of a large structure, a global structural coordinate system *XYZ*

should be established to consider the overall dynamic equilibrium conditions of the structure. A global wind coordinate system $X_uY_vZ_w$ is also required to define mean wind velocity and fluctuating wind components. The two global coordinate systems are then correlated using the global wind yaw angle and inclination.

There are many possible combinations between the XYZ-system and the $X_uY_vZ_w$-system in the buffeting analysis. Figure 4-1 shows a typical one of these combinations. In the global structural coordinate system, the axis X is along the bridge longitudinal axis and the axis Z is in the horizontal plane while the axis Y is vertical. In the global wind coordinate system, the axis X_u is along the direction of mean wind velocity $\overline{U}$ and the axis Y_v is located in a horizontal plane, which is parallel to the X-Z plane, whilst the axis Z_w is always upward. The three axes, X_u, Y_v and Z_w (or X, Y, and Z) are orthogonal to each other following a right-handed rule. The positive directions of the longitudinal (alongwind), lateral (horizontal) and upward components of wind turbulence, $u(t)$, $v(t)$, and $w(t)$, are defined as the positive directions of the three axes, X_u, Y_v and Z_w, respectively. The global wind yaw angle β_0 is then defined as the angle between the vertical plane normal to the bridge longitudinal axis and the vertical plane with the mean wind velocity included. The global yaw angle is positive when mean wind comes from the right side of the Z-Y plane. The global wind inclination θ_0 is interpreted as the angle between the mean wind velocity and the horizontal plane. It is positive when the vertical component of the mean wind velocity is upward.

4.3.2 Local Structural Coordinate Systems

With the use of finite element method, a local structural coordinate system $x'y'z'$ is necessary for each element to define the matrices of elemental mass, stiffness, damping and loading. The transformation matrix between the local structural coordinate system and the global structural coordinate system is then used to assemble the local dynamic matrices into the global dynamic matrices. It is noted that the buffeting analysis of a long span bridge is usually performed with respect to the deformed static configuration of the bridge caused by the mean wind velocity. Therefore, another local structural coordinate system xyz is required to refer to the static equilibrium position of the bridge. Since the rotational angle (static inclination) of the element caused by the mean wind velocity is the most influencing factor to the

buffeting of the bridge, it is included in the following transformation between the two local structural coordinate systems.

Figure 4-2 shows an arbitrary k^{th} element in the finite element model of a concerned bridge. *I*, *J*, and *R* denote the left, right and reference nodes of the element, respectively. Both the *xyz*-system and the $x'y'z'$-system are two local structural coordinate systems of the element. The axis x and the axis x' coincide with the longitudinal axis of the element and they are positive from the left node *I* to the right node *J*. The axis y' is located in the plane formed by the left node *I*, right node *J* and reference point *R* of the element. The positive direction of axis z' is determined by the cross product of unit directional vectors of the axis x' and the vector ***IR***. The positive direction of the axis y' can be obtained by the cross product of unit directional victors of the axis z' and the axis x'. The coordinate *xyz*-system is then obtained by rotating the system $x'y'z'$ about the axis x' with an initial angle of α_0, which is the average torsional angle of the element due to the mean wind loads. The two local structural systems obey the right-handed rule. The reference point should be selected in such a way that one of the axes y' and z' is parallel to the major plane of the element.

4.3.3 Local Reference Coordinate System

The aerodynamic and aeroelastic coefficients of bridge components are often measured via wind tunnel tests, as demonstrated in Chapters 6 to 8, or determined with some approximate/empirical formulae as introduced in Chapter 5. When performing wind tunnel tests, wind yaw angle and inclination are often defined with respect to local wind and reference coordinate systems. The measured coefficients are then expressed as the functions of local mean wind yaw angle and inclination, which are different from the global mean wind yaw angle and inclination. It is thus necessary to introduce a local reference coordinate system and a local mean wind coordinate system for each element in buffeting analysis with FEM, which should be consistent with those used in the wind tunnel tests. It is noted that though the vector of wind speed shows its different appearances in the global structural coordinate system and the local reference coordinate system, the absolute wind speed and direction are actually independent of the used coordinate systems. Therefore, the values of the local mean wind yaw angle $\bar{\beta}$ and the local mean wind inclination $\bar{\theta}$ of

each element can be computed from the global wind direction via a transformation between the global wind coordinate system and the local reference coordinate system.

Figure 4-3 shows a typical local reference coordinate *qph*-system. The axis q is along the longitudinal axis of the element. The axis p is located in either the deck plane or the tower plane. Its positive direction should be determined in such a way that the angle between the axis p and the mean wind direction is less than 90° and when both $\overline{\beta}$ and $\overline{\theta}$ are equal to zero, the axis p is in parallel to the mean wind direction. The axis h is then determined according to the right-handed rule. For the system shown in Figure 4-3, the local mean wind yaw angle $\overline{\beta}$ is defined as the angle between the *ph*-plane and the component $\overline{U}_{qp}$ of the mean wind projected onto the *qp*-plane. The angle $\overline{\beta}$ is positive when the mean wind component $\overline{U}_q$ along the axis q is negative. The local wind inclination $\overline{\theta}$ is defined as the angle between the mean wind velocity and the *qp*-plane. It takes a positive direction when the mean wind component $\overline{U}_h$ along the axis h is positive. The *qph*-system together with the local mean wind yaw angle $\overline{\beta}$ and the local mean wind inclination $\overline{\theta}$ should be consistent with those adopted in the wind tunnel tests for determining aerodynamic coefficients and flutter derivatives. In addition, Figure 4-3 also shows the instantaneous wind velocity V(t) and its components and the local instantaneous wind yaw angle $\tilde{\beta}$ and the local instantaneous wind inclination $\tilde{\theta}$. The rules for defining the angles $\tilde{\beta}$ and $\tilde{\theta}$ are the same as those for the angles $\overline{\beta}$ and $\overline{\theta}$. The further details are provided in the next section.

4.3.4 Local Mean and Instantaneous Wind Coordinate Systems

Traditionally, the instantaneous wind velocity is decomposed into the mean wind velocity and the three fluctuating wind components. Buffeting analysis is performed mainly considering three fluctuating wind components but based on the statically deformed configuration of the bridge under mean wind. Therefore, it is necessary to introduce a local mean wind coordinate system and an instantaneous wind coordinate system. It is noted that the local instantaneous wind yaw angle and inclination are related to the three fluctuating wind components. The instantaneous aerodynamic

forces are derived regarding the local instantaneous wind coordinate system and then converted to the local mean wind coordinate system through the transformation matrix between the two local wind coordinate systems. The buffeting forces on each element will be then further converted to the global structural coordinate system. Finally, the global vector of buffeting forces, $\mathbf{F}^b(t)$, will be assembled in the global structural coordinate system.

Figure 4-4 depicts the local mean wind coordinate $\bar{q}\bar{p}\bar{h}$-system and the local reference coordinate *qph*-system while Figure 4-5 displays the local instantaneous wind coordinate $\tilde{q}\tilde{p}\tilde{h}$-system and the local reference coordinate *qph*-system. The $\bar{q}\bar{p}\bar{h}$-system is attained by rotating the local reference coordinate *qph*-system by the angle $\bar{\beta}$ around the axis h first and then by the angle $\bar{\theta}$ around the axis $\bar{q}$. Similarly, the $\tilde{q}\tilde{p}\tilde{h}$-system is attained by rotating the *qph*-system by the angle $\tilde{\beta}$ around the axis h first and then by the angle $\tilde{\theta}$ around the axis $\tilde{q}$. As a result, the axes $\bar{q}$ and $\tilde{q}$ are located in the *qp*-plane. The axis $\bar{p}$ is along the mean wind direction whilst the axis $\tilde{p}$ is along the instantaneous wind direction. Both the $\bar{q}\bar{p}\bar{h}$-system and the $\tilde{q}\tilde{p}\tilde{h}$-system follow the right-hand rule.

4.4 TRANSFORMATION BETWEEN COORDINATE SYSTEMS

4.4.1 Global Structural and Wind Coordinate Systems

In terms of the arithmetic of vectors, the relationship between the global structural coordinate *XYZ*-system and the global wind coordinate $X_uY_vZ_w$-system can be expressed as

$$(X,Y,Z)^{\mathrm{T}} = \mathbf{T}_{GsGw}(X_u,Y_v,Z_w)^{\mathrm{T}} \tag{4-7a}$$

$$(X_u,Y_v,Z_w)^{\mathrm{T}} = \mathbf{T}_{GwGs}(X,Y,Z)^{\mathrm{T}} \tag{4-7b}$$

where $\mathbf{T}_{GsGw}$ is the 3×3 transformation matrix from the $X_uY_vZ_w$-system to the *XYZ*-system; $\mathbf{T}_{GwGs}$ is the 3×3 transformation matrix from the *XYZ*-system to the $X_uY_vZ_w$-system; the subscripts *Gw* and *Gs* represent the global wind coordinate $X_uY_vZ_w$-system and the global structural *XYZ*-system, respectively; and the superscript T

denotes a transpose operation of a vector or a matrix. For the two global coordinate systems shown in Figure 4-1, the transformation matrices can be derived using the arithmetic of vectors as follows:

$$\mathbf{T}_{GsGw} = \mathbf{T}_{GwGs}^{\mathrm{T}} = \begin{bmatrix} -\cos\theta_0 \sin\beta_0 & -\cos\beta_0 & \sin\theta_0 \sin\beta_0 \\ \sin\theta_0 & 0 & \cos\theta_0 \\ -\cos\theta_0 \cos\beta_0 & \sin\beta_0 & \sin\theta_0 \cos\beta_0 \end{bmatrix} \tag{4-8}$$

It can be easily proved that $\mathbf{T}_{GwGs} = \mathbf{T}_{GsGw}^{-1} = \mathbf{T}_{GsGw}^{\mathrm{T}}$. The other types of the two global coordinate systems and the corresponding transformation matrices can be found in Chapter 5.

4.4.2 Global and Local Structural Coordinate Systems

The local structural coordinate *xyz*-system and *x'y'z'*-system of an arbitrary k^{th} element are shown in Figure 4-2 together with the global structural coordinate *XYZ*-system. The relationships between the three coordinate systems can then be expressed as follows:

$$(x,y,z)^{\mathrm{T}} = \mathbf{T}_{LsLs'}(x',y',z')^{\mathrm{T}}$$

$$= \mathbf{T}_{LsLs'}\mathbf{T}_{Ls'Gs}(X,Y,Z)^{\mathrm{T}} = \mathbf{T}_{LsGs}(X,Y,Z)^{\mathrm{T}} \tag{4-9a}$$

$$(\theta_x,\theta_y,\theta_z)^{\mathrm{T}} = \mathbf{T}_{LsLs'}(\theta_{x'},\theta_{y'},\theta_{z'})^{\mathrm{T}}$$

$$= \mathbf{T}_{LsLs'}\mathbf{T}_{Ls'Gs}(\theta_X,\theta_Y,\theta_Z) = \mathbf{T}_{LsGs}(\theta_X,\theta_Y,\theta_Z)^{\mathrm{T}} \tag{4-9b}$$

$$(X,Y,Z)^{\mathrm{T}} = \mathbf{T}_{GsLs'}(x',y',z')^{\mathrm{T}}$$

$$= \mathbf{T}_{GsLs'}\mathbf{T}_{Ls'Ls}(x,y,z)^{\mathrm{T}} = \mathbf{T}_{GsLs}(x,y,z)^{\mathrm{T}} \tag{4-9c}$$

$$(\theta_X,\theta_Y,\theta_Z)^{\mathrm{T}} = \mathbf{T}_{GsLs'}(\theta_{x'},\theta_{y'},\theta_{z'})^{\mathrm{T}}$$

$$= \mathbf{T}_{GsLs'}\mathbf{T}_{Ls'Ls}(\theta_x,\theta_y,\theta_z)^{\mathrm{T}} = \mathbf{T}_{GsLs}(\theta_x,\theta_y,\theta_z)^{\mathrm{T}} \tag{4-9d}$$

where θ_x, θ_y and θ_z are the angular coordinates around the axes *x*, *y* and *z*, respectively, in the *xyz*-system; $\theta_{x'}$, $\theta_{y'}$ and $\theta_{z'}$ are the angular coordinates around the axes *x'*, *y'* and *z'*, respectively, in the *x'y'z'*-system; θ_X, θ_Y and θ_Z are the angular coordinates around the axes *X*, *Y* and *Z*, respectively, in the *XYZ*-system; the subscripts *Ls*, *Ls'* and *Gs* represent the local structural coordinate *xyz*-system and *x'y'z'*-system and the global structural *XYZ*-system, respectively; $\mathbf{T}_{Ls'Gs}$ is the 3×3

transformation matrix from the *XYZ*-system to the *x'y'z'*-system whilst $\mathbf{T}_{GsLs'}$ is one from the *x'y'z'*-system to the *XYZ*-system; $\mathbf{T}_{LsLs'}$ is the 3×3 transformation matrix from the *x'y'z'*-system to the *xyz*-system while $\mathbf{T}_{Ls'Ls}$ is one from the *xyz*-system to the *x'y'z'*-system; $\mathbf{T}_{LsGs}$ is the 3×3 transformation matrix from the *XYZ*-system to the *xyz*-system and $\mathbf{T}_{GsLs}$ is one from the *xyz*-system to the *XYZ*-system. It can be further proved that these transformation matrices possess the properties such as $\mathbf{T}_{GsLs'} = \mathbf{T}_{Ls'Gs}^{-1} = \mathbf{T}_{Ls'Gs}^{\mathrm{T}}$, $\mathbf{T}_{LsLs'} = \mathbf{T}_{Ls'Ls}^{-1} = \mathbf{T}_{Ls'Ls}^{\mathrm{T}}$, $\mathbf{T}_{GsLs} = \mathbf{T}_{GsLs'}\mathbf{T}_{Ls'Ls} = \mathbf{T}_{LsGs}^{-1} = \mathbf{T}_{LsGs}^{\mathrm{T}}$.

To derive the transformation matrices, in particular $\mathbf{T}_{LsGs}$, denote $\mathbf{c}_{x'}$, $\mathbf{c}_{y'}$ and $\mathbf{c}_{z'}$, respectively, the direction-cosine vectors of the axes *x'*, *y'* and *z'* in the *XYZ*-system and $\mathbf{c}_x$, $\mathbf{c}_y$ and $\mathbf{c}_z$, respectively, as the direction-cosine vectors of the axes *x*, *y* and *z* in the *XYZ*-system. Also denote $\mathbf{c}_{IR}$ the direction-cosine vector of the reference vector ***IR*** (see Figure 4-2) in the *XYZ*-system. Then, these direction-cosine vectors can be expressed in terms of the corresponding coordinates.

$$\mathbf{c}_{x'} = (c_{x'X},\ c_{x'Y},\ c_{x'Z}) = (X_J - X_I, Y_J - Y_I, Z_J - Z_I)/L_k \tag{4-10}$$

$$\mathbf{c}_{IR} = (c_{IRX},\ c_{IRY},\ c_{IRZ}) = (X_R - X_I, Y_R - Y_I, Z_R - Z_I)/L_{IR} \tag{4-11}$$

$$\begin{aligned}\mathbf{c}_{z'} &= (c_{z'X},\ c_{z'Y},\ c_{z'Z}) = \mathbf{c}_{x'} \times \mathbf{c}_{IR}/|\mathbf{c}_{x'} \times \mathbf{c}_{IR}| \\ &= \frac{(c_{x'Y}c_{IRZ} - c_{x'Z}c_{IRY},\ c_{x'Z}c_{IRX} - c_{x'X}c_{IRZ},\ c_{x'X}c_{IRY} - c_{x'Y}c_{IRX})}{\sqrt{(c_{x'Y}c_{IRZ} - c_{x'Z}c_{IRY})^2 + (c_{x'Z}c_{IRX} - c_{x'X}c_{IRZ})^2 + (c_{x'X}c_{IRY} - c_{x'Y}c_{IRX})^2}}\end{aligned} \tag{4-12}$$

$$\begin{aligned}\mathbf{c}_{y'} &= (c_{y'X},\ c_{y'Y},\ c_{y'Z}) = \mathbf{c}_{z'} \times \mathbf{c}_{x'}/|\mathbf{c}_{z'} \times \mathbf{c}_{x'}| \\ &= \frac{(c_{z'Y}c_{x'Z} - c_{z'Z}c_{x'Y},\ c_{z'Z}c_{x'X} - c_{z'X}c_{x'Z},\ c_{z'X}c_{x'Y} - c_{z'Y}c_{x'X})}{\sqrt{(c_{z'Y}c_{x'Z} - c_{z'Z}c_{x'Y})^2 + (c_{z'Z}c_{x'X} - c_{z'X}c_{x'Z})^2 + (c_{z'X}c_{x'Y} - c_{z'Y}c_{x'X})^2}}\end{aligned} \tag{4-13}$$

where (X_I, Y_I, Z_I), (X_J, Y_J, Z_J) and (X_R, Y_R, Z_R) are the coordinates of the left node *I*, the right node *J* and the reference point *R* of the kth element in the *XYZ*-system. L_k and L_{IR} are the lengths of the kth element and the reference vector ***IR***, respectively. They can be calculated as

$$L_k = \sqrt{(X_J - X_I)^2 + (Y_J - Y_I)^2 + (Z_J - Z_I)^2} \tag{4-14}$$

$$L_{IR} = \sqrt{(X_R - X_I)^2 + (Y_R - Y_I)^2 + (Z_R - Z_I)^2} \tag{4-15}$$

As a result,

$$\mathbf{T}_{Ls'Gs} = \mathbf{T}_{GsLs'}^{\mathrm{T}} = \begin{bmatrix} c_{x'X} & c_{x'Y} & c_{x'Z} \\ c_{y'X} & c_{y'Y} & c_{y'Z} \\ c_{z'X} & c_{z'Y} & c_{z'Z} \end{bmatrix} \tag{4-16a}$$

Since the coordinate *xyz*-system is attained by rotating the *x'y'z'*-system about the axis *x'* by an initial torsional angle of α_0 of the element caused by the mean wind loads (see Figure 4-2), one may obtain

$$\mathbf{T}_{LsLs'} = \mathbf{T}_{Ls'Ls}^{\mathrm{T}} = \begin{bmatrix} 1 & 0 & 0 \\ 0 & \cos(\alpha_0) & \sin(\alpha_0) \\ 0 & -\sin(\alpha_0) & \cos(\alpha_0) \end{bmatrix} \tag{4-16b}$$

Then,

$$\mathbf{T}_{LsGs} = \mathbf{T}_{LsLs'}\mathbf{T}_{Ls'Gs} = \mathbf{T}_{GsLs}^{\mathrm{T}}$$

$$= \begin{bmatrix} c_{x'X} & c_{x'Y} & c_{x'Z} \\ c_{y'X}\cos\alpha_0 + c_{z'X}\sin\alpha_0 & c_{y'Y}\cos\alpha_0 + c_{z'Y}\sin\alpha_0 & c_{y'Z}\sin\alpha_0 + c_{z'Z}\cos\alpha_0 \\ c_{z'X}\sin\alpha_0 - c_{y'X}\cos\alpha_0 & c_{z'Y}\cos\alpha_0 - c_{y'Y}\sin\alpha_0 & c_{z'Z}\sin\alpha_0 - c_{y'Z}\cos\alpha_0 \end{bmatrix} \tag{4-16c}$$

4.4.3 Local Structural and Reference Coordinate Systems

The relationship between the local structural coordinate *xyz*-system and the local reference coordinate *qph*-system (see Figure 4-3) can be described by

$$(q, p, h)^{\mathrm{T}} = \mathbf{T}_{LrLs}(x, y, z)^{\mathrm{T}} \tag{4-17a}$$

$$(\alpha, \gamma, \phi)^{\mathrm{T}} = \mathbf{T}_{LrLs}(\theta_x, \theta_y, \theta_z)^{\mathrm{T}} \tag{4-17b}$$

$$(x, y, z)^{\mathrm{T}} = \mathbf{T}_{LsLr}(q, p, h)^{\mathrm{T}} \tag{4-17c}$$

$$(\theta_x, \theta_y, \theta_z)^{\mathrm{T}} = \mathbf{T}_{LsLr}(\alpha, \gamma, \phi)^{\mathrm{T}} \tag{4-17d}$$

where α, γ and ϕ are the angular coordinates around the axes q, p and h, respectively in the *qph*-system; the subscripts *Ls* and *Lr* represent the local structural coordinate *xyz*-system and the local reference coordinate *qph*-system; $\mathbf{T}_{LrLs}$ is the 3×3 transformation matrix from the *xyz*-system to the *qph*-system. On the contrary, $\mathbf{T}_{LsLr}$ is the transformation matrix from the *qph*-system to the *xyz*-system. It can be proved that $\mathbf{T}_{LsLr} = \mathbf{T}_{LrLs}^{-1} = \mathbf{T}_{LrLs}^{\mathrm{T}}$. Both $\mathbf{T}_{LrLs}$ and $\mathbf{T}_{LsLr}$ consist of elements equal to 1 or –1 or zero. There are several combinations of the local structural coordinate *xyz*-system and the local reference coordinate *qph*-system (see Chapter 5). For a typical

combination of the local coordinate systems shown in Figure 4-3, $\mathbf{T}_{LrLs}$ and $\mathbf{T}_{LsLr}$ is an identity matrix.

$$\mathbf{T}_{LrLs} = \mathbf{T}_{LsLr}^{\mathrm{T}} = \begin{bmatrix} 1 & 0 & 0 \\ 0 & 1 & 0 \\ 0 & 0 & 1 \end{bmatrix} \tag{4-18}$$

4.4.4 Global Structural Coordinate System and Local Reference Coordinate System

The global structural coordinate *XYZ*-system can be related to the local reference coordinate *qph*-system using the following equations.

$$(q,p,h)^{\mathrm{T}} = \mathbf{T}_{LrGs}\,(X,Y,Z)^{\mathrm{T}} \tag{4-19a}$$

$$(\alpha,\gamma,\phi)^{\mathrm{T}} = \mathbf{T}_{LrGs}(\theta_X,\theta_Y,\theta_Z)^{\mathrm{T}} \tag{4-19b}$$

$$(X,Y,Z)^{\mathrm{T}} = \mathbf{T}_{GsLr}\,(q,p,h)^{\mathrm{T}} \tag{4-19c}$$

$$(\theta_X,\theta_Y,\theta_Z)^{\mathrm{T}} = \mathbf{T}_{GsLr}(\alpha,\gamma,\phi)^{\mathrm{T}} \tag{4-19d}$$

where $\mathbf{T}_{LrGs}$ is the 3×3 transformation matrix from the *XYZ*-system to the *qph*-system and on the other hand, $\mathbf{T}_{GsLr}$ is one from the *qph*-system to the *XYZ*-system. Again it can be proved that $\mathbf{T}_{GsLr} = \mathbf{T}_{LrGs}^{-1} = \mathbf{T}_{LrGs}^{\mathrm{T}}$. These two transformation matrices can be easily determined in terms of the derived transformation matrices.

$$\mathbf{T}_{LrGs} = \mathbf{T}_{LrLs}\mathbf{T}_{LsGs} \tag{4-20a}$$

$$\mathbf{T}_{GsLr} = \mathbf{T}_{GsLs}\mathbf{T}_{LsLr} = \mathbf{T}_{LsGs}^{\mathrm{T}}\mathbf{T}_{LrLs}^{\mathrm{T}} = (\mathbf{T}_{LrLs}\mathbf{T}_{LsGs})^{\mathrm{T}} = \mathbf{T}_{LrGs}^{\mathrm{T}} \tag{4-20b}$$

4.4.5 Global Wind Coordinate System and Local Reference Coordinate System

Furthermore, the global wind coordinate $X_uY_vZ_w$-system can be related to the local reference coordinate *qph*-system using the following equations.

$$(q,p,h)^{\mathrm{T}} = \mathbf{T}_{LrGw}\,(X_u,Y_v,Z_w)^{\mathrm{T}} \tag{4-21a}$$

$$(X_u,Y_v,Z_w)^{\mathrm{T}} = \mathbf{T}_{GwLr}\,(q,p,h)^{\mathrm{T}} \tag{4-21b}$$

where $\mathbf{T}_{LrGw}$ is the 3×3 transformation matrix from the $X_uY_vZ_w$-system to the *qph*-system and $\mathbf{T}_{GwLr}$ is one from the *qph*-system to the $X_uY_vZ_w$-system. These

transformation matrices can also be determined in terms of the derived transformation matrices.

$$\mathbf{T}_{LrGw} = \mathbf{T}_{LrGs}\mathbf{T}_{GsGw} \tag{4-22a}$$

$$\mathbf{T}_{GwLr} = \mathbf{T}_{LrGw}^{-1} = \mathbf{T}_{GwGs}\mathbf{T}_{GsLr} = \mathbf{T}_{GsGw}^{T}\mathbf{T}_{LrGs}^{T} = (\mathbf{T}_{LrGs}\mathbf{T}_{GsGw})^{T} = \mathbf{T}_{LrGw}^{T} \tag{4-22b}$$

Now, express the transformation matrix $\mathbf{T}_{LrGw}$ as

$$\mathbf{T}_{LrGw} = \begin{bmatrix} t_{11} & t_{12} & t_{13} \\ t_{21} & t_{22} & t_{23} \\ t_{32} & t_{32} & t_{33} \end{bmatrix} \tag{4-23}$$

where t_{ij} $(i,j=1,2,3)$ is the element of $\mathbf{T}_{LrGw}$ at the ith row and j^{th} column. These elements are the functions of the global wind yaw angle β_0, the global wind inclination θ_0, the position of the element in the *XYZ*-system and the average torsional angle due to the mean wind loads. Because $\mathbf{T}_{LrGw}^{-1} = \mathbf{T}_{LrGw}^{T}$, both $\mathbf{T}_{LrGw}\mathbf{T}_{LrGw}^{T}$ and $\mathbf{T}_{LrGw}^{T}\mathbf{T}_{LrGw}$ are identity matrices. Their elements satisfy the following relationships.

$$\sum_{k=1}^{3} t_{ik}t_{jk} = \begin{cases} 1, & i = j \\ 0, & i \neq j \end{cases}, \qquad (i,j = 1,2,3) \tag{4-24a}$$

$$\sum_{k=1}^{3} t_{ki}t_{kj} = \begin{cases} 1, & i = j \\ 0, & i \neq j \end{cases}, \qquad (i,j = 1,2,3) \tag{4-24b}$$

4.4.6 Local Reference and Mean Wind Coordinate Systems

The relationship between the local reference coordinate *qph*-system and the local mean wind coordinate $\overline{qph}$-system, as shown in Figure 4-4, can be expressed by the following equations:

$$(q,p,h,\alpha,\gamma,\phi)^{T} = \overline{\mathbf{T}}_{Lr\overline{Lw}}(\overline{q},\overline{p},\overline{h},\overline{\alpha},\overline{\gamma},\overline{\phi})^{T} \tag{4-25a}$$

$$(\overline{q},\overline{p},\overline{h},\overline{\alpha},\overline{\gamma},\overline{\phi})^{T} = \overline{\mathbf{T}}_{\overline{Lw}Lr}(q,p,h,\alpha,\gamma,\phi)^{T} \tag{4-25b}$$

where $\overline{\alpha}$, $\overline{\gamma}$ and $\overline{\phi}$ are, respectively, the angular coordinates around the axes $\overline{q}$, $\overline{p}$ and $\overline{h}$; the subscripts $L\overline{w}$ represents the local mean wind coordinate $\overline{qph}$-system; $\overline{\mathbf{T}}_{Lr\overline{Lw}}$ is the 6×6 transformation matrix from the $\overline{qph}$-system to the *qph*-system whilst $\overline{\mathbf{T}}_{\overline{Lw}Lr}$ is one from the *qph*-system to the $\overline{qph}$-system. $\mathbf{T}_{\overline{Lw}Lr} = \mathbf{T}_{Lr\overline{Lw}}^{-1} = \mathbf{T}_{Lr\overline{Lw}}^{T}$.

$\overline{\mathbf{T}}_{LrL\bar{w}}$ and $\overline{\mathbf{T}}_{L\bar{w}Lr}$ can be determined in terms of local mean wind yaw angle and inclination.

$$\overline{\mathbf{T}}_{LrL\bar{w}} = \overline{\mathbf{T}}_{L\bar{w}Lr}^{\mathrm{T}} = \begin{bmatrix} \mathbf{T}_{LrL\bar{w}} & \mathbf{0} \\ \mathbf{0} & \mathbf{T}_{LrL\bar{w}} \end{bmatrix} \tag{4-26a}$$

$$\mathbf{T}_{LrL\bar{w}} = \begin{bmatrix} \cos\bar{\beta} & -\cos\bar{\theta}\sin\bar{\beta} & \sin\bar{\theta}\sin\bar{\beta} \\ \sin\bar{\beta} & \cos\bar{\theta}\cos\bar{\beta} & -\sin\bar{\theta}\cos\bar{\beta} \\ 0 & \sin\bar{\theta} & \cos\bar{\theta} \end{bmatrix} \tag{4-26b}$$

4.4.7 Local Reference and Instantaneous Wind Coordinate Systems

The relationship between the local reference coordinate *qph*-system and the local instantaneous wind coordinate $\tilde{q}\tilde{p}\tilde{h}$-system, as shown in Figure 4-5, can be expressed as

$$(q, p, h, \alpha, \gamma, \phi)^{\mathrm{T}} = \mathbf{T}_{LrL\tilde{w}}(\tilde{q}, \tilde{p}, \tilde{h}, \tilde{\alpha}, \tilde{\gamma}, \tilde{\phi})^{\mathrm{T}} \tag{4-27a}$$

$$(\tilde{q}, \tilde{p}, \tilde{h}, \tilde{\alpha}, \tilde{\gamma}, \tilde{\phi})^{\mathrm{T}} = \mathbf{T}_{L\tilde{w}Lr}(q, p, h, \alpha, \gamma, \phi)^{\mathrm{T}} \tag{4-27b}$$

where $\tilde{\alpha}$, $\tilde{\gamma}$ and $\tilde{\phi}$ are, respectively, the angular coordinates around the axes $\tilde{q}$, $\tilde{p}$ and $\tilde{h}$; the subscript $L\tilde{w}$ represents the local instantaneous wind coordinate $\tilde{q}\tilde{p}\tilde{h}$-system; $\overline{\mathbf{T}}_{LrL\tilde{w}}$ is the 6×6 transformation matrix from the $\tilde{q}\tilde{p}\tilde{h}$-system to the *qph*-system whilst $\overline{\mathbf{T}}_{L\tilde{w}Lr}$ is one from the *qph*-system to the $\tilde{q}\tilde{p}\tilde{h}$-system. $\mathbf{T}_{L\tilde{w}Lr} = \mathbf{T}_{LrL\tilde{w}}^{-1} = \mathbf{T}_{LrL\tilde{w}}^{\mathrm{T}}$. $\overline{\mathbf{T}}_{LrL\tilde{w}}$ and $\overline{\mathbf{T}}_{L\tilde{w}Lr}$ can be determined in terms of local instantaneous wind yaw angle and inclination.

$$\overline{\mathbf{T}}_{LrL\tilde{w}} = \overline{\mathbf{T}}_{L\tilde{w}Lr}^{\mathrm{T}} = \begin{bmatrix} \mathbf{T}_{LrL\tilde{w}} & \mathbf{0} \\ \mathbf{0} & \mathbf{T}_{LrL\tilde{w}} \end{bmatrix} \tag{4-28a}$$

$$\mathbf{T}_{LrL\tilde{w}} = \begin{bmatrix} \cos\tilde{\beta} & -\cos\tilde{\theta}\sin\tilde{\beta} & \sin\tilde{\theta}\sin\tilde{\beta} \\ \sin\tilde{\beta} & \cos\tilde{\theta}\cos\tilde{\beta} & -\sin\tilde{\theta}\cos\tilde{\beta} \\ 0 & \sin\tilde{\theta} & \cos\tilde{\theta} \end{bmatrix} \tag{4-28b}$$

4.5 DETERMINATION OF LOCAL WIND YAW ANGLE AND INCLINATION

The aerodynamic and aeroelastic forces acting on an element in the finite element model of the bridge depend on the local wind yaw angle and inclination, for the aerodynamic coefficients and the flutter derivatives of the element measured from the wind tunnel are described as the functions of both the local wind yaw angle and inclination. However, for the given global wind yaw angle β_0 and inclination θ_0, the local wind yaw angle and inclination vary from element to element. Therefore, only when the local wind yaw angle and inclination are identified for an element, wind-induced buffeting forces and self-excited forces on the element can be evaluated.

4.5.1 Wind Components in *qph*-system

Denote $\mathbf{U}_{Gw}$ and $\mathbf{V}_{Gw}(t)$ the mean wind vector and instantaneous wind vector in the global wind coordinate $X_u Y_v Z_w$-system, respectively. Use $\mathbf{U}_{Lr}$ and $\mathbf{V}_{Lr}(t)$ to represent the mean wind vector and instantaneous wind vector in the local reference *qph*-system, respectively. Then,

$$\mathbf{U}_{Gw} = \left(\overline{U},\ 0,\ 0\right)^{\mathrm{T}} \tag{4-29}$$

$$\mathbf{V}_{Gw} = \left(\overline{U} + u(t),\ v(t),\ w(t)\right)^{\mathrm{T}} \tag{4-30}$$

$$\mathbf{U}_{Lr} = \left(\overline{U}_q,\ \overline{U}_p,\ \overline{U}_h\right)^{\mathrm{T}} \tag{4-31}$$

$$\mathbf{V}_{Lr} = \left(V_q,\ V_p,\ V_h\right)^{\mathrm{T}} \tag{4-32}$$

$$|\mathbf{U}_{Gw}| = |\mathbf{U}_{Lr}| = \overline{U} \tag{4-33}$$

$$|\mathbf{V}_{Gw}(t)| = |\mathbf{V}_{Lr}(t)| = V(t) = \sqrt{[\overline{U} + u(t)]^2 + [v(t)]^2 + [w(t)]^2} \tag{4-34}$$

where $\overline{U}$ and $V(t)$ are the scalar mean and instantaneous wind speeds, respectively; $u(t)$, $v(t)$, and $w(t)$ are the alongwind, lateral-horizontal and upward components of the fluctuating wind, respectively. $\overline{U}_i$ and V_i, $(i = q, p, h)$ denote the components of $\mathbf{U}_{Lr}$ and $\mathbf{V}_{Lr}(t)$ projected onto the q, p, h-axes, respectively (see Figure 4-3). Because $\mathbf{U}_{Lr} = \mathbf{T}_{LrGw}\mathbf{U}_{Gw}$ and $\mathbf{V}_{Lr} = \mathbf{T}_{LrGw}\mathbf{V}_{Gw}$, one can obtain

$$\mathbf{U}_{Lr} = \left(\overline{U}_q, \overline{U}_p, \overline{U}_h\right)^{\mathrm{T}} = \left(t_{11}\overline{U},\ t_{21}\overline{U},\ t_{31}\overline{U},\right)^{\mathrm{T}} \tag{4-35}$$

$$\mathbf{V}_{Lr}=\begin{Bmatrix}V_q\\V_p\\V_h\end{Bmatrix}=\begin{Bmatrix}t_{11}\overline{U}+t_{11}u(t)+t_{12}v(t)+t_{13}w(t)\\t_{21}\overline{U}+t_{21}u(t)+t_{22}v(t)+t_{23}w(t)\\t_{31}\overline{U}+t_{31}u(t)+t_{32}v(t)+t_{33}w(t)\end{Bmatrix} \tag{4-36}$$

where t_{ij} $(i,j=1,2,3)$ is the element of $\mathbf{T}_{LrGw}$ of the ith row and j^{th} column given by Eq.(4-23). The components of mean wind and instantaneous wind onto the qp-plane of the local reference qph-system, denoted as $\overline{U}_{qp}$ and V_{qp}, can be expressed as

$$\overline{U}_{qp}=\sqrt{\overline{U}_q^2+\overline{U}_p^2}=\sqrt{t_{11}^2+t_{21}^2}\,\overline{U} \tag{4-37}$$

$$V_{qp}=\sqrt{V_q^2+V_p^2}=\sqrt{\left[t_{11}(\overline{U}+u)+t_{12}v+t_{13}w\right]^2+\left[t_{21}(\overline{U}+u)+t_{22}v+t_{23}w\right]^2} \tag{4-38}$$

4.5.2 Local Mean Wind Yaw Angle and Inclination

According to the definitions of the local mean wind yaw angle $\overline{\beta}$ and inclination $\overline{\theta}$, they can be determined by the following trigonometric formulas.

$$\cos\overline{\theta}=\overline{U}_{qp}/\overline{U}=\sqrt{t_{11}^2+t_{21}^2} \tag{4-39a}$$

$$\sin\overline{\theta}=\overline{U}_h/\overline{U}=t_{31} \tag{4-39b}$$

$$\cos\overline{\beta}=\overline{U}_p/\overline{U}_{qp}=t_{21}/\sqrt{t_{11}^2+t_{21}^2} \tag{4-39c}$$

$$\sin\overline{\beta}=-\overline{U}_q/\overline{U}_{qp}=-t_{11}/\sqrt{t_{11}^2+t_{21}^2} \tag{4-39d}$$

$$\cos\overline{\theta}\cos\overline{\beta}=t_{21} \tag{4-39e}$$

$$\cos\overline{\theta}\sin\overline{\beta}=-t_{11} \tag{4-39f}$$

$$\sin\overline{\theta}\cos\overline{\beta}=t_{21}t_{31}/\sqrt{t_{11}^2+t_{21}^2} \tag{4-39g}$$

$$\sin\overline{\theta}\sin\overline{\beta}=-t_{11}t_{31}/\sqrt{t_{11}^2+t_{21}^2} \tag{4-39h}$$

4.5.3 Local Instantaneous Wind Yaw Angle and Inclination

Similarly, according to the definitions of the local instantaneous wind yaw angle $\tilde{\beta}$ and inclination $\tilde{\theta}$, they can be determined from the following trigonometric functions.

$$\cos\tilde{\theta}=V_{qp}(u,v,w)/V(u,v,w) \tag{4-40a}$$

$$\sin\tilde{\theta}=V_h(u,v,w)/V(u,v,w) \tag{4-40b}$$

$$\cos\tilde{\beta}=V_p(u,v,w)/V_{qp}(u,v,w) \tag{4-40c}$$

$$\sin\tilde{\beta} = -V_q(u,v,w)/V_{qp}(u,v,w) \tag{4-40d}$$

$$\cos\tilde{\theta}\cos\tilde{\beta} = V_p(u,v,w)/V(u,v,w) \tag{4-40e}$$

$$\cos\tilde{\theta}\sin\tilde{\beta} = -V_q(u,v,w)/V(u,v,w) \tag{4-40f}$$

$$\sin\tilde{\theta}\cos\tilde{\beta} = [V_h(u,v,w)V_p(u,v,w)]/[V(u,v,w)V_{qp}(u,v,w)] \tag{4-40g}$$

$$\sin\tilde{\theta}\sin\tilde{\beta} = -[V_h(u,v,w)V_q(u,v,w)]/[V(u,v,w)V_{qp}(u,v,w)] \tag{4-40h}$$

It is noticed that all the trigonometric functions depend on the three fluctuating wind components. In consideration that the fluctuating wind components are much smaller than the mean wind speed, the trigonometric functions can be approximately expressed as the linear functions of u, v, and w after using the Taylor's formula to expand the trigonometric functions.

$$\cos\tilde{\theta} \approx \sqrt{t_{11}^2+t_{21}^2} - \frac{t_{31}t_{32}}{\sqrt{t_{11}^2+t_{21}^2}}\frac{v}{\overline{U}} - \frac{t_{31}t_{33}}{\sqrt{t_{11}^2+t_{21}^2}}\frac{w}{\overline{U}} \tag{4-41a}$$

$$\sin\tilde{\theta} \approx t_{31} + t_{32}\frac{v}{\overline{U}} + t_{33}\frac{w}{\overline{U}} \tag{4-41b}$$

$$\cos\tilde{\beta} \approx \frac{t_{21}}{\sqrt{t_{11}^2+t_{21}^2}} + \left(\frac{t_{22}}{\sqrt{t_{11}^2+t_{21}^2}} + \frac{t_{21}t_{31}t_{32}}{\sqrt{(t_{11}^2+t_{21}^2)^3}}\right)\frac{v}{\overline{U}} + \left(\frac{t_{23}}{\sqrt{t_{11}^2+t_{21}^2}} + \frac{t_{21}t_{31}t_{33}}{\sqrt{(t_{11}^2+t_{21}^2)^3}}\right)\frac{w}{\overline{U}} \tag{4-41c}$$

$$\sin\tilde{\beta} \approx -\frac{t_{11}}{\sqrt{t_{11}^2+t_{21}^2}} - \left(\frac{t_{12}}{\sqrt{t_{11}^2+t_{21}^2}} + \frac{t_{11}t_{31}t_{32}}{\sqrt{(t_{11}^2+t_{21}^2)^3}}\right)\frac{v}{\overline{U}} - \left(\frac{t_{13}}{\sqrt{t_{11}^2+t_{21}^2}} + \frac{t_{11}t_{31}t_{33}}{\sqrt{(t_{11}^2+t_{21}^2)^3}}\right)\frac{w}{\overline{U}} \tag{4-41d}$$

$$\cos\tilde{\theta}\cos\tilde{\beta} \approx t_{21} + t_{22}\frac{v}{\overline{U}} + t_{23}\frac{w}{\overline{U}} \tag{4-41e}$$

$$\cos\tilde{\theta}\sin\tilde{\beta} \approx -t_{11} - t_{12}\frac{v}{\overline{U}} - t_{13}\frac{w}{\overline{U}} \tag{4-41f}$$

$$\sin\tilde{\theta}\cos\tilde{\beta} \approx \frac{t_{21}t_{31}}{\sqrt{t_{11}^2+t_{21}^2}} + \left(\frac{t_{22}t_{31}}{\sqrt{t_{11}^2+t_{21}^2}} + \frac{t_{21}t_{32}}{\sqrt{(t_{11}^2+t_{21}^2)^3}}\right)\frac{v}{\overline{U}} + \left(\frac{t_{23}t_{31}}{\sqrt{t_{11}^2+t_{21}^2}} + \frac{t_{21}t_{33}}{\sqrt{(t_{11}^2+t_{21}^2)^3}}\right)\frac{w}{\overline{U}} \tag{4-41g}$$

$$\sin\tilde{\theta}\sin\tilde{\beta} \approx -\frac{t_{11}t_{31}}{\sqrt{t_{11}^2+t_{21}^2}} - \left(\frac{t_{12}t_{31}}{\sqrt{t_{11}^2+t_{21}^2}} + \frac{t_{11}t_{32}}{\sqrt{(t_{11}^2+t_{21}^2)^3}}\right)\frac{v}{\overline{U}} - \left(\frac{t_{13}t_{31}}{\sqrt{t_{11}^2+t_{21}^2}} + \frac{t_{11}t_{33}}{\sqrt{(t_{11}^2+t_{21}^2)^3}}\right)\frac{w}{\overline{U}} \tag{4-41h}$$

In the derivation of the above expressions, the relations given by Eqs.(4-24) are employed.

4.5.4 Increments of Local Wind Yaw and Inclination

Let $\Delta\beta$ and $\Delta\theta$ denote the increments of local wind yaw angle and inclination due to the fluctuating wind components. They can be then expressed as

$$\Delta\theta = \tilde{\theta} - \bar{\theta} \tag{4-42a}$$

$$\Delta\beta = \tilde{\beta} - \bar{\beta} \tag{4-42b}$$

By retaining only the linear terms of the fluctuating wind components and considering the relations given by Eqs.(4-24), $\Delta\beta$ and $\Delta\theta$ can be obtained as follows:

$$\Delta\theta \approx \sin\Delta\theta = \sin\tilde{\theta}\cos\bar{\theta} - \cos\tilde{\theta}\sin\bar{\theta} = \frac{t_{32}}{\sqrt{t_{11}^2 + t_{21}^2}}\frac{v}{\bar{U}} + \frac{t_{33}}{\sqrt{t_{11}^2 + t_{21}^2}}\frac{w}{\bar{U}} \tag{4-43a}$$

$$\Delta\beta \approx \sin\Delta\beta = \sin\tilde{\beta}\cos\bar{\beta} - \cos\tilde{\beta}\sin\bar{\beta} = \frac{t_{11}t_{22} - t_{12}t_{21}}{t_{11}^2 + t_{21}^2}\frac{v}{\bar{U}} + \frac{t_{11}t_{23} - t_{13}t_{21}}{t_{11}^2 + t_{21}^2}\frac{w}{\bar{U}} \tag{4-43b}$$

4.6 DETERMINATION OF BUFFETING FORCES AND SPECTRA

4.6.1 Buffeting Forces on Element per Unit Length

As is common, aerodynamic coefficients associated with local wind coordinate system are used in this study to express the aerodynamic buffeting forces/moments acting on bridge components. Thus, in the following context, the expressions of the buffeting forces per unit length related to the local mean wind coordinate $\bar{q}\bar{p}\bar{h}$-system are first derived. They are then transferred to those with respect to the local structural coordinate xyz-system. Afterwards, the nodal buffeting force vector of an arbitrary element of the bridge finite element model is established in the light of the principle of virtual work, and the global buffeting force vector is assembled by FEM. Finally, the spectral density function matrix of global buffeting forces is determined.

Furthermore, how much are the effects of aerodynamic crosswind force, rolling and yawing moments, acting on oblique strips of bridge components due to skew wind, on buffeting response of a long span cable-supported bridge is rarely reported and not very clear at present before a detailed parametric study. Therefore, the aerodynamic crosswind force, rolling and yawing moments are included in the

buffeting force model, in addition to aerodynamic drag, lift and pitching moment, to establish a complete and general buffeting force model for the skew wind case.

4.6.1.1 With Respect to Local Mean Wind Coordinate System

Denote $\tilde{\mathbf{f}}^{ad}(t)$ the total wind force vector on an element per unit length with respect to the local instantaneous wind coordinate $\tilde{q}\tilde{p}\tilde{h}$ -system. The element is an oblique strip with its two ends parallel to the direction of mean wind velocity. The total wind force vector can be expressed as

$$\tilde{\mathbf{f}}^{ad}(t) = \left(C_{\tilde{q}}^{ad}(t), D_{\tilde{p}}^{ad}(t), L_{\tilde{h}}^{ad}(t), M_{\tilde{\alpha}}^{ad}(t), M_{\tilde{\gamma}}^{ad}(t), M_{\tilde{\phi}}^{ad}(t)\right)^{\mathrm{T}}$$

$$= \frac{1}{2}\rho V(t)^2 \mathbf{B}\,\tilde{\mathbf{C}}(\tilde{\beta},\tilde{\theta}) \tag{4-44}$$

where $C_{\tilde{q}}^{ad}(t)$, $D_{\tilde{p}}^{ad}(t)$, $L_{\tilde{h}}^{ad}(t)$ are the total crosswind force, drag force and lift force, respectively, along the axis $\tilde{q}$, the axis $\tilde{p}$ and the axis $\tilde{h}$ in the $\tilde{q}\tilde{p}\tilde{h}$ -system; and $M_{\tilde{\alpha}}^{ad}(t)$, $M_{\tilde{\gamma}}^{ad}(t)$ and $M_{\tilde{\phi}}^{ad}(t)$ are, respectively, the total pitching moment, rolling moment and yawing moment around the axis $\tilde{q}$, the axis $\tilde{p}$ and the axis $\tilde{h}$, respectively (see Figure 4-6).

$$\mathbf{B} = \mathbf{Diag}(B, B, B, B^2, B^2, B^2) \tag{4-45}$$

where the term **Diag** represents a diagonal matrix; B is the characteristic width of the element true cross section. $\tilde{\mathbf{C}}(\tilde{\beta},\tilde{\theta})$ is the aerodynamic coefficient vector as the functions of the local instantaneous wind yaw angle $\tilde{\beta}$ and inclination $\tilde{\theta}$. The aerodynamic coefficient vector can be linearized using the Taylor's formula and ignoring all non-linear terms.

$$\tilde{\mathbf{C}}(\tilde{\beta},\tilde{\theta}) = \bar{\mathbf{C}}(\bar{\beta},\bar{\theta}) + \bar{\mathbf{C}}'^{\beta}(\bar{\beta},\bar{\theta})\Delta\beta + \bar{\mathbf{C}}'^{\theta}(\bar{\beta},\bar{\theta})\Delta\theta \tag{4-46}$$

where $\bar{\mathbf{C}}(\bar{\beta},\bar{\theta})$ is the aerodynamic coefficient vector as the functions of the local mean wind yaw angle $\bar{\beta}$ and inclination $\bar{\theta}$; and $\bar{\mathbf{C}}'^{\beta}(\bar{\beta},\bar{\theta}) = \partial\bar{\mathbf{C}}(\bar{\beta},\bar{\theta})/\partial\beta$, $\bar{\mathbf{C}}'^{\theta}(\bar{\beta},\bar{\theta}) = \partial\bar{\mathbf{C}}(\bar{\beta},\bar{\theta})/\partial\theta$. The detailed expressions are given as follows:

$$\bar{\mathbf{C}}(\bar{\beta},\bar{\theta}) = \left(C_{C_{\tilde{q}}}, C_{D_{\tilde{p}}}, C_{L_{\tilde{h}}}, C_{M_{\tilde{\alpha}}}, C_{M_{\tilde{\gamma}}}, C_{M_{\tilde{\phi}}}\right)^{\mathrm{T}}_{(\bar{\beta},\bar{\theta})} \tag{4-47a}$$

$$\overline{\mathbf{C}}'^{\beta}(\bar{\beta},\bar{\theta})=\left(\frac{\partial C_{C_{\bar{q}}}}{\partial\beta},\frac{\partial C_{D_{\bar{p}}}}{\partial\beta},\frac{\partial C_{L_{\bar{h}}}}{\partial\beta},\frac{\partial C_{M_{\bar{\alpha}}}}{\partial\beta},\frac{\partial C_{M_{\bar{\gamma}}}}{\partial\beta},\frac{\partial C_{M_{\bar{\phi}}}}{\partial\beta}\right)^{\mathrm{T}}_{(\bar{\beta},\bar{\theta})}$$

$$=\left(C'^{\beta}_{C_{\bar{q}}},C'^{\beta}_{D_{\bar{p}}},C'^{\beta}_{L_{\bar{h}}},C'^{\beta}_{M_{\bar{\alpha}}},C'^{\beta}_{M_{\bar{\gamma}}},C'^{\beta}_{M_{\bar{\phi}}}\right)^{\mathrm{T}}_{(\bar{\beta},\bar{\beta})} \tag{4-47b}$$

$$\overline{\mathbf{C}}'^{\theta}(\bar{\beta},\bar{\theta})=\left(\frac{\partial C_{C_{\bar{q}}}}{\partial\theta},\frac{\partial C_{D_{\bar{p}}}}{\partial\theta},\frac{\partial C_{L_{\bar{h}}}}{\partial\theta},\frac{\partial C_{M_{\bar{\alpha}}}}{\partial\theta},\frac{\partial C_{M_{\bar{\gamma}}}}{\partial\theta},\frac{\partial C_{M_{\bar{\phi}}}}{\partial\theta}\right)^{\mathrm{T}}_{(\bar{\beta},\bar{\beta})}$$

$$=\left(C'^{\theta}_{C_{\bar{q}}},C'^{\theta}_{D_{\bar{p}}},C'^{\theta}_{L_{\bar{h}}},C'^{\theta}_{M_{\bar{\alpha}}},C'^{\theta}_{M_{\bar{\gamma}}},C'^{\theta}_{M_{\bar{\phi}}}\right)^{\mathrm{T}}_{(\bar{\beta},\bar{\beta})} \tag{4-47c}$$

where $C_{C_{\bar{q}}}$, $C_{D_{\bar{p}}}$,$C_{L_{\bar{h}}}$, $C_{M_{\bar{\alpha}}}$, $C_{M_{\bar{\gamma}}}$ and $C_{M_{\bar{\phi}}}$ are, respectively, the aerodynamic coefficients of crosswind force, drag, lift, pitching moment, rolling moment, and yawing moment with respect to the local mean wind coordinate $\overline{qph}$-system; the subscript $(\bar{\beta},\bar{\theta})$ means that the aerodynamic coefficients take the values at the local mean wind yaw $\bar{\beta}$ and the local mean wind inclination $\bar{\theta}$ based on the concept of oblique strip; and $()'^{\beta}=\partial()/\partial\beta$ and $()'^{\theta}=\partial()/\partial\theta$ represent the partial derivative with respect to either the local mean wind yaw angle or the local mean wind inclination.

Now, denote $\bar{\mathbf{f}}^{b}(t)$ the buffeting force vector due to the fluctuating wind only and with respect to the $\overline{qph}$-system.

$$\bar{\mathbf{f}}^{b}(t)=\left(C^{b}_{\bar{q}}(t),D^{b}_{\bar{p}}(t),L^{b}_{\bar{h}}(t),M^{b}_{\bar{\alpha}}(t),M^{b}_{\bar{\gamma}}(t),M^{b}_{\bar{\phi}}(t)\right)^{\mathrm{T}} \tag{4-48}$$

where $C^{b}_{\bar{q}}(t)$, $D^{b}_{\bar{p}}(t)$ and $L^{b}_{\bar{h}}(t)$ are the crosswind, drag and lift buffeting forces due to the fluctuating wind, respectively, along the axis $\bar{q}$, the axis $\bar{p}$ and the axis $\bar{h}$ in the $\overline{qph}$-system; $M^{b}_{\bar{\alpha}}(t)$, $M^{b}_{\bar{\gamma}}(t)$ and $M^{b}_{\bar{\phi}}(t)$ are the buffeting pitching moment, rolling moment and yawing moment due to the fluctuating wind, respectively, around the axis $\bar{q}$, the axis $\bar{p}$ and the axis $\bar{h}$ (see Figure 4-7). The buffeting force vector can be then obtained in terms of the transformation of the total wind force vector and the mean wind force vector.

$$\bar{\mathbf{f}}^{b}(t)=\overline{\mathbf{T}}_{L\bar{w}L\tilde{w}}\tilde{\mathbf{f}}^{ad}(t)-\frac{1}{2}\rho\bar{U}^{2}\mathbf{B}\,\overline{\mathbf{C}}(\bar{\beta},\bar{\theta})$$

$$= \frac{1}{2}\rho V(t)^2 \overline{\mathbf{T}}_{L\bar{w}L\tilde{w}} \mathbf{B}\left[\overline{\mathbf{C}}(\bar{\beta},\bar{\theta}) + \overline{\mathbf{C}}^{,\beta}(\bar{\beta},\bar{\theta})\Delta\beta + \overline{\mathbf{C}}^{,\theta}(\bar{\beta},\bar{\theta})\Delta\theta\right]$$

$$-\frac{1}{2}\rho\bar{U}^2 \mathbf{B}\,\overline{\mathbf{C}}(\bar{\beta},\bar{\theta}) \tag{4-49}$$

where $\overline{\mathbf{T}}_{L\bar{w}L\tilde{w}}$ is the 6×6 transformation matrix from the $\tilde{q}\tilde{p}\tilde{h}$ -system to the $\bar{q}\bar{p}\bar{h}$ -system, determined by

$$\overline{\mathbf{T}}_{L\bar{w}L\tilde{w}} = \overline{\mathbf{T}}_{L\bar{w}Lr}\overline{\mathbf{T}}_{LrL\tilde{w}} = \overline{\mathbf{T}}_{LrL\bar{w}}^{-1}\overline{\mathbf{T}}_{LrL\tilde{w}} = \overline{\mathbf{T}}_{LrL\bar{w}}^{\mathrm{T}}\overline{\mathbf{T}}_{LrL\tilde{w}} \tag{4-50}$$

Inserting Eq.(4-26) and Eq.(4-28) into Eq.(4-50) and replacing the trigonometric functions of the local wind yaw angle and inclination by using Eq.(4-39) and Eq.(4-41) yield

$$\overline{\mathbf{T}}_{L\bar{w}L\tilde{w}} = \mathbf{I} + \overline{\mathbf{T}}_v \frac{v}{\bar{U}} + \overline{\mathbf{T}}_w \frac{w}{\bar{U}} \tag{4-51a}$$

where $\mathbf{I}$ is the 6×6 identity matrix, and

$$\overline{\mathbf{T}}_v = \begin{bmatrix} \mathbf{T}_v & \mathbf{0} \\ \mathbf{0} & \mathbf{T}_v \end{bmatrix}, \qquad \mathbf{T}_v = \begin{bmatrix} 0 & -s_1 & s_2 t_{31} \\ s_1 & 0 & -s_3 \\ -s_2 t_{31} & s_3 & 0 \end{bmatrix} \tag{4-51b}$$

$$\overline{\mathbf{T}}_w = \begin{bmatrix} \mathbf{T}_w & \mathbf{0} \\ \mathbf{0} & \mathbf{T}_w \end{bmatrix}, \qquad \mathbf{T}_w = \begin{bmatrix} 0 & -s_4 & s_5 t_{31} \\ s_4 & 0 & -s_6 \\ -s_5 t_{31} & s_6 & 0 \end{bmatrix} \tag{4-51c}$$

$$s_1 = \left(t_{11}t_{22} - t_{21}t_{12}\right)\Big/\sqrt{t_{11}^2 + t_{21}^2} \tag{4-52a}$$

$$s_2 = \left(t_{11}t_{22} - t_{21}t_{12}\right)\Big/\left(t_{11}^2 + t_{21}^2\right) \tag{4-52b}$$

$$s_3 = t_{32}\Big/\sqrt{t_{11}^2 + t_{21}^2} \tag{4-52b}$$

$$s_4 = \left(t_{11}t_{23} - t_{21}t_{13}\right)\Big/\sqrt{t_{11}^2 + t_{21}^2} \tag{4-52b}$$

$$s_5 = \left(t_{11}t_{23} - t_{21}t_{13}\right)\Big/\left(t_{11}^2 + t_{21}^2\right) \tag{4-52b}$$

$$s_6 = t_{33}\Big/\sqrt{t_{11}^2 + t_{21}^2} \tag{4-52b}$$

Substituting Eq.(4-51), Eq. (4-34), and Eq.(4-43) into Eq.(4-49) and retaining the linear terms only of the fluctuating wind components $u(t)$, $v(t)$, and $w(t)$ then result in

$$\tilde{\mathbf{f}}^b(t) \approx \overline{\mathbf{A}}^b\,\tilde{\mathbf{a}}(t) \tag{4-53}$$

where $\tilde{\mathbf{a}}(t)$ is the 3×1 vector of fluctuating wind components.

$$\tilde{\mathbf{a}}(t) = \left(u(t), v(t), w(t)\right)^{\mathrm{T}} \tag{4-54}$$

$\overline{\mathbf{A}}^b$ is the 6×3 aerodynamic coefficient matrix of buffeting forces.

$$\overline{\mathbf{A}}^b = \left[\overline{\mathbf{A}}^u, \overline{\mathbf{A}}^v, \overline{\mathbf{A}}^w\right] \tag{4-55a}$$

$$\overline{\mathbf{A}}^u = \rho\overline{U}\mathbf{B}\chi_u(\overline{\beta},\overline{\theta},K)\overline{\mathbf{C}}(\overline{\beta},\overline{\theta}) = \frac{1}{2}\rho\overline{U}\begin{Bmatrix} 2C_{C_{\overline{q}}}B\chi_{C_{\overline{q}}u} \\ 2C_{D_{\overline{p}}}B\chi_{D_{\overline{p}}u} \\ 2C_{L_{\overline{h}}}B\chi_{L_{\overline{h}}u} \\ 2C_{M_{\overline{\alpha}}}B^2\chi_{M_{\overline{\alpha}}u} \\ 2C_{M_{\overline{\gamma}}}B^2\chi_{M_{\overline{\gamma}}u} \\ 2C_{M_{\overline{\phi}}}B^2\chi_{M_{\overline{\phi}}u} \end{Bmatrix}_{(\overline{\beta},\overline{\theta})} \tag{4-55b}$$

$$\begin{aligned}\overline{\mathbf{A}}^v &= \frac{1}{2}\rho\overline{U}\left\{\overline{\mathbf{T}}_v\mathbf{B}\chi_v(\overline{\beta},\overline{\theta},K)\overline{\mathbf{C}}(\overline{\beta},\overline{\theta}) + s_2\mathbf{B}\chi_v(\overline{\beta},\overline{\theta},K)\overline{\mathbf{C}}'^{\beta}(\overline{\beta},\overline{\theta})\right. \\ &\quad \left. + s_3\mathbf{B}\chi_v(\overline{\beta},\overline{\theta},K)\overline{\mathbf{C}}'^{\theta}(\overline{\beta},\overline{\theta})\right) \\ &= \frac{1}{2}\rho\overline{U}\begin{Bmatrix} [-s_1C_{D_{\overline{p}}} + s_2t_{31}C_{L_{\overline{h}}} + s_2C'^{\beta}_{C_{\overline{q}}} + s_3C'^{\theta}_{C_{\overline{q}}}]B\chi_{C_{\overline{q}}v} \\ [s_1C_{C_{\overline{q}}} - s_3C_{L_{\overline{h}}} + s_2C'^{\beta}_{D_{\overline{p}}} + s_3C'^{\theta}_{D_{\overline{p}}}]B\chi_{D_{\overline{p}}v} \\ [-s_2t_{31}C_{C_{\overline{q}}} + s_3C_{D_{\overline{p}}} + s_2C'^{\beta}_{L_{\overline{h}}} + s_3C'^{\theta}_{L_{\overline{h}}}]B\chi_{L_{\overline{h}}v} \\ [-s_1C_{M_{\overline{\gamma}}} + s_2t_{31}C_{M_{\overline{\phi}}} + s_2C'^{\beta}_{M_{\overline{\alpha}}} + s_3C'^{\theta}_{M_{\overline{\alpha}}}]B^2\chi_{M_{\overline{\alpha}}v} \\ [s_1C_{M_{\overline{\alpha}}} - s_3C_{M_{\overline{\phi}}} + s_2C'^{\beta}_{M_{\overline{\gamma}}} + s_3C'^{\theta}_{M_{\overline{\gamma}}}]B^2\chi_{M_{\overline{\gamma}}v} \\ [-s_2t_{31}C_{M_{\overline{\alpha}}} + s_3C_{M_{\overline{\gamma}}} + s_2C'^{\beta}_{M_{\overline{\phi}}} + s_3C'^{\theta}_{M_{\overline{\phi}}}]B^2\chi_{M_{\overline{\phi}}v} \end{Bmatrix}_{(\overline{\beta},\overline{\theta})}\end{aligned} \tag{4-55c}$$

$$\begin{aligned}\overline{\mathbf{A}}^w &= \frac{1}{2}\rho\overline{U}\left(\mathbf{T}_w\mathbf{B}\chi_w(\overline{\beta},\overline{\theta},K)\overline{\mathbf{C}}(\overline{\beta},\overline{\theta}) + s_5\mathbf{B}\chi_w(\overline{\beta},\overline{\theta},K)\overline{\mathbf{C}}'^{\beta}(\overline{\beta},\overline{\theta})\right. \\ &\quad \left. + s_6\mathbf{B}\chi_w(\overline{\beta},\overline{\theta},K)\overline{\mathbf{C}}'^{\theta}(\overline{\beta},\overline{\theta})\right) \\ &= \frac{1}{2}\rho\overline{U}\begin{Bmatrix} [-s_4C_{D_{\overline{p}}} + s_5t_{31}C_{L_{\overline{h}}} + s_5C'^{\beta}_{C_{\overline{q}}} + s_6C'^{\theta}_{C_{\overline{q}}}]B\chi_{C_{\overline{q}}w} \\ [s_4C_{C_{\overline{q}}} - s_6C_{L_{\overline{h}}} + s_5C'^{\beta}_{D_{\overline{p}}} + s_6C'^{\theta}_{D_{\overline{p}}}]B\chi_{D_{\overline{p}}w} \\ [-s_5t_{31}C_{C_{\overline{q}}} + s_6C_{D_{\overline{p}}} + s_5C'^{\beta}_{L_{\overline{h}}} + s_6C'^{\theta}_{L_{\overline{h}}}]B\chi_{L_{\overline{h}}w} \\ [-s_4C_{M_{\overline{\gamma}}} + s_5t_{31}C_{M_{\overline{\phi}}} + s_5C'^{\beta}_{M_{\overline{\alpha}}} + s_6C'^{\theta}_{M_{\overline{\alpha}}}]B^2\chi_{M_{\overline{\alpha}}w} \\ [s_4C_{M_{\overline{\alpha}}} - s_6C_{M_{\overline{\phi}}} + s_5C'^{\beta}_{M_{\overline{\gamma}}} + s_6C'^{\theta}_{M_{\overline{\gamma}}}]B^2\chi_{M_{\overline{\gamma}}w} \\ [-s_5t_{31}C_{M_{\overline{\alpha}}} + s_6C_{M_{\overline{\gamma}}} + s_5C'^{\beta}_{M_{\overline{\phi}}} + s_6C'^{\theta}_{M_{\overline{\phi}}}]B^2\chi_{M_{\overline{\phi}}w} \end{Bmatrix}_{(\overline{\beta},\overline{\theta},t)}\end{aligned} \tag{4-55d}$$

in which

$$\chi_u(\overline{\beta},\overline{\theta},K) = \mathbf{Diag}(\chi_{C_{\overline{q}}u}, \chi_{D_{\overline{p}}u}, \chi_{L_{\overline{h}}u}, \chi_{M_{\overline{\alpha}}u}, \chi_{M_{\overline{\gamma}}u}, \chi_{M_{\overline{\phi}}u}) \tag{4-56a}$$

$$\chi_v(\overline{\beta},\overline{\theta},K) = \mathbf{Diag}(\chi_{C_{\overline{q}}v}, \chi_{D_{\overline{p}}v}, \chi_{L_{\overline{h}}v}, \chi_{M_{\overline{\alpha}}v}, \chi_{M_{\overline{\gamma}}v}, \chi_{M_{\overline{\phi}}v}) \tag{4-56b}$$

$$\chi_w(\overline{\beta},\overline{\theta},K) = \mathbf{Diag}(\chi_{C_{\overline{q}}w}, \chi_{D_{\overline{p}}w}, \chi_{L_{\overline{h}}w}, \chi_{M_{\overline{\alpha}}w}, \chi_{M_{\overline{\gamma}}w}, \chi_{M_{\overline{\phi}}w}) \tag{4-56c}$$

$K = 2\pi nB/\overline{U}$ is the reduced frequency of the turbulence eddy with frequency of n; $\chi_{\bar{f}a}(\overline{\beta},\overline{\theta},K)$ ($\bar{f} = C_{\bar{q}}$, $D_{\bar{p}}$, $L_{\bar{h}}$, $M_{\bar{\alpha}}$, $M_{\bar{\gamma}}$, $M_{\bar{\phi}}$; a = u, v, w) are the 18 aerodynamic admittance functions, considering the unsteadiness of wind turbulence and the partial coherence of the turbulence along the chord of the oblique cross section in skew wind direction (Davenport, 1962a, 1962b). All these aerodynamic admittance functions are the functions of the reduced frequency and the wind direction. The coherence of the wind turbulence is higher for the turbulence components with longer wavelength (lower frequency or higher velocity) than for the turbulence components with shorter wavelength (higher frequency or lower velocity). As a result, the values of the aerodynamic admittance functions will drop with an increase of K.

Eq. (4-53) is the most general expression for the buffeting force vector acting on the element under skew winds. The conventional cases can be deducted from this expression. For instance, let the local reference coordinate *qph*-system be consistent with the global structural coordinate *XYZ*-system and neglect the initial torsional angle of the element caused by mean wind loads. Then $\overline{\theta} = \theta_0$, $\overline{\beta} = \beta_0$, $\mathbf{T}_{LrGw} = \mathbf{T}_{GsGw}$, and $\alpha_0 = 0$. Consequently, one may obtain

$$\begin{bmatrix} t_{11} & t_{12} & t_{13} \\ t_{21} & t_{22} & t_{23} \\ t_{31} & t_{32} & t_{33} \end{bmatrix} = \begin{bmatrix} -\cos\theta_0 \sin\beta_0 & -\cos\beta_0 & \sin\theta_0 \sin\beta_0 \\ \cos\theta_0 \cos\beta_0 & -\sin\beta_0 & -\sin\theta_0 \cos\beta_0 \\ \sin\theta_0 & 0 & \cos\theta_0 \end{bmatrix} \tag{4-57}$$

and $s_1 = s_6 = 1$, $s_2 = 1/\cos\theta_0$, $s_3 = s_4 = s_5 = 0$,

$$\overline{\mathbf{A}}^b = \frac{1}{2}\rho\overline{U}\begin{bmatrix} 2BC_{C_{\bar{q}}}\chi_{C_{\bar{q}}u} & \left(-C_{D_{\bar{p}}} + C_{L_{\bar{h}}}\tan\theta_0 + \dfrac{C'^{\beta}_{C_{\bar{q}}}}{\cos\theta_0}\right)B\chi_{C_{\bar{q}}v} & C'^{\theta}_{C_{\bar{q}}}B\chi_{C_{\bar{q}}w} \\ 2BC_{D_{\bar{p}}}\chi_{D_{\bar{p}}u} & \left(C_{C_{\bar{q}}} + \dfrac{C'^{\beta}_{D_{\bar{p}}}}{\cos\theta_0}\right)B\chi_{D_{\bar{p}}v} & \left(-C_{L_{\bar{h}}} + C'^{\theta}_{D_{\bar{p}}}\right)B\chi_{D_{\bar{p}}w} \\ 2BC_{L_{\bar{h}}}\chi_{L_{\bar{h}}u} & \left(-C_{C_{\bar{q}}}\tan\theta_0 + \dfrac{C'^{\beta}_{L_{\bar{h}}}}{\cos\theta_0}\right)B\chi_{L_{\bar{h}}v} & \left(C_{D_{\bar{p}}} + C'^{\theta}_{L_{\bar{h}}}\right)B\chi_{L_{\bar{h}}w} \\ 2B^2C_{M_{\bar{\alpha}}}\chi_{M_{\bar{\alpha}}u} & \left(-C_{M_{\bar{\gamma}}} + C_{M_{\bar{\phi}}}\tan\theta_0 + \dfrac{C'^{\beta}_{M_{\bar{\alpha}}}}{\cos\theta_0}\right)B^2\chi_{M_{\bar{\alpha}}v} & C'^{\theta}_{M_{\bar{\alpha}}}B^2\chi_{M_{\bar{\alpha}}w} \\ 2B^2C_{M_{\bar{\gamma}}}\chi_{M_{\bar{\gamma}}u} & \left(C_{M_{\bar{\alpha}}} + \dfrac{C'^{\beta}_{M_{\bar{\gamma}}}}{\cos\theta_0}\right)B^2\chi_{M_{\bar{\gamma}}v} & \left(-C_{M_{\bar{\phi}}} + C'^{\theta}_{M_{\bar{\gamma}}}\right)B^2\chi_{M_{\bar{\gamma}}w} \\ 2B^2C_{M_{\bar{\phi}}}\chi_{M_{\bar{\phi}}u} & \left(-C_{M_{\bar{\alpha}}}\tan\theta_0 + \dfrac{C'^{\beta}_{M_{\bar{\phi}}}}{\cos\theta_0}\right)B^2\chi_{M_{\bar{\phi}}v} & \left(C_{M_{\bar{\gamma}}} + C'^{\theta}_{M_{\bar{\phi}}}\right)B^2\chi_{M_{\bar{\phi}}w} \end{bmatrix}_{(\beta_0,\theta_0)} \tag{4-58}$$

Furthermore, if the local mean wind yaw angle and inclination are equal to zero ($\bar{\beta}=\beta_0=0$, $\bar{\theta}=\theta_0=0$), the values of $C_{C_{\bar{q}}}$, $C_{M_{\bar{r}}}$, $C_{M_{\bar{\phi}}}$, and $C_{\bar{f}}^{'\beta}$ ($\bar{f}=C_{\bar{q}}$, $D_{\bar{p}}$, $L_{\bar{h}}$, $M_{\bar{\alpha}}$, $M_{\bar{r}}$, $M_{\bar{\phi}}$) are all equal to zero. Eq.4-58 can be further simplified as

$$\bar{\mathbf{A}}^b=\frac{1}{2}\rho\bar{U}\begin{bmatrix} 0 & -C_{D_{\bar{p}}}B\chi_{C_{\bar{q}}v} & 0 \\ 2BC_{D_{\bar{p}}}\chi_{D_{\bar{p}}u} & 0 & \left(-C_{L_{\bar{h}}}+C_{D_{\bar{p}}}^{'\theta}\right)B\chi_{D_{\bar{p}}w} \\ 2BC_{L_{\bar{h}}}\chi_{L_{\bar{h}}u} & 0 & \left(C_{D_{\bar{p}}}+C_{L_{\bar{h}}}^{'\theta}\right)B\chi_{L_{\bar{h}}w} \\ 2B^2C_{M_{\bar{\alpha}}}\chi_{M_{\bar{\alpha}}u} & 0 & C_{M_{\bar{\alpha}}}^{'\theta}B^2\chi_{M_{\bar{\alpha}}w} \\ 0 & C_{M_{\bar{\alpha}}}B^2\chi_{M_{\bar{\alpha}}v} & 0 \\ 0 & 0 & 0 \end{bmatrix}_{(0,0)} \tag{4-59}$$

In the traditional buffeting analysis, the mean wind is assumed to be normal to the bridge deck and the lateral component v of fluctuating wind along the bridge deck is often ignored. Thus, the 2nd column in Eq.(4-59) is often neglected in the traditional buffeting analysis. Furthermore, the term $-C_{L_{\bar{h}}}$ in the 2nd row and 3rd column of Eq.(4-59) is often ignored in the traditional buffeting analysis because $-C_{L_{\bar{h}}}$ is quite small when $\bar{\theta}$ is small. Consequently, Eq. (4-59) becomes the same as the equation used in the traditional buffeting analysis with these two assumptions. It is clear that when the wind yaw angle and inclination are considered, Eq. (4-53) other than Eq. (4-59) should be used in the buffeting analysis, as investigated in this thesis, and the aerodynamic coefficients should be measured based on the concept of oblique strip rather than the normal strip. Furthermore, it was pointed out in Zhu et al., (2000) that when $\bar{\theta}$ reaches a certain level, the neglect of the term $-C_{L_{\bar{h}}}$ in Eq. (4-59) may lead to some error in the estimation of buffeting response.

4.6.1.2 With Respect to Local Structural Coordinate System

The buffeting force vector in the local mean wind coordinate system should be converted to the local structural coordinate system that will be further converted to the global structural coordinate system. This kind of the transformation avoids the difficulties involved in the cosine decomposition method. Denote $\mathbf{f}^b(t)$ the buffeting force vector with respect to the local structural *xyz*-system and express it as

$$\mathbf{f}^b(t)=\left(f_x^b(t),f_y^b(t),f_z^b(t),m_{\theta_x}^b(t),m_{\theta_y}^b(t),m_{\theta_z}^b(t)\right)^{\mathrm{T}} \tag{4-60}$$

where $f_x^b(t)$, $f_y^b(t)$, and $f_z^b(t)$ are the three buffeting forces along the axis x, the axis y and the axis z in the xyz-system, respectively. $m_{\theta_x}^b(t)$, $m_{\theta_y}^b(t)$ and $m_{\theta_z}^b(t)$ represent the three buffeting moments around the axis x, the axis y and the axis z, respectively. Then, by means of coordinate transformations one may obtain

$$\mathbf{f}^b(t) = \overline{\mathbf{T}}_{LsLr}\overline{\mathbf{T}}_{LrL\overline{w}}\overline{\mathbf{f}}^b(t) = \overline{\mathbf{T}}_{LsLr}\overline{\mathbf{T}}_{LrL\overline{w}}\overline{\mathbf{A}}^b\overline{\mathbf{a}}(t) \tag{4-61}$$

where, $\overline{\mathbf{T}}_{LsLr}$ is the 6×6 transformation matrix from the local reference coordinate qph-system to the local structural coordinate xyz-system of the form (see Eq. (4-18)).

$$\overline{\mathbf{T}}_{LsLr} = \begin{bmatrix} \mathbf{T}_{LsLr} & 0 \\ 0 & \mathbf{T}_{LsLr} \end{bmatrix} \tag{4-62}$$

4.6.2 Buffeting Forces at Element Nodes

4.6.2.1 With Respect to Local Structural Coordinate System

In the finite element model of a long span cable-supported bridge, the lengths of some elements are quite long. To ensure the accuracy of buffeting analysis, these elements can be further divided into a number of segments so that a constant mean wind speed and a fully coherent turbulence wind can be assumed within the segment. Suppose that n_k is the total number of segments in the kth element; $L_{i,k}$ $(i = 1, \cdots, n_k)$ is the length of ith segment, according to the principle of virtual work, the 12×1 vector of buffeting forces at the nodes of the kth element, $\mathbf{f}_{e,k}^b(t)$, with respect to the xyz-system can be derived as:

$$\begin{aligned}
\mathbf{f}_{e,k}^b(t) &= \left(F_{xI}^b, F_{yI}^b, F_{zI}^b, M_{\theta_{xI}}^b, M_{\theta_{yI}}^b, M_{\theta_{zI}}^b, F_{xJ}^b, F_{yJ}^b, F_{zJ}^b, M_{\theta_{xJ}}^b, M_{\theta_{yJ}}^b, M_{\theta_{zJ}}^b\right)_k^{\mathrm{T}} \\
&= \int_0^l \mathbf{N}_{\delta,k}^{\mathrm{T}}(\xi)\,\mathbf{f}_k^b(t) L_k d\xi = L_k \int_0^l \mathbf{N}_{\delta,k}^{\mathrm{T}}(\xi)\,\overline{\mathbf{T}}_{LsLr,k}\,\overline{\mathbf{T}}_{LrL\overline{w},k}\,\overline{\mathbf{A}}_k^b\,\overline{\mathbf{a}}_k(\xi,t) d\xi \\
&= L_k \sum_{i=1}^{n_k} \left(\left[\overline{\mathbf{T}}_{LsLr,k}^{\mathrm{T}} \int_{\xi_{i-1,k}}^{\xi_{i,k}} \mathbf{N}_{\delta,k}(\xi) d\xi \right]^{\mathrm{T}} \overline{\mathbf{T}}_{LrL\overline{w},k}\,\overline{\mathbf{A}}_{i,k}^b\,\overline{\mathbf{a}}_{i,k}(t) \right) \\
&= \sum_{i=1}^{n_k} \mathbf{Q}_{i,k}^b \overline{\mathbf{a}}_{i,k}(t)
\end{aligned} \tag{4-63}$$

where, the subscript k indicates the kth element; the subscript i indicates the ith segment; I and J represent the left and right nodes of the element;

$\xi = x/L_k\ (0 \le \xi \le 1)$ is the reduced coordinate; $\xi_{i,k} = x_{i,k}/L_k$; $L_k = \sum_{i=1}^{n_k} L_{i,k}$ is the total length of the kth element; and $x_{i,k}$ is the distance between the right end of the ith segment and the left node of the kth element with $x_{0,k} = 0$; $\bar{\mathbf{a}}_{i,k}(t)$ is the 3×1 vector of fluctuating wind components (see Eq.(4-54)) at the center of the ith segment of the kth element; the two 6×6 transformation matrices $\overline{\mathbf{T}}_{LrL\bar{w},k}$ and $\overline{\mathbf{T}}_{LsLr,k}$ for the kth element are determined, respectively, by Eq.(4-26) and Eq.(4-62); the 6×3 aerodynamic coefficient matrix $\overline{\mathbf{A}}^b_{i,k}$ for the ith segment of the kth element is calculated using Eq.(4-55); $\mathbf{Q}^b_{i,k}$ is the 12×3 coefficient matrix of nodal buffeting forces with respect to the local *xyz*-system for the ith segment of the kth element and it is determined by

$$\mathbf{Q}^b_{i,k} = L_k \left[\overline{\mathbf{T}}^{\mathrm{T}}_{LsLr,k} \int_{\xi_{i-1,k}}^{\xi_{i,k}} \mathbf{N}_{\delta,k}(\xi) d\xi \right]^{\mathrm{T}} \overline{\mathbf{T}}_{LrL\bar{w},k} \overline{\mathbf{A}}^b_{i,k} = \tilde{\mathbf{N}}^T_{i,k} \overline{\mathbf{T}}_{LrL\bar{w},k} \overline{\mathbf{A}}^b_{i,k} \tag{4-64}$$

$\mathbf{N}_{\delta,k}(\xi)$ is the matrix of displacement interpolation function of the kth element with respect to the local *xyz*-system, reflecting the relationship between the displacement at an arbitrary position within the kth element and the nodal displacements. For 12-degree-of-freedom spatial beam element, it is expressed as

$$\mathbf{N}_{\delta,k}(\xi) = \begin{bmatrix} N_5 & 0 & 0 & 0 & 0 & 0 & N_6 & 0 & 0 & 0 & 0 & 0 \\ 0 & N_1 & 0 & 0 & 0 & N_2 & 0 & N_3 & 0 & 0 & 0 & N_4 \\ 0 & 0 & N_1 & 0 & -N_2 & 0 & 0 & 0 & N_3 & 0 & -N_4 & 0 \\ 0 & 0 & 0 & N_5 & 0 & 0 & 0 & 0 & 0 & N_6 & 0 & 0 \\ 0 & 0 & N_7 & 0 & N_8 & 0 & 0 & 0 & -N_7 & 0 & -N_9 & 0 \\ 0 & -N_7 & 0 & 0 & 0 & N_8 & 0 & N_7 & 0 & 0 & 0 & -N_9 \end{bmatrix}_k \tag{4-65a}$$

where

$$N_{1,k}(\xi) = 1 - 3\xi^2 + 2\xi^3 \tag{4-65b}$$

$$N_{2,k}(\xi) = L_k\left(\xi - 2\xi^2 + \xi^3\right) \tag{4-65c}$$

$$N_{3,k}(\xi) = 3\xi^2 - 2\xi^3 \tag{4-65d}$$

$$N_{4,k}(\xi) = L_k\left(-\xi^2 + \xi^3\right) \tag{4-65e}$$

$$N_{5,k}(\xi) = 1 - \xi \tag{4-65f}$$

$$N_{6,k}(\xi) = \xi \tag{4-65g}$$

$$N_{7,k}(\xi)=\frac{6}{L_k}\left(\xi-\xi^2\right) \tag{4-65h}$$

$$N_{8,k}(\xi)=1-4\xi+3\xi^2 \tag{4-65i}$$

$$N_{9,k}(\xi)=2\xi-3\xi^2 \tag{4-65j}$$

The matrix $\tilde{\mathbf{N}}_{i,k}\,(i=1,\cdots,n_k)$ in Eq. (4-64) is then determined as follows:

$$\tilde{\mathbf{N}}_{i,k}=L_k\overline{\mathbf{T}}_{LsLr,k}^{\mathrm{T}}\int_{\xi_{i-1,k}}^{\xi_{i,k}}\mathbf{N}_{\delta,k}(\xi)d\xi$$

$$=\overline{\mathbf{T}}_{LsLr,k}^{\mathrm{T}}\begin{bmatrix}\tilde{N}_5 & 0 & 0 & 0 & 0 & 0 & \tilde{N}_6 & 0 & 0 & 0 & 0 & 0\\ 0 & \tilde{N}_1 & 0 & 0 & 0 & \tilde{N}_2 & 0 & \tilde{N}_3 & 0 & 0 & 0 & \tilde{N}_4\\ 0 & 0 & \tilde{N}_1 & 0 & -\tilde{N}_2 & 0 & 0 & 0 & \tilde{N}_3 & 0 & -\tilde{N}_4 & 0\\ 0 & 0 & 0 & \tilde{N}_5 & 0 & 0 & 0 & 0 & 0 & \tilde{N}_6 & 0 & 0\\ 0 & 0 & \tilde{N}_7 & 0 & \tilde{N}_8 & 0 & 0 & 0 & -\tilde{N}_7 & 0 & -\tilde{N}_9 & 0\\ 0 & -\tilde{N}_7 & 0 & 0 & 0 & \tilde{N}_8 & 0 & \tilde{N}_7 & 0 & 0 & 0 & -\tilde{N}_9\end{bmatrix}_{i,k} \tag{4-66a}$$

where

$$\tilde{N}_{1,i,k}=\frac{L_k}{2}\left[2\left(\xi_{i,k}-\xi_{i-1,k}\right)-2\left(\xi_{i,k}^3-\xi_{i-1,k}^3\right)+\left(\xi_{i,k}^4-\xi_{i-1,k}^4\right)\right] \tag{4-66b}$$

$$\tilde{N}_{2,i,k}=\frac{L_k^2}{12}\left[6\left(\xi_{i,k}^2-\xi_{i-1,k}^2\right)-8\left(\xi_{i,k}^3-\xi_{i-1,k}^3\right)+3\left(\xi_{i,k}^4-\xi_{i-1,k}^4\right)\right] \tag{4-66c}$$

$$\tilde{N}_{3,i,k}=\frac{L_k}{2}\left[2\left(\xi_{i,k}^3-\xi_{i-1,k}^3\right)-\left(\xi_{i,k}^4-\xi_{i-1,k}^4\right)\right] \tag{4-66d}$$

$$\tilde{N}_{4,i,k}=\frac{L_k^2}{12}\left[-4\left(\xi_{i,k}^3-\xi_{i-1,k}^3\right)+3\left(\xi_{i,k}^4-\xi_{i-1,k}^4\right)\right] \tag{4-66e}$$

$$\tilde{N}_{5,i,k}=\frac{L_k}{2}\left[2\left(\xi_{i,k}-\xi_{i-1,k}\right)-\left(\xi_{i,k}^2-\xi_{i-1,k}^2\right)\right] \tag{4-66f}$$

$$\tilde{N}_{6,i,k}=\frac{L_k}{2}\left[\xi_{i,k}^2-\xi_{i-1,k}^2\right] \tag{4-66g}$$

$$\tilde{N}_{7,i,k}=3\left(\xi_{i,k}^2-\xi_{i-1,k}^2\right)-2\left(\xi_{i,k}^3-\xi_{i-1,k}^3\right) \tag{4-66h}$$

$$\tilde{N}_{8,i,k}=L_k\left[\left(\xi_{i,k}-\xi_{i-1,k}\right)-2\left(\xi_{i,k}^2-\xi_{i-1,k}^2\right)+\left(\xi_i^3-\xi_{i-1,k}^3\right)\right] \tag{4-66i}$$

$$\tilde{N}_{9,i,k}=L_k\left[\left(\xi_{i,k}^2-\xi_{i-1,k}^2\right)-\left(\xi_{i,k}^3-\xi_{i-1,k}^3\right)\right] \tag{4-66j}$$

4.6.2.2 With Respect to Global Structural Coordinate System

The 12×1 nodal buffeting force vector of the kth element with respect to the global structural coordinate *XYZ*-system, denoted as $\mathbf{F}_{e,k}^{b}(t)$, can be obtained from the 12×1

nodal buffeting force vector, $\mathbf{f}_{e,k}^{b}(t)$, of the kth element in the local structural coordinate system through the coordinate transformation.

$$\mathbf{F}_{e,k}^{b}(t) = \left(F_{XI}^{b}, F_{YI}^{b}, F_{ZI}^{b}, M_{\theta_{XI}}^{b}, M_{\theta_{YI}}^{b}, M_{\theta_{ZI}}^{b}, F_{XJ}^{b}, F_{YJ}^{b}, F_{ZJ}^{b}, M_{\theta_{XJ}}^{b}, M_{\theta_{YJ}}^{b}, M_{\theta_{ZJ}}^{b}\right)_{k}^{T}$$

$$= \overline{\mathbf{T}}_{GsLs,k}\, \mathbf{f}_{e,k}^{b}(t) = \overline{\mathbf{T}}_{GsLs,k} \sum_{i=1}^{n_k} \mathbf{Q}_{i,k}^{b} \overline{\mathbf{a}}_{i,k}(t) = \sum_{i=1}^{n_k} \mathbf{P}_{i,k}^{b} \overline{\mathbf{a}}_{i,k}(t) \tag{4-67}$$

where

$$\overline{\mathbf{T}}_{GsLs,k} = \mathbf{Diag}\left(\mathbf{T}_{GsLs}, \mathbf{T}_{GsLs}, \mathbf{T}_{GsLs}, \mathbf{T}_{GsLs}\right)_{k} \tag{4-68}$$

It is the 12×12 transformation matrix of the kth element from the local *xyz*-system to the global *XYZ*-system; $\mathbf{T}_{GsLs}$ is given by Eq.(4-16). $\mathbf{P}_{i,k}^{b}(t)$ is the 12×3 coefficient matrix of nodal buffeting forces with respect to the global *XYZ*-system for the ith segment of the kth element and it can be determined by

$$\mathbf{P}_{i,k}^{b} = \overline{\mathbf{T}}_{GsLs,k} \mathbf{Q}_{i,k}^{b} \tag{4-69}$$

4.6.3 Global Buffeting Force Vector

Denote $\mathbf{F}^{b}(t)$ the system buffeting force vector assembled in the global structural coordinate *XYZ*-system. It is the same as that defined in the governing equation (4-3) and can be assembled from the nodal buffeting force vectors of all the elements in the global structural coordinate system.

$$\mathbf{F}^{b}(t) = \sum_{k=1}^{M} \left(\mathbf{T}_{k} \sum_{i=1}^{n_k} \mathbf{P}_{i,k}^{b} \overline{\mathbf{a}}_{i,k}(t) \right) = \mathbf{P}^{b} \mathbf{a}(t) \tag{4-70}$$

where M is the total number of elements; $\mathbf{T}_{k}$ is a transformation matrix for the kth element with the dimension equal to the dimension of the system buffeting force vector times 12. Suppose that there are N nodes in the finite element model of the bridge. The matrix $\mathbf{T}_{k}$ is a $6N$×12 matrix with the following topography.

$$\mathbf{T}_{k} = \begin{bmatrix} \mathbf{0} & \mathbf{0} \\ \mathbf{I}_{6} & \mathbf{0} \\ \mathbf{0} & \mathbf{0} \\ \mathbf{0} & \mathbf{I}_{6} \\ \mathbf{0} & \mathbf{0} \end{bmatrix} \tag{4-71}$$

where $\mathbf{0}$ is the zero matrix; $\mathbf{I}_{6}$ is the 6×6 identity matrix. The matrix $\mathbf{I}_{6}$ in the first column of the $\mathbf{T}_{k}$ is located in the 6 rows corresponding to the left node of the kth

element whilst the matrix $\mathbf{I}_6$ in the second column of the matrix $\mathbf{T}_k$ is situated in the 6 rows corresponding to the right node of the kth element. $\mathbf{P}^b$ is the $6N \times 3m$ coefficient matrix of buffeting forces of the form.

$$\mathbf{P}^b = \left[\mathbf{T}_1\mathbf{P}^b_{1,1}, \cdots, \mathbf{T}_1\mathbf{P}^b_{n_1,1}, \cdots, \mathbf{T}_k\mathbf{P}^b_{1,k}, \cdots, \mathbf{T}_k\mathbf{P}^b_{n_k,k}, \cdots, \mathbf{T}_M\mathbf{P}^b_{1,M}, \cdots, \mathbf{T}_M\mathbf{P}^b_{n_M,M}\right] \quad (4\text{-}72)$$

where $m = \sum_{k=1,\cdots M} n_k$ is the total number of segments of the entire bridge.

The vector $\mathbf{a}(t)$ is the $3m \times 1$ vector of the fluctuating wind components of the entire bridge.

$$\mathbf{a}(t) = \left(\bar{\mathbf{a}}^{\mathrm{T}}_{1,1}, \cdots, \bar{\mathbf{a}}^{\mathrm{T}}_{n_1,1}, \cdots, \bar{\mathbf{a}}^{\mathrm{T}}_{n1,k}, \cdots, \bar{\mathbf{a}}^{\mathrm{T}}_{n_k,k}, \cdots, \bar{\mathbf{a}}^{\mathrm{T}}_{1,M}, \cdots, \bar{\mathbf{a}}^{\mathrm{T}}_{n_M,M}\right)^{\mathrm{T}} \quad (4\text{-}73)$$

It should be noted that the multiplication between $\mathbf{T}_k$ and $\mathbf{P}^b_{i,k}$ in Eq.(4-72) is actually not necessary in the computation because $\mathbf{P}^b$ is attained by arranging each $\mathbf{P}^b_{i,k}$ in the proper position of the matrix $\mathbf{P}^b$ directly. The number of the non-zero elements in each row of $\mathbf{P}^b$ is not more than $\sum_{j=1,\cdots M_I} 3n_{k_j}$ ($<< 3m$). M_I is the number of elements with wind loads and associated with the node I; k_j (j=1,..., M_I) is the element number; and n_{k_j} is the number of segments in the k_j element. It is noted that $\mathbf{P}^b$ is a very sparse matrix because the number of elements M_I is small for a long span cable-supported bridge and the number of segments is often small for elements. The sparse property of the matrix $\mathbf{P}^b$ could be and should be utilized to enhance the computational efficiency. In addition, if the frequency-dependent aerodynamic admittance functions are included in the computation, the elements of $\mathbf{P}^b$ are the functions of frequency and complex in nature.

4.6.4 Spectral Density Function Matrix of Global Buffeting Forces

The Fourier transformation of the buffeting force vector $\mathbf{F}^b(t)$ is

$$\hat{\mathbf{F}}^b(\omega) = \mathbf{P}^b(\omega)\hat{\mathbf{a}}(\omega) \quad (4\text{-}74)$$

where $\hat{\mathbf{a}}(\omega)$ is the Fourier transformation of fluctuating wind vector $\mathbf{a}(t)$. By using the following relationship

$$\hat{\mathbf{F}}^{b^*}(\omega)\hat{\mathbf{F}}^{b\,\mathrm{T}}(\omega) = \mathbf{P}^{b^*}(\omega)\,\hat{\mathbf{a}}^*(\omega)\,\hat{\mathbf{a}}^{\mathrm{T}}(\omega)\,\mathbf{P}^{b\mathrm{T}}(\omega) \quad (4\text{-}75)$$

the spectral density matrix of buffeting forces , $\mathbf{S}_{FF}^{b}(\omega)$, can be determined as

$$\mathbf{S}_{FF}^{b}(\omega) = \mathbf{P}^{b^*}(\omega)\mathbf{S}_{aa}(\omega)\mathbf{P}^{b^{\mathrm{T}}}(\omega) \tag{4-76}$$

where the superscript asterisk denotes a complex conjugation operation; $\mathbf{S}_{aa}(\omega)$ is the spectral density function matrix of fluctuating wind components. It is a $3m \times 3m$ matrix and can be expressed as follows:

$$\mathbf{S}_{aa}(\omega) = \begin{bmatrix} \mathbf{S}_{\bar{a}_{1,1}\bar{a}_{1,1}}(\omega) & \cdots & \mathbf{S}_{\bar{a}_{1,1}\bar{a}_{n_k,1}}(\omega) & \cdots & \mathbf{S}_{\bar{a}_{1,1}\bar{a}_{1,M}}(\omega) & \cdots & \mathbf{S}_{\bar{a}_{1,1}\bar{a}_{n_M,M}}(\omega) \\ \vdots & \ddots & \vdots & \ddots & \vdots & \ddots & \vdots \\ \mathbf{S}_{\bar{a}_{n_k,1}\bar{a}_{1,1}}(\omega) & \cdots & \mathbf{S}_{\bar{a}_{n_k,1}\bar{a}_{n_k,1}}(\omega) & \cdots & \mathbf{S}_{\bar{a}_{n_k,1}\bar{a}_{1,M}}(\omega) & \cdots & \mathbf{S}_{\bar{a}_{n_k,1}\bar{a}_{n_M,M}}(\omega) \\ \vdots & \ddots & \vdots & \ddots & \vdots & \ddots & \vdots \\ \mathbf{S}_{\bar{a}_{1,M}\bar{a}_{1,1}}(\omega) & \cdots & \mathbf{S}_{\bar{a}_{1,M}\bar{a}_{n_k,1}}(\omega) & \cdots & \mathbf{S}_{\bar{a}_{1,M}\bar{a}_{1,M}}(\omega) & \cdots & \mathbf{S}_{\bar{a}_{1,M}\bar{a}_{n_M,M}}(\omega) \\ \vdots & \ddots & \vdots & \ddots & \vdots & \ddots & \vdots \\ \mathbf{S}_{\bar{a}_{n_M,M}\bar{a}_{1,1}}(\omega) & \cdots & \mathbf{S}_{\bar{a}_{n_M,M}\bar{a}_{n_k,1}}(\omega) & \cdots & \mathbf{S}_{\bar{a}_{n_M,M}\bar{a}_{1,M}}(\omega) & \cdots & \mathbf{S}_{\bar{a}_{n_M,M}\bar{a}_{n_M,M}}(\omega) \end{bmatrix} \tag{4-77a}$$

where, $\mathbf{S}_{\bar{a}_{i,k}\bar{a}_{j,l}}(\omega)$ $(i=1,\cdots,n_k; j=1,\cdots,n_l; k=1,\cdots,M, l=1,\cdots,M)$ is the 3×3 matrix of auto/cross spectral densities between the three fluctuating wind components at the center of the ith segment of the kth element as well as at the center of the jth segment of the lth element.

$$\mathbf{S}_{\bar{a}_{i,k}\bar{a}_{j,l}}(\omega) = \begin{bmatrix} S_{u_{i,k}u_{j,l}}(\omega) & S_{u_{i,k}v_{j,l}}(\omega) & S_{u_{i,k}w_{j,l}}(\omega) \\ S_{v_{i,k}u_{j,l}}(\omega) & S_{v_{i,k}v_{j,l}}(\omega) & S_{v_{i,k}w_{j,l}}(\omega) \\ S_{w_{i,k}u_{j,l}}(\omega) & S_{w_{i,k}v_{j,l}}(\omega) & S_{w_{i,k}w_{j,l}}(\omega) \end{bmatrix} \tag{4-77b}$$

The diagonal elements of $\mathbf{S}_{aa}(\omega)$ are the auto spectra of fluctuating wind at a designated location and they are real quantities. All the non-diagonal elements of $\mathbf{S}_{aa}(\omega)$ are the cross spectra and complex in general. In addition, it can be proved that $\mathbf{S}_{aa}(\omega)$ is a non-negative-determined Hermitian matrix (Wang, 1994), namely, it is a conjugate-symmetric non-negative-determined matrix.

4.7 DETERMINATION OF AEROELASTIC STIFFNESS AND DAMPING MATRICES

4.7.1 Aeroelastic Forces on Element per Unit Length

The buffeting force vector of the entire bridge under skew winds has been determined in the last section for the governing equation of motion, Eq.(4-3). This section aims to determine the aeroelastic stiffness and damping matrices of the entire

bridge under skew winds for the governing equation of motion. Figure 4-8 shows an arbitrary oblique segment of the bridge deck element submerged in a skew wind field with the mean wind speed $\overline{U}$ and the local mean wind yaw angle $\overline{\beta}$ and inclination $\overline{\theta}$. When the segment oscillates due to wind, there will be some motion-dependent aeroelastic forces and moments acting on the segment caused by the interaction between the segment motion and the air flow around the segment. These self-excited forces are often expressed in terms of the Scanlan's flutter derivatives. Since this investigation concerns skew winds, the Scanlan's flutter derivatives will be measured from the wind tunnel tests of oblique deck segments under skew winds. Thus, they are not only the function of the reduced frequency but also the functions of local mean wind yaw and inclination. Theoretically, there should be six components of the aeroelastic forces/moments but only the pitching moment M_α^{se}, drag D_p^{se} and lift L_h^{se}, as shown in Figure 4-8, are generally regarded to be important to the buffeting response prediction of the bridge (Scanlan and Gade, 1977; Scanlan and Jones, 1990; Jain et al., 1996a).

$$M_\alpha^{se} = \frac{1}{2}\rho\overline{U}^2B^2\left[KA_1^*(\overline{\beta},\overline{\theta},K)\frac{\dot{\delta}_h}{\overline{U}} + KA_2^*(\overline{\beta},\overline{\theta},K)\frac{B\dot{\delta}_\alpha}{\overline{U}} + K^2A_3^*(\overline{\beta},\overline{\theta},K)\delta_\alpha \right.$$
$$\left. + K^2A_4^*(\overline{\beta},\overline{\theta},K)\frac{\delta_h}{B} + KA_5^*(\overline{\beta},\overline{\theta},K)\frac{\dot{\delta}_p}{\overline{U}} + K^2A_6^*(\overline{\beta},\overline{\theta},K)\frac{\delta_p}{B}\right] \quad (4\text{-}78a)$$

$$D_p^{se} = \frac{1}{2}\rho\overline{U}^2B\left[KP_1^*(\overline{\beta},\overline{\theta},K)\frac{\dot{\delta}_p}{\overline{U}} + KP_2^*(\overline{\beta},\overline{\theta},K)\frac{B\dot{\delta}_\alpha}{\overline{U}} + K^2P_3^*(\overline{\beta},\overline{\theta},K)\delta_\alpha \right.$$
$$\left. + K^2P_4^*(\overline{\beta},\overline{\theta},K)\frac{\delta_p}{B} + KP_5^*(\overline{\beta},\overline{\theta},K)\frac{\dot{\delta}_h}{\overline{U}} + K^2P_6^*(\overline{\beta},\overline{\theta},K)\frac{\delta_h}{B}\right] \quad (4\text{-}78b)$$

$$L_h^{se} = \frac{1}{2}\rho\overline{U}^2B\left[KH_1^*(\overline{\beta},\overline{\theta},K)\frac{\dot{\delta}_h}{\overline{U}} + KH_2^*(\overline{\beta},\overline{\theta},K)\frac{B\dot{\delta}_\alpha}{\overline{U}} + K^2H_3^*(\overline{\beta},\overline{\theta},K)\delta_\alpha \right.$$
$$\left. + K^2H_4^*(\overline{\beta},\overline{\theta},K)\frac{\delta_h}{B} + KH_5^*(\overline{\beta},\overline{\theta},K)\frac{\dot{\delta}_p}{\overline{U}} + K^2H_6^*(\overline{\beta},\overline{\theta},K)\frac{\delta_p}{B}\right] \quad (4\text{-}78c)$$

where ρ is the air density; $\overline{U}$ is the mean wind speed of the incident wind at the oblique segment of the bridge deck; $\delta_p(t)$ and $\delta_h(t)$ are the dynamic displacements along the axis p and the axis h and $\delta_\alpha(t)$ is the dynamic angular displacement about the axis q; each over-dot denotes one order of partial differentiation with respect to

time; B is the characteristic width of the true cross section of the bridge segment; $K = B\omega/\overline{U}$ is the reduced frequency; ω is the circular frequency; and $P_i^*(\overline{\beta},\overline{\theta},K)$, $H_i^*(\overline{\beta},\overline{\theta},K)$ and $A_i^*(\overline{\beta},\overline{\theta},K)$ $(i=1,\cdots,6)$ are the flutter derivatives of the oblique bridge segment and thus they are the functions of the local mean wind yaw angle $\overline{\beta}$ and inclination $\overline{\theta}$ as well as the reduced frequency K or the reduced velocity $2\pi/K$.

It is noted that the above aeroelastic pitching moment M_α^{se}, drag D_p^{se} and lift L_h^{se} refer to the local reference coordinate *qph*-system of the bridge deck segment though the flutter derivatives are measured from the oblique segment. These are consistent with the motions of the bridge deck as well as the wind tunnel measurements of flutter derivatives described in Chapter 7. Thus, in spite of the variation of the local mean wind yaw angle and inclination, the positive M_α^{se} is always around the axis q while the positive D_p^{se} and L_h^{se} are always along the axis p and the axis h. For the convenience, the characteristic width still takes the width of the true cross section (see Figure 4-8 and Chapter 7). Furthermore, in this study the aeroelastic inertia forces associated with bridge acceleration response are ignored because air density is much smaller than structural density.

4.7.2 Aeroelastic Stiffness and Damping Matrices for Elements

4.7.2.1 With Respect to Local Structural Coordinate System

Designate $\mathbf{f}_{e,k}^{se}$ the nodal vector of aeroelastic forces and moments at the two ends of the kth element with respect to the local structural coordinate *xyz*-system (see Figure 4-9).

$$\mathbf{f}_{e,k}^{se} = \left(F_{xI}^{se}, F_{yI}^{se}, F_{zI}^{se}, M_{\theta_xI}^{se}, M_{\theta_yI}^{se}, M_{\theta_zI}^{se}, F_{xJ}^{se}, F_{yJ}^{se}, F_{zJ}^{se}, M_{\theta_xJ}^{se}, M_{\theta_yJ}^{se}, M_{\theta_zJ}^{se}\right)_k^{\mathrm{T}} \tag{4-79}$$

Following the traditional way, it can be further expressed in terms of aeroelastic stiffness and damping matrices.

$$\mathbf{f}_{e,k}^{se} = -\mathbf{K}_{e,k}^{'se}\boldsymbol{\delta}_{e,k} - \mathbf{C}_{e,k}^{'se}\dot{\boldsymbol{\delta}}_{e,k} \tag{4-80}$$

where $\mathbf{K}_{e,k}^{'se}$ and $\mathbf{C}_{e,k}^{'se}$ are, respectively, the 12×12 aeroelastic stiffness and damping matrices of the kth element with respect to the *xyz*-system; $\boldsymbol{\delta}_{e,k}$ and $\dot{\boldsymbol{\delta}}_{e,k}$ are,

respectively, the 12×1 nodal displacement vector and the nodal velocity vector of the kth element in the *xyz*-system.

$$\boldsymbol{\delta}_{e,k} = \left(\delta_{xI}, \delta_{yI}, \delta_{zI}, \delta_{\theta_xI}, \delta_{\theta_yI}, \delta_{\theta_zI}, \delta_{xJ}, \delta_{yJ}, \delta_{zJ}, \delta_{\theta_xJ}, \delta_{\theta_yJ}, \delta_{\theta_zJ}\right)_k^T \tag{4-81a}$$

$$\dot{\boldsymbol{\delta}}_{e,k} = \left(\dot{\delta}_{xI}, \dot{\delta}_{yI}, \dot{\delta}_{zI}, \dot{\delta}_{\theta_xI}, \dot{\delta}_{\theta_yI}, \dot{\delta}_{\theta_zI}, \dot{\delta}_{xJ}, \dot{\delta}_{yJ}, \dot{\delta}_{zJ}, \dot{\delta}_{\theta_xJ}, \dot{\delta}_{\theta_yJ}, \dot{\delta}_{\theta_zJ}\right)_k^T \tag{4-81b}$$

On the other hand, express the dynamic displacements and aeroelastic forces at an arbitrary position of the element in the local reference coordinate system and the local structural coordinate system as

$$\boldsymbol{\delta}_{Lr,k} = \left(\delta_\alpha, \delta_p, \delta_h\right)_k^T, \text{ and } \dot{\boldsymbol{\delta}}_{Lr,k} = \left(\dot{\delta}_\alpha, \dot{\delta}_p, \dot{\delta}_h\right)_k^T \tag{4-82}$$

$$\boldsymbol{\delta}_{Ls,k} = \left(\delta_{\theta_x}, \delta_y, \delta_z\right)_k^T, \text{ and } \dot{\boldsymbol{\delta}}_{Ls,k} = \left(\dot{\delta}_{\theta_x}, \dot{\delta}_y, \dot{\delta}_z\right)_k^T \tag{4-83}$$

$$\mathbf{f}_{r,k}^{se} = \left(M_\alpha^{se}, D_p^{se}, L_h^{se}\right)_k^T \tag{4-84}$$

Then, using the coordinate transformation and the interpolation function yields

$$\boldsymbol{\delta}_{Lr,k} = \mathbf{T}_{LrLs,k}\boldsymbol{\delta}_{Ls,k} = \mathbf{T}_{LrLs}\mathbf{N}_{se,k}\boldsymbol{\delta}_{e,k} = \overline{\mathbf{N}}_{se,k}\boldsymbol{\delta}_{e,k} \tag{4-85a}$$

$$\dot{\boldsymbol{\delta}}_{Lr,k} = \mathbf{T}_{LrLs,k}\dot{\boldsymbol{\delta}}_{Ls,k} = \mathbf{T}_{LrLs}\mathbf{N}_{se,k}\dot{\boldsymbol{\delta}}_{e,k} = \overline{\mathbf{N}}_{se,k}\dot{\boldsymbol{\delta}}_{e,k} \tag{4-85b}$$

where, $\mathbf{T}_{LrLs}$ is the coordinate transformation matrix from the *xyz*-system to the *qph*-system, expressed by Eq.(4-18) and Eqs.(5-2a) to (5-2h) for various combination types of the local coordinate system shown in Figure 4-3 and Figures 5-4; and $\mathbf{N}_{se,k}$ is the matrix of displacement interpolation function of the kth element with respect to the local *xyz*-system. Eq.(4-85) reflects the relationship between the dynamic displacement vector $\boldsymbol{\delta}_{Ls,k}$ or velocity vector $\dot{\boldsymbol{\delta}}_{Ls,k}$ at any position of the kth element in the local reference coordinate system and the nodal dynamic displacement vector $\boldsymbol{\delta}_{e,k}$ or velocity vector $\dot{\boldsymbol{\delta}}_{e,k}$ of the same element in the local structural coordinate system; $\overline{\mathbf{N}}_{se,k} = \mathbf{T}_{LrLs}\mathbf{N}_{se,k}$ is the matrix of transformed displacement interpolation function of the kth element. For a 12-degree-of-freedom spatial beam element, the displacement interpolation function matrix $\mathbf{N}_{se,k}$ can be written as

$$\mathbf{N}_{se,k}(\xi) = \begin{bmatrix} 0 & 0 & 0 & N_5 & 0 & 0 & 0 & 0 & 0 & N_6 & 0 & 0 \\ 0 & N_1 & 0 & 0 & 0 & N_2 & 0 & N_3 & 0 & 0 & 0 & N_4 \\ 0 & 0 & N_1 & 0 & -N_2 & 0 & 0 & 0 & N_3 & 0 & -N_4 & 0 \end{bmatrix}_k \tag{4-86}$$

where the displacement interpolation functions $N_i(\xi)$ (i=1, ...,6) are the same as those given in Eqs.(4-65).

Eqs.(4-78) can be written in the form of matrix.

$$\begin{aligned}\mathbf{f}_{r,k}^{se}(\bar{\beta},\bar{\theta},K) &= \mathbf{A}_{S,k}(\bar{\beta},\bar{\theta},K)\boldsymbol{\delta}_{Lr,k} + \mathbf{A}_{D,k}(\bar{\beta},\bar{\theta},K)\dot{\boldsymbol{\delta}}_{Lr,k} \\ &= \mathbf{A}_{S,k}(\bar{\beta},\bar{\theta},K)\overline{\mathbf{N}}_{se,k}\boldsymbol{\delta}_{e,k} + \mathbf{A}_{D,k}(\bar{\beta},\bar{\theta},K)\overline{\mathbf{N}}_{se,k}\dot{\boldsymbol{\delta}}_{e,k}\end{aligned} \tag{4-87}$$

where

$$\mathbf{A}_{S,k}(\bar{\beta},\bar{\theta},K) = \frac{1}{2}\rho\bar{U}^2K^2\begin{bmatrix} B^2A_3^* & BA_6^* & BA_4^* \\ BP_3^* & P_4^* & P_6^* \\ BH_3^* & H_6^* & H_4^* \end{bmatrix}_{(\bar{\beta},\bar{\theta},K)} \tag{4-88}$$

$$\mathbf{A}_{D,k}(\bar{\beta},\bar{\theta},K) = \frac{1}{2}\rho\bar{U}BK\begin{bmatrix} B^2A_2^* & BA_5^* & BA_1^* \\ BP_2^* & P_1^* & P_5^* \\ BH_2^* & H_5^* & H_1^* \end{bmatrix}_{(\bar{\beta},\bar{\theta},K)} \tag{4-89}$$

The principle of virtual work is then used to find the aeroelastic stiffness and damping matrices in Eq. (4-80). Assuming that the element has virtual nodal displacements $\bar{\boldsymbol{\delta}}_{e,k}$, the corresponding virtual displacements at any position in the element can be expressed as

$$\bar{\boldsymbol{\delta}}_{Lr,k} = \overline{\mathbf{N}}_{se,k}\bar{\boldsymbol{\delta}}_{e,k} \tag{4-90}$$

The virtual work done by the nodal aeroelastic forces at the two ends of the element should be equal to that done by the distributed aeroelastic forces on the element.

$$\bar{\boldsymbol{\delta}}_{e,k}^{\mathrm{T}}\mathbf{f}_{e,k}^{se} = \int_0^1 \bar{\boldsymbol{\delta}}_{Lr,k}^{\mathrm{T}}\mathbf{f}_{r,k}^{se}L_k d\xi \tag{4-91}$$

The above equation together with Eqs. (4-80), (4-85) and (4-87) then produce the aeroelastic stiffness and damping matrices for the element in the local structural coordinate xyz-system.

$$\mathbf{K}_{e,k}^{rse} = -L_k\int_0^1 \mathbf{N}_{se,k}^{\mathrm{T}}\mathbf{T}_{LrLs}^{\mathrm{T}}\mathbf{A}_{S,k}\mathbf{T}_{LrLs}\mathbf{N}_{se,k}d\xi \tag{4-92a}$$

$$\mathbf{C}_{e,k}^{rse} = -L_k\int_0^1 \mathbf{N}_{se,k}^{\mathrm{T}}\mathbf{T}_{LrLs}^{\mathrm{T}}\mathbf{A}_{D,k}\mathbf{T}_{LrLs}\mathbf{N}_{se,k}d\xi \tag{4-92b}$$

Because the coordinate transformation matrix $\mathbf{T}_{LrLs}$ is different for different combinations of the local reference coordinate system and the local structural

coordinate system as discussed in Chapter 5, the expressions of the aeroelastic stiffness and damping matrices derived from Eqs.(4-92a) to (4-92b) will be also different, as presented in Appendix B with Eqs.(B-1a) to (B-1h) and Eqs.(B-2a) to (B-2h), for the different combinations of the local coordinate systems.

4.7.2.2 With Respect to Global Structural Coordinate System

The nodal vector of aeroelastic forces and moments at the two ends of the element in the global structural coordinate *XYZ*-system, as shown in Figure (4-9b), can be expressed as

$$\begin{aligned}\mathbf{F}_{e,k}^{se} &= \left(F_{XI}^{se}, F_{YI}^{se}, F_{ZI}^{se}, M_{\theta_X I}^{se}, M_{\theta_Y I}^{se}, M_{\theta_Z J}^{se}, F_{XJ}^{se}, F_{YJ}^{se}, F_{ZJ}^{se}, M_{\theta_X J}^{se}, M_{\theta_Y J}^{se}, M_{\theta_Z J}^{se}\right)_k^{\mathrm{T}} \\ &= -\mathbf{K}_{e,k}^{se}\boldsymbol{\Delta}_{e,k} - \mathbf{C}_{e,k}^{se}\dot{\boldsymbol{\Delta}}_{e,k} \end{aligned} \tag{4-93}$$

where $\mathbf{K}_{e,k}^{se}$ and $\mathbf{C}_{e,k}^{se}$ are, respectively, the aeroelastic stiffness and damping matrices of the kth element with respect to the *XYZ*-system; $\boldsymbol{\Delta}_{e,k}$ and $\dot{\boldsymbol{\Delta}}_{e,k}$ are, respectively, the dynamic displacement and velocity vectors of the kth element in the *XYZ*-system.

$$\boldsymbol{\Delta}_{e,k} = \left(\delta_{XI}, \delta_{YI}, \delta_{ZI}, \delta_{\theta_X I}, \delta_{\theta_Y I}, \delta_{\theta_Z I}, \delta_{XJ}, \delta_{YJ}, \delta_{ZJ}, \delta_{\theta_X J}, \delta_{\theta_Y J}, \delta_{\theta_Z J}\right)_k^{\mathrm{T}} \tag{4-94a}$$

$$\dot{\boldsymbol{\Delta}}_{e,k} = \left(\dot{\delta}_{XI}, \dot{\delta}_{YI}, \dot{\delta}_{ZI}, \dot{\delta}_{\theta_X I}, \dot{\delta}_{\theta_Y I}, \dot{\delta}_{\theta_Z I}, \dot{\delta}_{XJ}, \dot{\delta}_{YJ}, \dot{\delta}_{ZJ}, \dot{\delta}_{\theta_X J}, \dot{\delta}_{\theta_Y J}, \dot{\delta}_{\theta_Z J}\right)_k^{\mathrm{T}} \tag{4-94b}$$

Consider the following coordinate transformation.

$$\mathbf{f}_{e,k}^{se} = \overline{\mathbf{T}}_{LsGs,k}\mathbf{F}_{e,k}^{se} \tag{4-95}$$

$$\boldsymbol{\delta}_{e,k} = \overline{\mathbf{T}}_{LsGs,k}\boldsymbol{\Delta}_{e,k} \tag{4-96a}$$

$$\dot{\boldsymbol{\delta}}_{e,k} = \overline{\mathbf{T}}_{LsGs,k}\dot{\boldsymbol{\Delta}}_{e,k} \tag{4-96b}$$

where $\overline{\mathbf{T}}_{LsGs,k}$ is the 12×12 transformation matrix from the *XYZ*-system to the *xyz*-system, given by Eq.(4-68). Substituting Eqs.(4-95) and (4-96) into Eq.(4-80) and then comparing with Eq.(4-93) yield the following expressions for the aeroelastic stiffness and damping matrices for the element with respect to the global structural coordinate *XYZ*-system.

$$\mathbf{K}_{e,k}^{se} = \overline{\mathbf{T}}_{LsGs}^{\mathrm{T}}\mathbf{K}_{e,k}^{\prime se}\overline{\mathbf{T}}_{LsGs} \tag{4-97a}$$

$$\mathbf{C}_{e,k}^{se} = \overline{\mathbf{T}}_{LsGs}^{\mathrm{T}}\mathbf{C}_{e,k}^{\prime se}\overline{\mathbf{T}}_{LsGs} \tag{4-97b}$$

4.7.3 Global Aeroelastic Stiffness and Damping Matrices

The global aeroelastic stiffness matrix $\mathbf{K}^{se}$ and damping matrix $\mathbf{C}^{se}$ defined in Eq.(4-2) for the global structural coordinate system can be easily obtained by assembling the aeroelastic stiffness and damping matrices for all the elements in the same way as the assemblage of the global structural stiffness matrix and damping matrix from the elemental structural stiffness and damping matrices.

4.8 SOLUTIONS OF BUFFETING GOVERNING EQUATION

4.8.1 Traditional CQC Method and SRSS Method

Under the frame of finite element method, the number of degrees of freedom (DOF) of the buffeting governing equation of a long span bridge is often very large. Thus, the modal superposition scheme is commonly used to reduce computational efforts. Depending on the separation extent of modes of vibration, either the complete quadratic combination method (CQC) or the square root of the sum of square method (SRSS) can be applied (Clough and Penzien, 1975; Wilson, et al., 1981). A brief description of the two schemes is given in the following.

Denote Φ the $N \times M_\Phi$ modal matrix containing the M_Φ modes of vibration of the entire bridge and introduce the following linear transformation for the buffeting displacement response of the bridge.

$$\Delta(t) = \Phi\eta(t) = [\varphi_1, \cdots, \varphi_r, \cdots, \varphi_{M_\Phi}]\eta(t) \tag{4-98}$$

where φ_r is the N-dimensional mode shape vector of the rth mode; and $\eta(t)$ is the M_Φ-dimensional vector of generalized displacement coordinates. Then, the buffeting governing equation, Eq.(4-3), can be reduced to

$$\tilde{\mathbf{M}}\ddot{\eta}(t) + \tilde{\mathbf{C}}\dot{\eta}(t) + \tilde{\mathbf{K}}\eta(t) = \tilde{\mathbf{F}}^b(t) = \Phi^{\mathrm{T}}\mathbf{P}^b\mathbf{a}(t) \tag{4-99}$$

where $\tilde{\mathbf{M}}$, $\tilde{\mathbf{C}}$, and $\tilde{\mathbf{K}}$ are, respectively, the $M_\Phi \times M_\Phi$ matrices of the generalized mass, damping and stiffness. $\tilde{\mathbf{F}}^b(t)$ is the M_Φ-dimensional vector of the generalized buffeting force. They are determined with the following equations.

$$\tilde{\mathbf{M}} = \Phi^{\mathrm{T}}\mathbf{M}\Phi = \Phi^{\mathrm{T}}\mathbf{M}^s\Phi \tag{4-100}$$

$$\tilde{\mathbf{C}} = \Phi^{\mathrm{T}}\mathbf{C}\Phi = \tilde{\mathbf{C}}^s + \tilde{\mathbf{C}}^{se} \tag{4-101a}$$

$$\tilde{\mathbf{K}} = \boldsymbol{\Phi}^{\mathrm{T}}\mathbf{K}\boldsymbol{\Phi} = \tilde{\mathbf{K}}^{s} + \tilde{\mathbf{K}}^{se} \tag{4-102a}$$

$$\tilde{\mathbf{F}}^{b}(t) = \boldsymbol{\Phi}^{\mathrm{T}}\mathbf{F}^{b}(t) = \boldsymbol{\Phi}^{\mathrm{T}}\mathbf{P}^{b}\mathbf{a}(t) \tag{4-103}$$

in which $\tilde{\mathbf{K}}^{s}$ and $\tilde{\mathbf{C}}^{s}$ are, respectively, the diagonal matrices of the generalized structural stiffness and damping of dimension $M_{\Phi} \times M_{\Phi}$. $\tilde{\mathbf{K}}^{se}$ and $\tilde{\mathbf{C}}^{se}$ are, respectively, the $M_{\Phi} \times M_{\Phi}$ matrices of the generalized aeroelastic stiffness and damping; $\mathbf{P}^{b}$ is the $6N \times 3m$ coefficient matrix of nodal buffeting forces given by Eq.(4-72); $\mathbf{a}(t)$ is the $3m$-dimensional vector of fluctuating wind components; m is the number of the points at which the 3 fluctuating wind components act. The generalized structural stiffness and damping matrices and the generalized aeroelastic stiffness and damping matrices can be further expressed as

$$\tilde{\mathbf{C}}^{s} = \boldsymbol{\Phi}^{\mathrm{T}}\mathbf{C}^{s}\boldsymbol{\Phi} = \boldsymbol{\Phi}^{\mathrm{T}}\mathbf{M}^{s}\boldsymbol{\Phi}\,\mathbf{Diag}(2\zeta_{1}\omega_{1},\cdots,2\zeta_{M_{\Phi}}\omega_{M_{\Phi}}) \tag{4-101b}$$

$$\tilde{\mathbf{K}}^{s} = \boldsymbol{\Phi}^{\mathrm{T}}\mathbf{K}^{s}\boldsymbol{\Phi} = \boldsymbol{\Phi}^{\mathrm{T}}\mathbf{M}^{s}\boldsymbol{\Phi}\,\mathbf{Diag}(\omega_{1}^{2},\cdots,\omega_{M_{\Phi}}^{2}) \tag{4-102b}$$

$$\tilde{\mathbf{C}}^{se} = \boldsymbol{\Phi}^{\mathrm{T}}\mathbf{C}^{se}\boldsymbol{\Phi} \tag{4-101c}$$

$$\tilde{\mathbf{K}}^{se} = \boldsymbol{\Phi}^{\mathrm{T}}\mathbf{K}^{se}\boldsymbol{\Phi} \tag{4-102c}$$

where ω_{r} and ζ_{r} $(r = 1,\cdots,M_{\Phi})$ are the circular frequency and damping ratio, respectively, of the rth mode of vibration of the bridge. Since the buffeting response of the bridge is often attributed to the first a few modes of vibration, the size of the equation (4-99) is much smaller than that of equation (4-3). The computational efforts are significantly reduced.

Provided that the fluctuating wind components in the vector $\mathbf{a}(t)$ are stationary random processes and the vibration of the bridge is linear, $\tilde{\mathbf{F}}^{b}(t)$, $\boldsymbol{\eta}(t)$ and $\boldsymbol{\Delta}(t)$ are also stationary random processes. In accordance with random vibration theory, the cross spectral density matrices of $\boldsymbol{\eta}(t)$ and $\boldsymbol{\Delta}(t)$ can be founded from the cross spectral density matrix $\mathbf{S}_{aa}(\omega)$ of the wind excitation (Clough and Penzien, 1975; Newland, 1993).

$$\mathbf{S}_{\eta\eta}(\omega) = \tilde{\mathbf{H}}^{*}(\omega)\mathbf{S}_{\tilde{F}\tilde{F}}(\omega)\tilde{\mathbf{H}}^{\mathrm{T}}(\omega) = \tilde{\mathbf{H}}^{*}(\omega)\boldsymbol{\Phi}^{\mathrm{T}}\mathbf{P}^{b^{*}}\mathbf{S}_{aa}(\omega)\mathbf{P}^{b^{\mathrm{T}}}\boldsymbol{\Phi}\tilde{\mathbf{H}}^{\mathrm{T}}(\omega) \tag{4-104a}$$

$$\mathbf{S}_{\Delta\Delta}(\omega) = \boldsymbol{\Phi}\mathbf{S}_{\eta\eta}(\omega)\boldsymbol{\Phi}^{\mathrm{T}} = \boldsymbol{\Phi}\tilde{\mathbf{H}}^{*}(\omega)\boldsymbol{\Phi}^{\mathrm{T}}\mathbf{P}^{b^{*}}\mathbf{S}_{aa}(\omega)\mathbf{P}^{b^{\mathrm{T}}}\boldsymbol{\Phi}\tilde{\mathbf{H}}^{\mathrm{T}}(\omega)\boldsymbol{\Phi}^{\mathrm{T}} \tag{4-104b}$$

where

$$\tilde{\mathbf{H}}(\omega) = \left[-\omega^{2}\tilde{\mathbf{M}} + i\omega\tilde{\mathbf{C}} + \tilde{\mathbf{K}}\right]^{-1}$$

$$= \Big[\boldsymbol{\Phi}^{\mathrm{T}} \mathbf{M}^{s} \boldsymbol{\Phi} \Big[\mathbf{Diag}(\omega_1^2 - \omega^2, \cdots, \omega_{M_\Phi}^2 - \omega^2)$$

$$+ i\,\mathbf{Diag}(2\zeta_1\omega_1\omega, \cdots, \omega_{M_\Phi}\omega) \Big] + \boldsymbol{\Phi}^{\mathrm{T}} \mathbf{K}^{se} \boldsymbol{\Phi} + i\omega\, \boldsymbol{\Phi}^{\mathrm{T}} \mathbf{C}^{se} \boldsymbol{\Phi} \Big]^{-1} \qquad (4\text{-}105)$$

$\tilde{\mathbf{H}}(\omega)$ is the generalized matrix of frequency response functions of the bridge. If the aeroelastic stiffness and damping matrices are neglected, the matrix $\tilde{\mathbf{H}}(\omega)$ is diagonal. Eq.(4-104b) can be reduced to

$$\mathbf{S}_{\Delta\Delta}(\omega) = \sum_{r=1}^{M_\Phi} \sum_{s=1}^{M_\Phi} \left(H_r^*(\omega) H_s(\omega) \boldsymbol{\varphi}_r \boldsymbol{\varphi}_r^{\mathrm{T}} \mathbf{P}^{b^*}(\omega) \mathbf{S}_{aa}(\omega) \mathbf{P}^{b^{\mathrm{T}}}(\omega) \boldsymbol{\varphi}_s \boldsymbol{\varphi}_s^{\mathrm{T}} \right) \qquad (4\text{-}106)$$

Equation (4-106) is actually called the traditional CQC method for computing the spectral density matrix of bridge displacement response to turbulence. For a large structural system, the computational effort for obtaining the spectral matrix of structural displacement response using Eq. (4-106) is enormous. If a structure is lightly damped and has well separated modes of vibration, the buffeting responses from two different modes of vibration are almost statistically independent of each other. Therefore, the inter-mode terms in Eq.(4-106) are often ignored in engineering practice to reduce computational efforts. This leads to the so-called SRSS method as shown below.

$$\mathbf{S}_{\Delta\Delta}(\omega) = \sum_{r=1}^{M_\Phi} \left(|H_r(\omega)|^2 \boldsymbol{\varphi}_r \boldsymbol{\varphi}_r^{\mathrm{T}} \mathbf{P}^{b^*} \mathbf{S}_{aa}(\omega) \mathbf{P}^{b^{\mathrm{T}}} \boldsymbol{\varphi}_r \boldsymbol{\varphi}_r^{\mathrm{T}} \right) \qquad (4\text{-}107)$$

However, for long span cable-supported bridges, the natural modes of vibration are often closely spaced. The inter-mode (cross-correlation) terms in Eq. (4-106) may be significant and cannot be neglected. Furthermore, the aeroelastic matrices in Eq.(4-105) due to the self-excited loads on the bridge deck often play an important role on bridge buffeting response and must be included in the analysis. Hence, the global (system) damping matrix is no longer proportional and the frequency response function matrix is no longer diagonal. On the other hand, the direct use of Eq. (4-104) to compute the spectral response is very time consuming. All these factors lead to the difficulty in decision making as to which method should be used. In this study, the pseudo-excitation method proposed by Lin and Zhang (Lin, 1985; Lin, 1992; Lin, et al., 1993; Lin et al., 1994;) and extended to the buffeting response prediction of the bridge by Xu and Sun (Xu el al., 1998; Sun et al, 2000; Xu et al., 2000a) is employed.

4.8.2 Pseudo Excitation Method

The pseudo excitation method was first proposed for the structural seismic analysis with only a single random excitation concerned (Lin, 1985; Lin, 1992), It was then expanded to the problems of multi-excitations of fully or partially coherence (Lin, et al., 1993; Lin et al., 1994). Afterwards, it has been applied to the buffeting response analysis of long span bridges (Xu et al., 1998; Xu, 1999; Sun et al. 2000, Xu et al., 2000a).

When using this method, the cross-spectral matrix of random excitations is decomposed using the $\mathbf{L}^*\mathbf{D}\mathbf{L}^T$ decomposition scheme of a non-negative-determined Hermitian matrix. The decomposition scheme is similar to the $\mathbf{L}\mathbf{D}\mathbf{L}^T$ decomposition of a real symmetric matrix (Jennings and McKeown, 1992), where all the elements of the diagonal matrix $\mathbf{D}$ are non-negative. Then, a series of harmonic pseudo excitations are established using the non-zero elements of the diagonal matrix $\mathbf{D}$ and the corresponding columns of the lower triangular matrix $\mathbf{L}$. These harmonic pseudo excitations are then applied to the system to find the pseudo response. Suppose $\mathbf{R}_j$ is the jth pseudo response of either displacement or internal force caused by the jth pseudo excitation. The final spectral response matrix of the response can be obtained as

$$\mathbf{S}_{RR}(\omega) = \sum_{j=1}^{m_p} \mathbf{R}_j^*(\omega)\mathbf{R}_j^T(\omega) \tag{4-108}$$

where m_p is the number of the pseudo harmonic excitations which are equal to the rank of the cross-spectral matrix of the random excitations.

4.8.3 Solution for Bridge Buffeting Response

Because the cross-spectral matrix of wind turbulence, $\mathbf{S}_{aa}(\omega)$, is a non-negative-determined Hermitian matrix (Wang, 1994), it can be expressed as the sum of sub-spectral matrices using the $\mathbf{L}^*\mathbf{D}\mathbf{L}^T$ decomposition.

$$\mathbf{S}_{aa}(\omega) = \mathbf{l}^*(\omega)\mathbf{d}(\omega)\mathbf{l}^T(\omega) = \sum_{j=1}^{m_p} \mathbf{S}_{aa,j}(\omega) \tag{4-109a}$$

$$\mathbf{S}_{aa,j}(\omega) = d_j \mathbf{l}_j^*(\omega)\mathbf{l}_j^T(\omega) \tag{4-109b}$$

where $m_p \le 3m$ is the rank of the spectral matrix $\mathbf{S}_{aa}(\omega)$; $\mathbf{d}(\omega)$ is a $3m \times 3m$ real diagonal matrix; $\mathbf{l}(\omega)$ is a $3m \times 3m$ lower triangular matrix with all its diagonal elements being unity; $d_j(\omega)$ is the jth non-zero diagonal element of $\mathbf{d}(\omega)$; $\mathbf{l}_j(\omega)$ is the jth column of $\mathbf{l}(\omega)$. Corresponding to each sub-spectral matrix, $\mathbf{S}_{aa,j}(\omega)$ $(j = 1, \cdots, m_p)$, a harmonic pseudo wind excitation can be constituted as follows

$$\mathbf{a}_{p,j}(\omega,t) = \mathbf{l}_j(\omega)\sqrt{d_j(\omega)}\, e^{i\omega t} \quad (j = 1, \cdots, m_p) \tag{4-110}$$

The substitution of $\mathbf{a}(t)$ and $\boldsymbol{\eta}(t)$ in Eq. (4-99) by $\mathbf{a}_{p,j}(\omega,t)$ and $\boldsymbol{\eta}_{p,j}(\omega,t)$ respectively produces

$$\tilde{\mathbf{M}}\ddot{\boldsymbol{\eta}}_{p,j}(\omega,t) + \tilde{\mathbf{C}}\dot{\boldsymbol{\eta}}_{p,j}(\omega,t) + \tilde{\mathbf{K}}\boldsymbol{\eta}_{p,j}(\omega,t) = \boldsymbol{\Phi}^T\mathbf{P}^b(\omega)\mathbf{a}_{p,j}(\omega,t) \tag{4-111}$$

in which $\boldsymbol{\eta}_{p,j}(\omega,t)$ is the jth harmonic generalized pseudo displacement response vector corresponding to the jth harmonic pseudo wind excitation $\mathbf{a}_{p,j}(\omega,t)$. Since this is a determinate dynamic problem, the pseudo displacement response can be easily found.

$$\boldsymbol{\eta}_{p,j}(\omega,t) = \tilde{\mathbf{H}}(\omega)\tilde{\mathbf{l}}_j(\omega)\sqrt{d_j(\omega)}\, e^{i\omega t} \tag{4-112}$$

where

$$\tilde{\mathbf{l}}_j(\omega) = \boldsymbol{\Phi}^{\mathrm{T}}\mathbf{P}^{\mathrm{b}}(\omega)\mathbf{l}_j(\omega) \tag{4-113}$$

Substituting Eq.(4-112) into Eq.(4-98) yields

$$\boldsymbol{\Delta}_{p,j}(\omega,t) = \boldsymbol{\Phi}\tilde{\mathbf{H}}(\omega)\tilde{\mathbf{l}}_j(\omega)\sqrt{d_j(\omega)}\, e^{i\omega t} = \sqrt{d_j(\omega)}\,\tilde{\boldsymbol{\Delta}}_j(\omega)e^{i\omega t} \tag{4-114a}$$

and

$$\dot{\boldsymbol{\Delta}}_{p,j}(\omega,t) = i\omega\sqrt{d_j(\omega)}\,\tilde{\boldsymbol{\Delta}}_j(\omega)e^{i\omega t} \tag{4-114b}$$

$$\ddot{\boldsymbol{\Delta}}_{p,j}(\omega,t) = -\omega^2\sqrt{d_j(\omega)}\,\tilde{\boldsymbol{\Delta}}_j(\omega)e^{i\omega t} \tag{4-114c}$$

where $\boldsymbol{\Delta}_{p,j}(\omega,t)$, $\dot{\boldsymbol{\Delta}}_{p,j}(\omega,t)$ and $\ddot{\boldsymbol{\Delta}}_{p,j}(\omega,t)$ are the pseudo displacement, velocity and acceleration responses corresponding to the jth pseudo excitation $\mathbf{a}_{p,j}(\omega,t)$ and

$$\tilde{\boldsymbol{\Delta}}_j(\omega) = \boldsymbol{\Phi}\tilde{\mathbf{H}}(\omega)\tilde{\mathbf{l}}_j(\omega) \tag{4-115}$$

In light of Eq.(4-108), the response spectra of bridge displacement, velocity and acceleration can be obtained as follows:

$$\mathbf{S}_{\Delta\Delta}(\omega) = \sum_{j=1}^{m_p}\boldsymbol{\Delta}_{p,j}^{*}\boldsymbol{\Delta}_{p,j}^{\mathrm{T}} = \sum_{j=1}^{m_p} d_j\tilde{\boldsymbol{\Delta}}_j^{*}\tilde{\boldsymbol{\Delta}}_j^{\mathrm{T}} \tag{4-116a}$$

$$\mathbf{S}_{\dot{\Delta}\dot{\Delta}}(\omega)=\sum_{j=1}^{m_p}\dot{\mathbf{\Delta}}_{p,j}^{*}\dot{\mathbf{\Delta}}_{p,j}^{\mathrm{T}}=\omega^2\mathbf{S}_{\Delta\Delta}(\omega) \tag{4-116b}$$

$$\mathbf{S}_{\ddot{\Delta}\ddot{\Delta}}(\omega)=\sum_{j=1}^{m_p}\ddot{\mathbf{\Delta}}_{p,j}^{*}\ddot{\mathbf{\Delta}}_{p,j}^{\mathrm{T}}=\omega^4\mathbf{S}_{\Delta\Delta}(\omega) \tag{4-116c}$$

It has been proved that the spectral matrices of buffeting response determined by Eq. (4-116) are the same as those using Eq.(4-104b), but the computation efforts required by Eq. (4-116) are much less.

To further enhance the computation efficiency, the $\mathbf{L}^{*}\mathbf{D}\mathbf{L}^{\mathrm{T}}$ decomposition method will be used twice in this study (Sun 1999). By substituting Eq.(4-115) into Eq(4-116a), one obtains

$$\mathbf{S}_{\Delta\Delta}(\omega)=\mathbf{\Phi}\tilde{\mathbf{H}}^{*}(\omega)\left(\sum_{j=1}^{m_p}d_j\tilde{\mathbf{l}}_j^{*}(\omega)\tilde{\mathbf{l}}_j^{\mathrm{T}}(\omega)\right)\tilde{\mathbf{H}}^{\mathrm{T}}(\omega)\mathbf{\Phi}^{\mathrm{T}}(\omega) \tag{4-117}$$

On the other hand, $\mathbf{S}_{\Delta\Delta}(\omega)$ in Eq. (4-104b) can be expressed as

$$\mathbf{S}_{\Delta\Delta}(\omega)=\mathbf{\Phi}\tilde{\mathbf{H}}^{*}(\omega)\mathbf{S}_{\tilde{\mathbf{F}}\tilde{\mathbf{F}}}^{b}(\omega)\tilde{\mathbf{H}}^{\mathrm{T}}(\omega)\mathbf{\Phi}^{\mathrm{T}}(\omega) \tag{4-118}$$

where $\mathbf{S}_{\tilde{\mathbf{F}}\tilde{\mathbf{F}}}^{b}(\omega)$ is the cross-spectral matrix of the generalized buffeting force $\tilde{\mathbf{F}}^{b}(t)$. Comparing Eq.(4-117) with Eq. (4-118) leads to

$$\mathbf{S}_{\tilde{\mathbf{F}}\tilde{\mathbf{F}}}^{b}=\mathbf{\Phi}^{\mathrm{T}}\mathbf{P}^{b^{*}}(\omega)\mathbf{S}_{aa}(\omega)\mathbf{P}^{b^{\mathrm{T}}}(\omega)\mathbf{\Phi}=\sum_{j=1}^{m_p}d_j\tilde{\mathbf{l}}_j^{*}(\omega)\tilde{\mathbf{l}}_j^{T}(\omega) \tag{4-119}$$

Thus, instead of computing the response spectral matrix using Eq.(4-116a), the cross-spectral matrix of the generalized buffeting force $\mathbf{S}_{\tilde{\mathbf{F}}\tilde{\mathbf{F}}}^{b}$ is first founded using Eq.(4-119). Then, the $\mathbf{L}^{*}\mathbf{D}\mathbf{L}^{\mathrm{T}}$ decomposition is applied once more to the Hermitian matrix $\mathbf{S}_{\tilde{\mathbf{F}}\tilde{\mathbf{F}}}^{b}$.

$$\mathbf{S}_{\tilde{\mathbf{F}}\tilde{\mathbf{F}}}^{b}(\omega)=\mathbf{L}^{*}(\omega)\mathbf{D}(\omega)\mathbf{L}^{\mathrm{T}}(\omega)=\sum_{r=1}^{M_p}D_r(\omega)\mathbf{L}_r^{*}(\omega)\mathbf{L}_r^{\mathrm{T}}(\omega) \tag{4-120}$$

where $M_p \le M_\Phi$ is the rank of the generalized spectral matrix $\mathbf{S}_{\tilde{\mathbf{F}}\tilde{\mathbf{F}}}^{b}(\omega)$; $\mathbf{D}(\omega)$ is a real $M_\Phi \times M_\Phi$ diagonal matrix; $\mathbf{L}(\omega)$ is a $M_\Phi \times M_\Phi$ lower triangular matrix with all its diagonal elements being unity; $D_r(\omega)$ is the rth non-zero diagonal element of $\mathbf{D}(\omega)$; $\mathbf{L}_r(\omega)$ is the rth column of $\mathbf{L}(\omega)$; Physically, $\sqrt{D_r}\mathbf{L}_r(\omega)e^{i\omega t}$ can be regarded as a harmonic generalized pseudo excitation directly for $\tilde{\mathbf{F}}^{b}(t)$ in Eq.(4-99). By

using the principle of pseudo excitation method again, the cross-spectral matrices of buffeting responses can be found as follows:

$$\mathbf{S}_{\Delta\Delta}(\omega)=\sum_{r=1}^{M_p}D_r(\omega)\tilde{\boldsymbol{\Delta}}_{p,r}^{*}(\omega)\tilde{\boldsymbol{\Delta}}_{p,r}^{T}(\omega) \tag{4-121a}$$

$$\mathbf{S}_{\dot{\Delta}\dot{\Delta}}(\omega)=\omega^2\sum_{r=1}^{M_p}D_r(\omega)\tilde{\boldsymbol{\Delta}}_{p,r}^{*}(\omega)\tilde{\boldsymbol{\Delta}}_{p,r}^{T}(\omega)=\omega^2\mathbf{S}_{\Delta\Delta}(\omega) \tag{4-121b}$$

$$\mathbf{S}_{\ddot{\Delta}\ddot{\Delta}}(\omega)=\omega^4\sum_{r=1}^{M_p}D_r(\omega)\tilde{\boldsymbol{\Delta}}_{p,r}^{*}(\omega)\tilde{\boldsymbol{\Delta}}_{p,r}^{T}(\omega)=\omega^4\mathbf{S}_{\Delta\Delta}(\omega) \tag{4-121c}$$

where

$$\tilde{\boldsymbol{\Delta}}_{p,r}(\omega)=\boldsymbol{\Phi}\tilde{\mathbf{H}}(\omega)\mathbf{L}_r(\omega) \tag{4-122}$$

Furthermore, the RMS (standard deviation) responses of the nodal displacement, velocity and acceleration can be calculated through the integral of corresponding spectrum in the frequency domain as follows.

$$\boldsymbol{\sigma}_{\Delta_i}=\sqrt{2\int_0^{+\infty}\mathbf{S}_{\Delta_i}(\omega)d\omega} \tag{4-123a}$$

$$\boldsymbol{\sigma}_{\dot{\Delta}_i}=\sqrt{2\int_0^{+\infty}\mathbf{S}_{\dot{\Delta}_i}(\omega)d\omega} \tag{4-123b}$$

$$\boldsymbol{\sigma}_{\ddot{\Delta}_i}=\sqrt{2\int_0^{+\infty}\mathbf{S}_{\ddot{\Delta}_i}(\omega)d\omega} \tag{4-123c}$$

where $\Delta_i=(x_i,y_i,z_i,\theta_{xi},\theta_{yi},\theta_{zi})^T$, $\dot{\Delta}_i=(\dot{x}_i,\dot{y}_i,\dot{z}_i,\dot{\theta}_{xi},\dot{\theta}_{yi},\dot{\theta}_{zi})^T$, $\ddot{\Delta}_i=(\ddot{x}_i,\ddot{y}_i,\ddot{z}_i,\ddot{\theta}_{xi},\ddot{\theta}_{yi},\ddot{\theta}_{zi})^T$ are, respectively, the vectors of displacement, velocity and acceleration responses of ith node. $\boldsymbol{\sigma}_{\Delta_i}$, $\boldsymbol{\sigma}_{\dot{\Delta}_i}$ and $\boldsymbol{\sigma}_{\ddot{\Delta}_i}$ are, respectively, the vectors of RMS responses of nodal displacement, velocity and acceleration of ith node; $\mathbf{S}_{\Delta_i}$, $\mathbf{S}_{\dot{\Delta}_i}$ and $\mathbf{S}_{\ddot{\Delta}_i}$ are, respectively, the vectors of corresponding auto-spectra of ith node, extracted from the diagonal elements of the cross-spectral matrices $\mathbf{S}_{\Delta\Delta}(\omega)$, $\mathbf{S}_{\dot{\Delta}\dot{\Delta}}(\omega)$ and $\mathbf{S}_{\ddot{\Delta}\ddot{\Delta}}(\omega)$.

4.9 SUMMARY

A modified buffeting analysis method of long span cable-supported bridges under skew winds has been developed in this chapter based on the quasi-steady linear theory and the oblique strip theory in conjunction with the pseudo excitation method (PEM) and the finite element method (FEM). Major features of this modified method are summarised as follows:

(1) The modified method is capable of predicting the fully coupled buffeting response of long span cable-supported bridges to skew winds with acceptable computation efforts. The buffeting response predicted by the modified method naturally includes not only the effects of inter-mode, multi-mode, and spatial mode but also the interaction among major bridge components.

(2) A set of universal expressions for six component buffeting forces associated with the oblique segment has been derived using the quasi-steady linear theory. These buffeting forces are formed with respect to the local wind coordinate systems and then converted to the structural coordinate systems. Thus, the three orthogonal fluctuating wind components can be easily handled without artificial decomposition. This set of universal expressions is applicable to all the structural members including the bridge deck, cables and towers.

(3) Aeroelastic stiffness and damping matrices due to self-excited forces are taken into consideration in the modified method by introducing 18 flutter derivatives with respect to the oblique bridge segment. Non-proportional aeroelastic damping from the self-excited forces can be effectively handled by using the pseudo excitation method.

(4) The variations of mean wind speed, turbulence intensity, and auto-spectrum along the bridge longitudinal axis can be easily included in the prediction. The coherence of wind turbulence between any two arbitrary spatial points is considered in the global wind coordinate system rather than the global structural coordinate system.

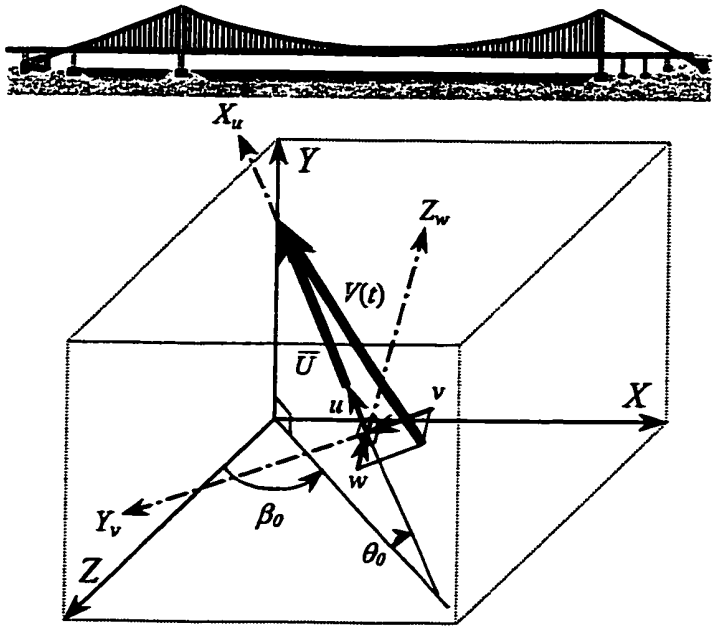

Figure 4-1 Global Structural and Wind Coordinate Systems

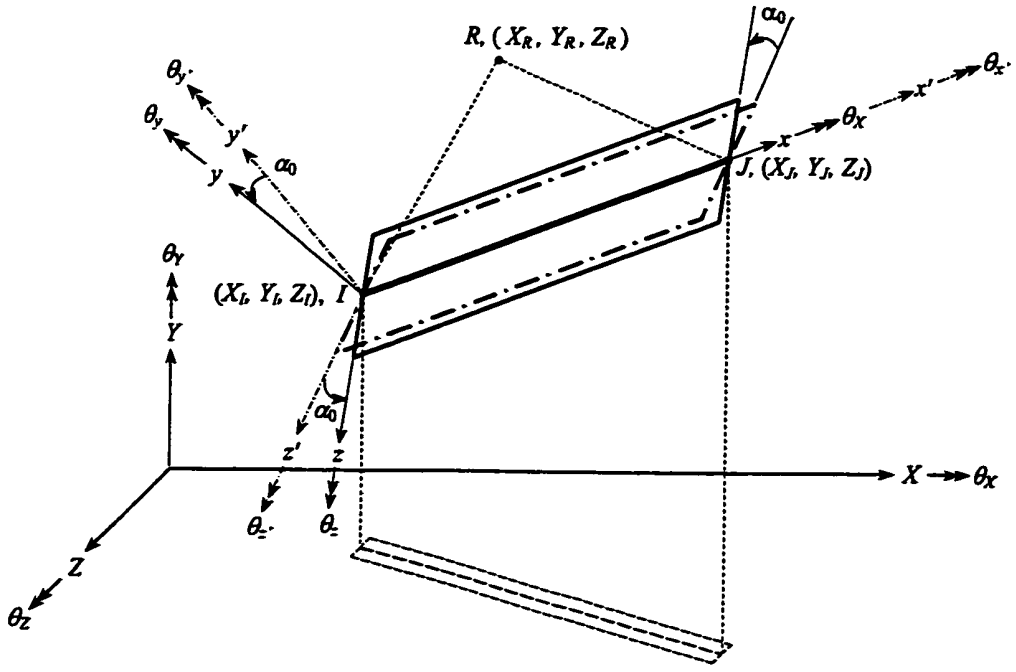

Figure 4-2 Local Structural Coordinate Systems

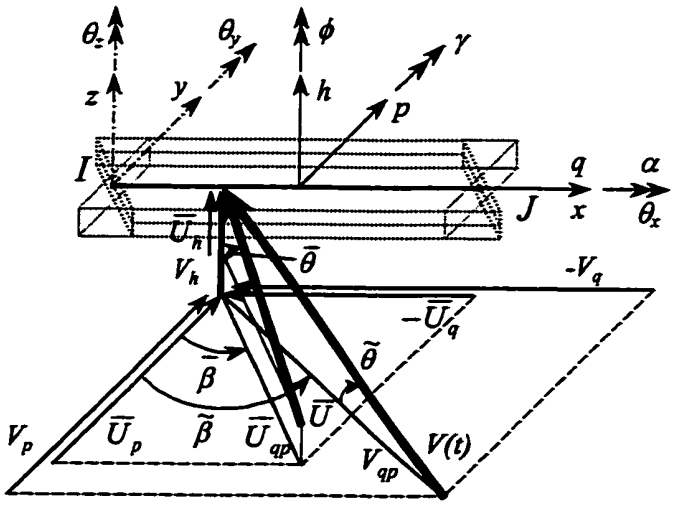

Figure 4-3 Local Reference Coordinate System

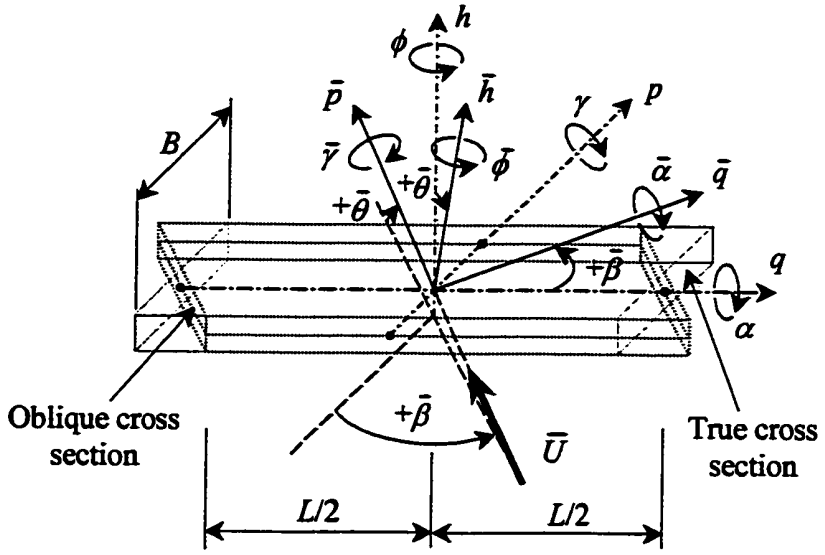

Figure 4-4 Local Mean Wind Coordinate System

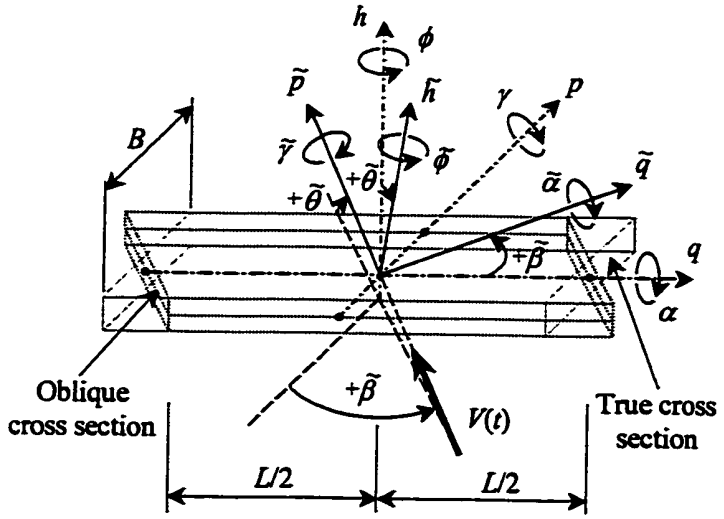

Figure 4-5 Local Instantaneous Wind Coordinate System

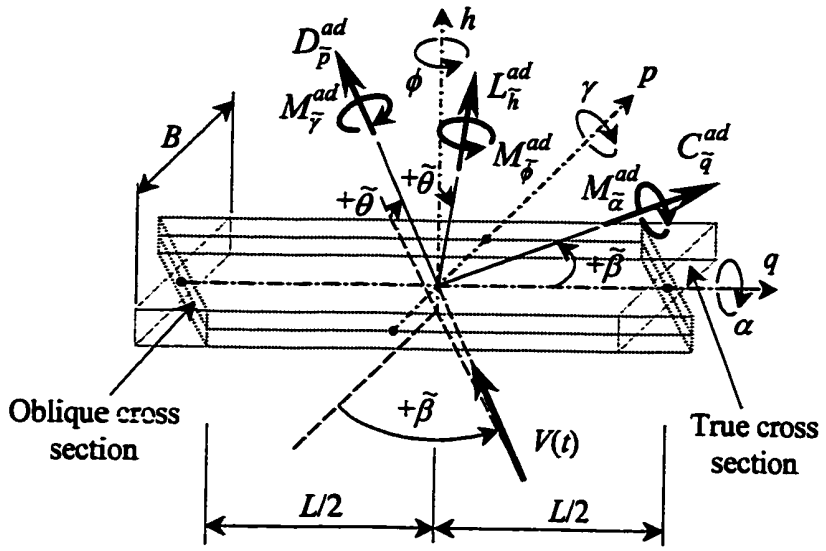

Figure 4-6 Aerodynamic Forces and Moments on Oblique Segment in Local instantaneous Coordinate system

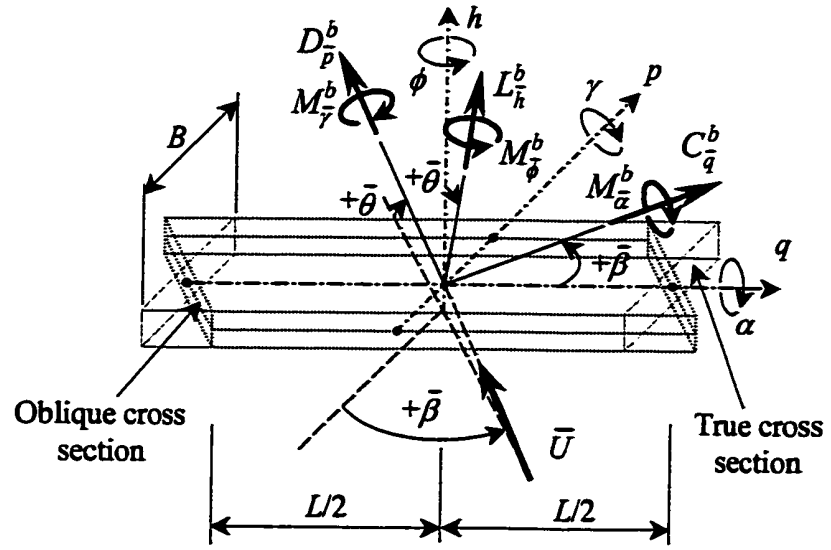

Figure 4-7 Buffeting Forces and Moments on Oblique Segment in Local Mean Wind Coordinate System

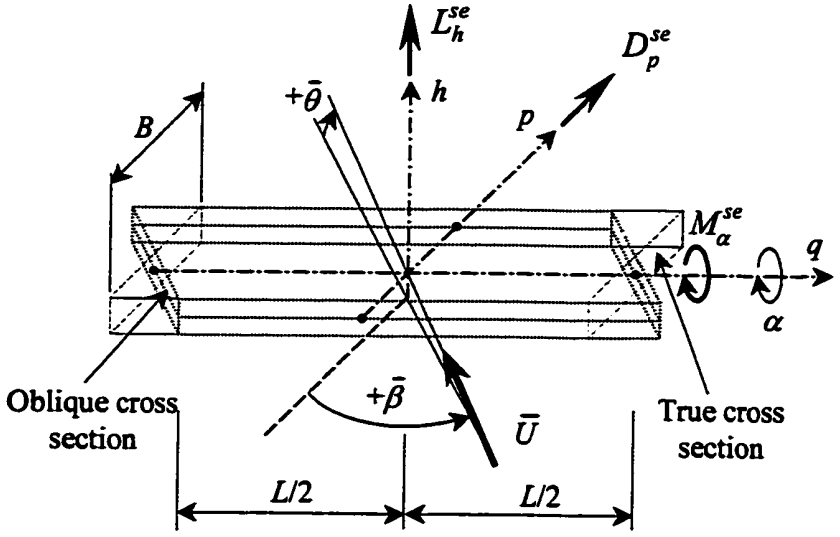

Figure 4-8 Aeroelastic Forces and Moment on Oblique Segment in Local Reference Coordinate System

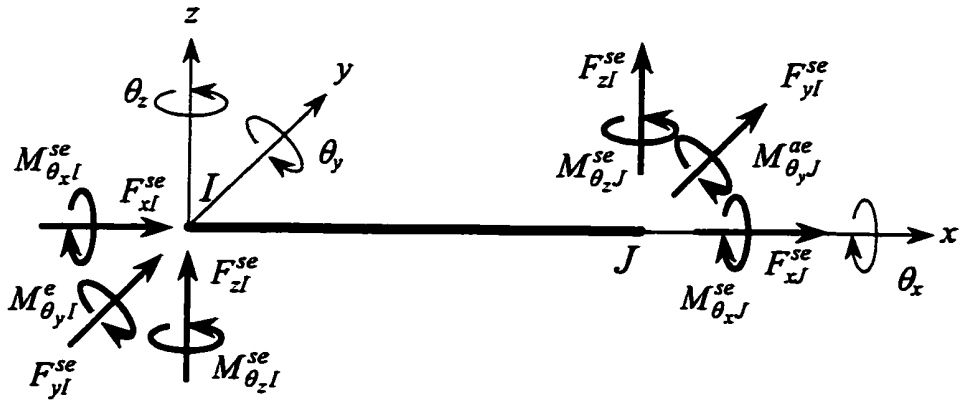

(a) Local structural coordinate system

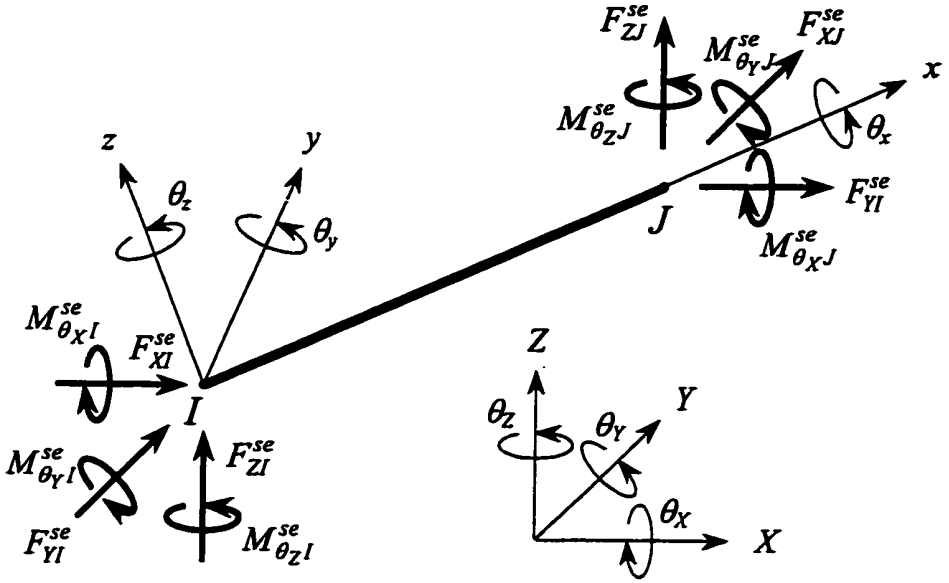

(b) Local structural coordinate system

Figure 4-9 Aeroelastic Forces and Moments at Element Nodes

Chapter 5

IMPLEMENTATION IN COMPUTER PROGRAM

5.1 INTRODUCTION

The new formulation for buffeting analysis of long span cable-supported bridges under skew winds has been derived in Chapter 4. A user-friendly computer program is also developed accordingly. To use the developed computer program to carry out the buffeting analysis of long span bridges under skew winds, a number of input data are required. The major input data include the global and local structural coordinate systems used in the modal analysis of the bridge, the aerodynamic coefficients and flutter derivatives of the bridge deck under skew winds, the aerodynamic coefficients of the bridge towers and cables under skew winds, the aerodynamic admittance functions of the bridge deck and cables, and the cross spectra of wind turbulence.

From a practical point of view, the modal analysis of a long span cable-supported bridge may be performed by engineers using different commercial computer programs with different global and local structural coordinate systems. To make it flexible, the computer program developed in this thesis provides various types of global and local structural coordinate systems to suit for real cases. This will be described in detail in this chapter.

For aerodynamic coefficients and flutter derivatives of a long span bridge under skew winds, Chapter 6 and Chapter 7 develop wind tunnel test techniques for measuring these quantities and provide the measured aerodynamic coefficients and flutter derivatives of the Tsing Ma suspension bridge deck under skew winds for the purpose of comparison and parameter analysis in Chapters 9 and 10. Chapter 8 also performs wind tunnel tests to measure the aerodynamic coefficients of structural members of the Tsing Ma bridge tower under yaw winds. In consideration that the aerodynamic coefficients and flutter derivatives of bridge components under skew winds may not be available for some of bridges. Some empirical and approximate expressions are provided in this chapter and incorporated in the computer program

for references or potential uses. Because of the time limitation in completing this thesis, some empirical formulae for both aerodynamic admittance functions and cross spectra of wind turbulence have to be employed in the buffeting analysis without detailed investigations.

To further enhance the computation efficiency of the modified method for buffeting analysis, the optimisation of position of wind excitation points involved in the cross spectral matrix of wind turbulence is introduced and incorporated in the computer program.

5.2 COMPUTER PROGRAM

5.2.1 Introduction

The computer program is developed in this study using the Fortran 95 language. It consists of a main program, 10 modules and more than 76 external procedures. The flowchart of main structure of the computer program is shown in Figure 5-1, and the flowchart of main structure of the computer algorithm is demonstrated in Figure 5.2. Since the finite element method is applied, the computer program is capable of handling skew winds with varying wind characteristics along major bridge components. These wind characteristics may include mean wind speed, friction velocity and wind spectrum. The effects of inter-modes, multi-modes, spatial modes and the interaction between different bridge components, such as bridge deck, towers and cables can also be taken into consideration. There are eight types of input files in the computer program: the project control file; the basic information file; the aerodynamic coefficient file; the flutter derivative file; the aerodynamic admittance file; the wind data file; the frequency and mode shapes file; and the initial displacement file. To make input files readable, the space line, annotation, and data line are used in addition to data elements. Furthermore, a free format is adopted for inputting the data in the program. However, the type of input data must be consistent with the type of the corresponding variables. For instance, a real number is required for a real variable whilst an integer variable demands an integer number. If the data number of an input element is less than the number of the required data, corresponding zeros will be added automatically at the end of the input element for

non-character data. The computer program can continuously perform a series of buffeting analysis of a given bridge with different parameters or requirements.

5.2.2 Combinations of Global Coordinates Systems

The global structural and wind coordinate systems introduced in Chapter 4 is only one representative. In practice, the global structural coordinate *XYZ*-system used in the modal analysis of a long span bridge by engineers to find the natural frequencies and modal shapes of the bridge may be different from one used in Chapter 4 or it may even follow the left-handed rule other than the right-handed rule. To make the current computer program user-friendly, 16 combinations of the global structural coordinate *XYZ*-system and the global wind coordinate $X_u Y_v Z_w$-system are provided to potential users of the program.

For the first 8 combinations shown in Figures 5-3a to 5-3h, the right-handed rule is adopted for the *XYZ*-system. The corresponding transformation matrices between these two global systems are respectively derived and expressed as follows:

$$\mathbf{T}_{GsGw} = \mathbf{T}_{GwGs}^{\mathrm{T}} = \begin{bmatrix} -\cos\theta_0 \sin\beta_0 & -\cos\beta_0 & \sin\theta_0 \sin\beta_0 \\ \sin\theta_0 & 0 & \cos\theta_0 \\ -\cos\theta_0 \cos\beta_0 & \sin\beta_0 & \sin\theta_0 \cos\beta_0 \end{bmatrix} \tag{5-1a}$$

$$\mathbf{T}_{GsGw} = \mathbf{T}_{GwGs}^{\mathrm{T}} = \begin{bmatrix} \cos\theta_0 \sin\beta_0 & \cos\beta_0 & -\sin\theta_0 \sin\beta_0 \\ \sin\theta_0 & 0 & \cos\theta_0 \\ \cos\theta_0 \cos\beta_0 & -\sin\beta_0 & -\sin\theta_0 \cos\beta_0 \end{bmatrix} \tag{5-1b}$$

$$\mathbf{T}_{GsGw} = \mathbf{T}_{GwGs}^{\mathrm{T}} = \begin{bmatrix} -\cos\theta_0 \sin\beta_0 & -\cos\beta_0 & \sin\theta_0 \sin\beta_0 \\ \cos\theta_0 \cos\beta_0 & -\sin\beta_0 & -\sin\theta_0 \cos\beta_0 \\ \sin\theta_0 & 0 & \cos\theta_0 \end{bmatrix} \tag{5-1c}$$

$$\mathbf{T}_{GsGw} = \mathbf{T}_{GwGs}^{\mathrm{T}} = \begin{bmatrix} \cos\theta_0 \sin\beta_0 & \cos\beta_0 & -\sin\theta_0 \sin\beta_0 \\ -\cos\theta_0 \cos\beta_0 & \sin\beta_0 & \sin\theta_0 \cos\beta_0 \\ \sin\theta_0 & 0 & \cos\theta_0 \end{bmatrix} \tag{5-1d}$$

$$\mathbf{T}_{GsGw} = \mathbf{T}_{GwGs}^{\mathrm{T}} = \begin{bmatrix} -\cos\theta_0 \sin\beta_0 & -\cos\beta_0 & \sin\theta_0 \sin\beta_0 \\ -\sin\theta_0 & 0 & -\cos\theta_0 \\ \cos\theta_0 \cos\beta_0 & -\sin\beta_0 & -\sin\theta_0 \cos\beta_0 \end{bmatrix} \tag{5-1e}$$

$$\mathbf{T}_{GsGw} = \mathbf{T}_{GwGs}^{\mathrm{T}} = \begin{bmatrix} \cos\theta_0 \sin\beta_0 & \cos\beta_0 & -\sin\theta_0 \sin\beta_0 \\ -\sin\theta_0 & 0 & -\cos\theta_0 \\ -\cos\theta_0 \cos\beta_0 & \sin\beta_0 & \sin\theta_0 \cos\beta_0 \end{bmatrix} \tag{5-1f}$$

$$\mathbf{T}_{GsGw} = \mathbf{T}_{GwGs}^{\mathrm{T}} = \begin{bmatrix} -\cos\theta_0 \sin\beta_0 & -\cos\beta_0 & \sin\theta_0 \sin\beta_0 \\ -\cos\theta_0 \cos\beta_0 & \sin\beta_0 & \sin\theta_0 \cos\beta_0 \\ -\sin\theta_0 & 0 & -\cos\theta_0 \end{bmatrix} \tag{5-1g}$$

$$\mathbf{T}_{GsGw} = \mathbf{T}_{GwGs}^{\mathrm{T}} = \begin{bmatrix} \cos\theta_0 \sin\beta_0 & \cos\beta_0 & -\sin\theta_0 \sin\beta_0 \\ \cos\theta_0 \cos\beta_0 & -\sin\beta_0 & -\sin\theta_0 \cos\beta_0 \\ -\sin\theta_0 & 0 & -\cos\theta_0 \end{bmatrix} \tag{5-1h}$$

For the last 8 combinations displayed in Figures 5-3i to 5-3p, the left-handed rule is applied. The transformation matrices for these 8 cases can be obtained based on the first 8 transformation matrices. That is, the left-handed *XYZ*-system is first converted in the program to the right-handed *XZY*-system by changing the sign of the axis *Z* for Types 9, 10, 13 and 14, or the sign of the axis *Y* for Types 11, 12, 15 and 16. The transformation matrices ($\mathbf{T}_{GsGw}$ and $\mathbf{T}_{GwGs}$) of the first 8 combinations can be then used correspondingly for the last 8 combinations. Meanwhile, φ_Z and φ_{θ_Y} are correspondingly multiplied by –1 for Types 9, 10, 13 and 14, and φ_Y and φ_{θ_Z} are correspondingly multiplied by –1 for Types 11, 12, 15 and 16. Here, φ_Z and φ_Y are the mode shape coordinates along the axis *Y* and the axis *Z*, respectively; φ_{θ_Y} and φ_{θ_Z} are the mode shape angular coordinates around the axis *Y* and the axis *Z*, respectively.

5.2.3 Combinations of Local Coordinates Systems

Similarly, the local coordinate *xyz*-system determined by engineers when carrying out the modal analysis of the bridge may be different from one introduced in Chapter 4. Therefore, 8 combinations of the local coordinate *xyz*-system and the local reference coordinate *qph*-system are provided in the computer program, as shown in Figures 5-4a to 4-5h. The corresponding transformation matrices $\mathbf{T}_{LrLs}$ and $\mathbf{T}_{LsLr}$ are listed as follows:

$$\mathbf{T}_{LrLs} = \mathbf{T}_{LsLr}^{\mathrm{T}} = \begin{bmatrix} 1 & 0 & 0 \\ 0 & 0 & -1 \\ 0 & 1 & 0 \end{bmatrix} \tag{5-2a}$$

$$\mathbf{T}_{LrLs} = \mathbf{T}_{LsLr}^{\mathrm{T}} = \begin{bmatrix} 1 & 0 & 0 \\ 0 & 0 & 1 \\ 0 & -1 & 0 \end{bmatrix} \tag{5-2b}$$

$$\mathbf{T}_{LrLs} = \mathbf{T}_{LsLr}^{\mathrm{T}} = \begin{bmatrix} -1 & 0 & 0 \\ 0 & 0 & 1 \\ 0 & 1 & 0 \end{bmatrix} \tag{5-2c}$$

$$\mathbf{T}_{LrLs} = \mathbf{T}_{LsLr}^{\mathrm{T}} = \begin{bmatrix} -1 & 0 & 0 \\ 0 & 0 & -1 \\ 0 & -1 & 0 \end{bmatrix} \tag{5-2d}$$

$$\mathbf{T}_{LrLs} = \mathbf{T}_{LsLr}^{\mathrm{T}} = \begin{bmatrix} 1 & 0 & 0 \\ 0 & 1 & 0 \\ 0 & 0 & 1 \end{bmatrix} \tag{5-2e}$$

$$\mathbf{T}_{LrLs} = \mathbf{T}_{LsLr}^{\mathrm{T}} = \begin{bmatrix} 1 & 0 & 0 \\ 0 & -1 & 0 \\ 0 & 0 & -1 \end{bmatrix} \tag{5-2f}$$

$$\mathbf{T}_{LrLs} = \mathbf{T}_{LsLr}^{\mathrm{T}} = \begin{bmatrix} -1 & 0 & 0 \\ 0 & -1 & 0 \\ 0 & 0 & 1 \end{bmatrix} \tag{5-2g}$$

$$\mathbf{T}_{LrLs} = \mathbf{T}_{LsLr}^{\mathrm{T}} = \begin{bmatrix} -1 & 0 & 0 \\ 0 & 1 & 0 \\ 0 & 0 & -1 \end{bmatrix} \tag{5-2h}$$

5.3 DRAG AND CROSSWIND COEFFICIENTS OF BRIDGE CABLES

Bridge cables and hangers often possess circular cross sections. Therefore, the corresponding aerodynamic coefficients can be determined using those of circular section. The coefficients of drag and crosswind force of a cylinder depend on Reynolds number (*Re*) and its surface roughness (Simiu and Scanlan, 1996; Sachs, 1978). According to Wooton and Scruton (1971), for a long smooth cylinder under normal wind condition, the drag coefficient is about 1.2 in the subcritical region ($Re < 2.0\times10^5$) and then drops sharply in the critical region ($2.0\times10^5 \le Re \le 5.0\times10^5$) up to a value of about 1/3 of its highest. With further increasing *Re*, the drag coefficient increases again in the supercritical region and the transcritical region, but remains much lower than its subcritical values. The main effect of

surface roughness is to move the onset of the critical and supercritical flow around cylinder to a lower Reynolds number leading to a subsequently high drag coefficient in the super-critical range (Güven et al., 1980; Sachs, 1978). Under yaw wind condition, the coefficients $C_{D_{\bar{p}}}(\bar{\beta})$ and $C_{C_{\bar{q}}}(\bar{\beta})$ of drag and crosswind force of a circular cylinder with respect to the local wind coordinate system are provided by Sachs (1978) for yaw angles between 0° to 90°, with an interval of 15° and Reynolds number lower than 3.5×10^5. Here, $\bar{\beta}$ is the local wind yaw angle and $C_{D_{\bar{p}}}(0°)=1.2$ and $C_{C_{\bar{q}}}(0°)=0.0$. These discrete data are plotted in Figure 5-5 with dots and hollow triangles, respectively, for the drag coefficient and the crosswind coefficient. To facilitate the computation, the application of the traditional cosine rule may lead to the following approximate formulae for the coefficients of drag and crosswind force of a circular cylinder as a function of wind yaw angle.

$$C_{D_{\bar{p}}}(\bar{\beta})=C_{D0}\cos^3\bar{\beta} \tag{5-3a}$$

$$C_{C_{\bar{q}}}(\bar{\beta})=C_{D0}\cos^2\bar{\beta}\sin\bar{\beta} \tag{5-3b}$$

where the local wind inclination $\bar{\theta}$ is assumed to be zero; $C_{D0}=C_{D_{\bar{p}}}(0°)$ is the drag coefficient at the zero yaw angle; and the diameter of the true cross section of the cylinder is referred. If C_{D0} is set to 1.2, it is found that Eq.(5-3) fits the discrete data from Sachs (1978) very well for both the coefficients of drag and crosswind force (see Figure 5-5). As a result, the approximate formulae given by Eq.(5-3) are incorporated in the computer program to estimate the coefficients of drag and crosswind force of bridge cables and hangers when lacking measured data. In the computation, the coefficient C_{D0} should be properly adjusted according to the cable surface roughness and the Reynolds number. It is suggested for engineering purposes to set C_{D0}=0.6 for a smooth surface with $Re\geq4.0\times10^5$ and C_{D0}=1.2 for a rough surface with all values of Reynolds number and for a smooth surface with $Re<4.0\times10^5$ (MacDonald, 1975; Xiang et al., 1996).

5.4 FLUTTER DERIVATIVES OF BRIDGE DECK

For a bridge deck under skew wind condition, the flutter derivatives are the functions of local wind yaw angle $\overline{\beta}$ and local wind inclination $\overline{\theta}$. In principle, they should be measured through wind tunnel tests of the bridge deck section model under a series of wind yaw angles and inclinations, as discussed in Chapter 7. However, this may not be feasible for some of the bridges in their preliminary design stage. Thus, this computer program also provides some empirical or approximate formulae for estimating the flutter derivatives of bridge deck under skew winds if the measured data are not available.

5.4.1 Empirical Formulae Based on Scanlan's Skew Wind Theory

A skew wind theory was proposed by Scanlan (1999) for estimating the critical wind speed of a long span bridge under skew winds. It is based on the oblique strip theory and the single DOF torsional flutter theory associated with the flutter derivative A_2^*. The skew wind is considered to cross the oblique cross section in the mean wind direction with an elongated deck width of $B' = B/\cos\overline{\beta}$. When wind yaw angle is not considerably large and the height-to-width ratio of the true cross section is small, the aeroelastic performance of the oblique cross section under skew wind is assumed to be the same as that of the true cross section under normal wind but with the elongated deck width. Base on this assumption, the critical wind speed of the bridge deck under the skew wind can be estimated using the single degree of freedom torsional flutter theory and the flutter derivative $A_2^*(0°,\overline{\theta},K')$ measured under the normal wind condition but with the reduced frequency K replaced by $K' = B'\omega/\overline{U} = K/\cos\overline{\beta}$. An approximate relationship can be also found between the flutter derivative $A_2^*(\overline{\beta},\overline{\theta},K)$ expressed in Eq.(4-78) for skew wind with the reduced frequency K and the flutter derivative $A_2^*(0°,\overline{\theta},K')$ under normal wind condition but with the reduced frequency K'. Though only the formula for estimating $A_2^*(\overline{\beta},\overline{\theta},K)$ was given by Scanlan, the formulae for estimating the other 17 flutter derivatives can also be derived using the same principle as described in the following.

As shown in Figure 5-6, the coordinate $q'p'h'$-system is attained by rotating the local reference qph-system around the axis h with an angle of $\bar{\beta}$. Thus, the axis h' is the same as the axis h and the axis p' is along the oblique cross section, and, both the axis p' and the axis q' are located in the qp-plane. Denote $\delta_p(t)$, $\delta_h(t)$ and $\delta_\alpha(t)$, respectively, the dynamic translation displacements along the axis p and the axis h and the dynamic angular displacement around the axis q of the deck segment. Let $\delta_{p'}(t)$, $\delta_{h'}(t)$ and $\delta_{\alpha'}(t)$, respectively, represent the dynamic translation displacements along the axis p' and the axis h' and the dynamic angular displacement around the axis q'. Then, the following approximate relations can be established.

$$\delta_{p'}(t) \approx \delta_p(t)\cos\bar{\beta} \tag{5-4a}$$

$$\delta_{h'}(t) = \delta_h(t) \tag{5-4b}$$

$$\delta_{\alpha'}(t) \approx \delta_\alpha(t)\cos\bar{\beta} \tag{5-4c}$$

Provided that the aeroelastic performance of the oblique cross section of a bridge deck is the same as that of the true cross section but with the reduced frequency K', the self excited pitching moment around the axis q' ($M^{se}_{\alpha'}$), drag along the axis p' ($D^{se}_{p'}$) and lift along the axis h' ($L^{se}_{h'}$) can then be expressed as follows:

$$M^{se}_{\alpha'} = \frac{1}{2}\rho\bar{U}^2B'^2\left[K'A_1^*(0°,\bar{\theta},K')\frac{\dot{\delta}_{h'}}{\bar{U}} + K'A_2^*(0°,\bar{\theta},K')\frac{B'\dot{\delta}_{\alpha'}}{\bar{U}} + K'^2A_3^*(0°,\bar{\theta},K')\delta_{\alpha'}\right.$$
$$\left. + K'^2A_4^*(0°,\bar{\theta},K')\frac{\delta_{h'}}{B'} + K'A_5^*(0°,\bar{\theta},K')\frac{\dot{\delta}_{p'}}{\bar{U}} + K'^2A_6^*(0°,\bar{\theta},K')\frac{\delta_{p'}}{B'}\right] \tag{5-5a}$$

$$D^{se}_{p'} = \frac{1}{2}\rho\bar{U}^2B'\left[K'P_1^*(0°,\bar{\theta},K')\frac{\dot{\delta}_{p'}}{\bar{U}} + K'P_2^*(0°,\bar{\theta},K)\frac{B'\dot{\delta}_{\alpha'}}{\bar{U}} + K'^2P_3^*(0°,\bar{\theta},K')\delta_{\alpha'}\right.$$
$$\left. + K'^2P_4^*(0°,\bar{\theta},K')\frac{\delta_{p'}}{B'} + K'P_5^*(0°,\bar{\theta},K')\frac{\dot{\delta}_{h'}}{\bar{U}} + K'^2P_6^*(0°,\bar{\theta},K')\frac{\delta_{h'}}{B'}\right] \tag{5-5b}$$

$$L^{se}_{h'} = \frac{1}{2}\rho\bar{U}^2B'\left[K'H_1^*(0°,\bar{\theta},K)\frac{\dot{\delta}_{h'}}{\bar{U}} + K'H_2^*(0°,\bar{\theta},K')\frac{B'\delta_{\alpha'}}{\bar{U}} + K'^2H_3^*(0°,\bar{\theta},K')\delta_{\alpha'}\right.$$
$$\left. + K'^2H_4^*(0°,\bar{\theta},K')\frac{\delta_{h'}}{B'} + K'H_5^*(0°,\bar{\theta},K')\frac{\dot{\delta}_{p'}}{\bar{U}} + K'^2H_6^*(0°,\bar{\theta},K')\frac{\delta_{p'}}{B'}\right] \tag{5-5c}$$

Substituting Eq.(5-4) into Eq.(5-5) and considering the following approximate relations

$$D_p^{se} \approx D_{p'}^{se} \cos\bar{\beta} \tag{5-6a}$$

$$L_h^{se} = L_{h'}^{se} \tag{5-6b}$$

$$M_\alpha^{se} \approx M_{\alpha'}^{se} \cos\bar{\beta} \tag{5-6c}$$

and comparing to the self-excited pitching moment, drag and lift expressed by Eq.(4-78), one can then establish the following approximate relations for estimating the flutter derivatives under yaw wind condition using those measured under normal wind condition.

$$P_1^*(\bar{\beta},\bar{\theta},K) \approx P_1^*(0,\bar{\theta},K') \tag{5-7a}$$

$$P_2^*(\bar{\beta},\bar{\theta},K) \approx P_2^*(0,\bar{\theta},K')/\cos\bar{\beta} \tag{5-7b}$$

$$P_3^*(\bar{\beta},\bar{\theta},K) \approx P_3^*(0,\bar{\theta},K')/\cos\bar{\beta} \tag{5-7c}$$

$$P_4^*(\bar{\beta},\bar{\theta},K) \approx P_4^*(0,\bar{\theta},K') \tag{5-7d}$$

$$P_5^*(\bar{\beta},\bar{\theta},K) \approx P_5^*(0,\bar{\theta},K')/\cos\bar{\beta} \tag{5-7e}$$

$$P_6^*(\bar{\beta},\bar{\theta},K) \approx P_6^*(0,\bar{\theta},K')/\cos\bar{\beta} \tag{5-7f}$$

$$H_1^*(\bar{\beta},\bar{\theta},K) \approx H_1^*(0,\bar{\theta},K')/\cos^2\bar{\beta} \tag{5-7g}$$

$$H_2^*(\bar{\beta},\bar{\theta},K) \approx H_2^*(0,\bar{\theta},K')/\cos^2\bar{\beta} \tag{5-7h}$$

$$H_3^*(\bar{\beta},\bar{\theta},K) \approx H_3^*(0,\bar{\theta},K')/\cos^2\bar{\beta} \tag{5-7i}$$

$$H_4^*(\bar{\beta},\bar{\theta},K) \approx H_4^*(0,\bar{\theta},K')/\cos^2\bar{\beta} \tag{5-7j}$$

$$H_5^*(\bar{\beta},\bar{\theta},K) \approx H_5^*(0,\bar{\theta},K')/\cos\bar{\beta} \tag{5-7k}$$

$$H_6^*(\bar{\beta},\bar{\theta},K) \approx H_6^*(0,\bar{\theta},K')/\cos\bar{\beta} \tag{5-7l}$$

$$A_1^*(\bar{\beta},\bar{\theta},K) \approx A_1^*(0,\bar{\theta},K')/\cos^2\bar{\beta} \tag{5-7m}$$

$$A_2^*(\bar{\beta},\bar{\theta},K) \approx A_2^*(0,\bar{\theta},K')/\cos^2\bar{\beta} \tag{5-7n}$$

$$A_3^*(\bar{\beta},\bar{\theta},K) \approx A_3^*(0,\bar{\theta},K')/\cos^2\bar{\beta} \tag{5-7o}$$

$$A_4^*(\bar{\beta},\bar{\theta},K) \approx A_4^*(0,\bar{\theta},K')/\cos^2\bar{\beta} \tag{5-7p}$$

$$A_5^*(\bar{\beta},\bar{\theta},K) \approx A_5^*(0,\bar{\theta},K')/\cos\bar{\beta} \tag{5-7q}$$

$$A_6^*(\bar{\beta},\bar{\theta},K) \approx A_6^*(0,\bar{\theta},K')/\cos\bar{\beta} \tag{5-7r}$$

5.4.2 Empirical Formulae Based on Flat Plate Theory

The earlier aeroelastic instability analysis of a bridge is based on the Theodorsen's flat plate theory developed for the flutter analysis of aircraft wings. The Thoedorsen's flat plate theory may be applied to a bridge deck with flat streamline cross section. As reviewed in Chapter 2, by using potential flow theory Theodorsen (1935) presented the explicit expressions for the self-excited lift and pitching moment of a 2 DOFs flat plate section under normal wind condition and zero wind inclination (see Eq.(2-2)). By combining the Theodorsen's expressions with the Scanlan's skew wind theory, this computer program provides a set of formulae for estimating the flutter derivatives of a bridge deck of streamline cross section and high width-to-height ratio under yaw wind condition without requiring wind tunnel tests of bridge deck section model.

Assume that the deck motions are harmonic and then compare the Scanlan's expressions of Eq.(2-4) with the Theodorsen's expressions of Eq.(2-2), one may find that the Scanlan's flutter derivatives for the flat plate under normal wind condition, $H_i^*(0°,0°,K)$, $A_i^*(0°,0°,K)$ (i=1,2,3,4) can be expressed in terms of the Theodorsen circulation function. Furthermore, by using Eq.(5-7), the flutter derivatives under yaw wind condition, $H_i^*(\bar{\beta},0°,K)$ and $A_i^*(\bar{\beta},0°,K)$ can be found as

$$H_1^*(\bar{\beta},0°,K) = -2\pi F(0.5K')/[K'\cos^2\bar{\beta}] \tag{5-8a}$$

$$H_2^*(\bar{\beta},0°,K) = -0.5\pi[K'+F(0.5K')K'+4G(0.5K')]/[K'\cos\bar{\beta}]^2 \tag{5-8b}$$

$$H_3^*(\bar{\beta},0°,K) = 0.5\pi[G(0.5K')K'-4F(0.5K')]/[K'\cos\bar{\beta}]^2 \tag{5-8c}$$

$$H_4^*(\bar{\beta},0°,K) = 0.5\pi[K'+4G(0.5K')]/[K'\cos^2\bar{\beta}] \tag{5-8d}$$

$$A_1^*(\bar{\beta},0°,K) = 0.5\pi F(0.5K')/[K'\cos^2\bar{\beta}] \tag{5-8e}$$

$$A_2^*(\bar{\beta},0°,K) = -0.125\pi[K'-F(0.5K')K'-4G(0.5K')]/[K'\cos\bar{\beta}]^2 \tag{5-8f}$$

$$A_3^*(\bar{\beta},0°,K) = 0.125\pi[0.125K'^2-G(0.5K')K'+4F(0.5K')]/[K'\cos\bar{\beta}]^2 \tag{5-8g}$$

$$A_4^*(\bar{\beta},0°,K) = -0.5\pi G(0.5K')/[K'\cos^2\bar{\beta}] \tag{5-8h}$$

where $F(k)$ and $G(k)$ are, respectively, the real part and the imaginary part of the Theodorsen's circulation function defined by Eq.(2-3) and they are expressed in terms of the first and second types of Bessel functions. To simplify the calculation of

the Theodorsen circulation function, efforts have been made by various investigators. It is known that the self-excited lift acting on the flat plate airfoil can be expressed in the time domain by the so-called Wagner function (Scanlan, 1993b). Thus, the Theodorsen circular function can be related to the Wagner function via the Fourier transform. The Wagner function may be replaced by the following approximation (Scanlan and Tomko, 1971).

$$\phi(s) = 1 - ae^{-b's} - ce^{-ds} \tag{5-9}$$

The Theodorsen circulation function can be thus approximated as

$$F(k) = 1 - a - c + \frac{ab'(b' - \xi k)}{(b' - \xi k)^2 + k^2} + \frac{cd(d - \xi k)}{(d - \xi k)^2 + k^2} \tag{5-10a}$$

$$G(k) = -\frac{ab'k}{(b' - \xi k)^2 + k^2} - \frac{cdk}{(d - \xi k)^2 + k^2} \tag{5-10b}$$

in which, $s = \overline{U}t/b$; $k = b\omega/\overline{U}$; ξ is the damping ratio; and the coefficients a, b', c, d are taken as 0.165, 0.0455, 0.335 and 0.300, respectively, by Jones, R.T.(1940), and as 0.165, 0.041, 0.335 and 0.320, respectively, by Jones, W.P., (1945). Furthermore, the effects of damping ratio on the values of $F(k)$ and $G(k)$ are negligibly small for a common range of damping ratio (Scanlan and Tomko, 1971). As a result, Eq.(5-10) can be further simplified into

$$F(k) = 1 - \frac{a}{1 + (b'/k)^2} + \frac{c}{1 + (d/k)^2} \tag{5-11a}$$

$$G(k) = -\frac{ab'/k}{1 + (b'/k)^2} - \frac{cd/k}{1 + (d/k)^2} \tag{5-11b}$$

5.4.3 Empirical Formulae Based on Quasi-steady Theory

The aeroelastic forces on a bluff body can also be estimated using the traditional quasi-steady theory but considering the changes of the instantaneous wind velocity and direction relative to the bridge deck caused by the motion of the bridge deck. In this connection, define the equivalent velocity fluctuations $\tilde{u}(t)$, $\tilde{v}(t)$ and $\tilde{w}(t)$ caused by the velocities of deck motion, and the additional increments of the local wind inclination ($\Delta\tilde{\theta}$) and yaw ($\Delta\beta$) caused by the deck rotation as

$$(\tilde{u}, \tilde{v}, \tilde{w})^{\mathrm{T}} = -(\dot{\delta}_{X_u}, \dot{\delta}_{Y_v}, \dot{\delta}_{Z_w})^{\mathrm{T}} = -\mathbf{T}_{GwLr}(\dot{\delta}_q, \dot{\delta}_p, \dot{\delta}_h)^{\mathrm{T}} \tag{5-12a}$$

$$(\Delta\tilde{\theta}, \Delta\tilde{\beta})^{\mathrm{T}} = -(\delta_{\tilde{\alpha}}, \delta_{\phi})^{\mathrm{T}} \tag{5-12b}$$

where $\dot{\delta}_{X_u}(t)$, $\dot{\delta}_{Y_v}(t)$ and $\dot{\delta}_{Z_w}(t)$ are, respectively, the velocities of deck motion along the three axes of the global wind coordinate $X_uY_vZ_w$-system; $\dot{\delta}_q(t)$, $\dot{\delta}_p(t)$ and $\dot{\delta}_h(t)$ are, respectively, the velocities of deck motion along the three axes of the local reference coordinate *qph*-system; $\delta_{\bar{\alpha}}$ and δ_{ϕ} are, respectively, the angular displacements of deck motion around the axis $\bar{q}$ of the local wind coordinate $\bar{q}\bar{p}\bar{h}$-system and the axis *h* of the local reference coordinate *qph*-system. $\mathbf{T}_{GwLr}$ is the 3×3 transformation matrix from the *qph*-system to the $X_uY_vZ_w$-system, given by Eqs.(4-22) and (4-23). Then, replacing $u(t)$, $v(t)$ and $w(t)$ in Eq. (4-54) with the equivalent velocity fluctuations $\tilde{u}(t)$, $\tilde{v}(t)$ and $\tilde{w}(t)$ and following the same procedure for deriving the buffeting forces in Chapter 4, one may find the quasi-steady self-excited forces with respect to the local mean wind coordinate $\bar{q}\bar{p}\bar{h}$-system as:

$$\begin{aligned}
\bar{\mathbf{f}}^{se}(t) &= \left(C_{\bar{q}}^{se}(t), D_{\bar{p}}^{se}(t), L_{\bar{h}}^{se}(t), M_{\bar{\alpha}}^{se}(t), M_{\bar{\gamma}}^{se}(t), M_{\bar{\phi}}^{se}(t)\right)^{\mathrm{T}} \\
&\approx -\bar{\mathbf{A}}^{se}\left(\tilde{u},\tilde{v},\tilde{w}\right)^{\mathrm{T}} - \frac{\rho\bar{U}^2}{2}\mathbf{B}\left[\bar{\mathbf{C}}'^{\theta},\bar{\mathbf{C}}'^{\beta}\right]\left(\Delta\tilde{\theta},\Delta\tilde{\beta}\right)^{\mathrm{T}} \\
&\approx -\bar{\mathbf{A}}^{se}\left(\dot{\delta}_{X_u},\dot{\delta}_{Y_v},\dot{\delta}_{Z_w}\right)^{\mathrm{T}} - \frac{\rho\bar{U}^2}{2}\mathbf{B}\left[\bar{\mathbf{C}}'^{\theta},\bar{\mathbf{C}}'^{\beta}\right]\left(\delta_{\bar{\alpha}},\delta_{\phi}\right)^{\mathrm{T}} \\
&= -\bar{\mathbf{A}}^{se}\,\mathbf{T}_{GwLr}\left(\dot{\delta}_q,\dot{\delta}_p,\dot{\delta}_h\right)^{\mathrm{T}} - \frac{\rho\bar{U}^2}{2}\mathbf{B}\left[\bar{\mathbf{C}}'^{\theta},\bar{\mathbf{C}}'^{\beta}\right]\begin{bmatrix}\cos\bar{\beta} & \sin\bar{\beta} & 0\\ 0 & 0 & 1\end{bmatrix}\left(\delta_{\alpha},\delta_{\gamma},\delta_{\phi}\right)^{\mathrm{T}} \quad (5\text{-}13)
\end{aligned}$$

where, $\bar{\mathbf{A}}^{se}$ is determined by Eq.(4-55), with all the aerodynamic admittance functions being unit; and the matrix **B** and the two coefficient vectors $\bar{\mathbf{C}}'^{\beta}$ and $\bar{\mathbf{C}}'^{\theta}$ are given by Eqs.(4-45), (4-47b) and (4-47c), respectively. The first term in the right hand of Eq.(5-13) is due to change of the instantaneous wind speed and direction relative to the bridge deck caused by the velocities of the deck motion and reflects the aerodynamic damping. The second term in the right hand of Eq.(5-13) is due to the change of the instantaneous wind direction relative to the bridge deck caused by the deck rotation and represents the aerodynamic stiffness. The quasi-steady self-excited forces with respect to the local reference coordinate *qph*-system can be obtained by the transformation.

$$\begin{aligned}
\mathbf{f}_r^{se}(t) &= \left(C_q^{se}(t), D_p^{se}(t), L_h^{se}(t), M_{\alpha}^{se}(t), M_{\gamma}^{se}(t), M_{\phi}^{se}(t)\right)^{\mathrm{T}} \\
&= \mathbf{A}_D\left(\dot{\delta}_q,\dot{\delta}_p,\dot{\delta}_h\right)^{\mathrm{T}} + \mathbf{A}_S\left(\delta_{\alpha},\delta_{\gamma},\delta_{\phi}\right)^{\mathrm{T}} \quad (5\text{-}14)
\end{aligned}$$

where

$$\mathbf{A}_D = -\overline{\mathbf{T}}_{LrL\overline{w}}\overline{\mathbf{A}}^{se}\,\mathbf{T}_{GwLr} \tag{5-15a}$$

$$\mathbf{A}_S = -\frac{\rho\overline{U}^2}{2}\overline{\mathbf{T}}_{LrL\overline{w}}\mathbf{B}\left[\overline{\mathbf{C}}^{'\theta},\overline{\mathbf{C}}^{'\beta}\right]\begin{bmatrix}\cos\overline{\beta} & \sin\overline{\beta} & 0\\ 0 & 0 & 1\end{bmatrix} \tag{5-15b}$$

in which $\overline{\mathbf{T}}_{LrL\overline{w}}$ is the 6×6 transformation matrix from the $\overline{qph}$-system to the *qph*-system, given by Eq.(4-26b).

By comparing Eq.(5-14) with Eq.(4-78), the quasi-steady expressions of some of the flutter derivatives, P_i^*, H_i^* and A_i^*, (i=1,3,5), can then be obtained.

$$\begin{aligned}P_1^*(\overline{\beta},\overline{\theta},K) = -\frac{1}{K}\Big\{&[(2\cos^2\overline{\theta}-1)\sin\overline{\beta}\cos\overline{\beta}/\cos\overline{\theta}\,]C_{C_{\overline{q}}}(\overline{\beta},\overline{\theta})\\ &+[1+\cos^2\overline{\beta}\cos^2\overline{\theta}\,]C_{D_{\overline{p}}}(\overline{\beta},\overline{\theta})\\ &-[(\sin^2\overline{\beta}+\cos^2\overline{\beta}\cos^2\overline{\theta})\tan\overline{\theta}\,]C_{L_{\overline{h}}}(\overline{\beta},\overline{\theta})\\ &-[\sin^2\overline{\beta}/\cos\overline{\theta}\,]C'^{\beta}_{C_{\overline{q}}}(\overline{\beta},\overline{\theta})-[\sin\overline{\beta}\cos\overline{\beta}\sin\overline{\theta}\,]C'^{\theta}_{C_{\overline{q}}}(\overline{\beta},\overline{\theta})\\ &-[\sin\overline{\beta}\cos\overline{\beta}\,]C'^{\beta}_{D_{\overline{p}}}(\overline{\beta},\overline{\theta})-[\cos^2\overline{\beta}\sin\overline{\theta}\cos\overline{\theta}\,]C'^{\theta}_{D_{\overline{p}}}(\overline{\beta},\overline{\theta})\\ &+[\sin\overline{\beta}\cos\overline{\beta}\tan\overline{\theta}\,]C'^{\beta}_{L_{\overline{h}}}(\overline{\beta},\overline{\theta})+[\cos^2\overline{\beta}\sin^2\overline{\theta}\,]C'^{\theta}_{L_{\overline{h}}}(\overline{\beta},\overline{\theta})\Big\}\end{aligned} \tag{5-16a}$$

$$\begin{aligned}P_3^*(\overline{\beta},\overline{\theta},K) = -\frac{1}{K^2}\Big\{&[\sin\overline{\beta}\cos\overline{\beta}\,]C'^{\theta}_{C_{\overline{q}}}(\overline{\beta},\overline{\theta})+[\cos^2\overline{\beta}\cos\overline{\theta}\,]C'^{\theta}_{D_{\overline{p}}}(\overline{\beta},\overline{\theta})\\ &-[\cos^2\overline{\beta}\sin\overline{\theta}\,]C'^{\theta}_{L_{\overline{h}}}(\overline{\beta},\overline{\theta})\Big\}\end{aligned} \tag{5-16b}$$

$$\begin{aligned}P_5^*(\overline{\beta},\overline{\theta},K) = -\frac{1}{K}\Big\{&[2\sin\overline{\beta}\sin\overline{\theta}\,]C_{C_{\overline{q}}}(\overline{\beta},\overline{\theta})+[\cos\overline{\beta}\sin\overline{\theta}\cos\overline{\theta}\,]C_{D_{\overline{p}}}(\overline{\beta},\overline{\theta})\\ &-[(2-\cos^2\overline{\theta})\cos\overline{\beta}\,]C_{L_{\overline{h}}}(\overline{\beta},\overline{\theta})+[\sin\overline{\beta}\cos\overline{\beta}\,]C'^{\theta}_{C_{\overline{q}}}(\overline{\beta},\overline{\theta})\\ &+[\cos\overline{\beta}\cos^2\overline{\theta}\,]C'^{\theta}_{D_{\overline{p}}}(\overline{\beta},\overline{\theta})-[\cos\overline{\beta}\sin\overline{\theta}\cos\overline{\theta}\,]C'^{\theta}_{L_{\overline{h}}}(\overline{\beta},\overline{\theta})\Big\}\end{aligned} \tag{5-16c}$$

$$\begin{aligned}H_1^*(\overline{\beta},\overline{\theta},K) = -\frac{1}{K}\Big\{&[2-\cos^2\overline{\theta}\,]C_{D_{\overline{p}}}(\overline{\beta},\overline{\theta})+\cos^2\overline{\theta}\,C'^{\theta}_{L_{\overline{h}}}(\overline{\beta},\overline{\theta})\\ &+[\sin\overline{\theta}\cos\overline{\theta}\,][C_{L_{\overline{h}}}(\overline{\beta},\overline{\theta})+C'^{\theta}_{D_{\overline{p}}}(\overline{\beta},\overline{\theta})]\Big\}\end{aligned} \tag{5-16d}$$

$$H_3^*(\overline{\beta},\overline{\theta},K) = -\frac{1}{K^2}\Big\{[\cos\overline{\beta}\sin\overline{\theta}\,]C'^{\theta}_{D_{\overline{p}}}(\overline{\beta},\overline{\theta})+[\cos\overline{\beta}\cos\overline{\theta}\,]C'^{\theta}_{L_{\overline{h}}}(\overline{\beta},\overline{\theta})\Big\} \tag{5-16e}$$

$$H_5^*(\overline{\beta},\overline{\theta},K) = -\frac{1}{K}\Big\{[\cos\overline{\beta}\sin\overline{\theta}\cos\overline{\theta}\,]C_{D_{\overline{p}}}(\overline{\beta},\overline{\theta})$$

$$+[\cos\bar{\beta}(1+\cos^2\bar{\theta})]C_{L_{\bar{h}}}(\bar{\beta},\bar{\theta})$$

$$-[\sin\bar{\beta}\tan\bar{\theta}]C'^{\beta}_{D_{\bar{p}}}-[\cos\bar{\beta}\sin^2\bar{\theta}]C'^{\theta}_{D_{\bar{p}}}$$

$$-[\sin\bar{\beta}]C'^{\beta}_{L_{\bar{h}}}(\bar{\beta},\bar{\theta})-[\cos\bar{\beta}\sin\bar{\theta}\cos\bar{\theta}]C'^{\theta}_{L_{\bar{h}}}(\bar{\beta},\bar{\theta})\Big\} \qquad (5\text{-}16f)$$

$$A_1^*(\bar{\beta},\bar{\theta},K)=-\frac{1}{K}\Big\{[2\cos\bar{\beta}\sin\bar{\theta}]C_{M_{\bar{\alpha}}}(\bar{\beta},\bar{\theta})-[\sin\bar{\beta}\sin\bar{\theta}\cos\bar{\theta}]C_{M_{\bar{\gamma}}}(\bar{\beta},\bar{\theta})$$

$$+[(2-\cos^2\bar{\theta})\sin\bar{\beta}]C_{M_{\bar{\phi}}}(\bar{\beta},\bar{\theta})+[\cos\bar{\beta}\cos\bar{\theta}]C'^{\theta}_{M_{\bar{\alpha}}}$$

$$-[\sin\bar{\beta}\cos^2\bar{\theta}]C'^{\theta}_{M_{\bar{\gamma}}}(\bar{\beta},\bar{\theta})+[\sin\bar{\beta}\sin\bar{\theta}\cos\bar{\theta}]C'^{\theta}_{M_{\bar{\phi}}}(\bar{\beta},\bar{\theta})\Big\} \qquad (5\text{-}16g)$$

$$A_3^*(\bar{\beta},\bar{\theta},K)=-\frac{1}{K^2}\Big\{[\cos^2\bar{\beta}]C'^{\theta}_{M_{\bar{\alpha}}}(\bar{\beta},\bar{\theta})-[\sin\bar{\beta}\cos\bar{\beta}\cos\bar{\theta}]C'^{\theta}_{M_{\bar{\gamma}}}(\bar{\beta},\bar{\theta})$$

$$+[\sin\bar{\beta}\cos\bar{\beta}\sin\bar{\theta}]C'^{\theta}_{M_{\bar{\phi}}}(\bar{\beta},\bar{\theta})\Big\} \qquad (5\text{-}16h)$$

$$A_5^*(\bar{\beta},\bar{\theta},K)=-\frac{1}{K}\Big\{[(\sin^2\bar{\beta}+2\cos^2\bar{\beta}\cos^2\bar{\theta})/\cos\bar{\theta}]C_{M_{\bar{\alpha}}}(\bar{\beta},\bar{\theta})$$

$$-[\sin\bar{\beta}\cos\bar{\beta}\cos^2\bar{\theta}]C_{M_{\bar{\gamma}}}(\bar{\beta},\bar{\theta})-[\sin\bar{\beta}\cos\bar{\beta}\sin^2\bar{\theta}\tan\bar{\theta}]C_{M_{\bar{\phi}}}(\bar{\beta},\bar{\theta})$$

$$-[\sin\bar{\beta}\cos\bar{\beta}/\cos\bar{\theta}]C'^{\beta}_{M_{\bar{\alpha}}}(\bar{\beta},\bar{\theta})-[\cos^2\bar{\beta}\sin\bar{\theta}]C'^{\theta}_{M_{\bar{\alpha}}}(\bar{\beta},\bar{\theta})$$

$$+[\sin^2\bar{\beta}]C'^{\beta}_{M_{\bar{\gamma}}}(\bar{\beta},\bar{\theta})+[\sin\bar{\beta}\cos\bar{\beta}\sin\bar{\theta}\cos\bar{\theta}]C'^{\theta}_{M_{\bar{\gamma}}}(\bar{\beta},\bar{\theta})$$

$$-[\sin^2\bar{\beta}\tan\bar{\theta}]C'^{\beta}_{M_{\bar{\phi}}}(\bar{\beta},\bar{\theta})-[\sin\bar{\beta}\cos\bar{\beta}\sin^2\bar{\theta}]C'^{\theta}_{M_{\bar{\phi}}}(\bar{\beta},\bar{\theta})\Big\} \qquad (5\text{-}16i)$$

The above formulae are also implemented into the computer program for an alternative if only the aerodynamic coefficients are available.

5.5 AERODYNAMIC ADMITTANCE FUNCTIONS

As noted previously, the quasi-steady theory used in the formulation of buffeting forces is applicable only to the turbulence components with turbulence wavelength, $\bar{U}/n$, being larger than ten times the representative width of the bridge component. The buffeting forces caused by the turbulence with small wavelength (high frequency) are frequency-dependent and cannot be taken into account properly using quasi-steady theory because fluctuating wind velocity is not spatial uniform and not fully correlated along cross sections of a bridge deck. Furthermore, the structure-induced signature turbulence may play an important role on buffeting forces,

particularly in the case of bluff sections (Singh, 1997; Jones and Scanlan, 1998). Thus, as a conventional approach (Davenport 1962a,1962b), the formulation of buffeting forces on long span bridges in Chapter 4 involves the aerodynamic admittance functions which account for the effects of turbulence unsteadiness and the chordwise partial turbulence correlation due to the high-frequency turbulence components. Actually, the aerodynamic admittances essentially measure the ratios of the aerodynamic forces in fluctuating flows to their quasi-static values which is commonly given by wind tunnel test in smooth flow for a bridge component (Davenport 1962b). Such ratios are functions of turbulence frequency or wavelength and wind direction.

The determination of aerodynamic admittance of a bluff section is a complicated and challenging problem. Although some wind tunnel test approaches have been proposed for measuring the aerodynamic admittance as the function of reduced frequency or wavelength (Walshe and Wyatt, 1983; Xie et al., 1989; Sarkar, 1992; Kawatai and Kim, 1992; Larose et al., 1997; Singh, 1997; Zhang, 1998), many issues still remain unsolved, in particular for the simulation of turbulence scales. Furthermore, rare measurement of aerodynamic admittance functions involved skew wind and oblique section of bridge deck. Therefore, some empirical expressions for aerodynamic admittance functions used in practice and introduced in this section have to be employed in this study and implemented in the computer program without further detailed investigation. However, it is still desirable to have a detailed investigation in the future to see how the aerodynamic admittance functions vary with local wind yaw angle and inclination as well as reduced frequency.

The concept of aerodynamic admittance was first introduced by Sears (1941) and Liepmann (1952) when studying the buffeting problem of thin airfoils due to the vertical component of wind turbulence w. Provided that the changing rate of the velocity following the particle is small compared with the changing rate of the velocity at a fixed location, it may be assumed that the turbulence pattern around an airfoil does not change appreciably during a time of the order $B/\overline{U}$ and that the turbulence $w(x,t)$ depends upon $t-x/\overline{U}$ only. Here, x is the coordinate along the chord of the airfoil. Considering the distributed harmonic vertical velocity fluctuation of the form

$$w(x,t) = w_0\, e^{i\omega(t-x/\overline{U})} \tag{5-17}$$

Sears found the following expression for the unsteady lift coefficient:

$$C_L(t) = 2\pi\left(w_0/\overline{U}\right)e^{i\omega t}\chi(k) \tag{5-18}$$

where $k = \pi nB/\overline{U}$ is essentially the ratio of chord width of the airfoil to wave length of the turbulence; $\chi(k)$ is the complex function called admittance function relating to wind turbulence for unsteady lift. The admittance function given by Sears is of the form

$$\chi(k) = \frac{J_0(k)K_1(ik) + iJ_1(k)K_0(ik)}{K_1(ik) + K_0(ik)} \tag{5-19}$$

where J_i is the first type Bessel function of order i (i=0,1); K_i is the modified second type Bessel function of order i (i=0,1). It is quite time consuming to calculate the admittance function according to Eq. (5-19). When only $|\chi|^2$ is needed, the above Sears function may be well approximated by the following expression suggested by Liepmann (1952).

$$\left|\chi(nB/\overline{U})\right|^2 \approx 1/[1 + 2\pi^2(nB/\overline{U})] \tag{5-20}$$

However, when carrying out a coupled buffeting analysis the admittance function χ is required other than its module $|\chi|^2$ (see Eqs.(4-55)). Thus, to facilitate the calculation of the Sears function, the two simplified expressions are suggested in this thesis for approximating the real part (χ_r) and imaginary part (χ_i) of the Sears function.

$$\chi_r(nB/\overline{U}) = \left(1 + 0.3448\, e^{-7.5nB/\overline{U}}\right)\cos\left[\pi\left(\frac{nB}{\overline{U}} - 0.2331\right)\right]\Big/\sqrt{1 + 2\pi^2\frac{nB}{\overline{U}}} \tag{5-21a}$$

$$\chi_i(nB/\overline{U}) = \left(\frac{nB}{\overline{U}}\right)^{0.39}\sin\left[\pi\left(\frac{nB}{\overline{U}} - 0.2331\right)\right]\Big/\sqrt{1 + 2\pi^2\left(\frac{nB}{\overline{U}}\right)^{1.78}} \tag{5-21b}$$

It is seen that the conditions of $\chi_r(0) = 1.0$ and $\chi_i(0) = 0.0$ are satisfied by Eq. (5-21) and $\chi_r(\infty) = \chi_i(\infty) = 0.0$. The above two expressions are plotted in Fig.5-7 as a function of reduced frequency and compared with the original Sears functions. It is found that the proposed simplified expressions fit the original Sears function quite well for both the real and imaginary parts, particularly in the higher frequency region. Figure 5-8 shows the modules of both the proposed simplified expression and

the original Sears function. It is seen again that they match each other quite well. Furthermore, it is seen from Fig. (5-8) that the proposed expressions are better than the Liepmann's approximate expression for the module of Sears function.

The Sears function is often used as the aerodynamic admittance function to correct the quasi-steady lift and sometimes to correct the pitching moment on bridge deck. For the drag on bridge deck, Davenport suggested the following expression as the admittance function to account for the total cross correlation over an effective flow area, which is supposed to be equal to the cross-sectional area of deck (Davenport, 1962b).

$$\chi(nH/\overline{U}) = \sqrt{2\left(c\frac{nH}{\overline{U}} - 1 + e^{-c\frac{nH}{\overline{U}}}\right)} \Big/ \left(c\frac{nH}{\overline{U}}\right) \tag{5-22}$$

where H is the height of bridge deck; and c=7. The Davenport expression, Eq. (5-22), was modified by Irwin (1977b) as

$$\chi(nB/\overline{U}) = \frac{2}{\eta_1\eta_3}\sqrt{\left(\eta_1 - 1 + e^{-\eta_1}\right)\left(\eta_3 - 1 + e^{-\eta_3}\right)} \tag{5-23a}$$

$$\eta_i = 0.95(B/L_i)\sqrt{1 + 70.78(nL_i/\overline{U})^2} \tag{5-23b}$$

where $L_1/B = 0.154$ and $L_3/B = 0.331$. This expression was used by Irwin in the buffeting analysis of Lion's Gate Bridge for not only the drag but also the lift and pitching moment of the bridge deck.

For the drag on circular cross sections, such as cable section, Vickery (1966) suggested the following admittance function.

$$\chi(nD/\overline{U}) = 1/\sqrt{1 + 4nD/\overline{U}} \tag{5-24}$$

where D is the diameter of cable cross section. Furthermore, Vickery (1965) suggested another expression of aerodynamic admittance for the drag on a flat plate, a disc or a prism normal to wind flow.

$$\chi(nD/\overline{U}) = 1/\sqrt{1 + (2nD/\overline{U})^{4/3}} \tag{5-25}$$

where D is the typical dimension of the front face of the body.

The empirical expressions of aerodynamic admittance functions given in this section are only for the normal wind case. Because there is no information available for the aerodynamic admittance functions for the skew wind case, the above empirical

expressions of aerodynamic admittance functions are also used in the developed computer program for the skew wind case with replacing the width of the true cross section with the width of the oblique cross section parallel to the skew wind direction.

5.6 CROSS SPECTRA OF WIND TURBULENCE

The conventional expressions of cross spectra between the turbulent components of the same kind at two different spatial points have been introduced in Chapter 2. To carry out the fully coupled buffeting analysis of 3D bridges, these expressions are extended in the developed computer program with the following forms, which take into account the turbulent coherence in all the three directions at the same time.

$$S_{uu}(P_1,P_2,n)=\lambda_{uu}\sqrt{S_{u1}(n)S_{u2}(n)}\exp\{-\hat{f}_{uu}(P_1,P_2,n)+i\varphi_{uu}(P_1,P_2,n)\} \quad (5\text{-}26a)$$

$$S_{vv}(P_1,P_2,n)=\lambda_{vv}\sqrt{S_{v1}(n)S_{v2}(n)}\exp\{-\hat{f}_{vv}(P_1,P_2,n)+i\varphi_{vv}(P_1,P_2,n)\} \quad (5\text{-}26b)$$

$$S_{ww}(P_1,P_2,n)=\lambda_{ww}\sqrt{S_{w1}(n)S_{w2}(n)}\exp\{-\hat{f}_{ww}(P_1,P_2,n)+i\varphi_{ww}(P_1,P_2,n)\} \quad (5\text{-}26c)$$

$$\hat{f}_{uu}(P_1,P_2,n)=\frac{2n_{xu}\sqrt{\left[C^u_{X_u}(X_{u1}-X_{u2})\right]^2+\left[C^u_{Y_v}(Y_{v1}-Y_{v2})\right]^2+\left[C^u_{Z_w}(Z_{w1}-Z_{w2})\right]^2}}{\overline{U}_1+\overline{U}_2} \quad (5\text{-}27a)$$

$$\hat{f}_{vv}(P_1,P_2,n)=\frac{2n_{xv}\sqrt{\left[C^v_{X_u}(X_{u1}-X_{u2})\right]^2+\left[C^v_{Y_v}(Y_{v1}-Y_{v2})\right]^2+\left[C^v_{Z_w}(Z_{w1}-Z_{w2})\right]^2}}{\overline{U}_1+\overline{U}_2} \quad (5\text{-}27b)$$

$$\hat{f}_{ww}(P_1,P_2,n)=\frac{2n_{xw}\sqrt{\left[C^w_{X_u}(X_{u1}-X_{u2})\right]^2+\left[C^w_{Y_v}(Y_{v1}-Y_{v2})\right]^2+\left[C^w_{Z_w}(Z_{w1}-Z_{w2})\right]^2}}{\overline{U}_1+\overline{U}_2} \quad (5\text{-}27c)$$

where $i=\sqrt{-1}$; X_{uj}, Y_{vj} and Z_{wj} are the coordinates of spatial point P_j (j=1,2) in the global wind coordinate $X_uY_vZ_w$-system. $\overline{U}_{P_j}$ is the mean wind speed at the point P_j, determined by the specified design wind speed and mean wind profile; S_{aj} is the auto spectra of turbulent component a (a=u, v, w) at point P_j, which can be obtained from either the field measurement results or the empirical formulae introduced in Chapter 2; $C^a_{X_u}$, $C^a_{Y_v}$ and $C^a_{Z_w}$ are the 9 decay coefficients of turbulence coherence, the empirical values of which may be found in Chapter 2 if no field measurement data are available; λ_{aa} may be set to unity as done by Davenport (see Eq.(2-94)) or set to $1.0-\hat{f}_{aa}$ as suggested by Krenk (see Eq.(2-95)); $\varphi_{aa}(P_1,P_2,n)$ is called the

phase spectra between the turbulent components of a at points P_1 and P_2 but there is little information on the phase spectra and they are traditionally set to zero in practice; n_{xa} are the modified frequency and it may simply take the original value of turbulence frequency (n) or it is determined by the following equation extended from Eq.(2-95c) and (2-96b).

$$n_{xa} = \sqrt{n^2 + \frac{1}{70.78}\left(\frac{\overline{U}(z)}{L_a^x}\right)^2} \tag{5-28}$$

where n is the turbulence frequency; L_a^x is the length scale of turbulence component a (a=u, v, w) in the alongwind direction, determined from either the measured data or the empirical formulae introduced in Chapter 2.

As for the cross spectra between two turbulence components of different kinds at two different spatial points, the expressions suggested by Jones and Scanlan (1998) and Katsuchi et al. (1999) are extended as follows:

$$S_{uv}(P_1,P_2,n) = \lambda_{uv}\sqrt{S_{uv1}(n)S_{uv1}(n)}\exp\{-\hat{f}_{uv}(P_1,P_2,n) + i\varphi_{uv}(P_1,P_2,n)\} \tag{5-29a}$$

$$S_{uw}(P_1,P_2,n) = \lambda_{uw}\sqrt{S_{uw1}(n)S_{uw2}(n)}\exp\{-\hat{f}_{uw}(P_1,P_2,n) + i\varphi_{uw}(P_1,P_2,n)\} \tag{5-29b}$$

$$S_{vw}(P_1,P_2,n) = \lambda_{vw}\sqrt{S_{vw1}(n)S_{vw2}(n)}\exp\{-\hat{f}_{vw}(P_1,P_2,n) + i\varphi_{vw}(P_1,P_2,n)\} \tag{5-29c}$$

$$S_{uvj}(n) = C_{uvj}(,n) + iQ_{uvj}(n), \qquad j=1,2 \tag{5-30a}$$

$$S_{uwj}(n) = C_{uwj}(n) + iQ_{uwj}(n), \qquad j=1,2 \tag{5-30b}$$

$$S_{vwj}(n) = C_{vwj}(n) + iQ_{vwj}(n), \qquad j=1,2 \tag{5-30c}$$

$$\hat{f}_{uv}(P_1,P_2,n) = [\hat{f}_{uu}(P_1,P_2,n) + \hat{f}_{vv}(P_1,P_2,n)]/2 \tag{5-31a}$$

$$\hat{f}_{uw}(P_1,P_2,n) = [\hat{f}_{uu}(P_1,P_2,n) + \hat{f}_{ww}(P_1,P_2,n)]/2 \tag{5-31b}$$

$$\hat{f}_{vw}(P_1,P_2,n) = [\hat{f}_{vv}(P_1,P_2,n) + \hat{f}_{ww}(P_1,P_2,n)]/2 \tag{5-31c}$$

$$\varphi_{uv}(P_1,P_2,n) = [\varphi_{uu}(P_1,P_2,n) + \varphi_{vv}(P_1,P_2,n)]/2 \tag{5-32a}$$

$$\varphi_{uw}(P_1,P_2,n) = [\varphi_{uu}(P_1,P_2,n) + \varphi_{ww}(P_1,P_2,n)]/2 \tag{5-32b}$$

$$\varphi_{vw}(P_1,P_2,n) = [\varphi_{vv}(P_1,P_2,n) + \varphi_{ww}(P_1,P_2,n)]/2 \tag{5-32c}$$

where λ_{a1a2} are set to either unity or $1.0-\hat{f}_{a1a2}$ in the computer program(a_1, a_2=u, v, w); $C_{a_1a_2j}$ (j=1,2) are the co-spectra between two turbulence components of different kinds at the spatial point P_j whilst $Q_{a_1a_2j}$ are the corresponding quad-

spectra. The value of two-side co-spectrum of C_{uw} may be estimated by Eq.(2-98). However, there is almost no information about the C_{uv}, C_{vw} and Q_{uw}, Q_{uv}, C_{vw}, which are thus often neglected in buffeting analysis. In this study, the curves of these co-spectra and quad-spectra fitted from the field measurement data are used in the buffeting analysis of Tsing Ma Bridge.

In addition, all the wind turbulence spectra are converted into the form of double-side spectra in the buffeting analysis when using the developed computer program. The computed double-side response spectra are then converted into the single-side response spectra before being output.

5.7 TOPOGRAPHIC IMPROVEMENT OF CROSS-SPECTRAL MATRIX

It is noticed that, except for the cases of very low frequency, the value of the cross spectra between two turbulence components at two spatial points decreases rapidly with the increase of the distance between the two points. Therefore, the cross spectral matrix of wind turbulence will be sparse if the sequence of wind excitations is properly arranged and all the cross spectra with values lower than a sufficiently small number are ignored. In this connection, a strategy of rearranging the wind excitation sequence is adopted in this computer program to promote the computing efficiency. The rule of rearranging the wind excitation sequence is introduced in this section.

To promote the efficiency of computation as far as possible, the topography of the cross-spectral matrix of wind turbulence, $\mathbf{S}_{aa}(\omega)$, to be improved by a proper rearrangement of wind excitation sequence is recommended here. The new sequence should be determined according to the corresponding priority number ($p_{i,k}$) determined with one of Eqs.(5-3a) to (5-3f) in an ascending or descending order, so as to make the mean semi-bandwidth (b_w) of the matrix $\mathbf{S}_{aa}(\omega)$ minimal.

$$p_{i,k} = M_p^2 Y_{vi,k} + M_p Z_{wi,k} + X_{ui,k} \tag{5-33a}$$

$$p_{i,k} = M_p^2 Y_{vi,k} + M_p X_{ui,k} + Z_{wi,k} \tag{5-33b}$$

$$p_{i,k} = M_p^2 Z_{wi,k} + M_p Y_{vi,k} + X_{ui,k} \tag{5-33c}$$

$$p_{i,k} = M_p^2 Z_{wi,k} + M_p X_{ui,k} + Y_{vi,k} \tag{5-33d}$$

$$p_{i,k} = M_p^2 X_{ui,k} + M_p Y_{vi,k} + Z_{wi,k} \tag{5-33e}$$

$$p_{i,k} = M_p^2 X_{ui,k} + M_p Z_{wi,k} + Y_{vi,k} \tag{5-33f}$$

where M_P is a sufficiently large positive number, say 1000; $X_{ui,k}$, $Y_{vi,k}$ and $Z_{wi,k}$ are the coordinates of the center of the ith segment of the kth element in the global wind coordinate $X_u Y_v Z_w$-system. For the cases of small or moderate wind yaw angle, Eq.(5-33a) is the most proper one for the determination of priority numbers, as used in this study. Because the magnitude of cross spectrum of two excitations decreases with the separated distance between the two excitations, the matrix $\mathbf{S}_{aa}(\omega)$ will be a spare matrix when neglecting the cross spectra with sufficiently small value, saying 10^{-3} or 10^{-5}. Then, the computational efforts required during the $\mathbf{L}^*\mathbf{D}\mathbf{L}^T$ decomposition of $\mathbf{S}_{aa}(\omega)$ based on a variable bandwidth algorithm (Jennings and McKeown, 1992) can be considerably and rapidly reduced with increasing frequency.

A detailed comparison of computational efficiency between the traditional CQC method and the pseudo excitation method with one or two times of $\mathbf{L}^*\mathbf{D}\mathbf{L}^T$ decomposition was carried out by Sun (1999). The pseudo excitation method has been proved to be much more efficiency than the traditional CQC method. Thus, the large scale buffeting analysis of long span bridges including multi-mode and spatial mode effects, inter-mode and coupling effects, bridge component interaction, and non-proportional damping can be performed with acceptable computational efforts.

5.8 SUMMARY

A computer program for buffeting analysis of long span bridges has been developed based on the modified method introduced in Chapter 4. The computer program provides various types of global and local structural coordinate systems to suit real applications. The program also includes a number of empirical or approximate expressions for estimating aerodynamic coefficients, flutter derivatives and aerodynamic admittance functions for the cases where no measured data are available. Some of the expressions are newly developed in this study and others are

extended from previous empirical and approximate expressions. They are summarized as follows:

(1) The approximate expressions for estimating the aerodynamic coefficients of drag and crosswind force on cables under yaw wind based on the traditional cosine rule.

(2) The approximate formulae for estimating the 18 flutter derivatives of bridge deck under skew wind based on those measured under normal wind condition. These formulae are developed based on the skew wind flutter theory proposed by Scanlan.

(3) The empirical formulae for flat plate flutter derivatives are extended to the yaw wind condition in conjunction with the skew wind flutter theory.

(4) The quasi-steady formulae for flutter derivatives are extended to the skew wind condition.

(5) The two simplified expressions are suggested for approximating the real part and imaginary part of the Sears function as aerodynamic admittance functions. They fit the actual Sears function quite well.

To further enhance the computation efficiency of the modified method for buffeting analysis, the optimisation of position of wind excitation points involved in the cross spectra of wind turbulence has been incorporated in the computer program.

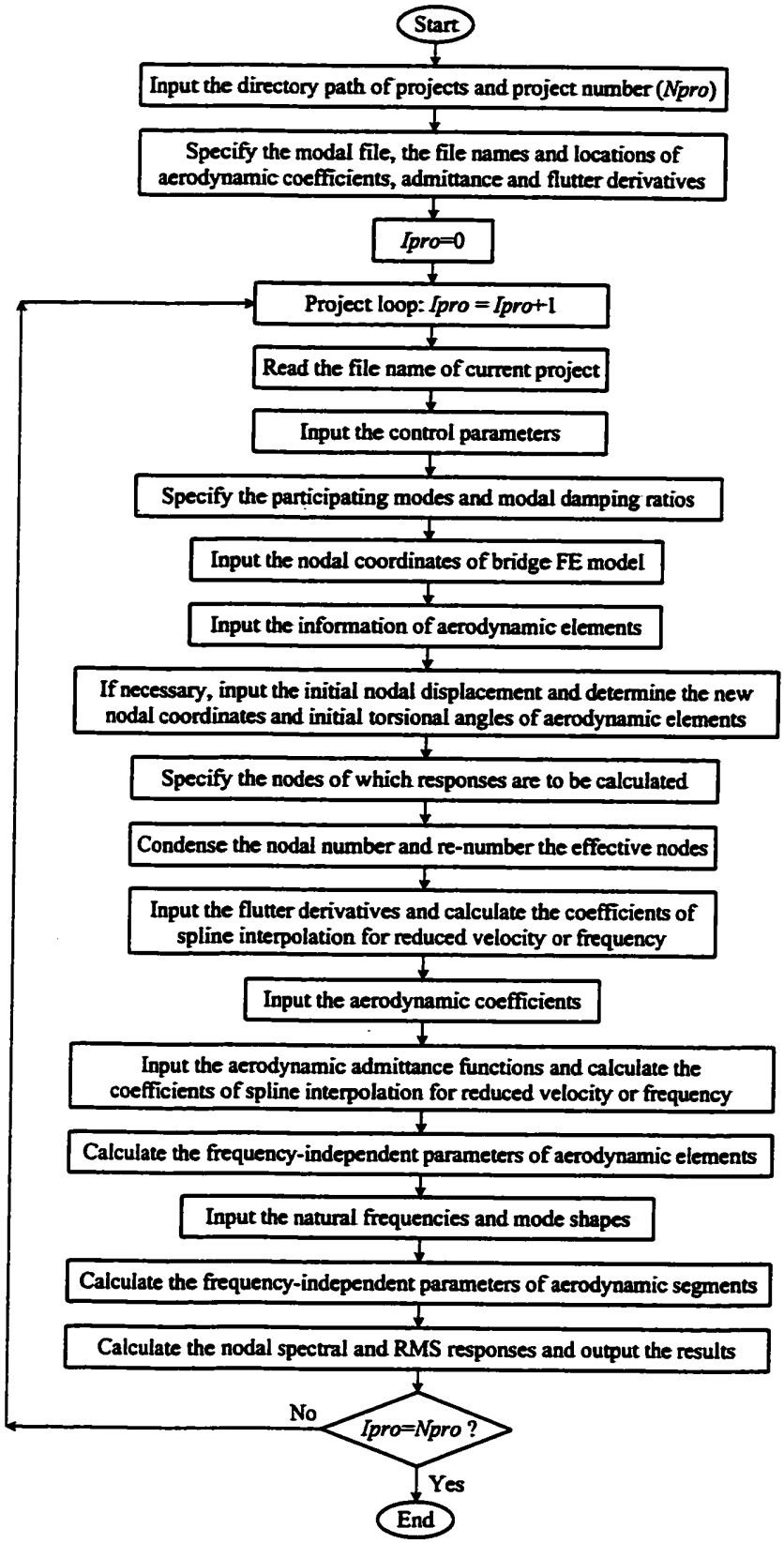

Figure 5-1 Main Flowchart of Computer Program

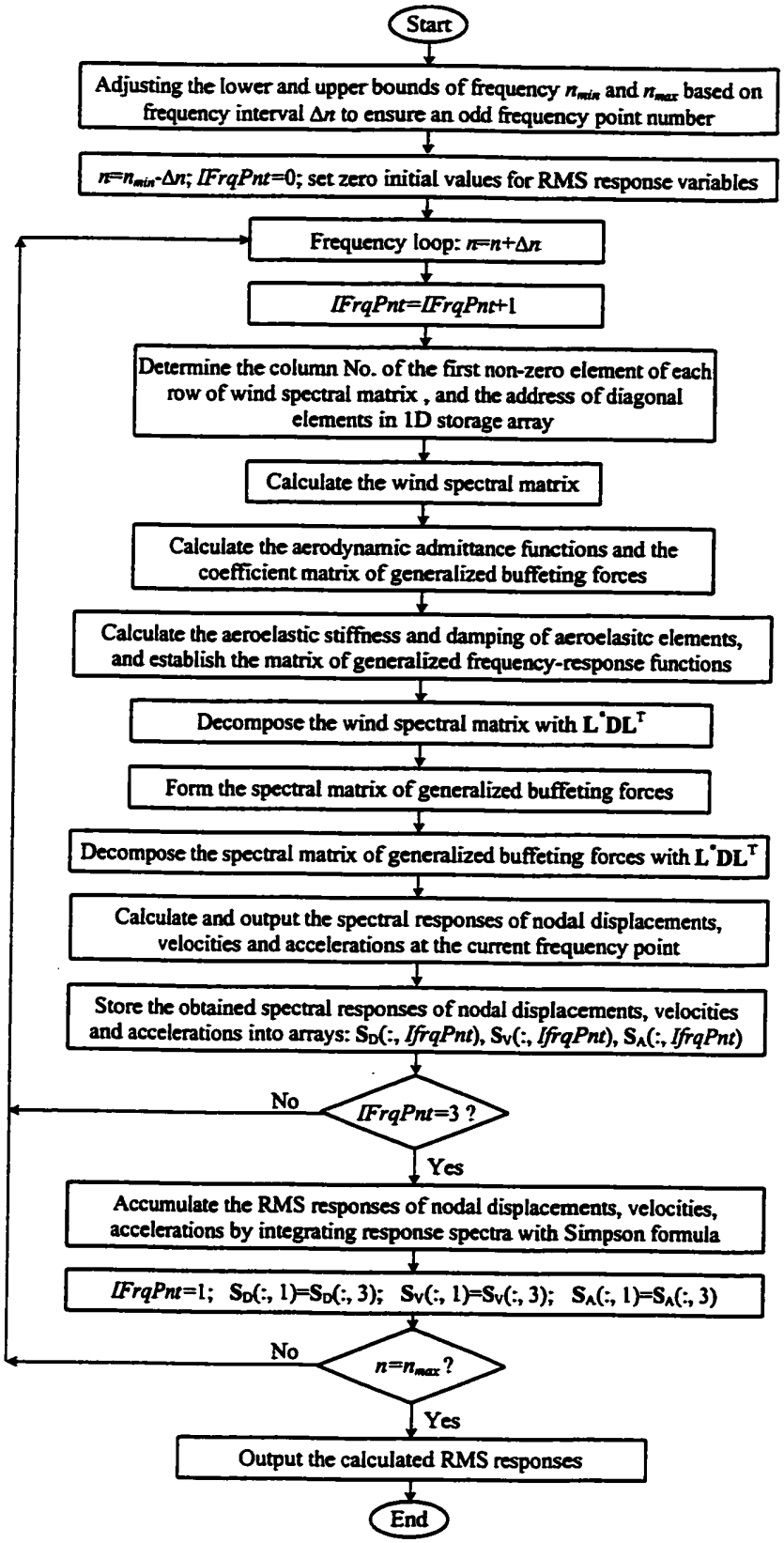

Figure 5-2 Flowchart of the Computing Algorithm

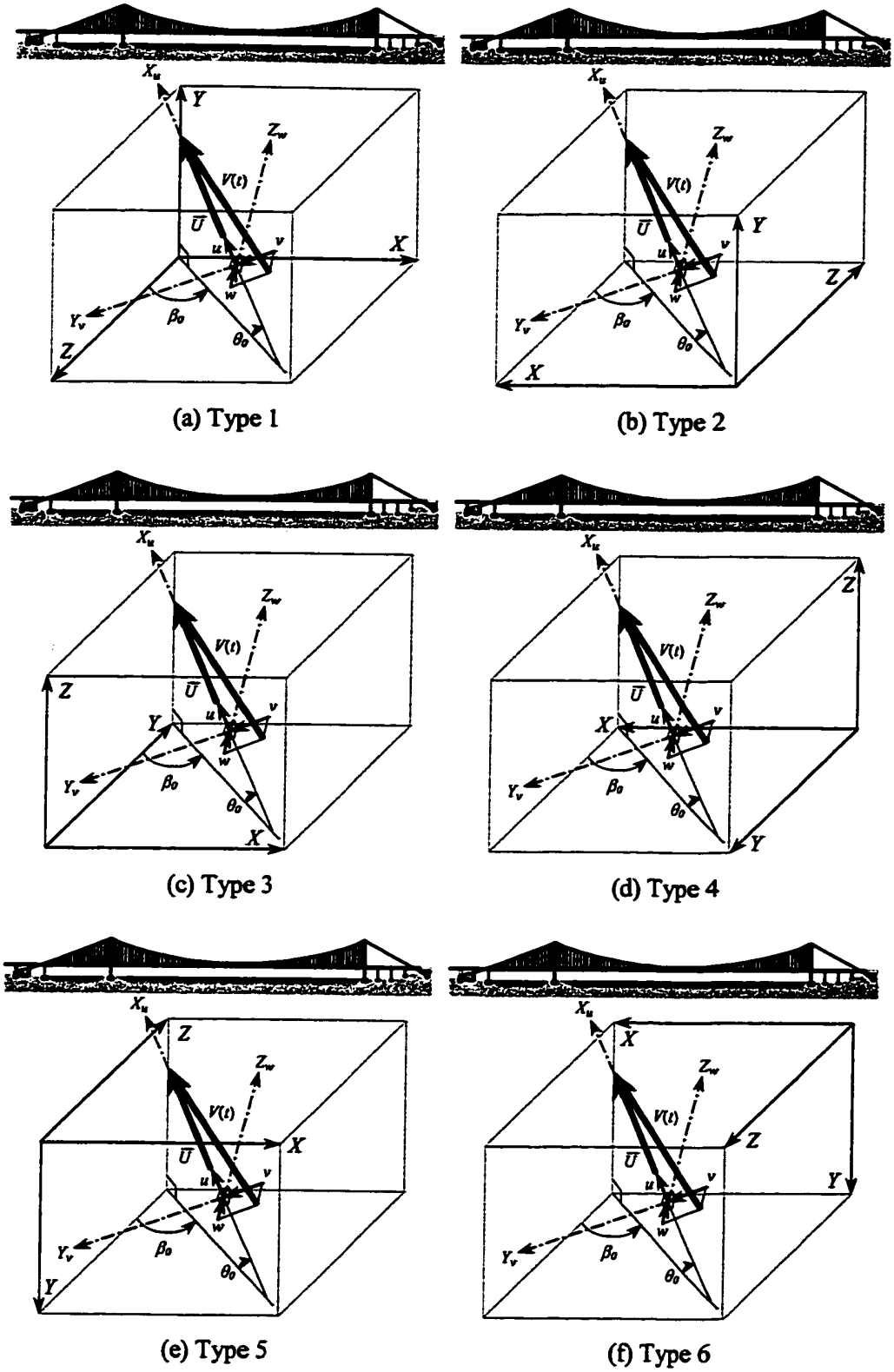

Figure 5-3 Combinations of Global Coordinate Systems

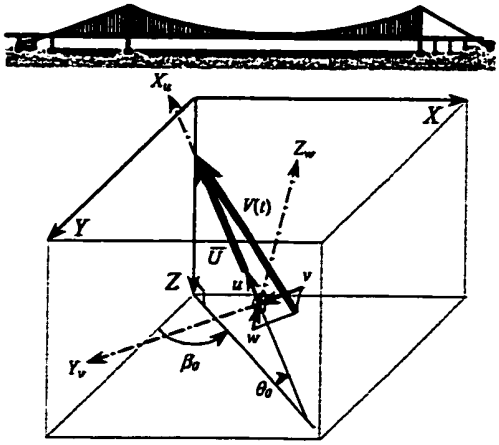

(g) Type 7

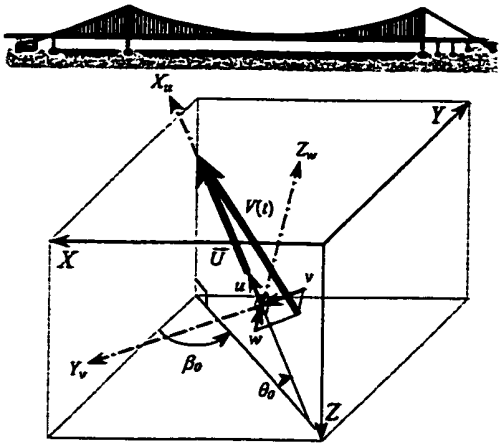

(h) Type 8

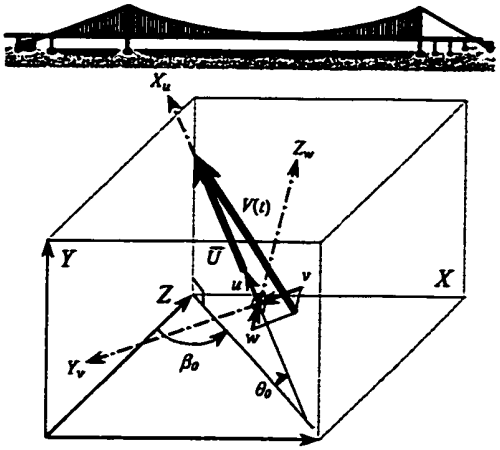

(i) Type 9

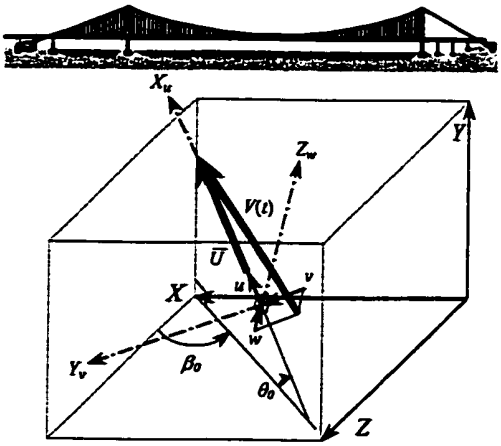

(j) Type 10

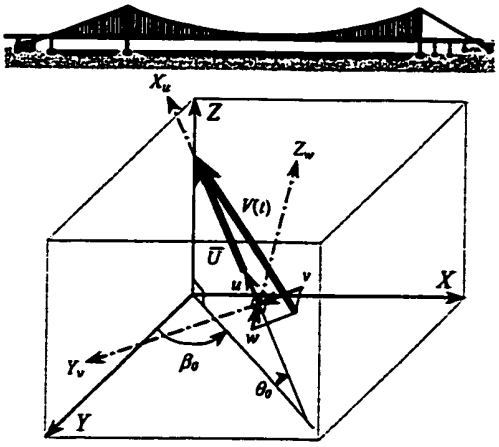

(k) Type 11

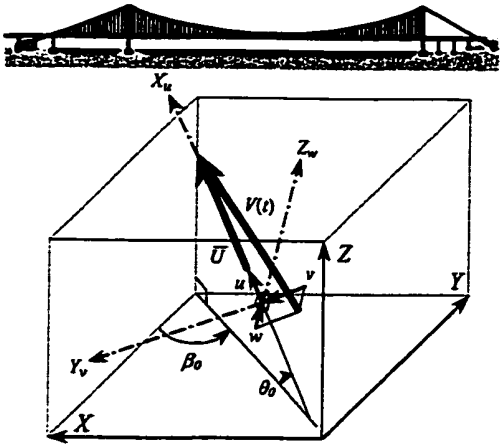

(l) Type 12

Figure 5-3(cont.) Combinations of Global Coordinate Systems

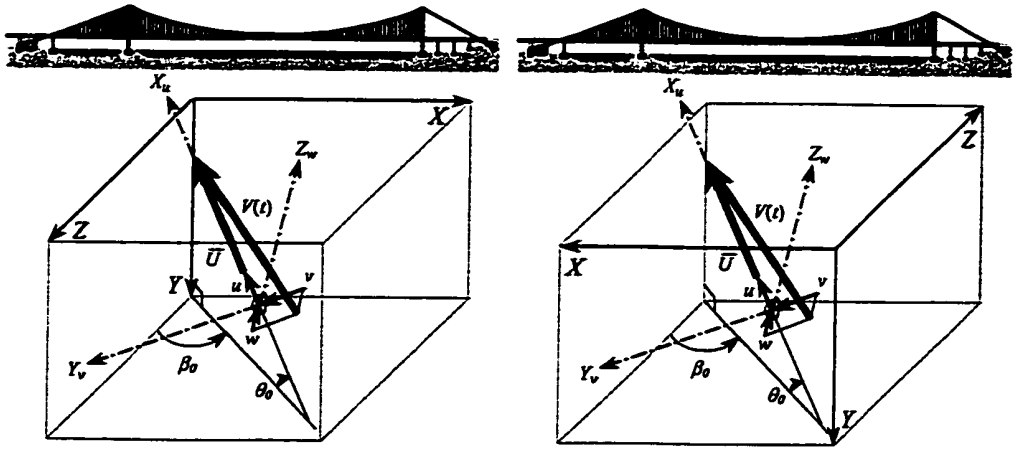

(m) Type 13

(n) Type 14

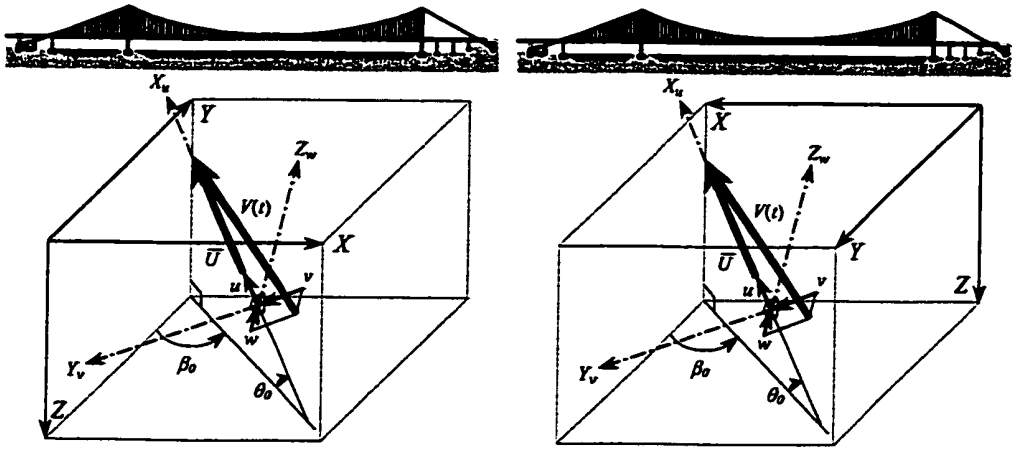

(o) Type 15

(p) Type 16

Figure 5-3(cont.) Combinations of Global Coordinate Systems

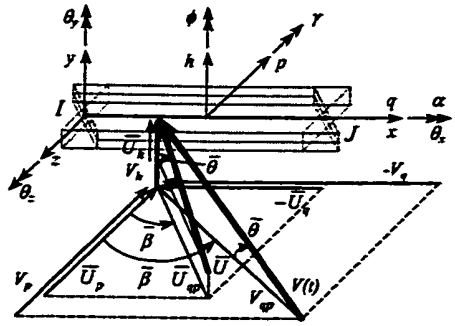

(a) Type 1

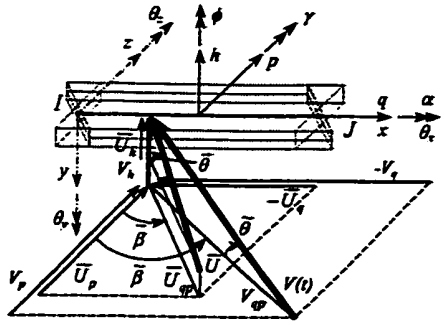

(b) Type 2

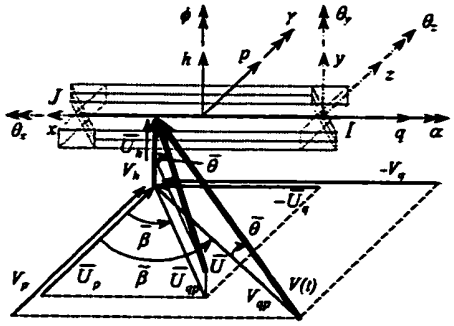

(c) Type 3

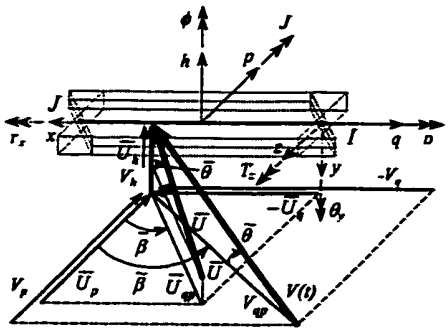

(d) Type 4

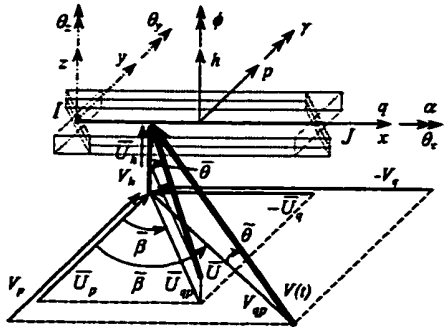

(e) Type 5

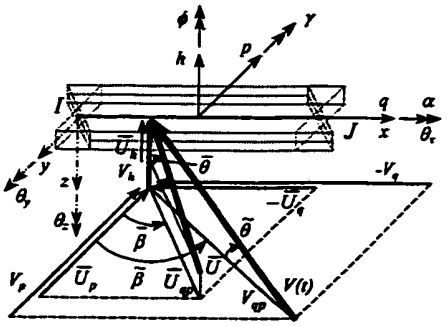

(f) Type 6

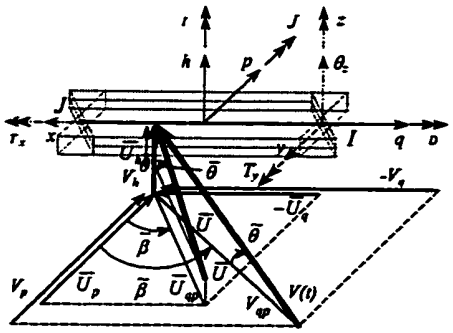

(g) Type 7

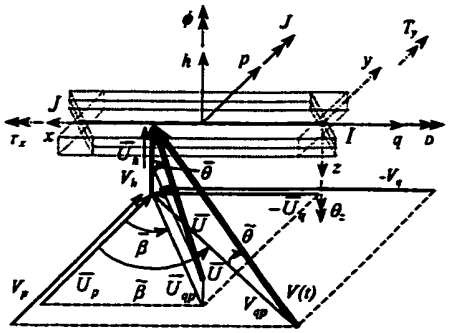

(h) Type 8

Figure 5-4 Combinations of Local Coordinate Systems

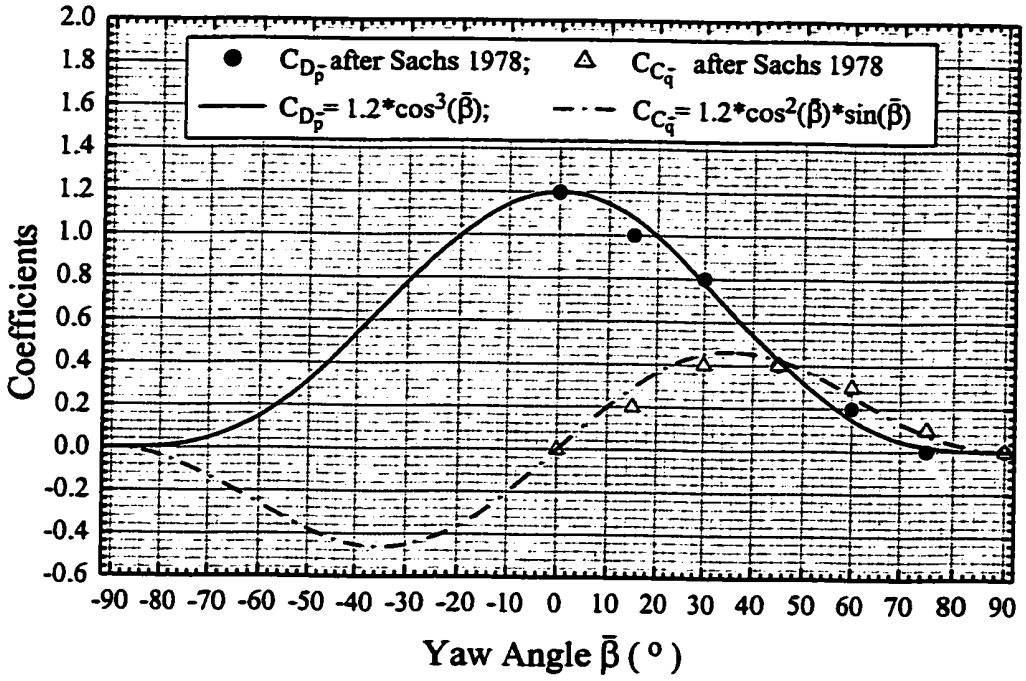

Figure 5-5 Aerodynamic Coefficients of Drag and Crosswind Force on Circular Section ($Re < 3.5 \times 10^5$)

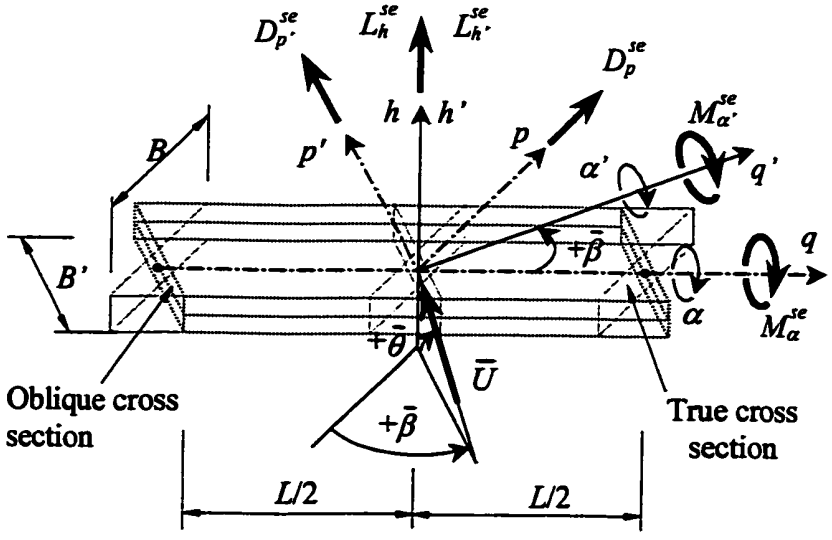

Figure 5-6 Positive Directions of Aeroelastic Forces/Moment

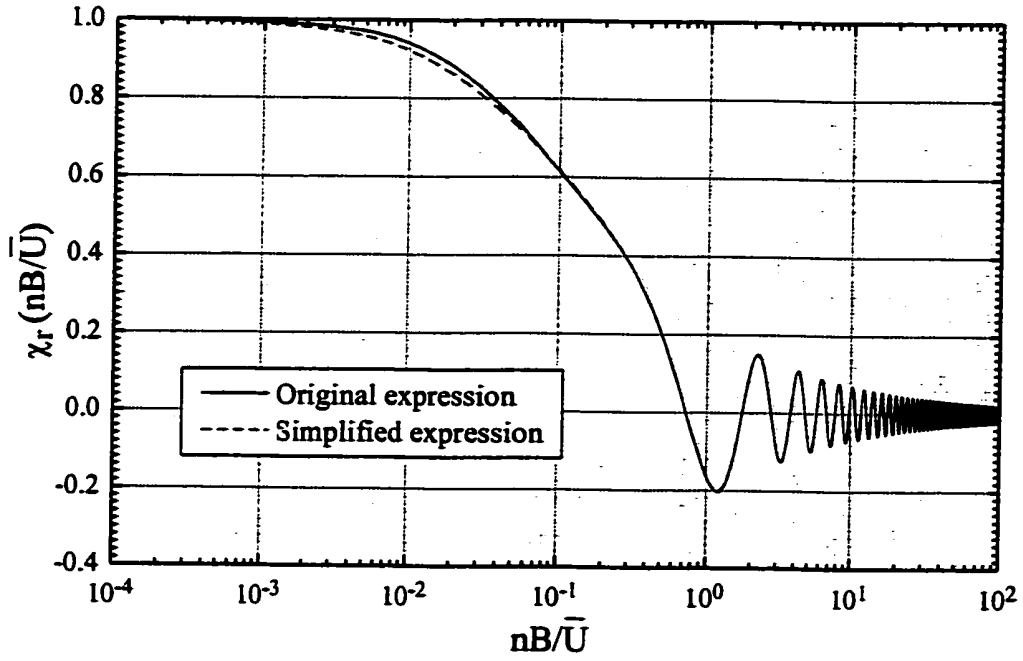

(a) Real part

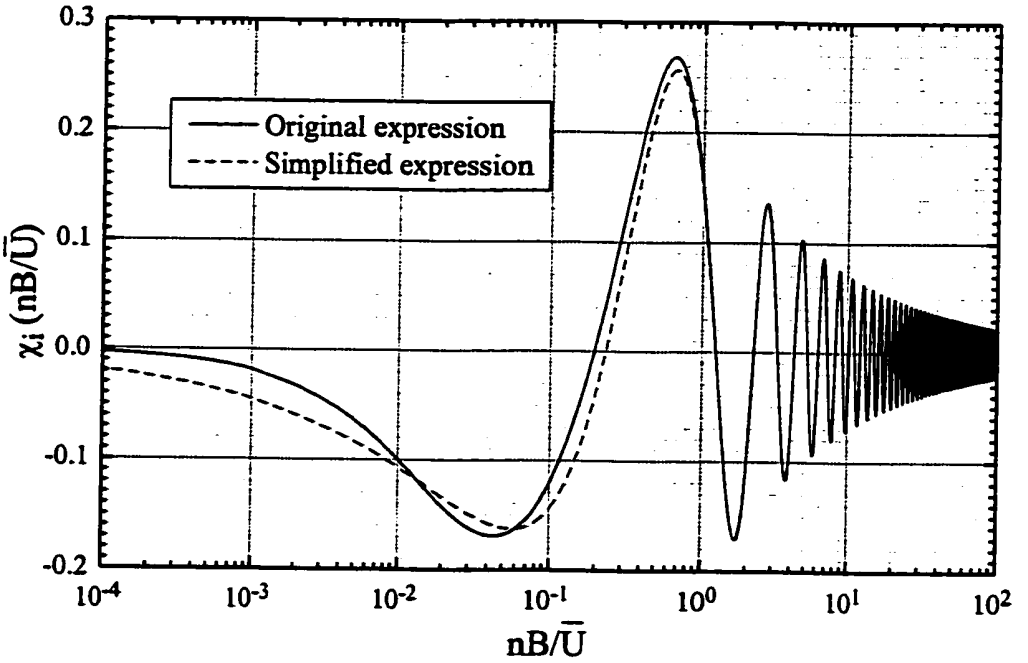

(b) Imaginary part

Figure 5-7 Comparison of Real and Imaginary Parts of Sears Function

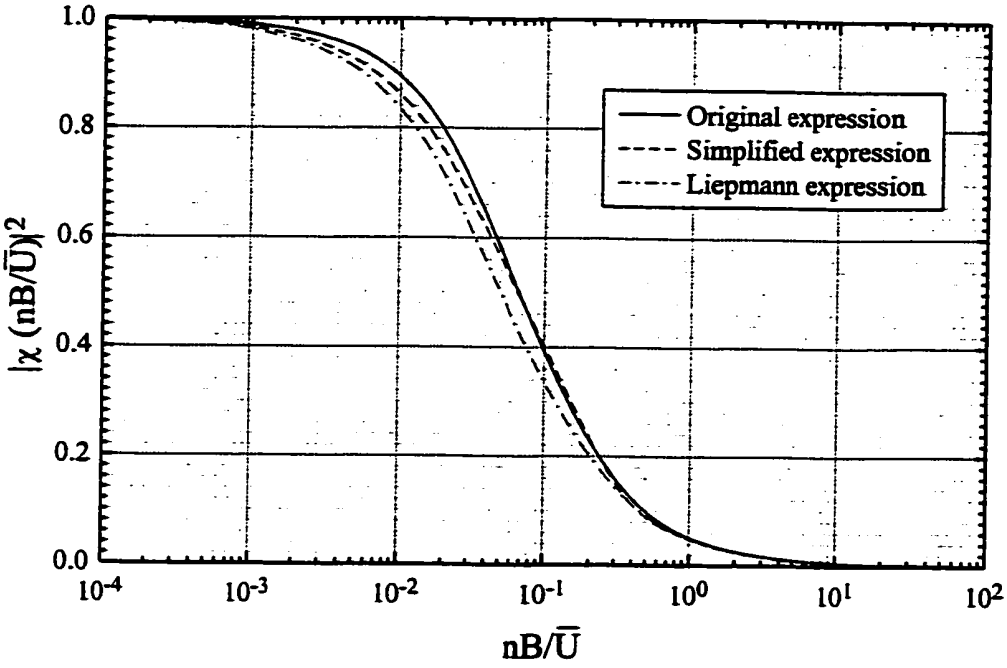

(c) Square of module

Figure 5-8 Comparison of Module of Sears Function

Chapter 6

WIND TUNNEL TEST FOR DECK AERODYNAMIC COEFFICIENTS UNDER SKEW WINDS

6.1 INTRODUCTION

The investigation carried out in Chapter 3 and the field measurements performed by other researchers manifest that the mean wind inclination and yaw angle relative to a bridge deck often deviate from the normal of the bridge deck. However, the traditional buffeting analysis often assumes that mean wind blows at a right angle to the longitudinal axis of the bridge deck. To achieve a better prediction of buffeting response of long span cable-supported bridges to skew winds and to conduct a fair comparison of buffeting response between field measurement and analysis, Chapter 4 presents a framework for fully-coupled buffeting analysis of long span bridges under skew winds and Chapter 5 provides a computer program written based on the proposed framework. To implement the proposed framework using the developed computer program, it is essential to obtain six component aerodynamic coefficients for typical oblique strips of a bridge deck. To this end, this Chapter presents a wind tunnel test technique for measuring such aerodynamic coefficients, which includes the design of sectional model, the development of test rig and measurement system, and the analysis of test results. Typical oblique strips of the Tsing Ma suspension bridge deck are selected and tested using the proposed wind tunnel test technique to obtain aerodynamic coefficients as functions of mean wind incidence and yaw angle. The measured results are then analyzed to find the relationship between the aerodynamic coefficients and the mean wind yaw angle and inclination for the later use in Chapters 9 and 10. The measured results are also used to examine the currently used cosine rule for buffeting analysis of a bridge under yaw winds.

6.2 DESIGN OF OBLIQUE SECTIONAL MODEL

The Tsing Ma suspension bridge deck is taken as an example to explain how to design sectional models of parallelogram (oblique strips) for measuring their six component aerodynamic coefficients. To cater for the comparison with the cosine rule and the later use in Chapters 9 and 10, the design of the oblique sectional models takes into consideration of a wide combination of mean wind inclinations and yaw angles.

6.2.1 Tsing Ma Suspension Bridge Deck

The Tsing Ma suspension bridge deck is a double layer deck carrying a dual three-lane highway on the upper level of the bridge deck and two railways and two carriage-ways on the lower level within the bridge deck (Figure 6-1). The dimension of a typical deck section is 41.0m wide and 7.643m high. It is mainly composed of a number of steel cross-frames which are connected together through two longitudinal steel trusses as well as upper and lower stiffened steel plates. The cross-frames are arranged with a longitudinal separation of 4.5m and covered with thin steel cladding at their two triangular edges to form two sets of wind fairing. Two bracing systems in the horizontal plane are set, respectively, at the center areas of the upper and lower layers. These bracing systems constitute the longitudinal vent system of the bridge deck, which together with the two sets of side fairing, are utilized to promote the aerodynamic performance of the bridge deck. The upper vent is 3.5m wide while the lower vent has an overall width of 11.7m. Laid on the lower chords of the cross-frames, two longitudinal railways of 2.1m wide each are arranged at the center area of the lower layer with a transverse space of 2.0m. Thus, the lower vent has three ventilation spaces of 2.75m wide for the two sides and 2.0m for the central one. Both the upper and lower vents are covered with steel grids of about 75% porosity ratio. The stiffened traffic plates are welded on the top of upper and lower chords of the cross-frames, resulting in direct exposure of the lower chords to wind. Thus, the aerodynamic exterior of the deck is quite complicated. In addition, four lines of parapets are mounted on the deck. Each of them consists of a series of posts separated at a central distance of 4.5m, and linked to each other with six horizontal taut steel wires of 12mm diameter with a vertical interval of 0.25m. The post has a square cross section of 0.35m×0.35m and a height of 1.64m in general. The

ventilation ratio of each line of parapet is typically about 85%. Wind shelters are installed on the deck in the vicinity of the two bridge towers to avoid a sudden change of lateral wind forces on vehicles passing through the towers and then serious traffic accidents. The length of wind shelter is 63m on both sides of Ma Wan Tower and on the central side of Tsing Yi Tower. The ventilation ratio drops gradually from 85% to 20% towards the tower. On the Tsing Yi side span, the wind shelter is 40.5m long, and its ventilation ratio reduces gradually from 40% to 20% towards the tower.

6.2.2 Design of Deck Sectional Model

Different from rectangular sectional models used in traditional wind tunnel tests for measuring aerodynamic force coefficients of a bridge deck under normal winds, a sectional model of parallelogram is used in this investigation to measure aerodynamic force coefficients of a bridge deck under skew winds. As shown in Figure 6-2, the longitudinal axis of the oblique sectional model is selected as the q-axis. The qph-system, called the local reference coordinates in whole bridge buffeting analysis (see Chapter 4) or called the model coordinates in this chapter, is used as a coordinate system for describing the longitudinal, lateral, and vertical motions of bridge deck in a common sense. The $\overline{qph}$-system, introduced to designate local wind coordinates in the whole bridge buffeting analysis, is simply called wind coordinates in this chapter, in which the $\overline{q}$-axis is in the "horizontal" plane (the qp-plane) and the $\overline{p}$-axis is along the mean wind direction. The mean wind yaw angle $\overline{\beta}$ is then defined as the angle between the vertical plane normal to the q-axis and the vertical plane normal to the $\overline{q}$-axis. The mean wind yaw angle is positive if it is counter-clockwise. The angle of inclination of mean wind $\overline{\theta}$ is defined as the angle between the mean wind and the horizontal plane. Figure 6-3 shows the positive directions of three aerodynamic forces and three aerodynamic moments to be measured for the oblique sectional model under skew winds, which are then used to determine the corresponding six component aerodynamic coefficients with respect to the $\overline{qph}$-system.

To facilitate wind tunnel tests, the oblique sectional model is installed vertically in a wind tunnel (Figure 6-4). To avoid 3D flow effects around the two ends of the oblique sectional model, two surrounding segments (the upper segment and the lower

segment) are introduced and each is mounted close to one end of, but free from any touch to, the sectional model (the middle segment) as shown in Figures 6-4 and 6-5. To accommodate a few yaw angles in the test using one sectional model, two adjustable parts are designed and placed between the top part and the middle part and between the bottom part and the middle part separately. Each adjustable part consists of four small triangle wedges used to adjust the middle part to form a measured segment and the top and bottom parts to form the upper and lower surrounding segments for five designated yaw angles (0°, 5°, 13°, 20° and 31°). The top part, the middle part, the bottom part, the upper adjustable set, and the lower adjustable set are regarded as different parts of the test model.

For instance, when the 0° yaw angle is concerned, the whole set of upper adjustable part is connected to the top part, forming the upper surrounding segment. The whole set of lower adjustable part is moved upwards to be connected to the middle part, forming the measured segment. The lower surrounding segment becomes the bottom part only. The sectional model (the measured segment) in the middle is rectangular in this case.

If the 31° yaw angle is considered, the whole set of upper adjustable part is attached to the middle part, forming the measured segment. The lower surrounding segment is composed of the whole set of lower adjustable part and the bottom part. The upper surrounding segment becomes the top part only.

When the yaw angle becomes either 5° or 13° or 20°, each of the two sets of adjustable parts as divided into two sub-parts correspondingly. The upper sub-part of the lower set adjustable part and the lower sub-part of the upper set adjustable part are moved to the middle part of the model, forming the measured segment. The upper sub-part of the upper set of adjustable parts is connected to the top part, constituting the upper surrounding segment. The lower sub-part of the lower set of adjustable parts is linked to the bottom part, forming the lower surrounding segment.

The geometric scale of the deck sectional model of the Tsing Ma Bridge was set as 1:100 after a careful consideration of many factors. These factors include the size of working section of the wind tunnel, the sufficiently large aspect ratio (length-over-width) requirement for the model, the high stiffness and lightweight requirement for

the measured segment of the model, and the sensitivity and capacity of the force balance. As a result, the width of sectional model is 410mm(Figure 6-5). The total length of the test model is 2210mm, in which the length of the oblique sectional model (the middle segment) is 1060mm, the length of longer side of the upper surrounding segment is 495mm, the length of shorter side of the lower segment is 647mm. The gap between the top part and the middle part and between the bottom part and the middle part is 4mm each. The deck exterior appearance, including the cross-frames, the central vents, and the parapets, are modeled in the light of the principle of geometric similarity. The details of the sectional model (the middle part), the top part, the bottom part, and the two adjustable parts are explained in the following and displayed in Figure 6-6 and Figure 6-7.

As shown in Figure 6-6a and Figure 6-7e, the bottom part of the model is a 647mm long rigid twin-box girder. It is used as a part of the lower surrounding segment other than the measured segment. The two heavy boxes of the bottom part were made of steel and connected with a steel end plate of 20mm thick, three pairs of transverse steel bars of 20mm wide and 3mm thick, and 14 cross-frames made of 0.3mm thick steel plate. There were two steel diaphragms of 5mm thick in each box, and one 20mm thick diaphragm near the top of each box on which other parts of the model and a six component balance were supported through two steel pipes. Two bars of wind fairing of the bottom part were made of plastic foam and were stuck on to the outer sides of the steel boxes with special glue. The nets of the vents on the central areas of the upper deck surface and lower deck surface were made of 2mm thick ABS plastic plate and were sculpted using computer controlled miller. The cross-frames were linked, at first, by welding four inverse T-style longitudinal beams through their lower beams (see Figure 6-7e). Then, the lower ABS nets, containing two solid belts simulating the two railways, were glued on to the lower chords of the cross-frames, and the upper ABS nets was glued on to the upper chords of the cross-frames. This led to a spatial frame structure. The inverse T-style longitudinal beams were also made of 0.3mm steel plates. This kind of spatial frame structure was also used for other parts of the model.

Displayed in Figure 6-6b is the middle part of the model, which is trapezoidal in deck plane and with only the top end perpendicular to the model axis. Its long side is

1060mm while its short side is 814mm. The middle part is the main body of the measured segment, requiring a high stiffness but a lightweight. The spatial frame system was comprised of 21 cross-frames and ABS vent nets. Two wood plates of 3mm thick were stuck on to the cantilevers of the spatial frame to simulate the two lower carriage-ways of the deck (Figures 6-7a and 6-7b). The wood webs and the two sets of wind fairing were then fixed on the traffic plates. To improve the stiffness and strength of the measured segment, the wind fairing on the left side of the model where the force balanced was installed was made of wood box and stiffened in its central part near to the balance bearing surface. On the other side, the wind fairing of short side was mad of plastic foam to reduce the mass and inertia of the measured segment. Two 3mm thick perspex plates simulating the upper carriage ways of the deck were dismountable to facilitate the installation of the test model and the force balance and the checking of free space between the model, the balance, and the steel pipes. Although perspex plates are heavier than wood plates, it was used as the removable plates to prevent from distortion in the operation.

The top part of the test model is also trapezoidal in deck plane and with only the top end perpendicular to the model axis (see Figure 6-6c). Its long and short sides are, respectively, 495mm and 249mm in length. Most of the part was made of plastic foam, except for the spatial frame system which consisted of 8 complete steel cross-frames and the short segment of wood box serving as the connection to the steel pipe (see Figures 6-7c and 6-7d).

The cross section of the upper adjustable set is similar to the cross section D-D (see Figures 6-6c and 6-7d). The cross section of the lower adjustable set is similar to the cross section A-A (see Figures 6-6b and 6-7a), except that both sets of wind fairing were made of plastic foam. The cross-frames for the two adjustable sets, however, were made of ABS plastic plate to avoid the difficulty of cutting.

6.3 Test Rig and Measurement System

6.3.1 Installation of Sectional Model and Force Balance

As shown in Figures 6-4 and 6-6a, the bottom part of the model was mounted rigidly on the turning table of a wind tunnel through a special apparatus. The special

apparatus was made of steel and designed in such a way that the model can be adjusted to meet the desired yaw angle. The special apparatus is thus called the yaw angle device. The desired angle of inclination was realized by rotating the turning table.

There were two steel pipes installed on the top of the bottom part of the model: one on the left and the other on the right, as shown in Figure 6-8. In Figure 6-8, the two carriage-way plates of the middle part were temporarily removed to reveal the internal connection details. The left steel pipe had an external diameter of 48mm. Fixed at the top of the left steel pipe was a six component force balance, shown in Figure 6-8 as a black cylinder. The middle measured segment of the model was then rigidly connected to the force balance through its strong diaphragm of 30mm thick and a steel link block of 12mm thick (see Figure 6-6b). The right steel pipe went through the middle part without any touch to rigidly support the top part of the model. The outer diameter of the right steel pipe was 42 mm. The reason why the six-component force balance was placed on the left side of the model rather than the longitudinal axis of the model is to ensure the rigidity of the measured segment and consider the real configuration of the deck. The top of the force balance was 508mm away from the top end of the middle part (see Figure 6-6b). The longitudinal axis of the force balance was parallel with the longitudinal axis of the deck model but away from the deck longitudinal axis at 97.5mm along the deck width and at 2.2 mm along the deck height with reference to the upper surface of the deck model.

Enough spaces were kept between the measured segment and the steel pipes to prevent from any contact during the test. For the same purpose, two gaps of about 4mm each were always set between the measured segment and the upper surrounding segment and between the measured segment and the lower surrounding segment.

6.3.2 Force/ Moment Measurement System

The force/moment measurement system used in the test for measuring the aerodynamic forces/moments acting on the deck model was composed of a six-component force (moment) balance, a potentiostatic DC power supply, a DC voltage amplifier of eight channels, a multi-channel data acquisition unit, and a computer.

The balance, used for measuring the six aerodynamic forces/moments acting on the measured segment of the model, is a high-accuracy internally-placed strain balance of six-components (See Figure 6-10a). The balance was elaborately designed and specially made for this investigation by Mr. F. Zhang of the State Key Laboratory for Disaster Reduction in Civil Engineering at Tongji University, China. Both high sensitivity and high stiffness requirements were considered in the balance design to ensure the measurement accuracy and to avoid model vibration. The balance was designed as a sufficiently small device to be placed inside the deck model. On the other hand, it should have enough capacity to take the forces and moments caused by the model weight, which was quite large when the model was set with a large yaw angle. As a result, it had an outer diameter of 48mm and a length of 235mm. Six groups of strain gauges were respectively installed on four separated sections to perceive three forces ($F_{\bar{x}}$, $F_{\bar{y}}$ and $F_{\bar{z}}$) and three moments ($M_{\bar{x}}$, $M_{\bar{y}}$ and $M_{\bar{z}}$) acting on the center of the balance top surface. The corresponding design bearing capacity are 100.0N, 150.0N and 150.0N, respectively, for three forces $F_{\bar{x}}$, $F_{\bar{y}}$ and $F_{\bar{z}}$, and 30.0Nm, 20.0Nm and 10.0Nm, respectively, for three moments $M_{\bar{x}}$, $M_{\bar{y}}$ and $M_{\bar{z}}$. As shown in Figure 6-9, $\bar{z}$ denotes the longitudinal axis of the balance while $\bar{x}$ and $\bar{y}$ denote, respectively, the two transverse axes with the $\bar{x}$, $\bar{y}$ and $\bar{z}$ axes perpendicular to each other. In this investigation, the $\bar{x}$ axis is located in the deck plane and the $\bar{y}$ axis is normal to the deck plane and $\bar{z}$ is along the longitudinal axis of the deck. The origin of the balance $\overline{xyz}$ coordinates is assigned at the center of the balance top surface.

The electric bridge of the strain balance was powered by a high-accuracy potentiostatic DC power supply (Ts1721) and connected to an eight channels DC voltage amplifier (Ts3815T), as shown in Figure 6-10. A temperature compensation system was built in the electric bridge to automatically eliminate the temperature effects and to cover a wide range of applied loads. The DC power supply and the DC voltage amplifier were specially made for the test. The variation of voltage amplitude of the power supply is less than $0.02\%V_0$, where V_0 is the selected output voltage of the DC power supply. The effect of wire resistance of the electric bridge on the output can also be automatically compensated by the power supply. The voltage amplifier was used to magnify the output signal of the force balance for data

acquisition. The output accuracy of the voltage amplifier is higher than 99.9%. The zero point of the amplifier can be automatically set and the amplification factor of the amplifier is adjustable.

The voltage signals from the amplifier were sampled at a frequency of 500Hz by a HP3852A data acquisition/control unit (Figure 6-10c) and saved in a HP9000-345 work station (Figure 6-10d). The HP3852A data acquisition unit is very stable and has an accuracy with an error less than 0.1% between the input and the output.

The force/moment measurement system was calibrated before the test. The voltage of the DC power supply applied to the electric bridge of the balance, V_b, was 10V and the amplification factors were set as 1000 for all the channels of the amplifier. These parameters were also used in the formal tests. During the calibration, the forces $F_{\bar{x}}$ along the axis $\bar{x}$, $F_{\bar{y}}$ along the axis $\bar{y}$, $F_{\bar{z}}$ along the axis $\bar{z}$, the moments $M_{\bar{x}}$ around the axis $\bar{x}$ and $M_{\bar{y}}$ around the axis $\bar{y}$ and $M_{\bar{z}}$ around the axis $\bar{z}$ was, respectively, applied to the balance in a proper way and at several intervals with respect to the center of the balance top surface. The pure output voltage from the balance after deducting the initial reading was then normalized by V_b ($\Delta V/V_b$ in $\mu V/V$) and expressed as a function of the applied force (in N) or moment (in Nm), as shown in Figures 6-11a to 6-11f. The data from the calibration were also fitted by a straight line and plotted in Figures 6-11a to 6-11f. It is found that the linear relationship between the applied force/moment and the balance output voltage is satisfactorily attained.

It is noted from Figures 6-11c and 6-11f that the applied moment $M_{\bar{x}}$, $M_{\bar{y}}$ or $M_{\bar{z}}$, or the applied force $F_{\bar{z}}$ mainly produced the output voltage of the balance in its own component and it almost did not affect the other components. However, it is seen from Figure 6-11a and 6-11b that the applied force $F_{\bar{x}}$ or $F_{\bar{y}}$ produced a significant output voltage in the component $M_{\bar{y}}$ or $M_{\bar{x}}$ besides the major output voltage in the component $F_{\bar{x}}$ or $F_{\bar{y}}$. This was due to the balance structure, in which the two strain gauges to measure the moment $M_{\bar{y}}$ or $M_{\bar{x}}$ were stuck on the balance section at a

certain distance from the top surface of the balance. The application of the force $F_{\bar{x}}$ or $F_{\bar{y}}$ thus led to the additional moment $M_{\bar{y}}$ or $M_{\bar{x}}$.

Based on the slopes of 36 fitted straight lines, the calibration matrix of the balance, reflecting the relationship between the applied forces/moments and the normalized output voltages, was obtained as follows:

$$\mathbf{S}_b = \begin{bmatrix} 9.1385 & -0.0038 & -0.0028 & 0.0978 & -0.1920 & 0.3123 \\ 0.0052 & -6.6897 & 0.0023 & 1.3135 & -0.1729 & -0.3684 \\ 0.0086 & 0.0301 & 7.1392 & 0.1360 & 0.4427 & 0.2656 \\ 0.0100 & -3.5157 & 0.0043 & 34.9915 & 0.1131 & 0.8907 \\ -1.9488 & 0.0470 & 0.0147 & 0.0394 & -26.7961 & 1.5227 \\ 0.0191 & 0.0056 & 0.0074 & 0.1974 & 0.4967 & -89.9394 \end{bmatrix} \quad (6\text{-}1)$$

The measurement error of the elements in the above matrix was less than 0.2% of the design bearing capacity for $M_{\bar{z}}$, and 0.1% of the design bearing capacity for the other five components, as indicated by an error analysis of the measurement data and fitted lines. As a result, if the output voltages of the six components of the balance are $\Delta V_{F_{\bar{x}}}$, $\Delta V_{F_{\bar{y}}}$, $\Delta V_{F_{\bar{z}}}$, $\Delta V_{M_{\bar{x}}}$, $\Delta V_{M_{\bar{y}}}$ and $\Delta V_{M_{\bar{z}}}$ in unit of μV, the forces and moments acting on the bridge tower component installed on the force balance can be calculated as

$$\left(F_{\bar{x}}, F_{\bar{y}}, F_{\bar{z}}, M_{\bar{x}}, M_{\bar{y}}, M_{\bar{z}}\right)^{\mathrm{T}} = \frac{1}{V_b}\mathbf{S}_b^{-1}\left(\Delta V_{F_{\bar{x}}}, \Delta V_{F_{\bar{y}}}, \Delta V_{F_{\bar{z}}}, \Delta V_{M_{\bar{x}}}, \Delta V_{M_{\bar{y}}}, \Delta V_{M_{\bar{z}}}\right)^{\mathrm{T}} \quad (6\text{-}2)$$

where, V_b is the voltage applied to the electric bridge of the balance in unit of V; and the obtained forces and moments are in unit of N and Nm, respectively.

6.4 Wind Tunnel Tests

6.4.1 Wind Tunnel

The tests were carried out in the TJ-2 Wind Tunnel of the State Key Laboratory for Disaster Reduction in Civil Engineering at Tongji University, China. The TJ-2 Wind Tunnel is a boundary layer tunnel of closed-circuit-type as shown in Figure 6-12. The working section of the tunnel is 3m wide, 2.5m high, and 15m long. The achievable mean wind speed ranges from 0.5m/s to 68.0m/s, adjustable continuously. All the tests for determining aerodynamic coefficients of the bridge deck were carried out in smooth flow. The thickness of boundary layers near the walls, floor

and ceiling of the tunnel is less than 150mm. The maximum non-uniformity of mean wind within the cross section, excluding the boundary areas, is less than 1% and the turbulence intensity within the same cross section is less than 0.5%. The horizontal yaw angle and vertical inclination angle of the mean wind in the tunnel are less than 0.5°.

6.4.2 Test Cases

For each of 5 major yaw angles (0°, 5°, 13°, 20° and 31°), the two ends of the measured segment, the bottom line of the upper surrounding segment and the top line of the lower surrounding segment were all kept in horizontal and in parallel to the mean wind direction. The wind yaw angle $\overline{\beta}$ was the same as the model end angle β_m (see Figures 6-5 and 6-9) in these five cases. However, to enrich the database for generating design curves of aerodynamic coefficients and to understand the effects of model end angle, it was decided to do the test under a wide combination of yaw angles from 0° to 34° at an interval of 1° or 2° and inclination angles from -10° to 10° at an interval of 1°. As a result, there were a total of 735 cases tested and listed in Table 6-1. For the other mean wind yaw angles around one of the five major yaw angles, only the model was adjusted to the target mean wind yaw angle $\overline{\beta}$ while the model end angle β_m remain unchanged. This is an approximate treatment but it is necessary for reducing test time and cost. This approximate treatment will be examined by the relevant test results.

Table 6-1 Test Cases for Six Aerodynamic Coefficients of Tsing Ma Bridge Deck

Case No.	Model end angle β_m (°)	Wind yaw angle $\overline{\beta}$ (°)	Inclination Angle $\overline{\theta}$ (°)
1 ~ 21	0	31	-10 ~ +10
22 ~ 42	0	20	-10 ~ +10
43 ~ 63	0	13	-10 ~ +10
64 ~ 84	0	5	-10 ~ +10
85 ~ 105	0	1	-10 ~ +10
106 ~ 126	0	0	-10 ~ +10

Table 6-1 (cont.) Test Cases for Six Aerodynamic Coefficients of Tsing Ma Bridge Deck

Case No.	Model end angle β_m (°)	Wind yaw angle $\bar{\beta}$ (°)	Inclination Angle $\bar{\theta}$ (°)
127 ~ 147	5	2	-10 ~ +10
148 ~ 168	5	3	-10 ~ +10
169 ~ 189	5	4	-10 ~ +10
190 ~ 210	5	5	-10 ~ +10
211 ~ 231	5	6	-10 ~ +10
232 ~ 252	5	8	-10 ~ +10
253 ~ 273	5	10	-10 ~ +10
274 ~ 294	13	8	-10 ~ +10
295 ~ 315	13	10	-10 ~ +10
316 ~ 336	13	12	-10 ~ +10
337 ~ 357	13	13	-10 ~ +10
358 ~ 378	13	14	-10 ~ +10
379 ~ 399	13	16	-10 ~ +10
400 ~ 420	13	17	-10 ~ +10
421 ~ 441	20	16	-10 ~ +10
442 ~ 462	20	17	-10 ~ +10
463 ~ 483	20	19	-10 ~ +10
484 ~ 504	20	20	-10 ~ +10
505 ~ 525	20	21	-10 ~ +10
526 ~ 546	20	23	-10 ~ +10
547 ~ 567	20	24	-10 ~ +10
568 ~ 588	20	25	-10 ~ +10
589 ~ 609	31	25	-10 ~ +10
610 ~ 630	31	27	-10 ~ +10
631 ~ 651	31	28	-10 ~ +10
652 ~ 672	31	30	-10 ~ +10
673 ~ 693	31	31	-10 ~ +10
694 ~ 714	31	32	-10 ~ +10
715 ~ 735	31	34	-10 ~ +10

6.4.3 Data Acquisition and Test Wind Speed

For each case, the measurement was repeated for at least three times, and the average values were used as final results. Each single measurement lasted for 10s with the sample frequency of 500Hz. The time-averaging method was used to analyze the data.

Although the measured segment of the model was quite stiff with its lowest frequency higher than 10Hz, small vibration of the model is inevitable if the wind speed is too high. Thus, it is important to select a proper test wind speed so that under this wind speed, the aerodynamic forces/moments on the measured segment are large enough to be measured and the vibration of the measured segment is small enough to be neglected. In this connection, pretests were carried out using three wind speeds of 10m/s, 15m/s, and 20m/s respectively. It was hard to perceive any model vibration for the wind speed of 10m/s. Only very small vibration was detected when the wind speed increased to 15m/s. When the wind speed further went up to 20m/s, small model vibration became observable. Nevertheless, the measured aerodynamic forces/moments were almost in proportion to the square of wind speed, which indicated that the measured aerodynamic coefficients were independent of wind speed used. Furthermore, no contact between the model components was perceived at all the levels of wind speeds. Finally, the mean wind speed of 15m/s was selected as the test mean wind speed $\overline{U}_m$.

6.5 Calculation of Aerodynamic Coefficients

The $\overline{xyz}$-system and the *qph*-system in Figure 6-11 represent the balance coordinates and the model coordinates, respectively. The origin of the $\overline{xyz}$-system, at which the loads measured by the balance are applied, is located at the center of the top surface of the balance. The origin of the model coordinate *qph*-system was located at the center of the measured segment. The signs e_x, e_y and e_z were used to denote the coordinates of the origin of the *qph*-system in the $\overline{xyz}$-system. The measured e_x and e_y were 0.0975m and 0.0022m, respectively, for all the test cases. However, the

coordinate e_z varied with the test case because it was the function of the model end angle β_m.

$$e_z = 0.205 \tan \beta_m - 0.022 \tag{6-3}$$

The aerodynamic coefficients of the oblique section model are defined with respect to the wind coordinates $\overline{qph}$-system, as shown in Figure 6-3. Therefore, the aerodynamic forces and moments directly measured by the balance should be transferred to those with respect to the wind coordinates $\overline{qph}$-system using the following equation.

$$\left(C_{\bar{q}}, D_{\bar{p}}, L_{\bar{h}}, M_{\bar{\alpha}}, M_{\bar{\gamma}}, M_{\bar{\phi}}\right)^{\mathrm{T}} = \mathbf{T}_{L\bar{w}Bl}\left(F_{\bar{x}}, F_{\bar{y}}, F_{\bar{z}}, M_{\bar{x}}, M_{\bar{y}}, M_{\bar{z}}\right)^{\mathrm{T}} \tag{6-4}$$

where, as shown in Figure 6-3, $C_{\bar{q}}$, $D_{\bar{p}}$ and $L_{\bar{h}}$ are the horizontal crosswind force, drag force, and lift force along the axes $\bar{q}$, $\bar{p}$ and $\bar{h}$ of the wind coordinates respectively. $M_{\bar{\alpha}}$, $M_{\bar{\gamma}}$ and $M_{\bar{\phi}}$ are the pitching, rolling and yawing moments around the axes $\bar{q}$, $\bar{p}$ and $\bar{h}$, respectively. $F_{\bar{x}}, F_{\bar{y}}$, $F_{\bar{z}}$, $M_{\bar{x}}$, $M_{\bar{y}}$ and $M_{\bar{z}}$ were three aerodynamic forces and three aerodynamic moments directly measured by the balance. The matrix $\mathbf{T}_{L\bar{w}Bl}$ is the transformation matrix from the balance coordinates $\overline{xyz}$ to the wind coordinates $\overline{qph}$, which can be expressed as

$$\mathbf{T}_{L\bar{w}BL} = \mathbf{T}_{L\bar{w}Lr} \times \begin{bmatrix} 0 & 0 & -1 & 0 & 0 & 0 \\ 1 & 0 & 0 & 0 & 0 & 0 \\ 0 & -1 & 0 & 0 & 0 & 0 \\ -e_y & e_x & 0 & 0 & 0 & -1 \\ 0 & e_z & -e_y & 1 & 0 & 0 \\ e_z & 0 & -e_x & 0 & -1 & 0 \end{bmatrix}$$

$$= \begin{bmatrix} \sin\bar{\beta} & 0 \\ \cos\bar{\theta}\cos\bar{\beta} & -\sin\bar{\theta} \\ -\sin\bar{\theta}\cos\bar{\beta} & -\cos\bar{\theta} \\ -e_y\cos\bar{\beta} & e_x\cos\bar{\beta} + e_z\sin\bar{\beta} \\ e_y\cos\bar{\theta}\sin\bar{\beta} + e_z\sin\bar{\theta} & -e_x\cos\bar{\theta}\sin\bar{\beta} + e_z\cos\bar{\theta}\cos\bar{\beta} \\ -e_y\sin\bar{\theta}\sin\bar{\beta} + e_z\cos\bar{\theta} & e_x\sin\bar{\theta}\sin\bar{\beta} - e_z\sin\bar{\theta}\cos\bar{\beta} \end{bmatrix}$$

$$\begin{bmatrix} -\cos\bar{\beta} & 0 & 0 & 0 \\ \cos\bar{\theta}\sin\bar{\beta} & 0 & 0 & 0 \\ -\sin\bar{\theta}\sin\bar{\beta} & 0 & 0 & 0 \\ -e_y\sin\bar{\beta} & \sin\bar{\beta} & 0 & -\cos\bar{\beta} \\ -e_y\cos\bar{\theta}\cos\bar{\beta}-e_x\sin\bar{\theta} & \cos\bar{\theta}\cos\bar{\beta} & -\sin\bar{\theta} & \cos\bar{\theta}\sin\bar{\beta} \\ e_y\sin\bar{\theta}\cos\bar{\beta}-e_x\cos\bar{\theta} & -\sin\bar{\theta}\cos\bar{\beta} & -\cos\bar{\theta} & -\sin\bar{\theta}\sin\bar{\beta} \end{bmatrix} \quad (6\text{-}5)$$

where, the matrix $\mathbf{T}_{L\bar{w}Lr}$ is the transformation matrix from the model coordinate *qph*-system to the wind coordinate $\bar{q}\bar{p}\bar{h}$ -system.

$$\mathbf{T}_{L\bar{w}Lr} = \begin{bmatrix} \mathbf{T}^0_{L\bar{w}Lr} & 0 \\ 0 & \mathbf{T}^0_{L\bar{w}Lr} \end{bmatrix} \quad (6\text{-}6)$$

$$\mathbf{T}^0_{L\bar{w}Lr} = \begin{bmatrix} \cos\bar{\beta} & \sin\bar{\beta} & 0 \\ -\cos\bar{\theta}\sin\bar{\beta} & \cos\bar{\theta}\cos\bar{\beta} & \sin\bar{\theta} \\ \sin\bar{\theta}\sin\bar{\beta} & -\sin\bar{\theta}\cos\bar{\beta} & \cos\bar{\theta} \end{bmatrix} \quad (6\text{-}7)$$

Finally, the aerodynamic coefficients of crosswind force, drag force, lift force, pitching moment, rolling moment, and yawing moment pertaining to the wind coordinate can be determined by

$$\left(C_{C_{\bar{q}}}, C_{D_{\bar{p}}}, C_{L_{\bar{h}}}, C_{M_{\bar{\alpha}}}, C_{M_{\bar{\gamma}}}, C_{M_{\bar{\phi}}}\right)^{\mathrm{T}} = \frac{2}{\rho\bar{U}_m^2 B_m^2 L_m}\left(B_m C_{\bar{q}}, B_m D_{\bar{p}}, B_m L_{\bar{h}}, M_{\bar{\alpha}}, M_{\bar{\gamma}}, M_{\bar{\phi}}\right)^{\mathrm{T}} \quad (6\text{-}8)$$

In this study, $B_m = 0.41\mathrm{m}$ is the width of model deck. $L_m = 1.060\mathrm{m}$ is the length of the measured segment of the model. $\rho = 1.225\mathrm{kg/m^3}$ is the air density. $\bar{U}_m = 15.0\mathrm{m/s}$ is the test wind speed. The wind tunnel tests were carried out only for positive yaw angles but the aerodynamic coefficients for the negative yaw angles could be obtained from those for positive yaw angles in terms of the principle of symmetry/asymmetry.

$$\left(C_{C_{\bar{q}}}, C_{D_{\bar{p}}}, C_{L_{\bar{h}}}, C_{M_{\bar{\alpha}}}, C_{M_{\bar{\gamma}}}, C_{M_{\bar{\phi}}}\right)^{\mathrm{T}}_{\bar{\beta}<0} = \left(-C_{C_{\bar{q}}}, C_{D_{\bar{p}}}, C_{L_{\bar{h}}}, C_{M_{\bar{\alpha}}}, -C_{M_{\bar{\gamma}}}, -C_{M_{\bar{\phi}}}\right)^{\mathrm{T}}_{\bar{\beta}>0} \quad (6\text{-}9)$$

6.6 MEASUREMENT RESULTS

In this section, the measurement data are first analyzed to ascertain the effects of model end angle distortion on the aerodynamic force and moment coefficients of the deck sectional model. The measurement data are then selected and grouped to form two databases: one for lift force, drag force, and pitching moment coefficients; and the other for crosswind force, rolling moment, and yawing moment coefficients. The interpolation and the curve fitting technique are finally employed on each database to generate the curves of six aerodynamic coefficients as functions of both mean wind inclination and yaw angle. Some discussion and comments are provided on the fitted curves of six aerodynamic coefficients of the Tsing Ma suspension bridge deck.

6.6.1 Effects of Model End Angle Distortion

To ascertain the effects of model end angle distortion, the six aerodynamic coefficients of the deck section model measured under skew winds with the same mean wind yaw angle and model end angle (5°, 13°, 20° or 31°) are compared with those under the same mean wind yaw angle but with the 0° model end angle. The comparative results are plotted in Figures 6-13 to 6-16. It is seen that the effects of model end angle on the lift and drag force coefficients are very small for all the concerned inclination angles from +10° to - 10°, even when the distortion of model end angle reaches 31°. For the pitching moment coefficients, the effects of model end angle are very small when the distortion of model end angle is less than 13° but the effects become evident with further increasing distortion of model end angle.

The values of crosswind force, rolling moment, and yawing moment coefficients are much smaller than the other three coefficients within the concerned ranges of both mean wind inclination and yaw angle. These three aerodynamic coefficients are sensitive to the distortion of model end angle, in particular the rolling moment and yawing moment coefficients.

Further examination of the effects of model end angle is performed using another five cases, each of which concerns two model end angles but one wind yaw angle between the two model end angles. These five cases are listed as (1) $\bar{\beta}=8°, \beta_m=5°$ vs. $\bar{\beta}=8°, \beta_m=13°$; (2) $\bar{\beta}=10°, \beta_m=5°$ vs. $\bar{\beta}=10°, \beta_m=13°$

(3) $\bar{\beta}=16°, \beta_m=13°$ vs. $\bar{\beta}=16°, \beta_m=20°$; (4) $\bar{\beta}=17°, \beta_m=13°$ vs. $\bar{\beta}=17°, \beta_m=20°$ and (5) $\bar{\beta}=25°, \beta_m=20°$ vs. $\bar{\beta}=25°, \beta_m=31°$, and the results are plotted in Figures 6-17 to 6-21. It is noted that the selected five cases include the maximum distortion of model end angle, 6°, in this investigation. The same conclusions can be drawn from these five cases as the four cases discussed before. That is, the effects of model end angle distortion on lift force, drag force, and pitching moment coefficients are very small. However, there are moderate effects on crosswind force coefficients, and significant effects on rolling moment and yawing moment coefficients.

6.6.2 Data Interpolation and Fitting

Since the effects of model end angle on lift force, drag force, and pitching moment coefficients are very small, the relevant data from the test cases 85 to 735 are used to form one database. In this database, the data from the overlapping case with the same wind yaw angle but different model end angles are first averaged and then stored into the database. In consideration that the effects of model end angle on crosswind force, rolling moment, and yawing moment coefficients are significant, only the data from the test cases without any model end angle distortion are used to form the second database. Clearly, the sample number in the second database is much smaller than that in the first database. The spline interpolation and the polynomial fitting are then applied to the first database to obtain the design curves of lift force, drag force, and pitching moment coefficients as functions of both mean wind inclination and yaw angle, and to the second database to obtain the design curves of crosswind force, rolling moment, and yawing moment coefficients.

The design curves for the bridge deck under yaw angles of 8°, 10°, 16°, 17° and 25° are plotted in Figure 6-17 to Figure 6-21 and compared with the measured data. Most of the design curves lie, as expected, between the two sets of measured data. For the crosswind force coefficient, the design curve somehow is located outside the two sets of measured data. This may be attributed to the lack of the relevant samples in the second database.

6.6.3 Main Features of Aerodynamic Coefficients

Figure 6-22 shows the 3D plots of the six aerodynamic coefficients as functions of mean wind inclination and yaw angle. It can be seen that, compared to the other three coefficients, the values of crosswind force, rolling moment, and yawing moment coefficients are much smaller even for a large yaw angle of 31°. The drag force coefficients are always positive.

To explore the main features of six aerodynamic coefficients, Figure 6-23 displays variations of six aerodynamic coefficients with yaw angle in the wind coordinates. It is seen that at zero yaw angle, the crosswind force, rolling moment, and yawing moment coefficients are all equal to zero while the slopes of lift force, drag force, and pitching moment coefficients are zero. This is because for a straight deck with uniform cross section, the former three coefficients are asymmetric about the zero yaw angle and the latter three coefficients are symmetric with respect to the zero yaw angle.

Relatively speaking, the variation of lift force coefficient with yaw angle is small for the angle of inclination less than 5°, indicating that the mean lift force on the bridge deck is hardly affected by mean wind yaw angle. The value of drag force coefficient, however, decreases with increasing yaw angle for all the concerned angles of inclination whereas the value of pitching moment increases with increasing yaw angle for the angle of inclination less than 10°. The variation of the crosswind force coefficient with yaw angle is similar to that of the yawing moment coefficient, which is not monotonic. There are rapid changes for the yaw angles within 5° to 15°. The variation of rolling moment coefficient with yaw angle depends on the angle of inclination as shown in Figure 6-23e.

Figure 6-24 depicts variations of six aerodynamic coefficients with the angle of inclination for a series of yaw angles. It is seen that with the increase of wind inclination, the lift force coefficient grows from negative to positive whilst the pitching moment coefficient goes down from positive to negative according to the sign convention set in this investigation. The drag force coefficient is always positive and attains the minimum value in the inclination range between 2.0° and 3.0° for all the concerned yaw angles. The slopes of drag coefficient curves are negative up to

the inclination of 2.0° and 3.0° and then become positive. Within the inclination range from –7.0° to 7.0°, the crosswind force coefficient decreases monotonically for all the concerned yaw angles. For yaw angles greater than 10°, the rolling moment coefficient decreases from positive value to negative value with the increase of inclination angle. When the yaw angle is less than 15°, the yawing moment coefficient becomes small as the inclination grows up. However, when the yaw angle ranges from 20° to 35°, the yawing moment coefficient curve has a maximum value around 0°. Both the rolling and yawing moment coefficients are very small when the yaw angle is less than 5°.

The six aerodynamic coefficients obtained above will be used in Chapters 9 and 10 for determining the buffeting response of the Tsing Ma suspension Bridge during Typhoon Sam and for performing a comparison of the bridge buffeting response between the field measurement and analysis, where the effects of skew winds on the buffeting response of the Tsing Ma Bridge will be demonstrated.

6.7 DISCUSSION ON COSINE RULE

In the traditional buffeting analysis of a bridge under a yaw wind, the yaw wind is often handled using the so-called "cosine rule". In the cosine rule, the yaw wind is decomposed into two perpendicular components: one is normal to the bridge longitudinal axis and the other is parallel to the bridge longitudinal axis. The parallel component is then ignored and the normal wind component is used in conjunction with the aerodynamic coefficients of true cross section obtained from the conventional rectangular sectional model tests. This approximation implies the following assumption.

$$\left(C_{C_q}, C_{D_p}, C_{L_h}, C_{M_\alpha}, C_{M_\gamma}, C_{M_\phi}\right)^{\mathrm{T}}_{(\bar{\beta},\bar{\theta})} = \left(C_{C_q}, C_{D_p}, C_{L_h}, C_{M_\alpha}, C_{M_\gamma}, C_{M_\phi}\right)^{\mathrm{T}}_{(0,\bar{\theta})} \cos^2\bar{\beta} \quad (6\text{-}10)$$

where, C_{C_q}, C_{D_p} and C_{L_h} are, respectively, the coefficients of aerodynamic force along the three axes q, p and h of the model qph-coordinate system; C_{M_α}, C_{M_γ} and C_{M_ϕ} are, respectively, the coefficients of aerodynamic moments around the three axes q, p and h. Because C_{C_q}, C_{M_γ} and C_{M_ϕ} are equal to zero at zero yaw angle,

Equation (6-10) indicates that these three coefficients are zero for any yaw angle and they are always neglected in the traditional buffeting analysis.

The six aerodynamic coefficients of oblique cross section obtained from the oblique sectional model with reference to the wind $\overline{qph}$-coordinate system in this study can be transformed to those with respect to the model *qph*-coordinate system using the following equation.

$$\left(C_{C_q}, C_{D_p}, C_{L_h}, C_{M_\alpha}, C_{M_\gamma}, C_{M_\phi}\right)^{\mathrm{T}}_{(\bar{\beta},\bar{\theta})} = \mathbf{T}_{Lr\bar{L}\bar{w}} \left(C_{C_{\bar{q}}}, C_{D_{\bar{p}}}, C_{L_{\bar{h}}}, C_{M_{\bar{\alpha}}}, C_{M_{\bar{\gamma}}}, C_{M_{\bar{\phi}}}\right)^{\mathrm{T}}_{(\bar{\beta},\bar{\theta})} \quad (6\text{-}11)$$

where $\mathbf{T}_{Lr\bar{L}\bar{w}} = \mathbf{T}^{\mathrm{T}}_{\bar{L}\bar{w}Lr}$. The transformed results are plotted in Figures 6-25. Clearly, it is seen from Figure 6-25 that the aerodynamic coefficients, C_{C_q}, C_{M_γ}, C_{M_ϕ}, with respect to the model *qph*-coordinate system are generally not zero for the non-zero yaw angle, as assumed in the cosine rule. They become noticeably large for larger yaw angles, which may have to be taken into account in the buffeting analysis of the bridge under yaw winds. To have a clear comparison of the aerodynamic coefficients, C_{D_p}, C_{L_h}, and C_{M_α} between the cosine rule and the measurement, three coefficient ratios R_{D_p}, R_{L_h}, R_{M_α} are defined as follows:

$$R_{D_p}(\bar{\beta},\bar{\theta}) = C_{D_p}(\bar{\beta},\bar{\theta}) / [C_{D_p}(0,\bar{\theta})\cos^2\bar{\beta}] \quad (6\text{-}12)$$

$$R_{L_h}(\bar{\beta},\bar{\theta}) = C_{L_h}(\bar{\beta},\bar{\theta}) / [C_{L_h}(0,\bar{\theta})\cos^2\bar{\beta}] \quad (6\text{-}13)$$

$$R_{M_\alpha}(\bar{\beta},\bar{\theta}) = C_{M_\alpha}(\bar{\beta},\bar{\theta}) / [C_{M_\alpha}(0,\bar{\theta})\cos^2\bar{\beta}] \quad (6\text{-}14)$$

These coefficient ratios are plotted in Figure 6-26. In light of cosine rule, these ratios are supposed to be unit for any yaw angle, as indicated by Eq.(6-10). However, this is not the case for any one of the three coefficient ratios. Particularly, the coefficient ratios become quite large or quite small for large yaw angles. All these results indicate that the traditional cosine rule may not be suitable for the buffeting analysis of long span bridges under yaw winds.

6.8 SUMMARY

A wind tunnel test technique for measuring the six aerodynamic coefficients of a bridge deck under skew winds was developed. This included the design of oblique sectional models, the development of test rig and six component force balance, and

the transformation of test data. Using the proposed wind tunnel test technique, typical oblique sectional models of the Tsing Ma suspension bridge deck were tested. The six aerodynamic coefficients were measured as functions of mean wind inclination and yaw angle and then analyzed and compared with those from the cosine rule. Major conclusions can be drawn as follows:

(1) The effects of model end angle distortion on lift force, drag force, and pitching moment coefficients were very small. However, there were moderate effects on crosswind force coefficients, and significant effects on rolling moment and yawing moment coefficients. Therefore, a simpler model without adjusting its end angles may be still acceptable if only the drag force, lift force and pitching moment coefficient are concerned.

(2) The drag force, lift force, and pitching moment coefficients were much larger than the crosswind force, rolling moment, and yawing moment coefficients even for a large yaw angle of 31°.

(3) At zero yaw angle, the crosswind force, rolling moment, and yawing moment coefficients were all equal to zero while the slopes of lift force, drag force, and pitching moment coefficients were zero.

(4) The variation of lift force coefficient with yaw angle was small for the angle of inclination less than 5°. The value of drag force coefficient, however, decreased with increasing yaw angle for all the concerned angles of inclination whereas the value of pitching moment increased with increasing yaw angle for the angle of inclination less than 10°.

(5) With the increase of wind inclination, the lift force coefficient changed from negative value to positive value whilst the pitching moment coefficient went down from positive to negative. The drag force coefficient was always positive and attained the minimum value in the inclination range between 2.0° and 3.0° for all the concerned yaw angles.

(6) The coefficients of the aerodynamic force along the model axis q, and the aerodynamic moments, respectively, around the model axes p and h were not

zero for the non-zero yaw angle, as assumed in the cosine rule. They became noticeably large for larger yaw angles, which may have to be taken into account in the buffeting analysis of the bridge under yaw winds.

(7) The coefficients of the aerodynamic forces respectively along the model axes p and h, and the aerodynamic moment around the model axis did not comply with the traditional cosine rule, particularly for large yaw angle cases.

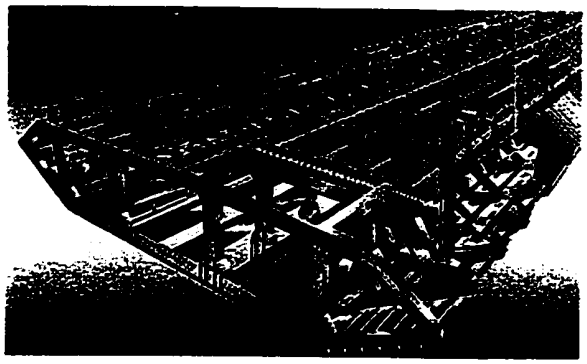

Figure 6-1 Schematic Diagram of Tsing Ma Bridge Deck

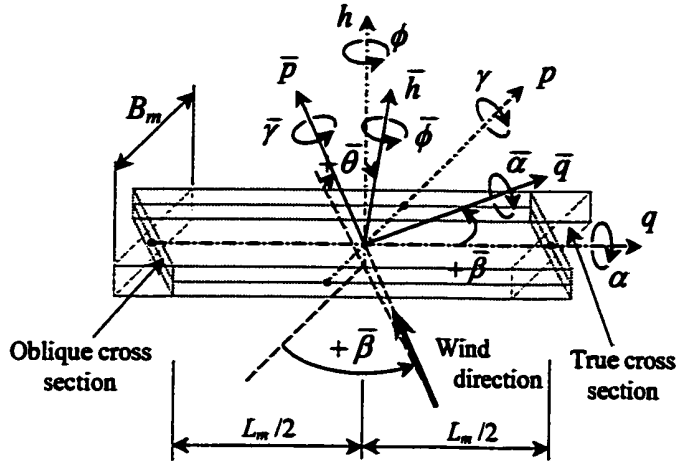

Figure 6-2 Definition of Mean Wind Inclination and Yaw Angle

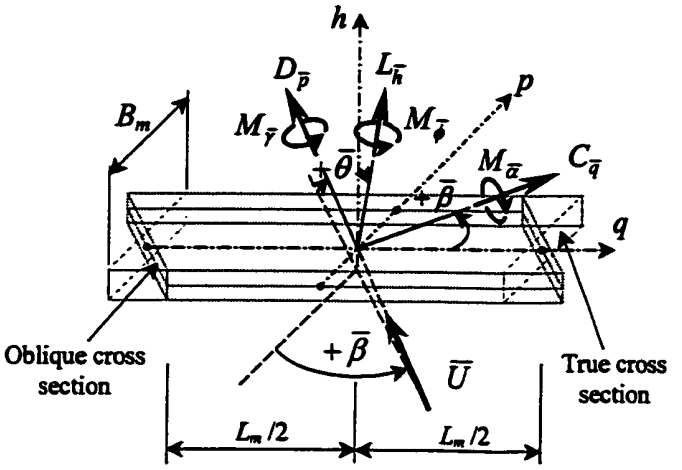

Figure 6-3 Positive Directions of Aerodynamic Forces/Moments



(a) Leeward view (b) View of deck top surface (c) View of deck bottom surface

Figure 6-4 Static Sectional Model of Tsing Ma Bridge Deck ($\bar{\beta} = 31°$, $\bar{\theta} = -10°$)

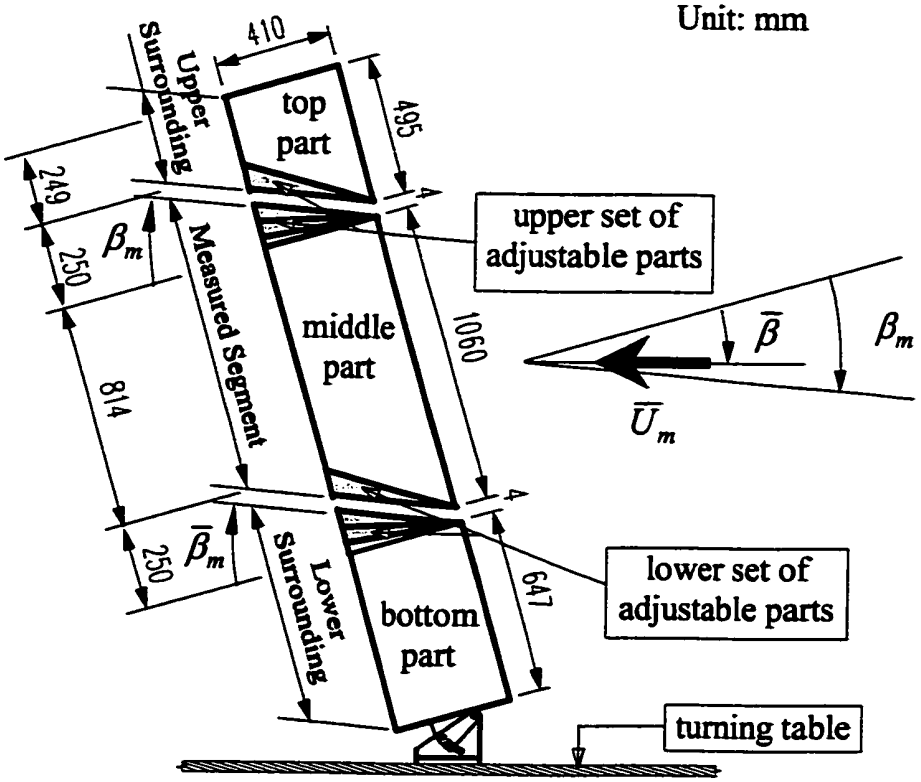

Figure 6-5 Configuration and Constitution of Static Deck Sectional Model

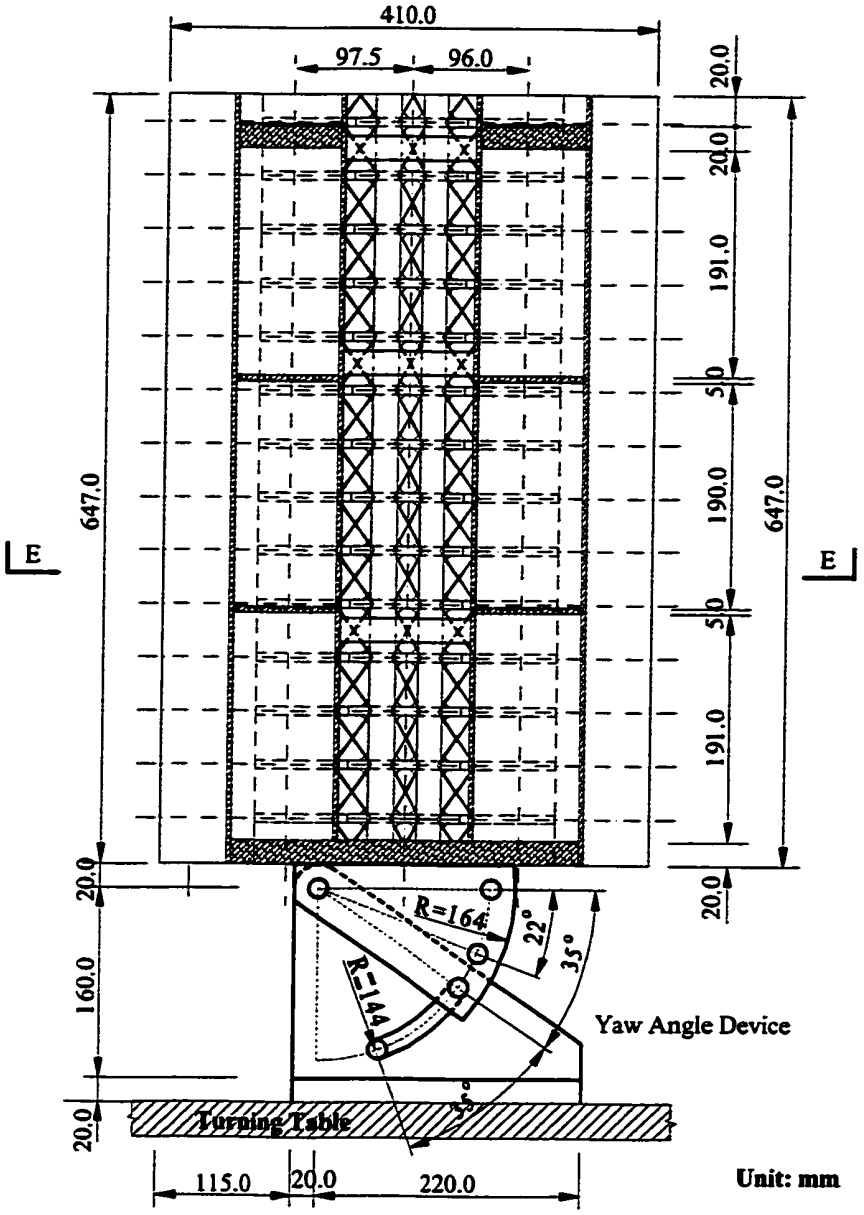

(a) bottom part and yaw angle device

Figure 6-6 Details of Static Deck Sectional Model

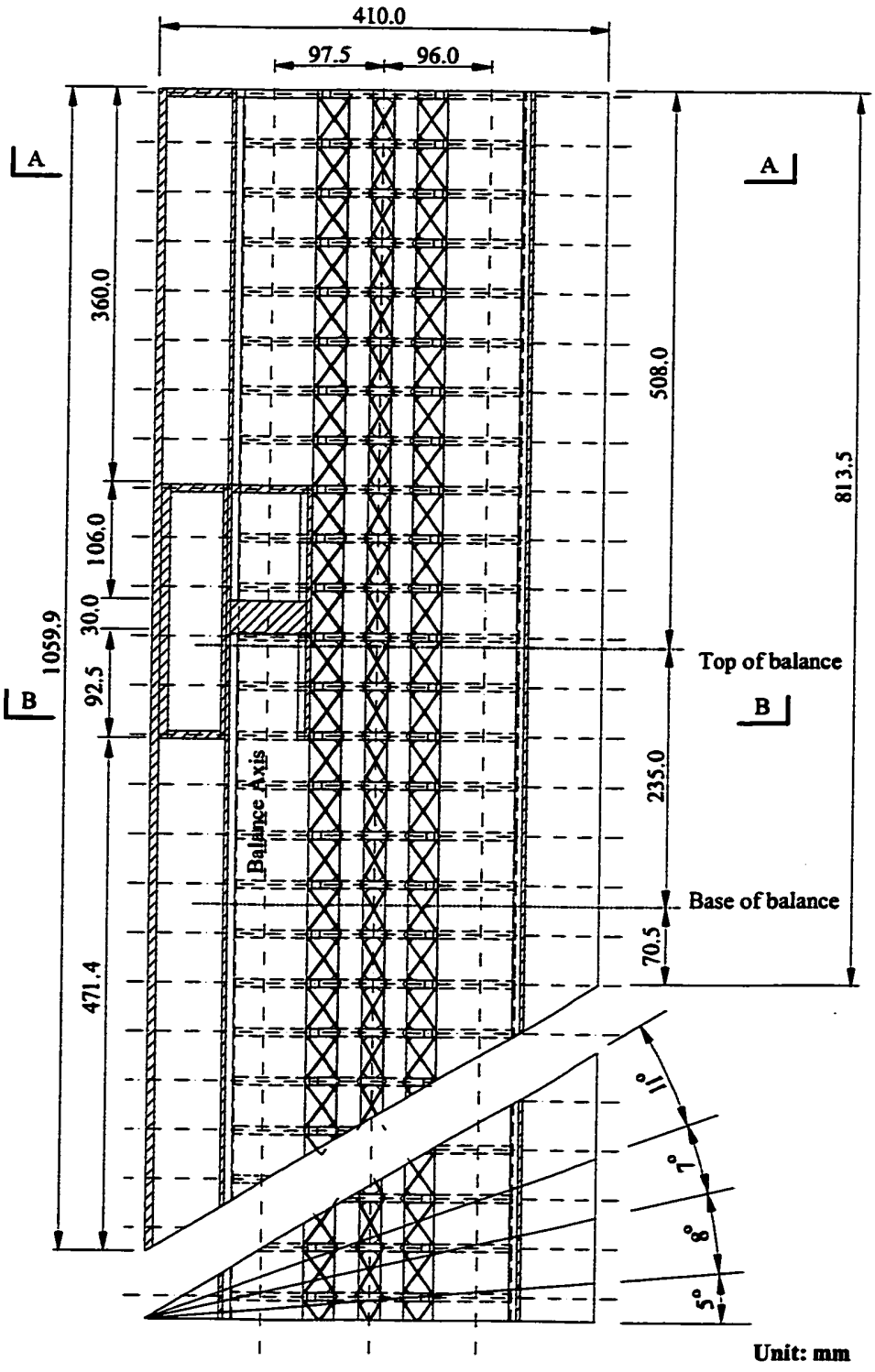

(b) Middle part and lower adjustable set

Figure 6-6 (cont.) Details of Static Deck Sectional Model

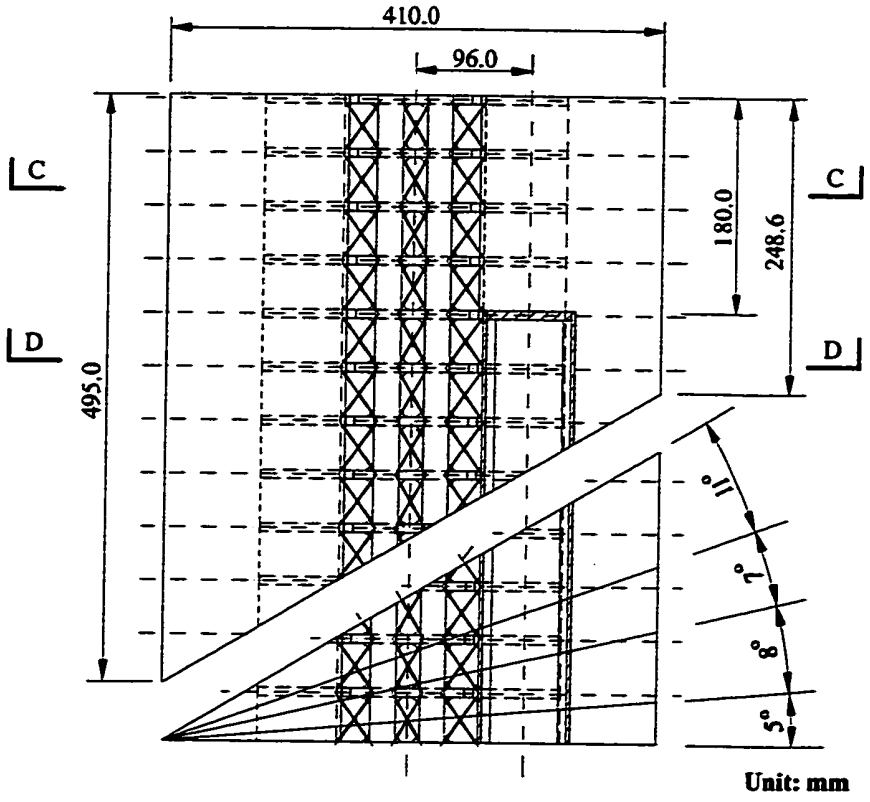

(c) Top part and upper adjustable set

Figure 6-6 (cont.) Details of Static Deck Sectional Model

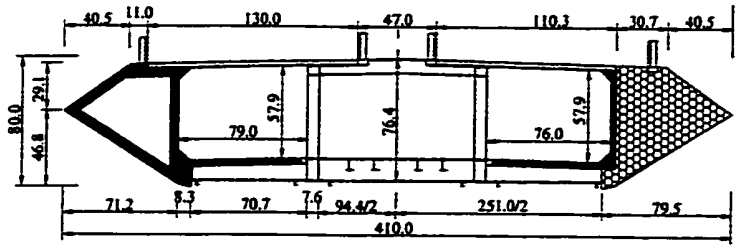

(a) Section A-A (wood; perspex; foam)

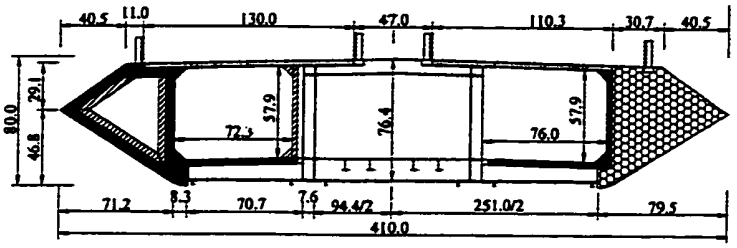

(b) Section B-B (wood; perspex; foam)

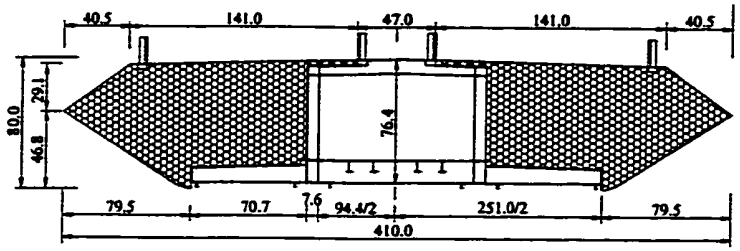

(c) Section C-C (wood; foam)

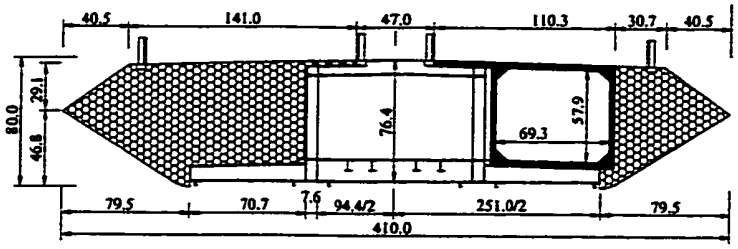

(d) Section D-D (wood; foam)

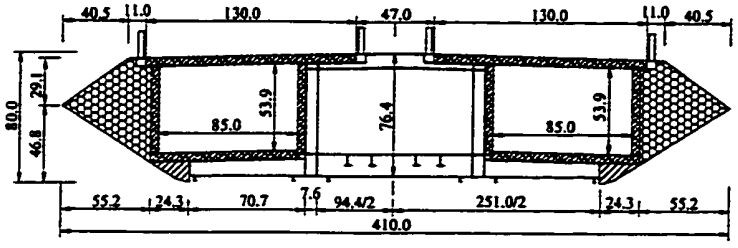

(e) Section E-E (steel; wood; foam)

Figure 6-7 Cross Sections of Static Deck Sectional Model

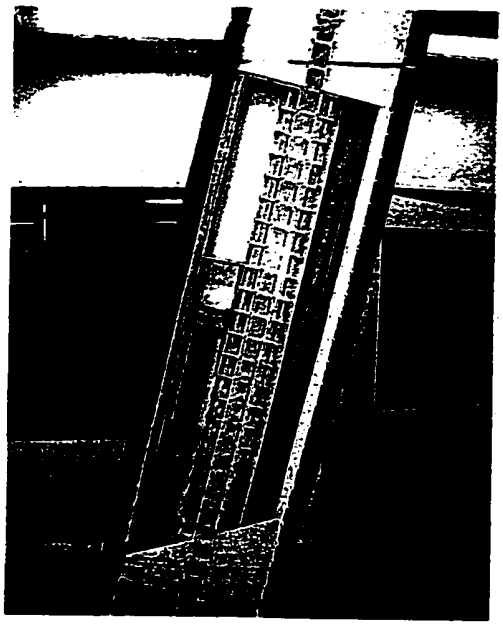

Figure 6-8 Force Balance and Steel-pipes in Model

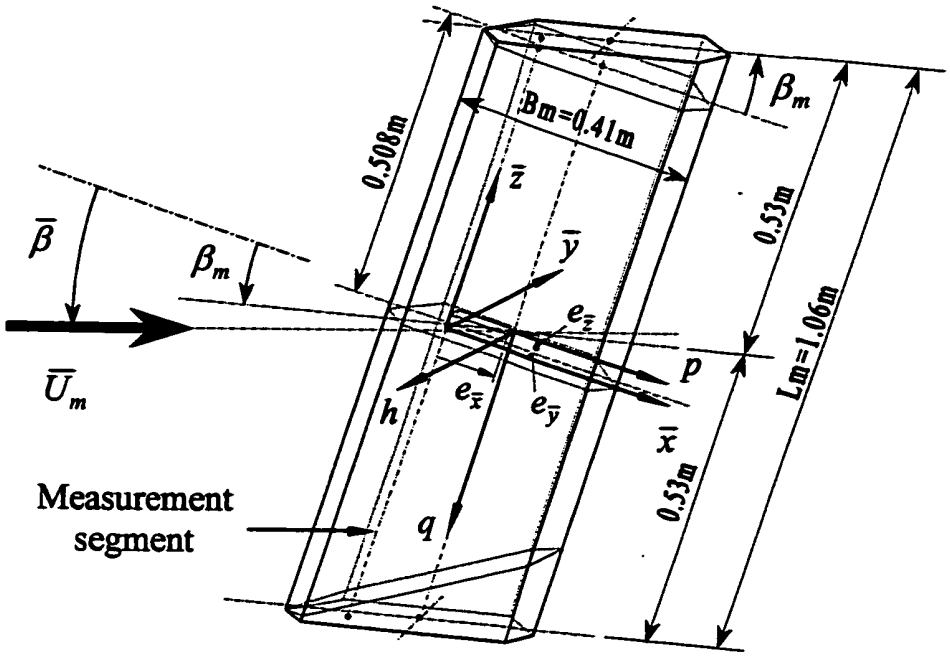

Figure 6-9 Balance Coordinates and Model Coordinates

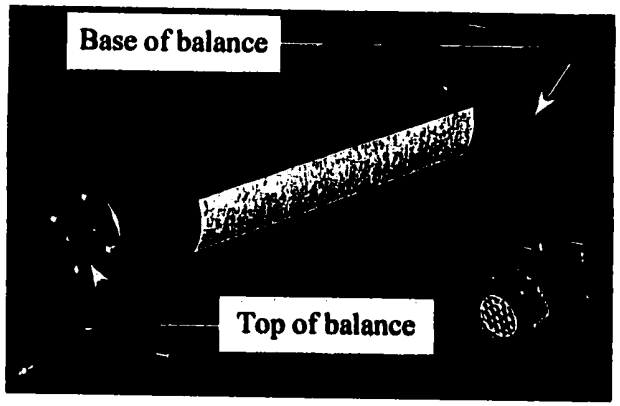

(a) Force balance of six-components

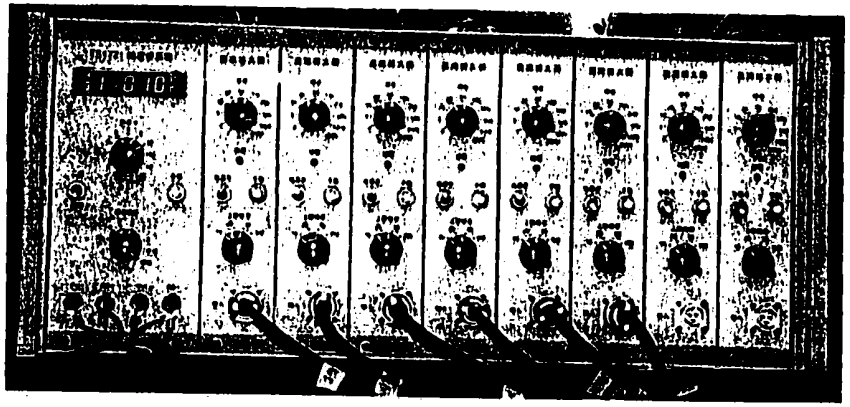

(b) Ts1721 potentiostatic DC supply and Ts3815T eight-channel DC voltage amplifier

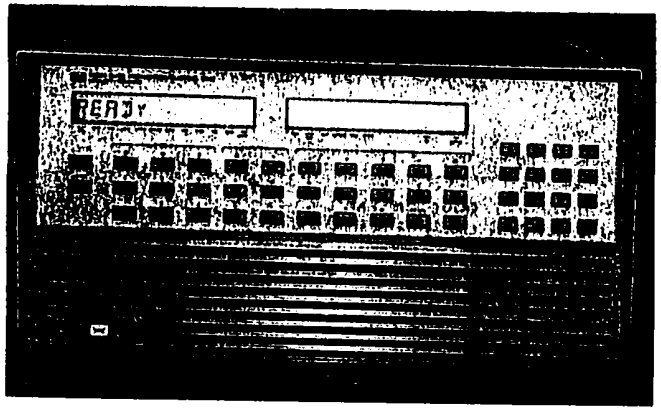

(c) HP3852A data acquisition/control unit

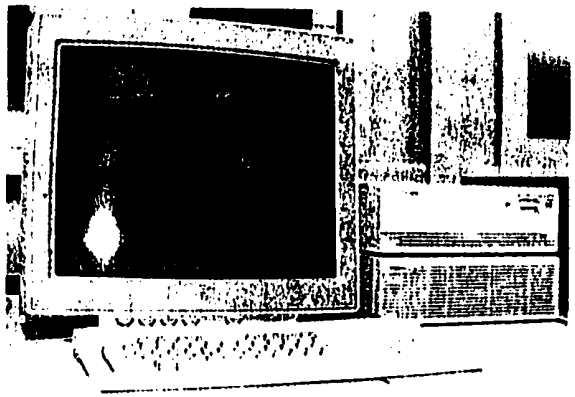

(d) HP9000-345 work station

Figure 6-10 Force/Moment Measurement System

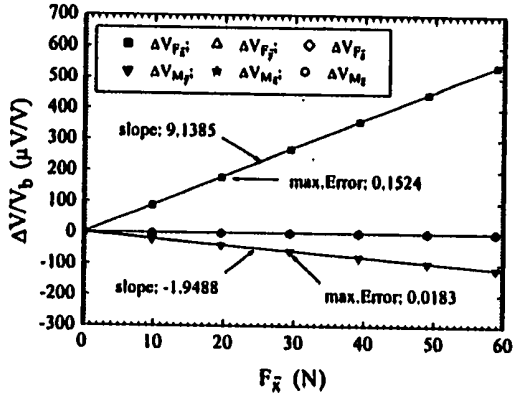

(a) Relation between $\Delta V/V_b$ and $F_{\bar{x}}$

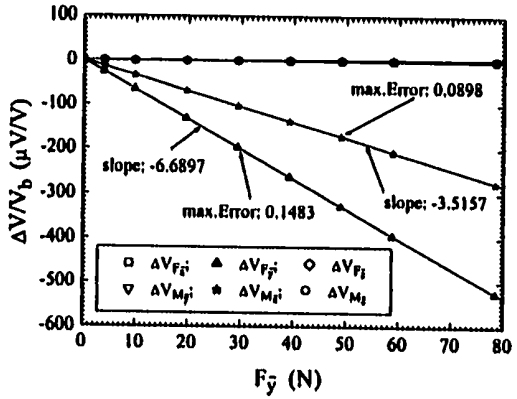

(b) Relation between $\Delta V/V_b$ and $F_{\bar{y}}$

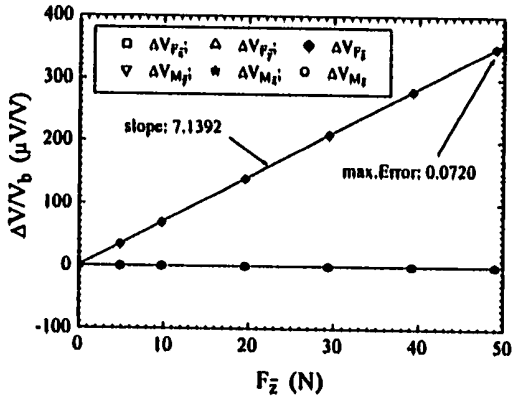

(c) Relation between $\Delta V/V_b$ and $F_{\bar{z}}$

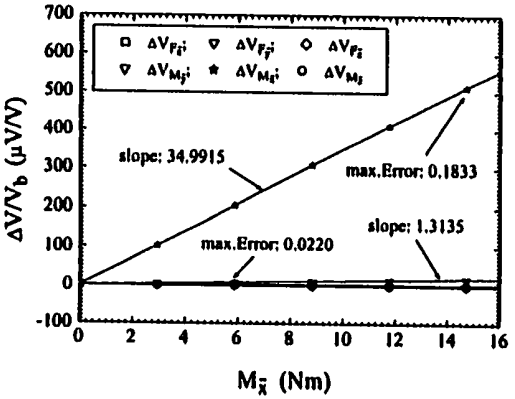

(d) Relation between $\Delta V/V_b$ and $M_{\bar{x}}$

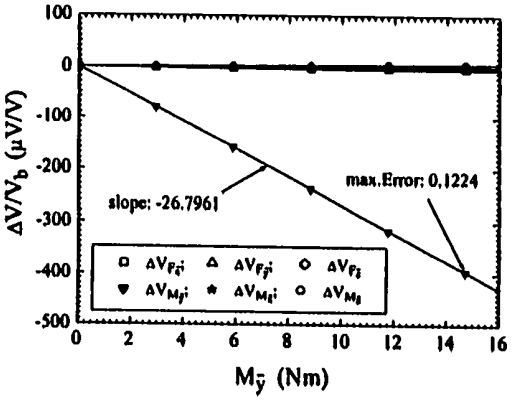

(e) Relation between $\Delta V/V_b$ and $M_{\bar{y}}$

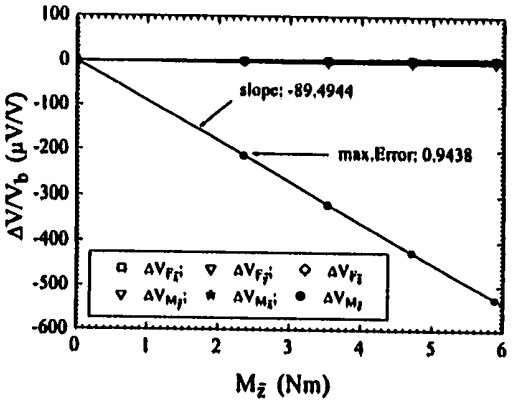

(f) Relation between $\Delta V/V_b$ and $M_{\bar{z}}$

Figure 6-11 Calibration Curves of Six-component Force Balance

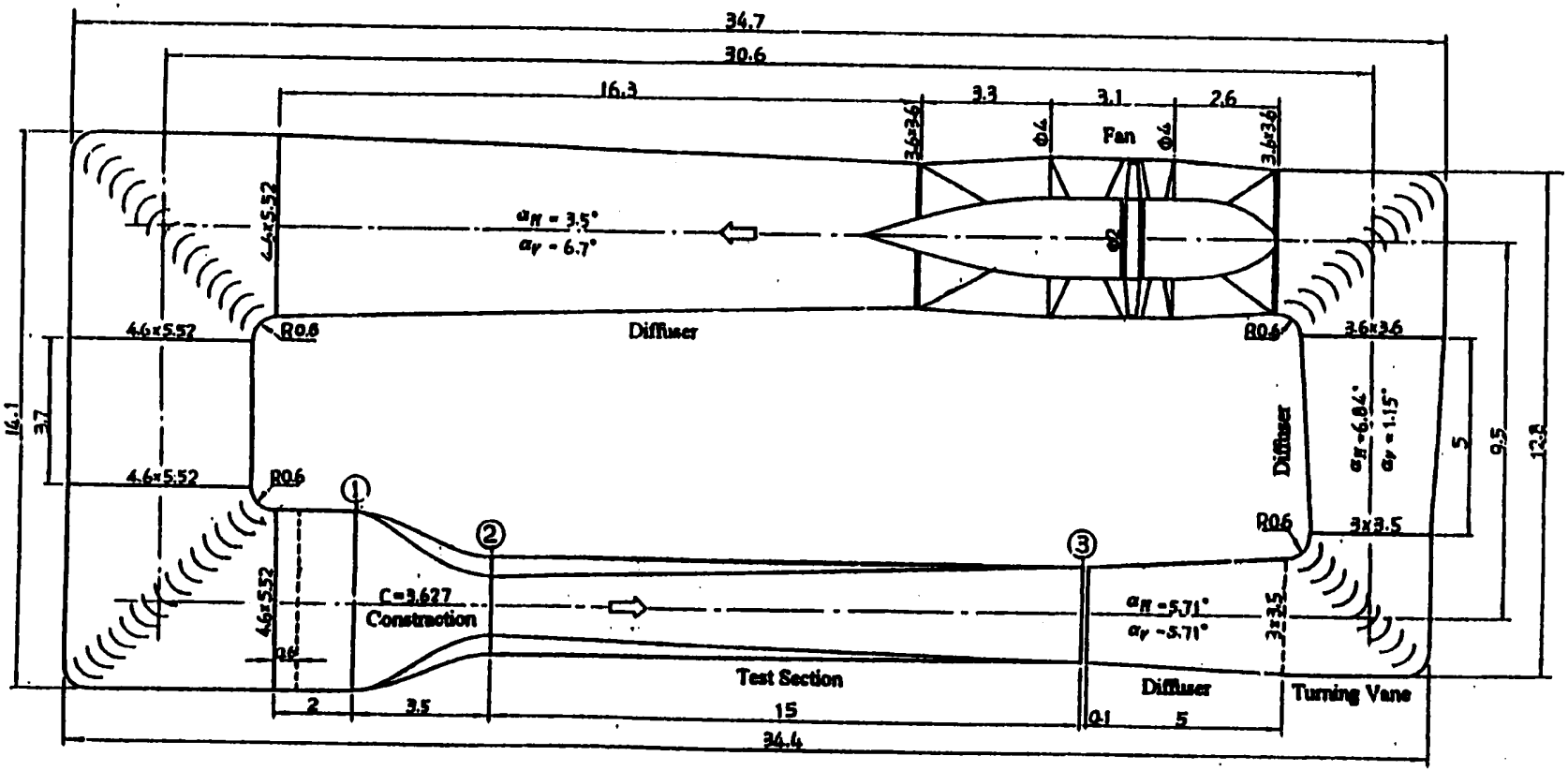

Figure 6-12 Layout of TJ-2 Boundary Layer Wind Tunnel

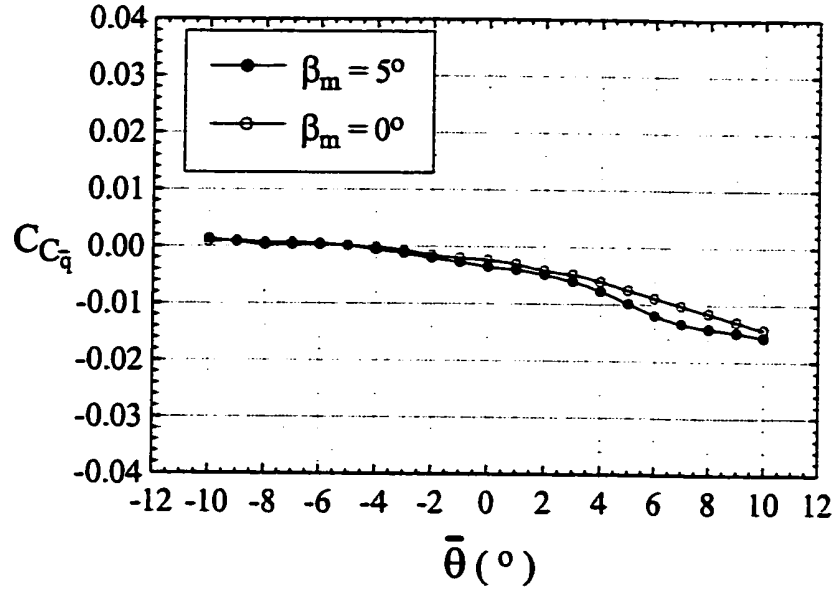

(a) Coefficient of crosswind force

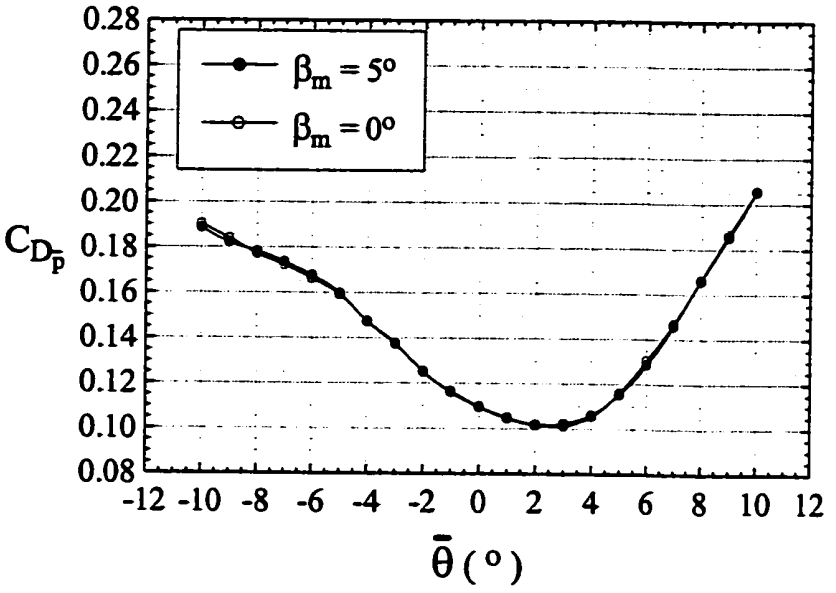

(b) Coefficient of drag force

Figure 6-13 Comparison of Aerodynamic Coefficients ($\bar{\beta} = 5°$, $\beta_m = 5°$ **vs.** $\bar{\beta} = 5°$, $\beta_m = 0°$)

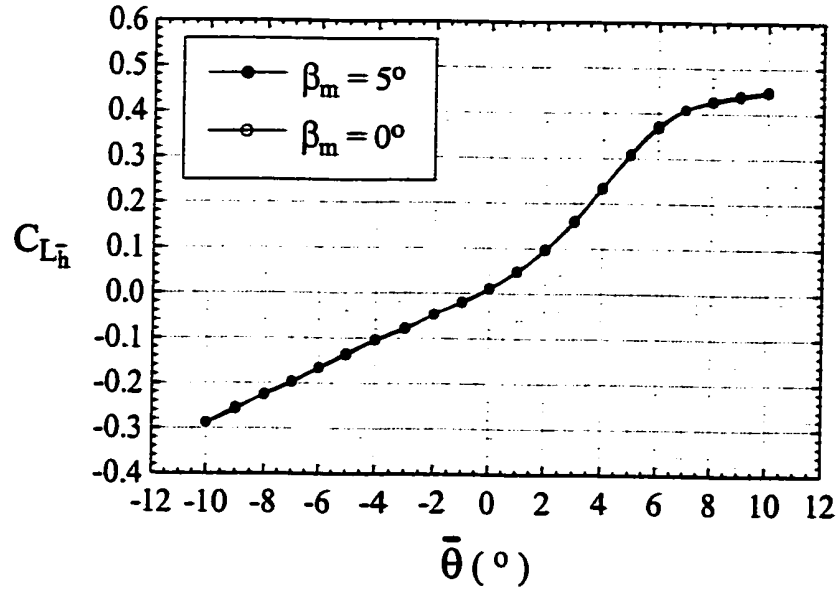

(c) Coefficient of lift force

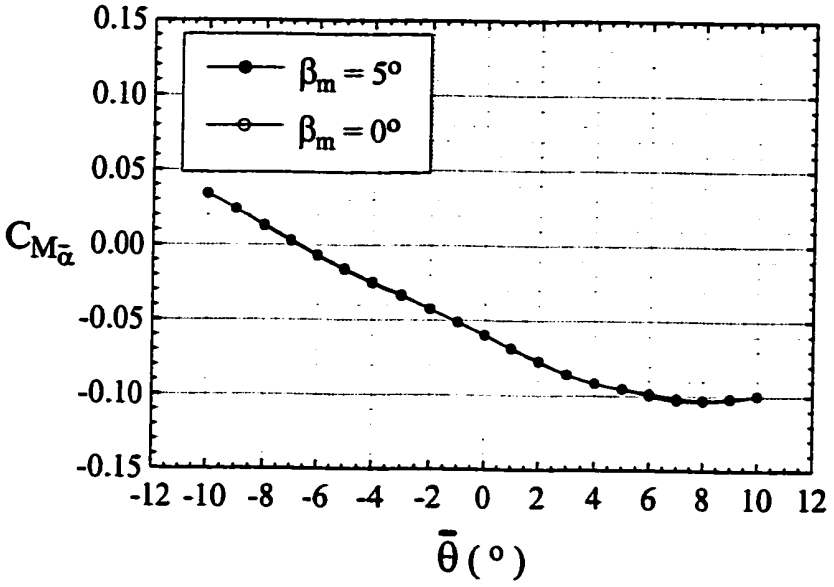

(d) Coefficient of pitching moment

Figure 6-13 (cont.) Comparison of Aerodynamic Coefficients ($\bar{\beta} = 5°$, $\beta_m = 5°$ **vs.** $\bar{\beta} = 5°$, $\beta_m = 0°$)

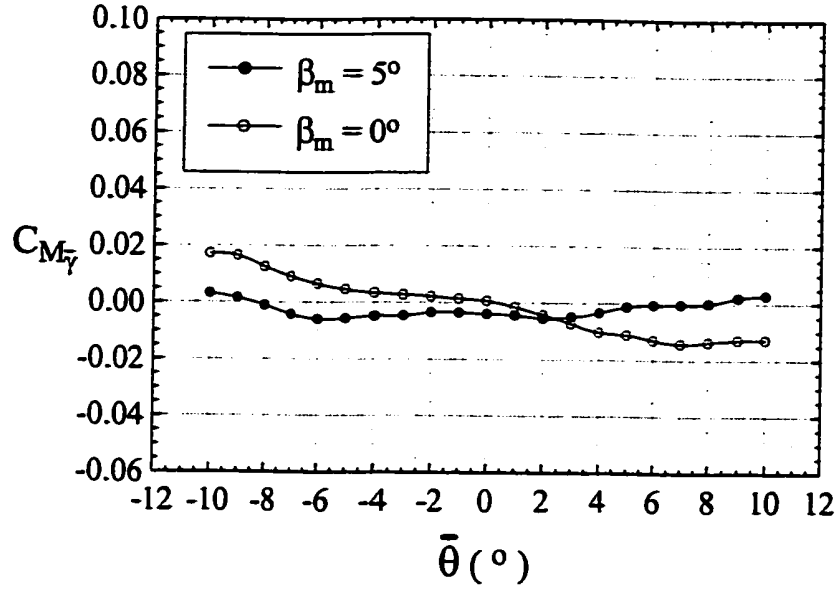

(e) Coefficient of rolling moment

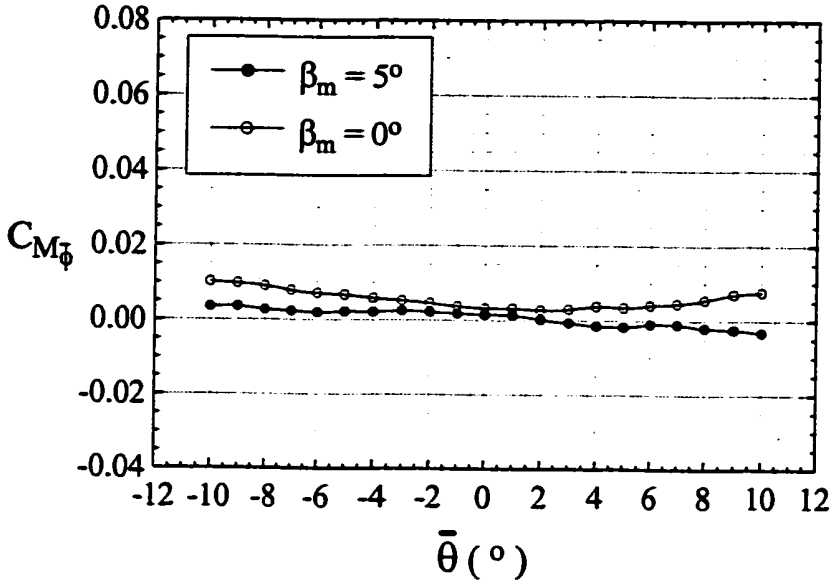

(f) Coefficient of yawing moment

Figure 6-13 (cont.) Comparison of Aerodynamic Coefficients ($\bar{\beta} = 5°$, $\beta_m = 5°$ **vs.** $\bar{\beta} = 5°$, $\beta_m = 0°$)

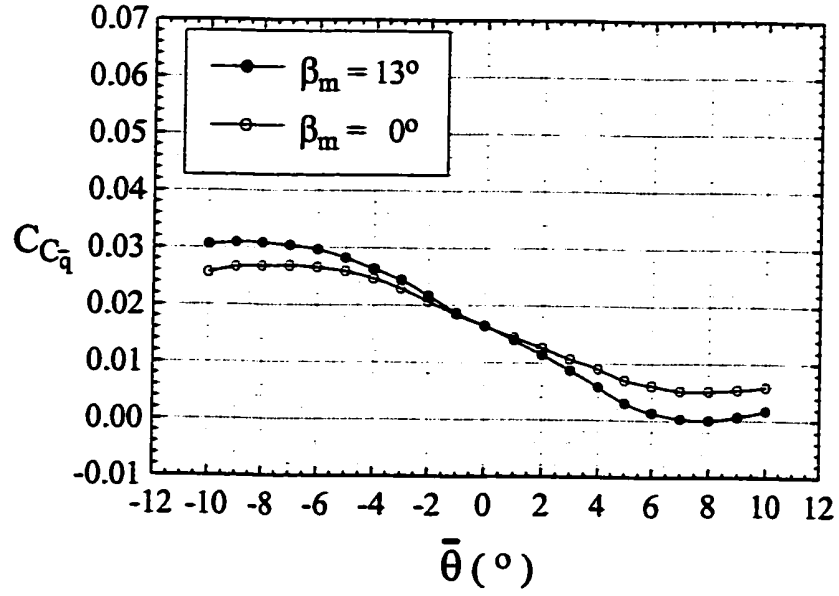

(a) Coefficient of crosswind force

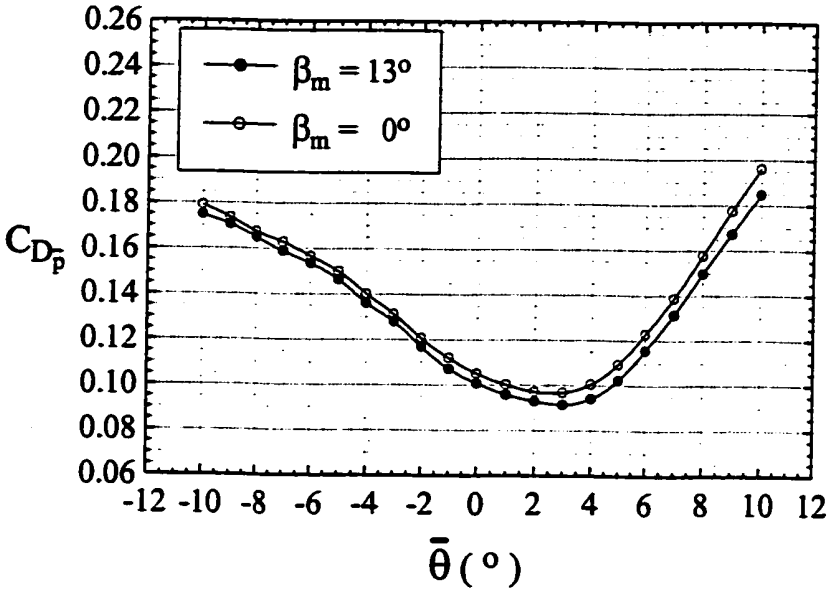

(b) Coefficient of drag force

Figure 6-14 Comparison of Aerodynamic Coefficients ($\bar{\beta} = 13°$, $\beta_m = 13°$ vs. $\bar{\beta} = 13°$, $\beta_m = 0°$)

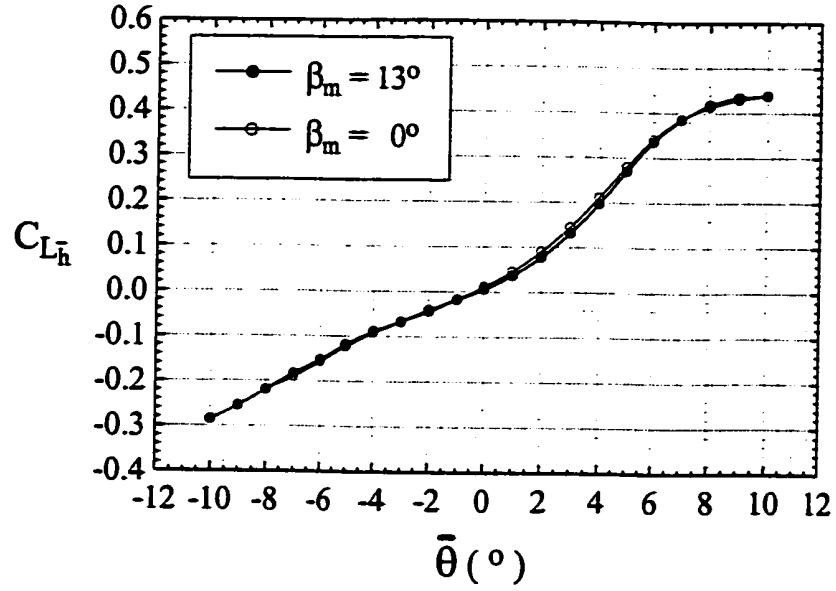

(c) Coefficient of lift force

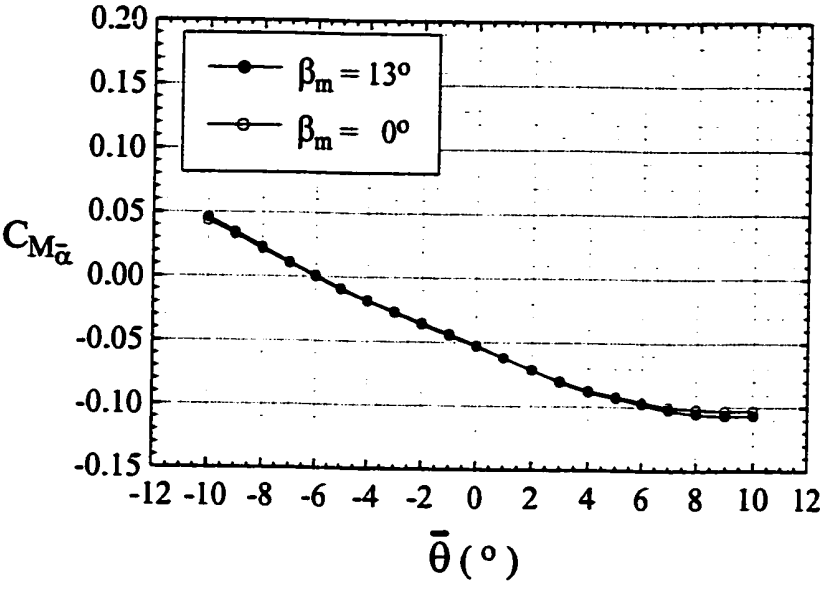

(d) Coefficient of pitching moment

Figure 6-14 (cont.) Comparison of Aerodynamic Coefficients ($\bar{\beta} = 13°$, $\beta_m = 13°$ vs. $\bar{\beta} = 13°$, $\beta_m = 0°$)

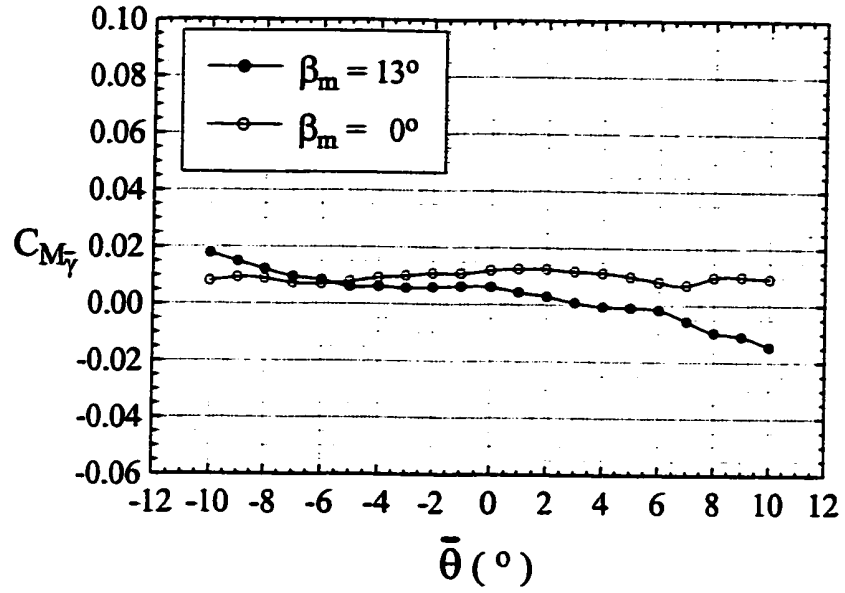

(e) Coefficient of rolling moment

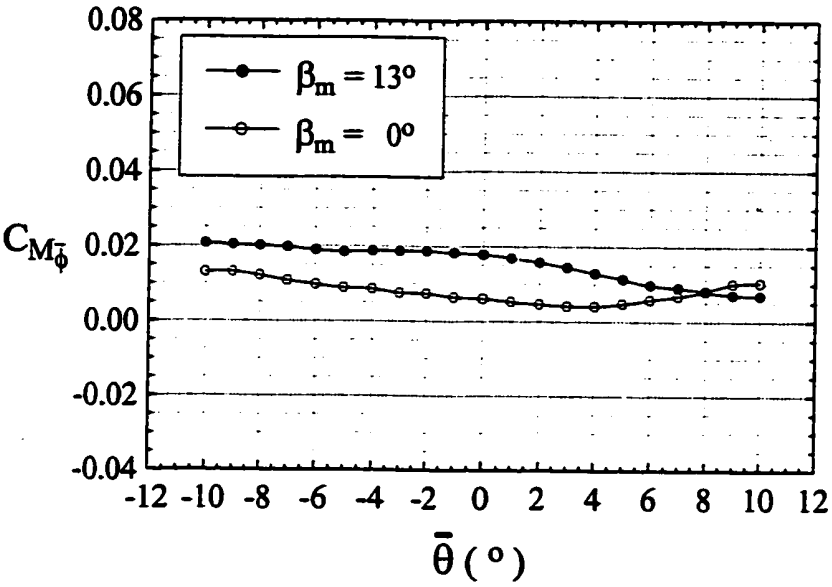

(f) Coefficient of yawing moment

Figure 6-14 (cont.) Comparison of Aerodynamic Coefficients ($\bar{\beta} = 13°$, $\beta_m = 13°$ vs. $\bar{\beta} = 13°$, $\beta_m = 0°$)

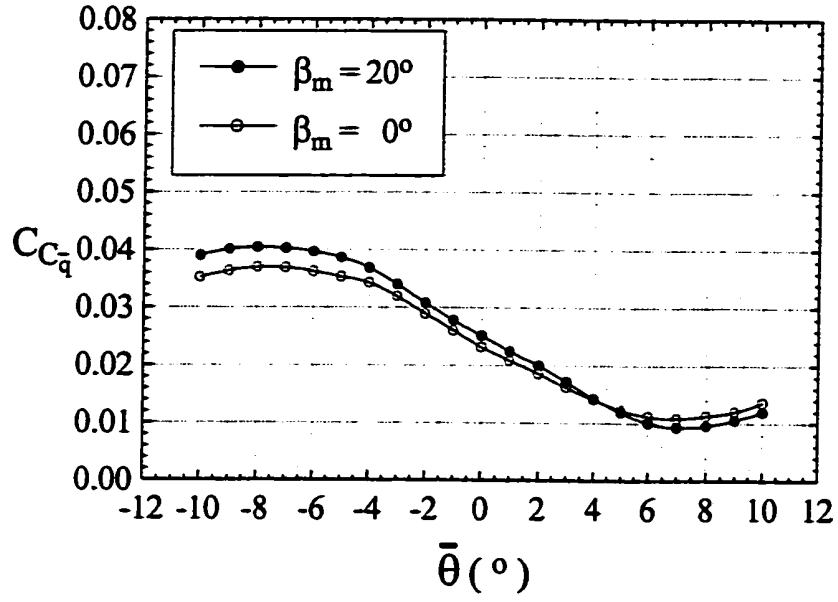

(a) Coefficient of crosswind force

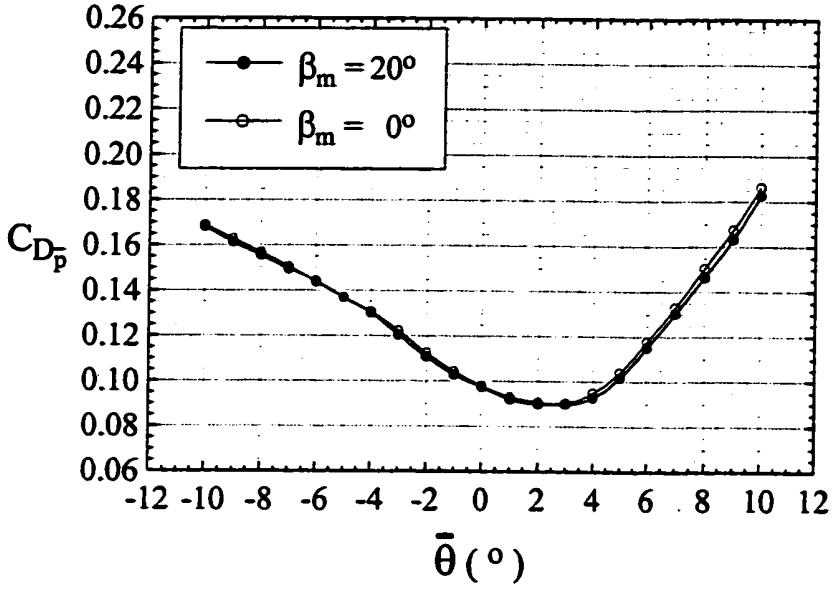

(b) Coefficient of drag force

Figure 6-15 Comparison of Aerodynamic Coefficients ($\bar{\beta} = 20°$, $\beta_m = 20°$ **vs.** $\bar{\beta} = 20°$, $\beta_m = 0°$)

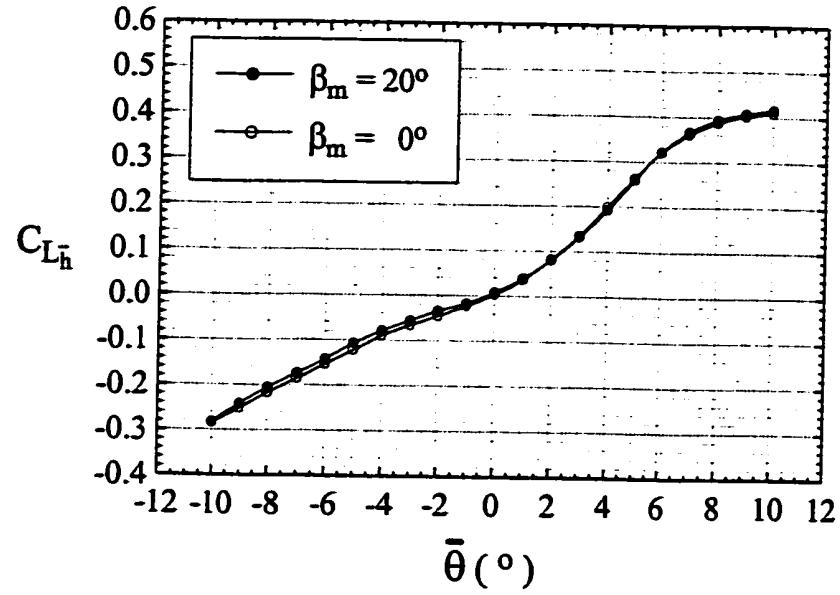

(c) Coefficient of lift force

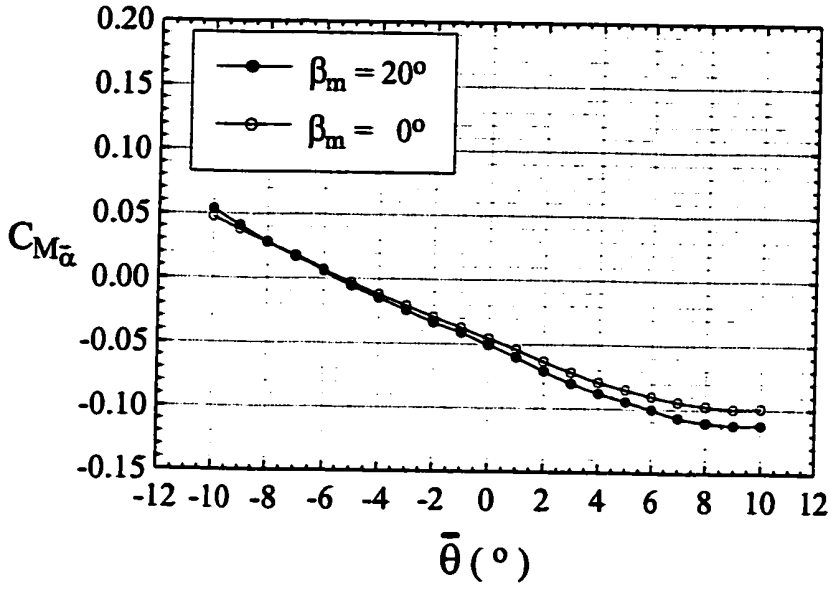

(d) Coefficient of pitching moment

Figure 6-15 (cont.) Comparison of Aerodynamic Coefficients ($\bar{\beta} = 20^o$, $\beta_m = 20^o$ **vs.** $\bar{\beta} = 20^o$, $\beta_m = 0^o$)

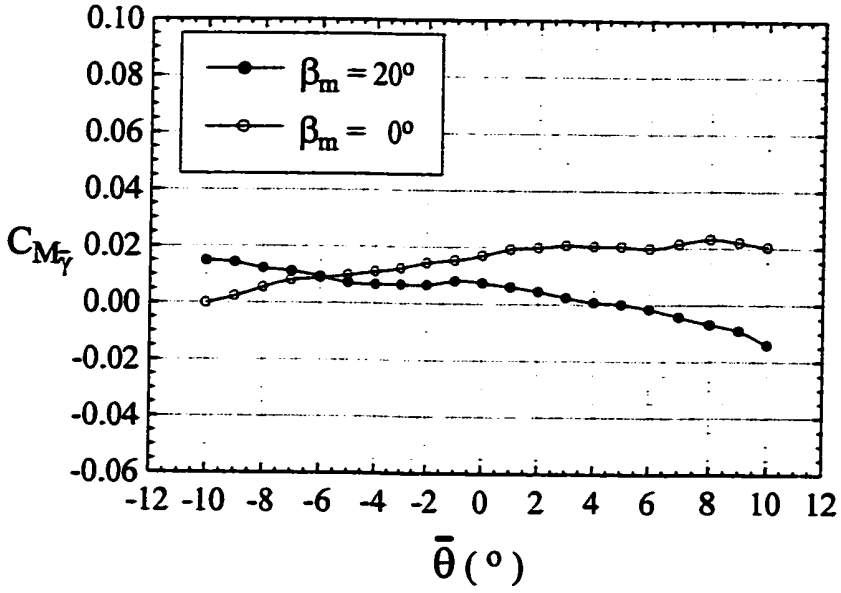

(e) Coefficient of rolling moment

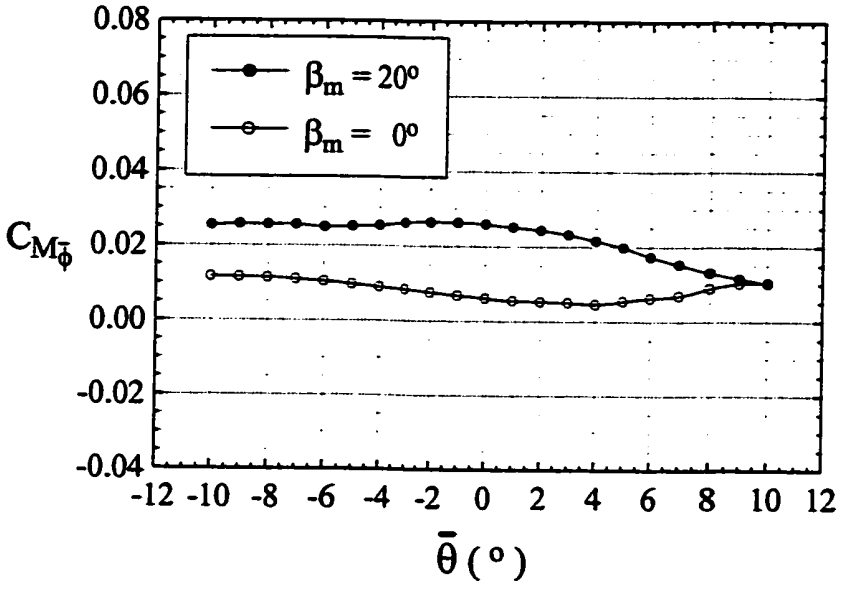

(f) Coefficient of yawing moment

Figure 6-15 (cont.) Comparison of Aerodynamic Coefficients ($\bar{\beta} = 20°$, $\beta_m = 20°$ **vs.** $\bar{\beta} = 20°$, $\beta_m = 0°$)

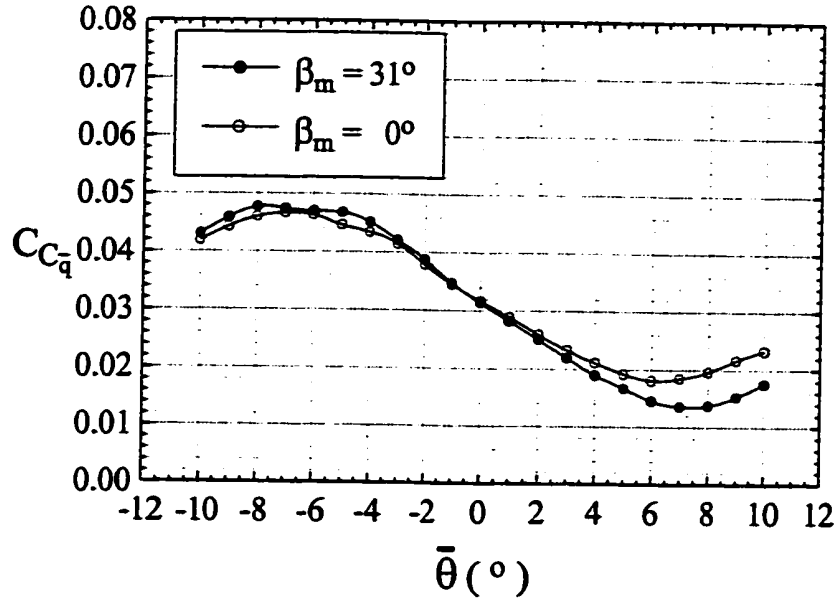

(a) Coefficient of crosswind force

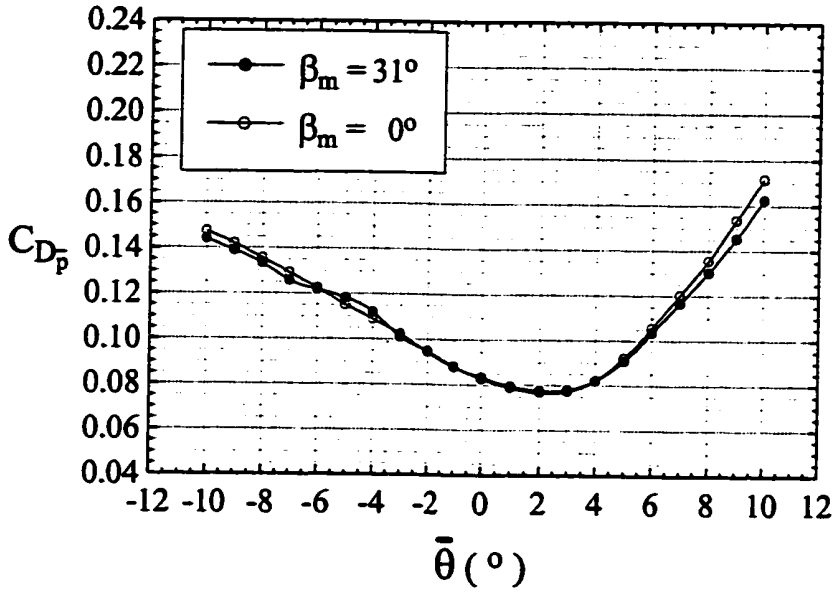

(b) Coefficient of drag force

Figure 6-16 Comparison of Aerodynamic Coefficients ($\bar{\beta} = 31°$, $\beta_m = 31°$ **vs.** $\bar{\beta} = 31°$, $\beta_m = 0°$)

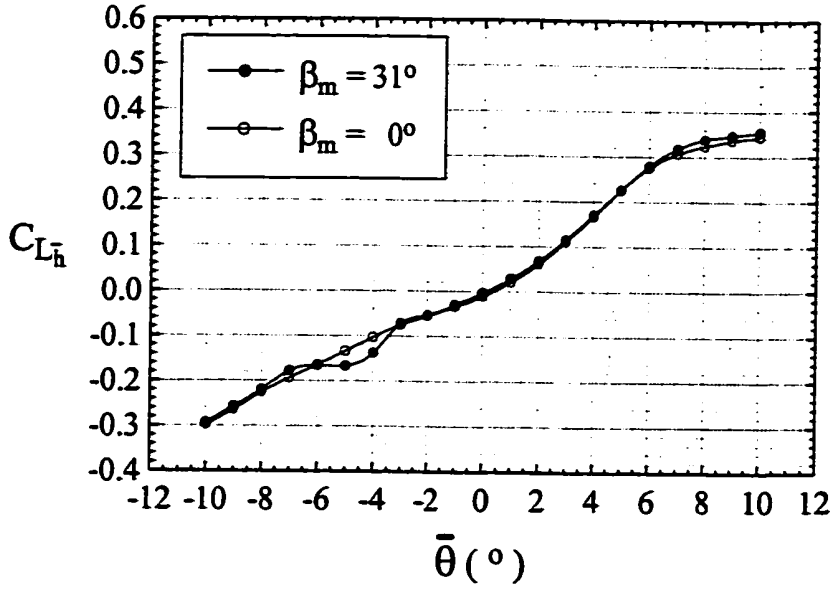

(c) Coefficient of lift force

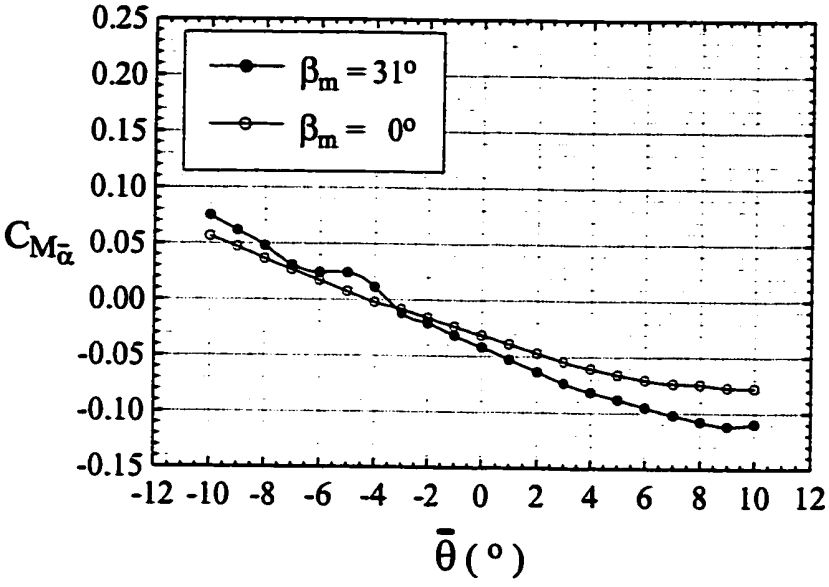

(d) Coefficient of pitching moment

Figure 6-16 (cont.) Comparison of Aerodynamic Coefficients ($\bar{\beta} = 31°$, $\beta_m = 31°$ vs. $\bar{\beta} = 31°$, $\beta_m = 0°$)

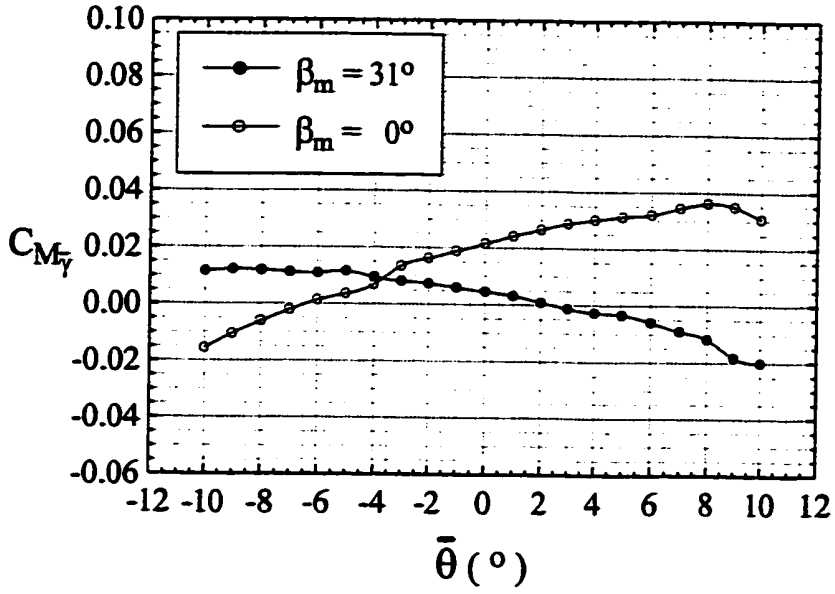

(e) Coefficient of rolling moment

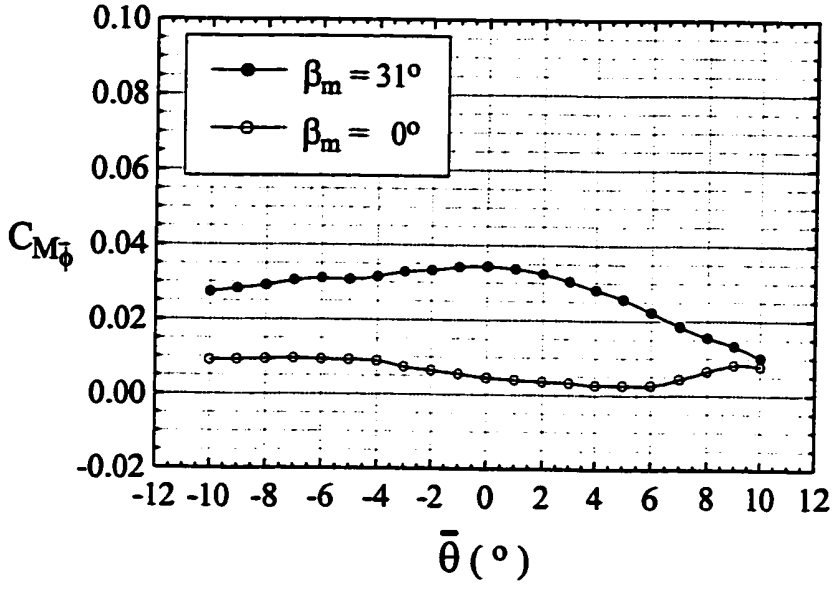

(f) Coefficient of yawing moment

Figure 6-16 (cont.) Comparison of Aerodynamic Coefficients ($\bar{\beta} = 31°$, $\beta_m = 31°$ vs. $\bar{\beta} = 31°$, $\beta_m = 0°$)

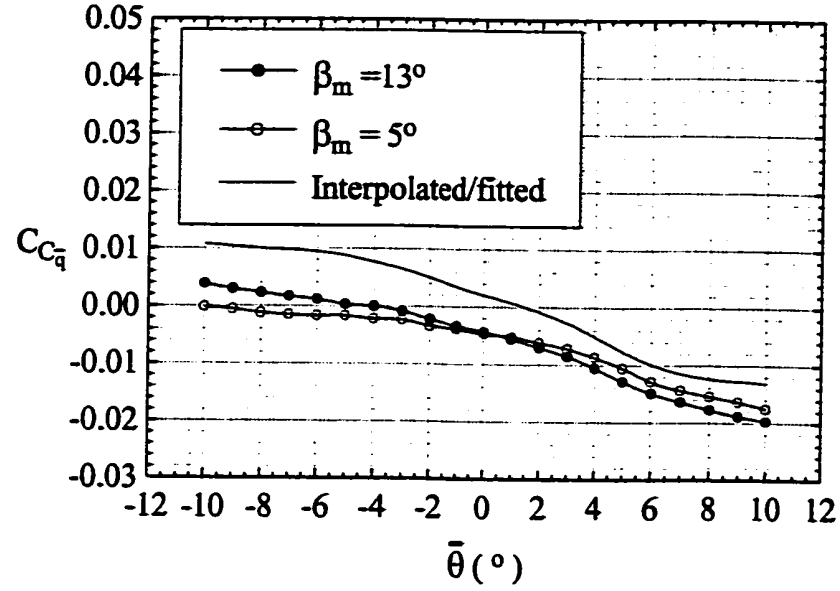

(a) Coefficient of crosswind force

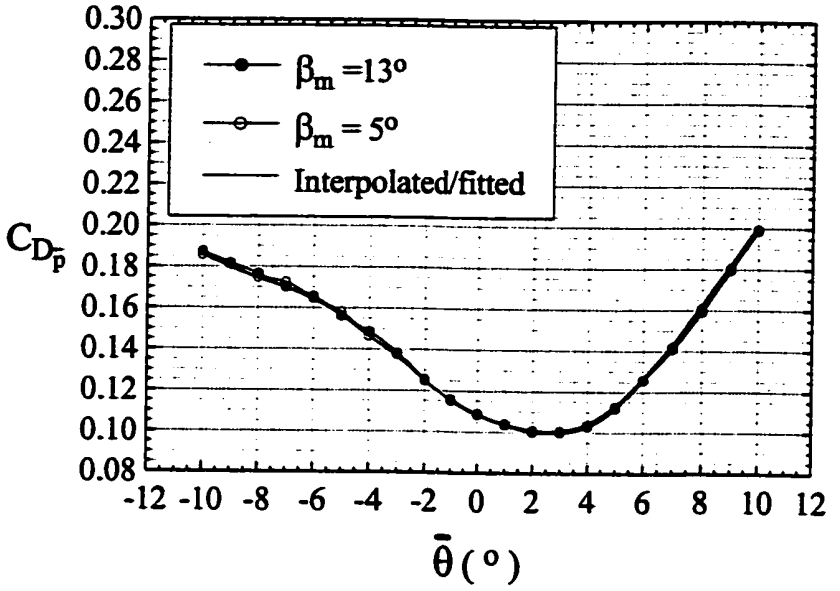

(b) Coefficient of drag force

Figure 6-17 Comparison of Aerodynamic Coefficients ($\bar{\beta}$ = 8°, β_m = 13° vs. $\bar{\beta}$ = 8°, β_m = 5°)

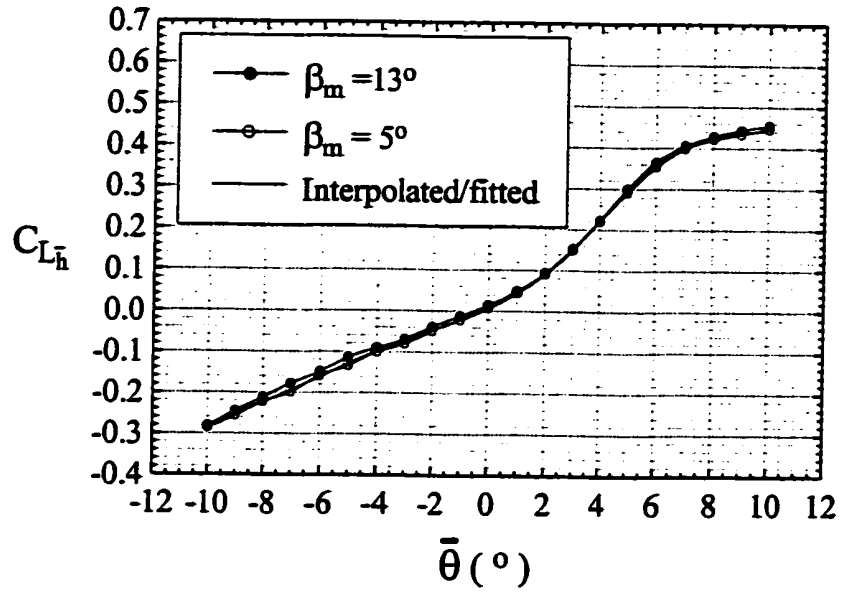

(c) Coefficient of lift force

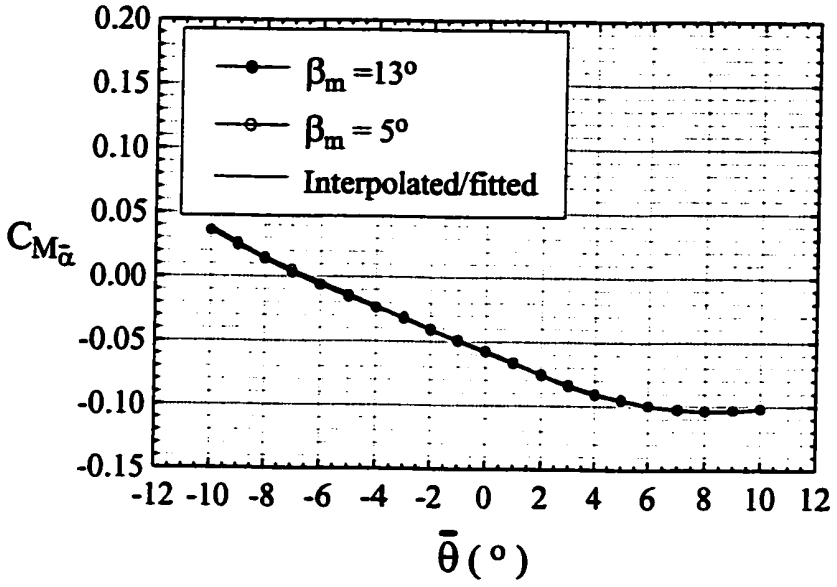

(d) Coefficient of pitching moment

Figure 6-17 (cont.) Comparison of Aerodynamic Coefficients ($\bar{\beta}$ =8°, β_m =13° vs. $\bar{\beta}$ =8°, β_m =5°)

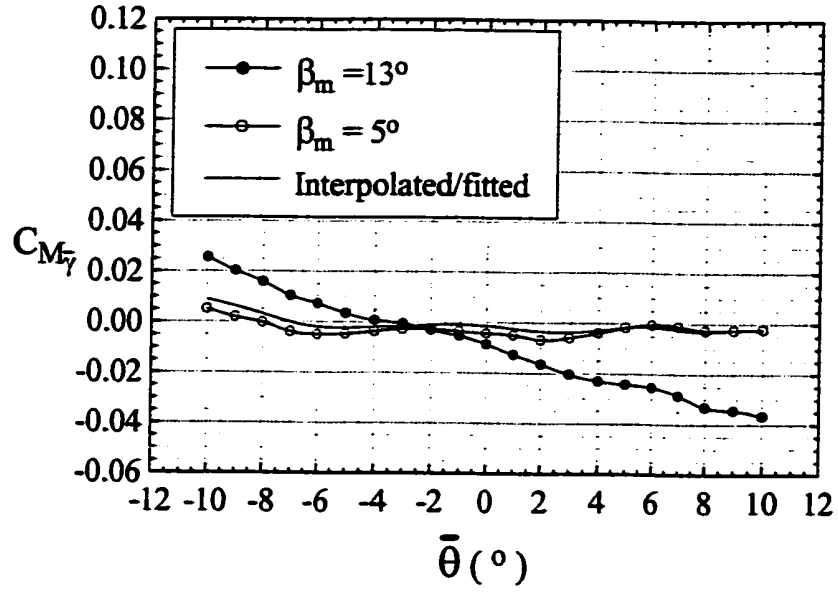

(e) Coefficient of rolling moment

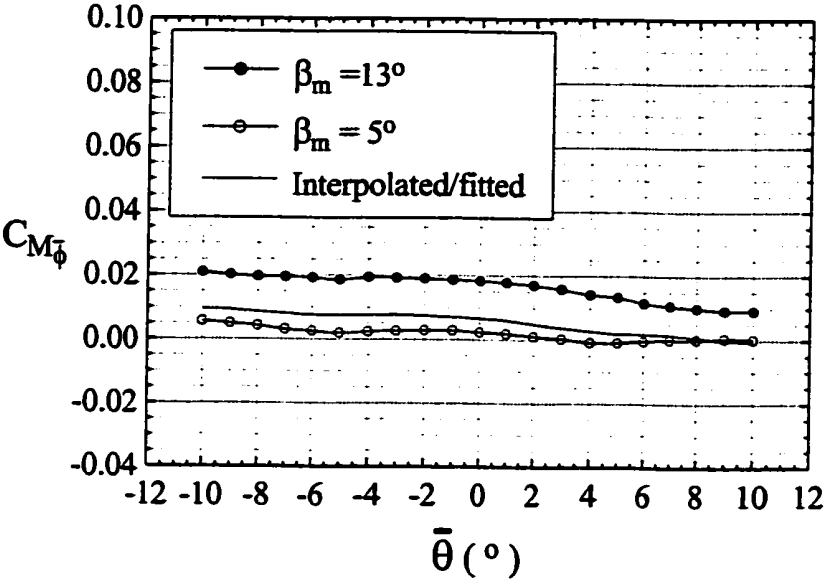

(f) Coefficient of yawing moment

Figure 6-17 (cont.) Comparison of Aerodynamic Coefficients ($\bar{\beta} = 8°$, $\beta_m = 13°$ vs. $\bar{\beta} = 8°$, $\beta_m = 5°$)

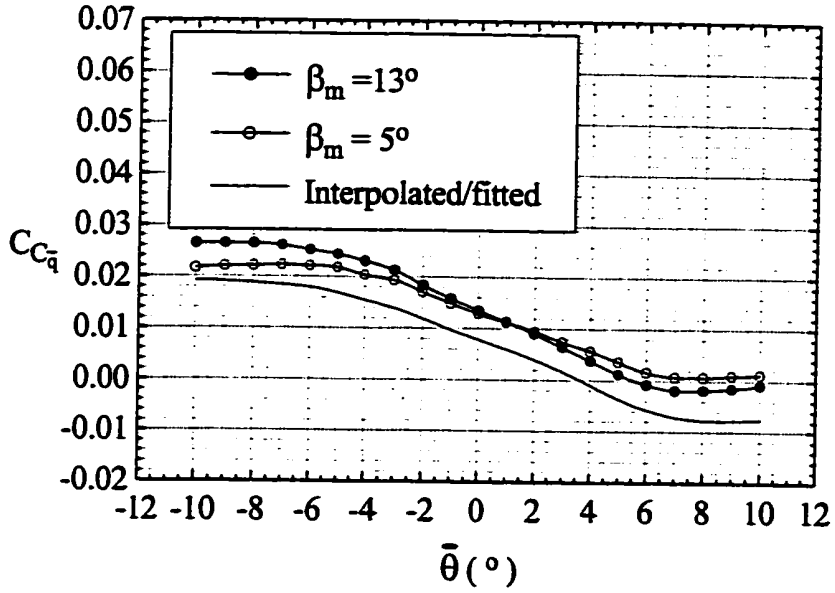

(a) Coefficient of crosswind force

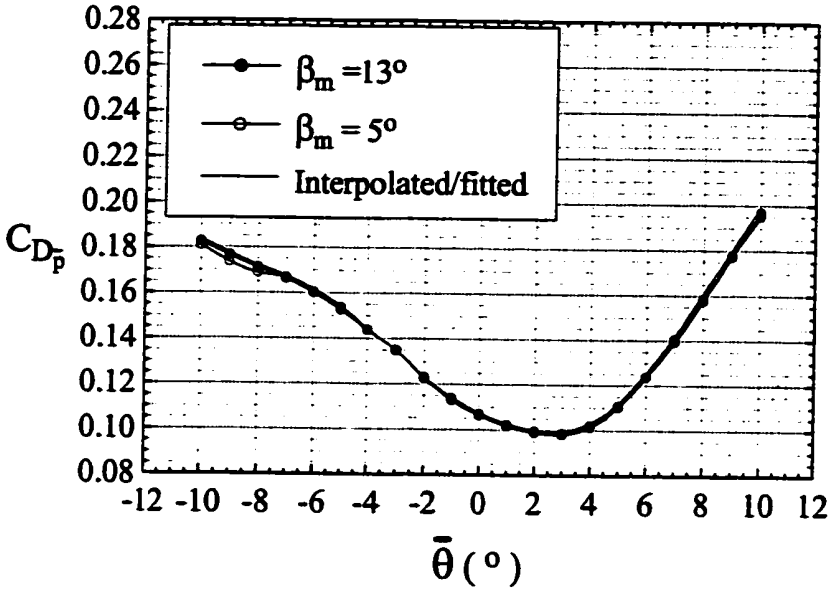

(b) Coefficient of drag force

Figure 6-18 Comparison of Aerodynamic Coefficients ($\bar{\beta} = 10°$, $\beta_m = 13°$ vs. $\bar{\beta} = 10°$, $\beta_m = 5°$)

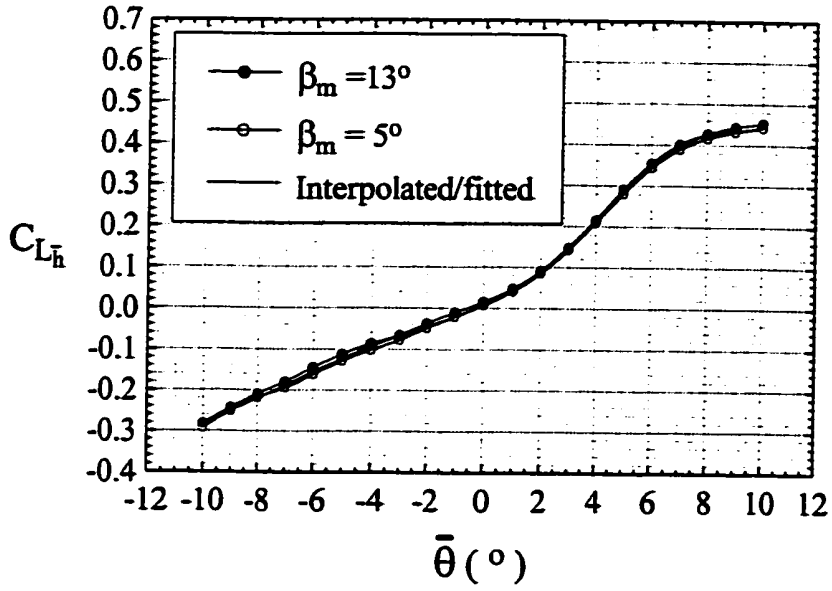

(c) Coefficient of lift force

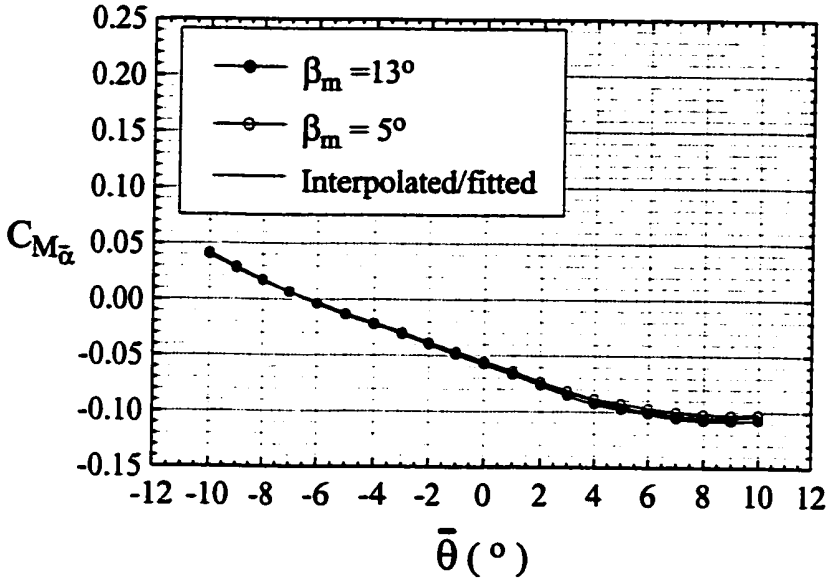

(d) Coefficient of pitching moment

Figure 6-18 (cont.) Comparison of Aerodynamic Coefficients ($\bar{\beta} = 10°$, $\beta_m = 13°$ vs. $\bar{\beta} = 10°$, $\beta_m = 5°$)

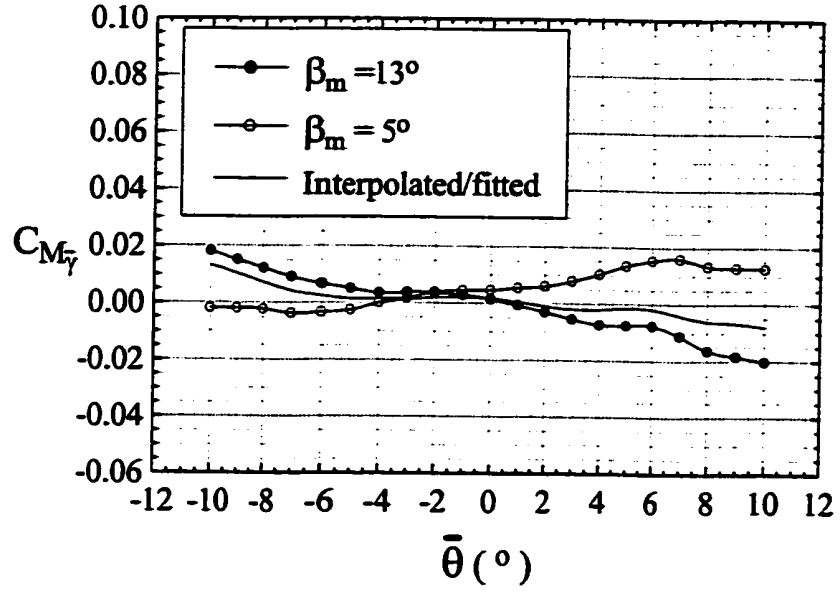

(e) Coefficient of rolling moment

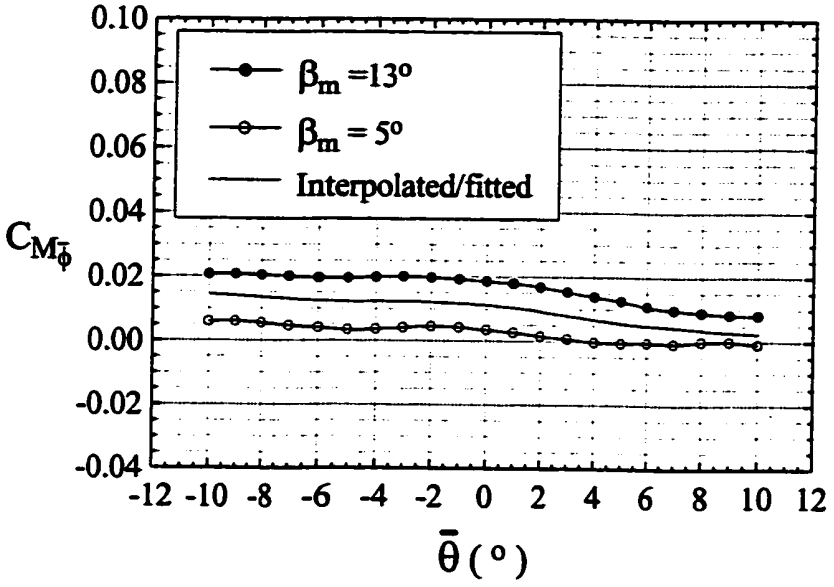

(f) Coefficient of yawing moment

Figure 6-18 (cont.) Comparison of Aerodynamic Coefficients ($\bar{\beta} = 10°$, $\beta_m = 13°$ vs. $\bar{\beta} = 10°$, $\beta_m = 5°$)

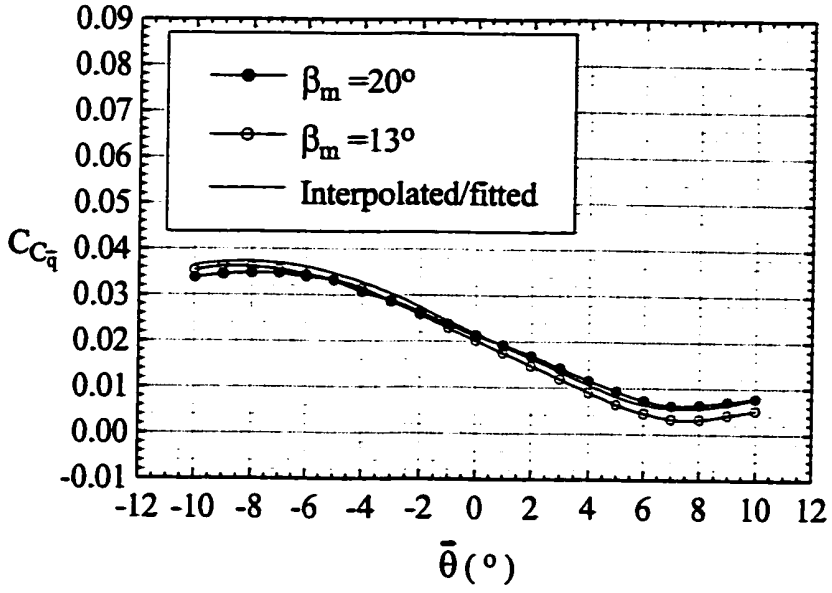

(a) Coefficient of crosswind force

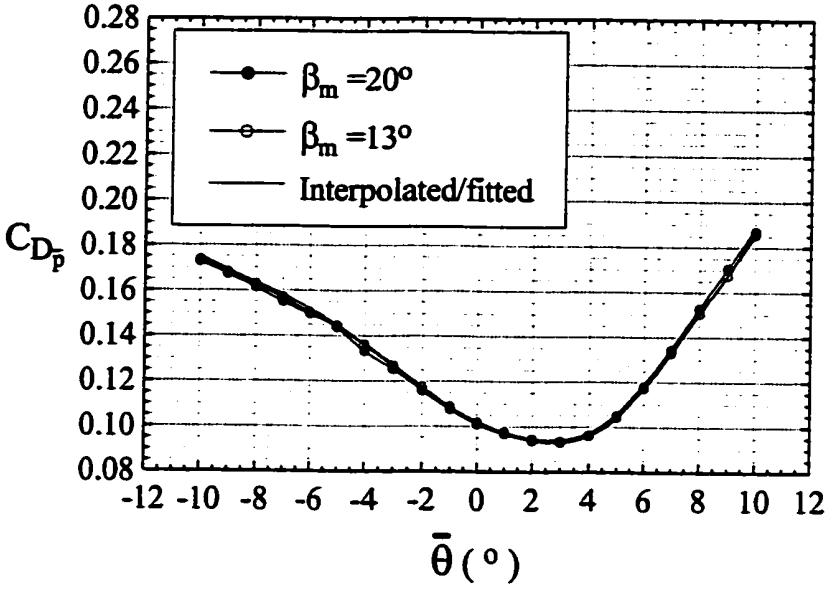

(b) Coefficient of drag force

Figure 6-19 Comparison of Aerodynamic Coefficients ($\bar{\beta} = 16°$, $\beta_m = 20°$ **vs.** $\bar{\beta} = 16°$, $\beta_m = 13°$)

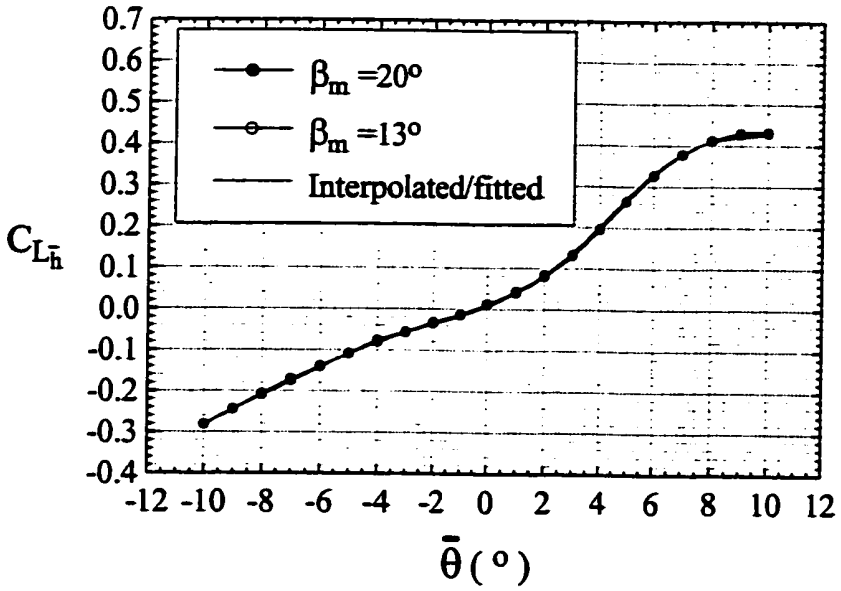

(c) Coefficient of lift force

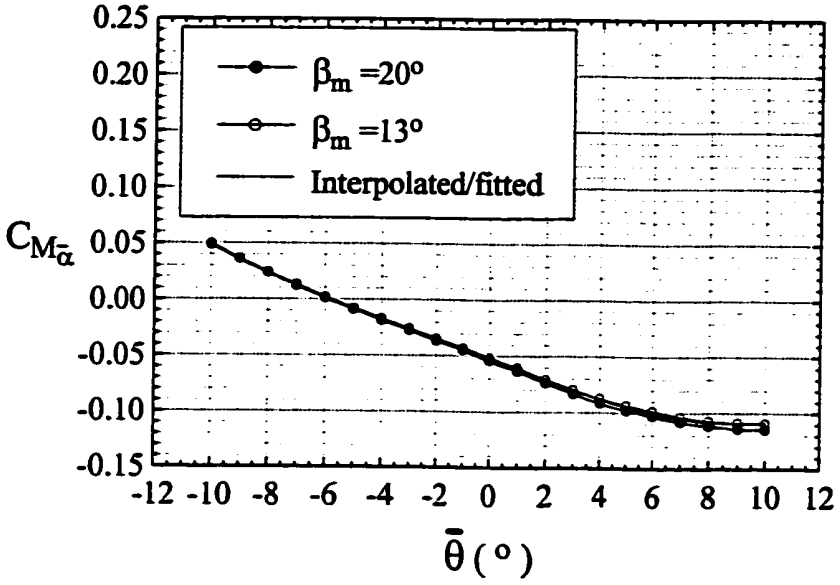

(d) Coefficient of pitching moment

Figure 6-19 (cont.) Comparison of Aerodynamic Coefficients ($\bar{\beta}=16°$, $\beta_m=20°$ vs. $\bar{\beta}=16°$, $\beta_m=13°$)

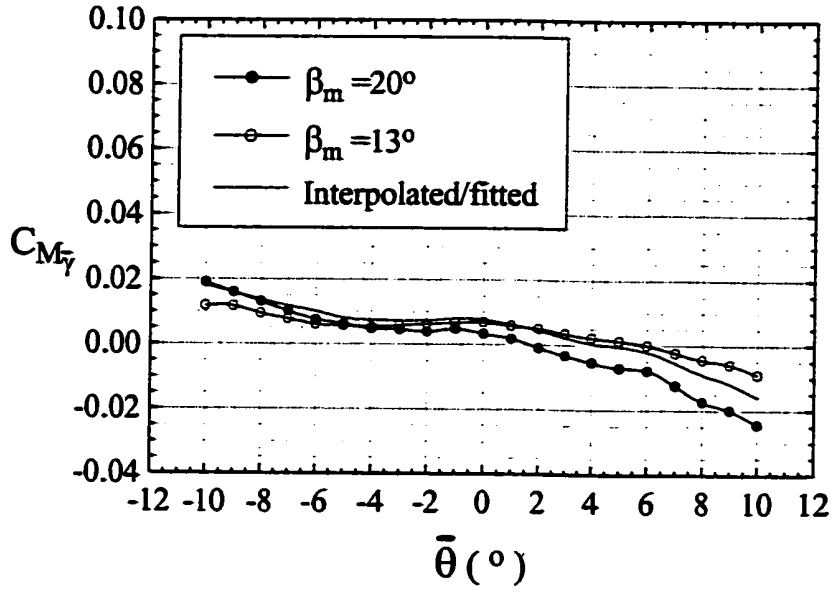

(e) Coefficient of rolling moment

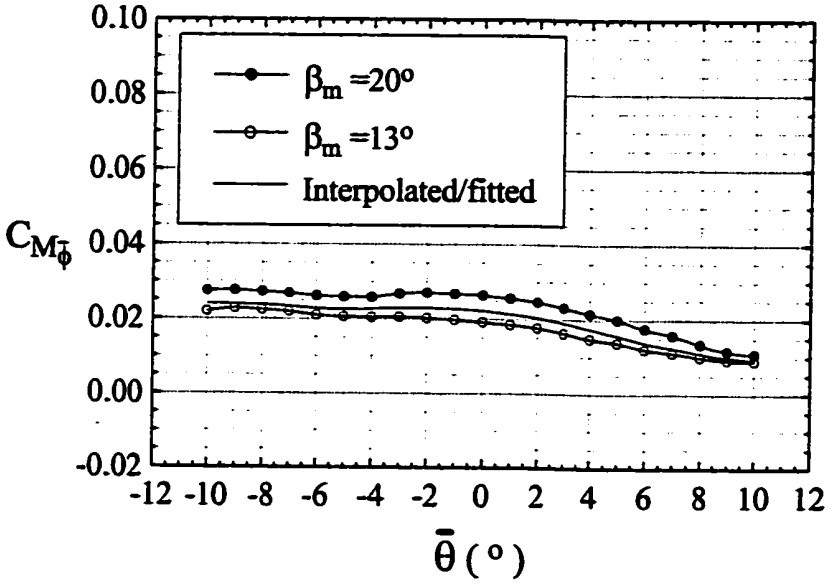

(f) Coefficient of yawing moment

Figure 6-19 (cont.) Comparison of Aerodynamic Coefficients ($\bar{\beta}=16°$, $\beta_m=20°$ vs. $\bar{\beta}=16°$, $\beta_m=13°$)

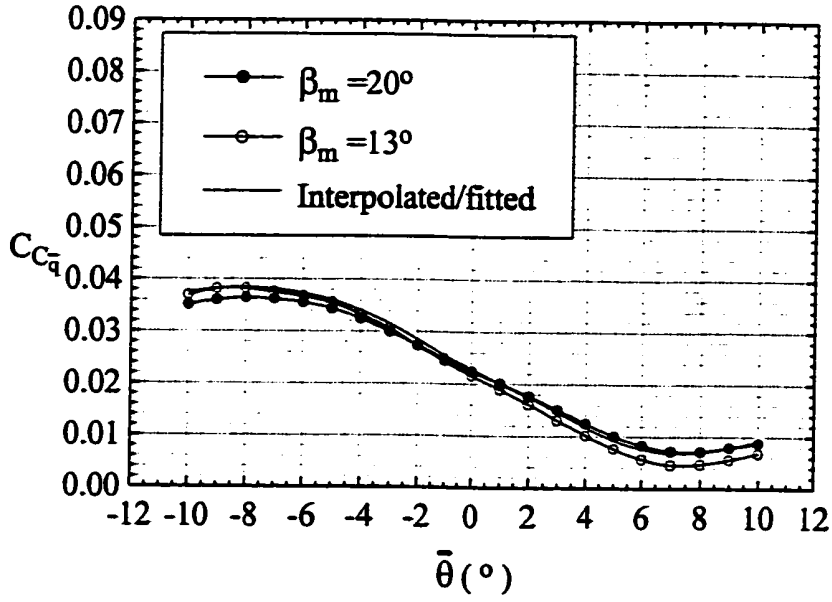

(a) Coefficient of crosswind force

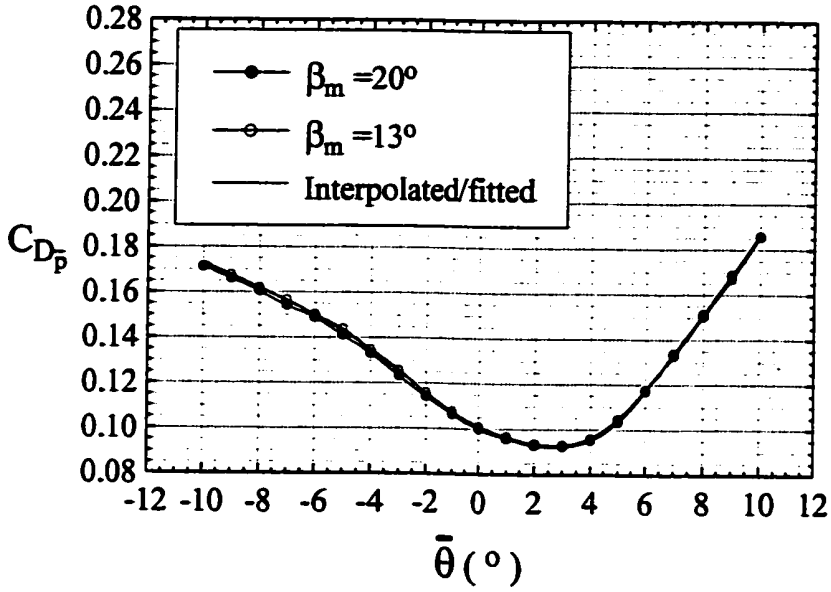

(b) Coefficient of drag force

Figure 6-20 Comparison of Aerodynamic Coefficients ($\bar{\beta}=17°$, $\beta_m=20°$ **vs.** $\bar{\beta}=17°$, $\beta_m=13°$)

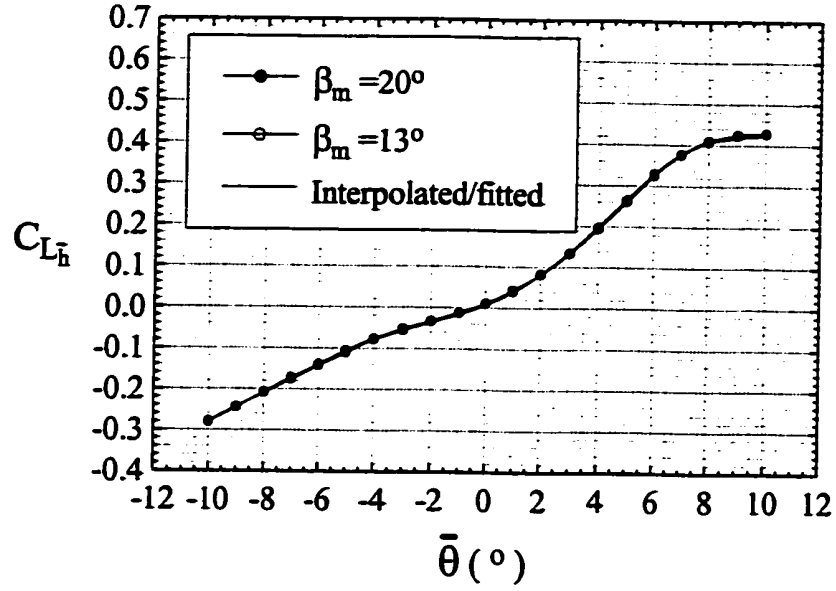

(c) Coefficient of lift force

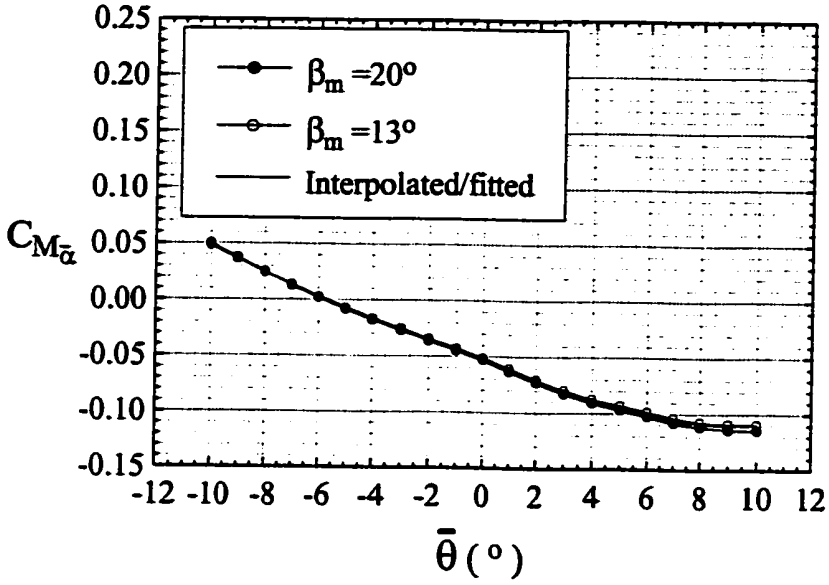

(d) Coefficient of pitching moment

Figure 6-20 (cont.) Comparison of Aerodynamic Coefficients ($\bar{\beta}$ =17°, β_m =20° **vs.** $\bar{\beta}$ =17°, β_m =13°)

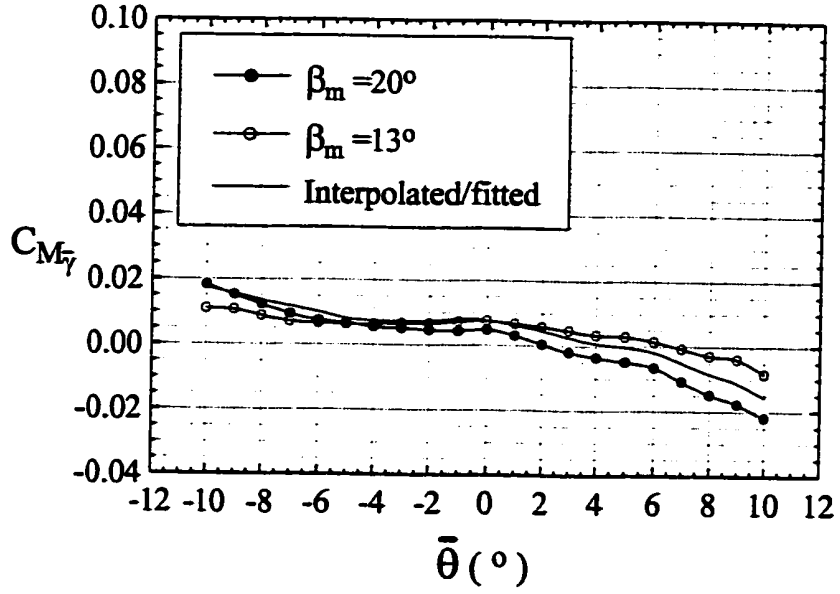

(e) Coefficient of rolling moment

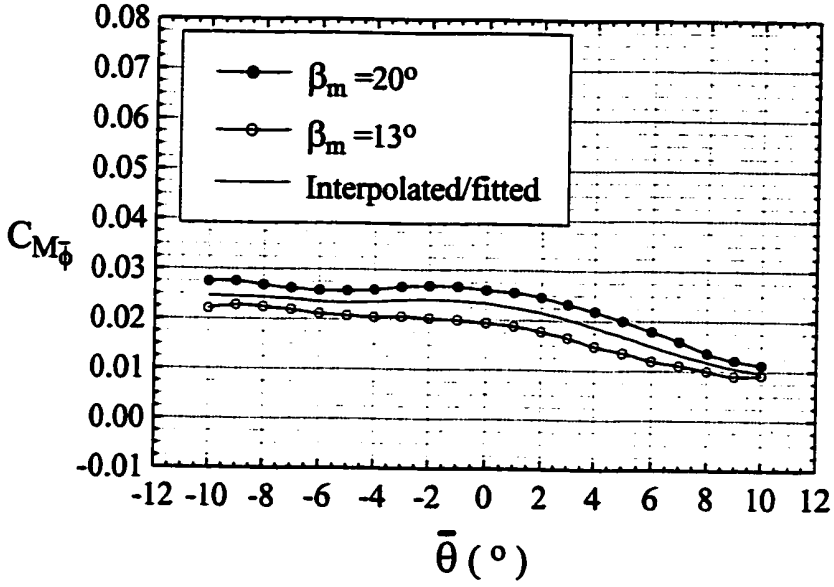

(f) Coefficient of yawing moment

Figure 6-20 (cont.) Comparison of Aerodynamic Coefficients ($\bar{\beta}$ =17°, β_m =20° vs. $\bar{\beta}$ =17°, β_m =13°)

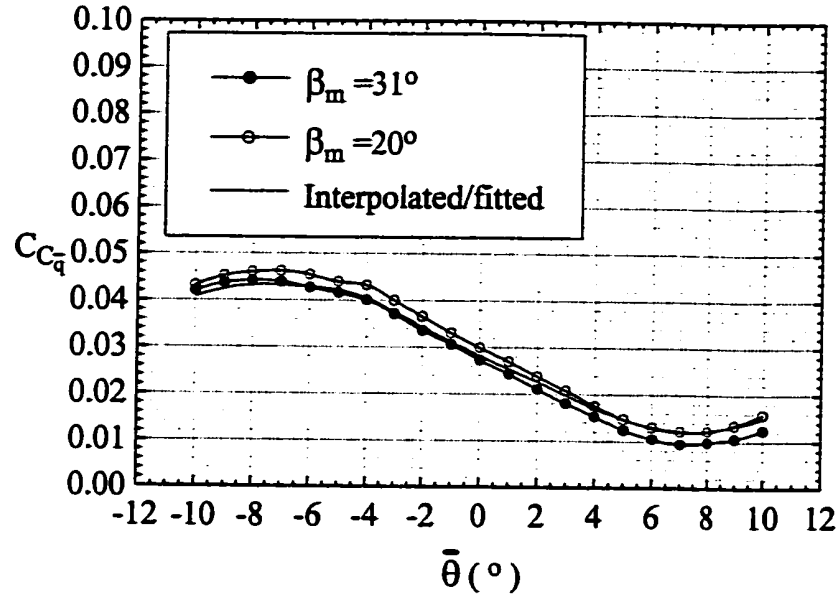

(a) Coefficient of crosswind force

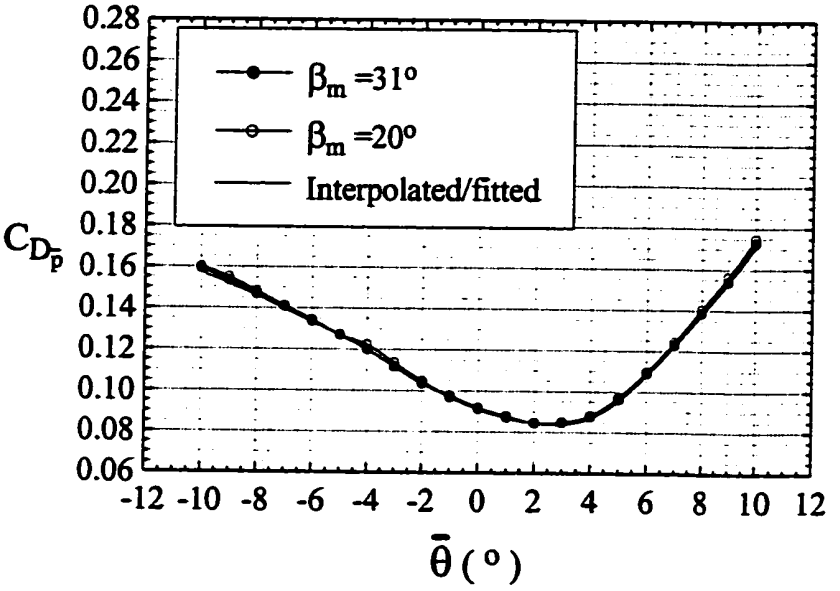

(b) Coefficient of drag force

Figure 6-21 Comparison of Aerodynamic Coefficients ($\bar{\beta} = 25°$, $\beta_m = 31°$ **vs.** $\bar{\beta} = 25°$, $\beta_m = 20°$)

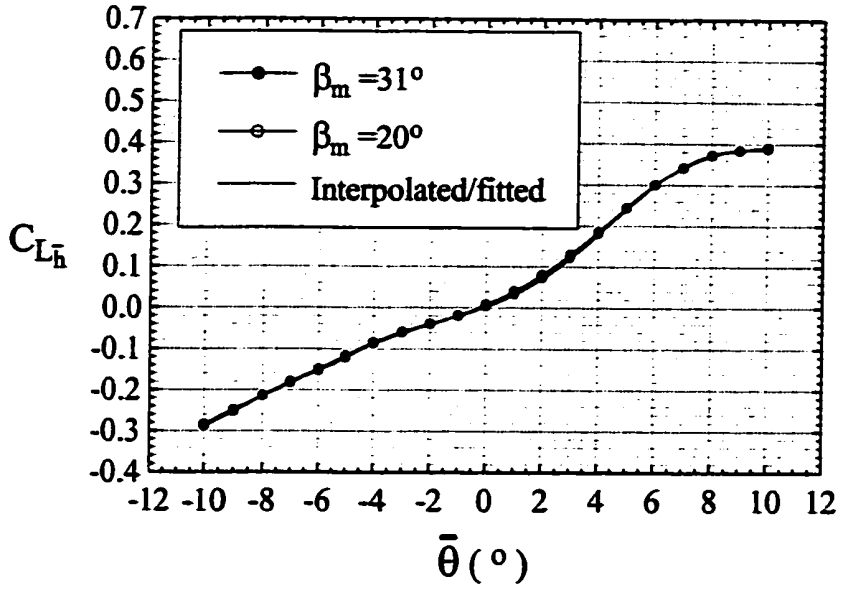

(c) Coefficient of lift force

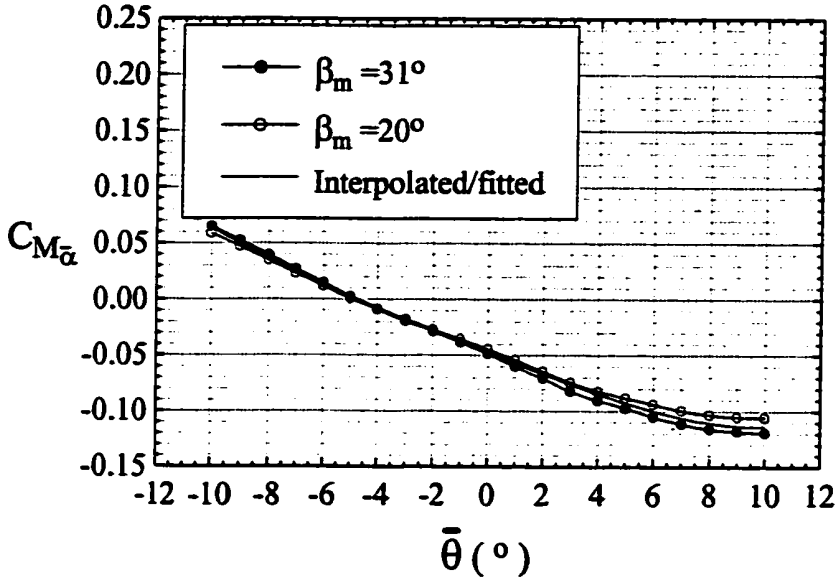

(d) Coefficient of pitching moment

Figure 6-21 (cont.) Comparison of Aerodynamic Coefficients ($\bar{\beta} = 25°$, $\beta_m = 31°$ vs. $\bar{\beta} = 25°$, $\beta_m = 20°$)

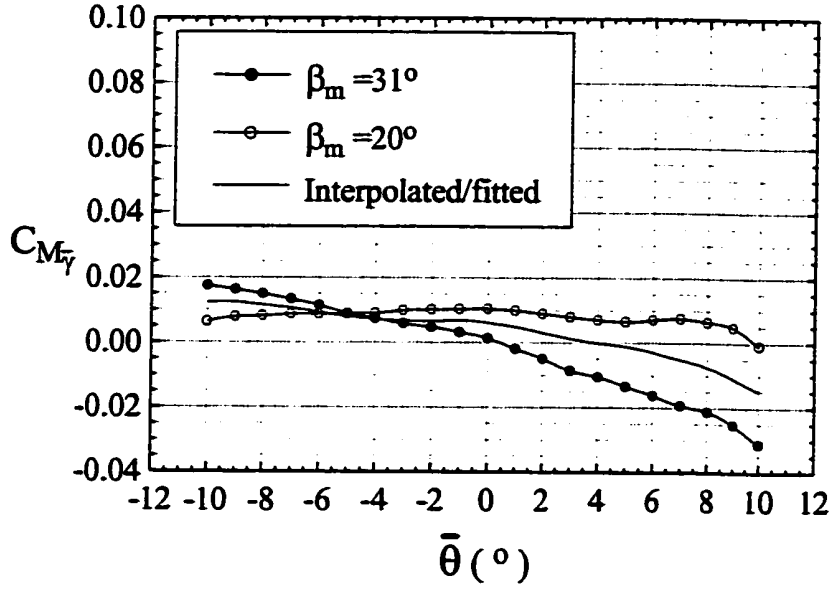

(e) Coefficient of rolling moment

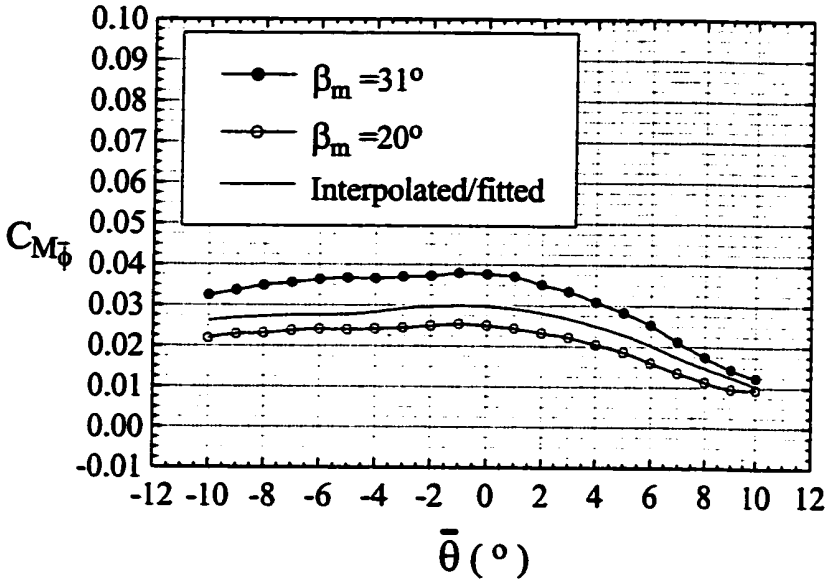

(f) Coefficient of yawing moment

Figure 6-21 (cont.) Comparison of Aerodynamic Coefficients ($\bar{\beta} = 25°$, $\beta_m = 31°$ vs. $\bar{\beta} = 25°$, $\beta_m = 20°$)

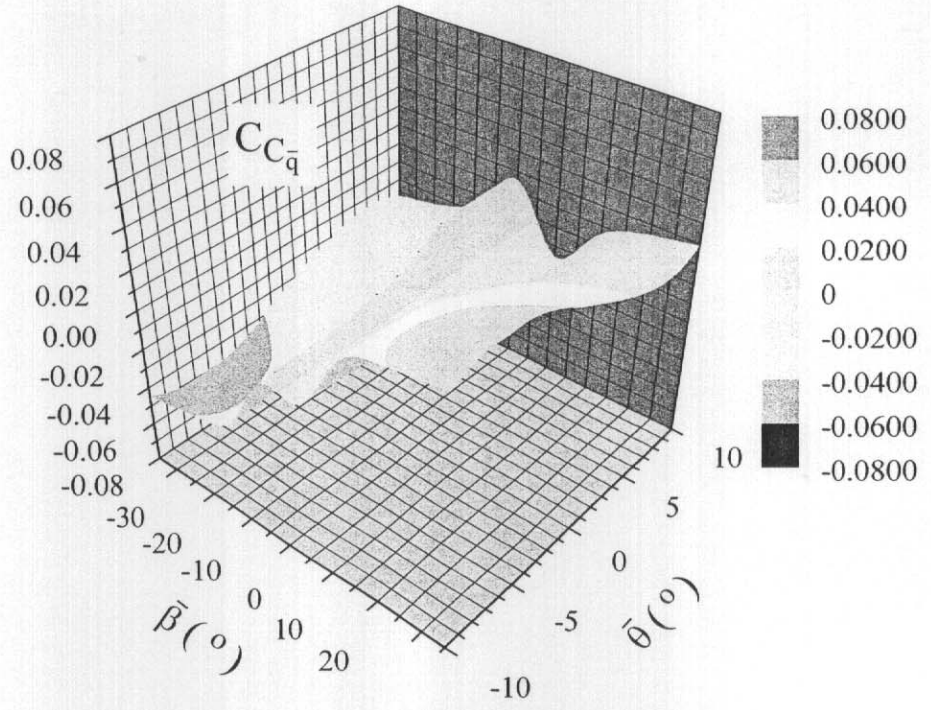

(a) Coefficient of crosswind force

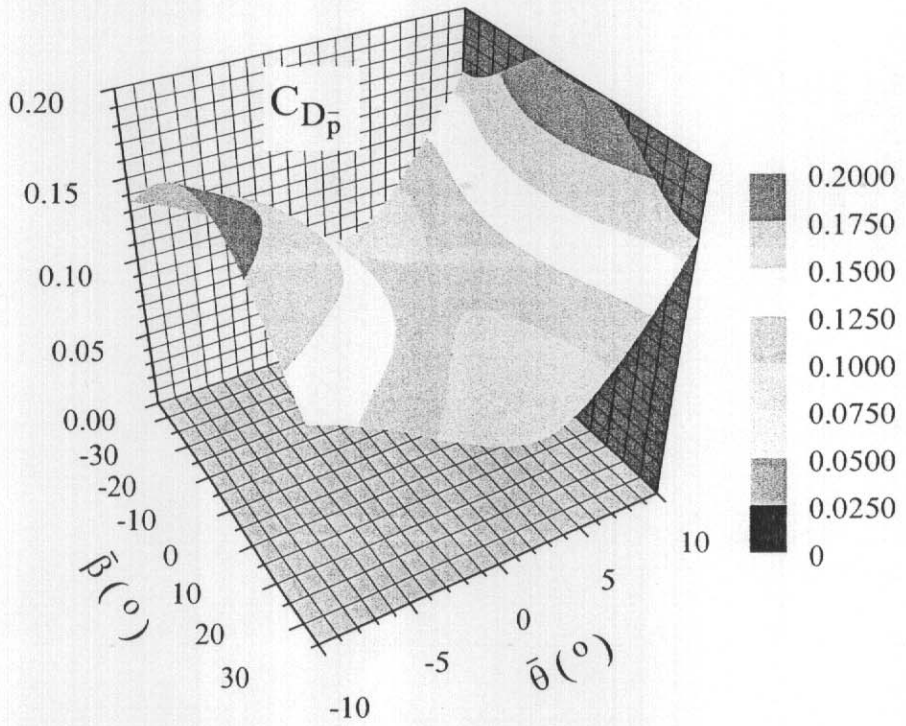

(b) Coefficient of drag force

Figure 6-22 Aerodynamic Coefficients of Tsing Ma Bridge Deck

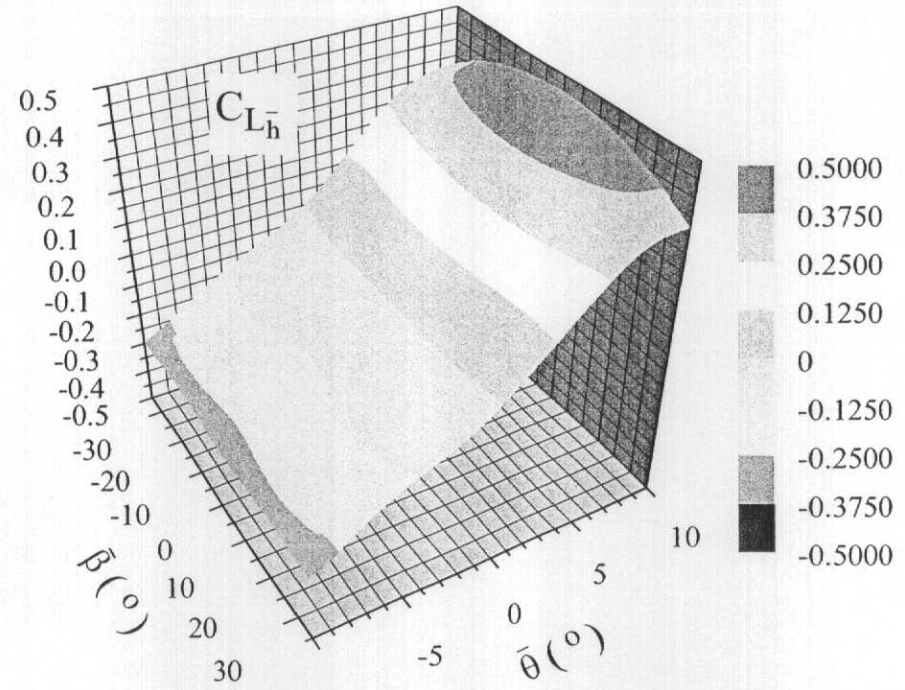

(c) Coefficient of lift force

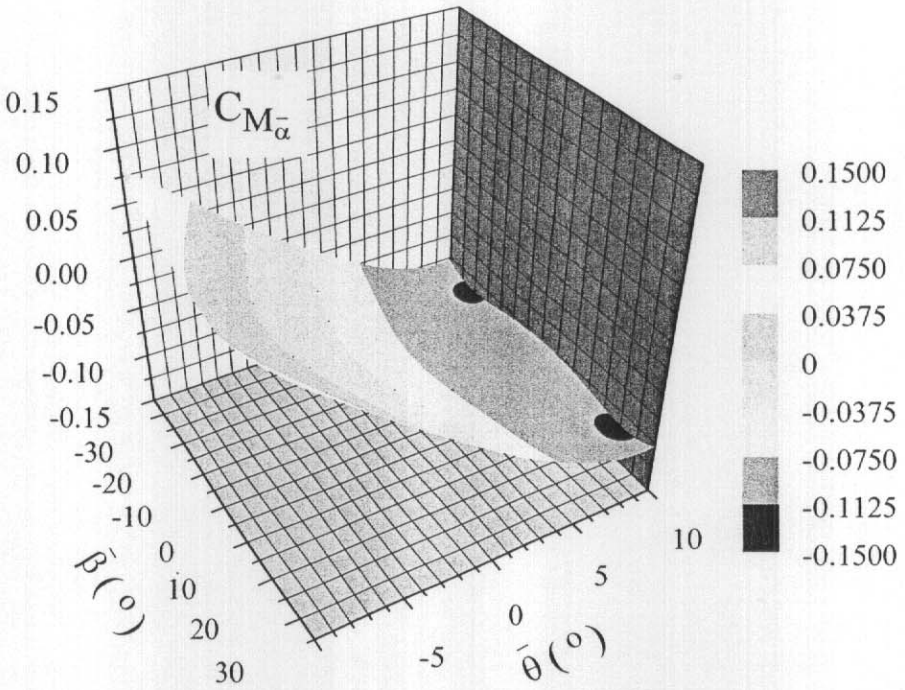

(d) Coefficient of pitching moment

Figure 6-22 (cont.) Aerodynamic Coefficients of Tsing Ma Bridge Deck

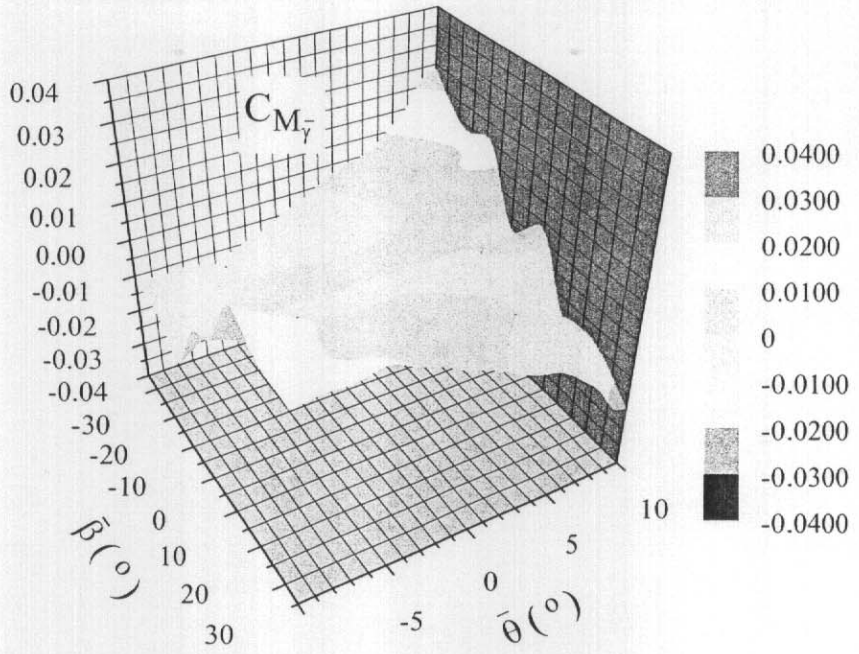

(e) Coefficient of rolling moment

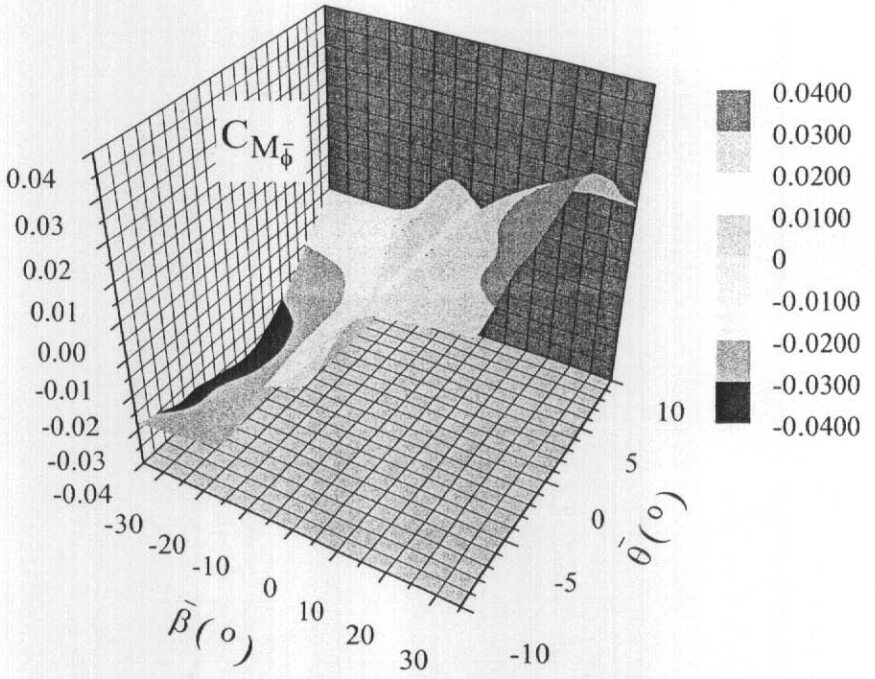

(f) Coefficient of yawing moment

Figure 6-22 (cont.) Aerodynamic Coefficients of Tsing Ma Bridge Deck

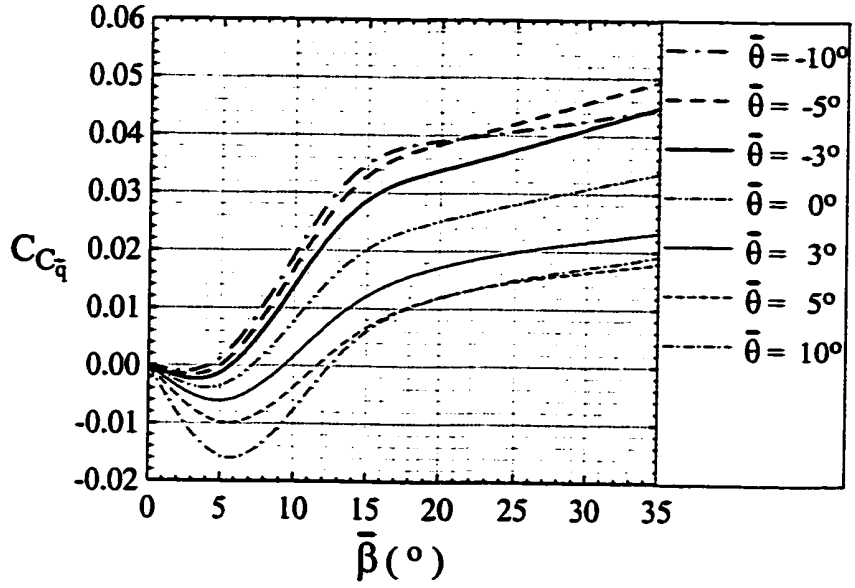

(a) Coefficient of crosswind force

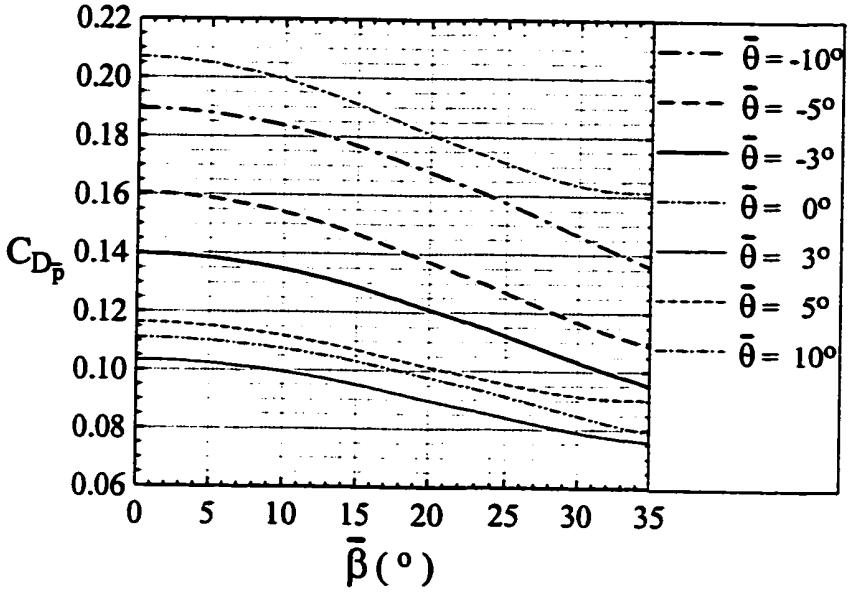

(b) Coefficient of drag force

Figure 6-23 Variations of Aerodynamic Coefficients with Yaw Angle

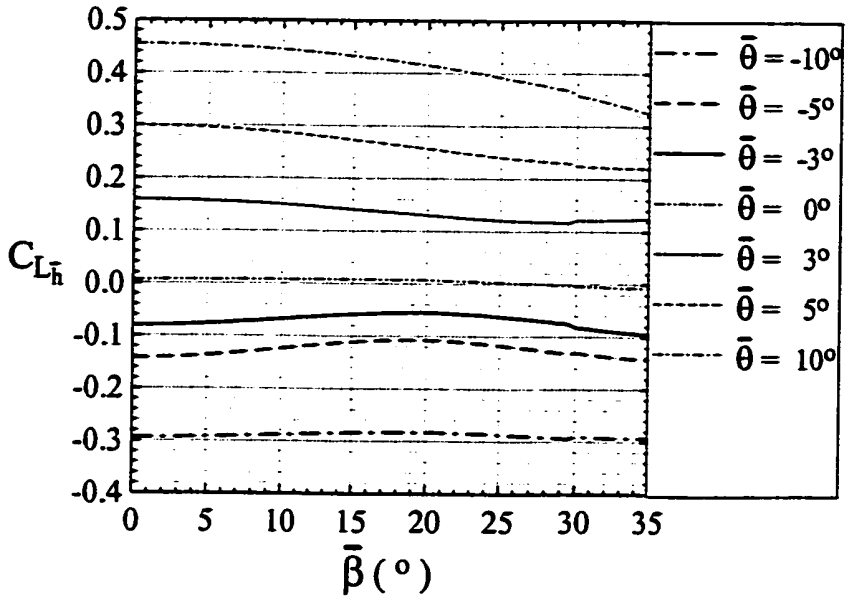

(c) Coefficient of lift force

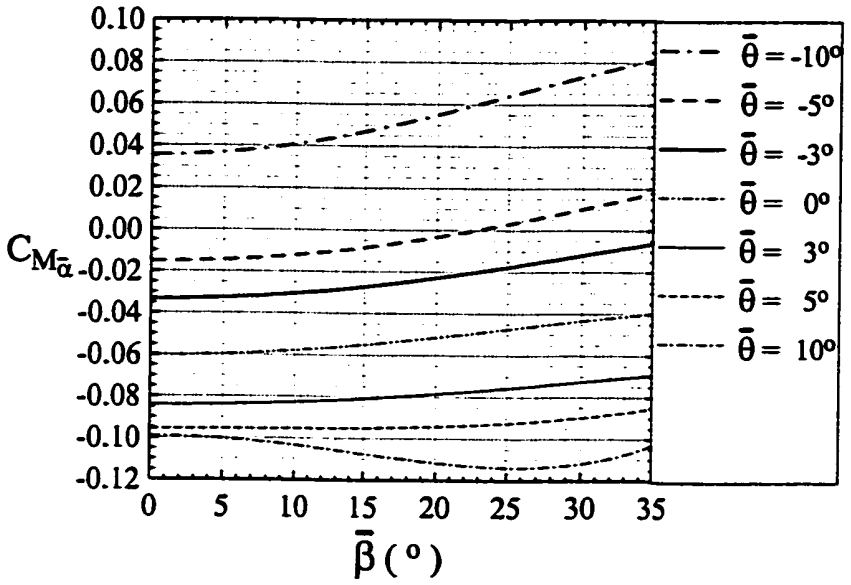

(d) Coefficient of pitching moment

Figure 6-23 (cont.) Variations of Aerodynamic Coefficients with Yaw Angle

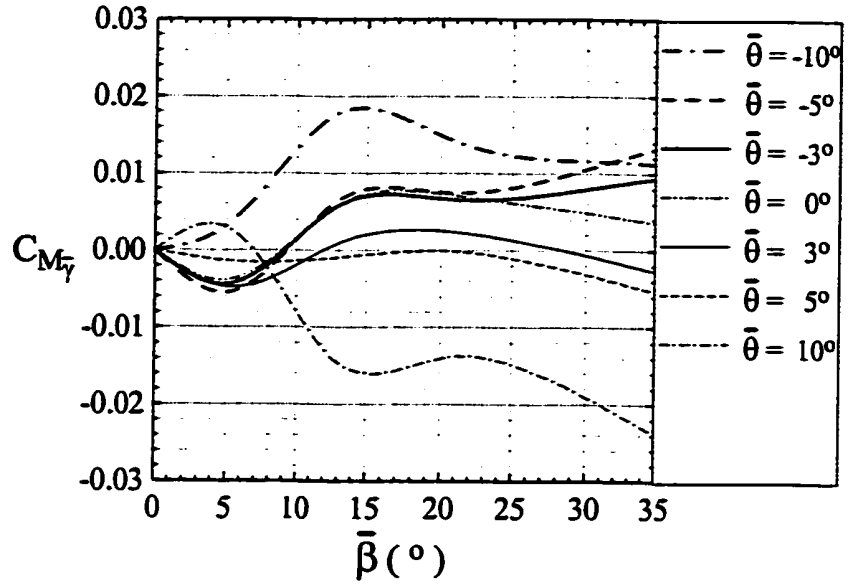

(e) Coefficient of rolling moment

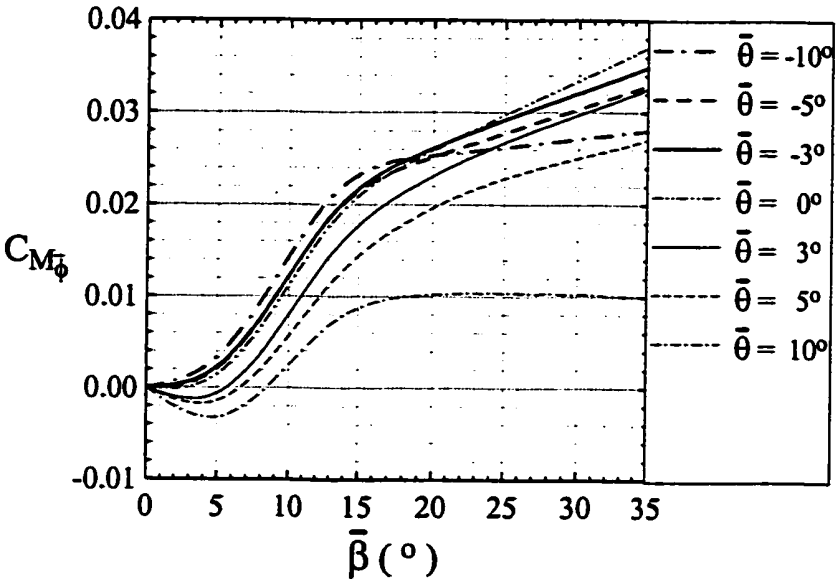

(f) Coefficient of yawing moment

Figure 6-23 (cont.) Variations of Aerodynamic Coefficients with Yaw Angle

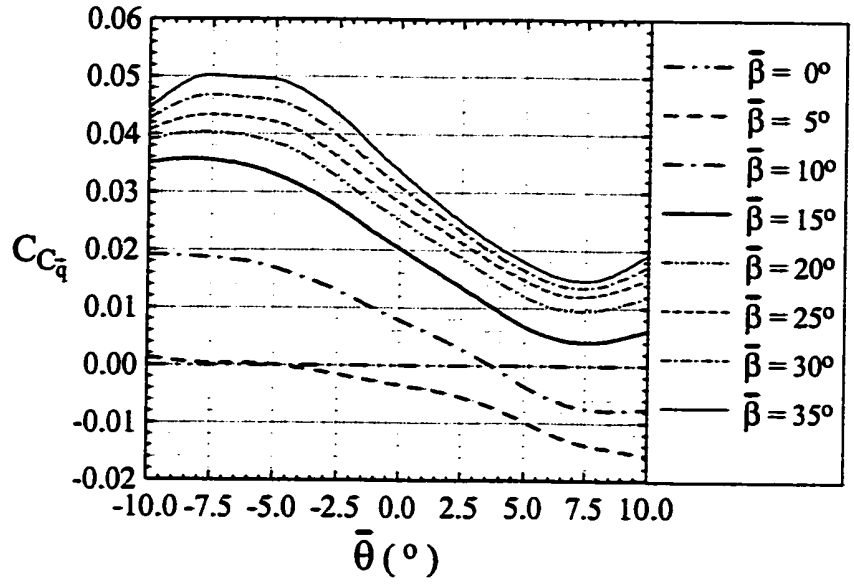

(a) Coefficient of crosswind force

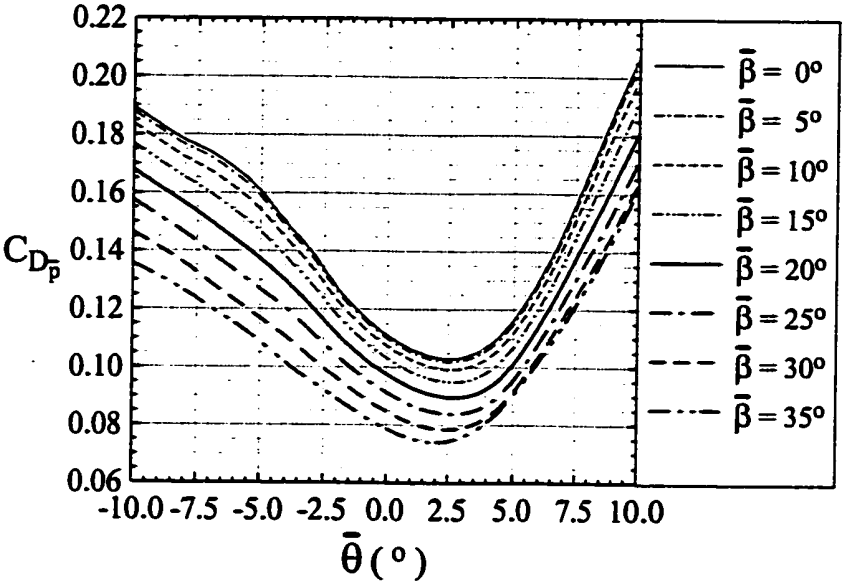

(b) Coefficient of drag force

Figure 6-24 Variations of Aerodynamic Coefficients with Angle of Inclination

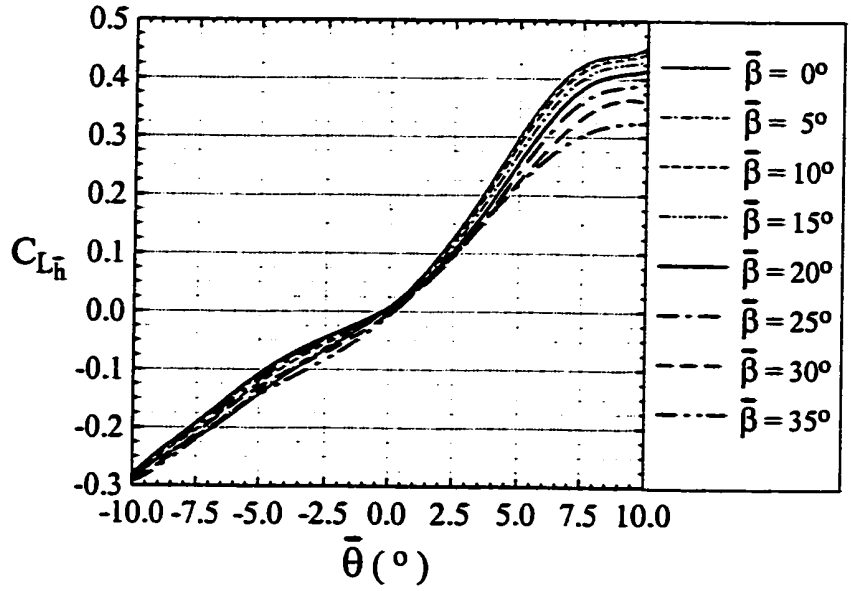

(c) Coefficient of lift force

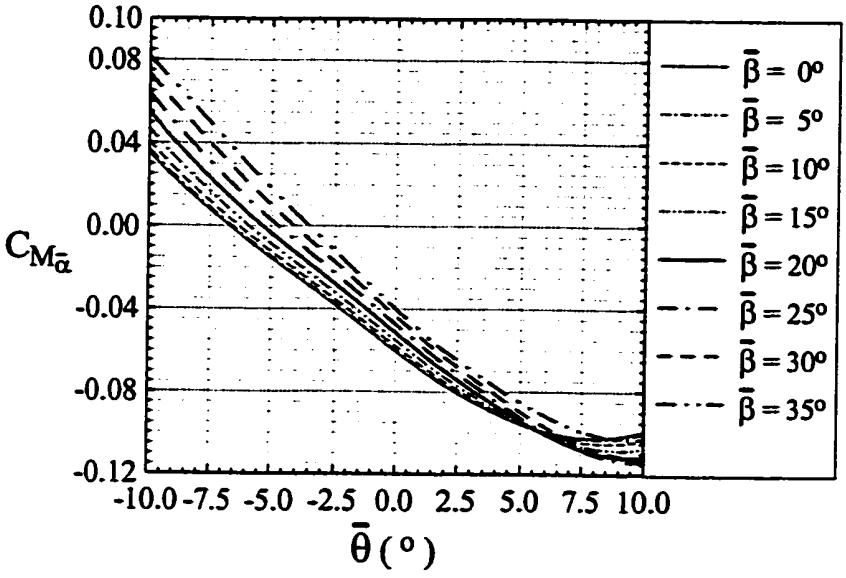

(d) Coefficient of pitching moment

Figure 6-24 (cont.) Variations of Aerodynamic Coefficients with Angle of Inclination

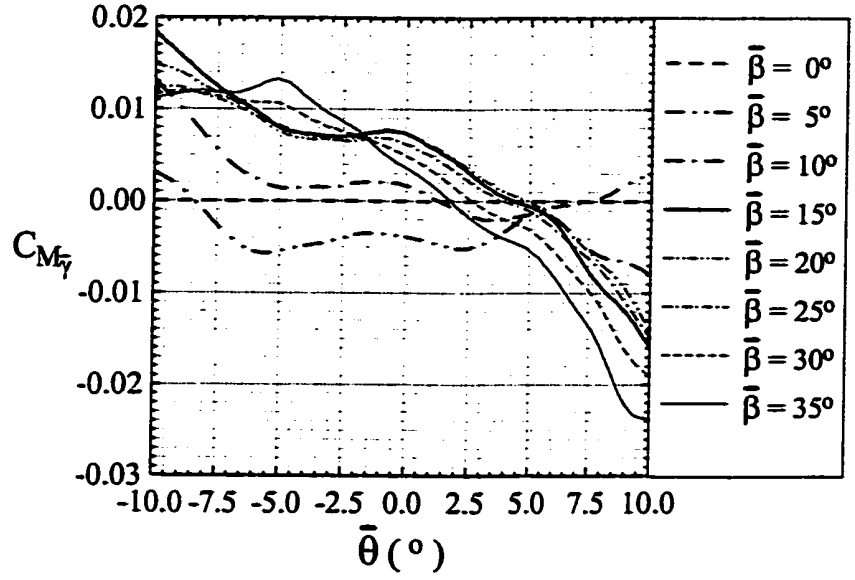

(e) Coefficient of rolling moment

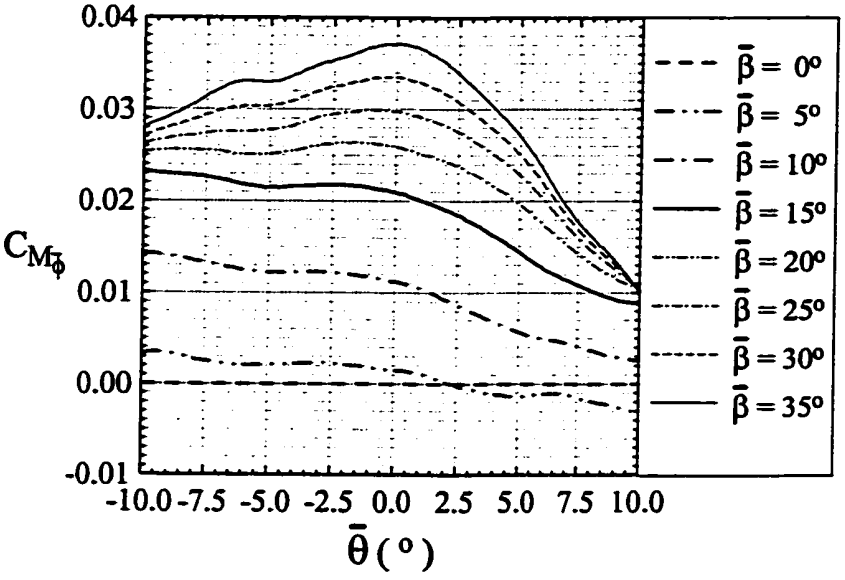

(f) Coefficient of yawing moment

Figure 6-24 (cont.) Variations of Aerodynamic Coefficients with Angle of Inclination

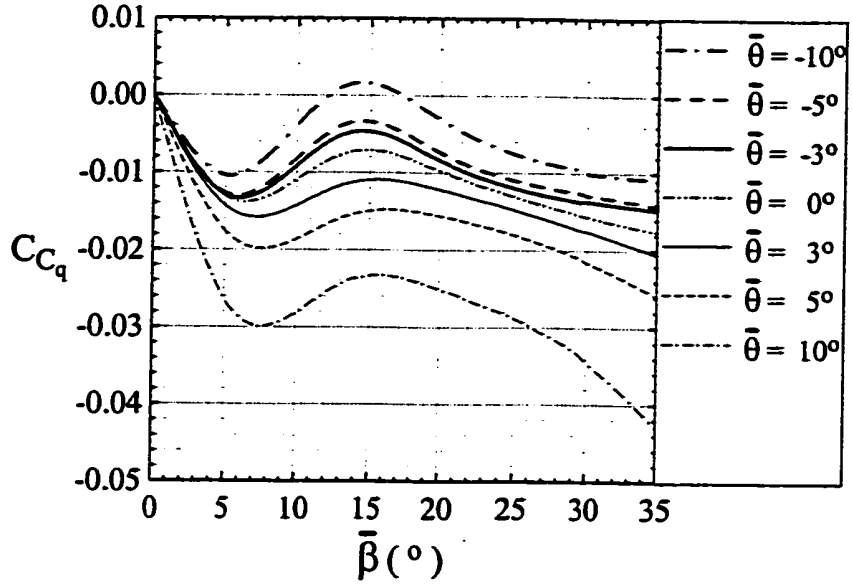

(a) Coefficient of force along the model axis *q*

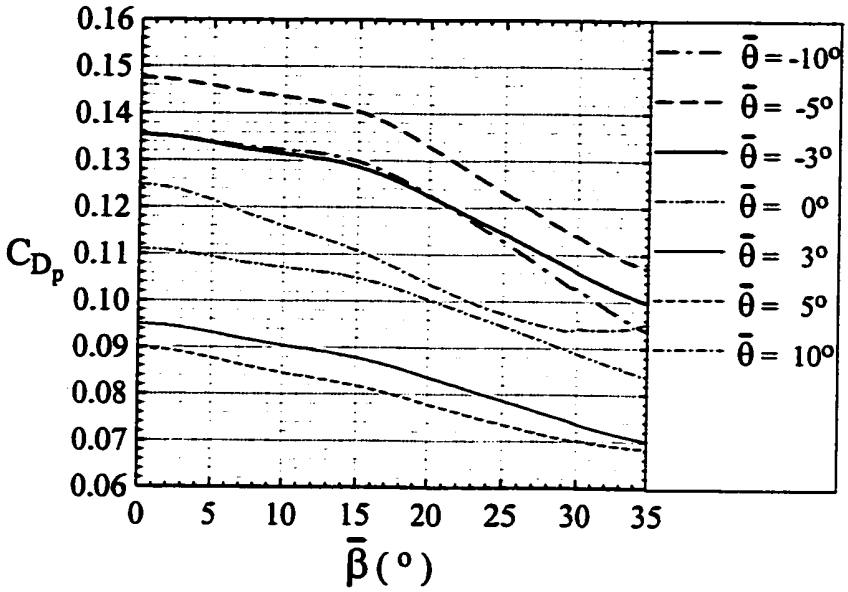

(b) Coefficient of force along the model axis *p*

Figure 6-25 Variations of Aerodynamic Coefficients with Yaw Angle (Model Coordinates)

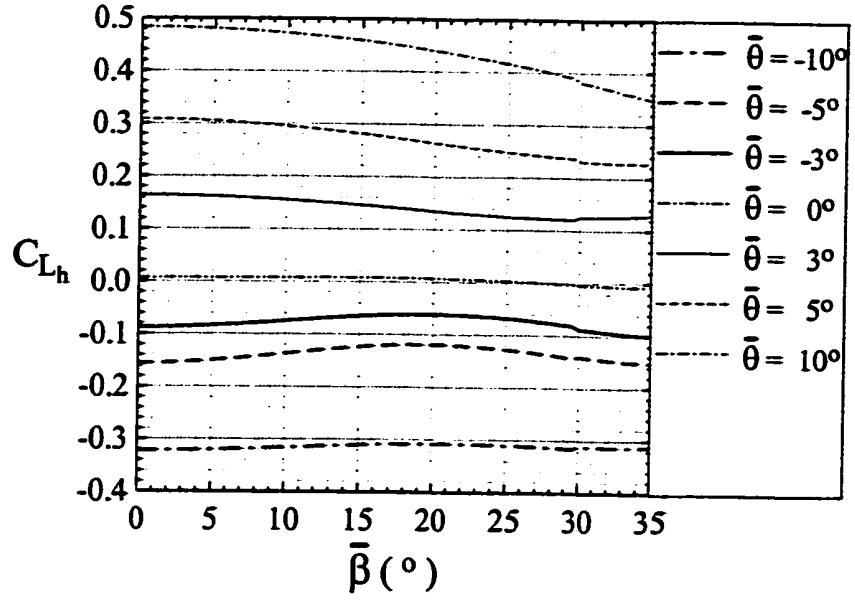

(c) Coefficient of force along the model axis *h*

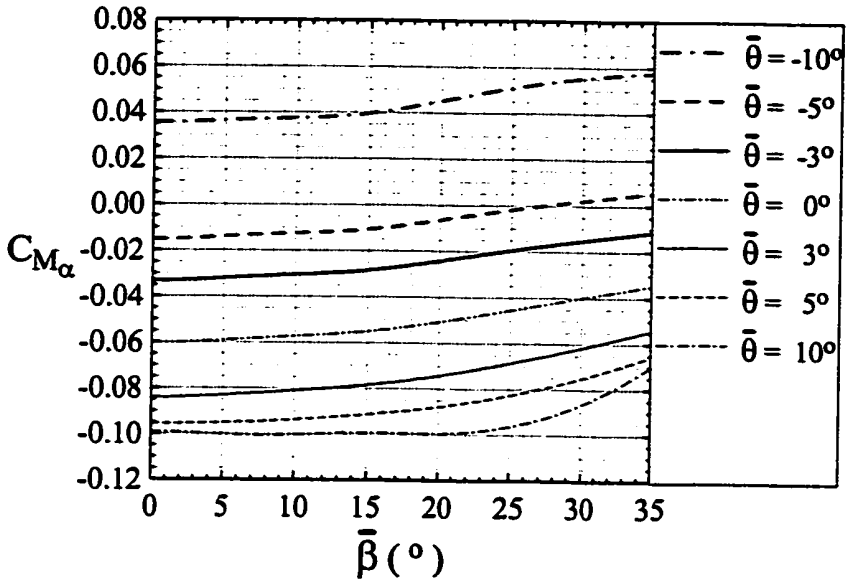

(d) Coefficient of momemt around the model axis *q*

Figure 6-25 (cont.) Variations of Aerodynamic Coefficients with Yaw Angle (Model Coordinates)

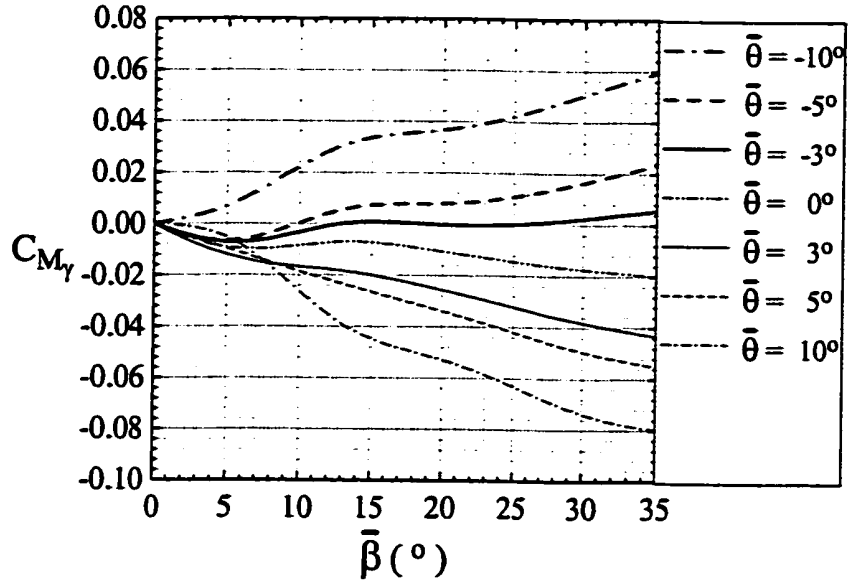

(e) Coefficient of moment around the model axis *p*

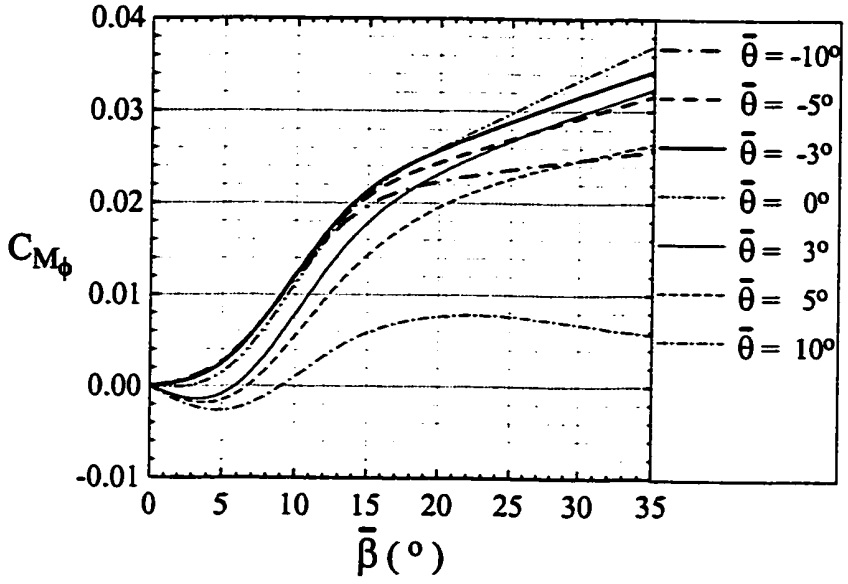

(f) Coefficient of moment around the model axis *h*

Figure 6-25 (cont.) Variations of Aerodynamic Coefficients with Yaw Angle (Model Coordinates)

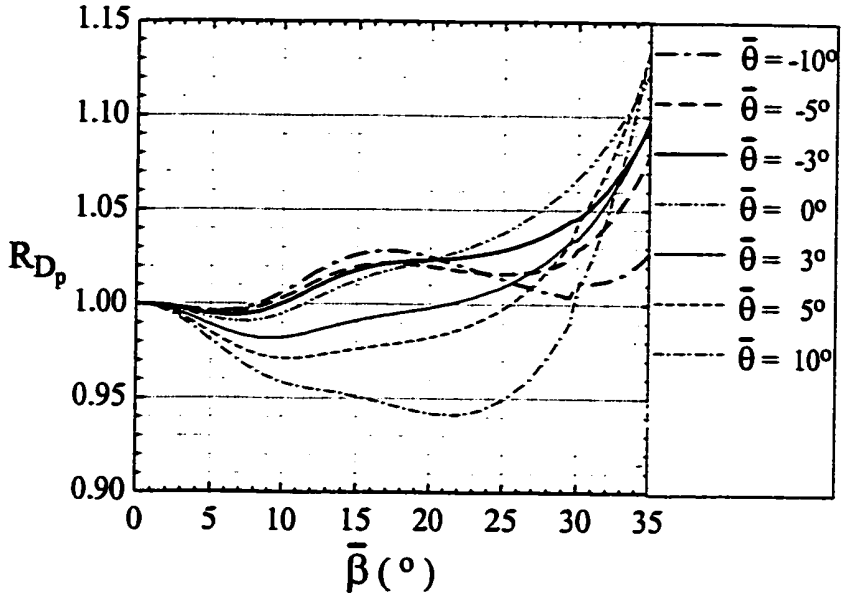

(a) Coefficient ratio of force along the model axis *p*

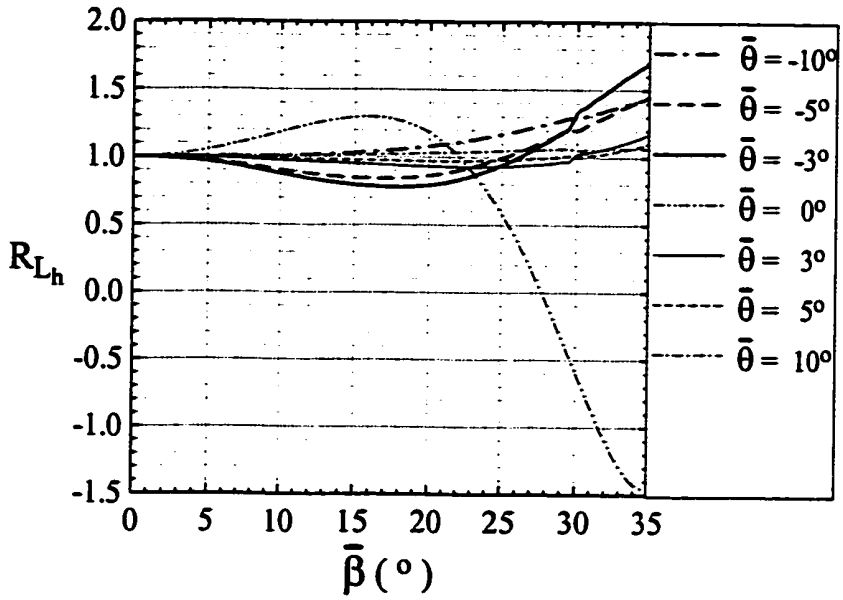

(b) Coefficient ratio of force along the model axis *h*

Figure 6-26 Aerodynamic Coefficient Ratios (Model Coordinates)

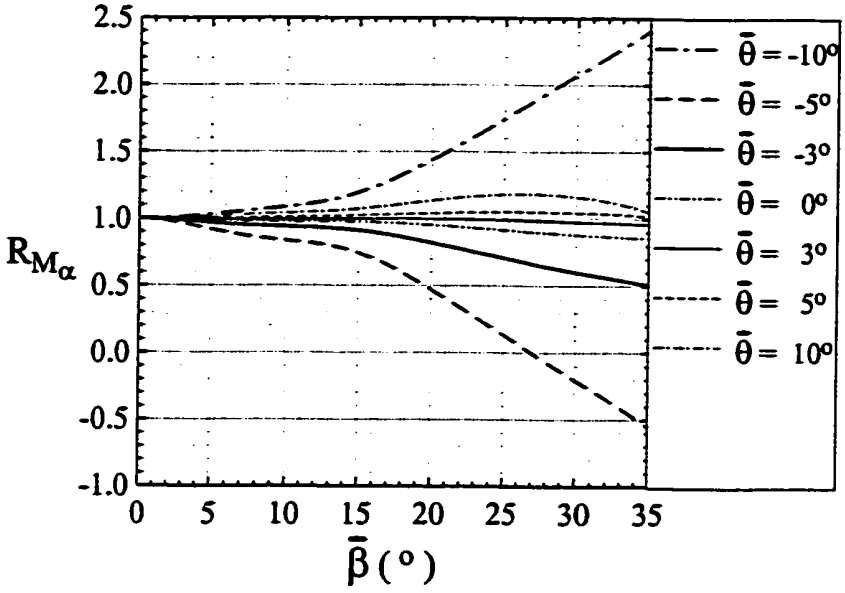

(c) Coefficient ratio of moment around the model axis *q*

Figure 6-26 (cont.) Aerodynamic Coefficient Ratios (Model Coordinates)

Chapter 7

WIND TUNNEL TEST FOR DECK FLUTTER DERIVATIVES UNDER SKEW WINDS

7.1 INTRODUCTION

To account for the aeroelastic effect on buffeting response of a long span bridge, Scanlan and his co-workers introduced self-excited forces into the equations of motion of the bridge for predicting its buffeting response (Scanlan and Gade, 1977; Scanlan, 1978b). The self-excited forces per unit length were expressed in terms of a set of flutter derivatives. These flutter derivatives are also essential for the flutter analysis of a long span bridge to estimate its critical wind speed. They are often obtained through wind tunnel tests in conjunction with system identification methods. Chapter 2 reviews various system identification methods for gaining the flutter derivatives.

To the best of the writer's recollection, the previous wind tunnel tests for flutter derivatives are carried out for the case in which mean wind speed is perpendicular to the longitudinal axis of a bridge deck model. This practice is based on the assumption that the flutter instability of a long span bridge occurs most likely when incident wind is normal to the longitudinal axis of the bridge. However, the field measurements of long span cable-supported bridges during strong winds demonstrate that strong winds seldom attack the bridge deck perpendicularly (Bietry 1994; Zhu et al., 1999; Xu et al., 2000). In fact, when designing a long span bridge, the bridge alignment is deliberately chosen such that its normal can be away, as far as possible, from the direction of predominant wind. This leads to some technical difficulties in performing a satisfactory comparison of buffeting response between field measurement and analysis. Furthermore, some wind tunnel test results revealed that buffeting response of a long span bridge under yaw wind might reach the same level as that under normal wind (Davenport et al., 1969; Tanaka and Davenport, 1982; Irwin and Gamble, 1985; Zan, 1987; Diana et al., 1995; Diana et al., 1999b; Kimura

and Ohara, 1999). The reasonable risk analysis or probability evaluation of a bridge to local wind climate also needs the directionality of wind to be taken into account. Thus, for a better prediction of buffeting response of a long span bridge and a reasonable comparison with field measurement results, the aerodynamic coefficients and flutter derivatives of a bridge deck under skew winds may have to be measured.

The wind tunnel tests and data analyses of the six aerodynamic coefficients of the Tsing Ma Bridge deck under skew winds have been presented in Chapter 6. To parallel this, this chapter presents an investigation on the flutter derivatives of the Tsing Ma Bridge deck under skew winds. The wind tunnel test rig developed for measuring the flutter derivatives for skew wind cases is first introduced. A unifying least-square (ULS) method, as introduced in Chapter 2, is then used to identify the flutter derivatives of the bridge deck under skew winds. Theoretically, the ULS method can be used to identify all the 18 flutter derivatives using a 3DOF sectional bridge deck model. However, due to the lack of a more inclusive experimental setup to accommodate the 3DOF bridge deck model, only the 8 important flutter derivatives associated with the vertical and torsional motions, namely H_i^*, A_i^* (i=1,2,3,4), will be measured using a 2DOF sectional model. The measured data are finally analyzed to find the relationship between the flutter derivatives, the reduced frequency, and the wind yaw angle and inclination for the later use in Chapters 9 and 10 in conjunction with the measured aerodynamic coefficients presented in Chapter 6. The results are also used to examine the approximate formula suggested for estimating the flutter derivatives of a bridge deck under yaw winds based on Scanlan's skew wind theory (Scanlan, 1999).

7.2 Model Design and Test Technique

7.2.1 Prototype Parameters

The structural configuration and the finite element model of the Tsing Ma suspension Bridge have been introduced in Chapter 3 in detail. The modal analysis of the Bridge was carried out by Xu et al (1997) and major results were provided in Chapter 3. The first torsional natural frequency dominated by the bridge deck with a symmetric torsional mode shape is 0.2712Hz. The lowest vertical natural frequency dominated

by the bridge deck with a symmetric mode shape is 0.1366Hz. The frequency ratio between the first torsional mode and the vertical bending mode of corresponding shape is thus

$$\varepsilon = f_t / f_v = 0.2712/0.1366 = 1.985 \tag{7-1}$$

This frequency ratio should be targeted in the design of a 2DOF sectional model for the measurement of flutter derivatives of the bridge deck under skew winds. To have a better wind tunnel simulation using a 2DOF sectional deck model, the effects of motion of other bridge components, such as towers and cables, and the effects of other modal components could be taken into consideration to some extent. In this connection, the effective mass and the effective mass moment of inertia of the prototype bridge deck are determined by (Zhu and Xiang, 1995)

$$m^e = \tilde{M}_v \Big/ \int_{L_d} \varphi_v^2(s) ds \tag{7-2a}$$

$$I_m^e = \tilde{M}_t \Big/ \int_{L_d} \varphi_t^2(s) ds \tag{7-2b}$$

where $\tilde{M}_v$ and $\tilde{M}_t$ are, respectively, the generalized mass of the whole bridge corresponding to the lowest symmetric vertical bending mode of vibration and the generalized mass moment of inertia of the whole bridge corresponding to the first symmetric torsional mode of vibration; φ_v is the vertical bending mode shape component of the bridge deck in the selected vertical mode of the whole bridge; φ_t is the torsional mode shape component of the bridge deck in the selected torsional mode of the whole bridge; and L_d is the length of the bridge deck, indicating that the integral should be carried out over the bridge deck only. The effective mass and the effective mass moment of inertia of the Tsing Ma Bridge per unit length are calculated as 44365.6kg/m and 8676036.8kgm^2/m, respectively, using Eq.7-2. The effective radius of gyration of the prototype bridge deck is then

$$r^e = \sqrt{I_m^e / m^e} = 13.984\text{m} \tag{7-3}$$

7.2.2 Model Design

The structural configuration of the Tsing Ma bridge deck has been described in Chapter 6 for the measurement of six aerodynamic coefficients of a typical deck section under skew winds. The same typical deck section was used in the design of the 2DOF sectional bridge deck model for the measurement of eight flutter

derivatives under skew winds. The length scale was selected as λ_L=1/100. The width of the sectional model was thus 0.41m. To facilitate the investigation of flutter derivatives of the deck model under skew winds, the dynamic sectional model was designed and composed of five major parts: one middle part, two end parts, and two support arms between the middle and end parts (see Figures 7-1 and 7-2). The length of the middle part was 2.407m and it remained unchanged in all the test cases. The two end parts of the dynamic sectional model were trapezoidal and its length changed with yaw angle designated. The five yaw angles, that is, 0°, 5°, 13°, 20° and 31°, were concerned in this study, which are the same as those used in Chapter 6 for the measurement of six aerodynamic coefficients. The definition of yaw angle $\overline{\beta}$ is the same as that used in Chapter 6 and shown in Figure 7-1. In corresponding to the five yaw angles, five pairs of the end parts were made. The short side length of the end part was 0.013m for all the test cases whilst the long side length varied according to the function of $0.013+0.41\tan\overline{\beta}$. The two support arms, 0.024m wide each, were suspended by eight helical springs from the wind tunnel and kept horizontal in all the test cases when there is no wind in the tunnel. The middle part and the two end parts were then properly connected to the two supporting arms to form a complete test model.

The plane view of the sectional model was generally of parallelogram (see Figure 7-2) except for the case of $\overline{\beta}=0°$, where the model plane view was rectangular. The two ends of the model were always kept in parallel to the incident wind in the wind tunnel. The end plates were not used in the tests to prevent from the distortion of axial flow along the longitudinal axis of deck model. The length-to-width ratio of the model in all the test cases was greater than 6.0. Thus, the 3-dimensional flow effect around the two ends of the model was regarded insignificant. Figures 7-2a and 7-2b show, respectively, the top surface and the bottom surface of the bridge deck model. All the important aerodynamic appearance of the prototype bridge deck, including the parapets and vents, was carefully modeled. It is seen that the bottom surface of the bridge deck model was quite complicated because the transverse beams were exposed to wind.

Figure 7-3 displays the cross section of the middle part of the dynamic model. Two 2391mm×38mm×26mm aluminum boxes, symmetrically arranged with a center-to-center distance of 281mm, were fixed to two aluminum end plates of 8mm thick (see Figure 7-4) to form a aluminum frame for the deck model. Two large circular openings were drilled on each of the end plates for reducing the model mass and mass moment of inertia. Several major wood plates were then fixed onto the aluminum frame to have the structural configuration properly modeled. To provide a space for adding mass to adjust the mass and the mass moment of inertia of the deck model towards the targeted values, the two wood plates just above the aluminum boxes were made removable, as shown in Figure 7-3. The distance between the center of the weighting space and the center of the whole model was 140.5mm, which was close to the design value of radius gyration, that is 139.84mm. This design kept the model radius of gyration almost unchanged when symmetrically adding the additional mass in the weighting spaces. Finally, a skeleton consisting of 54 cross frames linked by the upper and lower ventilation grids was installed into the central space of the model. The modeling details of the ventilation grids and the parapets were very similar to those used for the measurement of aerodynamic coefficients introduced in Chapter 6. The only difference is that the cross frames used here were made of 1mm thick ABS plastic other than 0.3mm thick steel plate. The cross section of the two end parts was similar to Section D-D of the model used for measuring aerodynamic coefficients (see Figure 6-7(d)). Two foam bodies were stuck to the ABS cross frames and ventilation grids and then they all were stuck to a 5mm ABS end plate. The ABS end plate was finally connected to the aluminum support arm and the end plate of middle part. The complete deck model with the aluminum frame turned out to be very rigid.

7.2.3 Model Installation and Position Adjustment

The oblique sectional model was suspended with four helical springs from the ceiling of the wind tunnel in the way as shown in Figures 7-5 and 7-6. The model was then pulled down and connected to the wind tunnel floor with another four helical springs. The sectional model was connected to the springs through the two aluminum support arms. Four rectangular openings on each of the two support arms were arranged for minimizing the disturbance to the wind flow near the two ends of the model. The distance between each pair of springs across the model width was determined in

accordance with the similarity law, which will be explained later. The eight springs were carefully selected from many springs to ensure that the eight springs had almost the same mechanical properties, such as weight, stiffness, and linear range of load-extension curve. The linear force and extension limitations of the eight springs were taken into account in the design to keep all the springs work in linear-elastic range during all the tests. To prevent the model from lateral motion, it was restrained by four very long wires in along-wind direction: two in the leeward and two in the windward. The horizontal wires were tied at the centers of the two ends of the model. They were so long and so flexible that their influence on the vertical and torsional motion of the model was negligible.

To facilitate the arrangement of the sectional model for each of the five designated wind yaw angles, there were two broken-line tracks fixed on the ceiling and another two on the floor of the wind tunnel (see Figure 7-5). Each broken-line track consists of 3 channel members. Five sets of screw eyes, with each set having eight screw eyes for the eight helical springs correspondingly, were bored on the channel members for the five designated yaw angles. All the screw eyes on either the floor tracks or the ceiling tracks were positioned on a circle of 1.247m radius. The center of circle on the floor was on the central line of the wind tunnel while the projection of the circle on the ceiling was the same as that on the floor. Each screw eye was labeled according to the designated yaw angle and the location. The projection of each screw eye on the ceiling track was the same as the corresponding labeled screw eye on the floor track. The anticipated yaw angle of the bridge deck model during the test was finally achieved by mounting each of the eight springs onto the corresponding labeled screw eye via an adjustable bolt (Figure 7-5).

As shown in Figure 7-6, there were two sets of holes on the aluminum support arm just next to the rectangular openings. Each set had five holes. Corresponding to the two sets of holes on the support arm, there were two sets of screw eyes drilled on the aluminum end plate of the middle part just next the big hole (see Figure 7-4). Each set had ten screw eyes. These holes and screw eyes were used to adjust the inclination of the model. The inclination of the model concerned in this study ranged from $0°$ to $\pm 5°$. It is defined as the rotational angle of the model around its longitudinal axis, as shown in Figure 7-6 denoted by θ_m. θ_m takes a negative value

if it is in counter clockwise. For each inclination, the middle part of the model was connected to the two support arms by three bolts at each end. The bolt of 10mm diameter at the center of the model was put into the position first and used also as a rotation shaft for the middle and end parts of the model. The model was then adjusted to the designated inclination. Each side bolt of 4mm diameter was finally put through the corresponding hole and fastened into the corresponding labeled screw eye on the aluminum end plate. For instance, if the inclination of the model should be set as -2°, the left side bolt should go through the opening L4 on the support arm (Figure 7-6) and then it is fastened tightly into the screw eye labeled with -2° on the left side of the aluminum end plate. Meanwhile, the right side bolt should pass through the opening R2 on the same support arm and it is fastened into the screw eye labeled with -2° on the right side of the same aluminum end plate.

After having fixed the middle part onto the two support arms, the two end parts of the model were installed. Each of them was connected to the aluminum end plate of the middle part by two bolts of 5mm diameter through the kidney-form openings on the support arm (see Figures 7-4 and 7-6). The two bolts were arranged symmetrically with respect to the center of the model and the distance between the two bolts was 70 mm. Apart from the two bolts, the end part was also fastened by another bolt at the center of the model. This bolt is also extended out of the end part of the model with a proper length on which the wires used for eliminating the model alongwind motion were tied. Since the two support arms were kept in horizontal no matter what was the model inclination and its height was less than the thickness of the model itself, adhesive tapes were used to seal the gap between the middle part and the end part of the model.

7.2.4 Model Parameters

After the installation of the model, the calibration was conducted on the model. The natural frequencies and damping ratios of the model were measured and examined against the prototype parameters and the similarity law, and then the adjustment was made if necessary. The final model parameters are listed in Table 7-1, where L_m is the model length; m_m and I_{mm} are the mass and mass moment of inertia per unit length, respectively; f_{vm} and f_{tm} are, respectively, the natural frequencies of the

vertical and torsional motion of the model in still air whilst ξ_{vm} and ξ_{tm} are the corresponding damping ratios; $\varepsilon_m = (f_t/f_v)_m$ is the frequency ratio; λ_L, λ_f and λ_V are the scales of length, frequency and wind velocity, respectively. The targeted values of the model mass and mass moment of inertia per unit length were 4.4356kg/m and 0.08676kgm^2/m, respectively. The requirement for mass simulation was met satisfactorily by weighing out the deck model and the 8 springs, where only a third of the spring mass was counted in according to the equivalent principle of kinetic energy. The mass moment of inertia was evaluated using the following relationship.

$$I_{mm} = \frac{K_{tm}}{(2\pi f_{tm})^2 L_m} = \frac{K_{vm} e_m^2}{(2\pi f_{tm})^2 L_m} = (e_m/\varepsilon_m)^2 m_m \tag{7-4}$$

where K_{vm} and $K_{tm} = K_{vm} e_m^2$ are the vertical and torsional stiffness of the deck model; e_m is a half of the distance between the two suspending springs connected to the same support arm (see Figure 7-6), which was determined by the similarity law as

$$e_m = \varepsilon r^e \lambda_L = 1.985 \times 13.984/100 = 0.278\text{m} \tag{7-5}$$

Table 7-1 Model Parameters

$\bar{\beta}$	0°	5°	13°	20°	31°
L_m (m)	2.4810	2.5169	2.5757	2.6302	2.7274
m_m (kg/m)	4.4356	4.4356	4.4356	4.4356	4.4356
I_{mm} (kgm^2/m)	0.08727	0.08814	0.08794	0.08694	0.08664
f_{vm} (Hz)	2.0103	1.9214	1.9048	1.8887	1.8578
f_{tm} (Hz)	3.9842	3.7892	3.7609	3.7504	3.6954
$\varepsilon_m = f_{tm}/f_{vm}$	1.9819	1.9721	1.9744	1.9857	1.9891
ξ_{vm} (%)	0.65~0.80	0.68~0.89	0.81~0.85	0.75~0.90	0.79~0.87
ξ_{tm} (%)	0.28~0.45	0.26~0.50	0.40~0.57	0.35~0.44	0.33~0.45
λ_L	1/100	1/100	1/100	1/100	1/100
λ_f	14.7	14.0	13.9	13.8	13.6
$\lambda_V = \lambda_L \lambda_f$	1/6.8	1/7.1	1/7.2	1/7.2	1/7.4

It is seen from Table 7-1 that the maximum error of the targeted mass moment of inertia is 1.6% in the case of $\bar{\beta} = 5°$. The maximum error of the targeted frequency ratio is 0.65% in the case of $\bar{\beta} = 5°$ as well. Because of the change of set-up for each inclination, the measured damping ratios slightly scatter within a range for a given wind yaw angle.

Table 7-2 Range of Wind Speed Used in Tests (m/s)

θ_m	$\bar{\beta}$				
	0°	5°	13°	20°	31°
-5°	2.0 ~ 22.0	2.0 ~ 20.0	2.0 ~ 20.0	2.0 ~ 20.0	2.0 ~ 20.0
-3°	2.0 ~ 20.0	2.0 ~ 22.0	2.0 ~ 20.0	2.0 ~ 20.0	2.0 ~ 20.0
-2°	2.0 ~ 22.0	2.0 ~ 21.0	2.0 ~ 20.0	2.0 ~ 20.0	2.0 ~ 20.0
0°	2.0 ~ 18.5	2.0 ~ 20.0	2.0 ~ 18.5	2.0 ~ 19.0	2.0 ~ 21.0
2°	2.0 ~ 16.0	2.0 ~ 14.0	2.0 ~ 16.0	2.0 ~ 15.5	2.0 ~ 18.0
3°	2.0 ~ 13.0	2.0 ~ 11.5	2.0 ~ 14.0	2.0 ~ 11.5	2.0 ~ 14.5
5°	1.0 ~ 12.0	2.0 ~ 9.0	2.0 ~ 9.0	2.0 ~ 8.5	2.0 ~ 11.0

7.3 WIND TUNNEL TEST

The coupled 2DOF free decay vibration was performed to identify the flutter derivatives of the Tsing Ma bridge deck in conjunction with the unifying least square (ULS) method (Zhang, 1998; Gu et al., 2000). The principle of the ULS method has been introduced in Chapter 2 in detail. The tests were carried out under smooth flow in the TJ-2 Wind Tunnel of the State Key Laboratory for Disaster Reduction in Civil Engineering at Tongji University of China. The configuration and the quality of wind field in the TJ-2 Wind Tunnel has been given in Chapter 6. The flutter derivatives are functions of reduce velocity/frequency, wind inclination, and wind yaw angle. Therefore, seven model inclinations (θ_m = 0°, ±2°, ±3°, ±5°) and five yaw angles ($\bar{\beta}$ = 0°, 5°, 13°, 20°, 31°) were considered, resulting in a total of 35 cases with respect to the model position. For each given position, the model was given a series

of coupled 2DOF free vibrations corresponding to a series of wind speeds to obtain flutter derivative curves as a function of reduced velocity. The wind speed was selected such that the number of test points on each curve of the flutter derivatives ranged from 10 and 15. The increment of wind speed was not uniform and it was adjusted during the test in the light of the on-site situation. The test points would be more if the curve tended to have a rapid change around a certain wind speed. The range of wind speeds used in the test for 35 position cases is listed in Table 7-2.

It should be pointed out that for any one of the cases in which θ_m and $\bar{\beta}$ are not zero, the model inclination (θ_m) defined in this Chapter is slightly different from the effective wind inclination ($\bar{\theta}$) defined as the angle between the mean wind and the deck plane in Chapters 3 and 6. The relation between the two angles of inclination can be expressed as

$$\bar{\theta} = \theta_m \cos\bar{\beta} \tag{7-6}$$

To obtain the time-histories of free decay curves of the model at a given position and a given wind speed, two accelerometers were mounted on one support arm and the third one was mounted on the other support arm, as shown in Figure 7-6. The distance (e_a) between one accelerometer and the longitudinal axis of the model was 0.263m. The vertical response of the model was obtained by averaging the outputs from the two accelerometers arranged in the diagonal. The torsional response was gained by multiplying the difference between the two outputs from the two accelerometers on the same support arm by a factor of $1/(2e_a)$. Figure 7-7 shows the data acquisition and analysis system used in the tests. The measurement system includes a six-channel charge amplifier (TS5865), an AD data acquisition, a computer, and a dynamic signal analyzer (HP35670A). The HP35670A dynamic signal analyzer shown in Figure 7-7c was used to monitor the vibration signals in real time. The acceleration signals from the accelerometers were amplified by the charge amplifier and sampled at 500Hz by the AD data acquisition and saved in the computer. The digital acceleration data from the three channels were immediately analyzed using a computer program implementing the ULS method to extract the flutter derivatives. For each wind speed and each model position, the test was

repeated for at least three times and the average values of flutter derivatives were stored into the test database for further action.

7.4 MEASUREMENT RESULTS

The identification of flutter derivatives using the coupled 2DOF free vibration method in this study is based on the following expressions for the self-excited lift (L_h^{se}) and pitching moment (M_α^{se}) acting on the oblique sectional model.

$$L_h^{se} = \frac{1}{2}\rho \overline{U}_m^2 B_m \left[K_1 H_1^*(\overline{\beta},\overline{\theta},K_1)\frac{\dot{\delta}_h}{\overline{U}_m} + K_2 H_2^*(\overline{\beta},\overline{\theta},K_2)\frac{B_m\dot{\delta}_\alpha}{\overline{U}_m} + K_2^2 H_3^*(\overline{\beta},\overline{\theta},K_2)\delta_\alpha + K_1^2 H_4^*(\overline{\beta},\overline{\theta},K_1)\frac{\delta_h}{B_m}\right] \quad (7\text{-}7a)$$

$$M_\alpha^{se} = \frac{1}{2}\rho \overline{U}_m^2 B_m^2 \left[K_1 A_1^*(\overline{\beta},\overline{\theta},K_1)\frac{\dot{\delta}_h}{\overline{U}_m} + K_2 A_2^*(\overline{\beta},\overline{\theta},K_2)\frac{B_m\dot{\delta}_\alpha}{\overline{U}_m} + K_2^2 A_3^*(\overline{\beta},\overline{\theta},K_2)\delta_\alpha + K_1^2 A_4^*(\overline{\beta},\overline{\theta},K_1)\frac{\delta_h}{B_m}\right] \quad (7\text{-}7b)$$

where, H_i^* and A_i^* (i=1,2,3,4) are the eight flutter derivatives to be identified, which are 2 times of those output by Zhang and Gu's computer program of ULS method (see Eqs.(2-33)); $\overline{U}_m$ is the test wind speed; ρ of 1.225 kg/m^3 is the air density; $B_m = 0.41$m is the width of the true cross section of the oblique sectional model (see Figure 7-8); $K_i = 2\pi f_{mi} B_m / \overline{U}_m$ (i=1,2) are reduced frequencies; f_{m1} and f_{m2} are the identified natural frequencies of the vertical motion dominant mode and the torsional motion dominant mode of the sectional model under wind speed $\overline{U}_m$; δ_h and δ_α are, respectively, the vertical displacement and torsional displacement of the model center, that is, the origin of the *qph*-system in Figure 7-8. The local reference coordinate (the model coordinate) *qph*-system and the local wind coordinate $\overline{qph}$-system in Figure 7-8 are the same as those used in previous chapters. Figure 7-8 also shows the definition of the self-excited lift (L_h^{se}) and pitching moment (M_α^{se}), which are along the axis h and around the axis q, respectively, of the local reference coordinate *qph*-system.

The test data of flutter derivatives for given model positions and wind speeds were interpolated/extrapolated and fitted to generate the design curves of eight flutter

derivatives H_i^* and A_i^* (i=1,2,3,4) as functions of reduced velocity ($\overline{U}/fB = 0 \sim 18$), wind inclination ($\overline{\theta}$ = -5° ~ 5°), and wind yaw angle ($\overline{\beta}$ = -31° ~ 31°). The flutter derivatives at negative yaw angles were the same as those of the corresponding positive yaw angles. The obtained eight flutter derivative curves are displayed in Figures 7-9 to 7-16 for wind inclinations ($\overline{\theta}$) of 0°, ±3° and ±5° and wind yaw angles ($\overline{\beta}$) of 0°, 5°, 13°, 20° and 31°. It is seen that H_1^* curves are basically negative for all the concerned wind inclinations and yaw angles, which indicates positive aeroelastic damping generated in the vertical motion of the bridge deck. The effects of wind inclination and yaw angle on H_1^* are relatively small when the reduced velocity is less than 10. The flutter derivative curves H_2^* are negative for the cases of $\overline{\theta} = -3°$ and $\overline{\theta} = -5°$, implying also positive aeroelastic damping in the vertical motion but caused by angular velocity. However, for the cases of $\overline{\theta} = 3°$ and $\overline{\theta} = 5°$, H_2^* becomes positive when reduced velocity exceeds about 12, except for the case of $\overline{\theta} = 5°$ and $\overline{\beta} = 13°$, in which H_2^* is small and negative. The positive H_2^* provides negative aeroelastic damping in the vertical motion of the bridge deck. It is also seen from Figure 7-10 that the effect of yaw angle on H_2^* becomes larger and larger with increasing reduced velocity. The curves H_3^* are negative for all wind inclinations and yaw angles within the reduced velocities concerned. The negative H_3^* means positive aeroelastic stiffness added to the vertical motion of the bridge deck. For most cases except the case of $\overline{\theta} = -5°$ and $\overline{\beta} = 13°$, the effects of both wind inclination and yaw angle on H_3^* are not significant when the reduced velocity is less than 8, but become considerable as the reduced velocity further increases. The flutter derivative H_4^* varies with reduced velocity in complicated pattern, leading to the addition of either positive or negative aeroelastic stiffness to the vertical motion of the bridge deck. Only for the case of $\overline{\theta} = 3°$, the values of H_4^* are negative for all yaw angles within the concerned reduced velocity range.

The flutter derivative A_1^* is associated with aeroelastic damping in the torsional motion of the bridge deck. It is seen from Figure 7-13 that in the cases of $\overline{\theta} \leq 0°$,

A_1^* is generally positive, indicating negative aeroelastic damping in the torsional motion. The effects of wind yaw angle and inclination on A_1^* are significant. The flutter derivative A_2^* is the most important derivative directly related to the critical wind speed of the Bridge. Positive value of A_2^* results in positive aeroelastic damping added to the torsional motion of the bridge deck. It is seen from Figure 7-14 that with the increasing wind inclination, A_2^* tends to have the positive values, which implies a low critical wind speed. The effect of wind yaw angle is considerable within the larger reduced velocity range. The flutter derivatives A_3^* and A_4^* are associated with aeroelastic stiffness in the torsional motion of the bridge deck. From Figure 7-15, it is seen that except for the case of $\bar{\theta} = 3^\circ$ and $\bar{\beta} = 13^\circ$ in the higher reduced velocity range, A_3^* is always positive, generating a negative torsional stiffness. The variation of A_4^* with reduced velocity is quite fluctuating and it takes a positive value sometimes but a negative value at other times. Both the wind inclination and yaw angle influence A_4^* significantly.

As mentioned before, the flutter derivative A_2^* is the most important derivative and it is directly related to the critical wind speed of the Bridge. To evaluate the effects of both wind inclination and yaw angle on the critical wind speed (flutter instability) of the Tsing Ma Bridge, the single DOF torsional flutter theory (Scanlan, 1999) is used. The portion of the flutter derivative A_2^* curves shown in Figure 7-14 at lower reduced velocities has been expanded in Figure 7-17 to permit a more detailed examination. An additional horizontal threshold line for flutter instability is also plotted in Figure 7-17. The threshold value of the critical wind speed is obtained based on the flutter derivative A_2^* only, that is

$$A_2^* = 4\xi_{st} I_m^e / \rho B^4 \tag{7-8}$$

where, the effect of the wind stiffness on vibration frequency via the flutter derivative A_3^* is regarded to be small and thus ignored; ρ is the air density and it is taken as 1.225kg/m^3; ξ_{st} is the structural torsional modal damping ratio. For the Tsing Ma suspension Bridge, I_m^e is equal to 8676.0368 tm^2/m and B is 41.0m. Thus,

provided that ξ_{st} is 0.005, the threshold value of A_2^* is about 0.05, by which the critical wind speed of the Bridge can be identified as listed in Table 7-3 and the effects of wind inclination and yaw angle on the critical wind speed can be evaluated.

Table 7-3 Flutter Critical Wind Speed of Tsing Ma Bridge Based on Measured A_2^* Curves (m/s)

$\bar{\theta}$	$\bar{\beta}$				
	0°	5°	13°	20°	31°
0°	149.1	>200.0	153.9	167.8	171.3
3°	74.1	74.1	86.2	77.4	88.5
5°	56.3	43.0	49.1	48.2	61.0

Figure 7-17 and Table 7-3 demonstrates that for the case of $\bar{\theta} = 0°$, the lowest critical wind speed occurs at $\bar{\beta} = 0°$ and then $\bar{\beta} = 13°$, $\bar{\beta} = 20°$, $\bar{\beta} = 31°$, and $\bar{\beta} = 5°$ in an ascending order. For the case of $\bar{\theta} = 3°$, the lowest critical wind speed occurs not only at $\bar{\beta} = 0°$ but also at $\bar{\beta} = 5°$ and then $\bar{\beta} = 20°$, $\bar{\beta} = 13°$, and $\bar{\beta} = 31°$ in an ascending order. As the wind inclination ($\bar{\theta}$) increases to 5°, the lowest critical wind speed takes place at $\bar{\beta} = 5°$ and then $\bar{\beta} = 20°$, $\bar{\beta} = 13°$, $\bar{\beta} = 0°$, and $\bar{\beta} = 31°$ in an ascending order. Clearly, the critical wind speed does not increase with increasing wind yaw angle. In particular, when $\bar{\theta}$ is equal to 5° the lowest critical wind speed occurs when wind yaw angle is 5°. Apparently, this can not be predicted by the traditional skew wind flutter theory based on "cosine rule" which assumes that a given skew wind velocity will be critical for flutter if its cosine component normal to the bridge deck equals the critical bridge normal-wind velocity. The reason behind this may be due to the complicated deck bottom surface of the Tsing Ma Bridge. The flow pattern around the transverse girder system, which is exposed to incident wind, is sensitive to wind inclination and wind yaw angle. Thus, even though the wind speed component normal to the bridge deck is reduced due to wind yaw angle, the aeroelastic resistant performance of the bridge deck is also reduced. Furthermore, if

comparing the three lowest critical wind speeds for the three inclinations, one may find that the larger is wind inclination, the less the lowest critical wind speed.

7.5 COMPARISON WITH SCANLAN'S SKEW WIND THEORY

Based on the oblique strip theory and the single DOF torsional flutter theory, Scanlan (1999) proposed his skew wind theory for estimating the critical flutter wind speed of long span bridges under skew wind. In this skew wind theory, the trace of the skew wind is assumed to cross an oblique cross section in mean wind direction with an elongated deck width of $B'=B/\cos\bar{\beta}$. Where, B is the width of the true cross section of the bridge deck, $\bar{\beta}$ is yaw angle of wind from the normal of the bridge deck. Then, an approximate relation can be established between the flutter derivatives A_2^* of the bridge deck under the skew wind and that one under the normal wind, which is often measured through wind tunnel sectional model test. The former can thus be estimated in terms of the test data of the latter.

Though only the formula for estimating A_2^* for the skew wind case was given by Scanlan, the formulae for estimating other 17 flutter derivatives have been derived by the writer in Chapter 5 using the same principle. In this section, the flutter derivatives of the Tsing Ma Bridge measured under skew winds using an oblique sectional model are compared with those estimated using those measured under normal wind based on the Scanlan's skew wind theory. For the sake of clarification, only the most important three flutter derivatives, H_1^*, A_2^* and A_3^* are discussed. The corresponding formulae for estimating the three major flutter derivatives under skew winds are given as follows.

$$A_2^*(\bar{\beta},\bar{\theta},K)\approx A_2^*(0^\circ,\bar{\theta},K')/\cos^2\bar{\beta} \tag{7-9a}$$

$$A_3^*(\bar{\beta},\bar{\theta},K)\approx A_3^*(0,\bar{\theta},K')/\cos^2\bar{\beta} \tag{7-9b}$$

$$H_1^*(\bar{\beta},\bar{\theta},K)\approx H_1^*(0,\bar{\theta},K')/\cos^2\bar{\beta} \tag{7-9c}$$

Then, the flutter critical wind speed can also be estimated according to the estimated $A_2^*(\bar{\beta},\bar{\theta},K)$ curves. The corresponding estimated results for Tsing Ma Bridge are shown in Table 7-4, where, the threshold is also taken as 0.05 corresponding to

torsional modal damping ratio of 0.005. The percentage numbers in Table 7-4 indicate the relative deviation of the flutter critical wind speed based on the estimated $A_2^*(\bar{\beta},\bar{\theta},K)$ curves from those based on the measured $A_2^*(\bar{\beta},\bar{\theta},K)$ curves. From Table 7-4, it can be found that two sets of flutter critical speed could be very close to each other in some cases, such as ($\bar{\theta}=0°$; $\bar{\beta}=13°$ and $\bar{\beta}=31°$) and ($\bar{\theta}=3°$; $\bar{\beta}=5°$ and $\bar{\beta}=20°$), but could significantly deviate from each other in some other cases, such as ($\bar{\beta}=5°$; $\bar{\theta}=0°$ and $\bar{\theta}=5°$), ($\bar{\beta}=13°$; $\bar{\theta}=3°$ and $\bar{\theta}=5°$) and ($\bar{\beta}=20°$;$\bar{\theta}=5°$).

Table 7-4 Flutter Critical Wind Speed of Tsing Ma Bridge Based on the Estimated A_2^* Curves (m/s)

$\bar{\theta}$	$\bar{\beta}$			
	5°	13°	20°	31°
0°	149.6 (—)	152.7 (-0.8%)	157.8 (-6.0%)	171.9 (0.4%)
3°	74.4 (0.4%)	75.7 (-12.2%)	77.9 (0.6%)	83.8 (-5.3%)
5°	56.5 (31.4%)	57.6 (17.3%)	59.3 (23.0%)	64.2 (5.2%)

Figures 7-18 to 7-21 show the comparisons between the flutter derivative curves A_2^*, measured under the skew winds of $\bar{\beta}=5°, 13°, 20°, 31°$ and under the normal wind of $\bar{\beta}=0°$, and those estimated using Eq. (7-9a) for the wind inclination of 0°, ±3° and ±5°. From these figures, one may see that the shapes of the estimated curves A_2^* are very similar to those of the A_2^* curves measured under normal wind (i.e. $\bar{\beta}=0°$), and the estimated flutter derivative curves A_2^* are closer to the measured ones under the normal wind than the measured ones under yaw winds. In many cases, the estimated flutter derivative curve A_2^* under yaw winds rather approaches that measured under yaw wind in the lower range of the reduced velocity. However, for the higher range of reduced velocity, the estimated flutter derivative curves A_2^* under yaw winds considerably deviate from the measured curves A_2^* under yaw winds in

most cases. Only in a few cases, such as ($\bar{\theta}=0°$, $\bar{\beta}=31°$) and ($\bar{\theta}=3°$, $\bar{\beta}=20°$), the estimated flutter derivative A_2^* under skew winds are close to the measured flutter derivatives under the same skew winds in the whole concerned range of reduced velocity.

The comparisons between the flutter derivative curves A_3^*, measured under the skew winds of $\bar{\beta}=5°, 13°, 20°, 31°$ and under the normal wind of $\bar{\beta}=0°$, and those estimated using Eq.7-9b are displayed in Figures 7-23 and 7-27 for the wind inclination of 0°, ±3° and ±5°. It is also found that the shapes of the estimated curves A_3^* are very similar to the shapes of the A_3^* curves measured under normal wind (i.e. $\bar{\beta}=0°$), and the estimated flutter derivative curves A_3^* are closer to the measured ones under the normal wind than the measured ones under yaw winds. Furthermore, in the cases of ($\bar{\theta}=-5°$, $\bar{\beta}\leq 20°$) and ($\bar{\theta}=-3°, \bar{\beta}\leq 13°$), the estimated flutter derivative curves A_3^* are close to the measured ones under both the skew winds and normal wind. This may be because in such wind inclinations, the flutter derivative A_3^* of the concerned bridge deck is not very sensitive to wind yaw angle. For the larger yaw angle or other wind inclinations, the differences between the estimated and measured flutter derivatives under skew winds are significant in the range of higher reduced velocity. However, within a certain lower range of reduced velocity, there are good agreements between the estimated and measured flutter derivatives A_3^* under skew wind.

Figures 7-28 to 7-32 show the comparisons between the flutter derivative curves H_1^*, measured under the skew winds of $\bar{\beta}=5°, 13°, 20°, 31°$ and under the normal wind of $\bar{\beta}=0°$, and those estimated using Eq. (7-9c) for the wind inclination of 0°, ±3° and ±5°. Compared with the flutter derivatives A_2^* and A_3^*, the differences between the estimated and measured flutter derivative H_1^* under skew winds are small in general with a similar curve pattern. Nevertheless, in most cases, the values of the estimated flutter derivative H_1^* in higher range of reduced velocity deviate quite evidently from the corresponding measured ones.

From the above comparisons, one may conclude that the empirical formulae Eqs. (7-9) for estimating the three major flutter derivatives under skew winds of Tsing Ma Bridge based on Scanlan's skew wind theory may be adequate only in a certain lower range, but generally not in the whole concerned range of reduced velocity. Thus, the reasonable comparison of buffeting response of Tsing Ma Bridge between the field measurement and the analysis should be performed using the flutter derivatives of the bridge deck measured under skew winds.

7.6 SUMMARY

A wind tunnel test technique for measuring the eight flutter derivatives of a bridge deck under skew winds has been developed. This included the design of oblique sectional model, the development of test rig, and the use of the unifying least square method for identification. By using the proposed wind tunnel test technique, the eight flutter derivatives of the Tsing Ma Bridge deck were measured as functions of wind inclination and yaw angle. The effects of wind inclination and yaw angle on the flutter derivatives, in particular A_2^*, were discussed in detail. The measured flutter derivatives were compared with those estimated based on the skew wind theory proposed by Scanlan. Furthermore, the flutter critical wind speeds based on the measured A_2^* curves were also compared with those based on the estimated A_2^* curves. Major conclusions can be drawn from as follows:

(1) The effect of wind yaw angle on the flutter derivatives H_1^*, H_2^*, H_3^*, A_2^* and A_3^* was in general not conspicuous in the lower range of the reduced velocity, but became considerable in the range of higher reduced velocity. The flutter derivatives H_4^*, A_1^* and A_4^*, however, oscillated remarkably with reduced velocity and were affected by the wind yaw angle within the whole range of reduced velocity.

(2) The eight flutter derivatives were sensitive to wind inclination, particularly in the range of higher reduced velocity.

(3) The critical wind speed of the Tsing Ma Bridge, estimated based on the SDOF torsional flutter theory, did not increase with increasing wind yaw angle. The lowest critical wind speed could occur when mean wind deviated from the normal of the bridge longitudinal axis.

(4) In general, the flutter derivatives for yaw wind cases estimated by the empirical formulae derived in the light of Scanlan's skew theory deviated significantly from the measured results. However, for lower reduced velocities, reasonable estimated values of the major flutter derivatives for yaw wind cases could be obtained using these empirical formulae.

(5) The critical wind speeds based on the estimated A_2^* using the skew wind theory were very close to those based on the measured A_2^* in some cases, but significantly deviated from those based on the measured A_2^* in other cases.

(6) The reasonable comparison of buffeting response of the Tsing Ma Bridge between the field measurement and the analysis should be performed using the flutter derivatives of the Bridge measured under skew winds.

However, it should be pointed out that the above conclusions were drawn from the Tsing Ma Bridge only. More investigations are needed in order to have a clear understanding of the effects of wind inclination and yaw angle on the flutter derivatives.

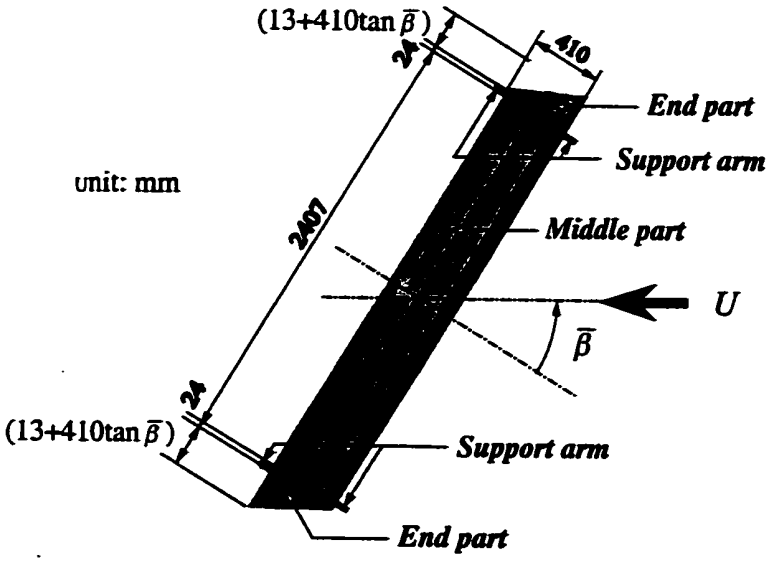

Figure 7-1 Dynamic Sectional Model of Bridge Deck under Yaw Wind

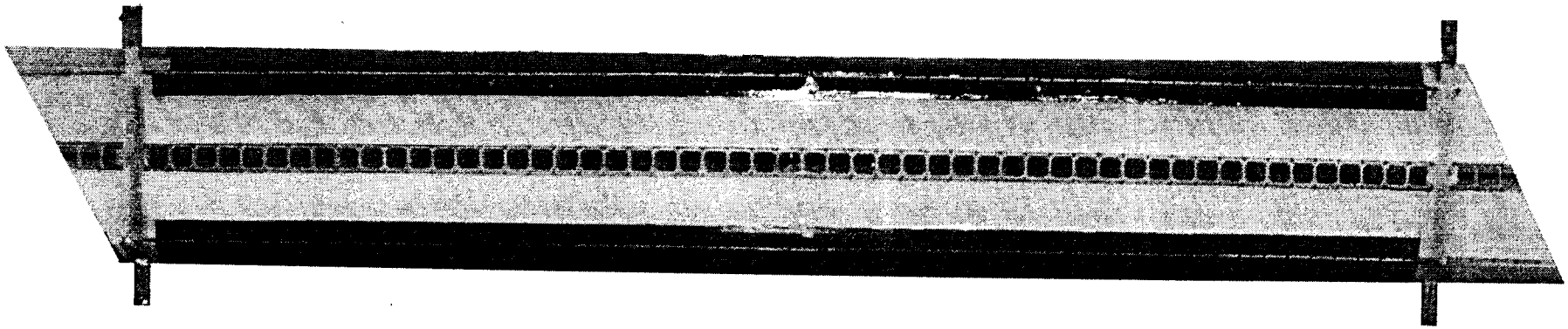

(a) Top view

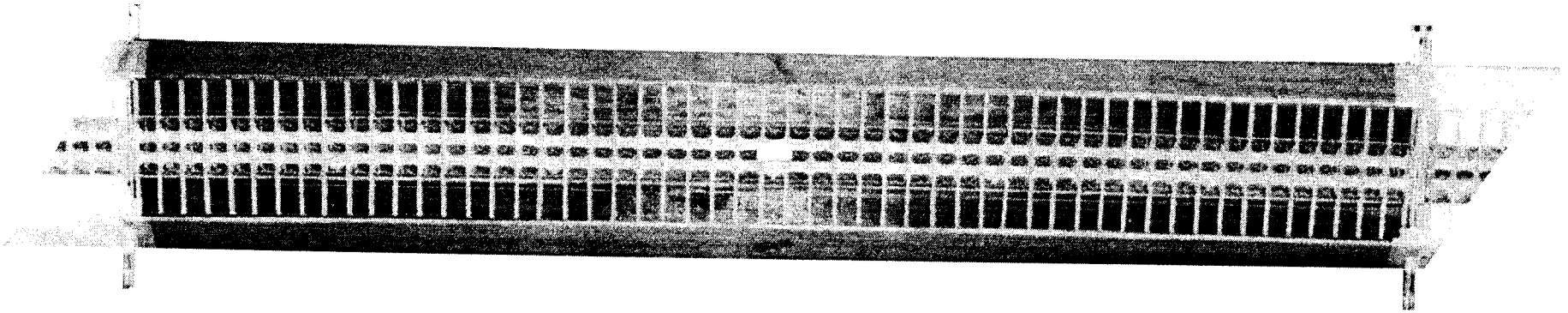

(b) Bottom view

Figure 7-2 Top and Bottom Views of Dynamic Sectional Model ($\overline{\beta} = 31^{\circ}$)

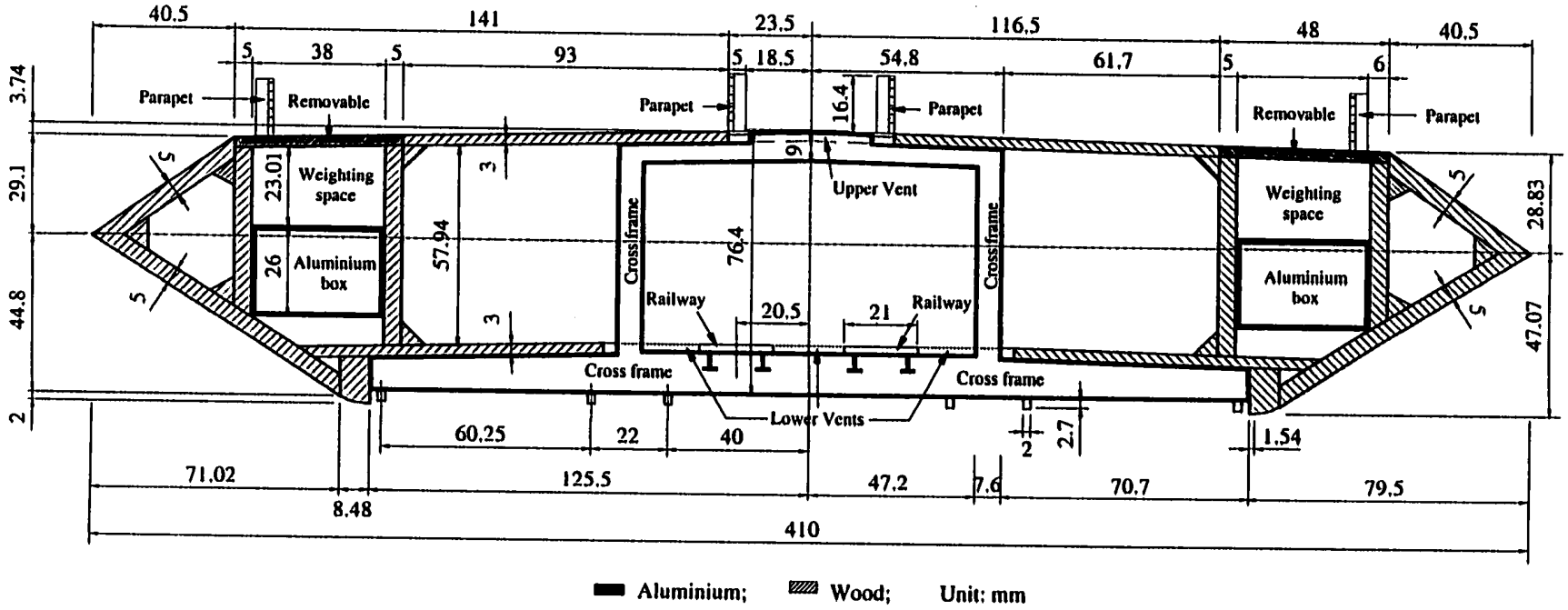

Figure 7-3 Cross Section of Middle Part of Dynamic Model

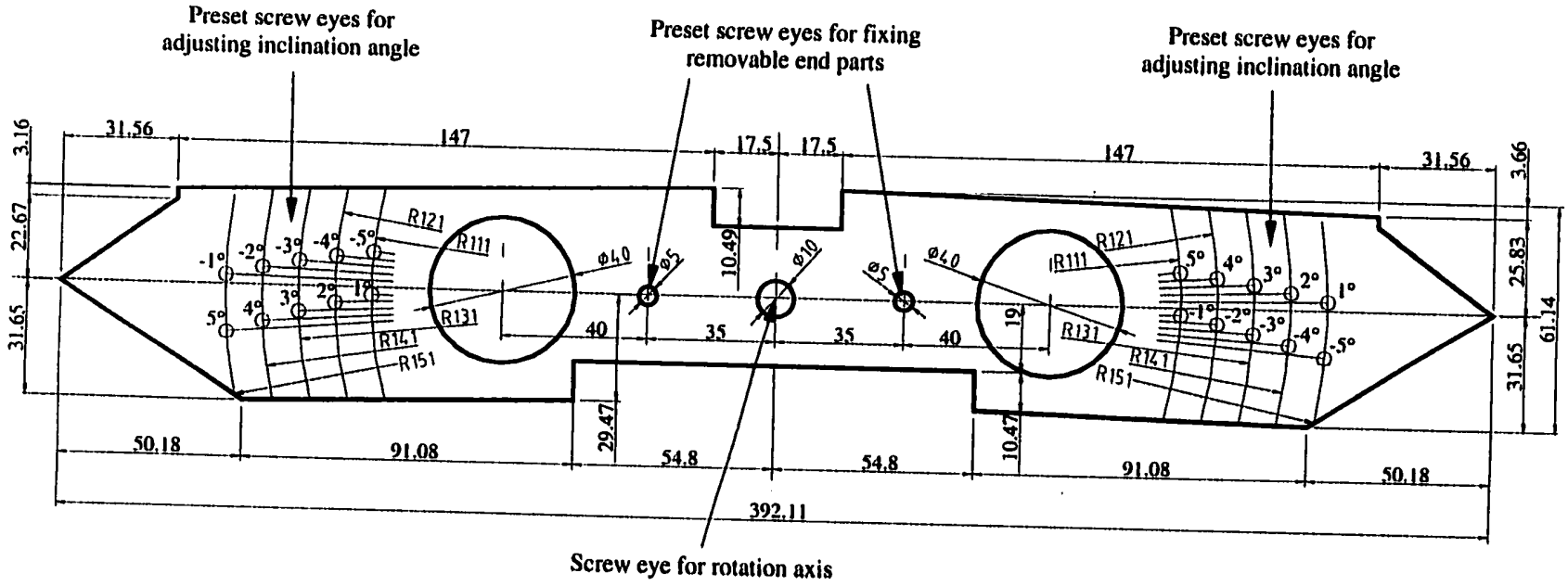

Figure 7-4 Aluminium End Plate of Middle Part of Dynamic Model

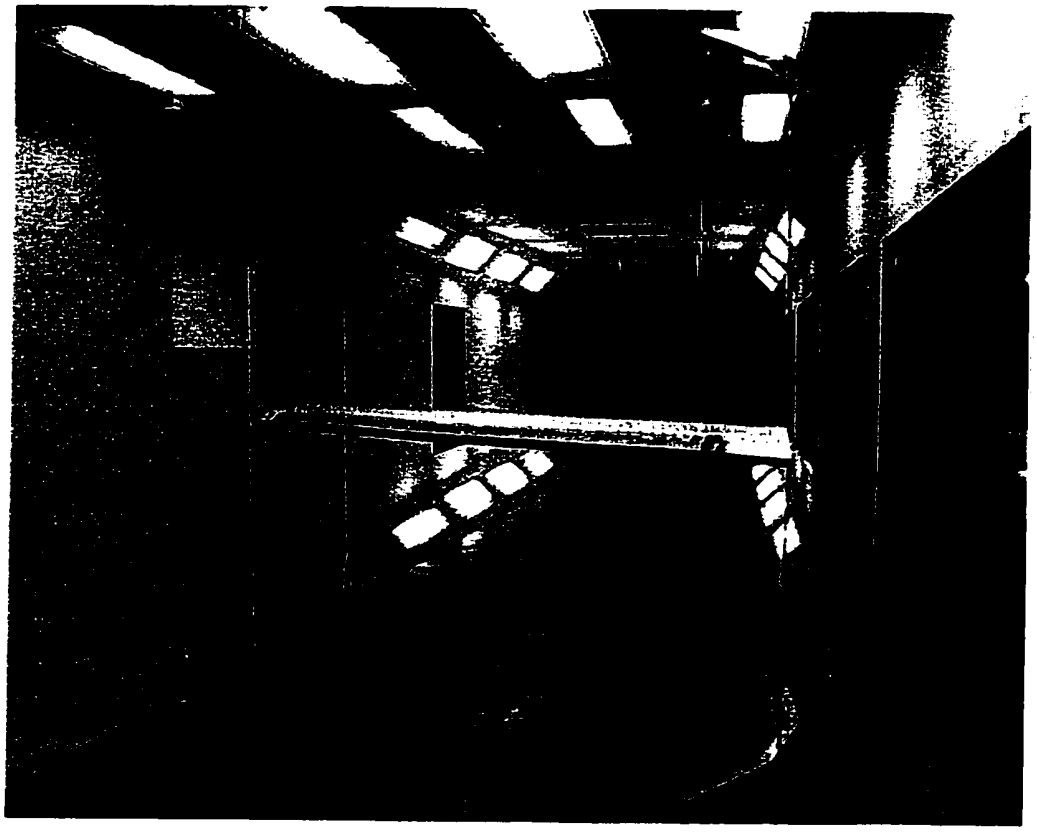

Figure 7-5 Installation of Dynamic Sectional Model in TJ-2 Wind Tunnel ($\overline{\beta} = 31°$)

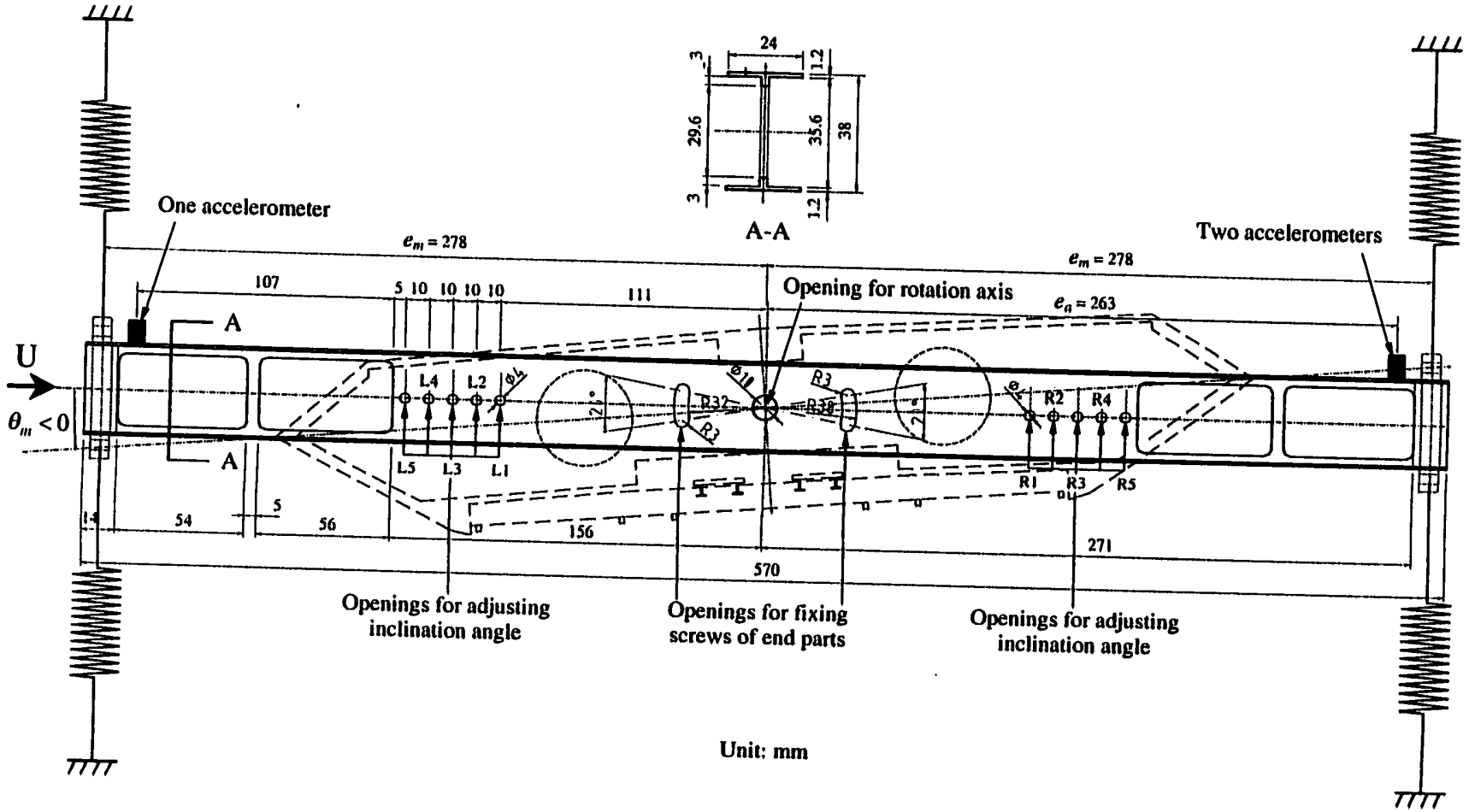

Figure 7-6 Aluminium Support Arms

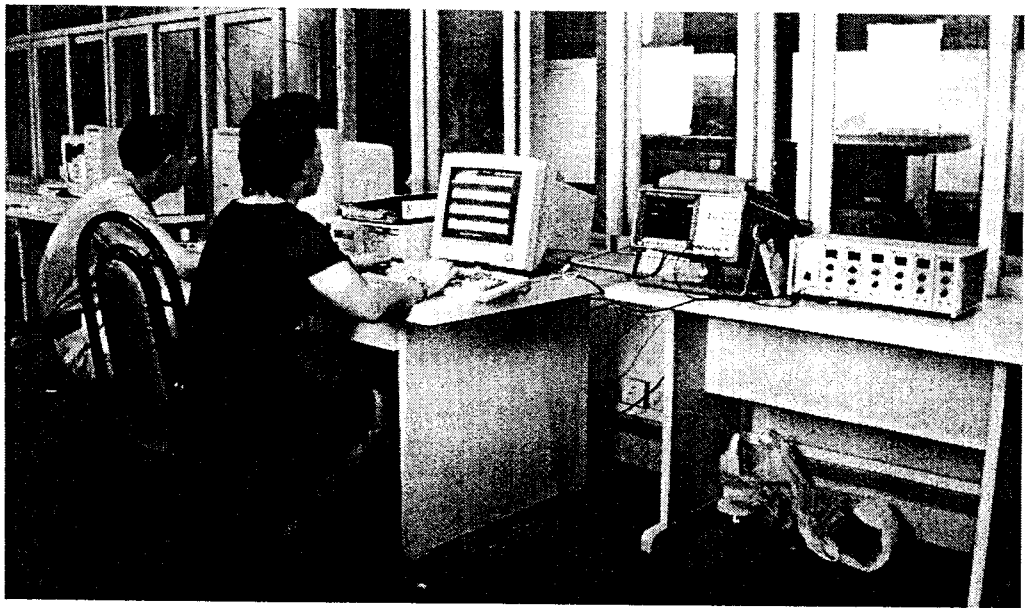

(a) System in Operation

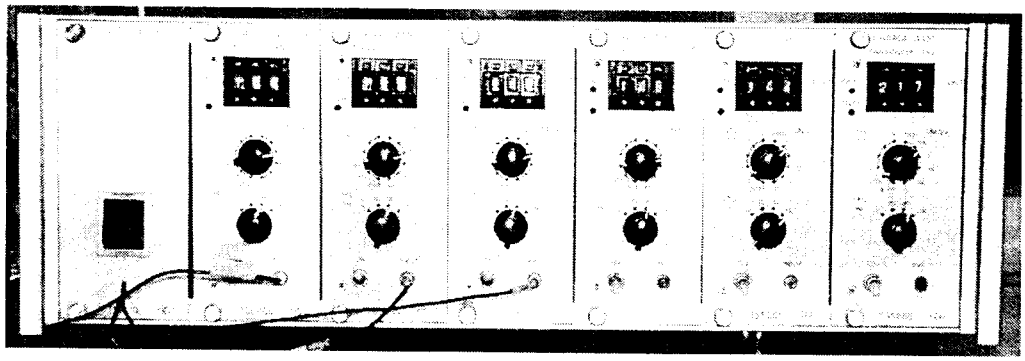

(b) TS5865 Charge Amplifiers

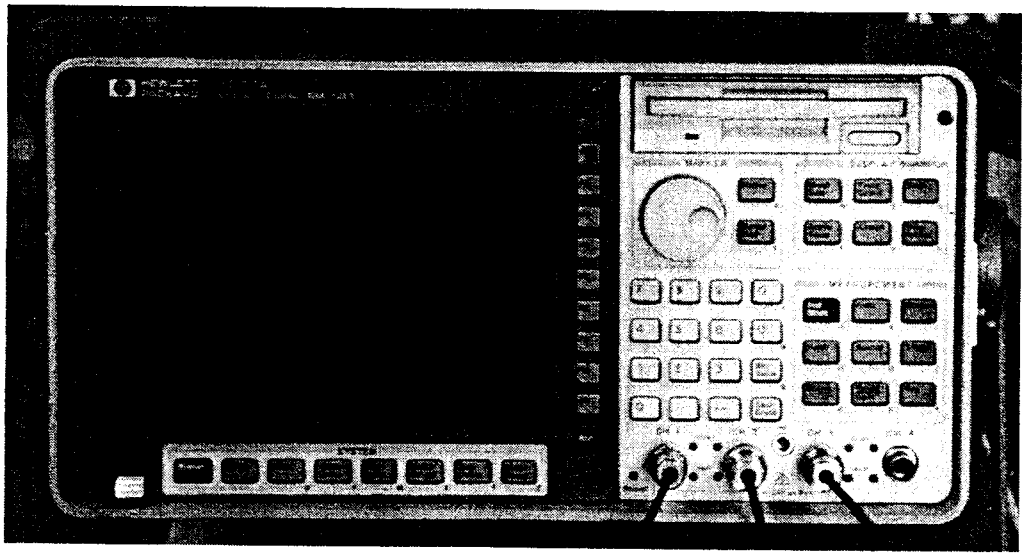

(c) HP35670A Dynamic Signal Analyzer

Figure 7-7 Data Acquisition and Analysis System Used Tests

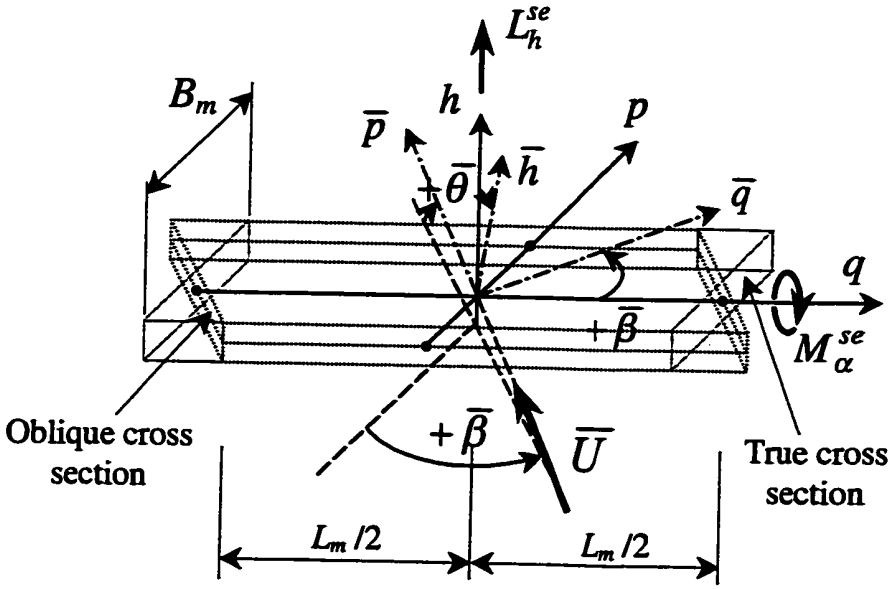

Figure 7-8 Definition of Local Reference Coordinates and Self-excited Forces

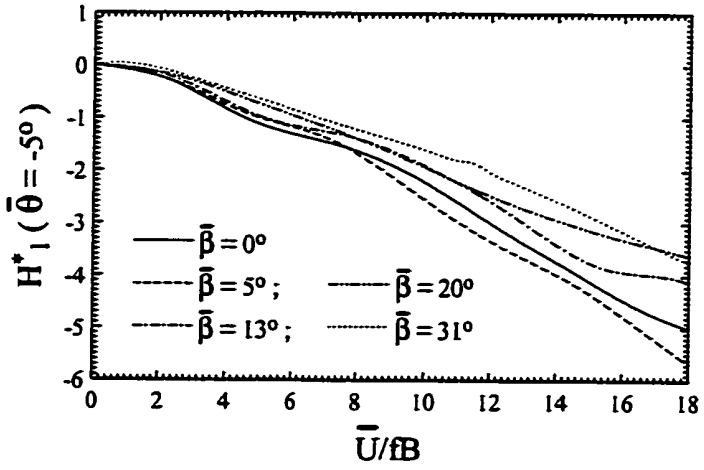

(a) $\theta = -5°$

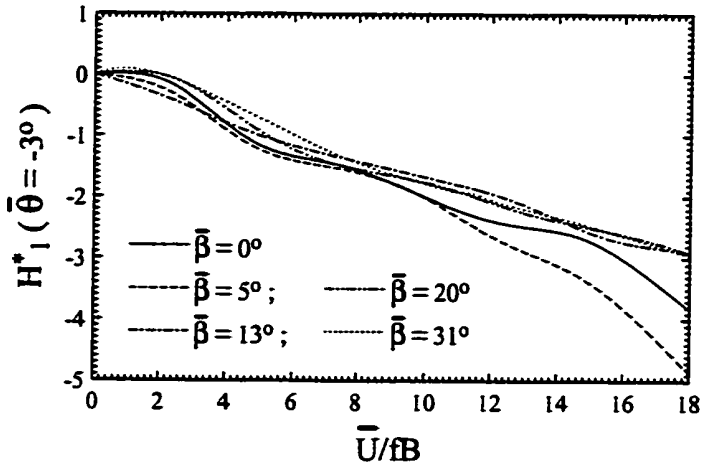

(b) $\theta = -3°$

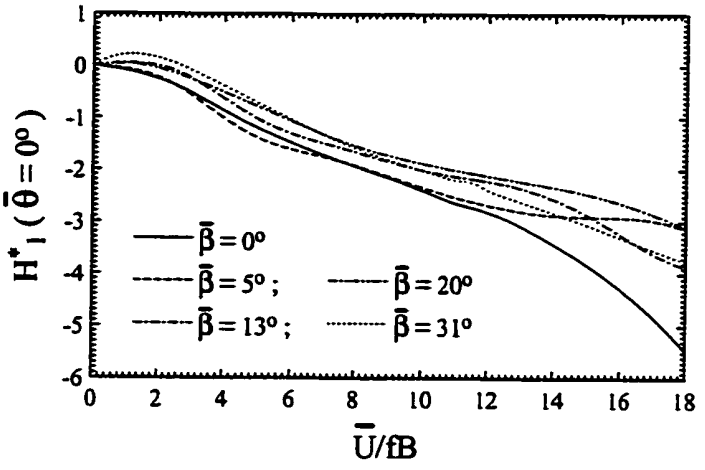

(c) $\theta = 0°$

Figure 7-9 Flutter Derivative Curves: H_1^* vs. $\bar{U}/fB$

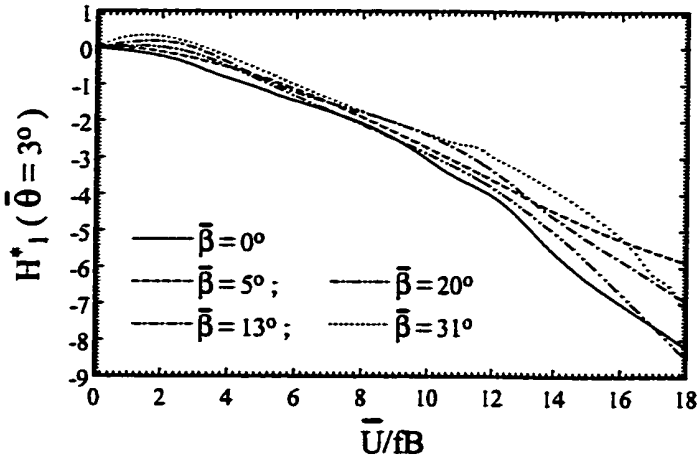

(d) $\theta = 3°$

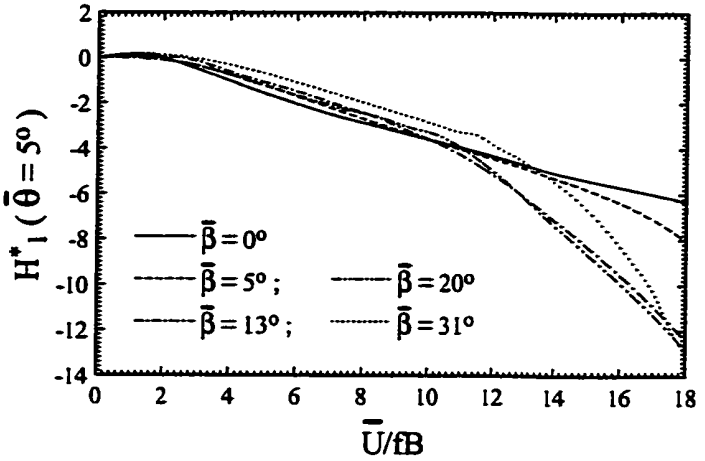

(e) $\theta = 5°$

Figure 7-9 (cont.) Flutter Derivative Curves: H_1^* vs. $\overline{U}/fB$

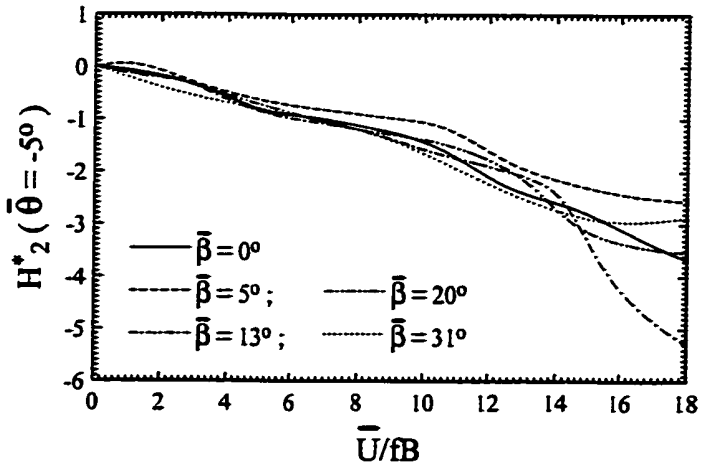

(a) θ = -5°

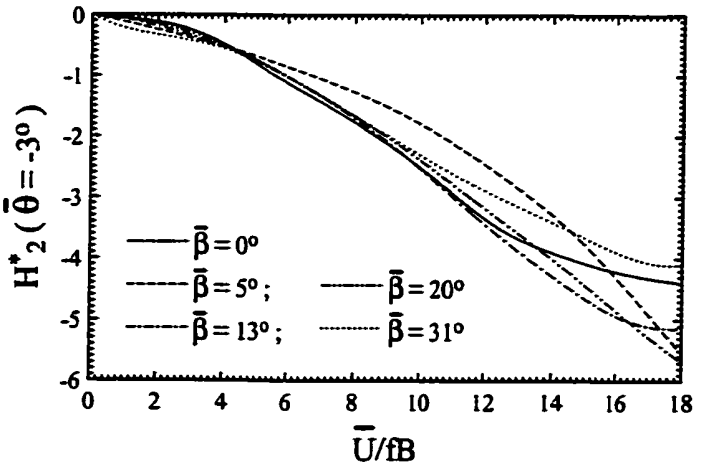

(b) θ = -3°

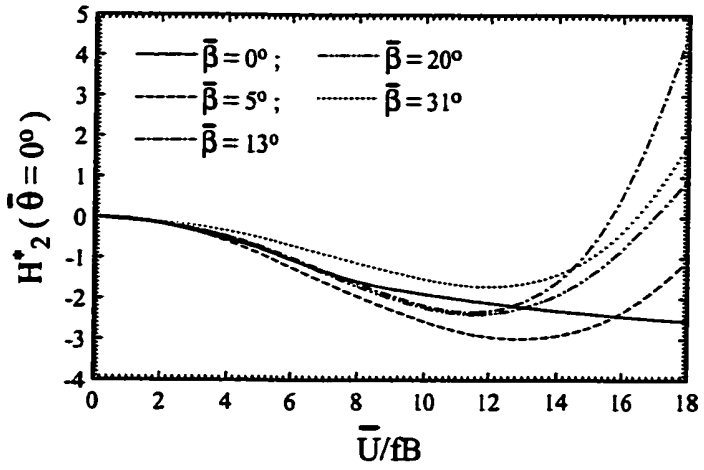

(c) θ = 0°

Figure 7-10 Flutter Derivative Curves: H_2^* vs. $\bar{U}/fB$

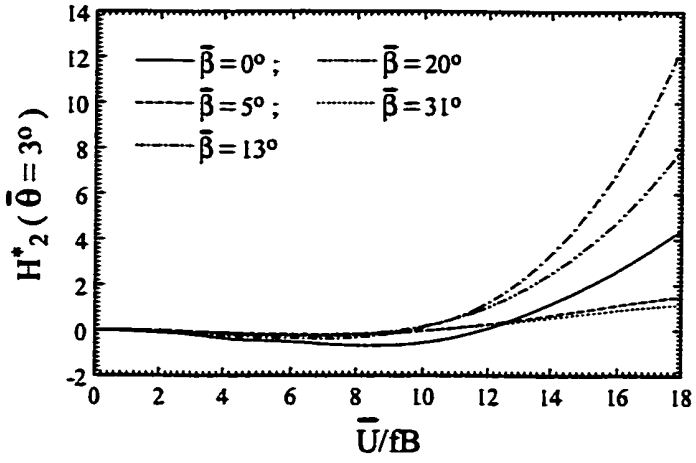

(d) $\theta = 3°$

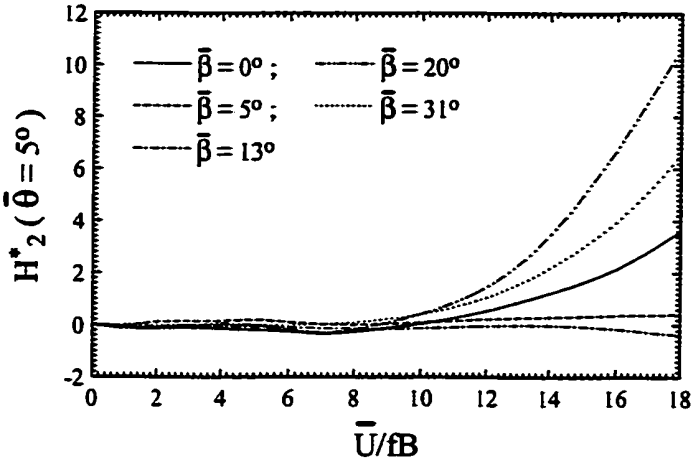

(e) $\theta = 5°$

Figure 7-10 (cont.) Flutter Derivative Curves: H_2^* vs. $\bar{U}/fB$

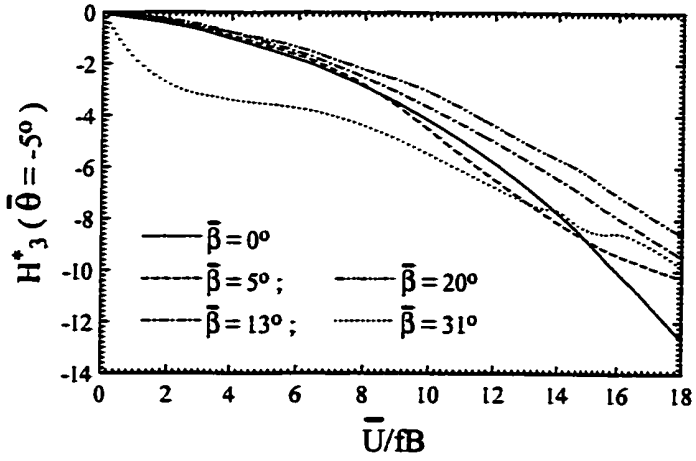

(a) $\theta = -5°$

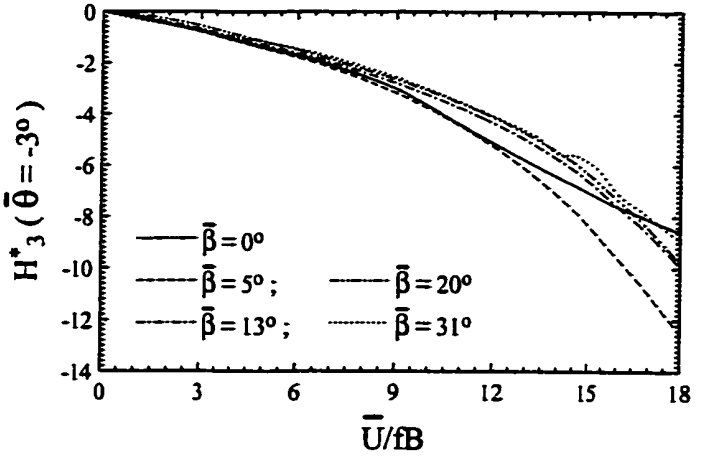

(b) $\theta = -3°$

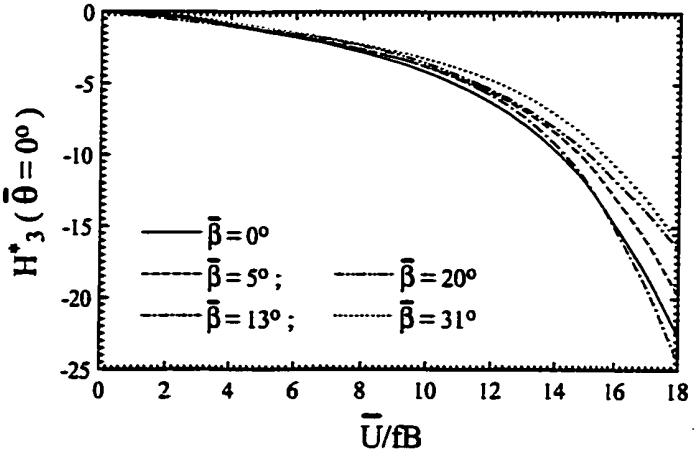

(c) $\theta = 0°$

Figure 7-11 Flutter Derivative Curves: H_3^* vs. $\bar{U}/fB$

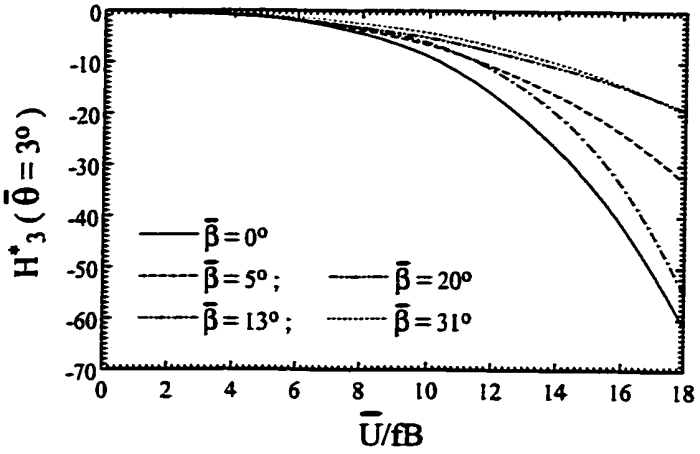

(d) $\theta = 3°$

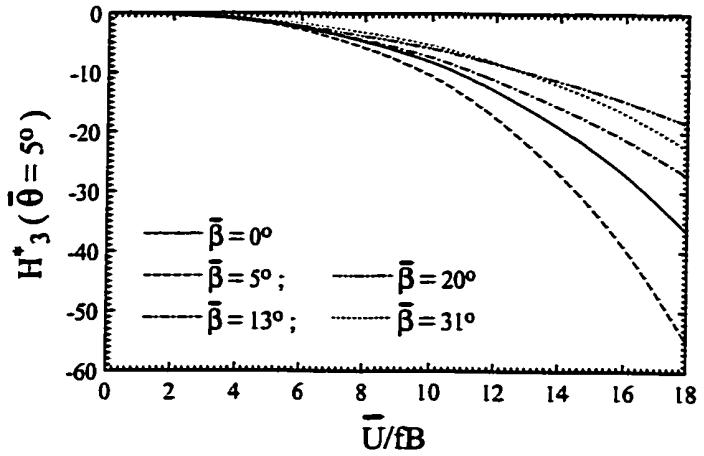

(e) $\theta = 5°$

Figure 7-11 (cont.) Flutter Derivative Curves: H_3^* vs. $\overline{U}/fB$

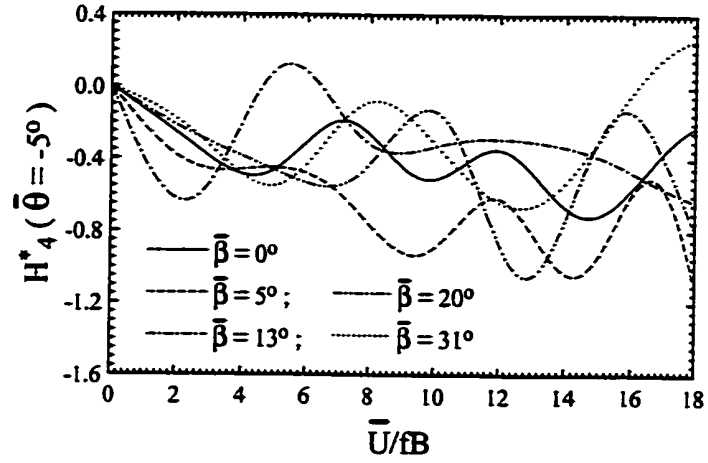

(a) $\theta = -5°$

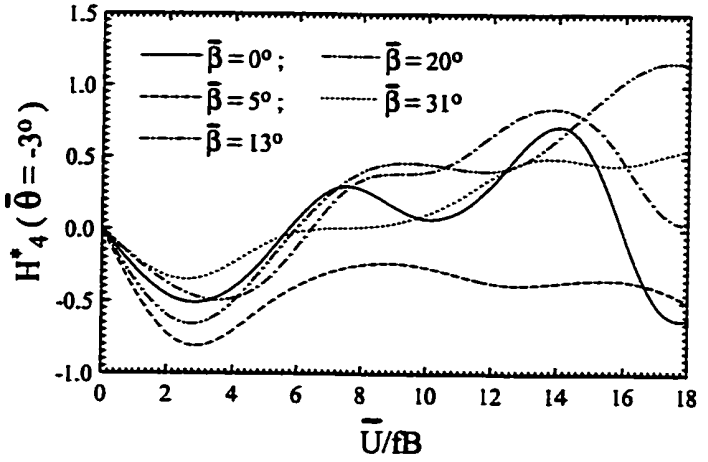

(b) $\theta = -3°$

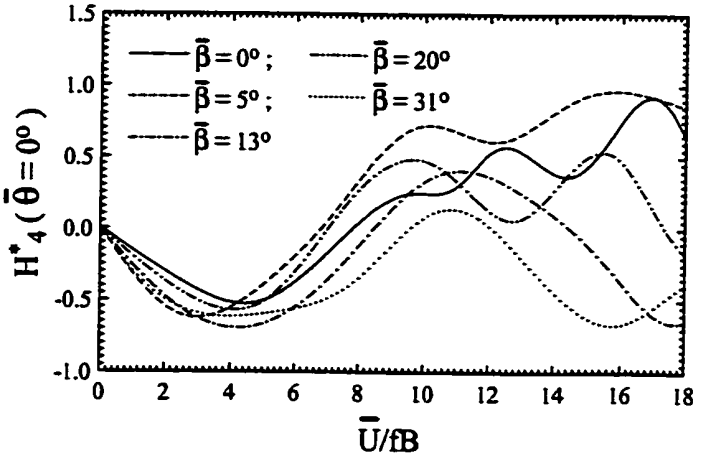

(c) $\theta = 0°$

Figure 7-12 Flutter Derivative Curves: H_4^* vs. $\bar{U}/fB$

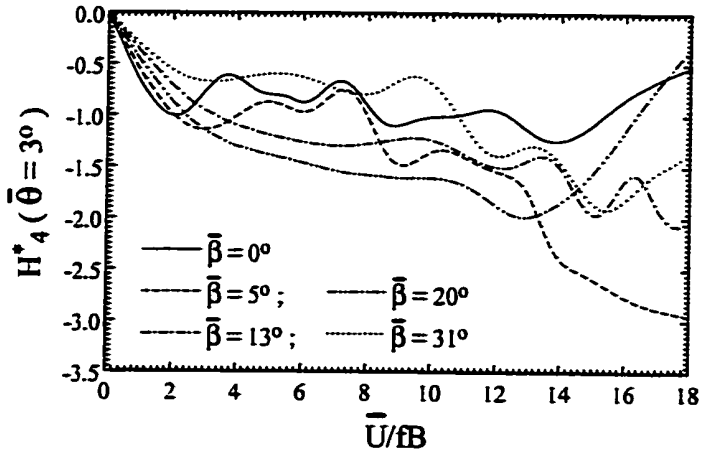

(d) $\theta = 3°$

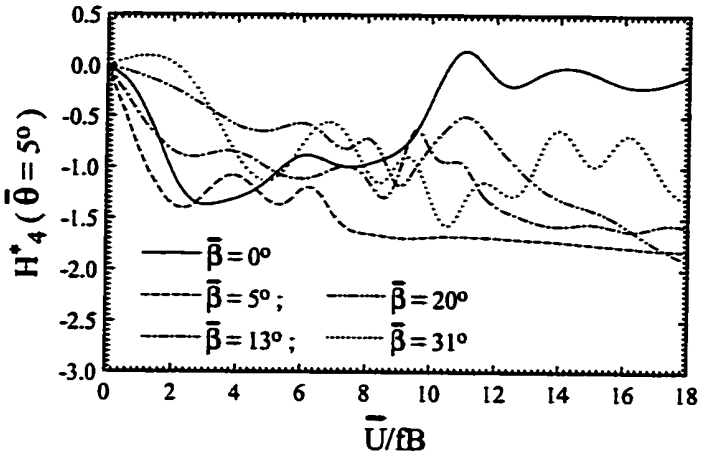

(e) $\theta = 5°$

Figure 7-12 (cont.) Flutter Derivative Curves: H_4^* vs. $\overline{U}/fB$

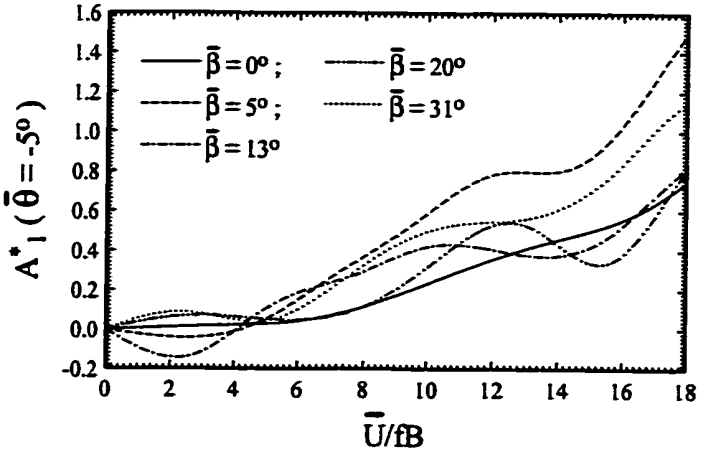

(a) $\theta = -5°$

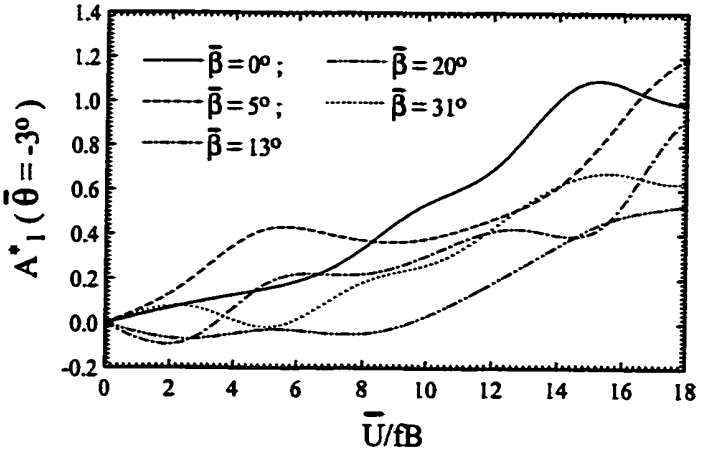

(b) $\theta = -3°$

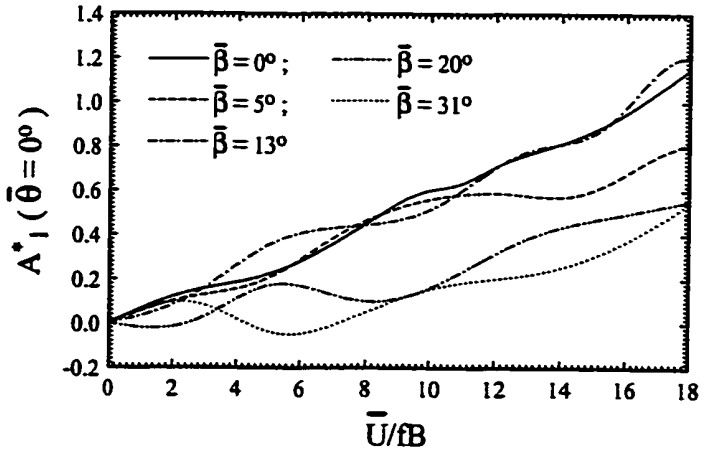

(c) $\theta = 0°$

Figure 7-13 Flutter Derivative Curves: A_1^* vs. $\bar{U}/fB$

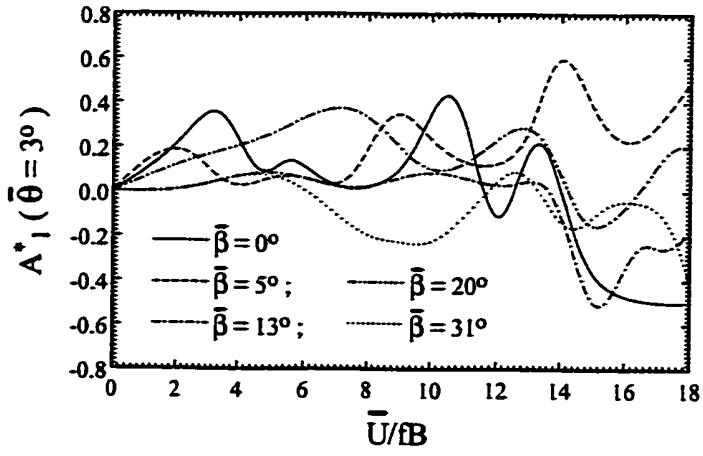

(d) $\theta = 3°$

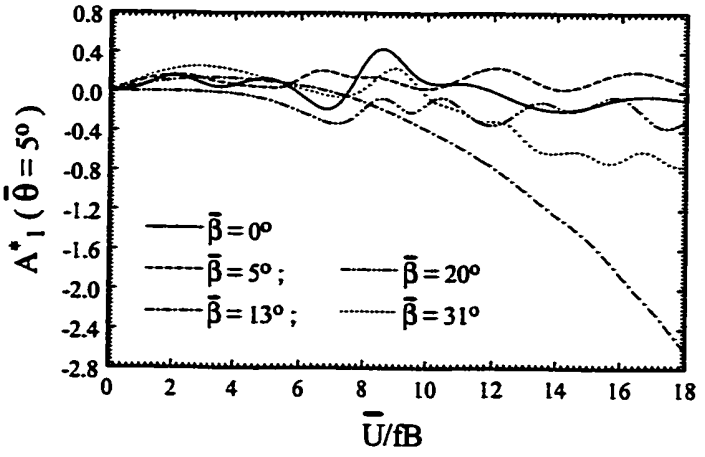

(e) $\theta = 5°$

Figure 7-13 (cont.) Flutter Derivative Curves: A_1^* vs. $\bar{U}/fB$

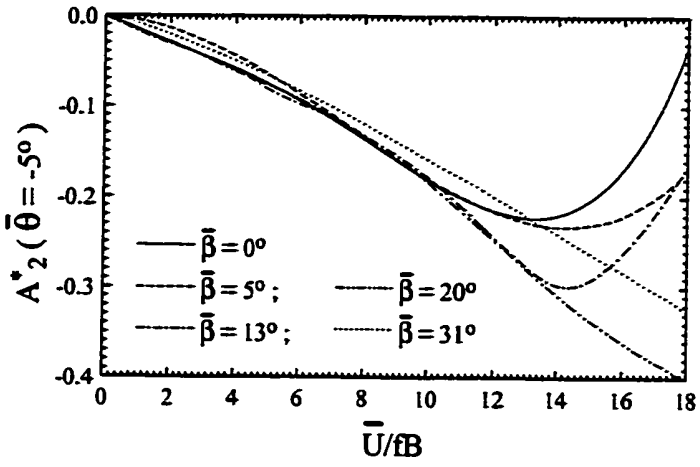

(a) $\bar{\theta} = -5°$

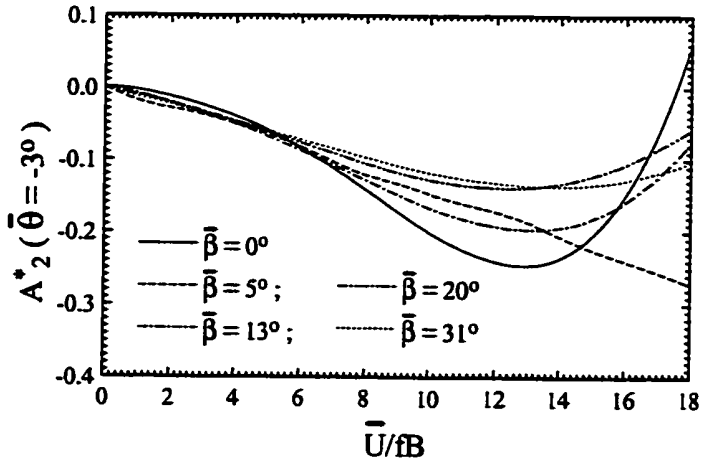

(b) $\bar{\theta} = -3°$

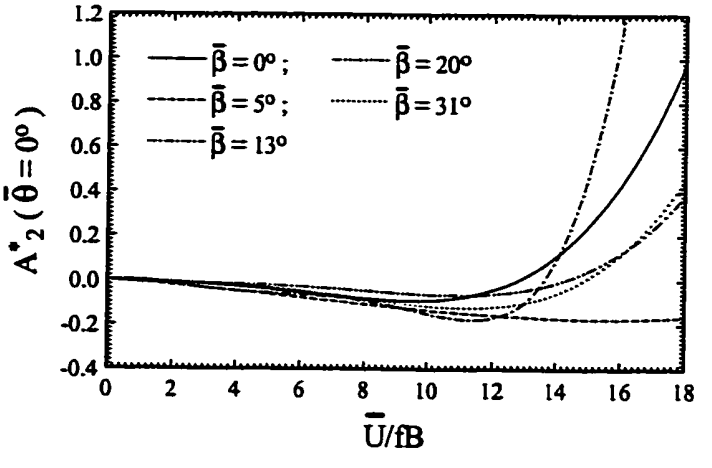

(c) $\bar{\theta} = 0°$

Figure 7-14 Flutter Derivative Curves: A_2^* vs. $\overline{U}/fB$

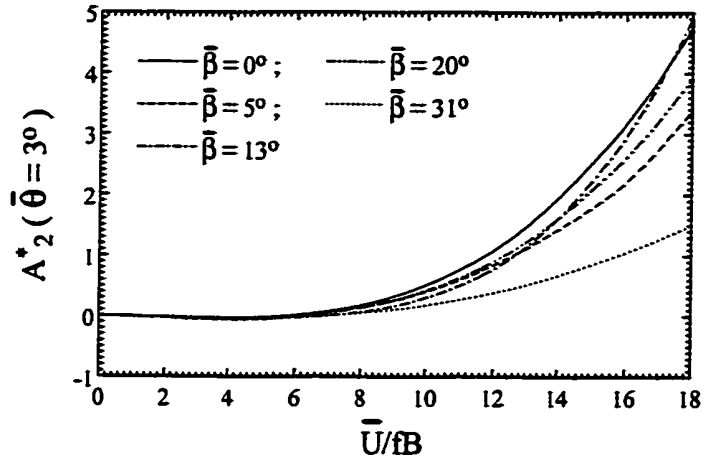

(d) $\theta = 3°$

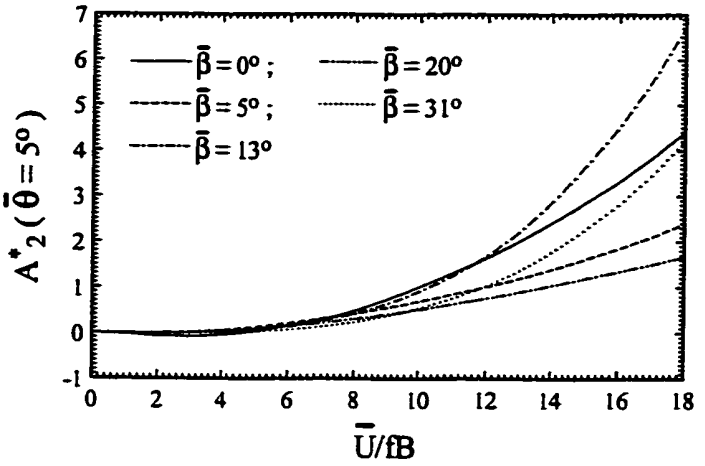

(e) $\theta = 5°$

Figure 7-14 (cont.) Flutter Derivative Curves: A_2^* vs. $\overline{U}/fB$

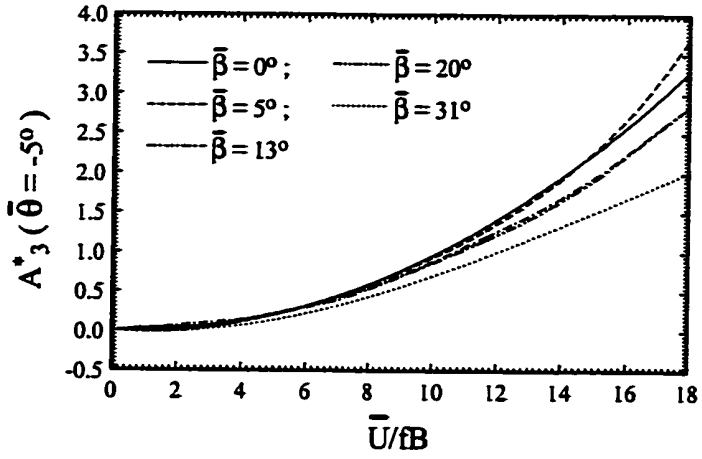

(a) $\theta = -5°$

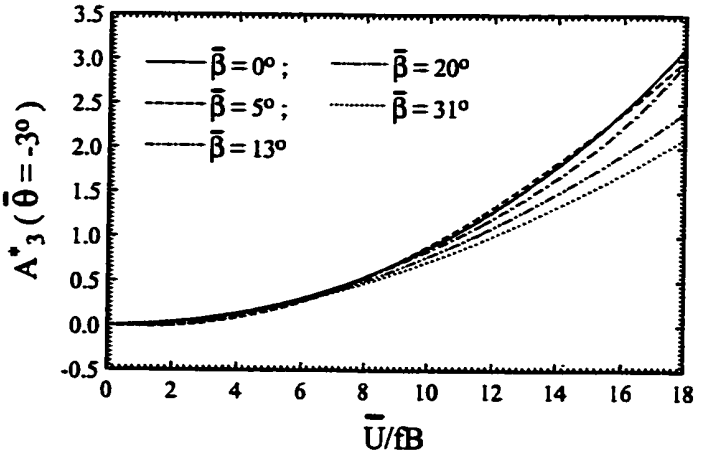

(b) $\theta = -3°$

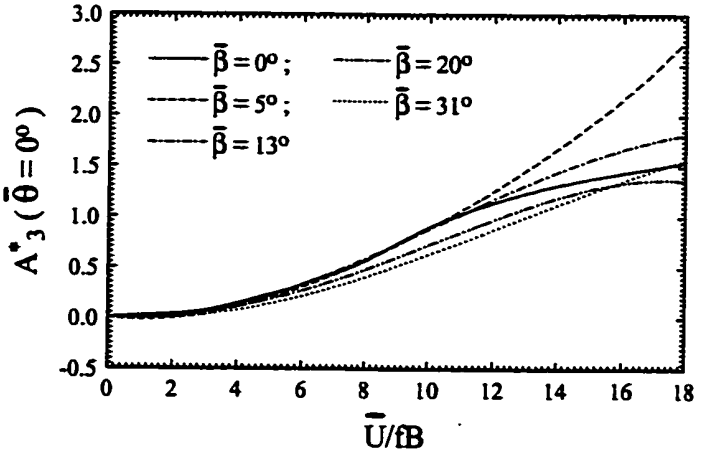

(c) $\theta = 0°$

Figure 7-15 Flutter Derivative Curves: A_3^* vs. $\bar{U}/fB$

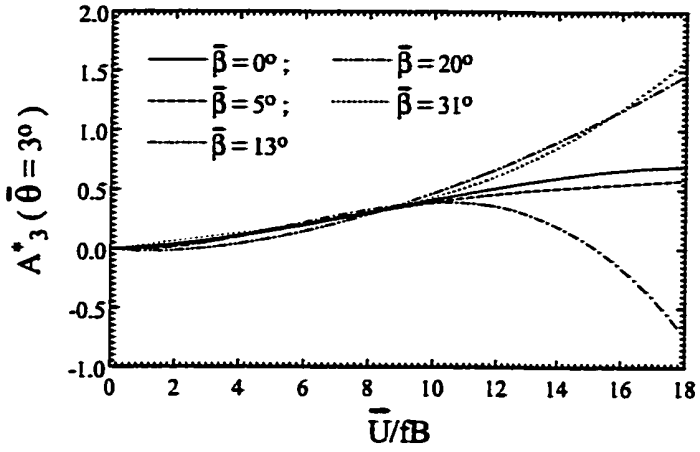

(d) $\theta = 3°$

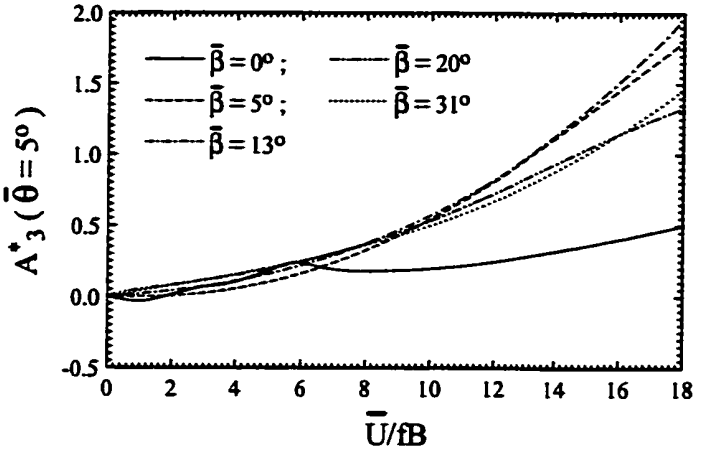

(e) $\theta = 5°$

Figure 7-15 (cont.) Flutter Derivative Curves: A_3^* vs. $\bar{U}/fB$

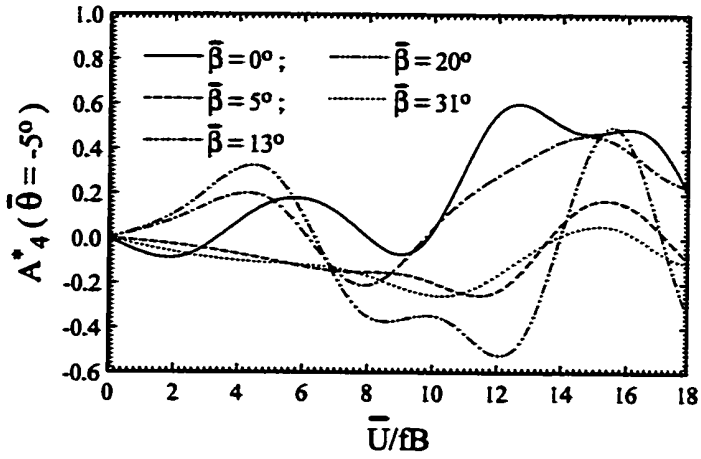

(a) $\theta = -5°$

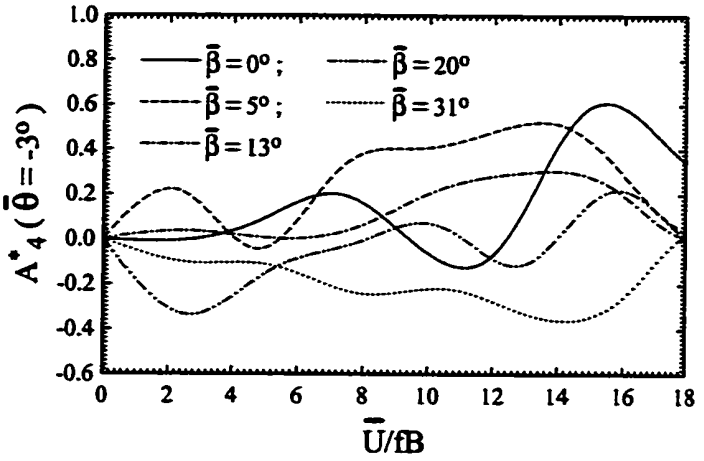

(b) $\theta = -3°$

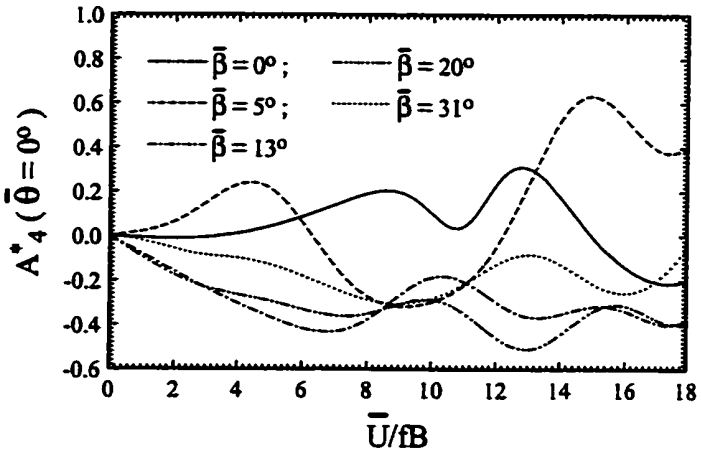

(c) $\theta = 0°$

Figure 7-16 Flutter Derivative Curves: A_4^* vs. $\bar{U}/fB$

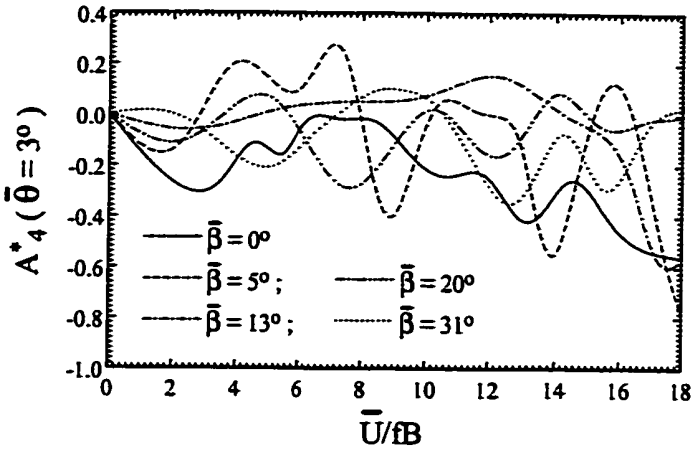

(d) $\theta = 3°$

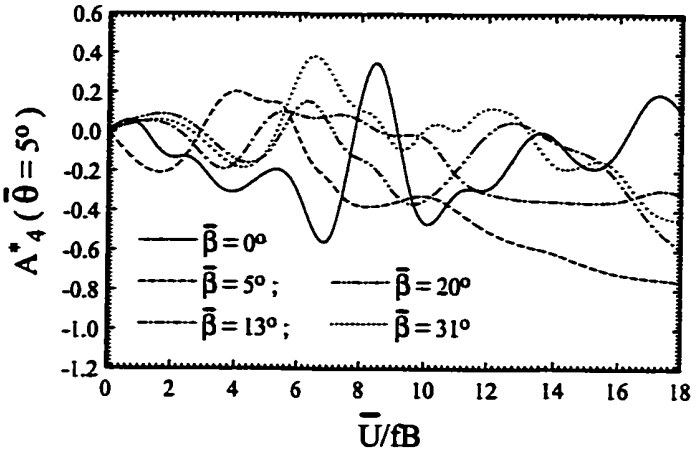

(e) $\theta = 5°$

Figure 7-16 (cont.) Flutter Derivative Curves: A_4^* vs. $\bar{U}/fB$

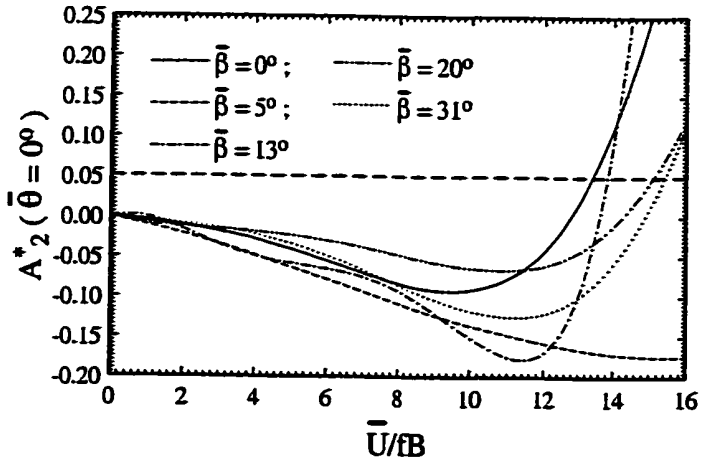

(a) $\theta = 0°$

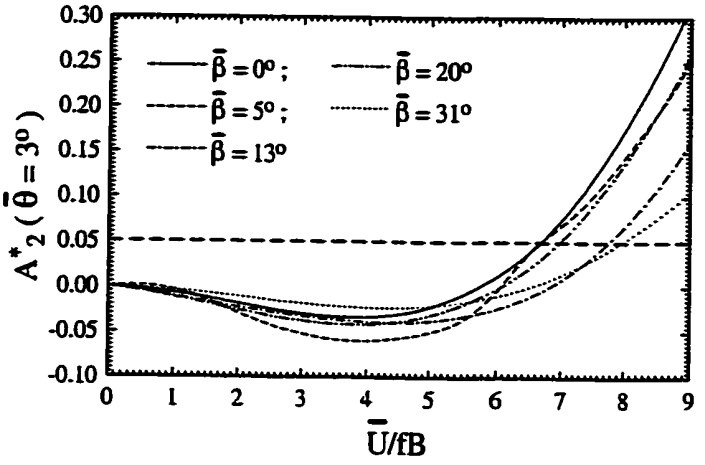

(b) $\theta = 3°$

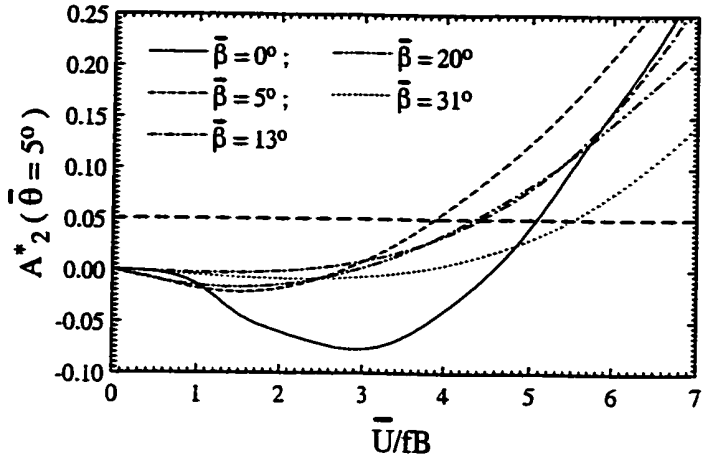

(c) $\theta = 5°$

Figure 7-17 Curves of A_2^* for Critical Wind Speeds

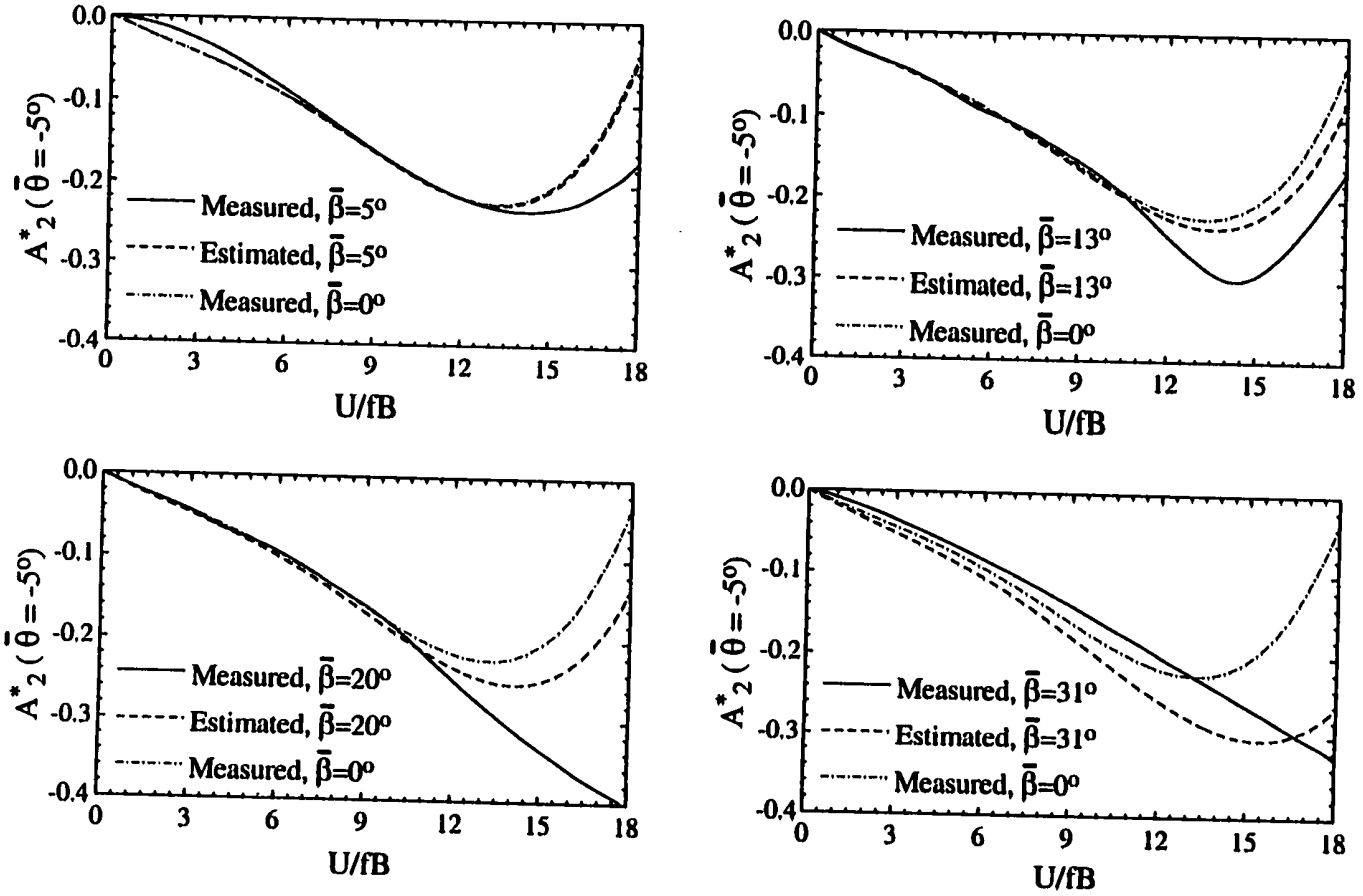

Figure 7-18 Measured and estimated A_2^* at $\bar{\theta}$ = -5°

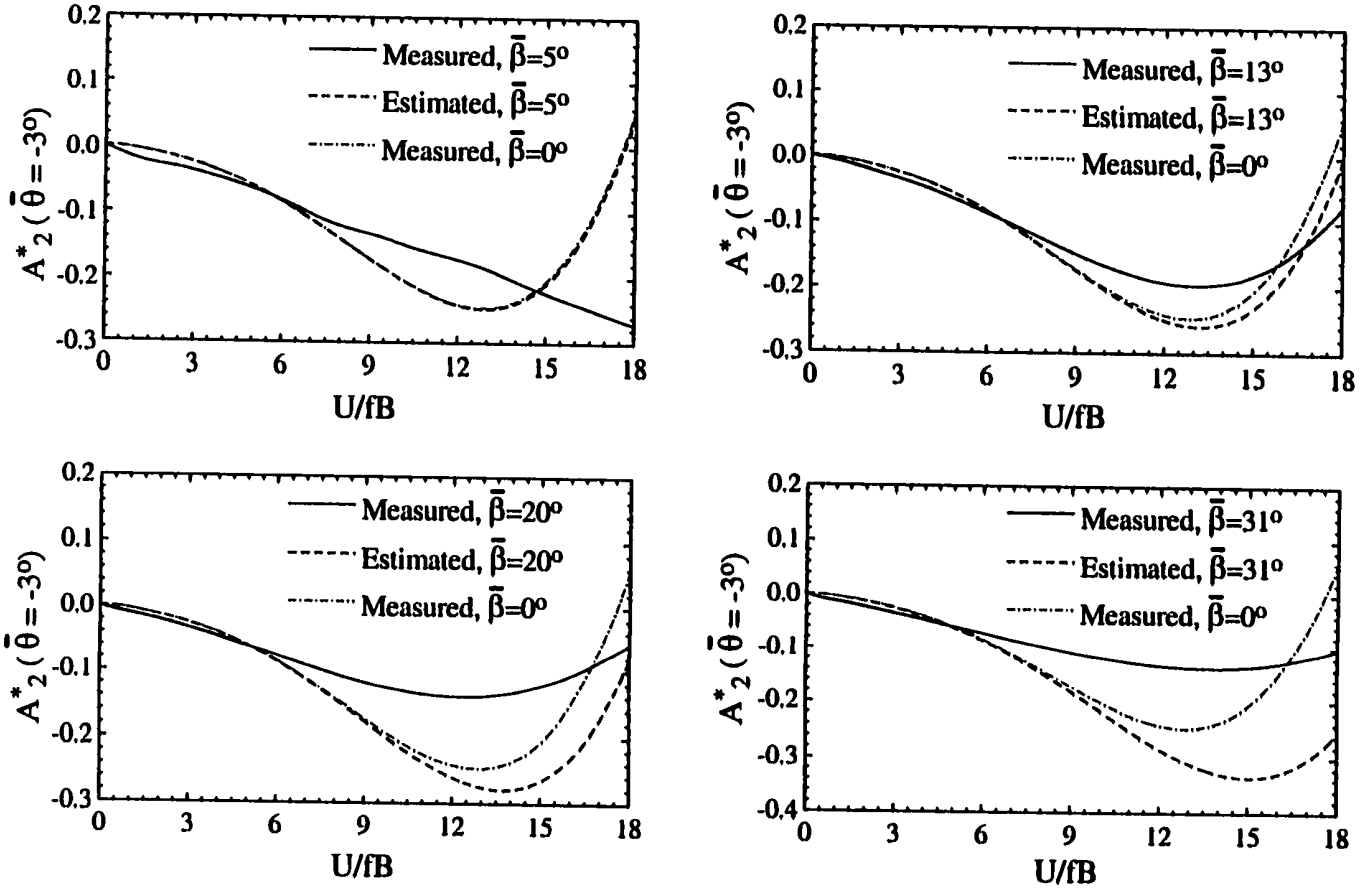

Figure 7-19 Measured and estimated A_2^* at $\bar{\theta}$ = -3°

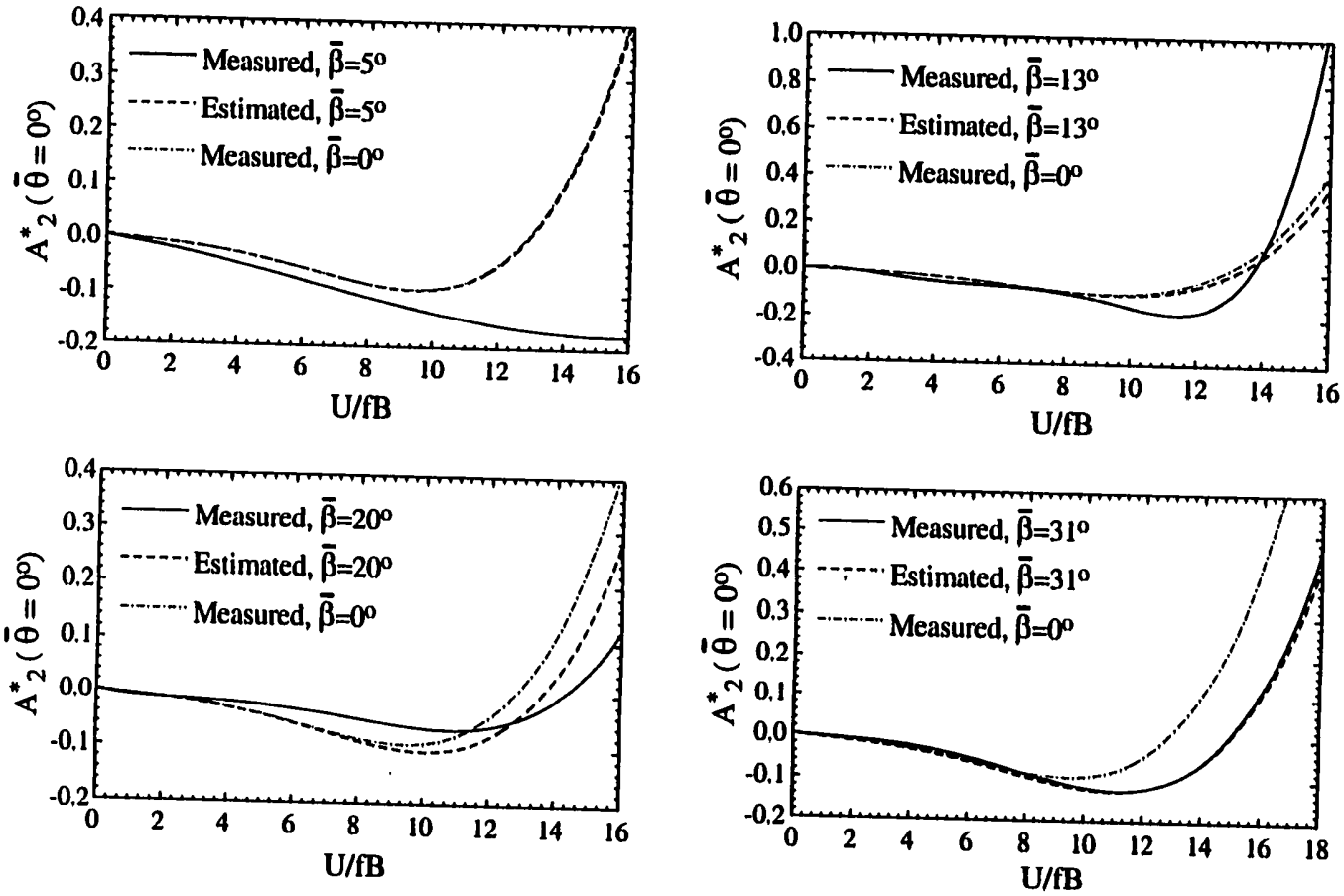

Figure 7-20 Measured and estimated A_2^* at $\bar{\theta}$ = 0°

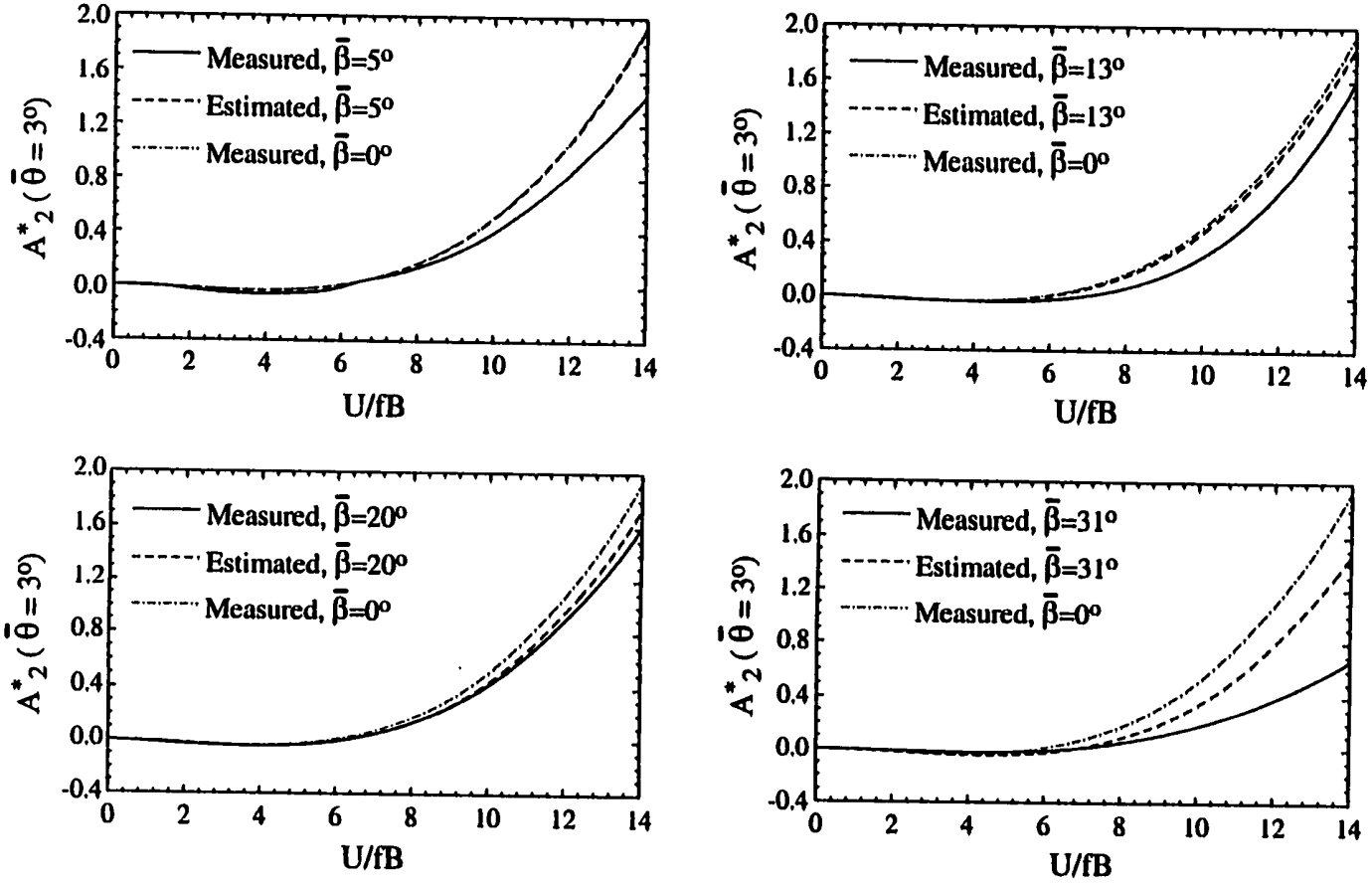

Figure 7-21 Measured and estimated A_2^* at $\bar{\theta} = 3°$

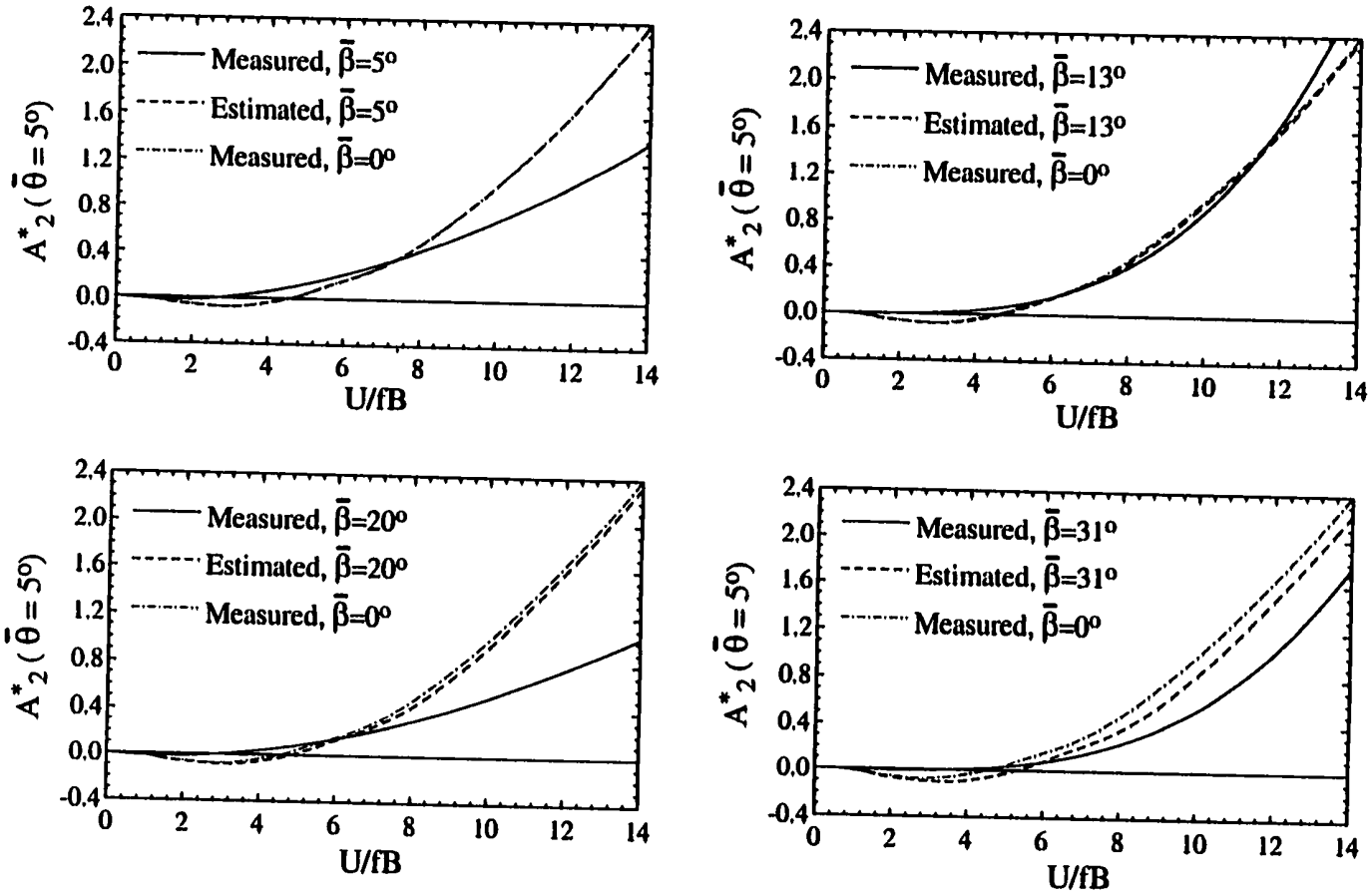

Figure 7-22 Measured and estimated A_2^* at $\bar{\theta}$ = 5°

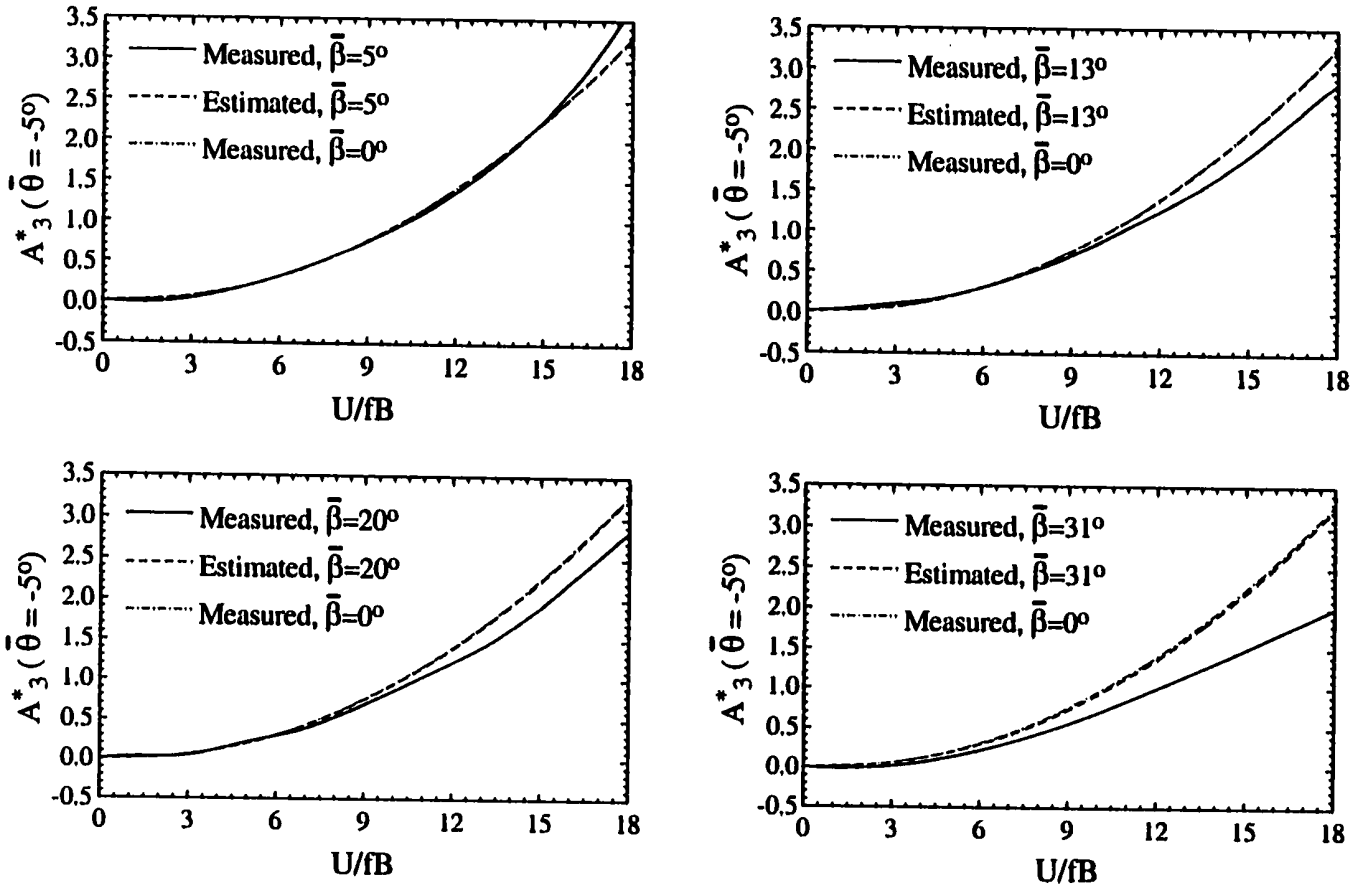

Figure 7-23 Measured and estimated A_3^* at $\bar{\theta}$ = -5°

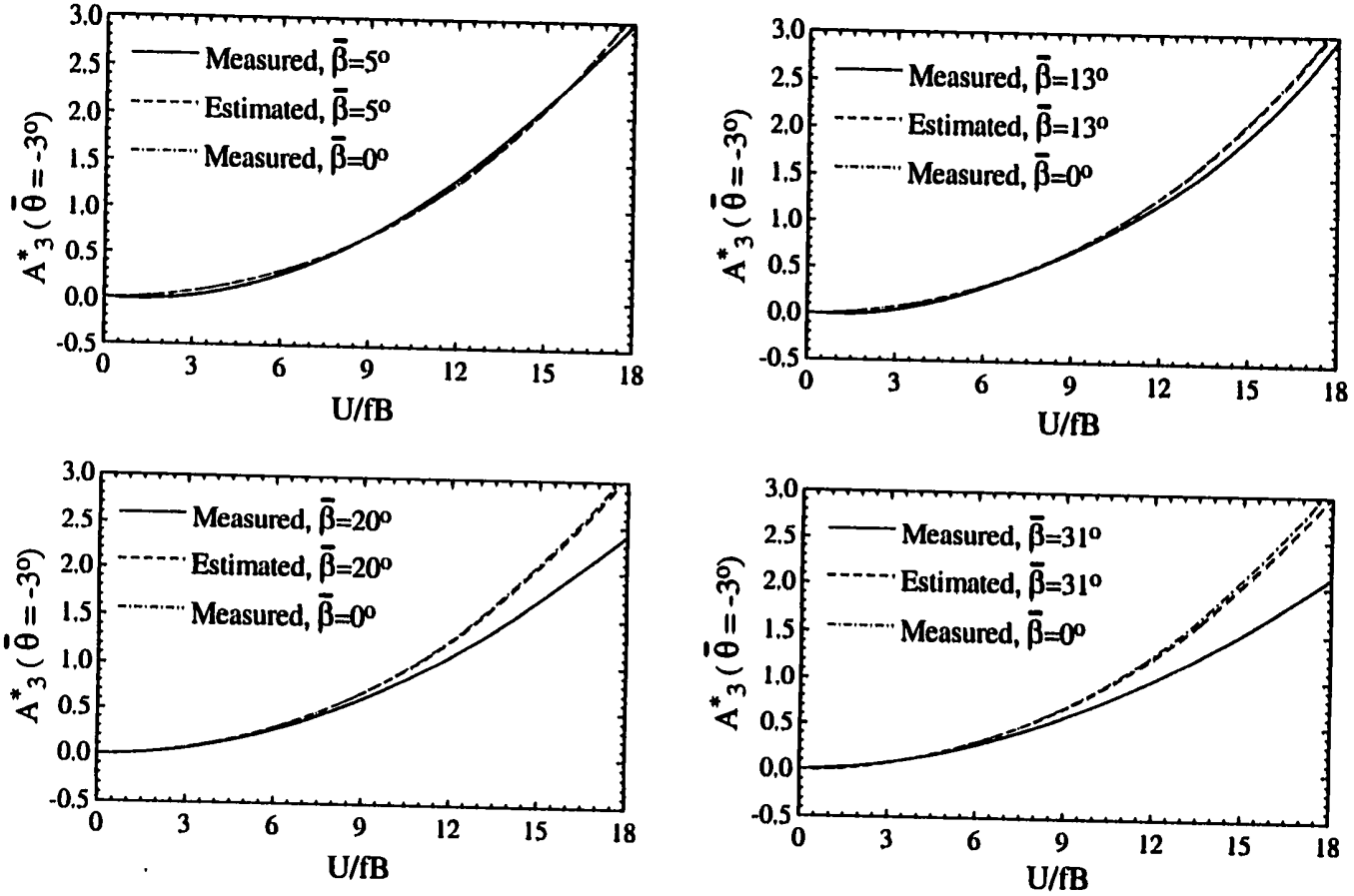

Figure 7-24 Measured and estimated A_3^* at $\bar{\theta}$ = -3°

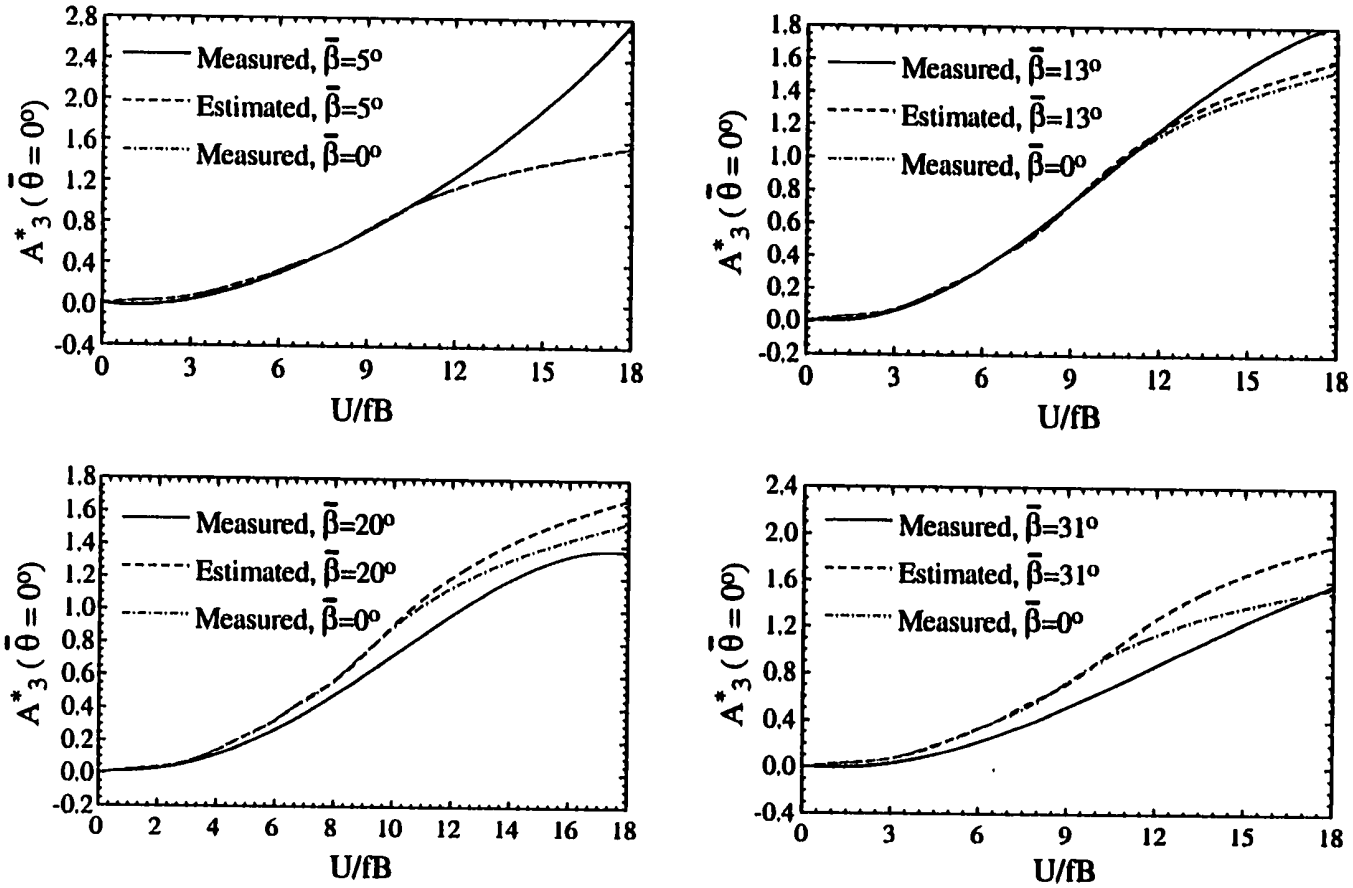

Figure 7-25 Measured and estimated A_3^* at $\bar{\theta} = 0°$

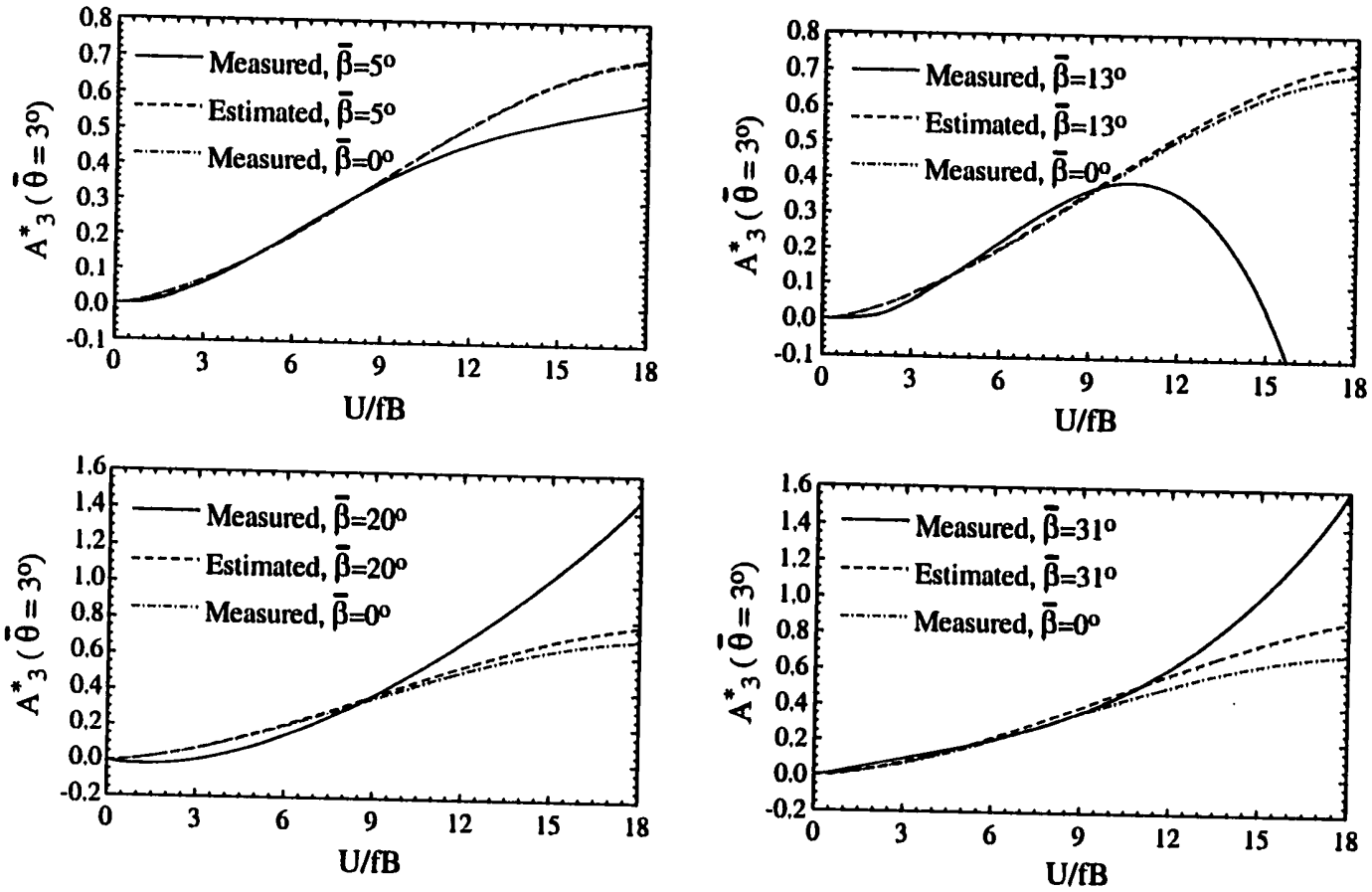

Figure 7-26 Measured and estimated A_3^* at $\bar{\theta}$ = 3°

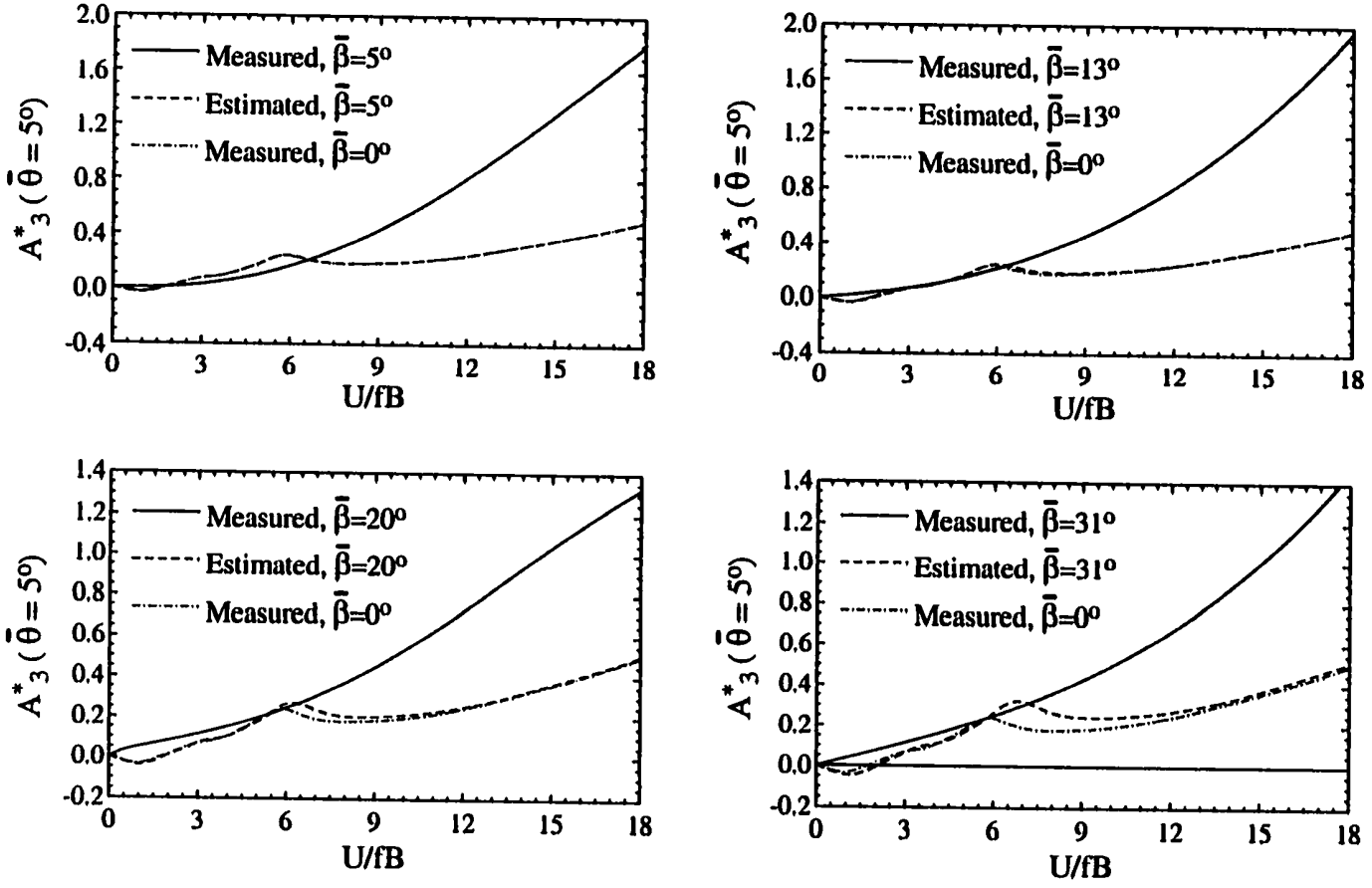

Figure 7-27 Measured and estimated A_3^* at $\bar{\theta}$ = 5°

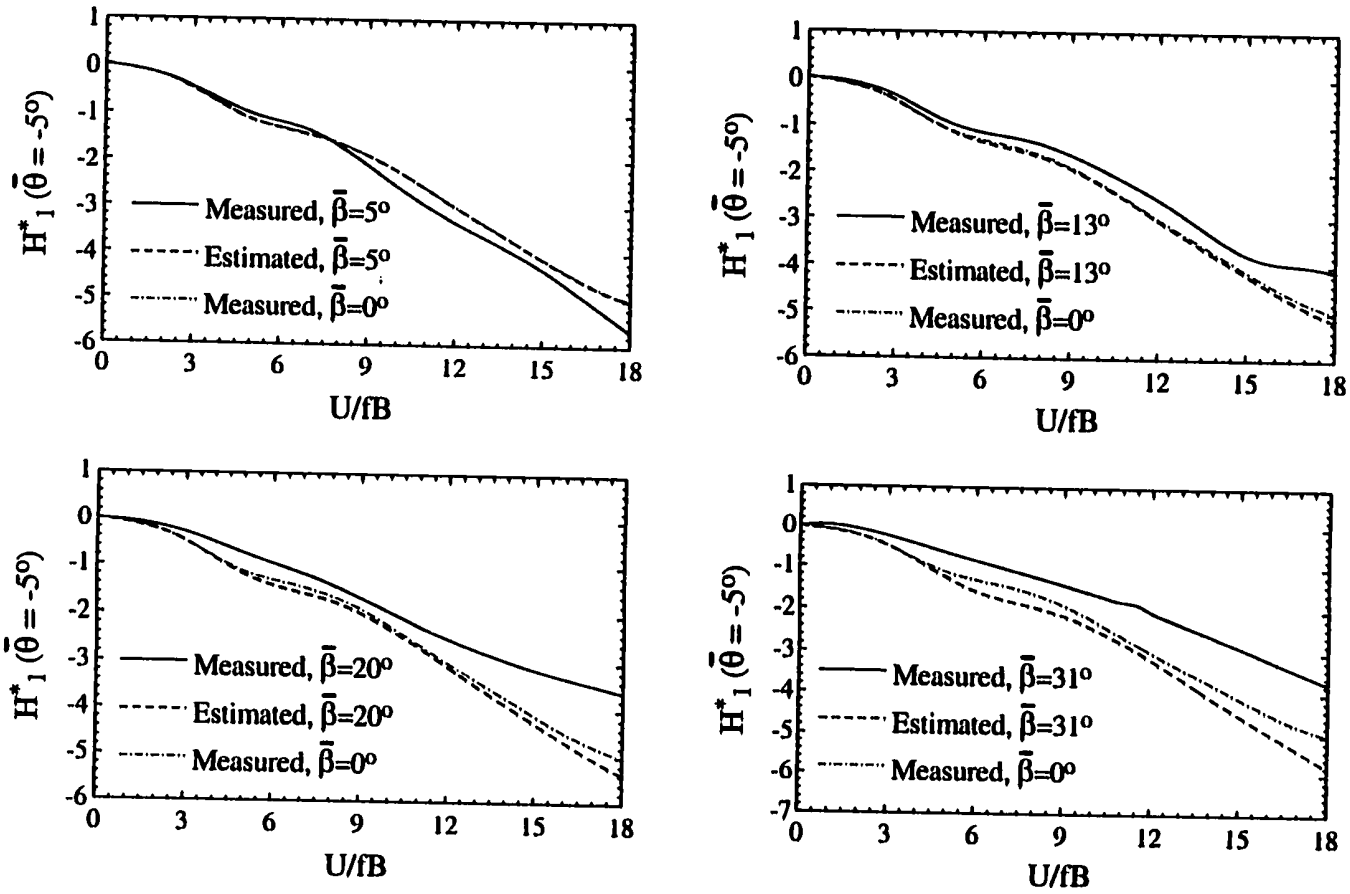

Figure 7-28 Measured and estimated H_1^* at $\bar{\theta}$ = -5°

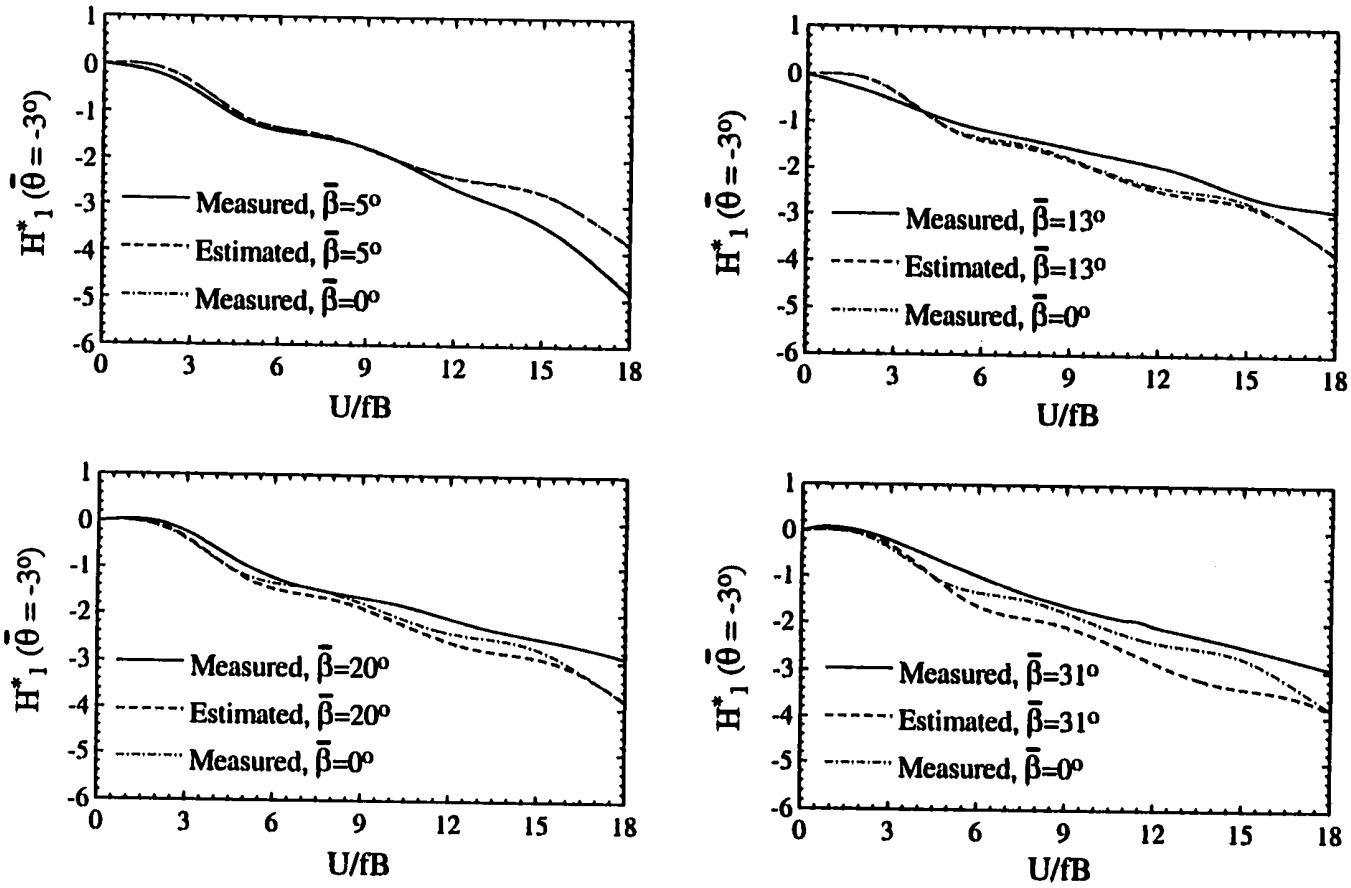

Figure 7-29 Measured and estimated H_1^* at $\bar{\theta}$ = -3°

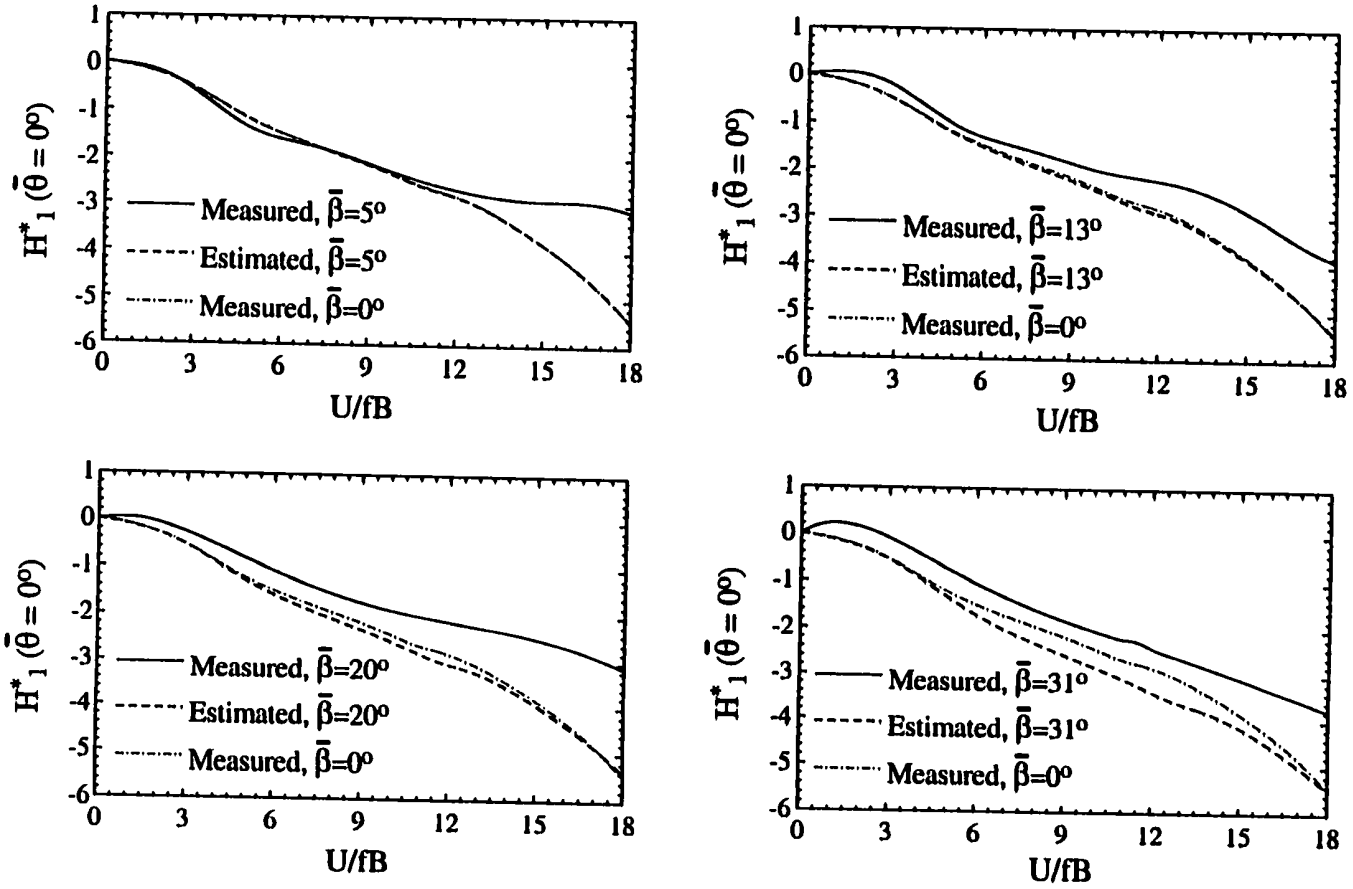

Figure 7-30 Measured and estimated H_1^* at $\bar{\theta} = 0°$

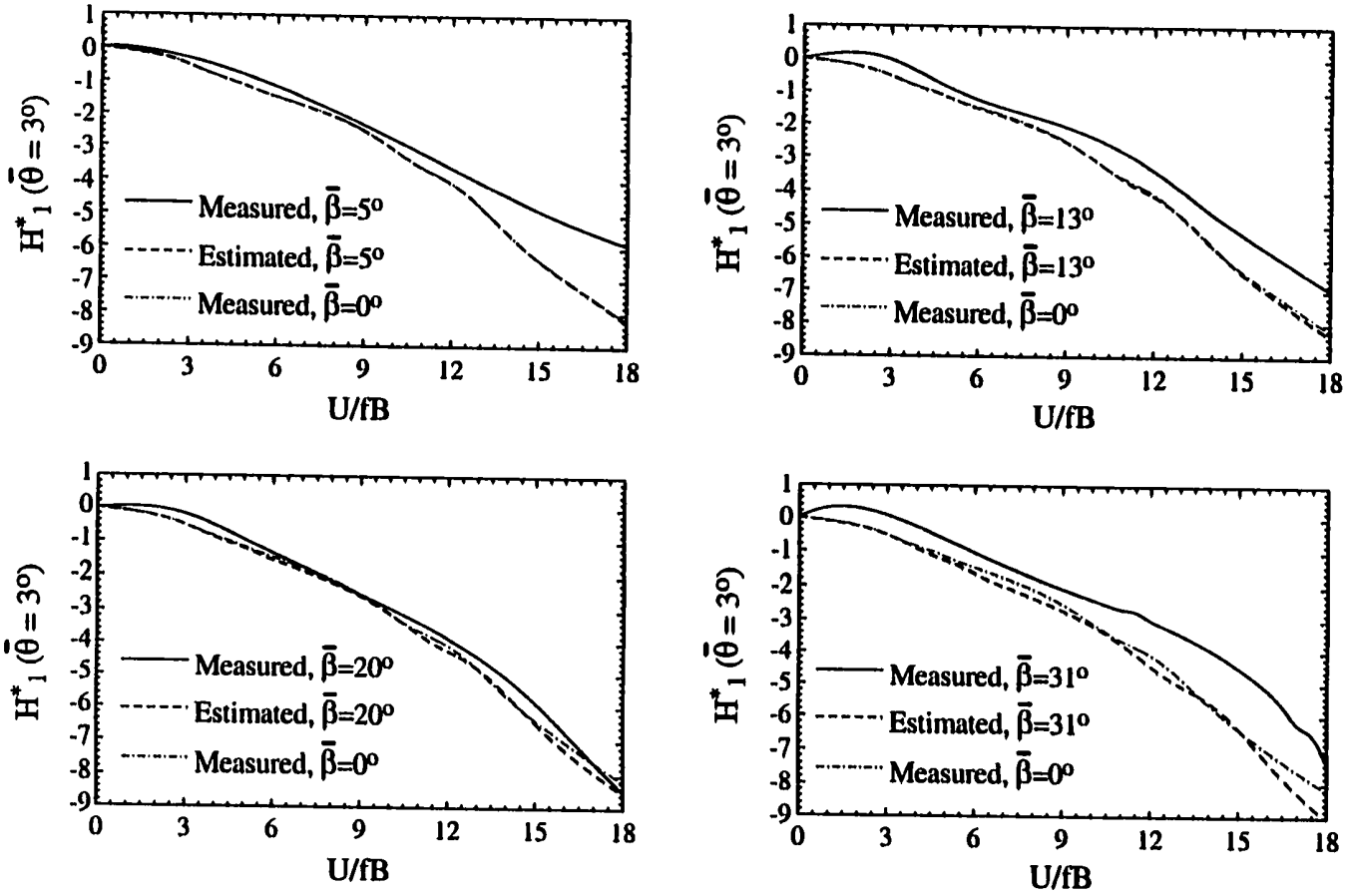

Figure 7-31 Measured and estimated H_1^* at $\bar{\theta} = 3^o$

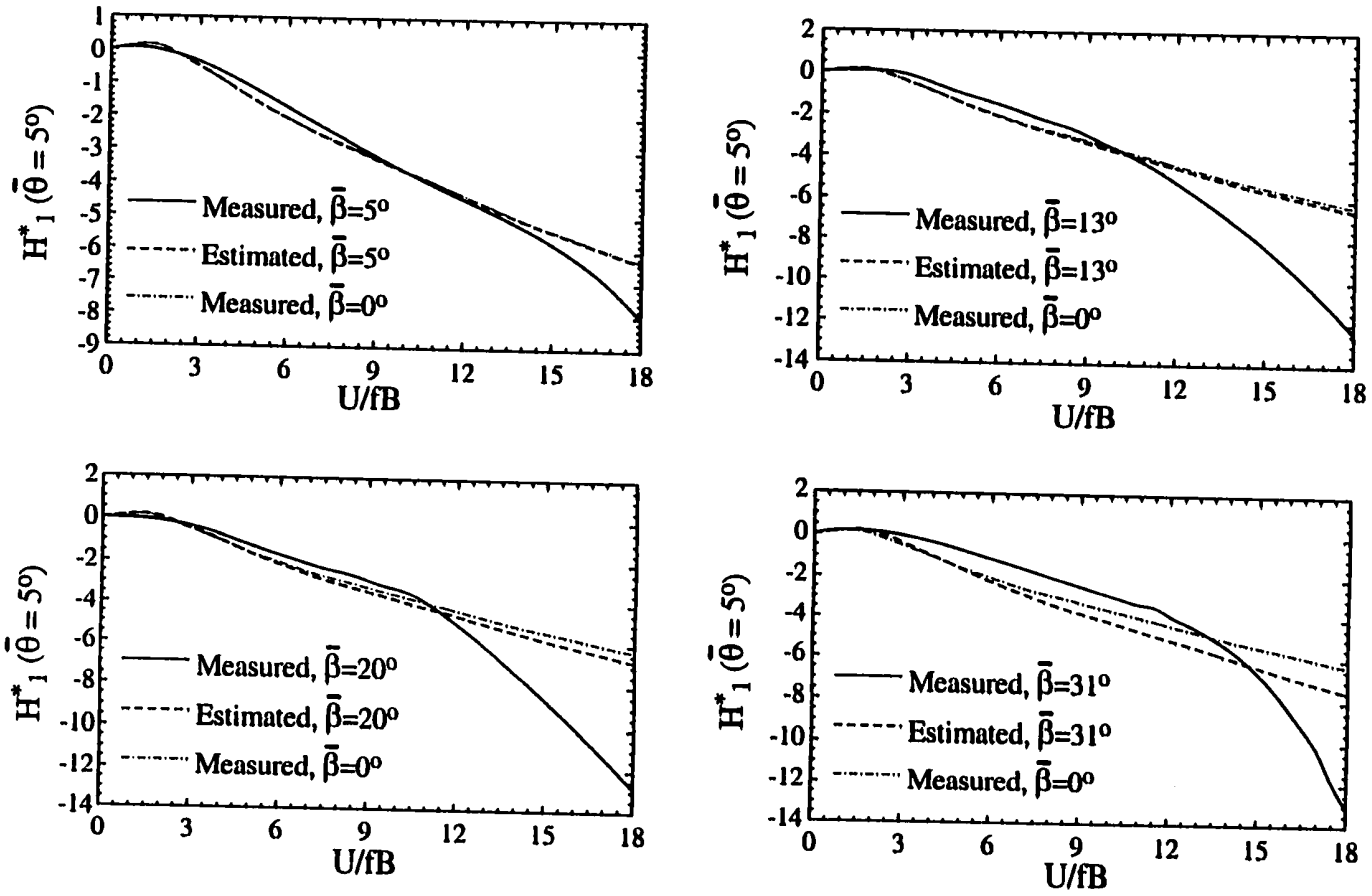

Figure 7-32 Measured and estimated H_1^* at $\bar{\theta} = 5°$

Chapter 8

WIND TUNNEL TEST FOR TOWER AERODYNAMIC COEFFICIENTS UNDER YAW WINDS

8.1 INTRODUCTION

The framework for fully coupled buffeting analysis of long span bridges as described in Chapter 4 is expected to provide a better comparison between the analyzed and measured buffeting responses of long span bridges under skew winds. Under this framework, the aerodynamic forces on bridge towers and the interaction between bridge deck and towers can be included. Furthermore, the framework is formulated using the finite element approach. The aerodynamic forces on a bridge tower can be thus detailed up to structural members such as tower legs and transverse beams. This treatment may be necessary for achieving a good comparison when the configuration of bridge tower is complicate and the bridge is under yaw winds.

In this connection and to be consistent with wind tunnel tests for deck aerodynamic coefficients and flutter derivatives under skew winds as described in Chapters 6 and 7, this chapter presents a wind tunnel investigation for determining aerodynamic coefficients of structural components of the Tsing Ma bridge tower under yaw winds. Though the sectional model test using either pressure or force balance test technique is often employed to measure the aerodynamic coefficient of bridge tower leg for its convenience and economy (Larose et al., 1993; Ricciardelli and Vickery, 1994, 1998), the effects of the horizontal transverse beams of the tower and the bridge deck can not be easily included. Also as observed in either full-scale measurements (Larose et al., 1997) or wind tunnel tests (Ricciardelli and Vickery, 1994 , 1998), the aerodynamic interference between two tower legs must be taken into consideration and the degree of aerodynamic interference depends on the separation of two tower legs and wind incidence. Thus, the present wind tunnel tests are performed on the entire single tower leg, part of single tower leg, and individual transverse beam. All other structural components of the bridge tower remain as dummy models when the

aerodynamic force on one structural component is measured in the wind tunnel. Furthermore, the effect of the existence of bridge deck on aerodynamic coefficients of the structural components of the tower is also investigated by including the part of bridge deck as a dummy model.

It may be worthwhile to point out that though wind inclination will significantly affect the aerodynamic forces on the bridge deck and thus should be considered in the global buffeting analysis, the influence of small wind inclination on aerodynamic forces on the bridge tower will be negligible. Therefore, wind inclination was not simulated in the wind tunnel for the measurement of aerodynamic forces on the bridge tower.

In the following, the design and installation of tower model and the test technique are first described. The force measurement system is then introduced. The test results and observations are finally presented. Some of the results obtained in this chapter will be used in Chapters 9 and 10 for the comparison between the analyzed and measured buffeting responses of the Tsing Ma Bridge.

8.2 DESIGN OF TOWER MODEL

8.2.1 Tsing Ma bridge tower

As shown in Figure 3-1, the Tsing Ma suspension Bridge has two H-shape prestress concrete towers: one is called the Tsing Yi tower and the other is the Ma Wan tower. Each tower is composed of two reinforce concrete legs and four deep prestressed transverse concrete beams (Figure 8-1). The two towers are almost identical. Therefore, only the Ma Wan tower is selected and tested in this study.

As shown in Figure 8-1, the horizontal distance between the axes of two tower legs is 36.0m at the top of the leg and 39.94 m at the base of the leg, resulting in a small slope ratio about 1%. The cross-section of a tower leg is composed of a central rectangle and two hemi-circles with a radius of 3.0m. The hemi-circle is constant but the rectangle varies along the height of the tower leg. According to the local coordinate system selected in this thesis, the windward side of a cross section (normal to wind) is defined as the height for all the bridge members while the side in

parallel to incident wind is defined as the width of the cross section. To this end, the height (H) of the cross section of the tower leg, as shown in Figure 8-1, is about 17.307m at the base of the leg. It then tapers off circularly (at a radius of 622.323 m) to 10.0m at a level of 70.0m and further tapers off linearly to 9.0m at the top surface of the upper transverse beam. The height of the cross section is finally enlarged linearly from 9.0m to 13.0m and then keeps constant until the top of the leg. The width (B) of the cross section of the tower leg, however, keeps constant of 6m along the entire height of the leg. All the transverse beams possess a rectangular cross section. The lower transverse beam just beneath the bridge deck is 12.0m high and 4.2m wide whilst the upper beam is 7.0m high and 2.8m wide. The lower-middle beam is 10.0m in height and 3.4m in width and the upper-middle beam is 8.0m in height and 3.1m in width.

8.2.2 Design of tower model

The wind tunnel tests of the bridge tower were conducted in the TJ-2 Wind Tunnel of the State Key Laboratory for Disaster Reduction in Civil Engineering at Tongji University, China. The configuration of this wind tunnel can be seen in Figure 6-12 and the further details of the tunnel can be found in Chapter 6. According to the wind tunnel size, the geometrical scale of the Ma Wan tower was selected as 1:100. The tower was carefully modeled for its appearance but the base line of the tower model was selected at a height of 7.5m in the prototype tower (Figures 8-1 and 8-2). The space between the levels of 5.0m and 7.5m in the prototype was then left in the model for installing an aluminum link between the base of the tower model and the force balance (see Figure 8-2). As a result, the height of the tower model excluding the link was 1935.1mm. The model was made of hard wood except that half of a perspex pipe of 30mm radius was glued onto the each side surface of the wood cores for the hemi-circle parts of tower legs. The tower model was assembled from two tower legs and four transverse beams. Fixed on the base of each leg was one circular steel plate. The diameter of the circular plate was 350 mm and its thickness was 5mm. The two legs and four transverse beams could be disconnected and remounted in different ways, depending on the test cases.

To consider the influence of bridge deck on wind flow around the bridge tower, a 180m long segment of the real bridge deck connected to the bridge tower was

considered as a dummy model in the wind tunnel tests. The configuration and dimension of the dummy deck segment model is shown in Figure 8-3. The parapet and wind shelter on the bridge deck was modeled but the central ventilation slots of the bridge deck were not included for simplification. The 1800 mm long dummy deck model was made of foam plastic and mounted to the tower model symmetrically with respect to the tower plane.

8.2.3 Test Cases and Model Installation

There were a total of 9 cases considered in this wind tunnel investigation. In Case 1, the aerodynamic force acting on one single tower leg was measured with dummy deck and dummy tower leg and transverse beams presented. The four transverse beams were connected to the dummy tower leg, which was fixed on the top surface of the turning table. Meanwhile, the measured (active) tower leg was centrally mounted on a five-component force balance through the link (Figures 8-2 and 8-4). The top surface of the turning table (i.e. the wind tunnel floor) was taken as a level of 2.0m in the prototype. The top surface of the balance was set at 30mm above the wind tunnel floor, thus corresponding to a level of 5.0 m in the prototype. The top face of the link of 20 mm thick was tightly connected to the steel plate using four bolts while its low face was connected to the top surface of the force balance using eight bolts. The five-component force balance was vertically connected to the balance support post, which was firmly mounted at the center of the turning table (Figure 8-5). The dummy deck model was symmetrically installed with respect to the tower but it was fixed directly on the turning table through the four vertical thin bars (Figure 8-6). Small gaps about 3mm were set between the measured tower leg and the four transverse beams and between the measured tower leg and the deck model. To make the model stiff enough, the dummy tower leg was properly tied down to the turning table using wires while the active tower leg was properly tied down to its own circular steel plate by thin wires.

In Case 2 to Case 5, the aerodynamic force acting on each transverse beam was measured with the presence of the dummy deck model. The measurement of aerodynamic force on each transverse beam was indirect in this study. For example, to determine the aerodynamic force on the upper transverse beam, the upper transverse beam was dismounted from the dummy tower leg and fixed to the active

tower leg at its original position. The total aerodynamic force acting on both the active tower leg and the upper transverse beam was measured in a similar way in Case 1. The aerodynamic force on the upper transverse beam was then calculated by the subtraction of the aerodynamic force on the active tower leg obtained in Case 1 from the total aerodynamic force obtained from the present case.

The aerodynamic force acting on the active tower leg without the presence of dummy deck model was measured in Case 6. In this case, the dummy deck model in Case 1 was removed and all the others in Case 1 remained unchanged (Figure 8-7). The comparison of the measured aerodynamic force between Case 1 and Case 6 could reveal the influence of existence of the dummy deck model.

The aerodynamic force acting on an isolated tower leg without any dummy models was measured in Case 7. In this case, the dummy tower leg and four transverse beams in Case 6 were removed, leaving only one tower leg supported by the force balance in the tunnel. The influence of the dummy tower leg and four transverse beams on the aerodynamic force on the active tower leg could be evaluated through the comparison of the measured aerodynamic force between Case 6 and Case 7.

In consideration that the height of cross section of a tower leg has a large change from the base of the tower leg to a level of 70.0m, the measured tower leg was thus further divided into two parts at 700 mm high to have the upper segment of 1310.1 mm high and the lower segment of 625mm excluding the base steel plate and the link. The upper segment was connected to the dummy tower leg while the lower segment was still mounted on the force balance. All other arrangements including the dummy four transverse beams and the dummy deck model were kept the same as those in Case 1. Figure 8-8 displays the set-up of the measurement for Case 8. The aerodynamic force on the lower segment of the tower leg was measured in this case. The aerodynamic force on the upper leg segment was calculated by deducting the aerodynamic force on the lower segment measured in the present case from the aerodynamic force on the entire leg measured in Case 1. To ensure the stability of the dummy models during the test, the upper leg segment was stiffened with wires tied up to the tunnel ceiling and down to the tunnel floor (Figure 8-8). A small horizontal gap of about 3mm was set between the upper segment and lower segment.

In the last case, that is Case 9, the aerodynamic force on the lower segment of the tower leg without the deck influence was measured. To fulfill this task, the dummy deck model in Case 8 was removed from the tunnel. After the aerodynamic force on the lower segment was measured, the aerodynamic force on the upper segment of the tower leg without deck influence was taken as the difference between the aerodynamic force on the entire tower leg measured in Case 6 and the aerodynamic force on the lower segment measured in Case 9.

8.3 MEASUREMENT SYSTEM

The measurement system used in wind tunnel tests for measuring the aerodynamic forces/moments on different structural components of the bridge tower was composed of a five-component force (moment) balance, a potentiostatic DC power supply, a multi-channel DC voltage amplifier, a multi-channel data acquisition unit, and a computer. Except for the force balance, the other components in the measurement system were the same as those introduced in Chapter 6 for the bridge deck tests.

The five-component force balance was elaborately designed by Mr. F. Zhang of the State Key Laboratory for Disaster Reduction in Civil Engineering at Tongji University, China. The balance met the requirements for high sensitivity and high stiffness to avoid the model vibration and to ensure the measurement accuracy. The balance was a base-supported strain balance with an outer diameter of 130mm (see Figure 8-9). Five groups of strain gauges were respectively stuck on three separated sections of the balance to perceive two forces ($F_{\bar{x}}$ and $F_{\bar{y}}$) and three moments ($M_{\bar{x}}$, $M_{\bar{y}}$ and $M_{\bar{z}}$) with respect to the center of the balance top surface. The corresponding design bearing capacity was 100.0N and 200.0N, respectively, for two forces $F_{\bar{x}}$, $F_{\bar{y}}$, and 100.0Nm, 50.0Nm and 10.0Nm, respectively, for three moments $M_{\bar{x}}$, $M_{\bar{y}}$ and $M_{\bar{z}}$. The balance was "rigid" in its longitudinal direction, and hence not able to perceive the longitudinal force $F_{\bar{z}}$. As shown in Figure 8-2, $\bar{z}$ denotes the longitudinal (vertical) axis of the balance while $\bar{x}$ and $\bar{y}$ denotes, respectively, the two transverse (horizontal) axes with the $\bar{x}$, $\bar{y}$ and $\bar{z}$ axes perpendicular to each

other. In this investigation, the $\bar{x}$ axis is located in the tower plane and the $\bar{y}$ axis is along the bridge deck axis. The origin of the balance $\overline{xyz}$ coordinates is assigned at the center of the balance top surface.

The force/moment measurement system was calibrated before the wind tunnel test of the bridge tower. The voltage of the DC power supply applied to the electric bridge of the balance V_b was 20V and the amplification factors were set as 1000 for all the channels of the amplifier. These parameters were also used in the formal wind tunnel tests. During the calibration, the forces $F_{\bar{x}}$ along the axis $\bar{x}$, the force $F_{\bar{y}}$ along the axis $\bar{y}$, the moments $M_{\bar{x}}$ around the axis $\bar{x}$, the moment $M_{\bar{y}}$ around the axis $\bar{y}$, and $M_{\bar{z}}$ around the axis $\bar{z}$ was, respectively, applied to the balance in a proper way and at several intervals with respect to the center of the balance top surface. The pure output voltage from the balance after deducting the initial reading was then normalized by V_b ($\Delta V/V_b$ in $\mu V/V$) and expressed as a function of the applied force (in N) or moment (in Nm), as shown in Figures 8-10a to 8-10e. The data from the calibration were also fitted by the straight line and plotted in Figures 8-10a to 8-10e. It is seen that the linear relationship between the applied force/moment and the balance output voltage is satisfactorily achieved.

It is noted from Figures 8-10a and 8-10e that the applied moment $M_{\bar{x}}$, $M_{\bar{y}}$ or $M_{\bar{z}}$ mainly produced the output voltage of the balance in its own component and it almost did not affect the other components. However, the applied force $F_{\bar{x}}$ or $F_{\bar{y}}$ produced a significant output voltage in the component $M_{\bar{y}}$ or $M_{\bar{x}}$ besides the major output voltage in the component $F_{\bar{x}}$ or $F_{\bar{y}}$. This was due to the balance structure, in which the two strain gauges to measure the moment $M_{\bar{y}}$ or $M_{\bar{x}}$ were stuck on the balance section at a certain distance from the top surface of the balance. The application of the force $F_{\bar{x}}$ or $F_{\bar{y}}$ thus led to the additional moment $M_{\bar{y}}$ or $M_{\bar{x}}$.

Based on the slopes of 25 fitted straight lines, the calibration matrix of the balance, reflecting the relationship between the applied forces/moments and the normalized output voltages, was obtained as follows:

Table 8-1 Test Cases for Aerodynamic Coefficients of Tsing Ma Bridge Tower

Case	Measured component	Surrounding components	Range of β_T	Interval of β_T
1	One tower leg	One tower leg; 4 transverse beams; Deck segment	0°~180°	3°
2	One tower leg; Upper transverse beam	One tower leg; Lower, lower-middle and upper-middle transverse beams; Deck segment	0°~180°	3°
3	One tower leg; Upper-middle transverse beam	One tower leg; Lower, lower-middle and upper transverse beams; Deck segment	0°~180°	3°
4	One tower leg; Lower-middle transverse beam	One tower leg; Lower, upper-middle and upper transverse beams; Deck segment	0°~180°	3°
5	One tower leg; Lower transverse beam	One tower leg; Lower-middle, upper-middle and upper transverse beams; Deck segment	0°~180°	3°
6	One tower leg	One tower leg; 4 transverse beams;	0°~180°	6°
7	One tower leg	None	0°,3°, 6°~90°	6°
8	Lower segment of one tower leg	One tower leg; 4 transverse beams; Deck segment; Upper segment of measured leg	0°~180°	3°
9	Lower segment of one tower leg	One tower leg; 4 transverse beams; Upper segment of measured leg	0°~180°	6°

$$\mathbf{S}_b = \begin{bmatrix} 2.7768 & -0.0405 & 0.0306 & -0.2090 & -0.1193 \\ -0.0026 & -1.6441 & -0.1537 & 0.0831 & -0.0867 \\ -0.0355 & -0.7726 & 4.4332 & -0.2049 & -0.1754 \\ 0.8292 & -0.0302 & 0.2142 & 6.6355 & 0.0785 \\ 0.0228 & -0.0094 & 0.0146 & 0.0963 & 50.3014 \end{bmatrix} \quad (8\text{-}1)$$

The measurement error of the elements in the above matrix was less than 0.3% of the design bearing capacity for $M_{\bar{x}}$ and 0.2% of the design bearing capacity for the other four components, as indicated by an error analysis of the measurement data and fitted lines. As a result, if the output voltages of the five components of the balance are $\Delta V_{F_{\bar{x}}}$, $\Delta V_{F_{\bar{y}}}$, $\Delta V_{M_{\bar{x}}}$, $\Delta V_{M_{\bar{y}}}$ and $\Delta V_{M_{\bar{z}}}$ in unit of μV, the forces and moments acting on the bridge tower component installed on the force balance can be calculated as

$$\left(F_{\bar{x}}, F_{\bar{y}}, M_{\bar{x}}, M_{\bar{y}}, M_{\bar{z}}\right)^{\mathrm{T}} = \frac{1}{V_b}\mathbf{S}_b^{-1}\left(\Delta V_{F_{\bar{x}}}, \Delta V_{F_{\bar{y}}}, \Delta V_{M_{\bar{x}}}, \Delta V_{M_{\bar{y}}}, \Delta V_{M_{\bar{z}}}\right)^{\mathrm{T}} \quad (8\text{-}2)$$

where V_b is the voltage applied to the electric bridge of the balance in unit of V; and the obtained forces and moments are in unit of N and Nm, respectively.

8.4 Wind Tunnel Test

All the 9 test cases as listed in Table 8-1 were investigated for a series of wind directions, where the angle β_T represents the rotation angle of the turning table in clockwise direction (see Figure 8-11). In consideration of the symmetry of the bridge tower in its plane, the test range of β_T was from 0° to 180° at a proper interval. It is reminded that in this thesis, the global wind yaw β_0 is defined as zero when the wind is normal to the longitudinal axis of the bridge deck or parallel to the tower plane (see Figure 8-11). The designated angle β_0 was then achieved by changing the angle β_T. In fact, when β_T varied from 0° and 90°, the measured tower leg was in windward position corresponding to the angle β_0 from 0° to 90° for the windward tower leg (see Figure 8-11a). When the angle β_T further increased from 90° and 180°, the measured tower leg was in leeward position corresponding to the angle β_0 from -90° to 0° for the leeward tower leg (see Figure 8-11b). Because of the symmetry of the bridge tower, the aerodynamic coefficients of the windward tower leg for the global yaw angle β_0 between -90° to 0° could be obtained from those of the windward tower

leg measured for the angle β_0 between 0° to 90° with the drag coefficient being symmetric and the lift coefficient being anti-symmetric. Similarly, the aerodynamic coefficients of the leeward tower leg for β_0 between 0° to 90° could be obtained from those measured for β_0 between -90° to 0°.

In this investigation, the aerodynamic coefficients of structural components of the bridge tower obtained from Cases 1 to 5 and Case 8 were used in Chapter 9 and 10 for the comparison between the field measurement and the analysis. The others were used for estimating the interference effects of the bridge deck, the windward or leeward tower leg on the aerodynamic forces/moments on the active tower leg or leg segment.

For each test case, the measurement was repeated for at least three times, and the average values were presented. Each single measurement lasted for 10 seconds with a sample frequency of 500Hz. The time-averaging method was used to analyze the data to obtain the aerodynamic coefficients.

As done in the wind tunnel tests for deck aerodynamic coefficients described in Chapter 6, some trial tests were also carried out here to select a test mean wind speed. To this end, three wind speeds of 10m/s, 15m/s, and 20m/s were respectively tried. The model vibration was hardly observed under all the three wind speeds, and the measured aerodynamic forces were found to be almost in proportion to the square of wind speed, indicating that the measured aerodynamic coefficients were independent of wind speed used. Furthermore, no contact between the model components was perceived. The mean wind speed of 15m/s was finally selected as the test mean wind speed $\overline{U}_m$. Correspondingly, the Reynolds number was between 0.603×10^5 and 1.809×10^5 while the Reynolds number in full scale was between 0.603×10^7 and 1.809×10^7 at the same wind speed. It is believed that the difference in Reynolds number would not significantly affect the measured aerodynamic forces/moments in consideration of the configuration of the tower.

8.5 CALCULATION OF AERODYNAMIC COEFFICIENTS

8.5.1 Drag and Lift Coefficients of Tower Leg

As mentioned before, global wind inclination is often within several degrees. Though small wind inclination does affect the aerodynamic and aeroelastic forces on the bridge deck, the small variation of global wind inclination seems not to affect the aerodynamic forces/moments acting on the tower legs because of their relative large dimension to wind inclination. Thus, the aerodynamic forces/ moments on the tower were measured under horizontal wind only in this investigation. The measured results will be used to approximate the aerodynamic coefficients of the Tsing Ma bridge tower for any wind inclination within ±5° in the comparison and parameter analysis of buffeting response of the Bridge in Chapter 9 and Chapter 10. Furthermore, in the buffeting analysis using the modified method presented in Chapter 4, the aerodynamic coefficients of any structural member in the Bridge were determined in the local wind coordinate systems with the local wind yaw $\bar{\beta}$ and local wind inclination $\bar{\theta}$. Therefore, after ignoring the influence of small local wind yaw on the tower, the aerodynamic coefficients of the tower leg could be expressed as function of local wind inclination ($\bar{\theta}$) only.

For the bridge tower leg, Figure 8-11 shows the balance coordinates (the $\overline{xyz}$-system), the local reference coordinates (the *qph*-system), and the local wind coordinates (the $\overline{qph}$-system). In the $\overline{xyz}$-system originating at the center of the top surface of the balance and following a right-hand rule, the $\bar{z}$-axis is in the vertical direction and the $\bar{x}$-axis and the $\bar{y}$-axis are in the horizontal plane with the $\bar{x}$-axis in the tower plane. The local reference coordinates and the local wind coordinates are simply called the model coordinates and the wind coordinates in this chapter for convenience. The *q*-axis in the model coordinates is upward and along the longitudinal axis of the tower leg and the *h*-axis is horizontal and normal to the tower plane. The *p*-axis in the model coordinates lies within the tower plane and always constitutes an acute angle with the mean wind direction. In the wind coordinates, the $\bar{q}$-axis is in the vertical direction whilst the $\bar{h}$-axis and the $\bar{p}$-axis are in the horizontal plane with the $\bar{p}$-axis along the mean wind direction. In light of the sign

convention used in this study, the local wind inclination $\bar{\theta}$ for the tower leg with respect to the *qph*-system is equal to β_0, the angle between the mean wind direction and the *qp* plane (i.e., the tower plane). The relation between the local wind inclination $\bar{\theta}$ and the rotation angle of the turning table β_T can then be expressed as

$$\bar{\theta} = \beta_0 = \begin{cases} \beta_T, & \text{when } 0^\circ \le \beta_T \le 90^\circ, \text{for windward tower leg} \\ \beta_T - 180^\circ, & \text{when } 90^\circ \le \beta_T \le 180^\circ, \text{for leeward tower leg} \end{cases} \tag{8-3}$$

Although the five aerodynamic forces/moments were measured on the tower leg, only the lift and drag forces are presented in this study because all the others were quite small and would not significantly affect the buffeting response of the whole bridge. The positive directions of the aerodynamic forces along the balance axes $\bar{x}$ and $\bar{y}$ ($F_{\bar{x}}$ and $F_{\bar{y}}$) and the lift and drag forces ($L_{\bar{h}}$ and $D_{\bar{p}}$) with respect to the wind coordinate $\bar{q}\bar{p}\bar{h}$-system are shown in Figure 8-11a for the windward tower leg and in Figure 8-11b for the leeward tower leg. Thus, the mean values of the lift and drag forces can be calculated from the measured mean aerodynamic forces using the following equations for both the windward and leeward tower legs.

$$L_{\bar{h}} = -F_{\bar{x}} \sin\beta_T + F_{\bar{y}} \cos\beta_T \tag{8-4}$$

$$D_{\bar{p}} = F_{\bar{x}} \cos\beta_T + F_{\bar{y}} \sin\beta_T \tag{8-5}$$

The average values of drag and lift coefficients of tower legs are then determined by

$$\left(C_{D_{\bar{p}}}, C_{L_{\bar{h}}}\right) = \frac{2}{\rho \bar{U}_m^2 B_m L_m} \left(D_{\bar{p}}, L_{\bar{h}}\right) \tag{8-6}$$

where ρ of 1.225kg/m^3 is the air density; $\bar{U}_m$ is the test wind speed of 15m/s; B_m of 0.06m is the width of tower leg; L_m is the length of the tower leg segment: 1.310m for the upper leg segment, 0.650m for the lower leg segment and 1.960m for the whole tower leg (including the link).

As mentioned before, the test range of local wind inclination $\bar{\theta}$ is from 0° to 90° for the windward tower leg and from 0° to -90° for the leeward tower leg. Because of the symmetry of the bridge tower, the drag coefficient $C_{D_{\bar{p}}}$ of tower leg is an even function of $\bar{\theta}$ whilst the lift coefficient $C_{L_{\bar{h}}}$ is an odd function of $\bar{\theta}$.

$$C_{D_{\bar{p}}}(-\bar{\theta}) = C_{D_{\bar{p}}}(\bar{\theta}) \tag{8-7}$$

$$C_{L_{\bar{h}}}(-\bar{\theta}) = -C_{L_{\bar{h}}}(\bar{\theta}) \tag{8-8}$$

Then, by using Eqs. 8-7 and 8-8, the aerodynamic coefficients of both the windward and leeward tower legs can be determined for the desirable range of $\bar{\theta}$ from -90° to 90°.

8.5.2 Coefficients of Drag and Crosswind Force of Tower Transverse Beam

The positive directions of the aerodynamic forces acting on a tower transverse beam are shown in Figures 8-12a and 8-12b for the angle β_T from 0° to 90° and from 90° and 180°, respectively. Figures 8-12a and 8-12b also show the balance coordinates (the $\bar{x}\bar{y}\bar{z}$ -system), the local reference coordinates (the *qph*-system), and the local wind coordinates (the $\bar{q}\bar{p}\bar{h}$ -system) for the tower transverse beam. In the figures, $F_{\bar{x}}$ and $F_{\bar{y}}$ are, respectively, the mean forces along the axes $\bar{x}$ and $\bar{y}$ on the transverse beam. They were obtained by the subtraction of the aerodynamic force on the active tower leg obtained in Case 1 from the total aerodynamic force obtained from one in Cases 2 to 5. $D_{\bar{p}}$ and $C_{\bar{q}}$ are the mean drag and crosswind forces along the wind axes $\bar{p}$ and $\bar{q}$. The aerodynamic moments on the transverse beam are not considered in this study. Because the tower transverse beam is a horizontal member, the axes q, p and $\bar{q}$, $\bar{p}$ are all in the same horizontal plane as the balance axes $\bar{x}$ and $\bar{y}$. The axes h and $\bar{h}$ are then in the vertical direction as the balance axis $\bar{z}$. Furthermore, the local wind inclination $\bar{\theta}$ for the transverse beam is zero and the local wind yaw angle $\bar{\beta}$ is determined by

$$\bar{\beta} = \beta_T - 90° = \begin{cases} \beta_0 - 90°, & \text{when } 0° \le \beta_T \le 90° \\ \beta_0 + 90°, & \text{when } 90° \le \beta_T \le 180° \end{cases} \tag{8-9}$$

The measured aerodynamic forces on the transverse beam are thus expressed as function of local wind yaw only ranging from -90° to 90°. The drag and crosswind forces are then calculated by

$$D_{\bar{p}} = F_{\bar{x}} \cos\beta_T + F_{\bar{y}} \sin\beta_T \tag{8-10}$$

$$C_{\bar{q}} = F_{\bar{x}} \sin\beta_T - F_{\bar{y}} \cos\beta_T \tag{8-11}$$

It may be worthwhile to point out that the measured aerodynamic forces and then the drag and crosswind forces on the transverse beam may not act at the center of the

beam, in particular in the case of yaw wind. However, the moments caused by the eccentricity of the aerodynamic forces on the transverse beam are too small to affect the buffeting response of the whole bridge. Furthermore, in the global buffeting analysis each transverse beam was modeled by two beam elements. Therefore, the average coefficients of drag and crosswind forces on the tower transverse beam were considered in this study and calculated by

$$\left(C_{C_{\bar{q}}}, C_{D_{\bar{p}}}\right) = \frac{2}{\rho \bar{U}_m^2 B_m L_m}\left(C_{\bar{q}}, D_{\bar{p}}\right) \tag{8-12}$$

where B_m and L_m are, respectively, the width and length of the tower transverse beam. Here, B_m is 0.028m, 0.031m, 0.034m, 0.042m and L_m is 0.300m, 0.307m, 0.316m, 0.327m for the upper, upper-middle, lower-middle and lower transverse beam, respectively. Theoretically, $C_{D_{\bar{p}}}$ is an even function of the local wind yaw angle $\bar{\beta}$ whilst $C_{C_{\bar{q}}}$ is an odd function of $\bar{\beta}$ because of the symmetry of the tower. However, in the actual model test, this symmetry was slightly violated because of the existence of narrow gap between the tower leg and the transverse beam. Therefore, the force coefficients averaged from the two cases with the positive and negative $\bar{\beta}$ were used, namely, for any $\bar{\beta}$ within –90° to 90°, the final aerodynamic coefficients are determined as follows

$$C_{D_{\bar{p}}}(\bar{\beta}) = [C_{D_{\bar{p}}}(\bar{\beta}) + C_{D_{\bar{p}}}(-\bar{\beta})]/2 \tag{8-13}$$

$$C_{C_{\bar{q}}}(\bar{\beta}) = [C_{C_{\bar{q}}}(\bar{\beta}) - C_{C_{\bar{q}}}(-\bar{\beta})]/2 \tag{8-14}$$

8.6 MEASUREMENT RESULTS

The aerodynamic forces measured by the balance under designated wind directions were first analyzed to obtain the mean coefficients of the drag/lift/crosswind force of the tower member. These discrete mean coefficients were then interpolated using spline functions and fitted using polynomial functions to obtain the aerodynamic coefficient curves, which are presented and analyzed in this section. Some of these curves will be used in Chapters 9 and 10 for the buffeting analysis of the whole bridge. It should be noted that all the coefficients provided here refer to the local wind coordinate system.

8.6.1 Drag and Lift Coefficients of Tower Legs

The drag and lift coefficients of the windward and leeward entire legs of the Tsing Ma bridge tower with and without the presence of the deck segment (Case 1 and Case 6) are depicted in Figures 8-13 and 8-14 as the functions of local wind inclination $\bar{\theta}$ from 0° to 90°. The drag and lift coefficients of the single tower leg without any dummy models presented (Case 7) are also plotted in Figures 8-13 and 8-14. From these measured results, the observations and comments are made in the following.

8.6.1.1 Drag and Lift Coefficients of Isolated Single Tower Leg

The drag coefficient of the single tower leg without any dummy model surrounded is about 1.7 and remains almost constant within the range of $0° \leq \bar{\theta} \leq 30°$, as shown in Figure 8-13. This means that the drag coefficient of the isolated single tower leg is not sensitive to local wind inclination with in this range. With the further increase of local wind inclination angle $\bar{\theta}$, the drag coefficient of the single tower leg decreases. In particular, the drag coefficient decreases almost linearly with the angle $\bar{\theta}$ when $\bar{\theta}$ is larger than 55°. As shown in Figure 8-14, the lift coefficient of the isolated single tower leg is negative within the range of $0° \leq \bar{\theta} \leq 76°$ and then positive afterwards. The lift coefficient reaches its minimum value of –0.75 at $\bar{\theta}$ of 54° and its maximum value of 0.35 at $\bar{\theta}$ of 82°. Such variations of drag and lift coefficients are mainly attributed to the shape and size of the tower leg.

8.6.1.2 Drag and Lift Coefficients of Windward Tower Leg

The drag coefficient of windward tower leg with the dummy models of leeward tower leg and transverse beams but without the dummy deck segment is smaller than that of the isolated single tower leg within the range of $0° \leq \bar{\theta} \leq 36°$, as shown in Figure 8-13. The small reduction in drag coefficient may be attributed to the obstruction of the transverse beams on the suction of leeward face of the windward tower leg. The drag coefficients from these two cases then become similar for $\bar{\theta}$ varying from 36° to 78°. After that (i.e., $\bar{\theta}$ >78°), the drag coefficient of windward tower leg is significantly larger than that of the isolated single tower leg mainly due

to the increase of wind speed caused by the blockage of transverse beams and leeward tower leg.

With the addition of the dummy bridge deck segment, the drag coefficient of windward tower leg has a slight increase within the range of $0° \leq \bar{\theta} \leq 40°$, compared with that of the same tower leg without the dummy deck segment. The drag coefficients from these two cases then become almost the same for $\bar{\theta}$ varying from 40° to 80°. One may thus conclude that the interference effect from the deck segment on the drag coefficient of the windward tower leg is insignificant when $0° \leq \bar{\theta} \leq 80°$.

Compared with the lift coefficient of the isolated single tower leg, the influence of the leeward leg and the transverse beams on the lift coefficient of the windward leg is relatively small when $\bar{\theta}$ <42°, as shown in Figure 8-14. This may be because for small $\bar{\theta}$, the leeward leg and the transverse beams could exert little influence on the flow patterns over the side faces of the windward tower leg. The difference between these two cases then becomes remarkable with the increase of $\bar{\theta}$ from 42° due to the interference from the transverse beams and leeward leg. Particularly, the lift force on the windward leg with the dummy models is not equal to zero when $\bar{\theta}$ =90°.

With the dummy deck segment in addition to other dummy models, the measured lift coefficients of the windward tower leg appear to be quite different from those of the isolated single tower leg within a wide range of local wind inclination. However, if compared with the lift coefficient of the windward tower leg without the dummy deck segment, the presence of the dummy deck segment exerts relatively small influence on the lift coefficient within the range of $0° \leq \bar{\theta} \leq 70°$.

8.6.1.3 Drag and Lift Coefficients of Leeward Tower Leg

Figure 8-13 clearly demonstrates that the drag coefficient of leeward tower leg with the dummy windward leg and transverse beams varies significantly differently from that of the isolated single tower leg and that of windward tower leg with the dummy models surrounded. Within a wide range of $\bar{\theta}$ from 0° to 70°, the drag coefficient of the leeward leg is considerably smaller than that of the windward tower leg. This is mainly because of the sheltering effect from the windward tower leg and the transverse beams. The sheltering effect from the windward leg is particularly

significant when $\bar{\theta}$ is small so that the drag coefficient of the leeward leg is only about 0.2 compared with 1.7 for the isolated leg and 1.6 for the windward leg. The sheltering effect from the windward leg, however, decreases with the increasing $\bar{\theta}$. Though the transverse beams still provide some degrees of sheltering effect on the leeward leg, they may also accelerate wind flow to the leeward leg along their surfaces. More vortexes may be also generated in the leeward face of the leeward leg because of the transverse beams, resulting in negative pressure area on the leeward face of the leeward leg. As a result of the mixture of all these factors, the drag coefficient of the leeward leg suddenly increases from 0.2 to 1.3 when the local wind inclination increases from 6° to15°. It then reduces gradually down to 0.9 at $\bar{\theta}$=66° and remains almost constant afterwards.

If compared with the drag coefficient of the leeward tower leg without the dummy deck segment, the drag coefficient of the leeward leg with the dummy deck segment is slightly increased when $0° \le \bar{\theta} \le 8°$, perhaps because of the increase of wind speed caused by the blockage of deck segment. Then, until $\bar{\theta}$=80° the influence from the dummy deck segment on the drag coefficient of the leeward leg is insignificant.

By comparing with the lift coefficients of the isolated single tower leg and the leeward tower leg with the dummy models surrounded, one may see that the lift coefficient of the leeward tower leg with the dummy models varies significantly differently with local wind inclination $\bar{\theta}$. Within the range of $0° \le \bar{\theta} \le 10°$, the presence of the windward leg and transverse beams leads to an increase in the lift coefficient of the leeward leg. The lift coefficient of the leeward leg then decreases when $\bar{\theta}$ increases from 10° to about 40°, but it is still larger that the lift coefficient of the windward tower leg. When $\bar{\theta}$ is further increased, the synthetic effect of the windward leg and the transverse beams makes the lift coefficient of the leeward leg not sensitive to $\bar{\theta}$ until 70°. It is also noticed that when $\bar{\theta}$=90°, the presence of the transverse beams leads to the wind flow passing the two side faces of the tower leg asymmetric, generating a non-zero lift force on the leg. Similar to the drag coefficient, it is seen from Figure 8-14 that the presence of the dummy deck segment

does not significantly affect the lift coefficient of the leeward tower leg except when local wind inclination is more than 80°.

8.6.2 Drag and Lift Coefficients of Upper and Lower Tower Leg Segments

Figures 8-15 and 8-17 show the drag and lift coefficient curves of the upper segment of the windward and leeward tower legs with and without the presence of the deck segment as the functions of local wind inclination $\bar{\theta}$ (Case 8 and Case 9). Figures 8-16 and 8-18, on the other hand, demonstrate the corresponding curves of the lower segment. The curves with solid dots in Figures 8-15 to 8-18 will be used in Chapters 9 and 10 for the buffeting analysis of the whole bridge.

8.6.2.1 Drag Coefficients of Upper and Lower Tower Leg Segments

It can be seen from Figure 8-15 that the variation of drag coefficient of the upper windward leg segment with local wind inclination ($\bar{\theta}$) is very similar to that of drag coefficient of the entire windward leg shown in Figure 8-13. The pattern of drag coefficient of the lower windward leg segment (see Figure 8-16) is, however, slightly different from that of the upper windward leg segment. The drag coefficient of the lower windward leg segment is greater than that of the upper windward leg segment when $\bar{\theta}$ is within 75°. This is mainly because the dimension of the lower windward leg segment is lager than that of the upper windward leg segment for $\bar{\theta}$ within this range. Thus, it is necessary to consider the difference of aerodynamic coefficient between the upper and lower leg segments in the buffeting analysis of the whole bridge. The drag coefficient reaches the maximum value about 1.6 at $\bar{\theta}$ about 36° for the upper windward leg segment and the maximum values about 2.0 at $\bar{\theta}$ about 36° and 6° for the lower windward leg segment.

For both the upper and lower windward leg segments, the presence of dummy deck segment leads to a small increase of the drag coefficient about 6% when $0° \le \bar{\theta} \le 40°$. This may be because the blockage of deck segment increases local wind pressures on the windward leg. This small effect diminishes as $\bar{\theta}$ becomes larger mainly because the deck dimension normal to wind direction reduces significantly. Nevertheless, the effect from the bridge deck on the drag coefficients of both upper and lower windward leg segments may be neglected.

The variation of drag coefficient of the upper segment of leeward leg with $\bar{\theta}$ is quite similar to that of drag coefficient of the entire leeward leg shown in Figure 8-13. The variation of drag coefficient of the lower segment of leeward leg with $\bar{\theta}$ is also similar to that of drag coefficient of the entire leeward leg except for $\bar{\theta}$ greater than 70°. The maximum value of the drag coefficient of the upper segment of the leeward leg is about 1.2 occurring at $\bar{\theta}$ about 18° and that of the lower segment of leeward leg is about 1.3 occurring at $\bar{\theta}$ about 24°. Nevertheless, the drag coefficients of both upper and lower segments of the leeward leg are significantly different from those of both upper and lower segments of the windward leg. Thus, it is necessary to distinguish the aerodynamic coefficients of the windward tower leg from those of the leeward tower leg.

The existence of deck segment affects the drag coefficient of the upper segment of the leeward tower leg when $0° \leq \bar{\theta} \leq 10°$ (see Figure 8-15). However, when $\bar{\theta}$ is greater than 10°, the deck influence on the drag coefficient of the leeward upper leg segment becomes insignificant. For the leeward lower leg segment, the existence of the bridge deck reduces the drag coefficient about 10% when $10° \leq \bar{\theta} \leq 70°$ (see Figure 8-16).

8.6.2.2 Lift Coefficients of Upper and Lower Tower Leg Segments

It is seen again that the lift coefficients of the upper segment of the windward tower leg with and without the dummy deck segment, as shown in Figure 8-17, are very similar to those of the entire windward tower leg, as shown in Figure 8-14. The lift coefficients of the lower segment of the windward tower leg, however, are different from the above two cases to some extent. The lift coefficient decreases approximately linearly with the increase of $\bar{\theta}$ up to 33° for the upper segment and 45° for the lower segment. There is a sudden change of lift coefficient of the upper segment of windward leg with the dummy deck segment when $\bar{\theta}$ is around 38°, but this does not occur in the lift coefficient of the lower segment of windward leg.

The similar observations can be made for the upper and lower segments of the leeward tower leg with and without the dummy deck segment. The lift coefficients of

the upper segment of the leeward leg, as shown in Figure 8-17, are similar to those of the entire leeward leg shown in Figure 8-14. The lift coefficients of the lower segment of the leeward leg, however, are different from the above two cases, in particular when $\overline{\theta}$ is greater than 60°. All these indicate that in the buffeting analysis of the Tsing Ma suspension Bridge and its comparison with the field measurement, it will be appropriate to use the separate aerodynamic coefficients for the upper and lower segments of windward and leeward tower legs rather than a tower as a whole.

8.6.3 Drag and Crosswind force Coefficients of Transverse Beams

The measured drag and crosswind force coefficients of the four transverse beams of the Tsing Ma bridge tower with the dummy deck segment are respectively plotted in Figures 8-19 to 8-22 as the functions of the local wind yaw angle $\overline{\beta}$. The measured data are fitted using polynomial functions, which are also depicted in Figures 8-19 to 8-22. The variations of both the drag and crosswind force coefficients with local yaw angle $\overline{\beta}$ are similar to each other for all the four transverse beams. The crosswind force coefficient varies with $\overline{\beta}$ in a manner similar to a sine wave. The drag coefficient, however, seems to have the shape of a cosine wave but it is distorted in the magnitude for $\overline{\beta}$ ranging from 0° to 27° for the lower transverse beam and from 0° to 15° for the other three transverse beams. It is interesting to see that such a distortion becomes weak for upper transverse beam. This kind of distortion may be attributed to the existence of the dummy deck segment.

8.7 SUMMARY

An extensive wind tunnel investigation has been performed to measure aerodynamic coefficients of all the major structural members of a long span suspension bridge tower to facilitate the buffeting analysis of the whole bridge and to understand the wind interference between the tower structural components. The wind tunnel tests taking the Tsing Ma bridge tower as an example included the measurements of the isolated single tower leg, the windward and leeward tower legs with the dummy tower leg and four transverse beams, the upper and lower segments of the windward

and leeward tower legs with the dummy tower leg and four transverse beams, the four transverse beams with the dummy tower legs, and the additional measurements with the dummy bridge deck segment. To fulfill this task, the tower model and the test rig have been carefully designed and the test procedure has been well planned. The following are major observations made from this investigation.

(1) The drag coefficient of the windward tower leg with the dummy leeward tower leg and four transverse beams has a slight difference from that of the isolated single tower leg for the most concerned local wind inclinations. The influence of the leeward leg and the transverse beams on the lift coefficient of the windward leg is also relatively small when $\bar{\theta}$ <42° but becomes remarkable with the increase of $\bar{\theta}$ from 42°. The interference effect from the deck segment on both the drag and lift coefficients of the windward tower leg is insignificant within the range of $0° \leq \bar{\theta} \leq 70°$.

(2) The drag coefficient of the leeward tower leg with the dummy windward leg and transverse beams is significantly different from either the isolated single tower leg or the windward tower leg because of the sheltering effect from the windward tower leg and the transverse beams. The same observation is made to the lift coefficient of the leeward tower leg. The influence from the dummy deck segment on both the drag and lift coefficients of the leeward leg is also insignificant when $0° \leq \bar{\theta} \leq 80°$.

(3) The variation of drag coefficient of the upper windward leg segment with local wind inclination $\bar{\theta}$ is very similar to that of drag coefficient of the entire windward leg. The pattern of drag coefficient of the lower windward leg segment is, however, slightly different from that of the upper windward leg segment. The drag coefficient of the lower windward leg segment is greater than that of the upper windward leg segment when $\bar{\theta}$ is within 75°.

(4) The variation of drag coefficient of the upper segment of leeward leg with $\bar{\theta}$ is quite similar to that of drag coefficient of the entire leeward leg. The variation of drag coefficient of the lower segment of leeward leg with $\bar{\theta}$ is also similar to that of drag coefficient of the entire leeward leg except for $\bar{\theta}$ greater than 70°. The

drag coefficients of both upper and lower segments of the leeward leg are significantly different from those of both upper and lower segments of the windward leg.

(5) The lift coefficients of the upper segment of either the windward or leeward tower leg with and without the dummy deck segment are very similar to those of either the entire windward or leeward tower leg. The lift coefficients of the lower segment of the windward and leeward tower legs, however, are different from the above two cases to some extent.

(6) The variations of both the drag and crosswind force coefficients with local yaw angle $\bar{\beta}$ are similar to each other for all the four transverse beams. The crosswind force coefficient varies with $\bar{\beta}$ in a manner similar to a sine wave. The drag coefficient, however, seems to have the shape of a cosine wave but it is distorted in the magnitude for $\bar{\beta}$ ranging from 0° to 27° for the lower transverse beam and from 0° to 15° for the other three transverse beams.

Based on the above test results, it may be concluded that in the buffeting analysis of the Tsing Ma suspension Bridge and its comparison with the field measurement, it will be appropriate to use the separate aerodynamic coefficients for the upper and lower segments of either the windward or leeward tower leg rather than taking a tower as a whole.

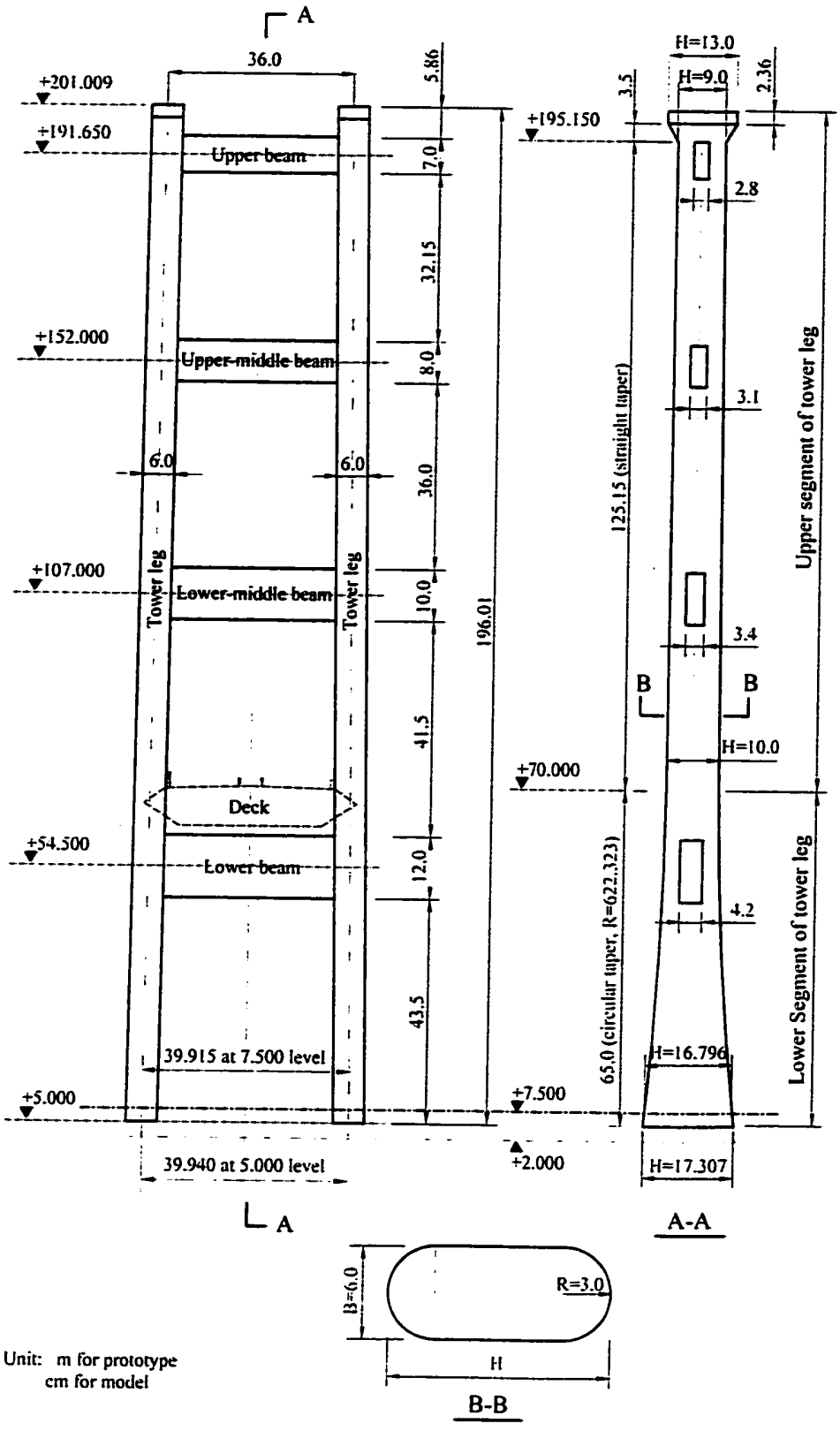

Figure 8-1 Ma Wan Tower of Tsing Ma Bridge

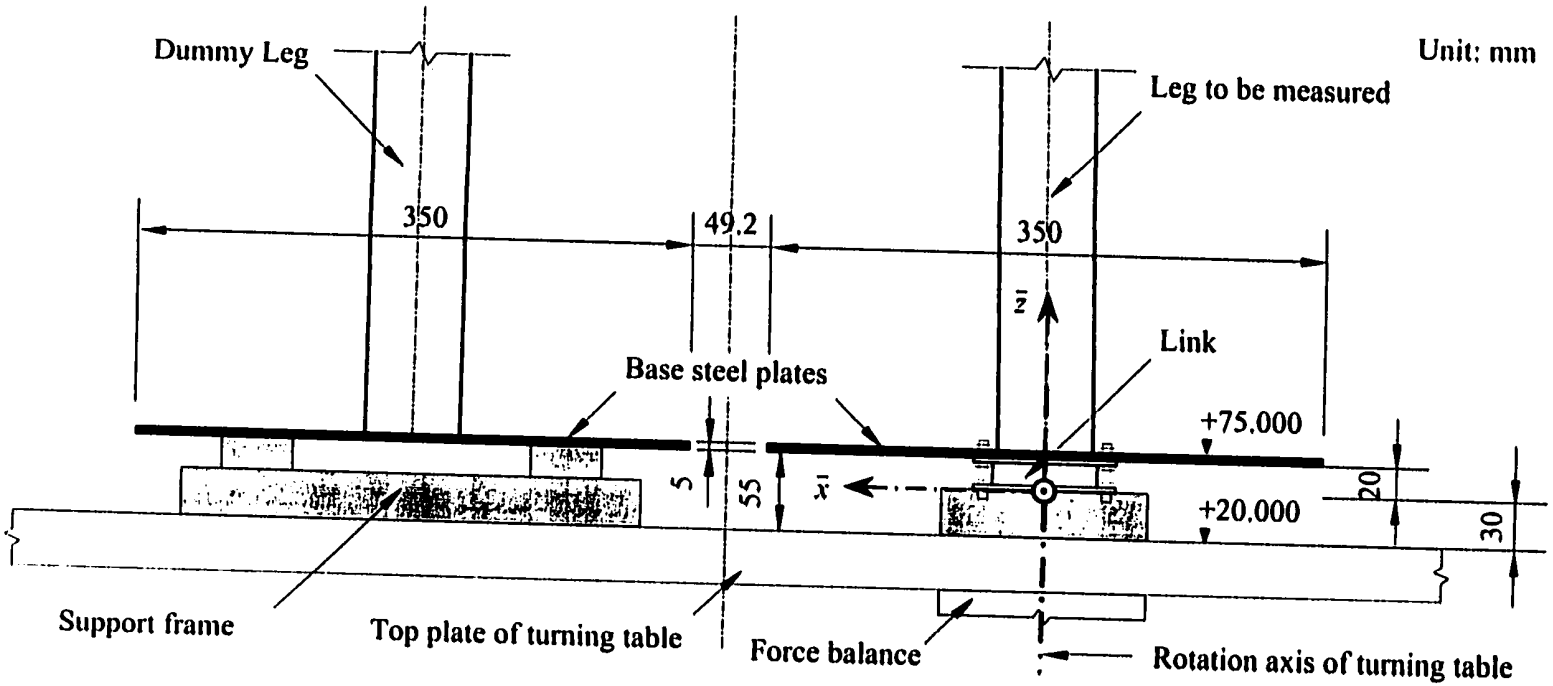

Figure 8-2 Schematic Diagram of Tower Model Installation

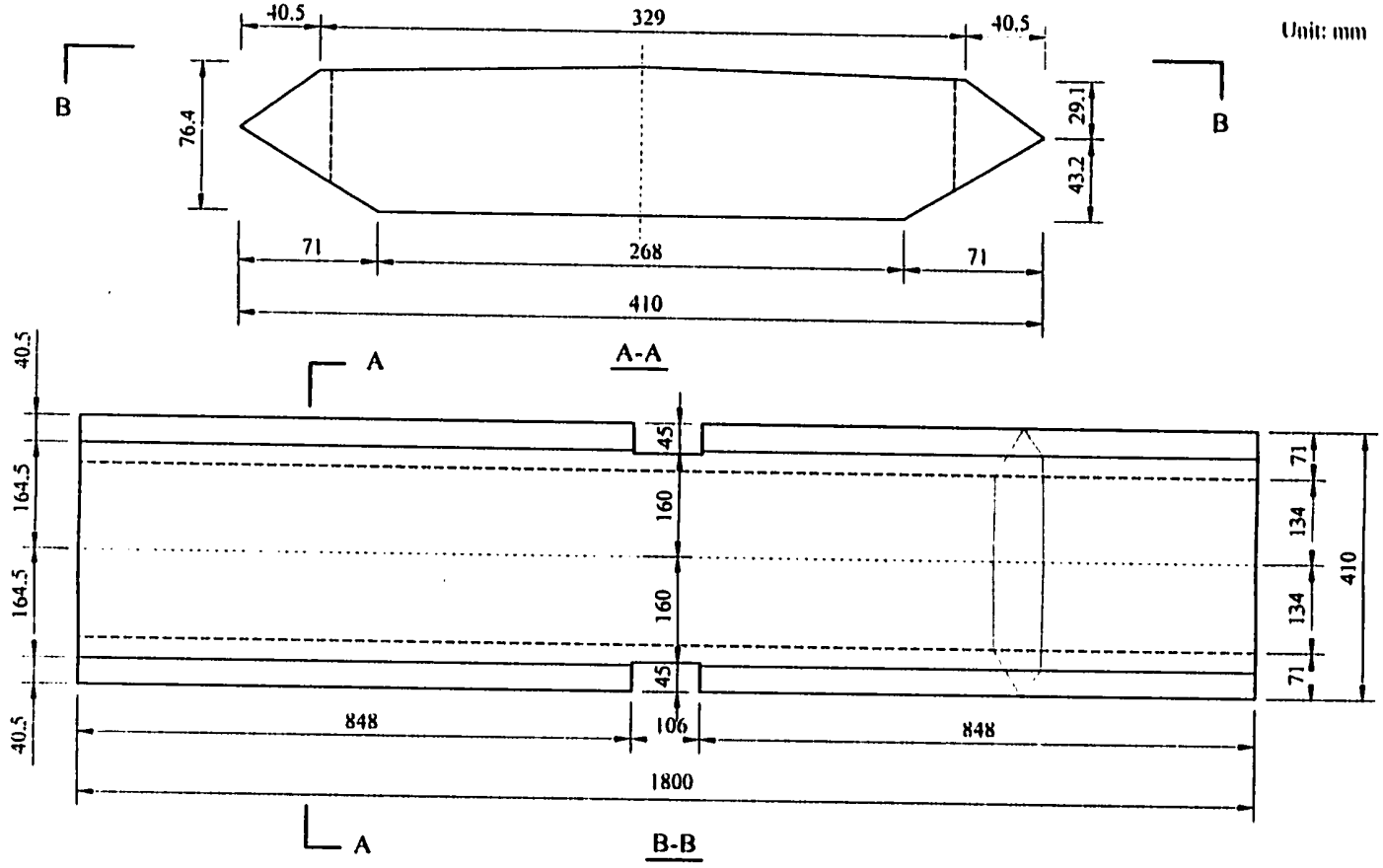

Figure 8-3 Configuration of Dummy Deck Segment Model

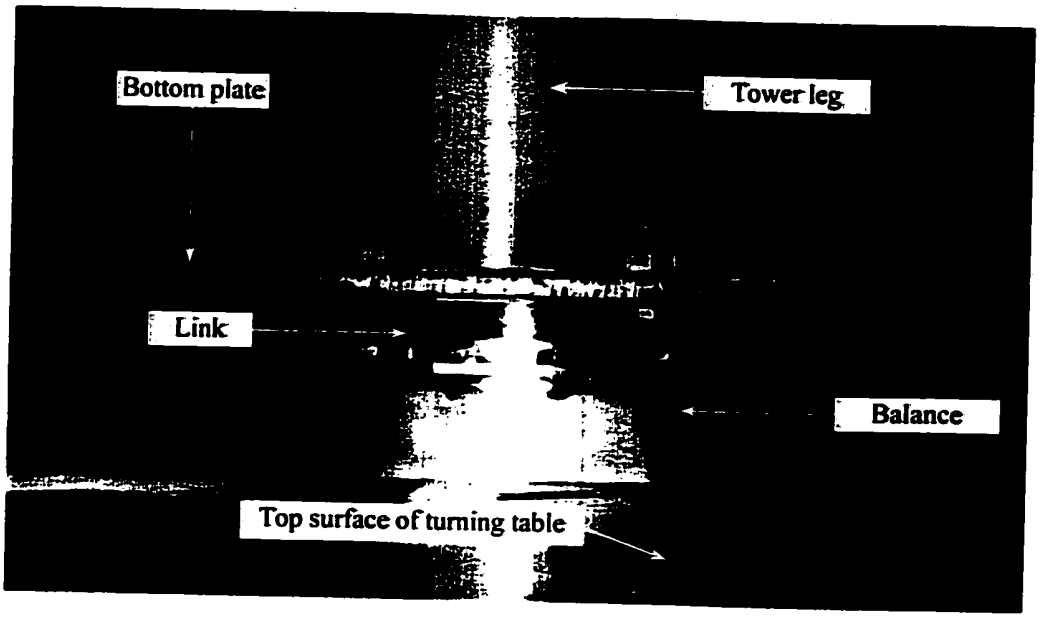

Figure 8-4 Connection of Tower Leg to Force Balance

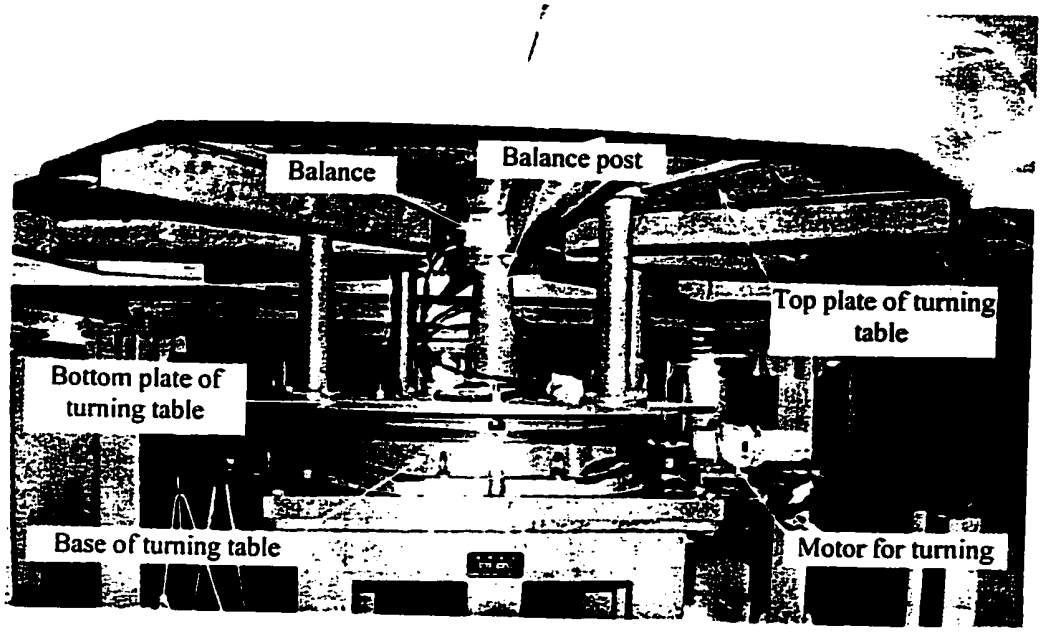

Figure 8-5 Installation of Force Balance on Turning Table

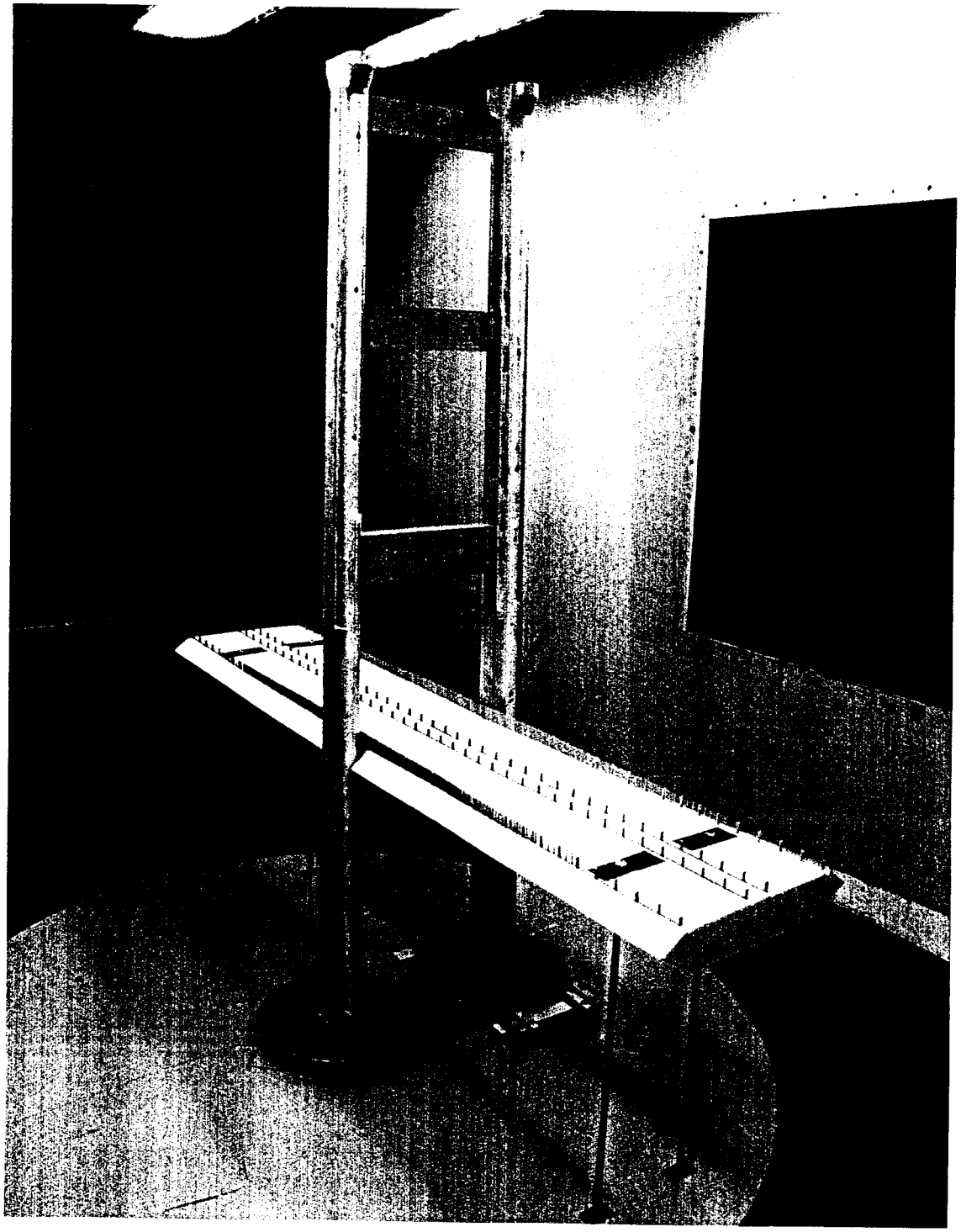

Figure 8-6 Single Leg Measurement with Bridge Deck

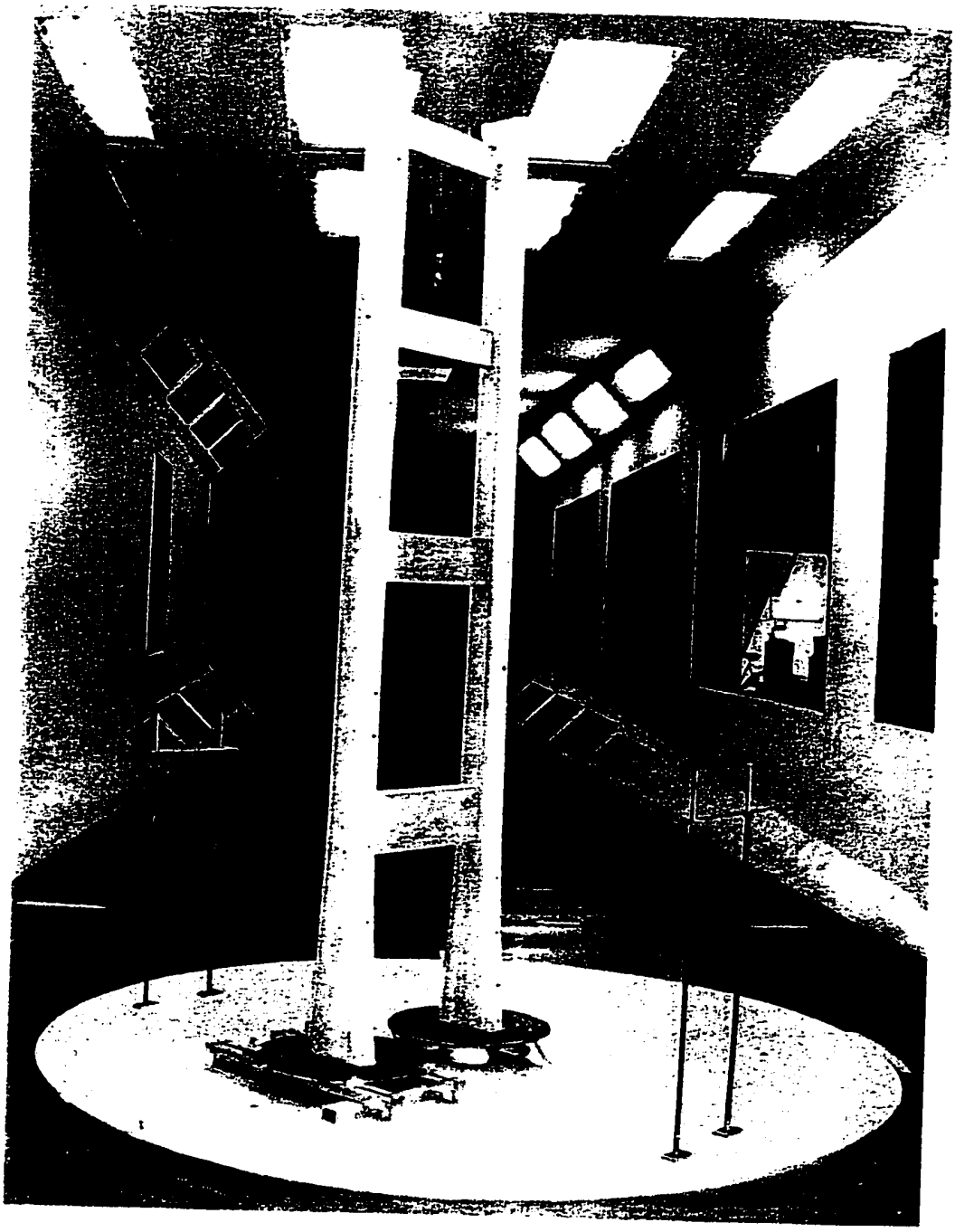

Figure 8-7 Single Leg Measurement without Bridge Deck

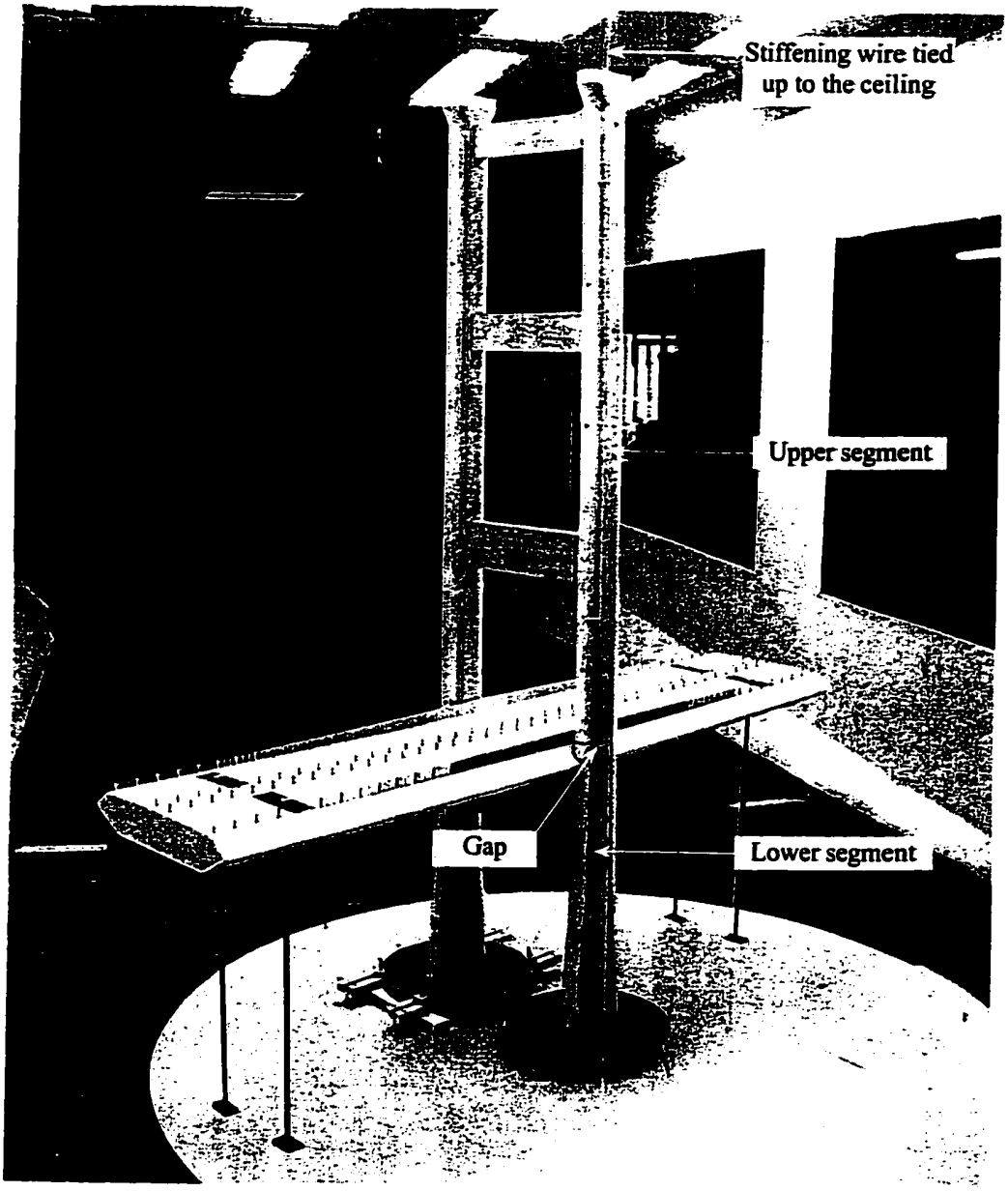

Figure 8-8 Lower Leg Segment Measurement with Bridge Deck

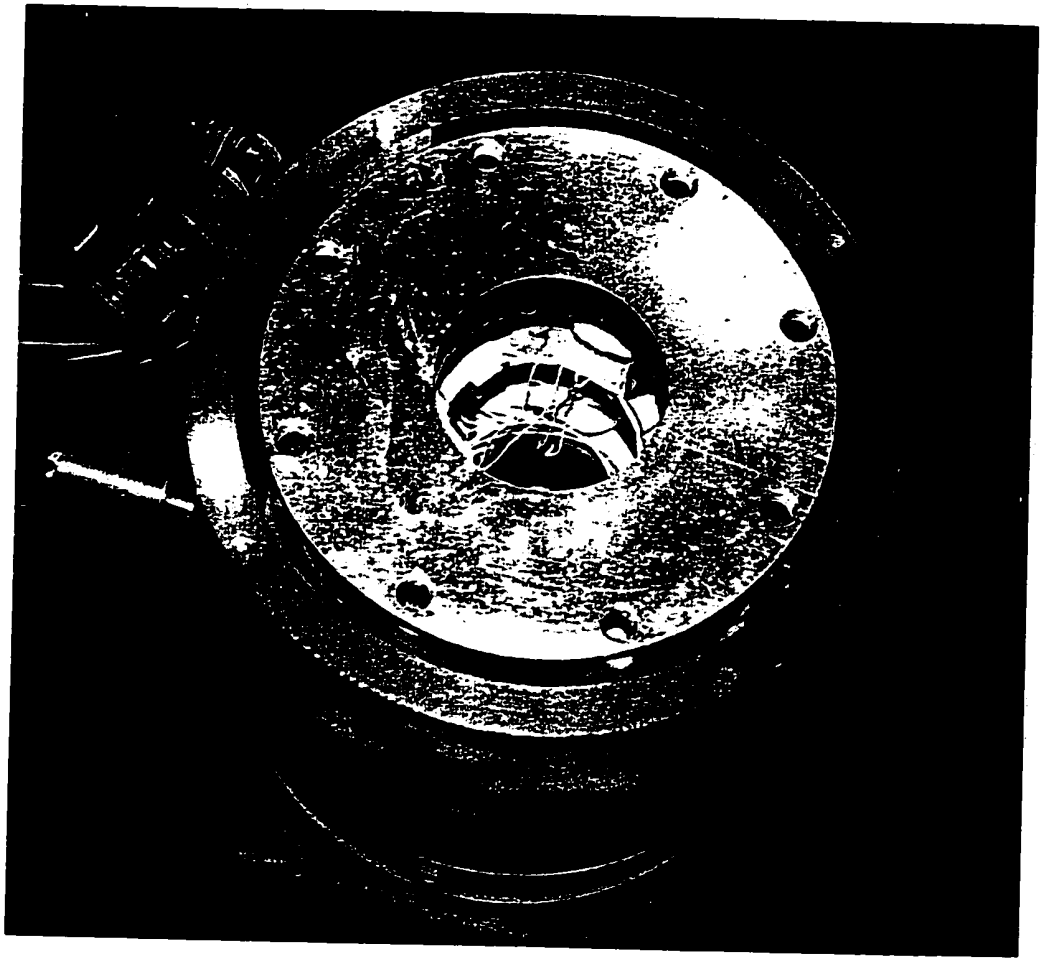

Figure 8-9 Five Component Force Balance

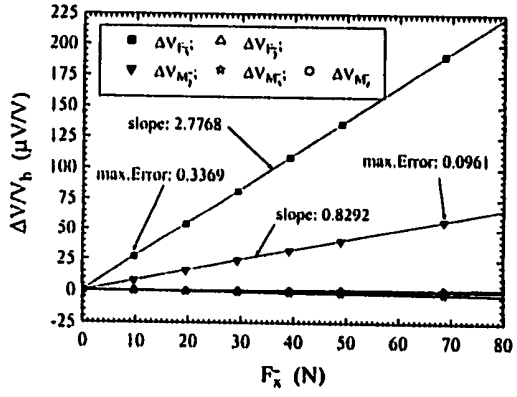

(a) Relation between $\Delta V/V_b$ and $F_{\bar{x}}$

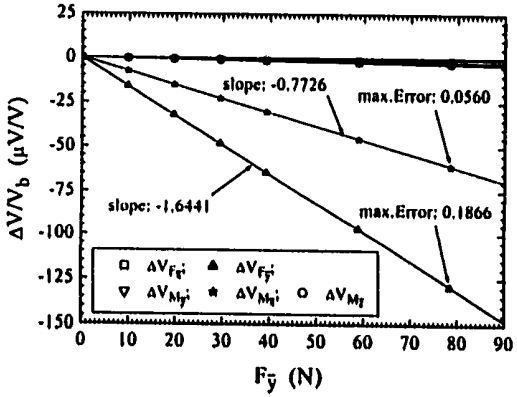

(b) Relation between $\Delta V/V_b$ and $F_{\bar{y}}$

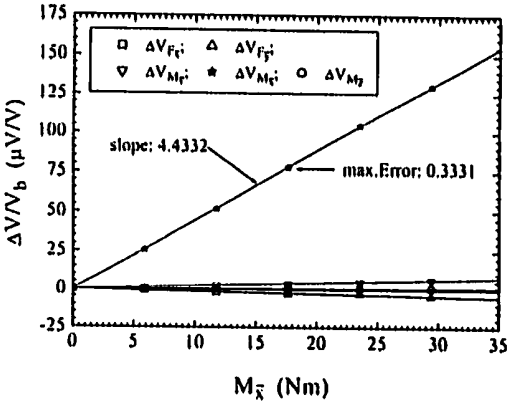

(d) Relation between $\Delta V/V_b$ and $M_{\bar{x}}$

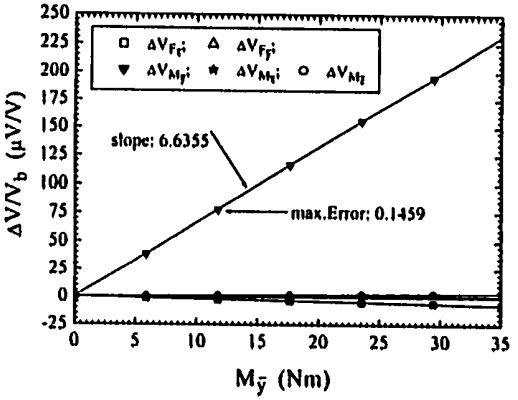

(e) Relation between $\Delta V/V_b$ and $M_{\bar{y}}$

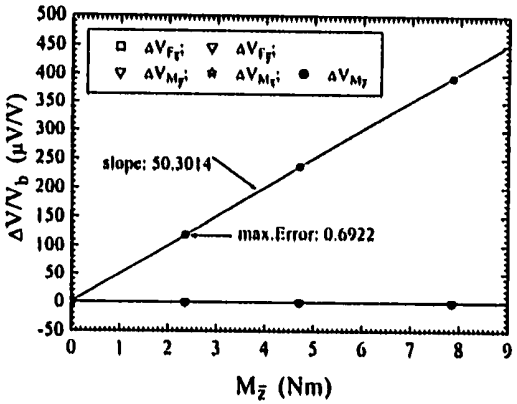

(f) Relation between $\Delta V/V_b$ and $M_{\bar{z}}$

Figure 8-10 Calibration Curves of Five-component Force Balance

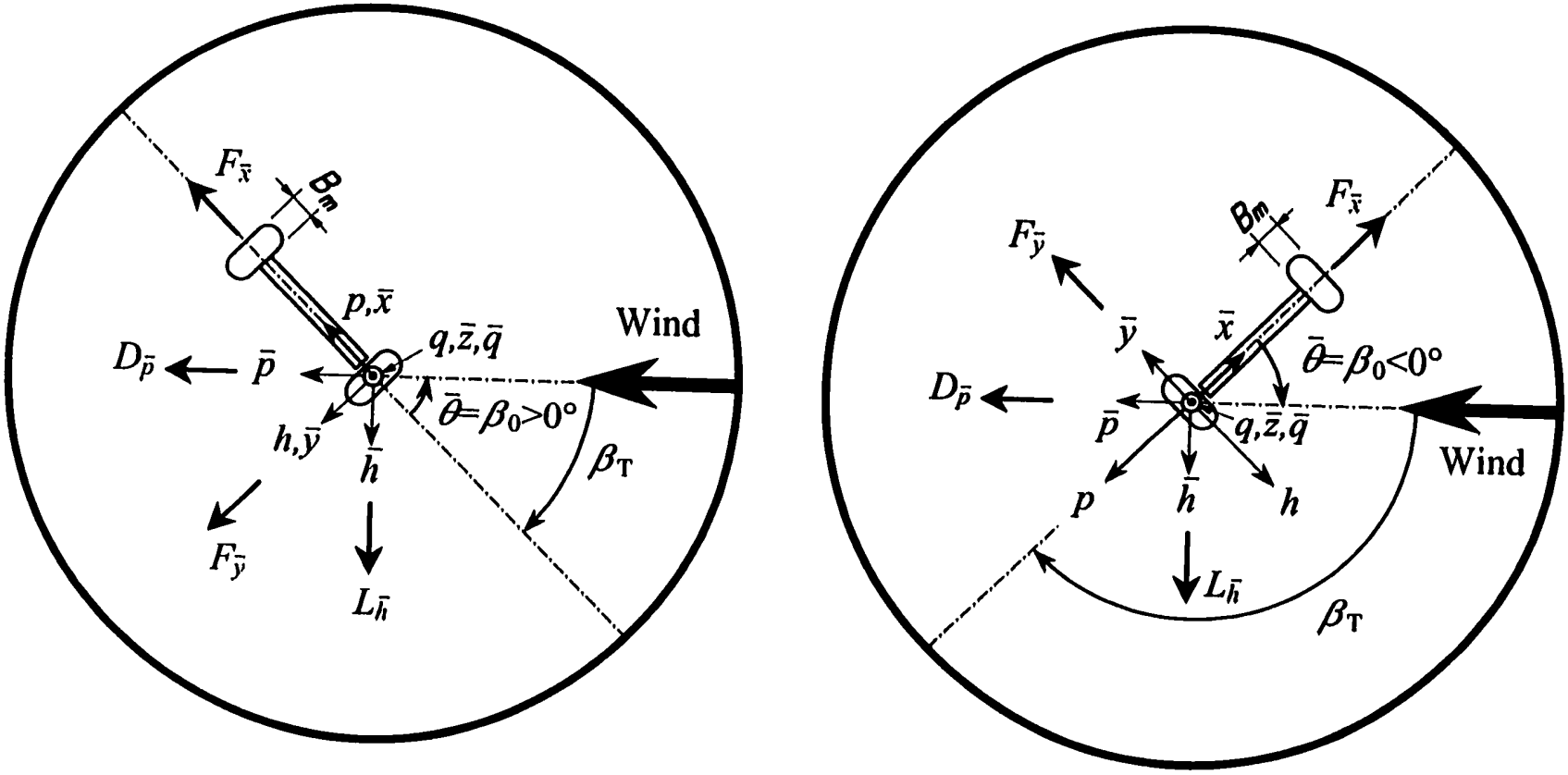

(a) $0° \le \beta_T \le 90°$ (windward tower leg)

(b) $90° \le \beta_T \le 180°$ (leeward tower leg)

Figure 8-11 Positive Directions of Aerodynamic Forces on Tower Legs

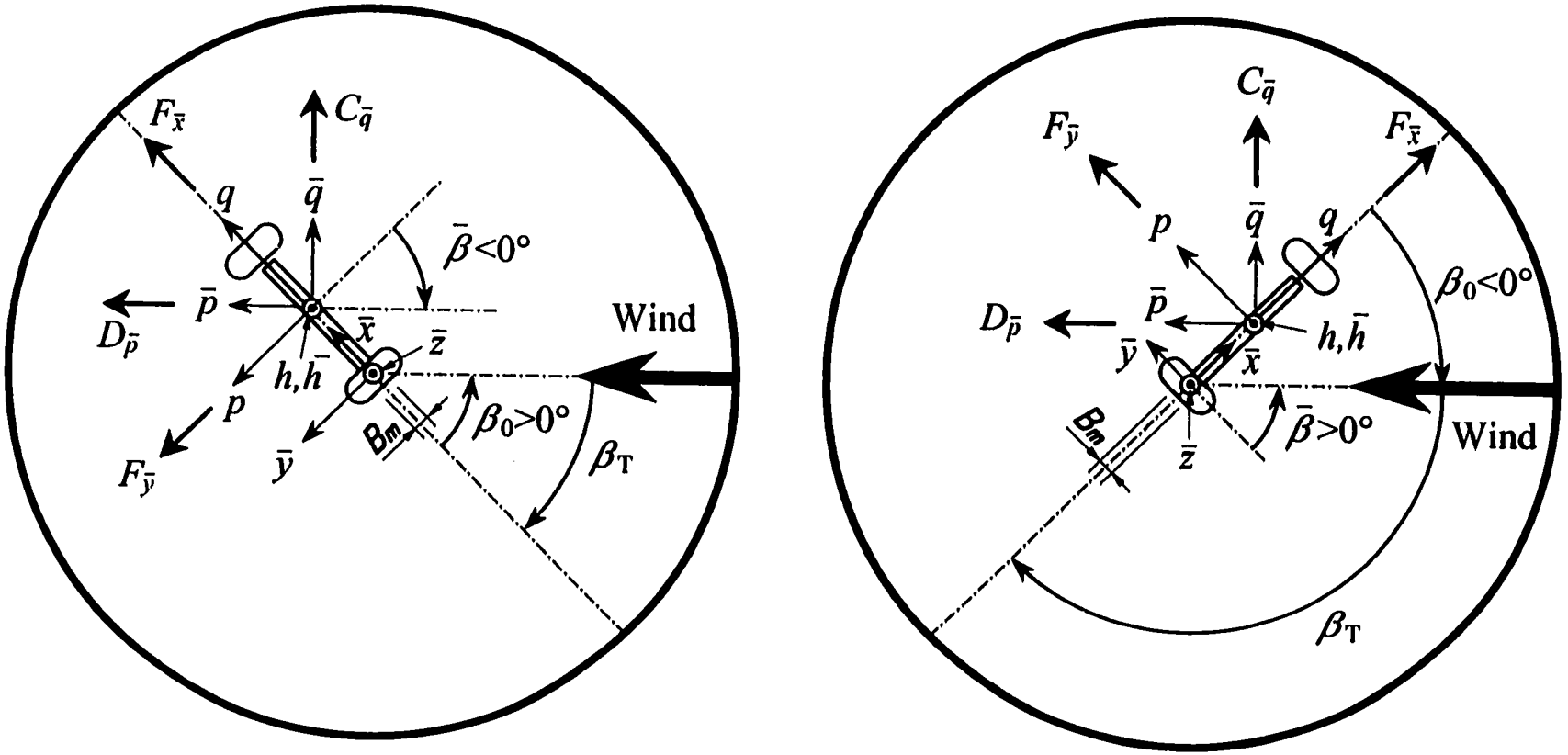

(a) $0° \le \beta_T \le 90°$ (leeward gap)

(b) $90° \le \beta_T \le 180°$ (windward gap)

Figure 8-12 Positive Directions of Aerodynamic Forces on Tower Transverse Beams

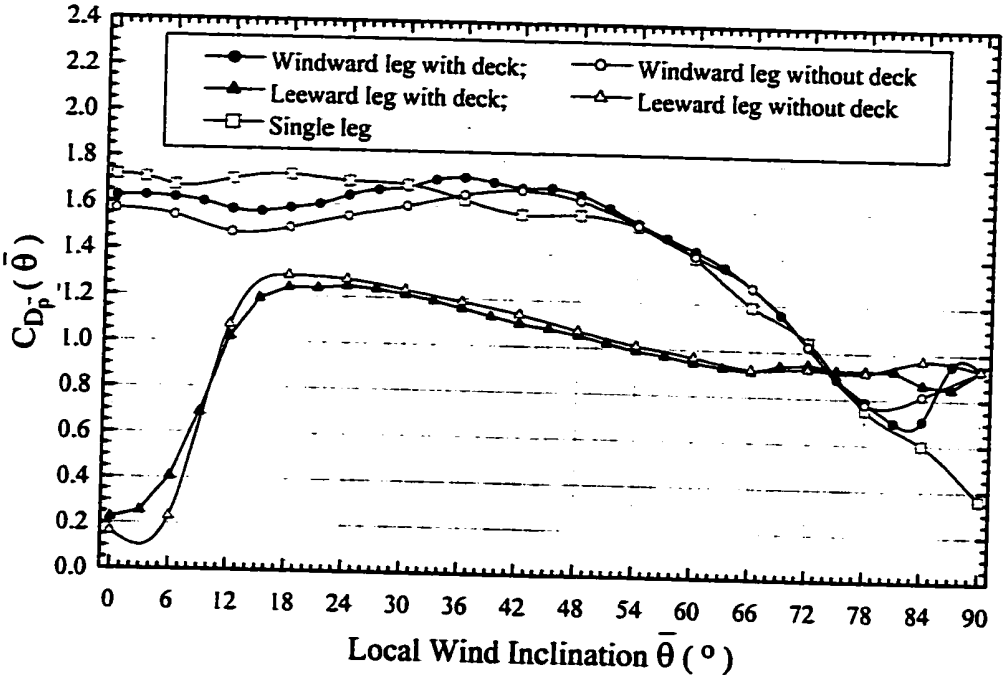

Figure 8-13 Drag Coefficients of Tower Legs

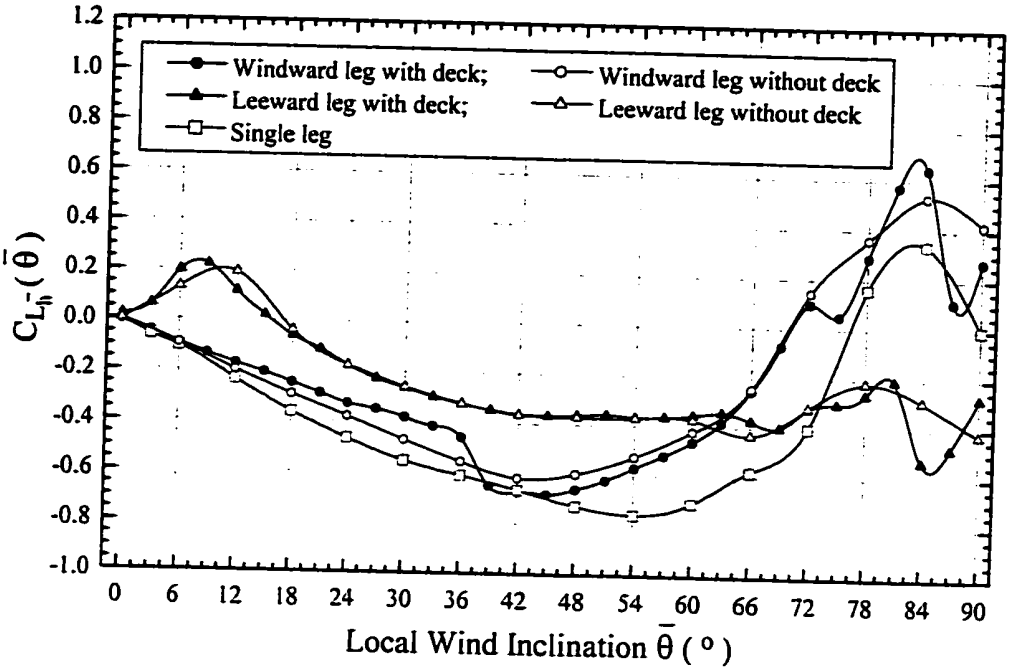

Figure 8-14 Lift Coefficients of Tower Leg

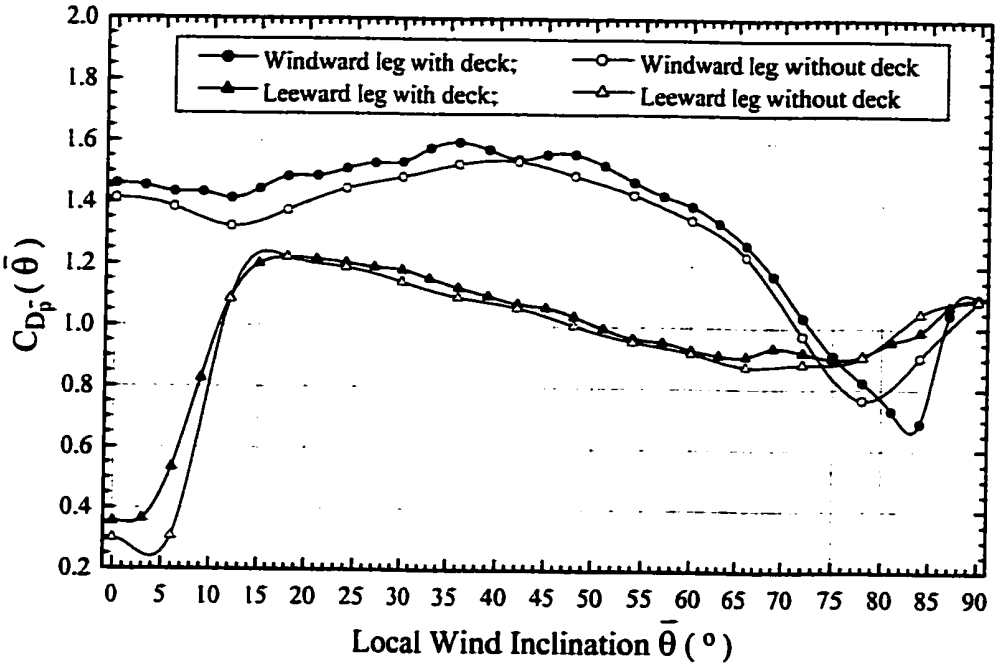

Figure 8-15 Drag Coefficients of Upper Segment of Tower Leg

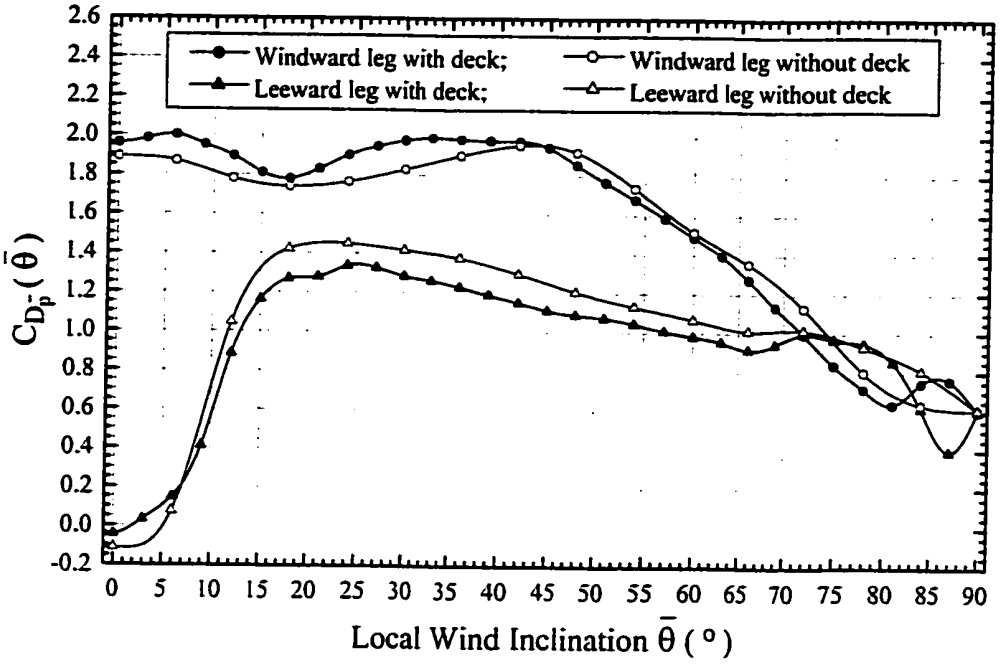

Figure 8-16 Drag Coefficients of Lower Segment of Tower Leg

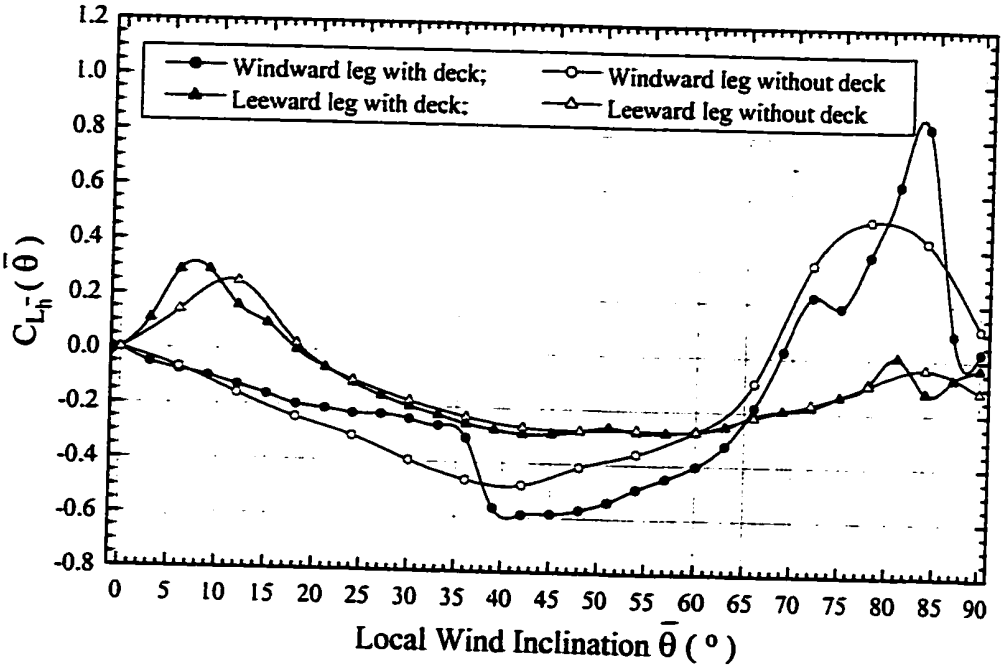

Figure 8-17 Lift Coefficients of Upper Segment of Tower Leg

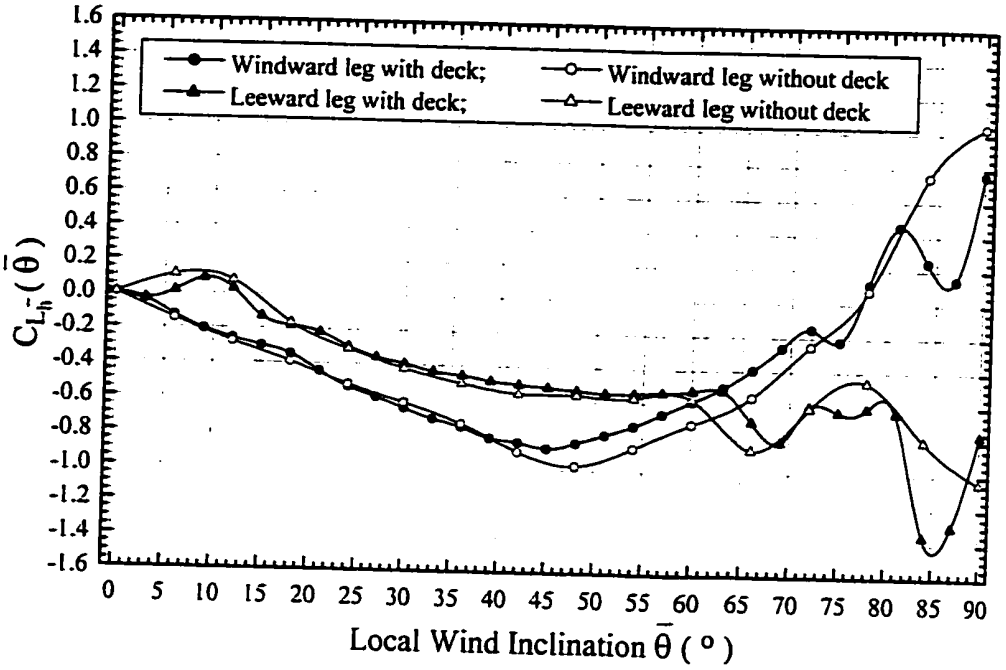

Figure 8-18 Lift Coefficients of Lower Segment of Tower Leg

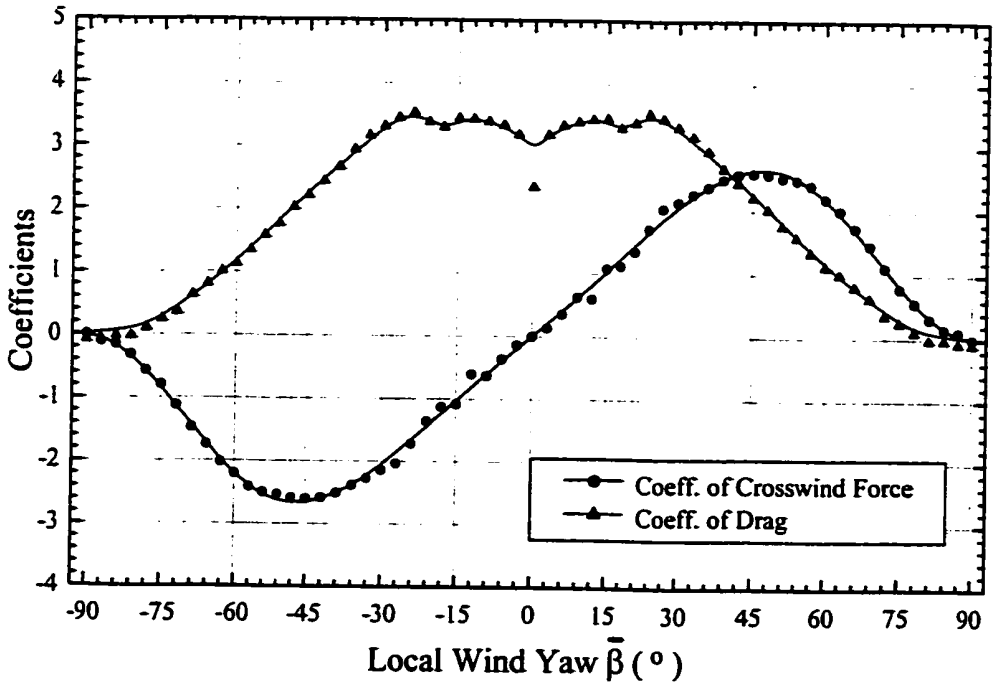

Figure 8-19 Coefficients of Drag and Crosswind Force of Lower Transverse Beam

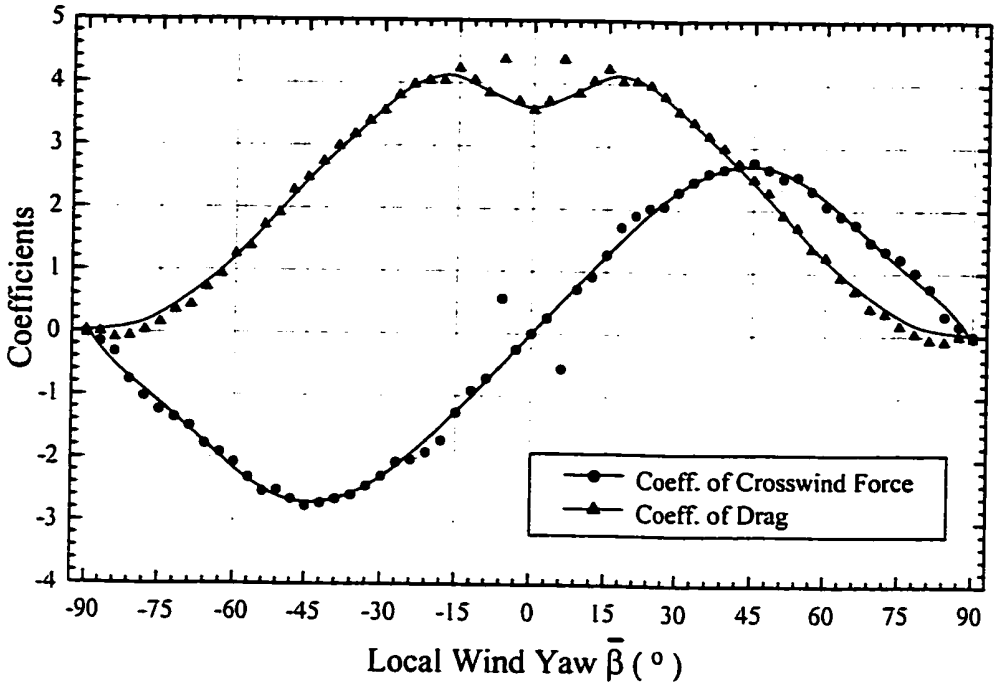

Figure 8-20 Coefficients of Drag and Crosswind Force of Lower-middle Transverse Beam

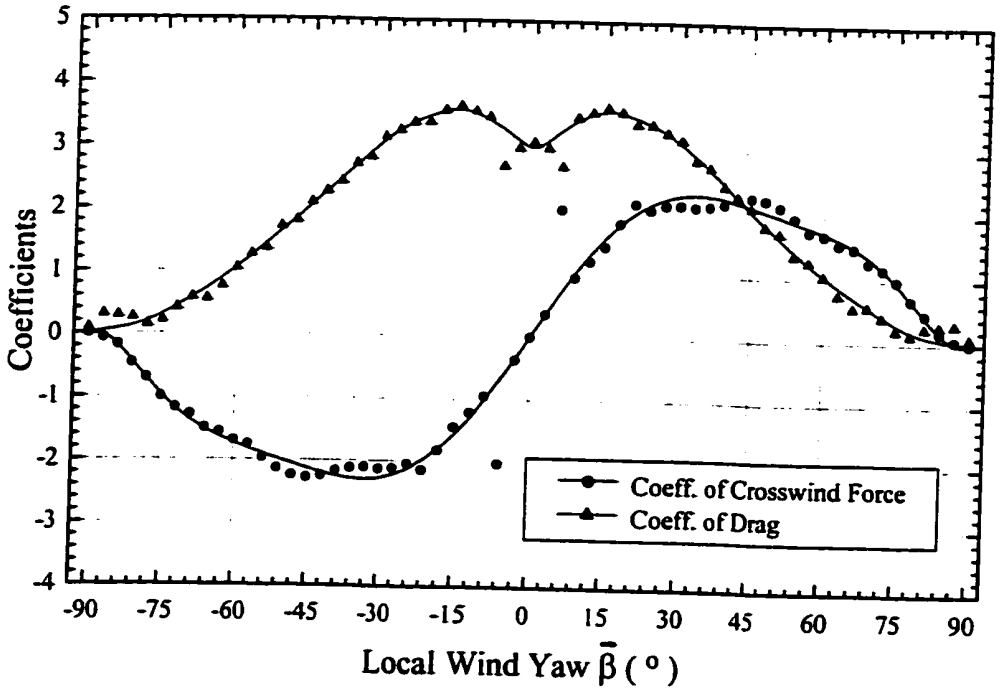

Figure 8-21 Coefficients of Drag and Crosswind Force of Upper-middle Transverse Beam

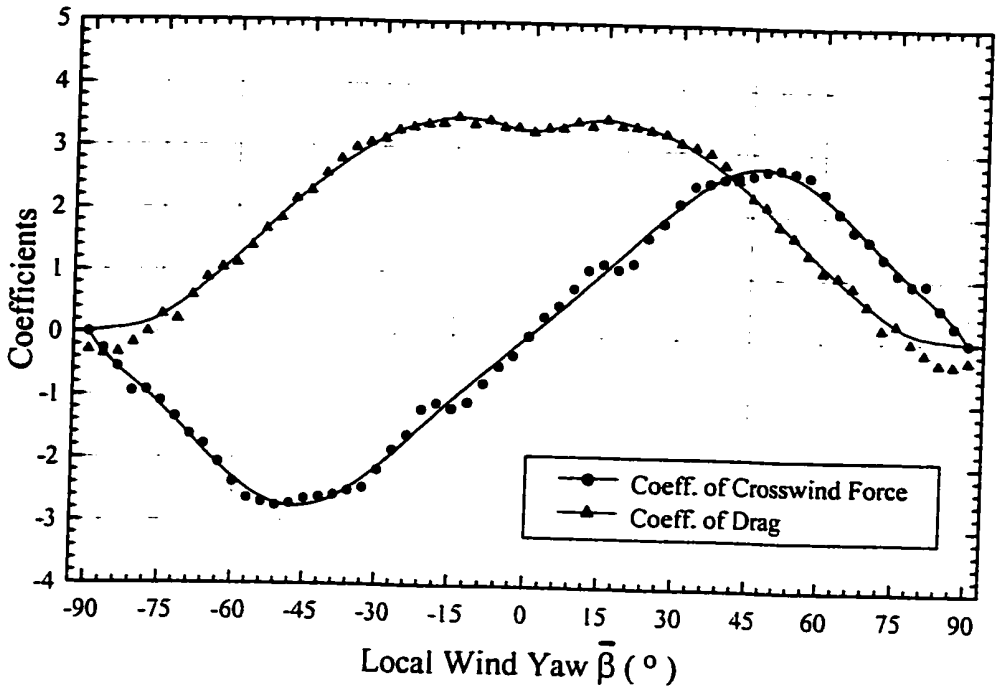

Figure 8-22 Coefficients of Drag and Crosswind Force of Upper Transverse Beam

Chapter 9

COMPARISON BTWEEN COMPUTED AND MEASURED BUFFETING RESPONSES

9.1 INTRODUCTION

The wind characteristics of Typhoon Victor related to the buffeting response of the Tsing Ma suspension Bridge analysed in Chapter 3 reveal that strong winds seldom attack a long span bridge at a right angle to the bridge longitudinal axis. The modified method for buffeting analysis of long span cable supported bridges under skew winds has been thus proposed in Chapter 4. The implementation of the modified method to the computer program has been introduced in Chapter 5 with some empirical formulae discussed. Wind tunnel test techniques for measuring aerodynamic coefficients and flutter derivatives of oblique bridge deck model have been developed in Chapters 6 and 7, by which the aerodynamic coefficients and flutter derivatives of the typical oblique deck section of the Tsing Ma suspension Bridge under skew winds have been measured. In Chapter 8, the aerodynamic coefficients of tower components of the Tsing Ma suspension Bridge under skew winds have also been measured. Therefore, a comparison between the computed and field-measured buffeting responses of the Tsing Ma suspension Bridge can reasonably be made. The modified method for predicting the buffeting response of long span cable supported bridges can be verified to some extent.

Unfortunately, the yaw angles of incident wind during Typhoon Victor to the Tsing Ma Bridge were more than 38°, which are out of the measured range of aerodynamic coefficients and flutter derivatives of the bridge deck provided in Chapters 6 and 7. Therefore, another typhoon called Sam experienced by the Tsing Ma suspension Bridge in 1999 has to be selected. Wind structures and structural responses of the Tsing Ma Bridge during Typhoon Sam are first analyzed in this chapter using the method and computer software used in Chapter 3. The wind characteristics of Typhoon Sam are obtained from the wind velocity time histories recorded by the

WASHMS and include the mean wind speed, wind yaw angle, wind inclination, friction velocity, and turbulence spectra. The measured wind structures of Typhoon Sam, the aerodynamic coefficients and flutter derivatives of the Tsing Ma bridge deck measured from the wind tunnel under skew winds, the aerodynamic coefficients of the Tsing Ma bridge tower measured from the wind tunnel under yaw winds, and other relevant information are then taken as input data to the computer program to compute the buffeting response of the Tsing Ma Bridge. The modal damping ratios used in the computation for the Tsing Ma Bridge are identified from the measured bridge response time histories during Typhoon Sam using the Hilbert-Huang method in conjunction with the random decrease technique in the frequency-time domain. Finally, the computed buffeting responses of the Tsing Ma Bridge are compared with the measured buffeting responses.

9.2 FIELD MEASUREMENT OF TSING MA BRIDGE DURING TYPHOON SAM

9.2.1 Typhoon Sam

After developed at about 680 km east-northeast of Manila on 19 August 1999, the tropical depression Sam moved west-northwestwards over the Pacific and intensified into a tropical storm that night. Sweeping across the northern part of Luzon on the next day, Sam then entered the South China Sea and intensified into a severe tropical storm on 21 August. It then moved north-west towards the coast of Guangdong Province, China and became a typhoon on late morning of 22 August near Hong Kong. Typhoon Sam finally made landfall over the eastern part of Sai Kung in Hong Kong at around 6 p.m. on 22 August. Following landfall, Sam traversed the northeastern part of the New Territories at a speed of about 25 km/h and crossed into Shenzhen, and then weakened gradually over inland Guangdong on 23 August, 1999 (Hong Kong Observatory, 2000). The moving track of Typhoon Sam is plotted in Fig. 9-1. The Hong Kong Observatory recorded a maximum hourly-mean wind speed of about 27m/s and a maximum gust wind speed of about 41m/s at 75m height at Waglan Island during the passage of Typhoon Sam. The lowest instantaneous pressure at mean sea level was recorded as 979.0hPa.

9.2.2 Wind Characteristics

The detailed information on the WASHMS has been given in Chapter 3. The locations of the anemometers can be found in Figures 3-2 and 3-3. The sampling frequency for wind velocity was 2.56Hz and the cut-off frequency was 1.28Hz. After a careful examination of all the measured wind velocity time histories, one-hour record of wind velocity between 14:11 to 15:11 on 22 Aug. 1999 was selected for the analysis. During this period, incident wind blew onto the Tsing Ma Bridge from the direction near to the north. Therefore, the wind data recorded by the anemometers at the south side of the bridge deck were contaminated by the bridge deck itself and were not suitable for the analysis of natural wind structures. Due to technical reason, the mechanical anemometers installed at the deck and the top of the towers failed to record the wind azimuth. As a result, wind characteristics of Typhoon Sam surrounding the bridge could be extracted only from the wind speed time histories recorded by the three-component ultrasonic anemometer WITJN01, as shown in Figure 9-2. The anemometer WITJN01 was installed on the north side of the bridge deck at the mid-span.

By analyzing the three components of the recorded wind velocity shown in Figure 9-2, it was found that the hourly-mean wind speed is about 17.1m/s and the mean wind blows from north-northeast. The global hourly-mean wind yaw angle β_0 and inclination θ_0 are, respectively, -29.15° and 2.25°. The time histories of fluctuating wind speeds $u(t)$, $v(t)$ and $w(t)$ in the longitudinal (along-wind), lateral, and upward directions are also extracted from the measured three components of wind velocity (see Figure 9-3). From the fluctuating wind speed time histories shown in Figure 9-3, it is found that the turbulence intensities are about 18.6%, 20.4% and 14.5%, for $u(t)$, $v(t)$ and $w(t)$, respectively, and the corresponding integral scales of turbulence are 228m, 116m, and 84m based on the Taylor's hypothesis (Simu and Scanlan, 1996). In the spectral analysis, the piecewise smoothing method and the hamming window are applied and the non-linear least square fitting approach are used to reduce the random error of spectral estimates. One-hour time history is divided into 11 sub-segments of 10-minute duration each with an overlapped length of 5 minutes between two neighboring segments. The 1536 data points in the 10-minute sub-segment are zero-padded to 2048 points to meet the requirement of Fast Fourier Transform (FFT). The frequency resolution in the wind spectral analysis is thus

0.00175Hz. Figure 9-4 shows the one-side normalized auto spectra of fluctuating wind speeds *u(t)*, *v(t)* and *w(t)*. The auto spectra are fitted using the non-linear least square method with the objective function expressed as Eq.(3-12) with c=5/3 and the friction velocity $u_* = 1.69$ m/s estimated from the measured horizontal shear stress (Tieleman and Mullins, 1980). The corresponding fitted parameters a, b, m and curves together with the von Karman spectra as Eqs.((2-73), (2-88) and (2-85), Kaimal spectra as Eqs.(2-78), (2-86) and (2-83), Simiu spectra as Eqs.(2-79) and (2-87), and Lumley spectrum as Eq.(2-82) are also displayed in Figure 9-4. It is seen that the spectra using Eq.(3-12) can fit the measured spectral data well in both low and high frequency regions. The von Karman spectra, using measured integral scales and intensities of turbulence, fit the measured spectral data better than Kaimal and Simiu spectra, especially in the low frequency region.

The co-spectra and quadrature spectra between every two of the three fluctuating wind speeds are also analyzed and plotted in Figures 9-5 and 9-6, respectively. The curve fitting of non-linear least square is also carried out for these cross spectra by taking Eq.(3-12) with c=2.4 and $u_* = 1.69$ m/s as the objective function. The fitted parameters and curves are also displayed in Figures 9-5 and 9-6. It can be seen that the above objective function is quite suitable for the co-spectra, but it seems not so good to the quadrature spectra. Furthermore, it is interesting to see from Figure 9-5b that the curve using the empirical formula of Eq.(2-98) suggested by Kaimal (Kaimal et al, 1972) for the co-spectrum C_{uw} is quite close to the fitted one.

9.2.3 Acceleration responses

Acceleration responses of the Tsing Ma Bridge during Typhoon Sam were also recorded by the WASHMS. The locations of the accelerometers can be referred to Figure 3-2. The sampling frequency of acceleration response was set as 25.6Hz and the cut-off frequency was 12.8 Hz. To be consistent with wind analysis, only the data recorded from 14:11 to 15:11 on 22 August, 1999 are analyzed and presented in this chapter. Figures 9-7 shows the time histories of lateral, vertical and torsional accelerations at the three deck sections in the main span (ATTJD, ATTID and ATTFD) and one deck section in the Ma Wan side span (ATTBD). Figure 9-8 shows the lateral and vertical acceleration responses at the four cable sections (ABTQC, ABTLC, ATTGC, and ABTCC) and the longitudinal acceleration response at

ATTGC. These time histories of acceleration responses are analyzed to obtain the measured RMS responses and response spectra. In the spectral analysis of acceleration response, the number of data point for the FFT and the overlapped length are selected as 8192 and 2.6 minutes, respectively. As a result, one-hour data are divided into 21 segments, which are then averaged and smoothed. Meanwhile, the hamming window is also applied, and thus the actual frequency resolution is 0.004375 Hz.

9.2.3.1 RMS Responses

The RMS acceleration responses at the four deck sections are calculated directly using the recorded one-hour time histories and are listed in Table 9-1. The maximum values are 0.014m/s^2, 0.074m/s^2 and 0.0024 rad/s^2, respectively, in the lateral, vertical and torsional directions. They all occur at the mid-main span (ATTJD) of the bridge.

Table 9-1 RMS Acceleration Responses of the Tsing Ma Bridge Deck (without any Filter)

Section	Lateral (m/s^2)	Vertical (m/s^2)	Torsional *13m (m/s^2)
ATTJD	0.014	0.074	0.032
ATTID	0.013	0.071	0.031
ATTFD	0.011	0.070	0.028
ATTBD	0.009	0.057	0.015

It is noted that when computing the buffeting response of the Tsing Ma Bridge in the frequency domain, a lower bound and an upper bound of frequency should be set. This depends on how many modes of vibration should be included in the computation and what is the valid frequency range for flutter derivatives measured from a wind tunnel. In this study, the upper bound of frequency used in the computation is 0.75 Hz, which is higher than the 45th natural frequency (0.7062 Hz) of the bridge. The lower bound of frequency used in the computation is set as 0.025Hz because the flutter derivatives measured from the wind tunnel are available only for the reduced velocity ($\overline{U}/fB$) lower than 18, namely, only for the frequency

higher than 0.0232Hz when the mean wind speed ($\overline{U}$) is 17.1m/s and the deck width (B) is 41m. Therefore, to have a reasonable comparison between computed and measured buffeting response, the measured response time histories should go through a digital bandpass filter with the same lower and upper bounds of frequency used in the computation. The RMS acceleration responses are then calculated using the filtered response time histories. The resulted RMS acceleration responses together with the reduction percentage (RP) are listed in Table 9-2. Furthermore, to evaluate the effects of the higher frequency components (>0.75Hz) and the lower frequency components (<0.025Hz) on the RMS response, the RMS acceleration responses are also calculated using the measured response time histories with lowpass filtering at a frequency of 0.75Hz. The corresponding results are given in Table 9-3.

Table 9-2 RMS Acceleration Responses of the Tsing Ma Bridge Deck (with Bandpass Filter)

Section	Lateral (m/s^2)		Vertical (m/s^2)		Tosional *13m (m/s^2)	
	RMS	RP (%)	RMS	RP (%)	RMS	RP (%)
ATTJD	0.012	14.3	0.073	1.4	0.029	9.4
ATTID	0.012	7.7	0.070	1.4	0.029	6.5
ATTFD	0.009	18.2	0.069	1.4	0.025	10.7
ATTBD	0.008	11.1	0.055	3.5	0.010	33.3

Table 9-3 RMS Acceleration Responses of the Tsing Ma Bridge Deck (with Lowpass Filter)

Section	Lateral (m/s^2)		Vertical (m/s^2)		Tosional *13m (m/s^2)	
	RMS	RP (%)	RMS	RP (%)	RMS	RP (%)
ATTJD	0.013	7.1	0.073	1.4	0.029	9.4
ATTID	0.013	0.0	0.070	1.4	0.029	6.5
ATTFD	0.010	9.1	0.069	1.4	0.025	10.7
ATTBD	0.008	11.1	0.055	3.5	0.010	33.3

It is seen from these tables that the reduction of the RMS responses of the vertical acceleration at the four deck sections owing to both the bandpass filter and lowpass filter is less than 3.5%. This means that the vertical responses are mainly contributed by the frequency components between 0.025Hz and 0.75Hz. The contribution of the higher frequency components to the lateral responses is less than 9.1% for the three deck sections (ATTJD, ATTID and ATTFD) in the main span and is 11.1% for the section ATTBD in the Ma Wan side span. The contribution of the lower frequency components to the lateral responses is also less than 9.1% for the three main span deck sections, but almost zero for the Ma Wan side span section. The reason why the lower frequency components have almost no effects on the acceleration response of the Ma Wan side span deck section is that the dominant natural frequencies associated with the Ma Wan side span are much higher than 0.025Hz and the dominate frequencies for the main span. The situation is reversed for the effects of higher frequency components.

As for the torsional acceleration responses, the lower frequency components have almost no effects. This is also because the natural torsional frequencies are much higher than 0.025Hz. The contribution of the higher frequency components to the torsional responses is from 6.5% to 10.7% for the three bridge sections in the man span and about 33.3% for the bridge section of the Ma Wan side span. Clearly, the higher frequency components play a significant role on the torsional acceleration response of the bridge deck in the Ma Wan side span. This is because the dominant torsional frequencies of the Ma Wan side span are much higher than those of the main span owing to its relative shorter span length.

The RMS acceleration responses at the four cable sections are also calculated in a similar way as done for the bridge deck. The results are listed in Tables 9-4 to 9-6 for the cases without any filter, with a bandpass filter, and with a lowpass filter, respectively. It is found that the lower frequency components (<0.025Hz) have almost no effects on the vertical and longitudinal acceleration responses of cables, and only small effect (<7%) on the lateral acceleration response of cables. However, the higher frequency components (>0.75Hz) exert significant effects on the lateral acceleration responses of all the concerned cable sections and the vertical acceleration response of the cable section in the Tsing Yi span. For the main cables

in the main span and the Ma Wan side span, the higher frequency components have 5% to 10% contribution to the vertical and longitudinal acceleration responses.

Table 9-4 RMS Acceleration Responses of the Tsing Ma Bridge Cable (without any Filter)

Section	Lateral (m/s^2)	Vertical (m/s^2)	Longitudinal (m/s^2)
ABTQC	0.028	0.040	—
ABTLC	0.034	0.084	—
ATTGC	0.030	0.082	0.020
ABTCC	0.022	0.062	—

Table 9-5 RMS Acceleration Responses of the Tsing Ma Bridge Cable (with Bandpass Filter)

Section	Lateral (m/s^2)		Vertical (m/s^2)		Longitudinal (m/s^2)	
	RMS	RP (%)	RMS	RP (%)	RMS	RP (%)
ABTQC	0.019	32.1	0.016	60.0	—	—
ABTLC	0.022	35.3	0.079	6.0	—	—
ATTGC	0.024	20.0	0.077	6.1	0.019	5.0
ABTCC	0.014	36.4	0.056	9.7	—	—

Table 9-6 RMS Acceleration Responses of the Tsing Ma Bridge Cable (with Lowpass Filter)

Section	Lateral (m/s^2)		Vertical (m/s^2)		Longitudinal (m/s^2)	
	RMS	RP (%)	RMS	RP (%)	RMS	RP (%)
ABTQC	0.020	28.6	0.016	60.0	—	
ABTLC	0.022	29.0	0.079	6.0	—	
ATTGC	0.024	20.0	0.077	6.1	0.019	5.0
ABTCC	0.014	36.4	0.057	8.1	—	

9.2.3.2 Response spectra

Figures 9-9 to 9-12 show the spectra of acceleration response at the four deck sections while Figures 9-13 to 9-16 are the spectra of acceleration response at the four cable sections. In these figures, the thin lines represent the spectra obtained from the original response time histories without filtering whilst the thick lines represent the spectra gained from the time histories filtered with the bandpass filtering from 0.025Hz to 0.75Hz. It is seen from these figures that within the frequency range between 0.025Hz and 0.75 Hz, the spectral amplitudes of the two sets of response time histories almost overlap, indicating the effectiveness and reliability of the digital filter used. The spectra with the filtering will be used to compare with the computed spectra in the next section.

Table 9-7 Computed and Measured Lateral Natural Frequencies

No.	Computed Frequency (Hz)	Measured Frequency (Hz)	Deviation (%)	Damping ratio (%)
1	0.0681	0.0688	1.0	1.018
4	0.1578	0.1594	1.0	1.139
6	0.2104	0.2250	6.9	0.210
7	0.2305	0.2375	3.0	0.2*
8	0.2324	0.2438~0.2469	4.9~6.2	0.682
9	0.2401	0.2438~0.2469	1.5~2.8	0.827
12**	0.2851	0.2875	0.8	1.0*
16	0.3331	0.3500	5.1	1.0*
17	0.3404	0.3625	6.5	0.2*
18	0.3651	0.3875	6.1	0.396
19	0.3671	0.3625	-1.3	0.089
20	0.3800	0.3969	4.4	0.139
21	0.3933	0.4188	6.5	0.094
22	0.3960	0.4125	4.2	0.2*

Table 9-7 (cont.) Computed and Measured Lateral Natural Frequencies

23	0.4040	—	—	0.2*
26	0.4344	—	—	1.0*
30	0.4832	0.4906	1.5	0.2*
31	0.4892	0.4875	-0.3	1.0*
32	0.4964	0.5125	3.2	0.2*
34	0.5260	—	—	0.2*
36	0.5461	0.5500	0.7	0.180
37	0.5798	0.5906	1.9	0.2*
38	0.5943	0.5719	-3.8	0.249
42	0.6686	0.6812	1.9	1.0*
43	0.6698	—	—	0.2*
44	0.6954	0.7000	0.7	1.0*

* Modal damping ratio estimated based on the other vibration mode of similar nature
** Coupled with deck torsional motion

Since the buffeting response of a long span bridge significantly depends on its natural frequencies, the computed and measured natural frequencies should be compared with each other in order to have a good comparison of buffeting response. The finite element model of the Tsing Ma Bridge used in this study was established by Xu et al. (1997) and the computed first 45 natural frequencies are listed in Tables 9-7, 9-8, and 9-9 for the lateral, vertical, and torsional modes of vibration, respectively. Each natural frequency number in the three tables is assigned according to the sequence of computed vibration modes of the whole bridge. The nature of each mode of vibration, such as either cable dominated mode or deck dominated mode, can be found either in Xu et al. (1997) or from the corresponding mode shape figures in Appendix A. The natural frequencies identified from the measured response spectra are also listed in the three tables. The identified natural frequencies cover most of the computed natural frequencies but some of the computed natural frequencies cannot be identified from the measured response spectra.

Table 9-8 Computed and Measured Vertical Natural Frequencies

No.	Computed Frequency (Hz)	Measured Frequency (Hz)	Deviation (%)	Damping ratio (%)
2	0.1166	0.1156	-0.9	2.235
3	0.1367	0.1406	2.9	1.084
5	0.1890	0.1844	-2.4	1.041
10	0.2448	0.2406	-1.7	0.941
13	0.2945	0.2812	-4.5	0.613 (1.0*)
15	0.3246	0.3281	1.1	0.497 (1.0*)
24	0.4060	0.4062	0.0	1.0*
25	0.4334	—	—	0.1*
27	0.4358	—	—	0.1*
28	0.4431	—	—	0.5*
33	0.4991	0.4969	-0.4	0.514(1.0*)
39	0.5989	0.5906	-1.3	1.0*
41	0.6481	0.6438	-0.7	0.6(1.0*)
45	0.7062	0.7188	1.8	1.0*

* Modal damping ratio estimated based on the other vibration mode of similar nature

It is seen from Table 9-7 that the differences between the measured and computed natural frequencies in the lateral direction are less than 7.0%. For the modes of vibration (Nos. 1, 4, 12, 31 and 44) dominated by the lateral motion of bridge deck in the main span, the differences are even less than 1.0%. The good agreement of natural frequencies between the computation and measurement provides a good foundation for the comparison of bridge buffeting response. The good agreement of natural frequencies also indicates that the aeroelastic stiffness of bridge deck in the lateral vibration is very small. It is seen that the lowest computed natural frequency of the bridge is 0.068 Hz, corresponding to the first lateral mode of vibration. Both the measured response spectra and the computed modes of vibration reveal that the lateral mode of vibration of the bridge deck at 0.2875Hz (No.12) is coupled with the

deck torsional motion (see Figure 9-9a, c and 9-10a,c). Furthermore, there are four modes of vibration (No. 23, 26, 34 and 43) failed to be identified from the measured acceleration spectra. The reason may be either that the accelerometers were installed close to the stationary points of the modes of vibration or that the signals were contaminated due to very closely spaced modes of vibration.

The computed and measured natural frequencies associated with the vertical vibration of bridge deck and cables are presented in Table 9-8. The 13th and 41th natural frequencies correspond to the vertical motion of the Ma Wan side span. The other measured natural frequencies are associated with the vertical motion of the main span of the bridge. The difference between the measured and computed natural frequencies is also insignificant, indicating small aeroelastic stiffness in the vertical motion of the bridge deck. The computed results show that the 25th, 27th natural frequencies are related to the vertical motion of the free cables in the Tsing Yi side span, and 28th natural frequency is associated with the deck longitudinal motion. The measured acceleration spectra of both deck and cable show the responses of these three natural modes are rather small. It is thus unable to identify these three natural frequencies from the measured acceleration spectra.

Table 9-9 Computed and Measured Torsional Natural Frequencies

No.	Computed Frequency (Hz)	Measured Frequency (Hz)	Deviation (%)	Damping ratio (%)
11**	0.2713	0.2656	-2.1	0.439
14	0.3106	0.3219	3.6	0.478
29	0.4755	0.4844	1.9	0.5*
35	0.5392	0.5969	10.7	0.542
40	0.6162	0.6344	3.0	0.488

* Modal damping ratio estimated based on the other vibration mode of similar nature
** Coupled with deck lateral motion

As listed in Table 9-9, there are a total of five torsional modes of vibration identified from the measured acceleration spectra with the cutting frequency of 0.75 Hz. Among these five torsional modes of vibration, the 35th mode of vibration reflects the

torsional motion of the deck in the Ma Wan side span. All the other torsional modes of vibration represent the torsional motion of the bridge deck in the main span. Both the measured response spectra and the computed mode shapes indicate that the 11th torsional mode (0.2656Hz) is coupled with the deck lateral motion. It is seen again that the difference between the measured and computed natural frequencies is insignificant except for the side span mode of vibration.

9.2.3.3 Modal Damping Ratios

The Hilbert-Huang transform (HHT) method (Huang et al., 1998, 1999) in conjunction with the random decrement technique (RDT) are used to identify the modal damping ratios from the measured acceleration response time histories. Each measured acceleration response time history is first decomposed using the empirical mode decomposition (EMD) method into a series of intrinsic mode functions (IMF) with an intermittency check. The RDT is then applied to the IMF which represents a specified modal response of the bridge to obtain the corresponding free modal response, and the Hilbert transform (HT) method is applied to the free modal response time history to identify the total damping ratio of the associated mode. Finally, the structural modal damping ratio is obtained by deducting the corresponding aerodynamic damping ratio from the identified total damping ratio. The measured flutter derivative curves presented in Chapter 7 were used for the flutter derivatives of H_1^* and A_2^*, and the measured aerodynamic coefficient curves presented in Chapter 6 were used for determining the values of P_1^* using the quasi-steady formula presented in Chapter 5. The reduced velocities or the reduced frequencies were determined using the wind speed simultaneously recorded during Typhoon Sam and the corresponding identified modal frequencies under wind. The measured wind yaw angle and inclination were also employed when determining the flutter derivatives and aerodynamic coefficients. The aerodynamic damping of cable vibration was also estimated based on the quasi-steady formula of H_1^* and P_1^* and the empirical formulae for aerodynamic coefficients of cables presented in Chapter 5. Nevertheless, the aerodynamic coupling effect on aerodynamic damping was neglected. The identified modal damping ratios are presented in Tables 9-7 to 9-9.

In general, the modal damping ratios associated with cable vibration are significantly lower than those related to deck vibration. For instance, the measured modal damping ratio is about 1% for the 1st and 4th modes of vibration which are dominated by the deck lateral motion. It becomes less than 0.1% for the 19th and 21th modes of vibration which are the pure cable lateral motion in the Ma Wan side span and the Tsing Yi side span, respectively.

It is noticed that even for the modes of vibration dominated by the bridge deck motion in the vertical direction, the identified modal damping ratios are somehow different to some extent. The modal damping ratio in the 2nd mode of vibration reaches 2.235%, which is more than two times the modal damping ratio in the 3rd, 5th, and 10th modes of vibration. The modal damping ratios in the 13th, 15th, and 33th modes of vibration are even small. They are only half the modal damping ratio in the 3rd, 5th, and 10th modes of vibration.

Inevitably, the damping ratios in some vibration modes failed to be extracted from the measured response time histories. This may be because some modes of vibration are closely spaced or the accelerometer is located close to the stationary point of vibration modes or the signal is contaminated by the measurement noise of similar level. To meet the demand in the later analysis of buffeting response of the Tsing Ma Bridge using the modified method, the damping ratios of these modes are then estimated based on the identified damping ratios of the other modes of vibration of similar nature. These estimated modal damping ratios are also listed in Tables 9-7 to 9-9 and distinguished using a star as superscript.

It should be mentioned that the comparison between the computed and measured mode shapes of the bridge cannot be made since the valid measurement points during Typhoon Sam are too small. Nevertheless, the computed mode shapes were verified by Xu et al. (1997) using the ambient vibration test technique.

9.3 COMPARISON BETWEEN COMPUTED AND MEASURED BUFFETING RESPONSES

9.3.1 Input Data

To perform a comparison between the measured and computed buffeting responses of the Tsing Ma Bridge, the computer program implementing the modified method as introduced in Chapters 4 and 5 is used in this section to computer the buffeting response of the Tsing Ma Bridge under skew wind during Typhoon Sam between 14:11 to 15:11 on 22 August, 1999. The information and data input into the computer program are presented here.

The detailed information on the three-dimensional finite element model of the Tsing Ma Bridge can be found in Xu et al. (1997). The first 45 computed natural frequencies listed in Tables 9-7 to 9-9 and the first 45 modes of vibration of the bridge, as shown in Appendix A, are included in the buffeting analysis. Most of the modal damping ratios identified from the measured response time histories and listed in Tables 9-7 to 9-9 are used, but for the 13th, 15th, 33th, and 41th vertical modes of vibration, the identified damping ratios are not used because they are too small compared with the other modes of vibration of similar nature. The modal damping ratio of 1.0% is assigned to these four vertical modes of vibration.

The measured mean wind speed of 17.1m/s at the elevation of 75.314m (the mid-manspan) with the global yaw angle of -29.15° and the global inclination of 2.25° are used as input wind parameters. Because of the limitation of measurement system, the mean wind speed and direction are considered to be uniform along the bridge deck in the computation. According to the Code of Practice on Wind Effect, Hong Kong (1983) and the wind characteristics during Typhoon Victor (see Chapter 3), the power low with the exponent of 0.33 was adopted to describe the mean wind profile. The cross spectra of the wind turbulence components at two spatial points (P_1 and P_2) used in the analysis are determined by Eqs.(5-26) and (5-27) and Eqs.(5-29) to (5-32). The auto-spectra (S_u, S_v and S_w), the co-spectra (C_{uv}, C_{uw} and C_{vw}) and the quadrature spectra (Q_{uv}, Q_{uw} and Q_{vw}) of three fluctuating wind speed components at a spatial point are taken as the fitted curves using Eq.(3-12) to the

measured spectra, as shown in Figures 9-4 to 9-6. The friction velocity u_* is estimated as 1.69m/s from the measured horizontal shear stress (Tieleman and Mullins, 1980). The exponential decay coefficients for the determination of the root-coherence functions ($e^{-\tilde{f}_{uu}}$, $e^{-\tilde{f}_{vv}}$ and $e^{-\tilde{f}_{ww}}$) cannot be estimated from the field measurement and are taken as $C^u_{X_u}=3.0$, $C^v_{X_u}=3.0$, $C^w_{X_u}=3.0$, $C^u_{Y_v}=16.0$, $C^v_{Y_v}=11.0$, $C^w_{Y_v}=8.0$, $C^u_{Z_w}=10.0$, $C^v_{Z_w}=7.0$, $C^w_{Z_w}=7.0$ as suggested in Simiu and Scanlan (1996) and Dyrbye and Hansen (1997). The phase spectra φ_{uu}, φ_{vv} and φ_{ww} are also not available at this stage and thus they are regarded as zero.

The aerodynamic coefficients of the bridge deck, tower legs, and tower transverse beams measured from the wind tunnel under skew wind condition and presented in Chapter 6 and Chapter 8 are used in the buffeting analysis. As for the coefficients of drag and crosswind forces of the main cables with respect to the local wind coordinate system $\overline{qph}$ under skew winds, the approximate formulae as Eqs.(5-3a) and (5-3b) with the drag coefficient at zero yaw angle (C_{D0}) being 1.0 for the Tsing Ma bridge cables based on the traditional cosine rule are employed in this analysis. When the local wind yaw angle is zero, the crosswind forces on the circular cross section are zero. However, when the local wind yaw angle is not zero, the oblique section of the cable becomes elliptic. The lift and pitching moment may not be zero but they cannot be taken into account in the traditional cosine rule. The aerodynamic forces on the bridge hangers (suspenders) are also neglected because they are relatively small.

To include the effects of aeroelastic forces in the buffeting analysis, the 8 flutter derivatives of H_i^* and A_i^* (i=1,2,3,4) of the bridge deck measured under skew wind and presented in Chapter 7 are used in the computation. The flutter derivatives of P_1^*, P_3^*, P_5^*, H_5^* and A_5^* are not available from the wind tunnel tests and hence the formulae derived based on the quasi-steady theory as expressed with Eqs.(5-16a) to (5-16c) and Eqs.(5-16f) and (5-16i) were employed in the analysis. The remaining five flutter derivatives were considered insignificant to the bridge buffeting response and neglected in the computation.

Furthermore, there are no measurement data available on the aerodynamic admittance functions of the Tsing Ma Bridge. The empirical formulae and other measures have to be used. For the bridge tower components including tower legs and transverse beams, the aerodynamic admittance functions are set to unity. For the main cables, the formula suggested by Vickery (1966) for the aerodynamic admittance function of circular cylinder shown as Eq.(5-24) is used. For the bridge deck, the aerodynamic admittance function proposed by Davenport (1962) shown as Eq.(5-22) is employed for the 9 aerodynamic admittance functions associated with the drag, crosswind force, and yawing moment of the bridge deck ($\chi_{C_{\bar{q}}u}$, $\chi_{C_{\bar{q}}v}$, $\chi_{C_{\bar{q}}w}$, $\chi_{D_{\bar{p}}u}$, $\chi_{D_{\bar{p}}v}$, $\chi_{D_{\bar{p}}w}$, $\chi_{M_{\bar{\phi}}u}$, $\chi_{M_{\bar{\phi}}v}$ and $\chi_{M_{\bar{\phi}}w}$), where the decay coefficient of the turbulence coherence along the deck chord (c) is set to 7. The other 9 admittance functions associated with the lift, pitching moment, and rolling moment are set to unity. The sensitivity of the aerodynamic admittance functions on the buffeting response of the Tsing Ma Bridge will be discussed in Chapter 10.

To have a reasonable comparison of bridge buffeting response between the field measurement and computation, the wind speed used in the buffeting analysis should not be in the vicinity of the wind speed associated with either aeroelastic instability or vortex shedding. In fact, the critical wind speed U_{vs} of the Tsing Ma Bridge associated with aeroelastic instability is estimated to be higher than 50.0m/s for wind inclination between ±5° (Lau and Wong, 1997). This critical wind speed is much higher than the wind speed of 17.1 m/s concerned in this comparison. The critical wind speed of the bridge related to vortex shedding may be estimated using the following equation.

$$U_{vs} = N_s D / S_t \tag{9-1}$$

where S_t is the Strouhal number; D is the characteristic dimension of the body projected on a plane normal to the mean wind and it is 7.64m for the Tsing Ma bridge deck; N_s is the primary frequency of vortex shedding transversely to the direction of mean wind and $2N_s$ is the primary frequency of vortex shedding along the direction of mean wind (Simiu and Scanlan, 1996). For the Tsing Ma bridge deck, the Strouhal number S_t is 0.14 (Lau and Wong, 1997). The first two natural frequencies of the bridge deck are 0.0681Hz and 0.1578Hz for the lateral vibration, and 0.1166Hz and 0.1367Hz for the vertical vibration. The first torsional natural

frequency is 0.2713Hz. Therefore, the critical wind speeds of the bridge deck associated with the significant vortex induced vibration are 1.8 to 4.3m/s for the lateral vibration, 6.3m/s to 7.5m/s for the vertical vibration, and 14.8 m/s for the torsional vibration. It is interesting to find that the critical wind speeds of the bridge deck associated with vortex shedding within wind inclination of ±7.5°, estimated from wind tunnel test results (Lau and Wong, 1997), are lower than 6.9m/s to 9.4m/s for the vertical vibration and 12.2m/s to 13.8m/s for the torsional vibration. The measured critical wind speeds for vortex shedding oscillation are comparable to the estimated results.

For the bridge cables, S_t can be taken approximately as 0.2 (Xiang et al., 1996; Simiu and Scanlan, 1996). The diameter of the cable D is 1.1m. The associated natural frequencies are 0.2014Hz to 0.2448Hz for the lateral vibration, 0.1166Hz and 0.1367Hz for the vertical vibration. As a result, the estimated critical wind speeds for vortex-induced cable vibration are approximately 0.5m/s to 0.7m/s for the lateral vibration and 0.6m/s to 0.75m/s for the vertical vibration. Therefore, there is no significant vortex-induced cable vibration in the current prediction of the bridge buffeting response.

For the bridge tower legs, S_t can also be taken approximately as 0.2 (Xiang et al., 1996). The characteristic dimension D varies from 6m to 10m depending on wind yaw angle. In the first 45 modes of vibration concerned, the natural frequencies related to the tower lateral vibration range between 0.48Hz to 0.60Hz. The estimated critical wind speed for vortex-induced lateral vibration of the tower is lower than (0.6/2)×10.0/0.2=15m/s. Furthermore, within the first 45 modes of vibration, there is no any mode of vibration associated with significant tower longitudinal vibration. Thus, it can be inferred that the vortex-induced vibration of the Tsing Ma Bridge is insignificant when wind speed is 17.1m/s. The mean wind speed of 17.1m/s used in the comparison of buffeting response of the Tsing Ma Bridge is appropriate.

9.3.2 Computed Acceleration Responses and Comparison

9.3.2.1 Acceleration Responses of Bridge Deck

The computed acceleration response spectra of the bridge deck at the four sections are shown in Figures 9-17 to 9-19 together with the measured response spectra with a

bandpss filtering from 0.025 Hz to 0.75 Hz. From the lateral response spectra shown in Figure 9-17, one may see that the computed response spectra agree with the measured ones quite well for the sections ATTJD, ATTID, and ATTFD in the main span for the frequency components below 0.2 Hz. This may indicate that the Davenport's aerodynamic admittance function used for the lateral vibration of the bridge seems quite adequate. In the high frequency range, the computed response spectra deviate from the measured response spectra to some extent. There are many factors attributed to this moderate discrepancy. However, this moderate discrepancy may not significantly affect the RMS acceleration response because the spectral amplitude in the high frequency range is relatively small compared with that in the low frequency range. For the deck section ATTBD in the Ma Wan side span, the dominant frequency range of large spectral amplitude is relatively high compared with the deck sections in the main span. The discrepancy between the computed and measured acceleration response spectra is also relatively large. For instance, the dominant peaks of the measured spectrum occur within the frequency range from 0.5Hz to 0.6Hz where no significant peaks can be observed for the computed spectrum. On the contrary, there are there major peaks on the computed spectrum in the frequency range between 0.3Hz and 0.45Hz, but the measured response spectrum is small within this region. Thus, one may expect that the difference between the computed and measured RMS acceleration responses in the lateral direction will be large for the deck section in the Ma Wan side span.

From the vertical acceleration response spectra displayed in Figure 9-18, one may find that in the frequency range lower than 0.35Hz, the computed response spectra are in good agreement with the measured spectra for all the four bridge sections except for a small drift of some spectral peaks. In the high frequency range, the computed spectral amplitudes are larger than the measured ones. This may be attributed to the unit aerodynamic admittance function used in the computation. The unit aerodynamic admittance may be a good approximation for the lower frequency components but may overstate the lift force on the bridge deck in high frequency components. One may also infer that the first vertical model damping ratio of 2.235% identified from the measured response time history is reasonable, for the computed spectra in the vicinity of the first vertical natural frequency are very close to the measured ones. On the other hand, the identified modal damping ratios

(1.084%, 1.041% and 0.941%) in the second, third and fourth vertical modes of vibration may be slightly underestimated.

It is seen from Figure 9-19 that the computed torsional response spectra of the three bridge deck sections in the main span are in excellent agreement with the measured torsional response spectra. The computed torsional response spectrum of the bridge deck section in the Ma Wan side span is also in good agreement with the measured one for the frequency components below 0.4 Hz. The unit aerodynamic admittance function used in the analysis for the torsional vibration of the bridge deck may be regarded satisfactory for the Tsing Ma Bridge. The first torsional modal damping ratio about 0.5% identified from the measured response time history using the HHT method seems to be reasonable. The discrepancy between the computed and measured spectra of the bridge deck in Ma Wan side span may come mainly from the drift of the computed 35th natural frequency, the deviation of the aerodynamic admittance from unity in the high-frequency region, the small damping ratio, the possible difference between the actual and used wind properties at Ma Wan side span. In addition, the interference effect of bridge tower on the aerodynamics of the bridge deck may have some contribution to the discrepancy between the computed and measured responses of Ma Wan side span as well.

From the computed acceleration response spectra of the bridge deck, the RMS acceleration responses of the bridge deck can be obtained by the integration of the spectra in the frequency domain. The frequency range for the integration is from 0.025Hz to 0.75Hz in order to have a fair comparison. The computed RMS acceleration responses of the bridge deck are plotted in Figure 9-20 for the lateral, vertical, and torsional vibrations, respectively. The computed RMS acceleration responses of the bridge deck at the four measured sections are also listed in Table 9-10. The RMS acceleration responses measured at the four specified deck sections are also plotted in Figure 9-20 for the comparison. The measured RMS acceleration responses are directly obtained from the measured acceleration time histories rather than the integration of the power spectra but the bandpass filter is applied between 0.025Hz and 0.75Hz.

It is seen that for the main span, the computed RMS acceleration responses of the bridge deck in the lateral, vertical and torsional directions are all close to the

measured results. The relative differences (RD) are less than 34% for lateral response and less than 20% for vertical and torsional response. For the Ma Wan side span, the computed RMS acceleration responses in the lateral and vertical directions are also close to the measured ones. The relative differences are less than 30%. However, for the torsional vibration, the relative difference (RD) between the computed and measured RMS response is as high as 140%.

Table 9-10 Computed Bridge Deck RMS Acceleration Responses and Relative Differences (with Bandpass Filter)

Section	Lateral (m/s^2)		Vertical (m/s^2)		Torsional *13m (m/s^2)	
	Computed	RD (%)	Computed	RD (%)	Computed	RD (%)
ATTJD	0.014	16.7	0.085	16.4	0.025	-13.8
ATTID	0.010	-16.7	0.078	11.4	0.026	-10.3
ATTFD	0.012	33.3	0.077	11.6	0.025	0.0
ATTBD	0.006	-25.0	0.071	29.1	0.024	140.0

9.3.2.2 Acceleration Responses of Bridge Cables

The computed and measured acceleration response spectra of the main cable on the south side of the Tsing Ma Bridge are plotted in Figures 9-21 to 9-23 for the lateral, vertical and longitudinal directions, respectively. The measured response spectra are obtained using the filtered time-histories with the bandpass filtering between 0.025Hz and 0.75Hz. From the lateral response spectra of the main cable at the four specified sections shown in Figure 9-21, one may see that there is a fairly good agreement between the computed and measured spectra for the cable in the main span but there are some moderate discrepancies in the response spectra for the cable in the two side spans. The Vickery's aerodynamic admittance used in the analysis seems to be adequate for the drag and crosswind forces on the main span cable.

Similar to the bridge deck, one may seen from Figure 9-22 that the computed vertical acceleration response spectra of the main cable at the four sections agree well with the measured spectra in the frequency range below than 0.4Hz. In the higher frequency range, the computed spectral amplitude is generally higher than the

measured spectral amplitude. This may be because the unit aerodynamic admittance used in the vertical vibration overestimates the lift forces on the main cable in the higher frequency components. The longitudinal acceleration response of the main cable was measured only at the section ATTGC. It is seen from Figure 9-23 that also there is a good agreement between the computed and measured response spectra of the longitudinal acceleration of the main cable.

Table 9-11 Computed Cable RMS Acceleration Responses and Relative Differences (with Bandpass Filter)

Section	Lateral (m/s^2)		Vertical (m/s^2)		Longitudinal (m/s^2)	
	Computed	RD (%)	Computed	RD(%)	Computed	RD (%)
ABTQC	0.021	10.5	0.016	0.0	0.008	—
ABTLC	0.019	-13.6	0.081	2.5	0.019	—
ATTGC	0.019	-20.8	0.081	5.2	0.020	5.3
ABTCC	0.021	50.0	0.076	35.7	0.027	—

The comparison between the computed and measured RMS acceleration responses of the main cable is shown in Figure 9-24 for the lateral, vertical, and longitudinal vibration, respectively. The computed RMS acceleration responses of the main cable at the four sections are listed in Table 9-11 together with the relative differences from the measured results. A good agreement is seen between the computed and measured RMS acceleration responses for the vertical and longitudinal vibration of the cable in the main span and for the lateral and vertical vibration of the free cable in the Tsing Yi side span. The relative differences between the computed and measured RMS responses are less than 11%. For the lateral acceleration of the main span cable, the computed RMS acceleration responses also agree with the measured results with the differences less than 21%. However, for the cable section ABTCC in the Ma Wan side span, the differences between the computed and measured RMS responses are significant for both the lateral and vertical vibrations with the relative differences of 50.0% and 36.0%, respectively. This trend is consistent with the comparative results of the bridge deck.

9.4 SUMMARY

Wind structures and structural responses of the Tsing Ma Bridge during Typhoon Sam have been analyzed in this chapter. The measured wind structures of Typhoon Sam, the aerodynamic coefficients and flutter derivatives of the Tsing Ma bridge deck measured from the wind tunnel under skew winds, the aerodynamic coefficients of the Tsing Ma bridge tower measured from the wind tunnel under skew winds, and other relevant information have been taken as input data to the computer program to compute the buffeting response of the Tsing Ma Bridge using the modified method. The modal damping ratios used in the computation for the Tsing Ma Bridge were identified from the measured bridge response time histories using the Hilbert-Huang method in conjunction with the random decrement technique. The computed buffeting response of the Tsing Ma Bridge was compared with the measured buffeting response. The major comparative results are summarized as follows:

(1) The vertical acceleration response of the Tsing Ma bridge deck during Typhoon Sam was mainly controlled by the excitation frequency components ranging from 0.025Hz and 0.75Hz. The lower frequency components (<0.025Hz) were also no considerable effects on the torsional acceleration response of the bridge deck but the higher frequency components (>0.75Hz) exerted a remarkable influence on the torsional acceleration response of the bridge deck in the Ma Wan side span. The lower frequency components (<0.025Hz) had moderate effects on the lateral acceleration response of the bridge deck in the main span but less effects on the lateral acceleration response of the bridge deck in the Ma Wan side span. The situation was reversed for the effects of higher frequency components (>0.75Hz) on the lateral acceleration responses of the bridge deck in the main span and the side span.

(2) The lower frequency components (<0.025Hz) had almost no effects on the acceleration response of the main cables of the bridge. However, the higher frequency components (>0.75Hz) significantly affected the lateral acceleration response of the cables in the main span and the vertical acceleration response of the free cables in the Tsing Yi side span.

(3) The modified method and the associated computer program developed in this thesis were verified to some extent through the comparison between the measured and computed bridge buffeting responses. The differences between the computed and measured RMS responses were less than 34%, 17% and 14% for the lateral, vertical and torsional vibration, respectively, of the bridge deck in the main span. The differences of RMS acceleration response of the main span cables were not more than 21%, 6% and 6% for the lateral, vertical and longitudinal vibration, respectively.

(4) The considerable differences between the computed and measured responses mostly occurred in the Ma Wan side span with 25%, 30%, and 140% for the bridge deck in the lateral, vertical, and torsional direction, respectively, and with 50% and 36% for the bridge cable in the lateral and vertical direction, respectively. Such differences are attributed to many factors, among which the modal characteristics and the aerodynamic admittance functions are most important.

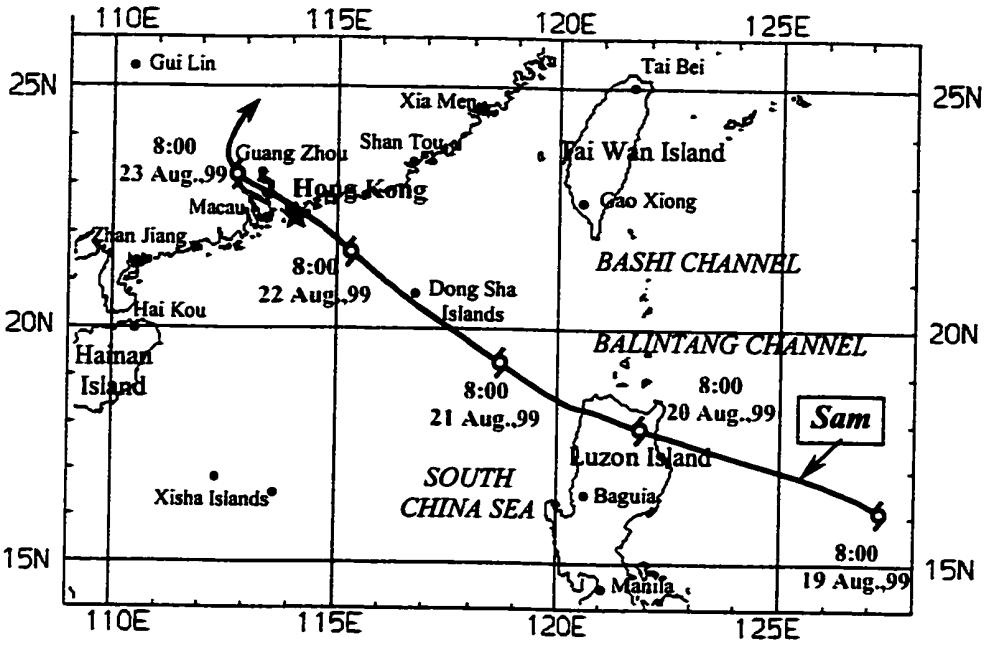

Figure 9-1 Moving Track of Typhoon Sam

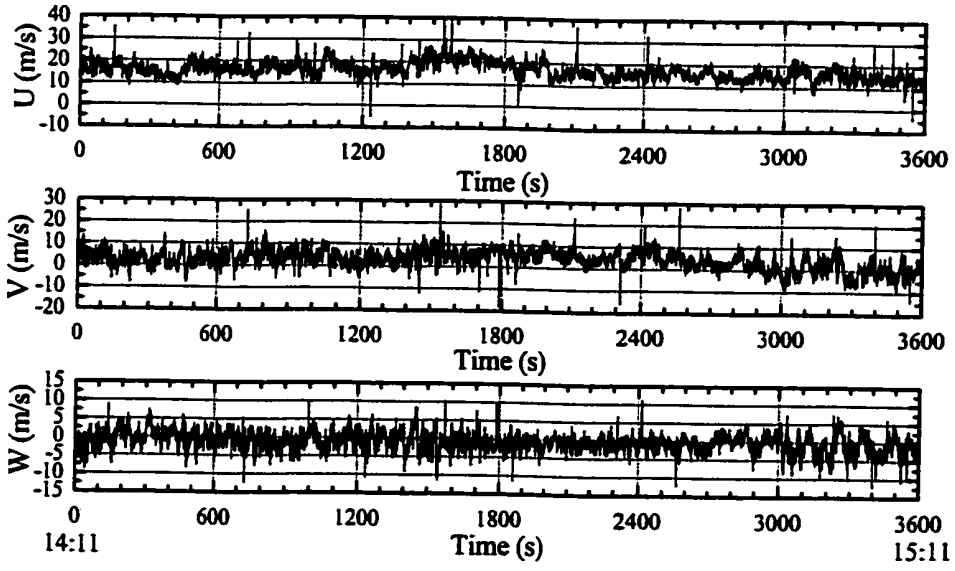

Figure 9-2 Three Components of Wind Velocity Recorded by Anemometer WITJN01

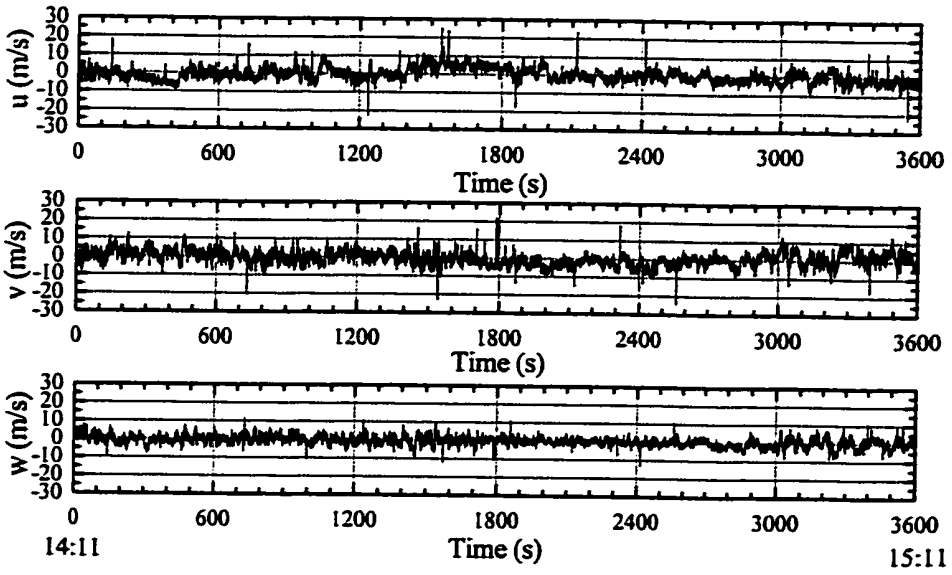

Figure 9-3 Three Components of Fluctuating Wind Velocity at Anemometer WITJN01

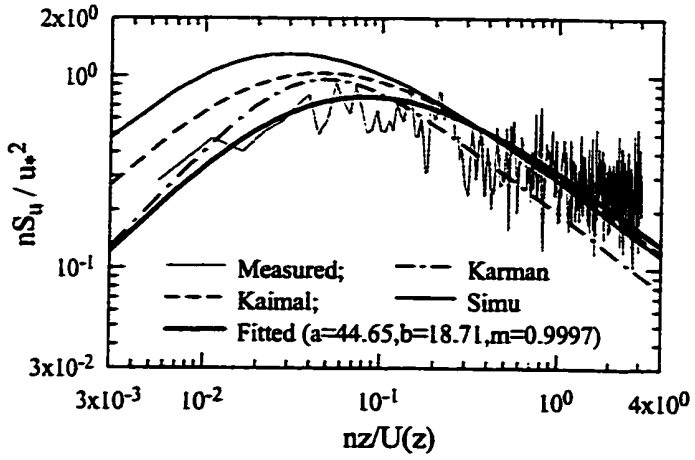

(a) Along-wind component u(t)

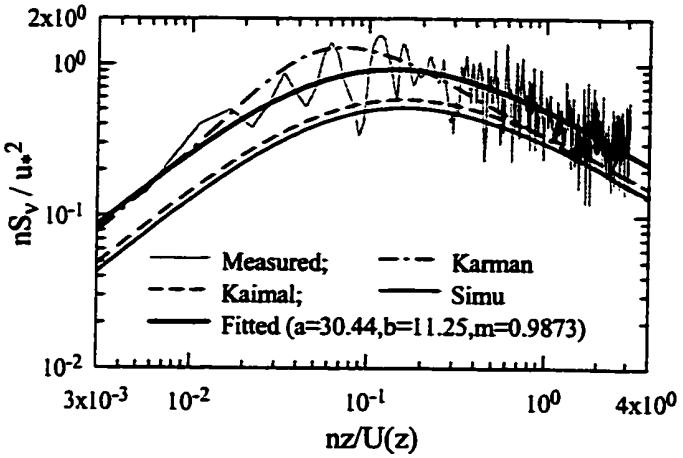

(b) Horizontal lateral component v(t)

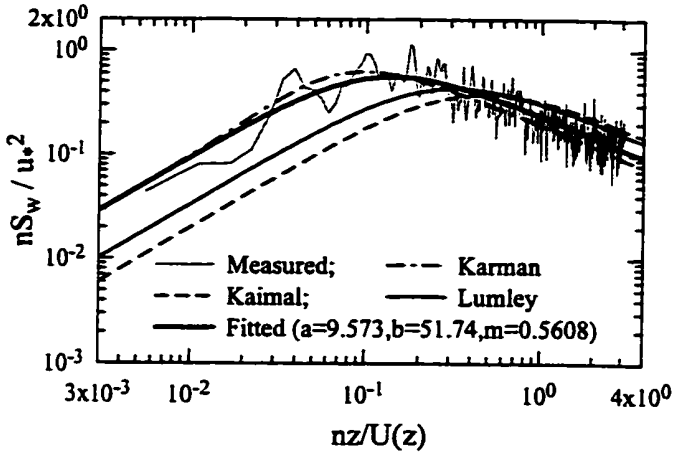

(c) Upward component w(t)

Figure 9-4 Auto Spectra of Fluctuating Wind Speeds

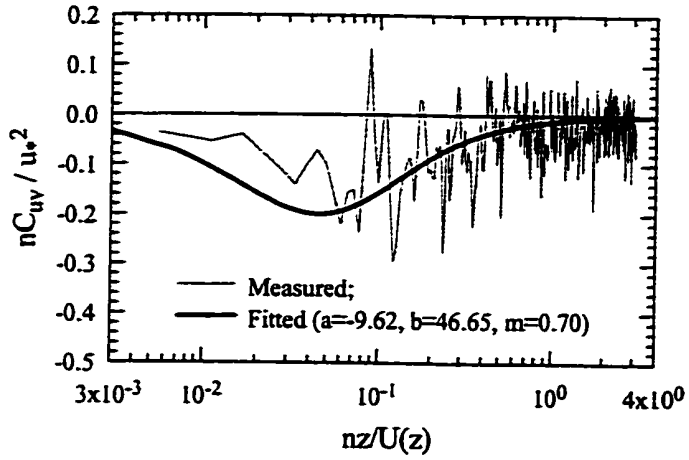

(a) Between along-wind and lateral components

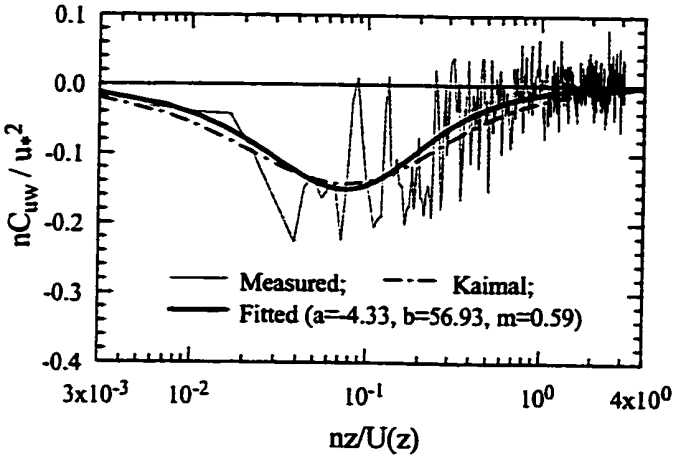

(b) Between along-wind and upward components

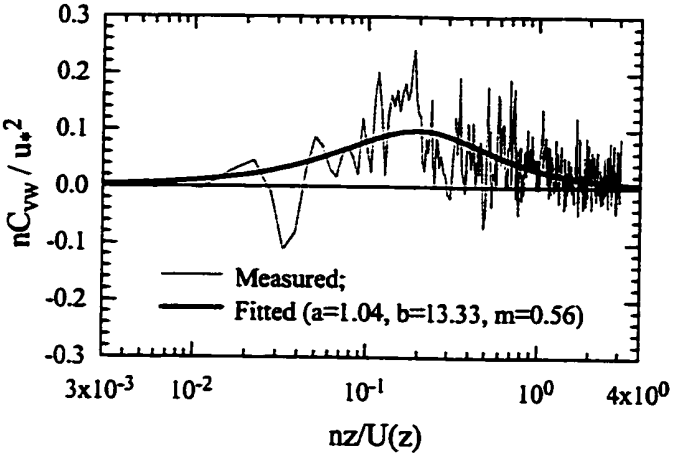

(c) Between lateral and upward components

Figure 9-5 Co-spectra of Fluctuating Wind Speeds

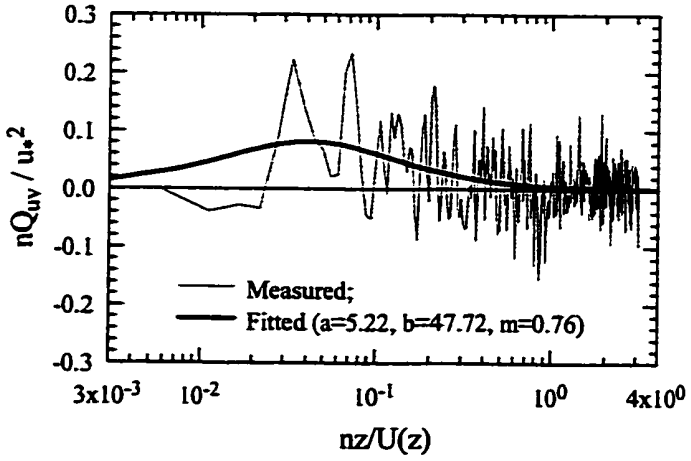

(a) Between along-wind and lateral components

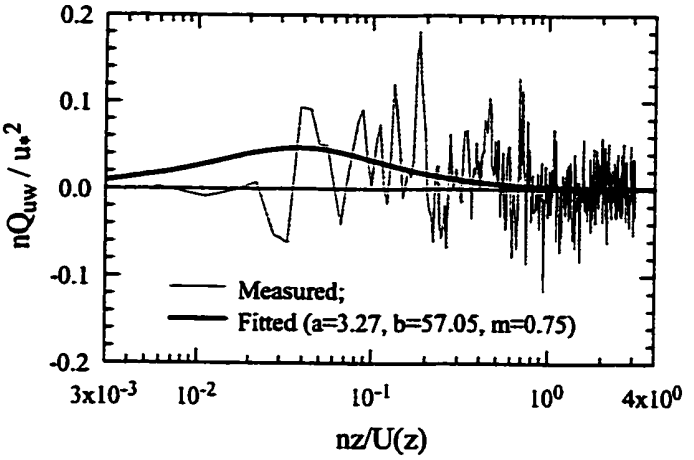

(b) Between along-wind and upward components

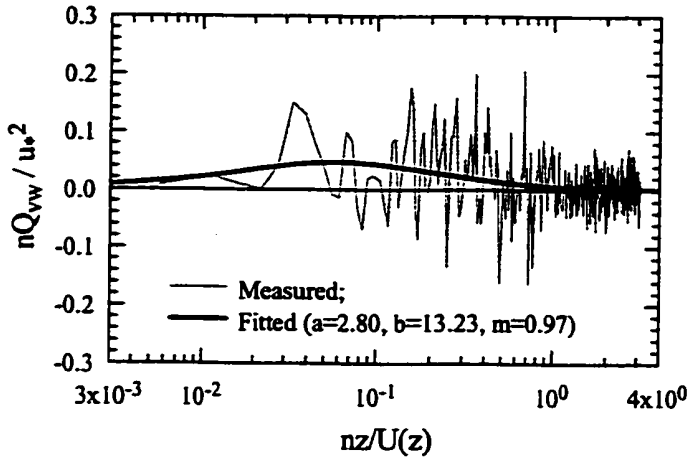

(c) Between lateral and upward components

Figure 9-6 Quadrature Spectra of Fluctuating Wind Speeds

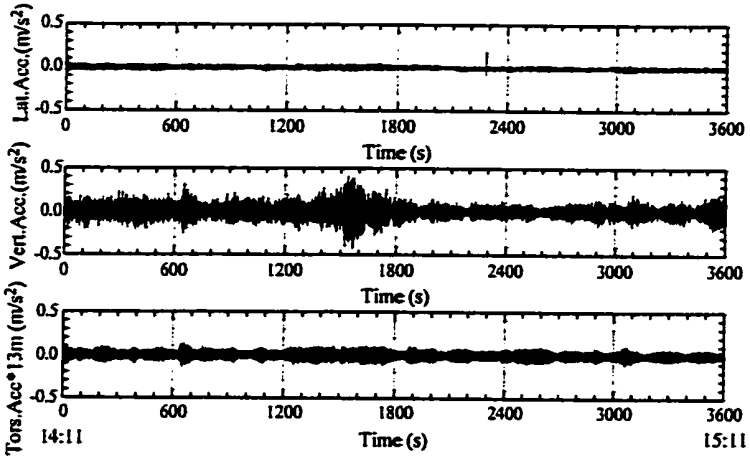

(a) Section ATTJD

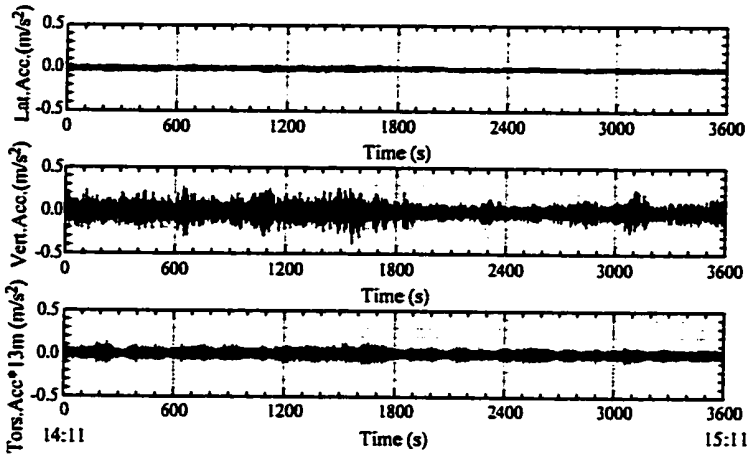

(b) Section ATTID

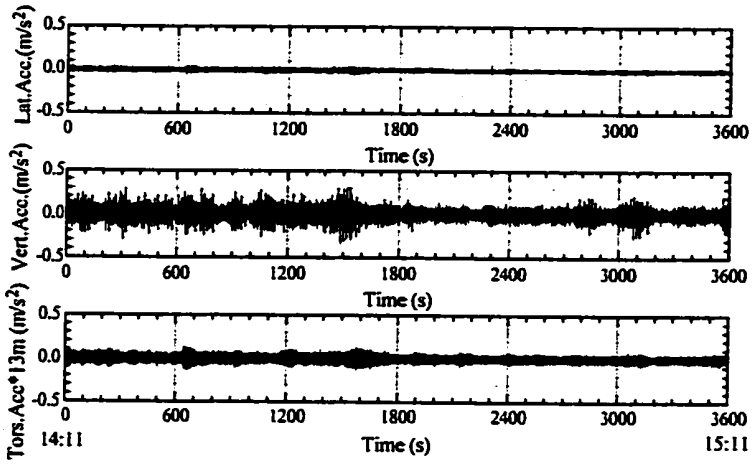

(c) Section ATTFD

Figure 9-7 Time Histories of Measured Deck Acceleration Responses to Typhoon Sam

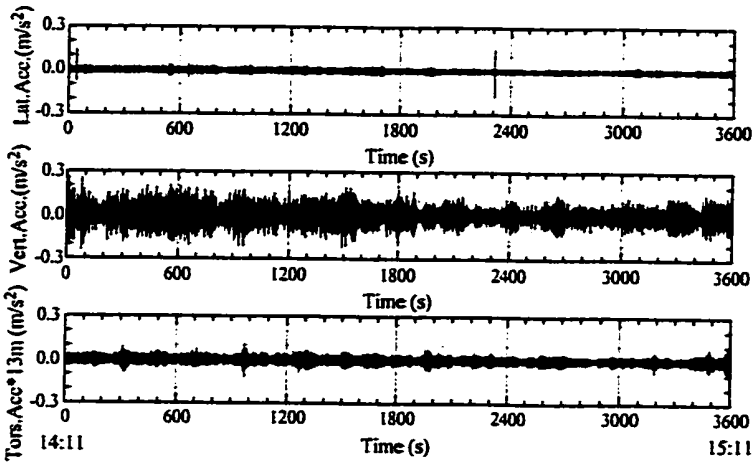

(d) Section ATTBD

Figure 9-7(cont.) Time Histories of Measured Deck Acceleration Responses to Typhoon Sam

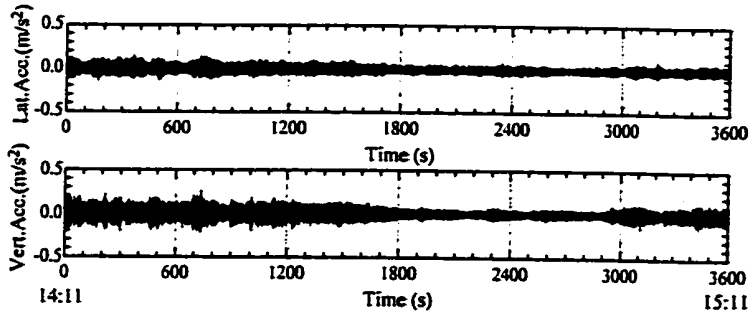

(a) Section ABTQC

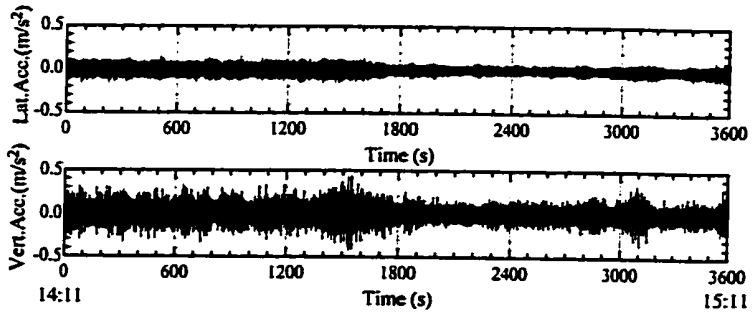

(b) Section ABTLC

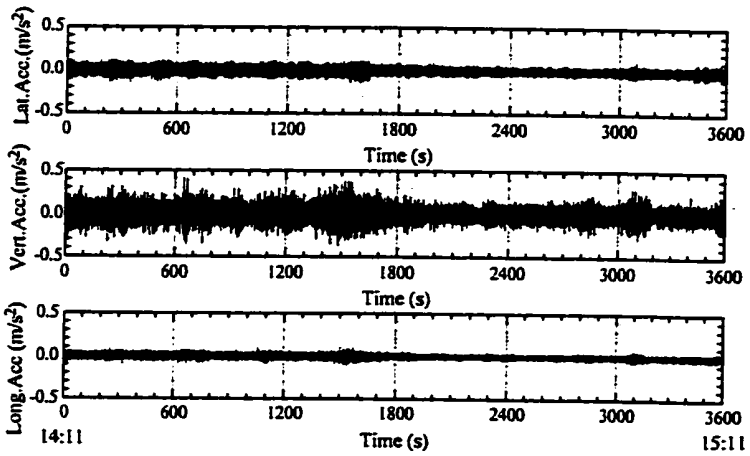

(c) Section ATTGC

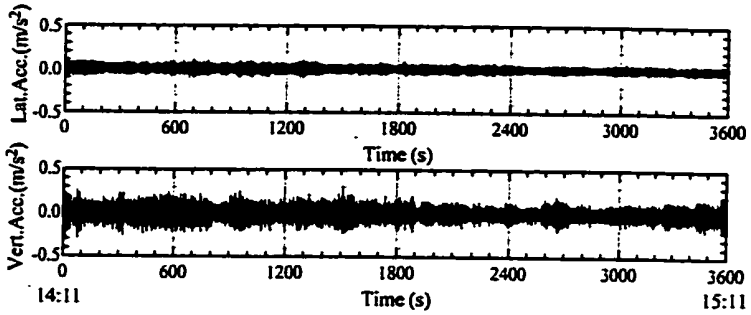

(d) Section ABTCC

Figure 9-8 Time Histories of Measured Cable Acceleration Responses to Typhoon Sam

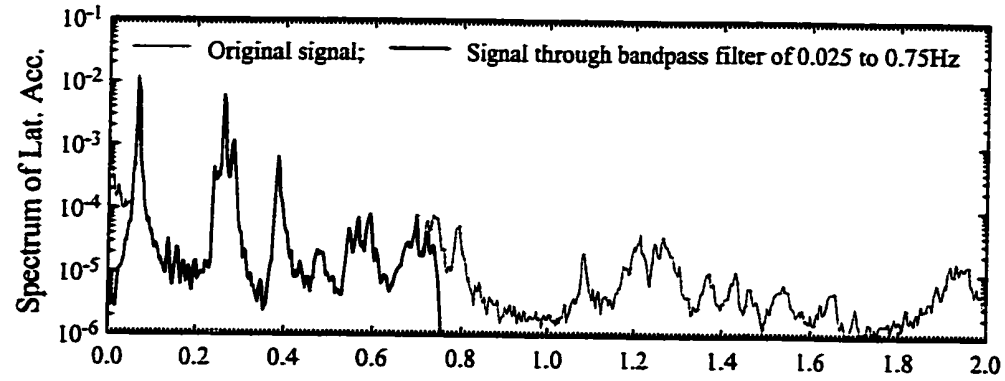

(a) Lateral

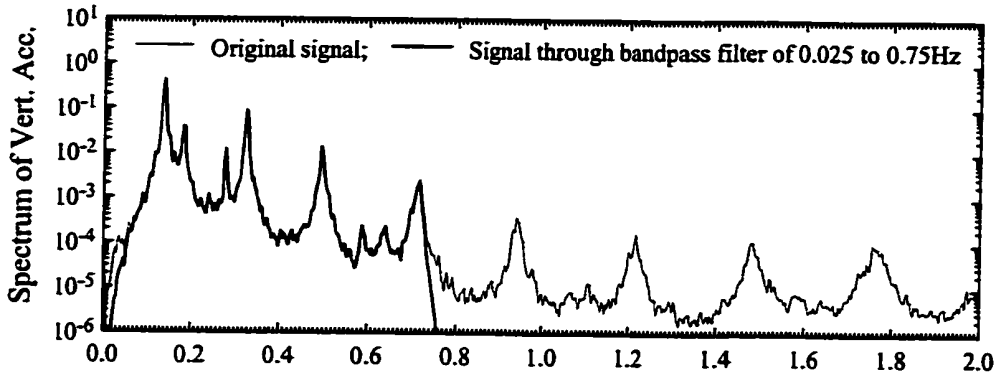

(b) Vertical

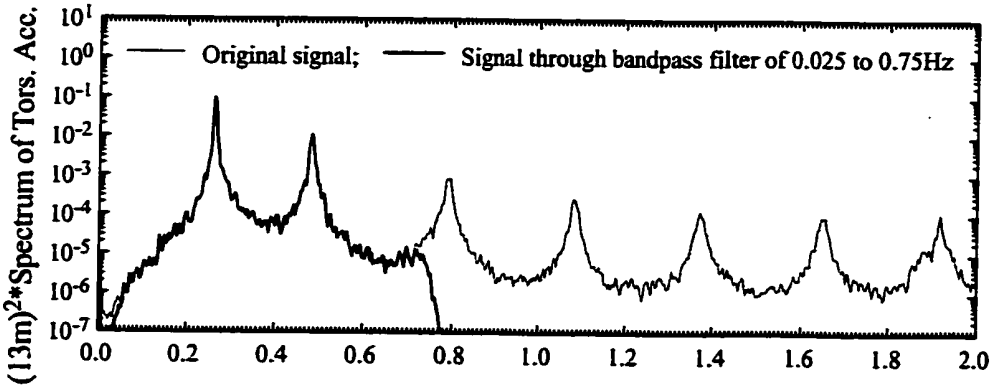

(c) Torsional

Figure 9-9 Measured Deck Acceleration Spectra at ATTJD

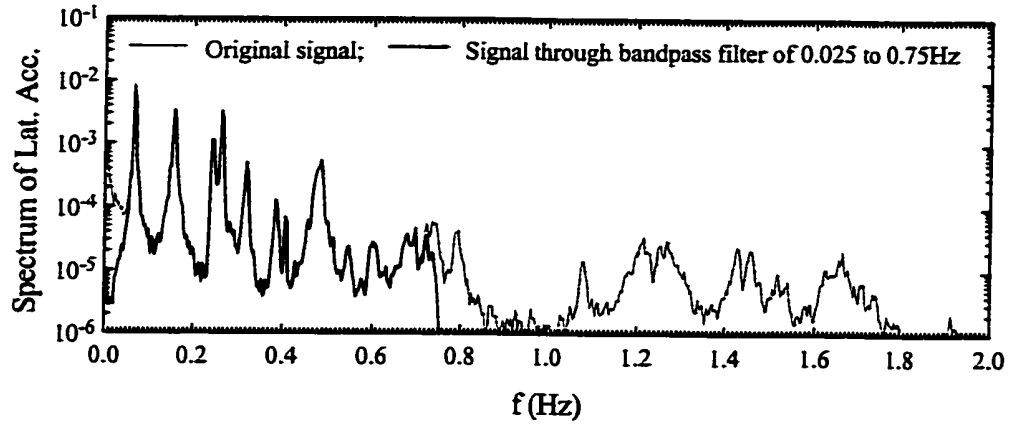

(a) Lateral

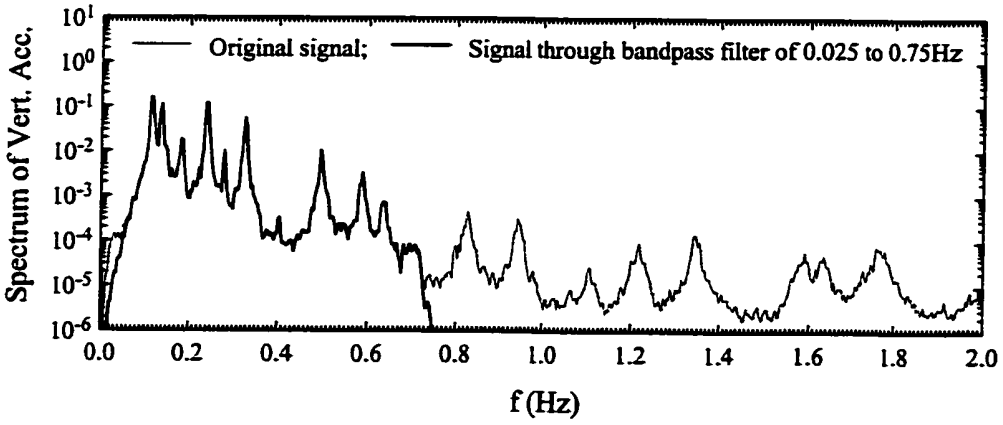

(b) Vertical

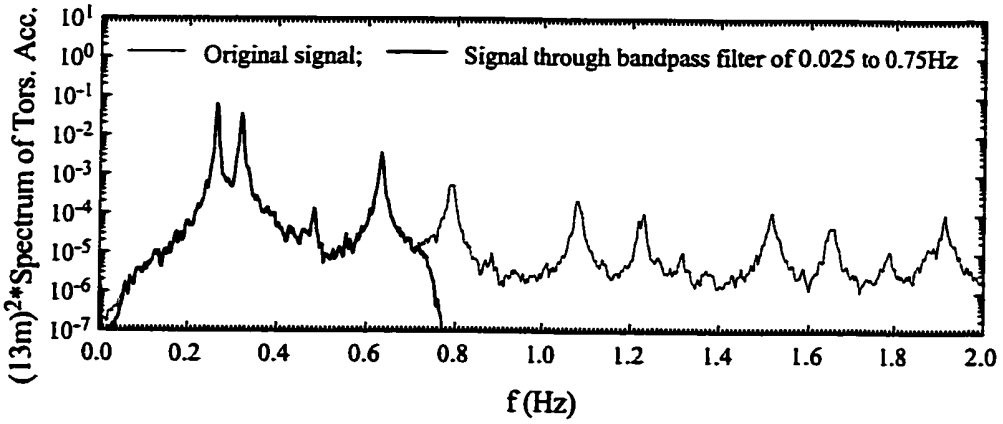

(c) Torsional

Figure 9-10 Measured Deck Acceleration Spectra at ATTID

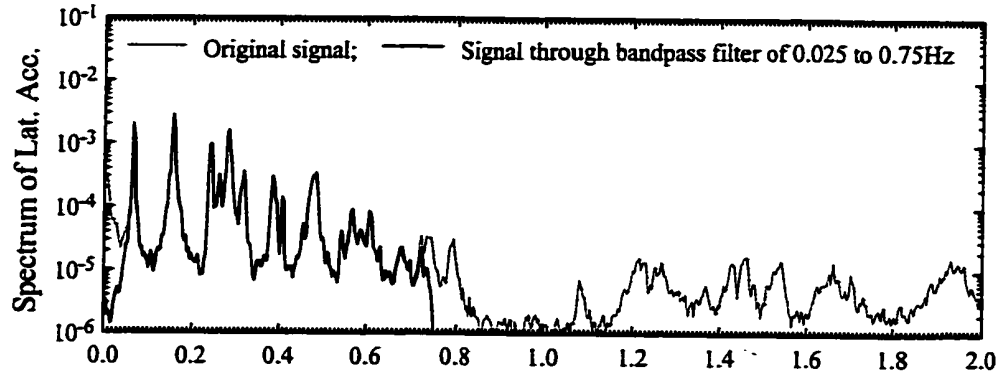

(a) Lateral

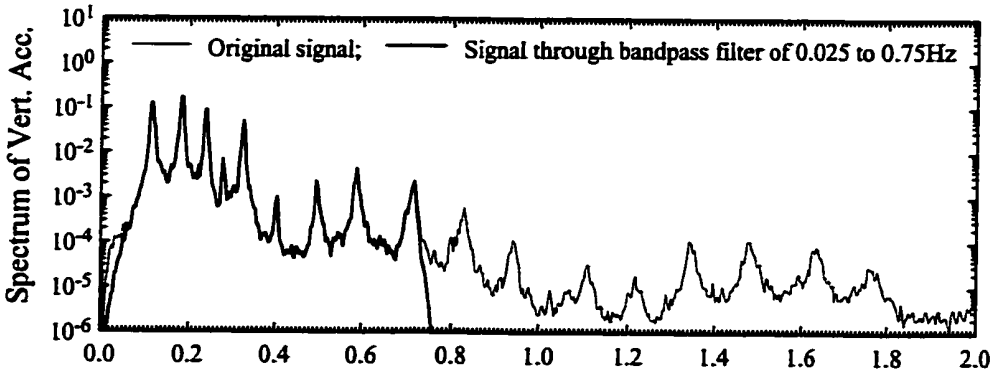

(b) Vertical

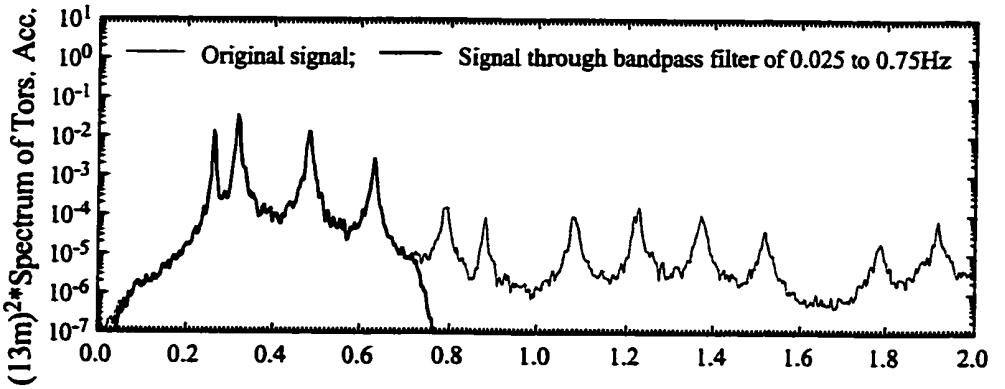

(c) Torsional

Figure 9-11 Measured Deck Acceleration Spectra at ATTFD

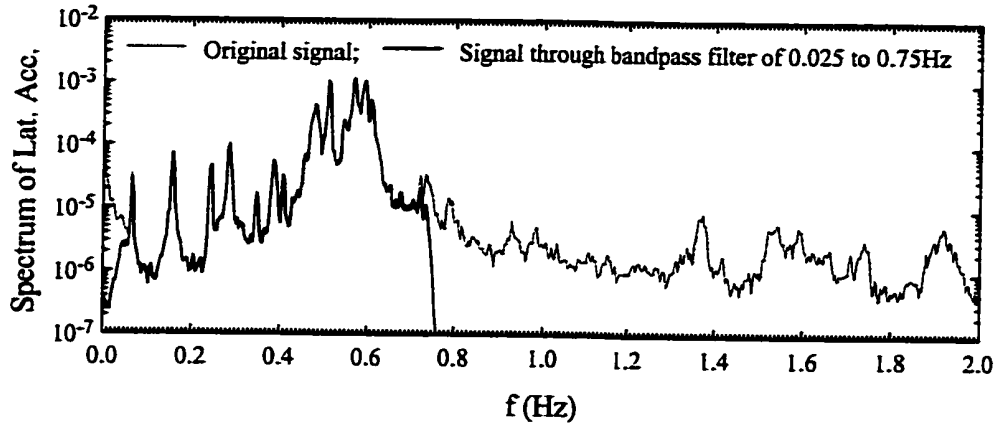

(a) Lateral

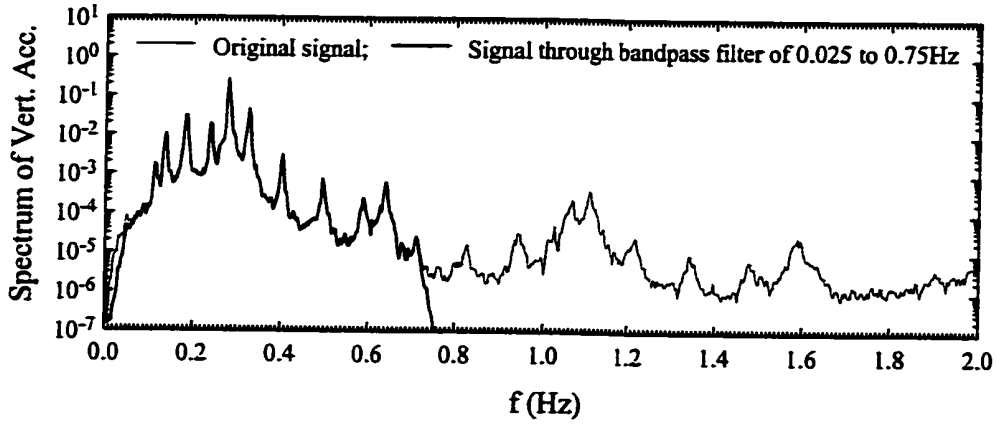

(b) Vertical

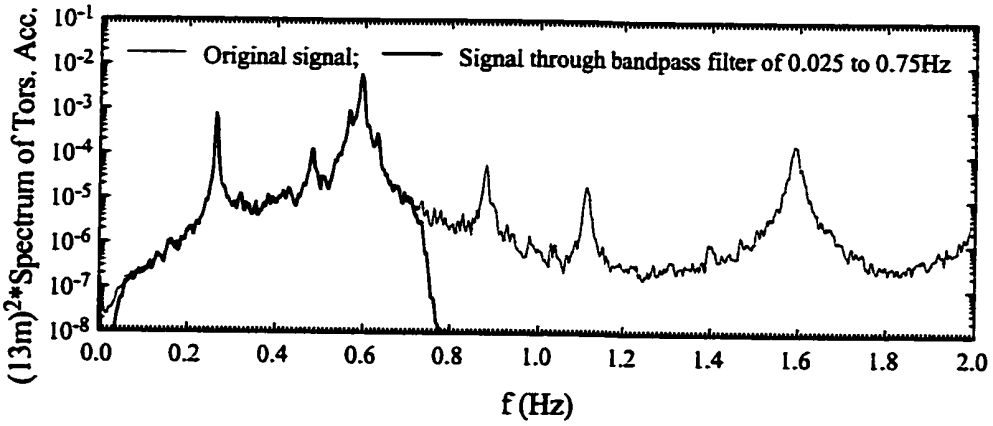

(c) Torsional

Figure 9-12 Measured Deck Acceleration Spectra at ATTBD

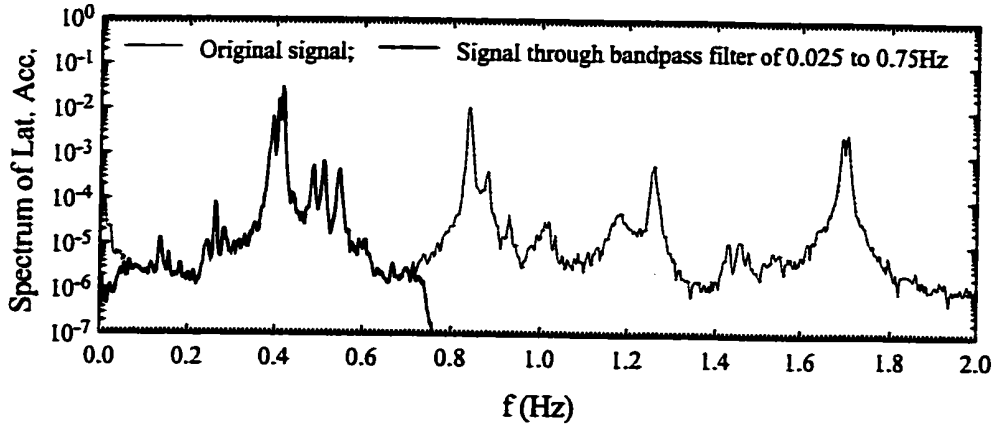

(a) Lateral

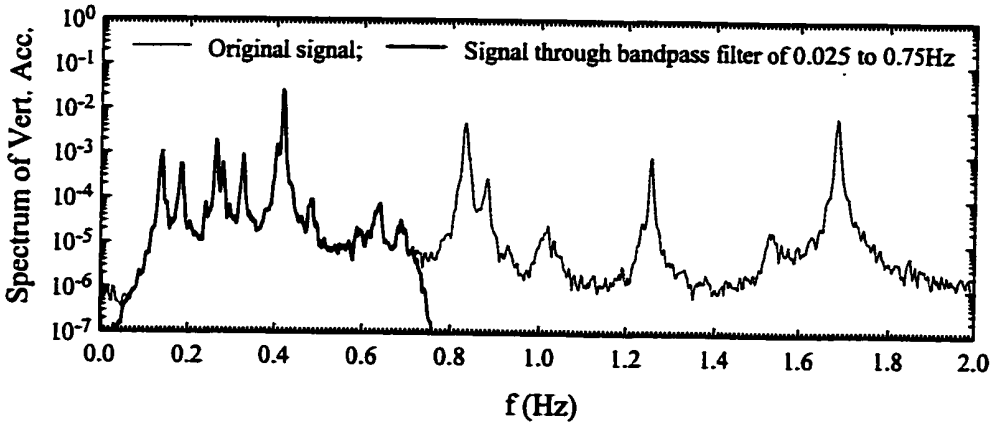

(b) Vertical

Figure 9-13 Measured Cable Acceleration Spectra at ABTQC

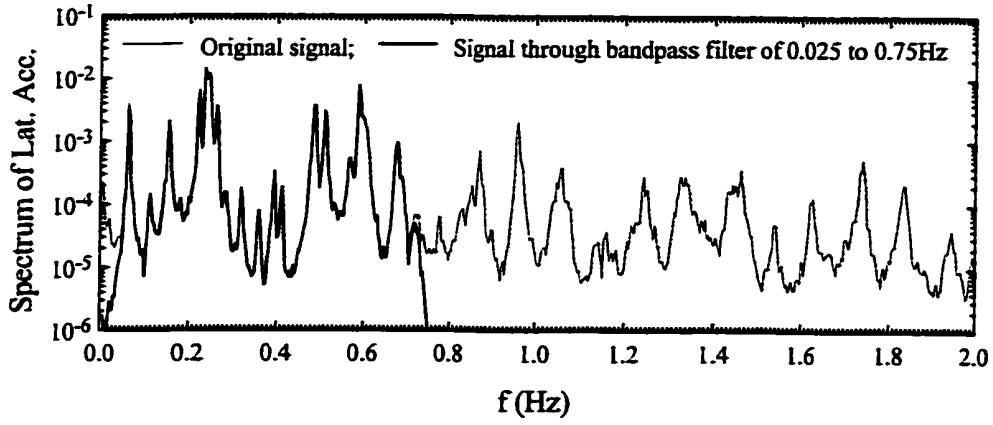

(a) Lateral

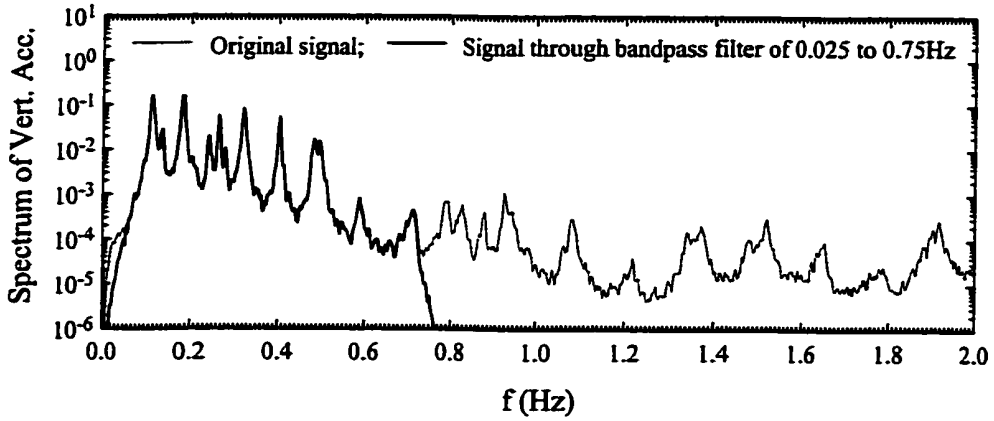

(b) Vertical

Figure 9-14 Measured Cable Acceleration Spectra at ABTLC

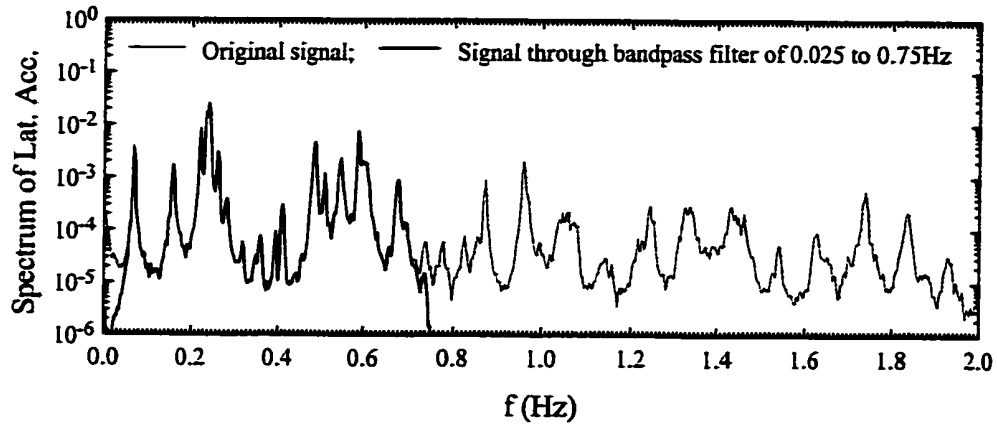

(a) Lateral

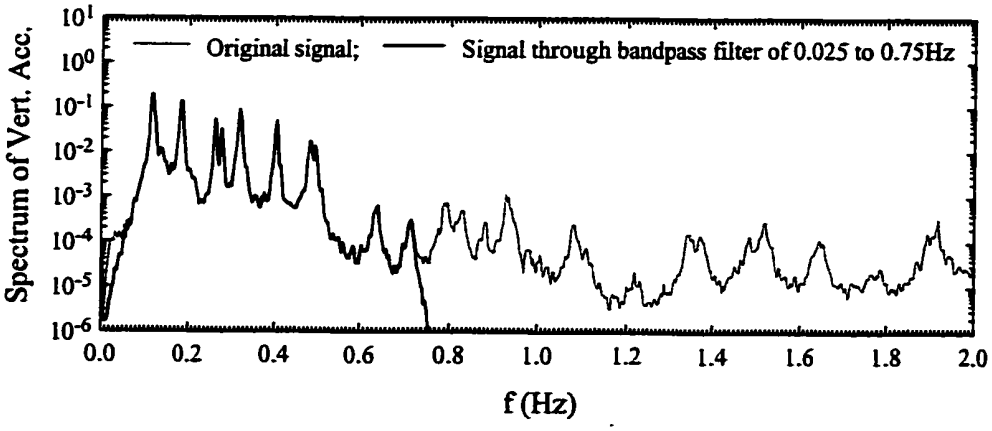

(b) Vertical

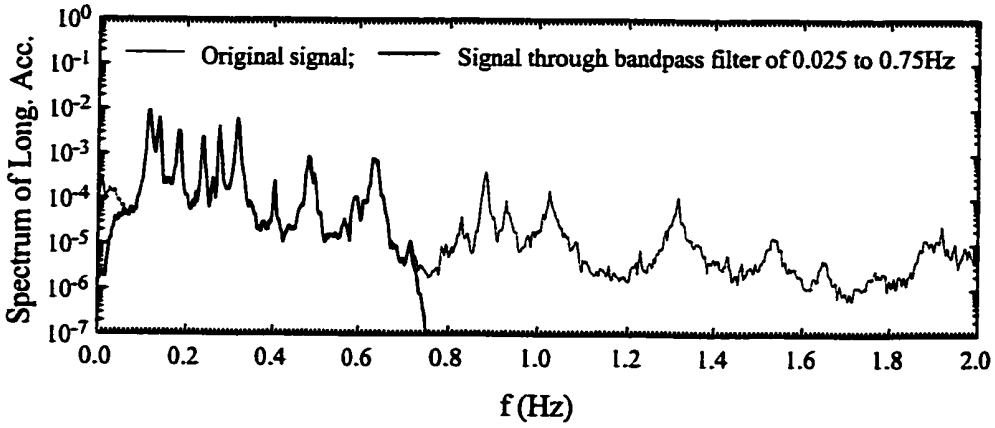

(c) Longitudinal

Figure 9-15 Measured Cable Acceleration Spectra at ATTGC

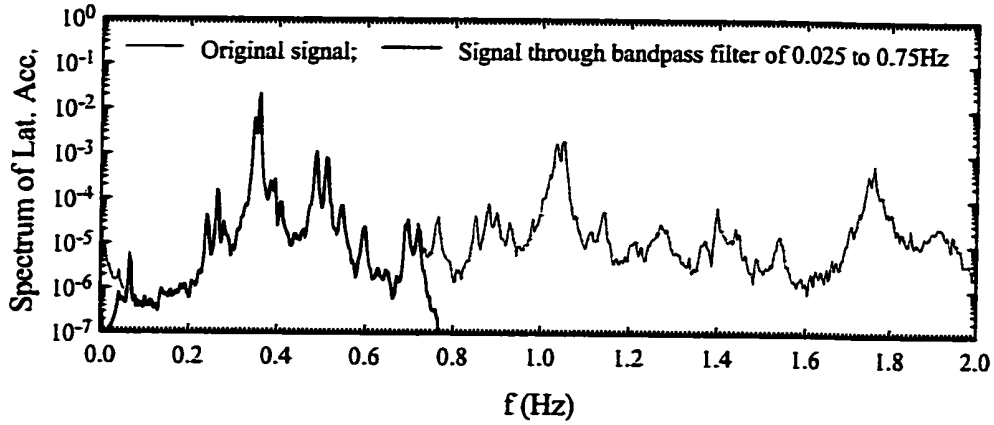

(a) Lateral

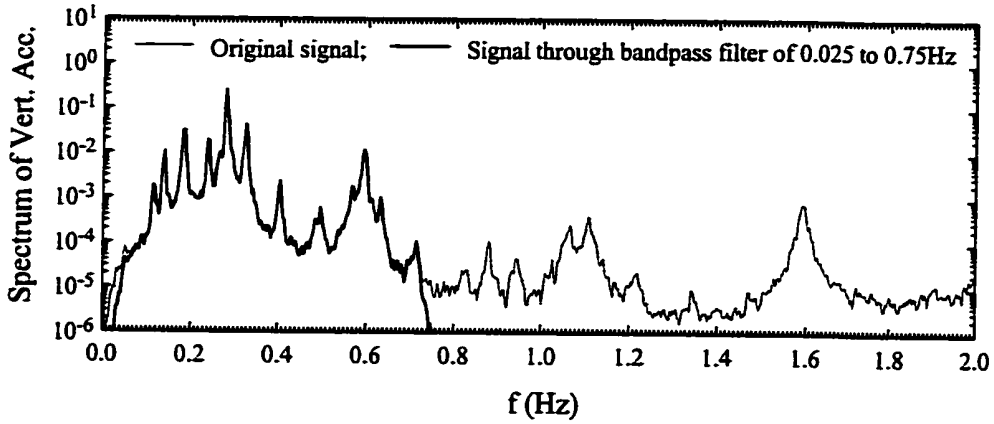

(b) Vertical

Figure 9-16 Measured Cable Acceleration Spectra at ABTCC

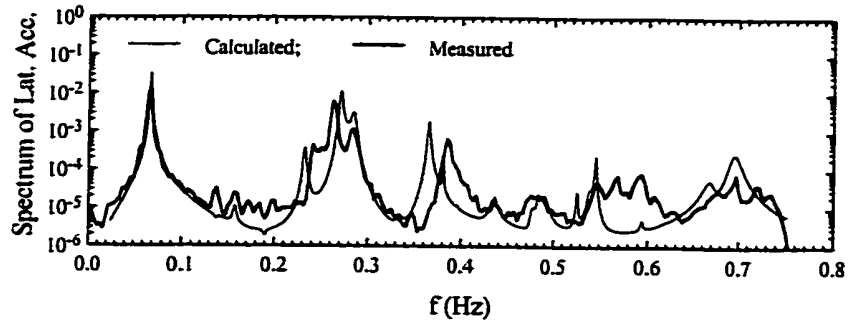

(a) At Section ATTJD

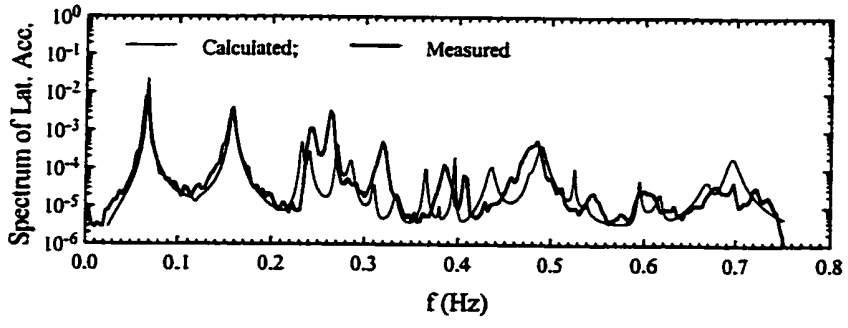

(b) At Section ATTID

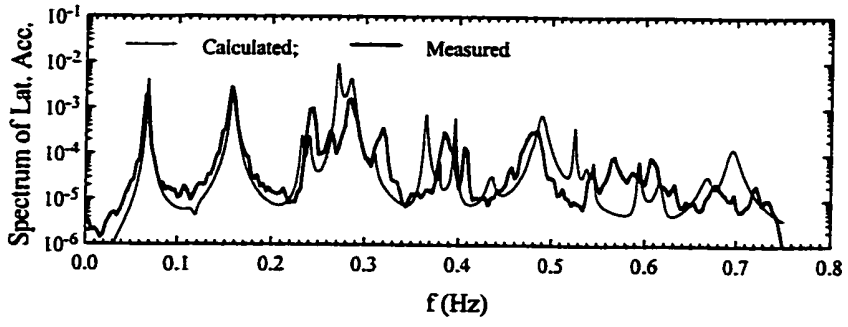

(c) At Section ATTFD

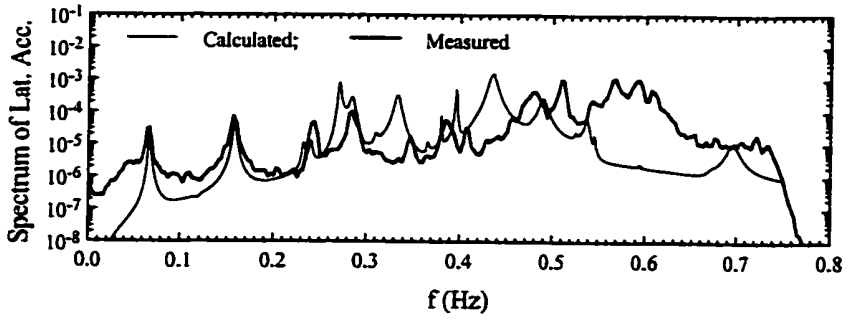

(d) At Section ATTBD

Figure 9-17 Comparison between Measured and Computed Spectra of Deck Lateral Acceleration

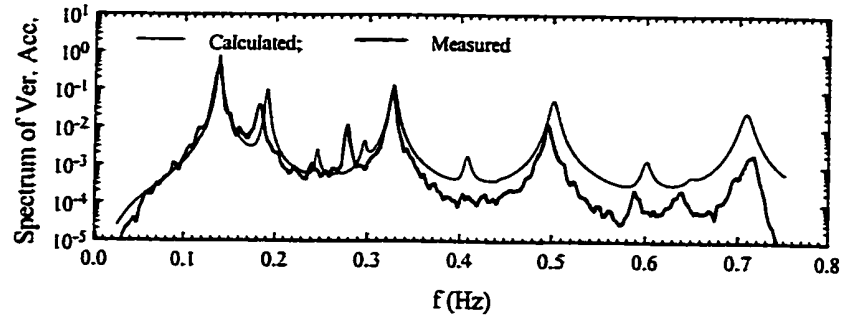

(a) At Section ATTJD

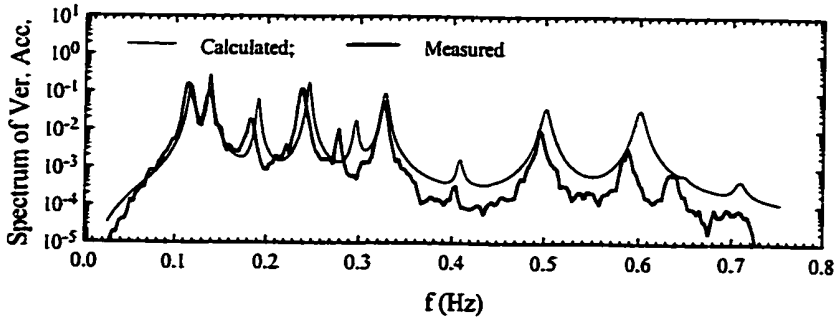

(b) At Section ATTID

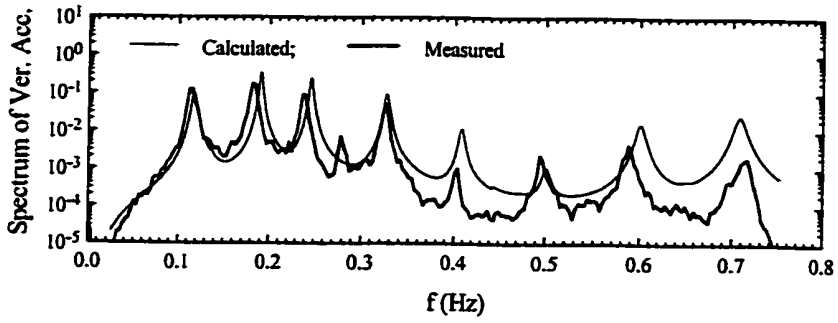

(c) At Section ATTFD

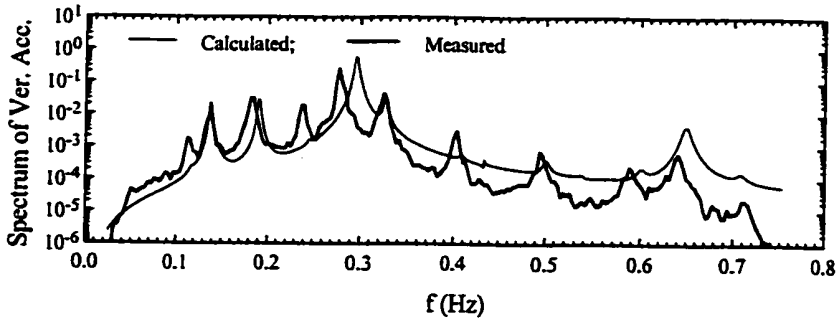

(d) At Section ATTBD

Figure 9-18 Comparison between Measured and Computed Spectra of Deck Vertical Acceleration

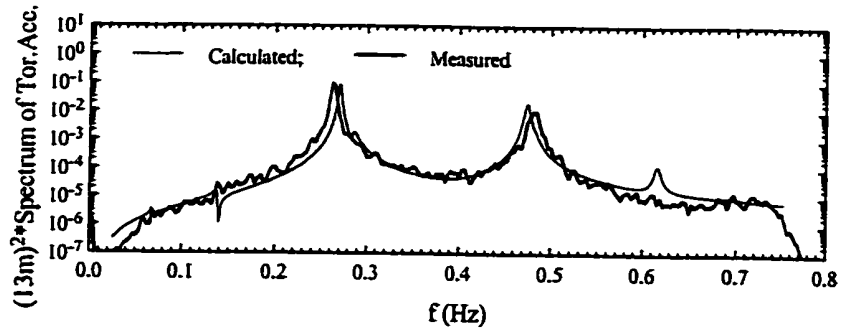

(a) At Section ATTJD

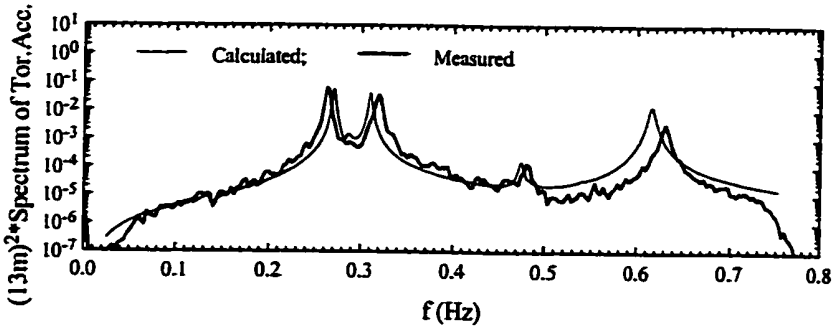

(b) At Section ATTID

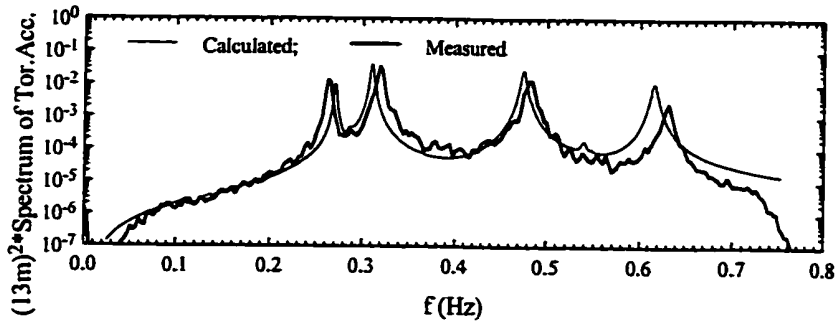

(c) At Section ATTFD

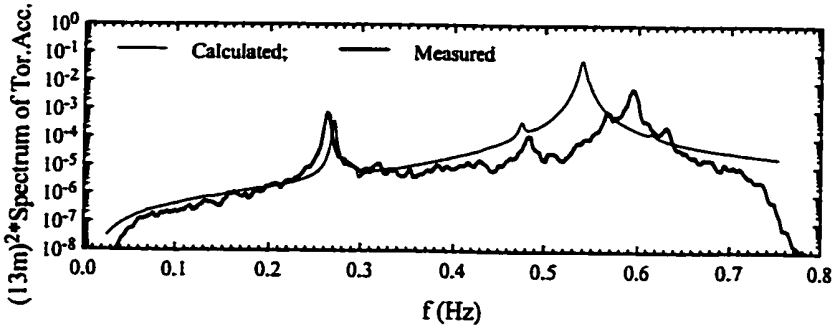

(d) At Section ATTBD

Figure 9-19 Comparison between Measured and Computed Spectra of Deck Torsinal Acceleration

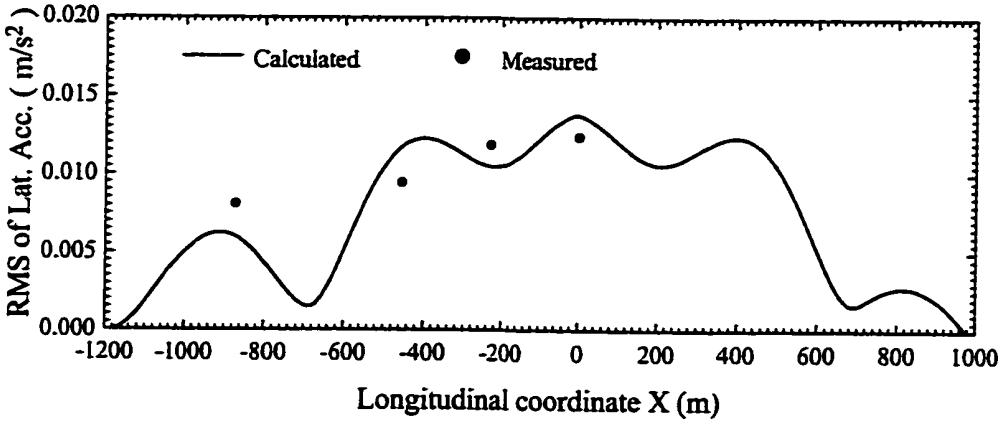

(a) Lateral

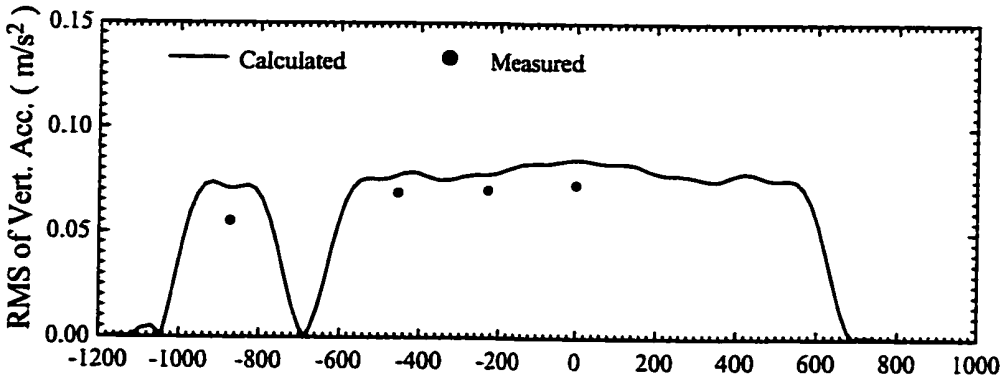

(b) Vertical

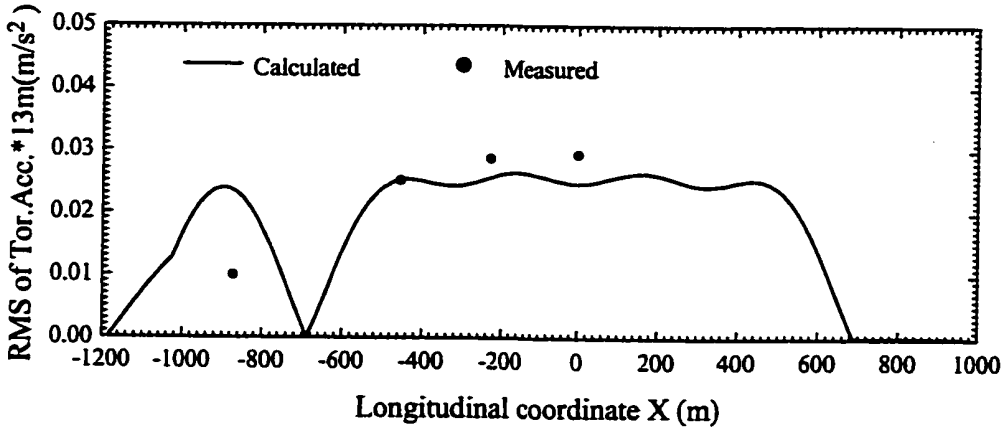

(c) Torsional

Figure 9-20 Comparison between Measured and Computed Deck RMS Acceleration Responses

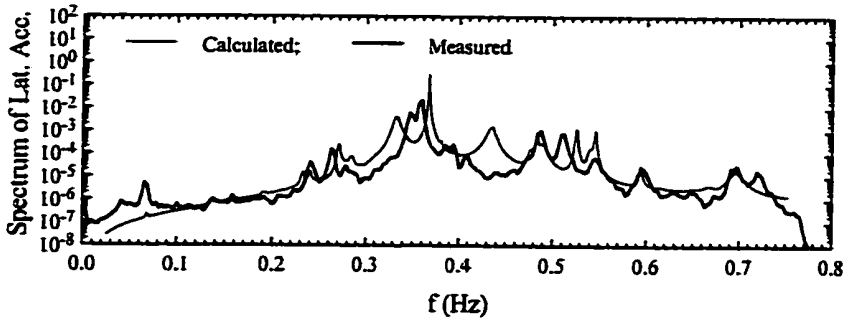

(a) At Section ABTCC

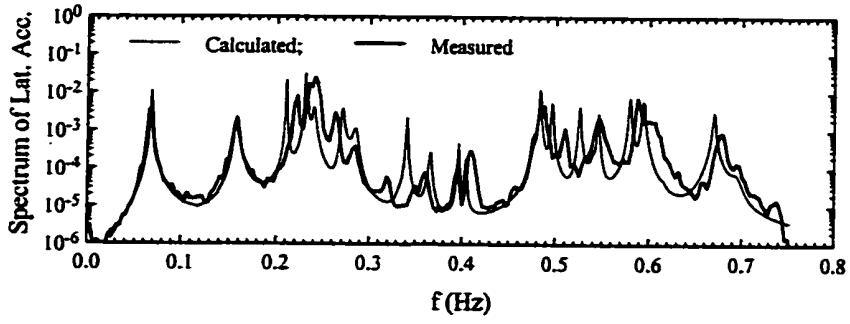

(b) At Section ATTGC

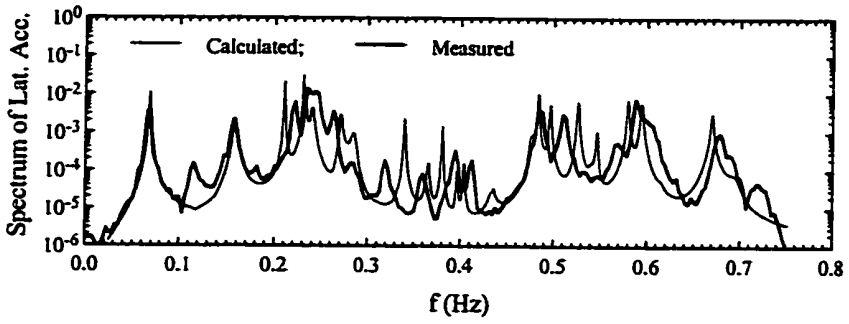

(c) At Section ABTLC

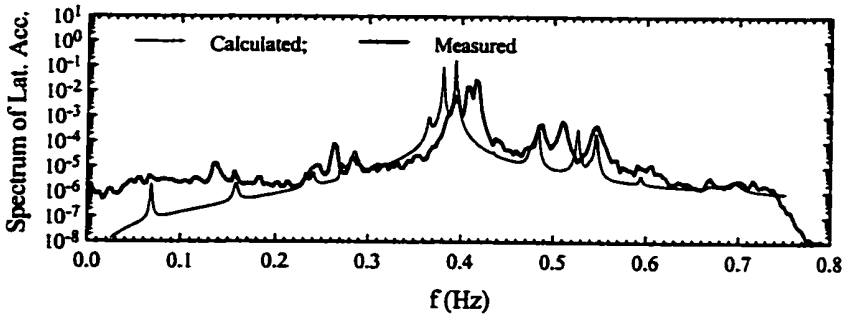

(d) At Section ABTQC

Figure 9-21 Comparison between Measured and Computed Spectra of Cable Lateral Acceleration

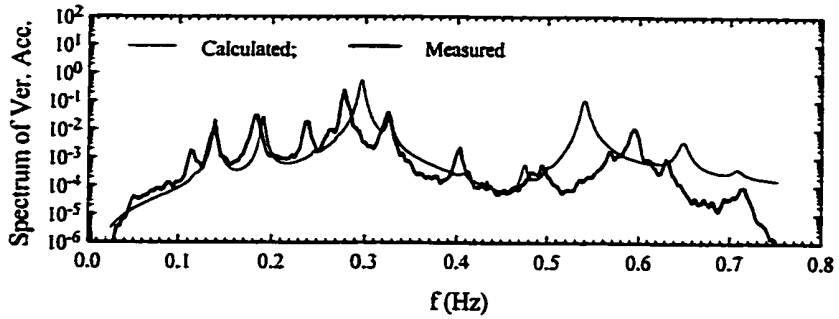

(a) At Section ABTCC

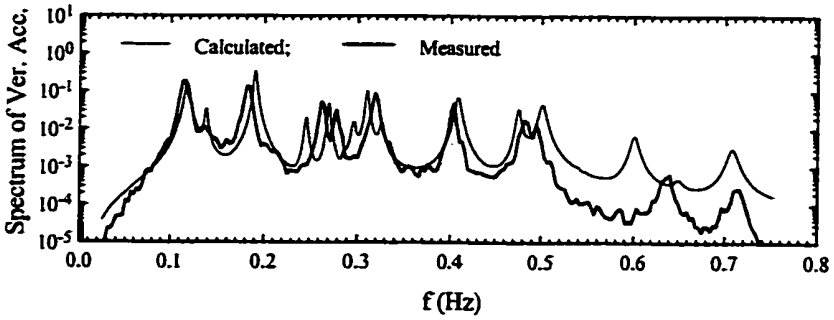

(b) At Section ATTGC

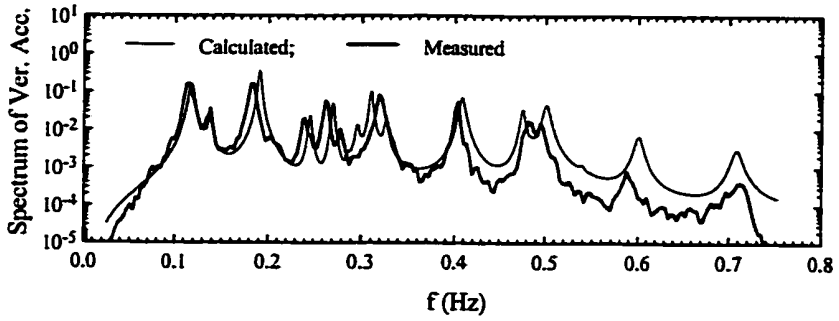

(c) At Section ABTLC

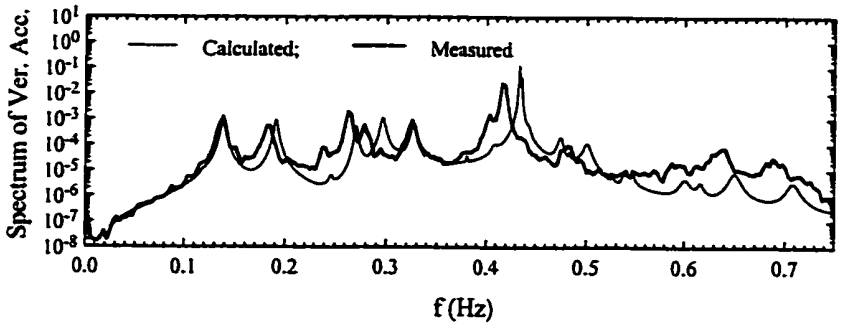

(d) At Section ABTQC

Figure 9-22 Comparison between Measured and Computed Spectra of Cable Vertical Acceleration

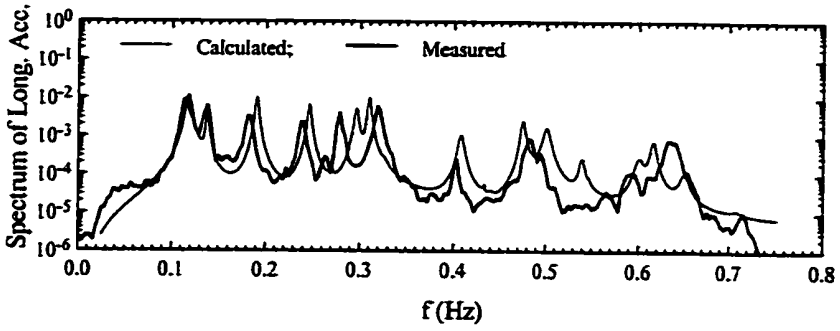

At Section ATTGC

Figure 9-23 Comparison between Measured and Computed Spectra of Cable Longitudinal Acceleration

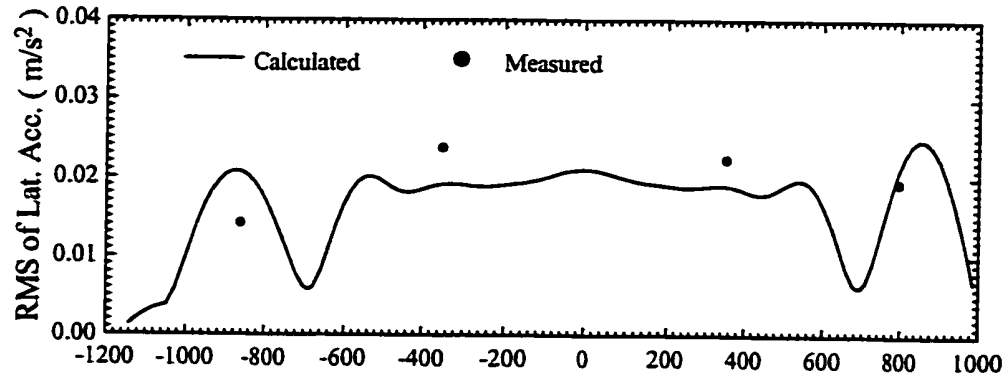

(a) Lateral

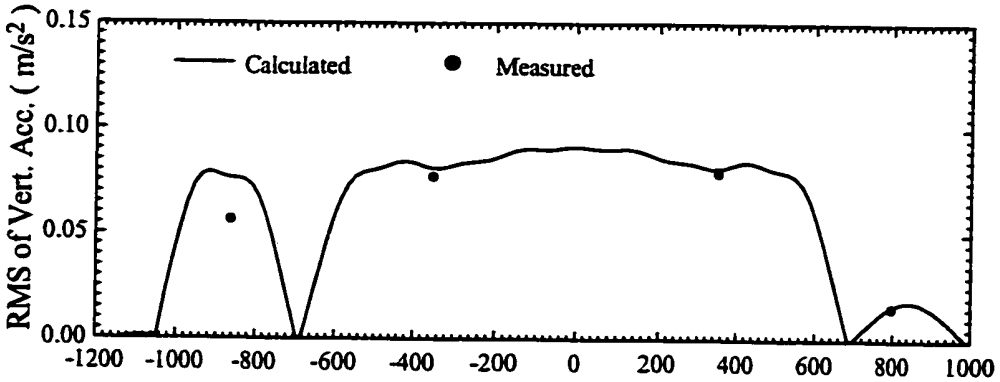

(b) Vertical

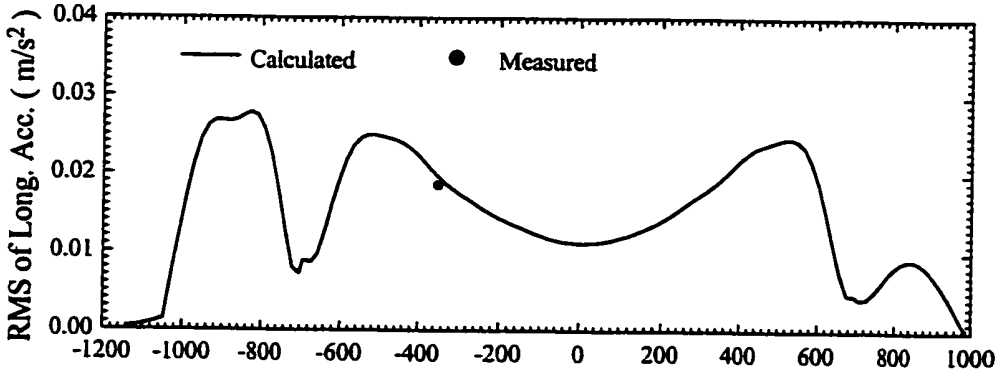

(c) Longitudinal

Figure 9-24 Comparison between Measured and Computed Cable RMS Acceleration Responses

Chapter 10

PARAMETRIC STUDIES

10.1 INTRODUCTION

In the last chapter, the modified buffeting analysis method developed in Chapter 4 and the associated computer program introduced in Chapter 5, together with the measured aerodynamic coefficients and flutter derivatives of the bridge deck and tower presented in Chapters 6 to 8, have been used to compute the buffeting response of the Tsing Ma Bridge during Typhoon Sam. The computed buffeting responses have been then compared with the field measurement data, and the comparison was found to be quite satisfactory. To understand further the buffeting behavior of long span cable-supported bridges under skew winds and to ascertain the influence of some empirical parameters and functions used in the comparison in the last chapter, this chapter performs extensive parametric studies.

Because of space limitation, the effects of wind loads acting on the bridge towers and cables on the buffeting responses of the whole bridge are not included in the parametric studies in this chapter. These effects were studied by Xu et al. (2000a) when carrying out the buffeting analysis of Tsing Ma Bridge under normal wind. According to their study, the buffeting forces on the bridge cables may increase the lateral response of the bridge deck by about 15%, but do not affect the vertical and torsional responses of the bridge deck. Furthermore, the buffeting forces acting on the bridge towers exert only small effect on the buffeting responses of the bridge deck. On the other hand, the lateral and vertical responses of the bridge cables are significantly affected by the bridge deck motion.

The buffeting response of the Tsing Ma Bridge to Typhoon Sam is first computed in this chapter again but using various types of aerodynamic admittance functions for the bridge deck so as to confirm the aerodynamic admittance function used in the last chapter. Then, the variations of the buffeting response of the Tsing Ma Bridge with wind yaw angle and inclination are analyzed, from which the unfavorable (critical)

wind yaw angle and inclination are identified and the mechanism behind the skew wind influence is pursued. Finally, the effects of self-excited forces, aerodynamic crosswind forces, and aerodynamic yawing and rolling moments are investigated.

10.2 EFFECT OF AERODYNAMIC ADMITTANCE FUNCTION

Aerodynamic admittance functions are introduced mainly to correct the quasi-steady buffeting forces to include the effects of turbulence unsteadiness and chordwise partial correlation on the buffeting response. These functions essentially measure the ratios of the aerodynamic forces in fluctuating flow to their quasi-steady values at different frequency points. Although some efforts have been made for the measurement of aerodynamic admittance functions of bluff sections, it is still a difficult and challenging task. Some empirical formulae, as introduced in Chapter 5, have been often used as approximations for engineering practice.

In the buffeting response comparison performed in Chapter 9, the Davenport's admittance function expressed by Eq.(5-22) were employed for the 9 aerodynamic admittance functions associated with the drag, crosswind force, and the yawing moment on the bridge deck ($\chi_{C_{\bar{q}}u}$, $\chi_{C_{\bar{q}}v}$, $\chi_{C_{\bar{q}}w}$, $\chi_{D_{\bar{p}}u}$, $\chi_{D_{\bar{p}}v}$, $\chi_{D_{\bar{p}}w}$, $\chi_{M_{\bar{\phi}}u}$, $\chi_{M_{\bar{\phi}}v}$ and $\chi_{M_{\bar{\phi}}w}$). The other 9 admittance functions associated with the lift, pitching, and rolling moments on the bridge deck ($\chi_{L_{\bar{h}}u}$, $\chi_{L_{\bar{h}}v}$, $\chi_{L_{\bar{h}}w}$, $\chi_{M_{\bar{\alpha}}u}$, $\chi_{M_{\bar{\alpha}}v}$, $\chi_{M_{\bar{\alpha}}w}$, $\chi_{M_{\bar{r}}u}$, $\chi_{M_{\bar{r}}v}$ and $\chi_{M_{\bar{r}}w}$) were set to unity. The computed buffeting responses of the Tsing Ma Bridge to Typhoon Sam were found in good agreement with the field measurement data for both the RMS response and response spectra.

In this section, the buffeting response of the Tsing Ma Bridge to Typhoon Sam are computed again but using different aerodynamic admittance functions for the bridge deck. Four additional cases are considered here. The first case is that all the 18 aerodynamic admittance functions are set to unity. In the other three cases, all the 18 aerodynamic admittance functions are determined using either the simplified Sears' function expressed by Eq.(5-21), or the Davenport's formula (Eq.(5-22)), or the Irwin formula (Eq.(5-23)). When using Eq. (5-21) or Eq. (5-22), the deck height is

used as the characteristic dimension to calculate the values of $\chi_{C_{\bar{q}}u}$, $\chi_{C_{\bar{q}}v}$, $\chi_{C_{\bar{q}}w}$, $\chi_{D_{\bar{p}}u}$, $\chi_{D_{\bar{p}}v}$, $\chi_{D_{\bar{p}}w}$, $\chi_{M_{\bar{\phi}}u}$, $\chi_{M_{\bar{\phi}}v}$ and $\chi_{M_{\bar{\phi}}w}$. When employing Eq. (5-23), the deck width is used as the characteristic dimension to calculate $\chi_{L_{\bar{h}}u}$, $\chi_{L_{\bar{h}}v}$, $\chi_{L_{\bar{h}}w}$, $\chi_{M_{\bar{\alpha}}u}$, $\chi_{M_{\bar{\alpha}}v}$, $\chi_{M_{\bar{\alpha}}w}$, $\chi_{M_{\bar{r}}u}$, $\chi_{M_{\bar{r}}v}$ and $\chi_{M_{\bar{r}}w}$. All the other parameters remain the same as those used in the comparison in Chapter 9.

The computed acceleration response spectra of the bridge deck at the mid-main span in the lateral, vertical, and torsional directions are shown in Figure 10-1 together with the acceleration response spectra measured between 14:11 to 15:11 HKT during Typhoon Sam and filtered between 0.025 Hz and 0.75 Hz. It is seen that, the computed response spectra of the deck lateral, vertical and torsional acceleration using the Sears' function are close to those using the Irwin's function. However, the spectral amplitudes are much lower than the measured spectral amplitudes over a wide frequency range. Thus, the Sears' admittance function and the Irwin's admittance function are not applicable to the Tsing Ma Bridge.

When the Davenport's admittance function is used in the analysis, the computed spectral curve is rather close to the measured one for the deck lateral acceleration response if ignoring the frequency shift at some resonant points. However, it is considerably lower than the measured one for the deck torsional acceleration response. For the deck vertical acceleration response, the spectral curve obtained using the Davenport's admittance function fits the measured one fairly well in the frequency range higher than about 0.35Hz, but is moderately lower than the measured one in the lower frequency range.

When all the 18 aerodynamic admittance functions are set to unity, the computed spectral amplitude of the deck lateral acceleration is higher than the measured one at most of the resonance points. For the vertical acceleration response, the computed spectral curve fits the measured one fairly well in the frequency range lower than about 0.35Hz, but it is significantly larger than the measured one in the higher frequency range. The computed spectral curve of the deck torsional response is quite close to the measured one in the whole frequency range concerned.

Based on the above parametric study results, the best combination used in the buffeting analysis of the Tsing Ma Bridge is to use the Davenport's admittance function for the 9 aerodynamic admittance functions associated with the buffeting crosswind force, drag force, and yawing moment (i.e., $\chi_{C_{\bar{q}}u}$, $\chi_{C_{\bar{q}}v}$, $\chi_{C_{\bar{q}}w}$, $\chi_{D_{\bar{p}}u}$, $\chi_{D_{\bar{p}}v}$, $\chi_{D_{\bar{p}}w}$, $\chi_{M_{\bar{\phi}}u}$, $\chi_{M_{\bar{\phi}}v}$ and $\chi_{M_{\bar{\phi}}w}$) and to set the aerodynamic admittance functions associated with the buffeting pitching moment ($\chi_{M_{\bar{\alpha}}u}$, $\chi_{M_{\bar{\alpha}}v}$ and $\chi_{M_{\bar{\alpha}}w}$) to unity. Furthermore, the response spectral components in the lower frequency range contribute most to the vertical RMS response of the deck. Therefore, the aerodynamic admittance functions associated with the buffeting lift and rolling moment ($\chi_{L_{\bar{h}}u}$, $\chi_{L_{\bar{h}}v}$, $\chi_{L_{\bar{h}}w}$, $\chi_{M_{\bar{\gamma}}u}$, $\chi_{M_{\bar{\gamma}}v}$ and $\chi_{M_{\bar{\gamma}}w}$) are also set to unity.

10.3 Effects of Wind Yaw Angle and Inclination

To investigate the effects of wind yaw angle and inclination on buffeting response of long span bridges, the buffeting response of the Tsing Ma Bridge is computed using the modified frequency-domain method for a wide combination of wind yaw angle from –30 ° to 30° at an interval of 2° and wind inclination from -5° to 5° at an interval of 0.5°. Except for wind yaw and inclination, which are regarded as variables, all the other wind parameters, such as mean wind speed, mean wind profile, friction velocity, turbulence spectra, and coherence decay coefficients, remain the same as those used in Chapter 9. Some of these wind parameters were measured between 14:11 and 15:11 HKT on 22 Aug 1999 during the passage of Typhoon Sam over Hong Kong. Some of them are selected empirically. For instance, the mean wind speed $\overline{U}$ of 17.1m/s at the level of 75.314m was the measured wind speed and the exponent of the mean wind profile taken as 0.33 was empirically selected. The friction velocity u_* was measured as 1.69m/s. The fitted auto spectra of three turbulence components shown in Figure 9-4 and the fitted co-spectra and quad-spectra between any two turbulent components at one point shown in Figures 9-5 and 9-6 are used as input data. Eqs.(5-26) to (5-27) and Eqs.(5-29) to (5-32) are used to determine the cross spectra between two turbulence components at

two different spatial points, in which the coherence decay coefficients are selected as $C_{X_u}^u = 3.0$, $C_{X_u}^v = 3.0$, $C_{X_u}^w = 3.0$, $C_{Y_v}^u = 16.0$, $C_{Y_v}^v = 11.0$, $C_{Y_v}^w = 8.0$, $C_{Z_w}^u = 10.0$, $C_{Z_w}^v = 7.0$, $C_{Z_w}^w = 7.0$. All the phase spectra are regarded as zero because no empirical or measured data are available at present.

The aerodynamic coefficients for the bridge deck and tower members used here were measured from wind tunnel static model tests under the skew wind condition as introduced in Chapter 6 and Chapter 8. The aerodynamic drag and crosswind coefficients of the bridge cables under yaw wind are estimated using Eqs.(5-3a) and (5-3b) with the drag coefficient under the normal wind being 1.0. The aerodynamic forces acting on the bridge hangers are neglected in the analysis since they are very small. The flutter derivatives of H_i^* and A_i^* (i =1,2,3,4) were obtained by the wind tunnel dynamic tests of 2DOF sectional models as introduced in Chapter 5. The flutter derivatives of H_5^*, A_5^* and P_i^* (i =1,3,5) are determined using the quasi-steady expressions shown by Eq.(5-16), and the other 5 of flutter derivatives are ignored. The first 45 modes of vibration with the lowest computed natural frequency of 0.0661 Hz and the highest computed natural frequency of 0.706Hz are taken into account in the analysis. The integration range of frequency for computing the bridge RMS response is from 0.025Hz to 0.75Hz. Thus, the highest reduced wind velocity occurring in the analysis is 16.7, which is a little bit lower than the upper bound of the reduced wind velocity, 18, in the flutter derivatives measured.

Figure 10-2 shows the contour plots of lateral, vertical, and torsional displacement RMS responses of the Tsing Ma bridge deck at mid-main span versus the global wind yaw angle β_0 and inclination θ_0. Figure 10-3 shows several profiles of the contour plots normal to the axis of the global wind yaw angle at five typical values of $\beta_0 = 0°, \pm 2°$ and $\pm 4°$. On the other hand, Figure 10-4 demonstrates several profiles of the contour plots normal to the axis of the global wind inclination at five typical values of $\theta_0 = 0°$, 6°, 12°, 18° and 24°. It is seen that the variations of buffeting response of the bridge are not monotonous with wind yaw angle and inclination. The maximum bridge response may not occur under normal wind condition (zero yaw angle) as indicated by the traditional cosine rule. For the Tsing Ma Bridge within a

range of wind yaw angles (±30°) and wind inclinations (±5°), the maximum displacement response of the bridge deck occurs at about ±12° (yaw angle) and 4° (inclination) in the vertical direction, about 5° (yaw angle) and –2.5° (inclination) in the lateral direction, and about 0° (yaw angle) and –2° (inclination) in the torsional direction.

Further details can be found from Figure 10-3. All the RMS response curves of the bridge deck versus wind inclination reach their summits at the wind inclination about –2.5° for the lateral displacement and within the wind inclination range from –2.0° to -1° for the torsional displacement. For the vertical displacement RMS response of the bridge deck, the response curves show the minimum RMS response occurring within the wind inclination range from -3° to -1° and the maximum RMS response at the wind inclination about 4°. The patterns of the RMS response curves of the bridge deck versus wind inclination for the lateral, vertical, and torsional responses are quite different.

Comparatively speaking, the RMS buffeting responses of the deck lateral and vertical displacements are much less sensitive to wind yaw angle than to wind inclination. The lateral RMS displacement response of the bridge deck is not sensitive to wind yaw angle within a range of ±15° when the global wind inclination is between -2° and -3° (see Figure 10-4). This insensitive range of wind yaw angle becomes larger for the wind inclination between -5° and -3° and between -2° and 5°, and it even becomes almost constant over the whole yaw angle range (±30°) when the wind inclination ranges from 0° to 2°. The RMS response curves of the deck vertical displacement versus the global wind yaw angle are also rather flat when the global wind inclination is less than 1°. The RMS response of the deck torsional displacement is also insensitive to wind yaw angle if wind inclination is equal to -4° or 2°. However, for other wind inclinations such as -2° and 4°, there are a few peaks in the RMS torsional response curves with the maximum (or minimum) peak occurring at zero yaw angle.

Depicted in Figure 10-5 is the contour plots of the RMS response of the bridge cables at quarter-mainspan near the Ma Wa tower for lateral, vertical, and longitudinal displacements. It can be seen that the variations of the lateral and vertical RMS

responses with the global wind yaw and inclination are close to those of the bridge deck at the mid-mainspan. The variation patterns of the longitudinal and vertical RMS displacement responses of the bridge cable are similar to each other though the longitudinal responses are much smaller than the vertical responses. This may be because these two kinds of cable responses are commonly dominated by the vertical and torsional vibration modes of the bridge deck.

The contour plots of the RMS responses of the lateral and longitudinal displacements at the top of the Ma Wa tower are plotted in Figure 10-6. It is interesting to see that the tower responses also vary with the global wind yaw angle and inclination in a pattern similar to those of the deck and cables. Nevertheless, the tower responses are significantly smaller than the responses of the deck and cables.

10.4 Influence Mechanism of Wind Yaw Angle and Inclination

It is known from Xu et al. (2000a) that the buffeting response of a long span bridge is caused mainly by the buffeting forces acting on the bridge deck. The buffeting forces on the cables and towers are only the secondary factors. It is thus reasonable to reckon that the lateral, vertical and torsional displacement responses of the bridge are mainly influenced by the buffeting drag, lift and pitching moments on the bridge deck. The variation patterns of the displacement responses of the bridge deck with wind yaw angle and inclination may follow those of the buffeting forces and moment with wind yaw angle and inclination if linear structures and linear dynamic analysis are considered. In this connection, the variations of buffeting forces and moment on the bridge deck with wind yaw angle and inclination are worthwhile to be investigated to understand the influence mechanism of wind yaw angle and inclination.

For a long span suspension bridge, the slope of the vertical configuration of the bridge deck in the bridge longitudinal direction is quite small. Hence, it is adequate to suppose that the local reference coordinate *qph*-system for the deck elements is consistent with the global coordinate *XYZ*-system. Let $\mathbf{f}_r^b(t)$ denote the 6×1 vector of

buffeting forces on a deck segment of unit length in the *qph*-system. This vector can be then expressed as follows

$$\mathbf{f}_r^b(t)=\begin{Bmatrix} C_q^b(t) \\ D_p^b(t) \\ L_h^b(t) \\ M_\alpha^b(t) \\ M_\gamma^b(t) \\ M_\phi^b(t) \end{Bmatrix}=\mathbf{A}_r^b\bar{\mathbf{a}}(t)=\begin{bmatrix} C_{C_q u} & C_{C_q v} & C_{C_q w} \\ C_{D_p u} & C_{D_p v} & C_{D_p w} \\ C_{L_h u} & C_{L_h v} & C_{L_h w} \\ C_{M_\alpha u} & C_{M_\alpha v} & C_{M_\alpha w} \\ C_{M_\gamma u} & C_{M_\gamma v} & C_{M_\gamma w} \\ C_{M_\phi u} & C_{M_\phi v} & C_{M_\phi w} \end{bmatrix}\begin{Bmatrix} u(t) \\ v(t) \\ w(t) \end{Bmatrix} \tag{10-1}$$

where $C_q^b(t)$, $D_p^b(t)$, $L_h^b(t)$ are the transient crosswind, drag, and lift forces due to wind turbulence, respectively, along the axis q, the axis p, and the axis h of the *qph*-system; $M_\alpha^b(t)$, $M_\gamma^b(t)$ and $M_\phi^b(t)$ are the transient pitching moment, rolling moment, and yawing moment due to wind turbulence, respectively, around the axis q, the axis p, and the axis h; $\bar{\mathbf{a}}(t)=(u(t),v(t),w(t))^{\mathrm{T}}$ is the 3×1 vector of fluctuating wind components; $\mathbf{A}_r^b=\bar{\mathbf{T}}_{Lr\bar{L}\bar{w}}\bar{\mathbf{A}}^b$; $\bar{\mathbf{T}}_{Lr\bar{L}\bar{w}}$ is the 6×6 transformation matrix from the local mean wind coordinate $\bar{q}\bar{p}\bar{h}$-system to the local reference coordinate *qph*-system, expressed by Eq.(4-26); $\bar{\mathbf{A}}^b$ is the 6×3 coefficient matrix of buffeting forces, determined by Eq.(4-55); and $C_{f_r a}$ ($f_r=C_q$, D_p, L_h, M_α, M_γ, M_ϕ; $a=u, v, w$) is one of the 18 elements of the matrix $\mathbf{A}_r^b$, and it is the coefficient of buffeting force f_r due to the fluctuating wind component a. When the *qph*-system is assumed to be consistent with the global coordinate *XYZ*-system, $\bar{\mathbf{A}}^b$ and then $\mathbf{A}_r^b$ can be determined by Eq. (4-58).

If all the cross spectra between any two wind turbulence components are ignored in Eq. (10-1), the buffeting forces and then the RMS buffeting responses of the lateral, vertical and torsional displacements of the bridge deck will be approximately and respectively proportional to the effective buffeting coefficients of drag, lift and pitching moment defined as follows:

$$C_{D_p}^e=\sqrt{C_{D_p u}^2+\mu_{vu}C_{D_p v}^2+\mu_{wu}C_{D_p w}^2} \tag{10-2a}$$

$$C_{L_h}^e=\sqrt{C_{L_h u}^2+\mu_{vu}C_{L_h v}^2+\mu_{wu}C_{L_h w}^2} \tag{10-2b}$$

$$C_{M_\alpha}^e=\sqrt{C_{M_\alpha u}^2+\mu_{vu}C_{M_\alpha v}^2+\mu_{wu}C_{M_\alpha w}^2} \tag{10-2c}$$

where μ_{vu} and μ_{wu} are the ratios of auto spectra of wind turbulence components.

$$\mu_{vu} = S_v(n)/S_u(n) \tag{10-3a}$$

$$\mu_{wu} = S_w(n)/S_u(n) \tag{10-3b}$$

As a result, it is expected that the variations of the effective buffeting coefficients of drag, lift, and pitching moment on the bridge deck in the *qph*-system with wind yaw angle and inclination may represent those of buffeting response of the bridge with wind yaw angle and inclination in the *XYZ*-system.

In this study, the following wind spectra achieved by fitting the measured wind spectra, as shown in Figure 9-4, are adopted.

$$nS_u(n)/u_*^2 \approx 44.65 f_z/(1+18.71 f_z)^{5/3} \tag{10-4a}$$

$$nS_v(n)/u_*^2 \approx 30.44 f_z/(1+11.25 f_z^{1.013})^{1.646} \tag{10-4b}$$

$$nS_w(n)/u_*^2 \approx 9.573 f_z/(1+51.74 f_z^{1.783})^{0.935} \tag{10-4c}$$

Therefore, the ratios of auto spectra, μ_{vu} and μ_{wu}, can plotted as the function of reduced frequency, as shown in Figure 10-7. It is seen that μ_{vu} and μ_{wu} are not sensitive to the reduced frequency when $f_z = nz/\overline{U}(z) > 0.5$. To facilitate the following discussion, the ratios of auto spectra can be seen as the constants. The values of 1.65 and 0.72 at $f_z = 4$ are used for μ_{vu} and μ_{wu}, respectively, in the following discussion.

Figure 10-8 shows the contour plots of the effective drag coefficient $C_{D_p}^e$, the effective lift coefficient $C_{L_h}^e$, and the effective pitching moment coefficient $C_{M_\alpha}^e$ versus the global wind yaw angle β_0 and inclination θ_0. Figure 10-9 depicts the several profiles of the contour plots normal to the axis β_0 at five typical values of $\beta_0 = 0°$, ±2° and ±4°. Figure 10-10 illustrates the several profiles of the contour plots normal to the axis θ_0 at five typical values of $\theta_0 = 0°$, 6°, 12°, 18° and 24°. By comparing Figure 10-2a with Figure 10-8a, one may find that the variation pattern of RMS response of the deck lateral displacement with β_0 and θ_0 is very similar to that of the effective drag coefficient $C_{D_p}^e$ with β_0 and θ_0. This similarity can be

seen more clearly if one compares Figure 10-3a with Figure 10-9a and Figure 10-4a with Figure 10-10a. Thus, the critical wind yaw angle and inclination for the RMS buffeting response of the lateral displacement of the bridge may be found from the variation of the effective drag coefficient $C_{D_p}^e$ with β_0 and θ_0. In this way, great computation efforts for determining the critical wind yaw angle and inclination from extensive lateral RMS displacement responses of the bridge can be avoided.

In the vertical direction, the comparison of Figure 10-2b with Figure 10-8b indicates some similarities in the negative region of θ_0 but not in the positive region of θ_0. The variations of the vertical RMS displacement response of the bridge deck with θ_0 shown in Figure 10-3b are very similar to those of the corresponding curves of the effective lift coefficient $C_{L_h}^e$ with θ_0 shown in Figure 10-9b. The variations of the vertical RMS displacement response of the bridge deck with β_0 are also similar to those of the effective lift coefficient $C_{L_h}^e$ with β_0 for the negative region of θ_0 but not for the positive region of θ_0, as shown in Figure 10-4b and Figure 10-10b. These results indicate that the critical wind inclination for the RMS buffeting response of the vertical displacement of the bridge may be found from the variation of the effective lift coefficient $C_{L_h}^e$ with θ_0. The critical wind yaw angle for the RMS buffeting response of the vertical displacement of the bridge may be also found from the variation of the effective lift coefficient $C_{L_h}^e$ with β_0 in the negative region of θ_0 but not in the positive region of θ_0.

The contour plot in Figure 10-2c for the torsional RMS displacement response of the bridge deck versus β_0 and θ_0 appears to be some different from the contour plot in Figure 10-8c for the effective pitching moment coefficient $C_{M_\alpha}^e$ versus β_0 and θ_0. However, if comparing Figure 10-3c with Figure 10-9c, one may see that the variation trend of torsional response with θ_0 is similar to that of the effective pitching moment coefficient with versus θ_0. The critical wind inclinations in the two figures are all around θ_0=-1.5° though it becomes not clear in the effective pitching moment coefficient curves when β_0 becomes smaller. This indicates that the

effective pitching moment coefficient $C^{e}_{M_\alpha}$ is a major factor affecting the variation pattern of the deck torsional response with θ_0. By comparing Figure 10-4c with Figure 10-10c, one may find that the variation pattern of the torsional response with β_0 is quite different from that of the effective pitching moment coefficient with β_0. Only for the case of θ_0=4°, the discrepancy between the two set curves becomes insignificant.

There are some discrepancies between the vertical RMS response curves and the effective lift coefficient curves with β_0 for the positive region of θ_0 and between the torsional RMS response curves and the effective pitching moment coefficient curves with β_0 for most of θ_0. The reason for this may be due to the inter-mode and aerodynamic coupling effects between the vertical and torsional modes of the Tsing Ma Bridge, which are not considered in the effective buffeting coefficients. The another possible reason may result from the neglect of the cross spectra between the wind turbulence components in the calculation of the effective buffeting coefficients. Nevertheless, further investigation is required to clarify these discrepancies so that the critical wind yaw angle and inclination may be identified directly from the effective buffeting coefficients rather than from the extensive computation of the buffeting responses.

10.5 EFFECTS OF SELF-EXCITED FORCES

Base on the above discussion on the critical wind yaw angle and inclination, two typical wind directions, (β_0=12°,θ_0=-2°) and (β_0=12°,θ_0=4°), are selected for the investigation of the effects of self-excited forces on the buffeting responses of the bridge under skew winds. For this purpose, the buffeting responses of the Tsing Ma Bridge are calculated for the selected typical wind directions. The input wind parameters, structural parameters, aerodynamic coefficients, and aerodynamic admittance functions of the bridge deck, tower and cables are all the same as those used in Section 10.3. Only the difference from Section 10.3 is to set the self-excited forces on the bridge deck as zero.

The computed RMS responses are plotted in the Figure 10-11 to Figure 10-14 and compared with those with the self-excited forces. From Figures 10-11 and 10-12 for bridge deck and cable responses under the wind speed of 17.1m/s and wind direction of β_0=12° andθ_0=-2°, one may see that if ignoring the self-excited forces on the bridge deck, the RMS responses of the bridge are overestimated by 10.8% at most for the lateral displacements of the bridge deck and cables, by 16.7% at most for the vertical displacement of the deck and cables, and by 2.6% at most for the deck torsional displacement and by 11.1% at most for the longitudinal displacement of cables. From Figures 10-13 and 10-14 for bridge deck and cable responses under the wind speed of 17.1m/s and wind direction of β_0=12° andθ_0=4°, one may find that the RMS responses of the bridge are also overestimated with the maximum values of 9.7%, 2.5%, 11.6% and 4.5%, respectively, for the lateral displacements of both bridge deck and cable, the vertical displacements of both bridge deck and cable, the torsional displacement of the deck only, and the longitudinal displacement of the cable only.

10.6 Effects of Crosswind Force, Rolling and Yawing Moments

This section investigates the effects of the crosswind force, rolling and yawing moments acting on the bridge deck on the buffeting response of the bridge for the two typical wind directions (β_0=12°, θ_0=-2°) and (β_0=12°, θ_0=4°), which are used in the last section for investigating the effects of self-excited forces. The input wind parameters, structural parameters, aerodynamic admittance functions, flutter derivatives, and the aerodynamic coefficients of drag, lift and pitching moment are all the same as those used in Section 10.3 except for the aerodynamic coefficients of crosswind force, rolling and yawing moments on the bridge deck. To distinguish the effects of the crosswind force from those of the rolling and yawing moments, two cases are considered. In the first case, the aerodynamic coefficients of the crosswind force on the bridge deck and the corresponding derivatives with respect to both wind yaw and wind inclination are set to zero whilst the aerodynamic coefficients of the rolling and yawing moments on the bridge deck are still included. The aerodynamic coefficients of the rolling and yawing moments used in this case are the same as

those employed in Section 10.3. In the second case, the aerodynamic coefficients of the crosswind force, rolling and yawing moments on the bridge deck all are neglected.

The computed RMS responses are also plotted in Figure 10-11 to Figure 10-14, in which "without $C_{\bar{q}}$ on deck" represents the first case and "without $C_{\bar{q}}$, $M_{\bar{r}}$ and $M_{\bar{\phi}}$ on deck" indicates the second case. It is seen from these figures that the aerodynamic coefficients of the crosswind force and rolling and yawing moments and their derivatives about wind yaw and inclination have almost no effect on the RMS responses of the deck vertical and torsional displacements and the cable vertical and longitudinal displacements. As for the lateral RMS responses of the bridge deck and cables, the exclusion of the aerodynamic coefficients of the crosswind force and their derivatives causes only small underestimation of about 3.1% at most for the wind direction of β_0=12° and θ_0=-2° and about 3.9% at most for the wind direction of β_0=12° and θ_0=4°. The aerodynamic coefficients of rolling and yawing moments and their derivatives with respect to β_0 and θ_0 exert no influence on the RMS buffeting responses of the lateral displacements of both bridge deck and cable. Similar conclusions are also found for the buffeting response of the Tsing Ma bridge tower.

10.7 SUMMARY

Extensive parameter studies on the buffeting response of the Tsing Ma Bridge under skew winds have been performed in this chapter. This includes the effects of aerodynamic admittance function, the effects of wind yaw and inclination, the effects of self-excited forces on the bridge deck, and the effects of crosswind force and rolling and yawing moments on the bridge deck. The influence mechanism of wind yaw and inclination on the buffeting response has been also explored. Major conclusions and remarks can be drawn as follows.

(1) The Sears' and Irwin's aerodynamic admittance functions are not suitable for the Tsing Ma bridge deck. The Davenport's aerodynamic admittance functions are adequate for the Tsing Ma bridge deck associated with the buffeting

crosswind force and drag. The Davenport's admittance functions may be also applicable to the bridge deck related to the lift force in the higher turbulence frequency range, but not in the lower turbulence frequency range. The Davenport's admittance functions are not suitable for the bridge deck related to the pitching moment. The satisfactory comparison with the field measurement data indicates that it is appropriate to set the aerodynamic admittance functions of the bridge deck to unity for the buffeting lift in the lower turbulence frequency range and for the buffeting pitching moment.

(2) The variations of buffeting response of the bridge are not monotonous with wind yaw angle and inclination. The maximum bridge response may not occur under normal wind condition (zero yaw angle). For the Tsing Ma Bridge within a range of wind yaw angles (±30°) and wind inclinations (±5°), the maximum displacement response of the bridge deck occurs at about ±12° (yaw angle) and 4° (inclination) in the vertical direction, about 5° (yaw angle) and –2.5° (inclination) in the lateral direction, and about 0° (yaw angle) and –2° (inclination) in the torsional direction.

(3) Comparatively speaking, the RMS buffeting responses of the deck lateral and vertical displacements are much more sensitive to wind inclination than to wind yaw angle. In particular, the lateral RMS displacement response of the bridge deck is almost insensitive to wind yaw angle within at least ±15° for all wind inclination within ±5°.

(4) The variation pattern of the RMS buffeting response of the lateral displacement of the bridge with wind yaw angle and inclination is mainly governed by the effective coefficient of buffeting drag on the bridge deck with wind yaw angle and inclination. Thus, the critical wind yaw angle and inclination for the RMS buffeting response of the lateral displacement of the bridge may be found from the variation of the effective drag coefficient with wind yaw angle and inclination. In this way, great computation efforts for determining the critical wind yaw angle and inclination from extensive lateral RMS displacement responses of the bridge can be avoided.

(5) The variation pattern of the RMS response of the vertical displacement of the bridge with wind inclination is also mainly governed by the effective coefficient of buffeting lift on the bridge deck with wind inclination. The variation of the effective coefficient of buffeting pitching moment with wind inclination is also the major factor affecting the variation pattern of the RMS torsional response of the bridge deck with wind inclination. However, due to the inter-mode and aerodynamic coupling effects, the variation pattern of the RMS response of either the deck vertical displacement or the deck torsional displacement with wind yaw angle depends upon both the effective lift and pitching moment coefficients versus wind yaw angle.

(6) If the self-excited forces on the bridge deck are ignored, the RMS response of the Tsing Ma Bridge under a mean wind speed of 17.1m/s may be overestimated by 17% for the vertical responses of deck and cables, and by 11% for the deck lateral and torsional responses and the cable lateral and longitudinal responses.

(7) The aerodynamic coefficients of crosswind force and rolling and yawing moments on the bridge deck and their derivatives about wind yaw angle and inclination have almost no effect on the RMS buffeting responses of the vertical, torsional and longitudinal displacements of the Tsing Ma Bridge.

(8) However, it should be noted that the above conclusions about the effects of the selected parameters on the buffeting responses of long span bridges were drawn from the Tsing Ma Bridge only. To get a general conclusion, further studies should be carried out in the future on more bridges with different types of cross section.

(9) It is noted from the parametric studies that for the Tsing Ma Bridge, adopting a wind yaw of zero instead of $\pm 12°$ may underestimate the maximum response by about 10%. Although, the underestimation is not very substantial in this case, but it is worthwhile to take wind yaw into account in the design of super long span bridges. As the bridges become longer and more flexible and the capability to accommodate deformation diminishes, 10% increment of

response may be important, particularly for assessing their remaining fatigue life and service conditions.

(10) The underestimation of buffeting response due to ignoring wind yaw may become more significant for other types of bridges deck sections, which are more sensitive to the wind yaw angle. In addition, it was found through flutter analysis of the Tsing Ma Bridge under skew wind that the lowest critical wind speed may occur in yaw wind cases. Therefore, skew wind effects should be considered in wind-resistant design of super long span cable-supported bridges.

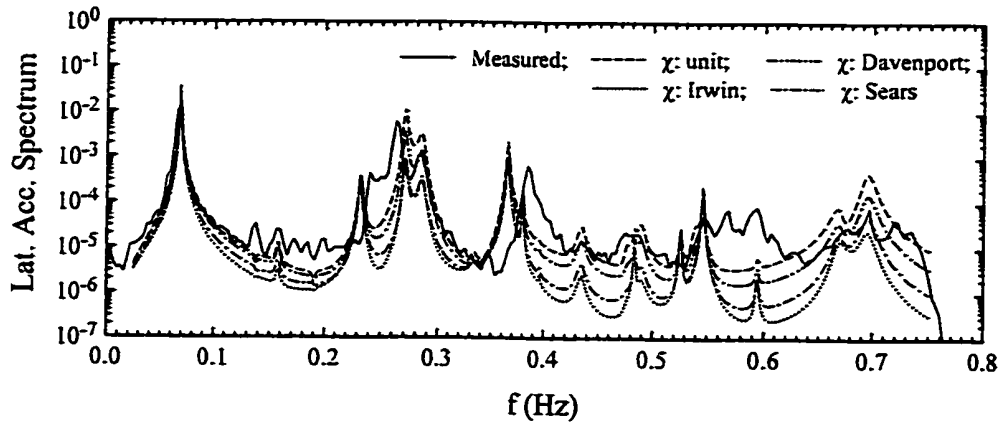

(a) Lateral

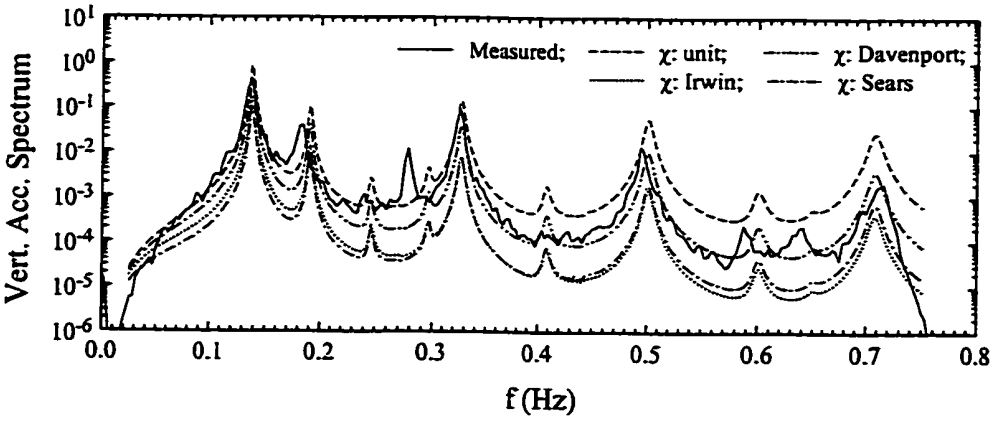

(b) Vertical

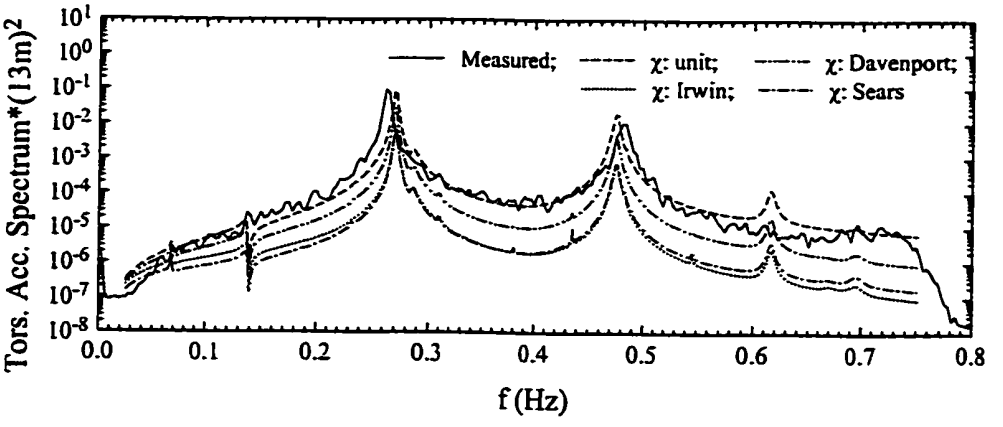

(c) Torsional

Figure 10-1 Response Spectra of Deck Accelerations at Mid-mainspan with Different Aerodynamic Admittance Functions

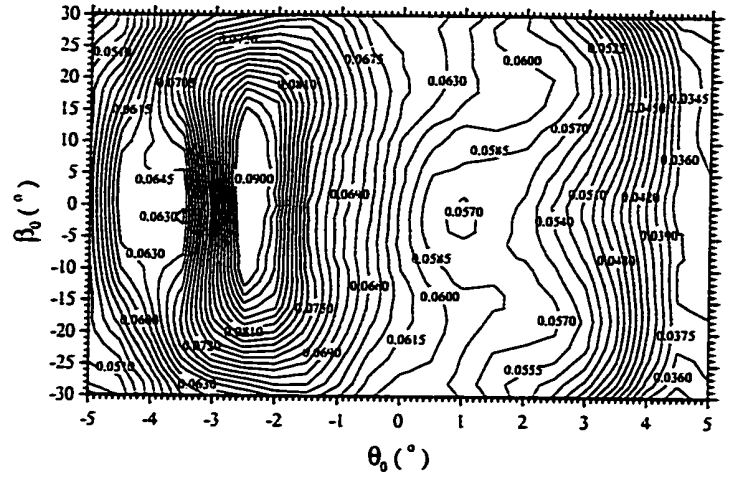

(a) Lateral RMS (m)

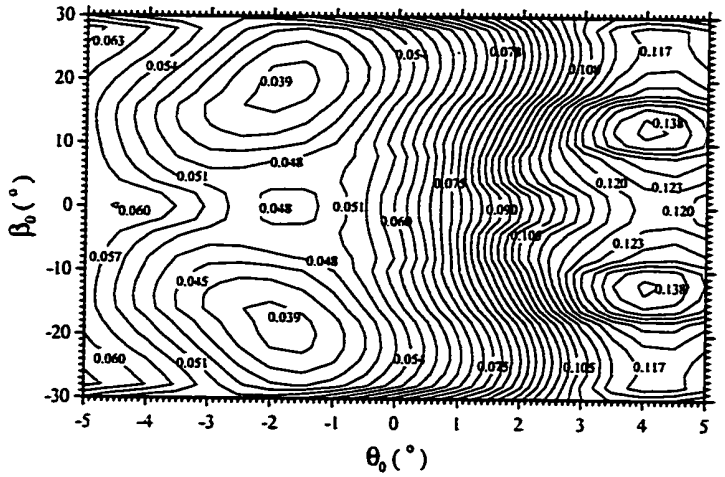

(b) Vertical RMS (m)

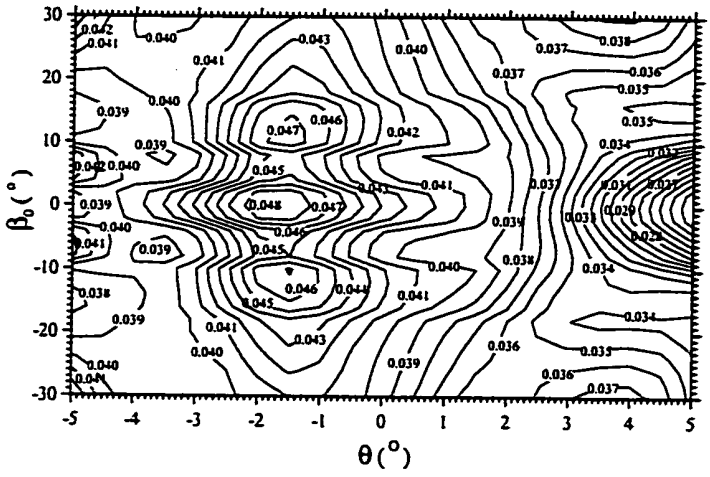

(c) Torsional RMS (°)

Figure 10-2 Contour Plots of RMS Responses of Deck Displacements at Mid-mainspan

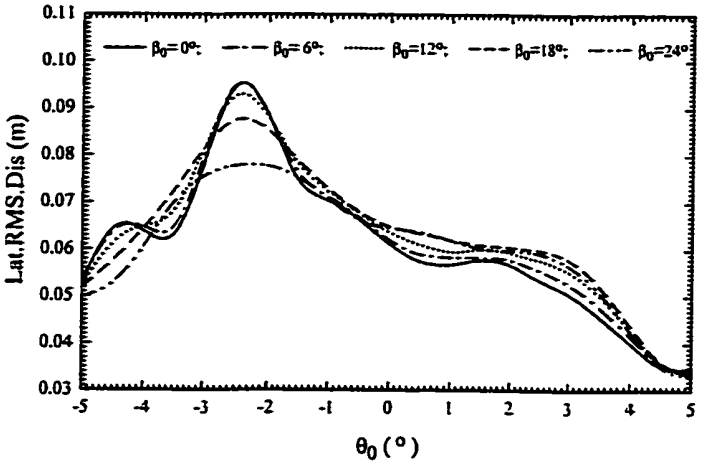

(a) Lateral RMS (m)

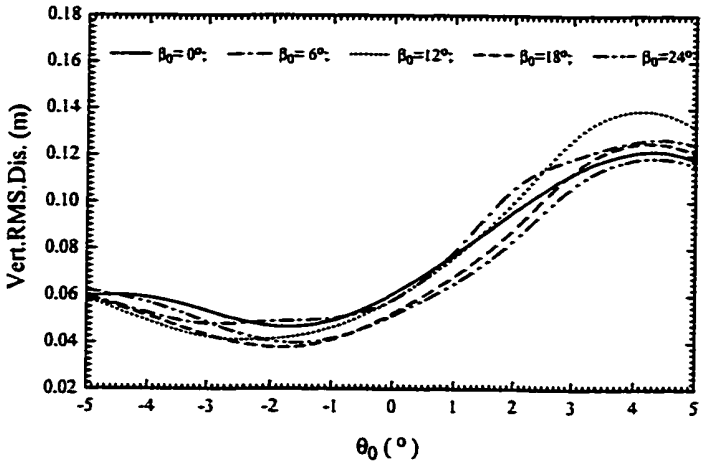

(b) Vertical RMS (m)

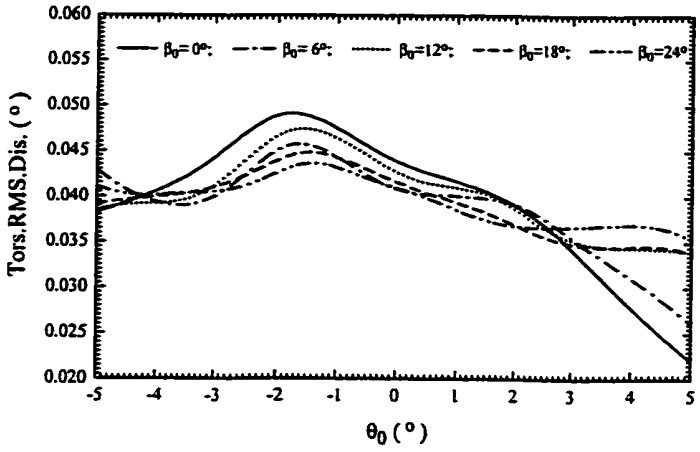

(c) Torsional RMS (°)

Figure 10-3 Variations of RMS Responses of Deck Displacements at Mid-mainspan with θ_0

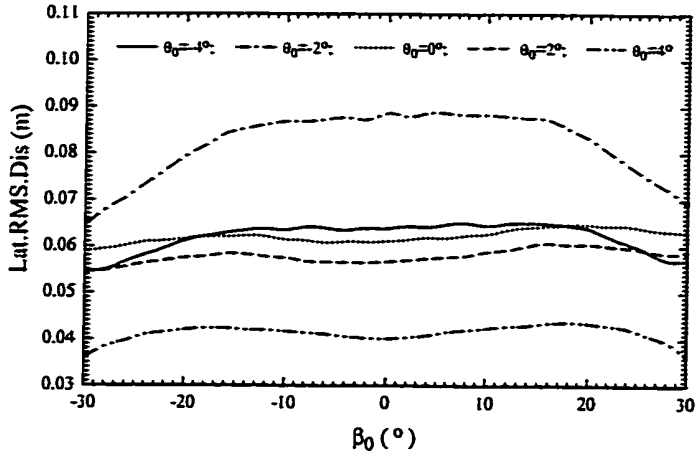

(a) Lateral RMS (m)

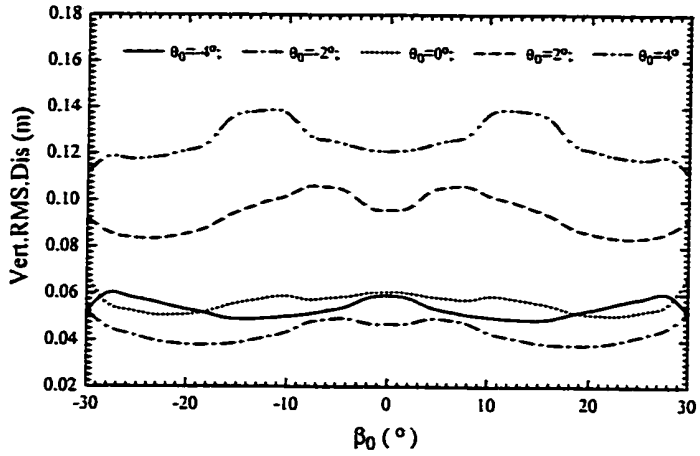

(b) Vertical RMS (m)

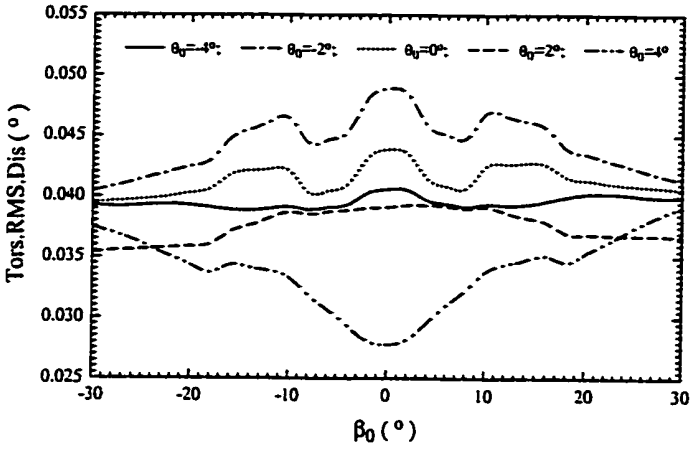

(c) Torsional (°)

Figure 10-4 Variations of RMS Responses of Deck Displacements at Mid-mainspan with β_0

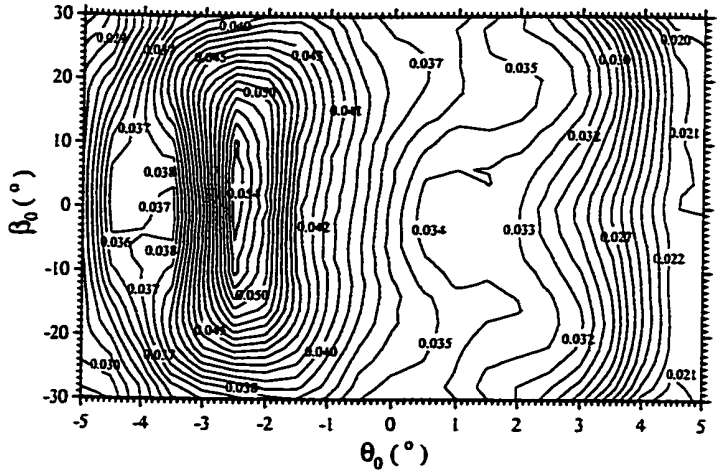

(a) Lateral RMS (m)

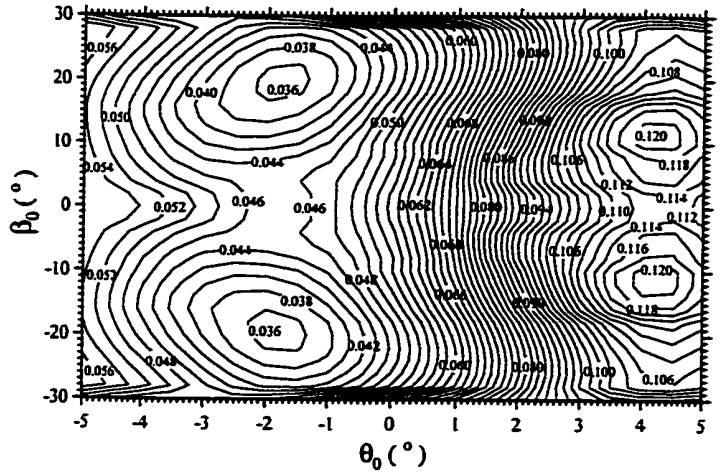

(b) Vertical RMS (m)

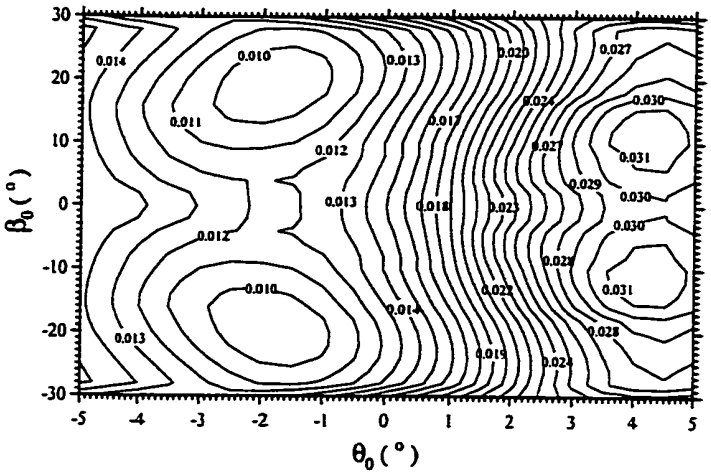

(c) Longitudinal RMS (m)

Figure 10-5 Contour Plots of RMS Responses of Cable Displacements at Quarter-mainspan

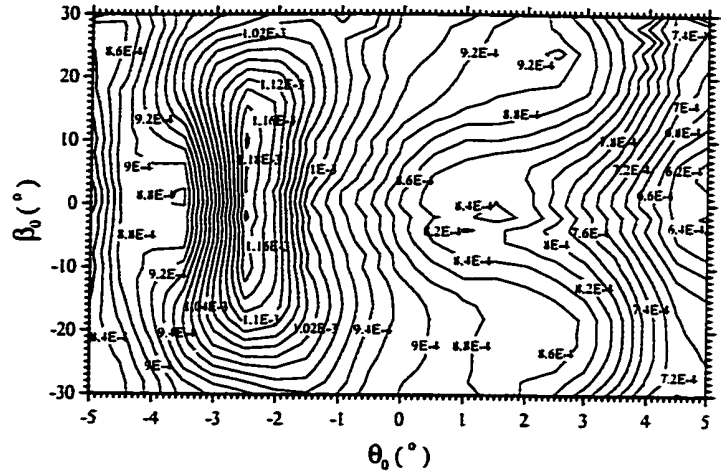

(a) Lateral RMS (m)

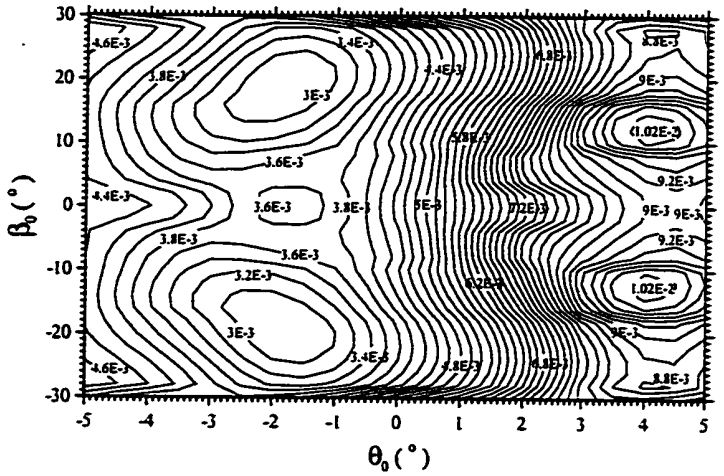

(b) Longitudinal RMS (m)

Figure 10-6 Contour Plots of RMS Displacement Responses at the Top of Ma Wan Tower

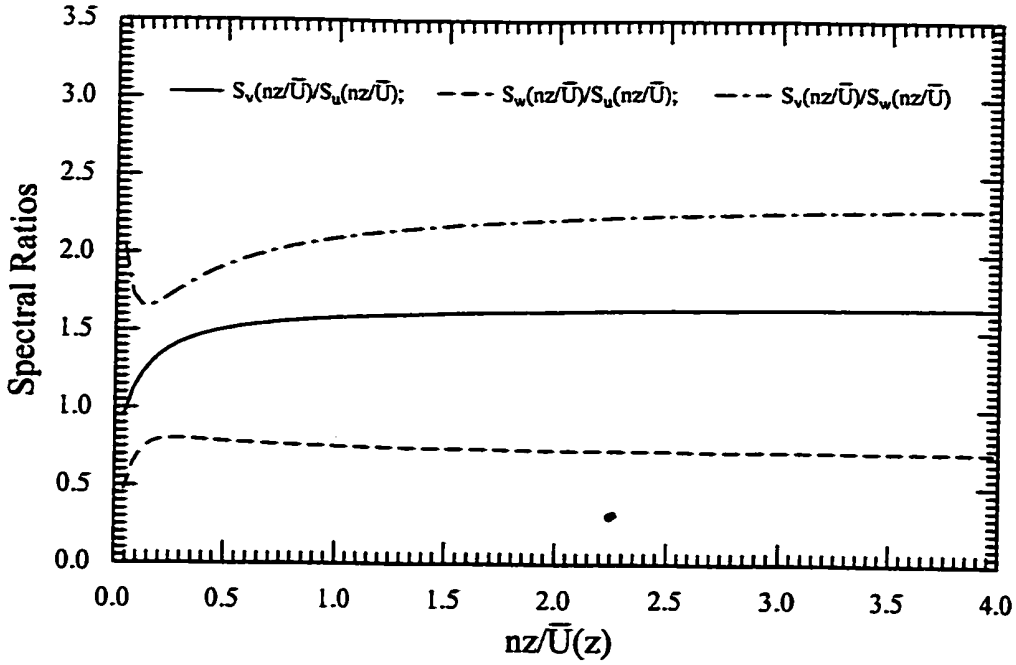

Figure 10-7 Ratios of Auto Spectra as Functions of Reduced Frequency

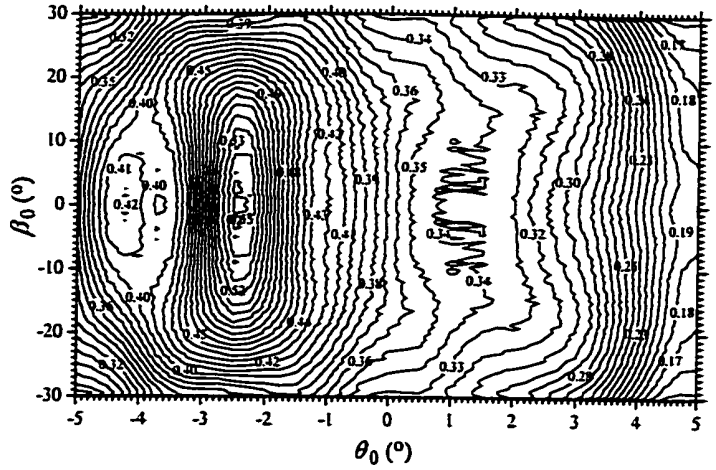

(a) Effective coefficient of buffeting drag ($C_{D_p}^e$)

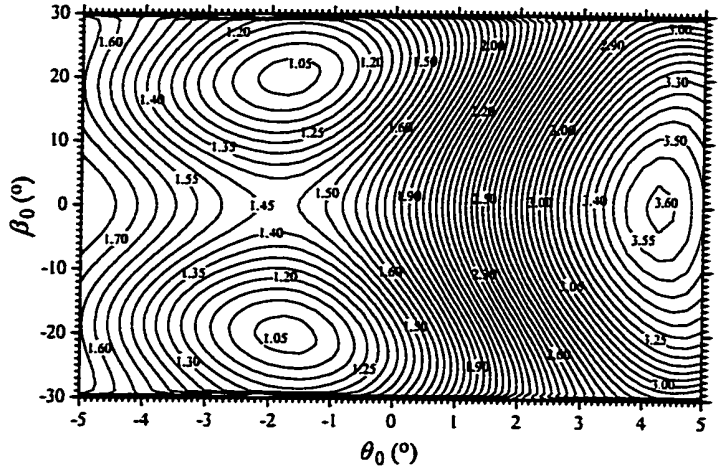

(b) Effective coefficient of buffeting lift ($C_{L_h}^e$)

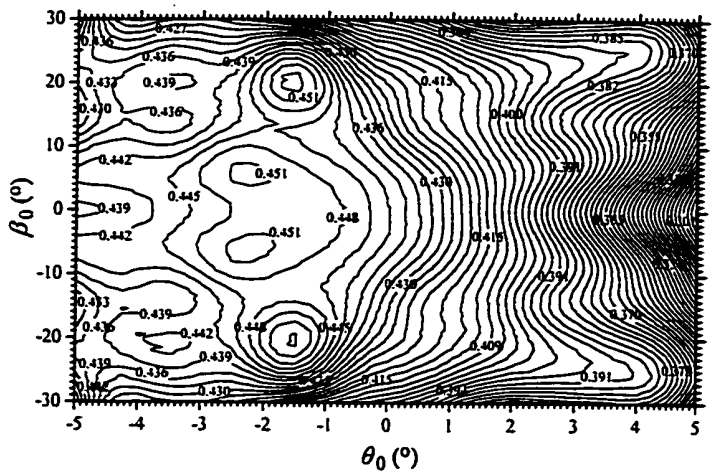

(c) Effective coefficient of buffeting pitching moment ($C_{M_\alpha}^e$)

Figure 10-8 Contour Plots of Effective Coefficients of Buffeting Forces/Moment on Bridge Deck

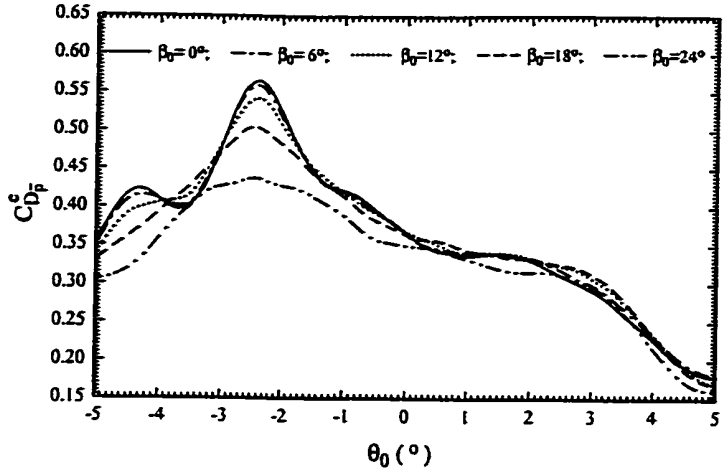

(a) Effective coefficient of buffeting drag ($C^e_{D_p}$)

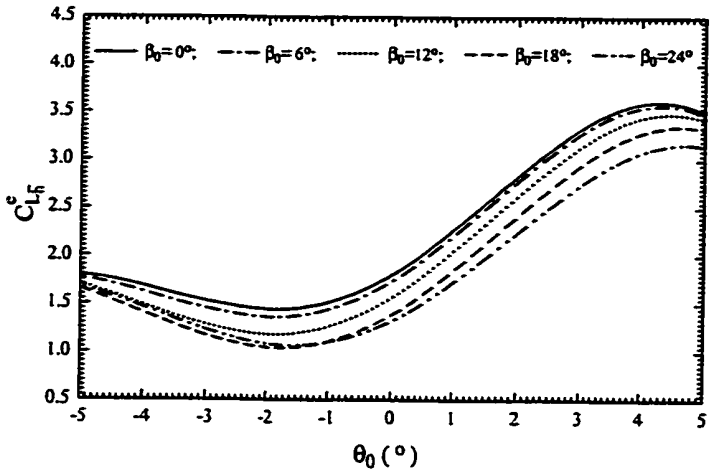

(b) Effective coefficient of buffeting lift ($C^e_{L_h}$)

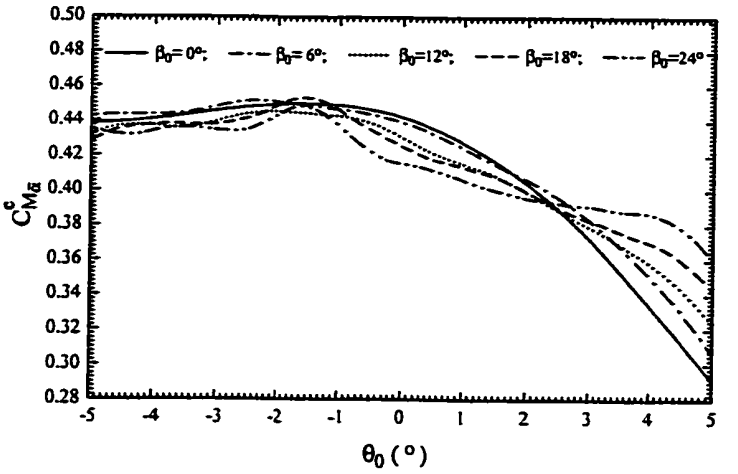

(c) Effective coefficient of buffeting pitching moment ($C^e_{M_\alpha}$)

Figure 10-9 Variations of Effective Coefficients of Buffeting Forces/ Moment on Bridge Deck with θ_0

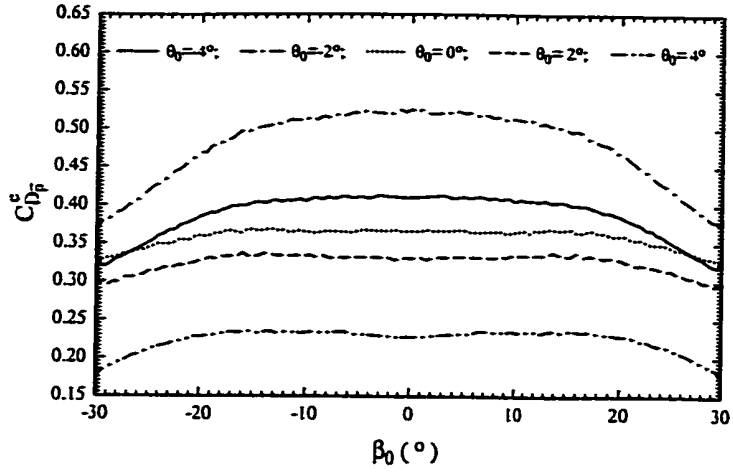

(a) Effective coefficient of buffeting drag ($C^e_{D_p}$)

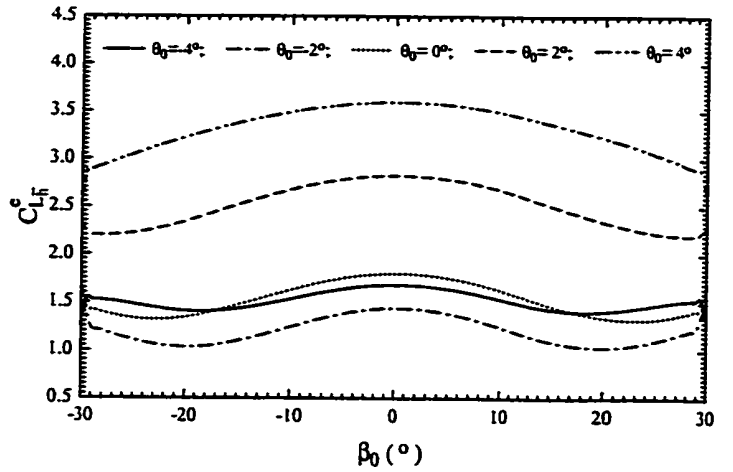

(b) Effective coefficient of buffeting lift ($C^e_{L_h}$)

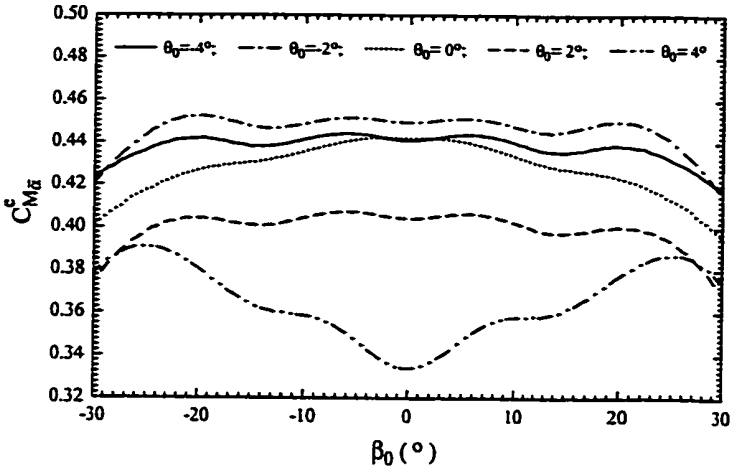

(c) Effective coefficient of buffeting pitching moment ($C^e_{M_\alpha}$)

Figure 10-10 Variations of Effective Coefficients of Buffeting Forces/ Moment on Bridge Deck with β_0

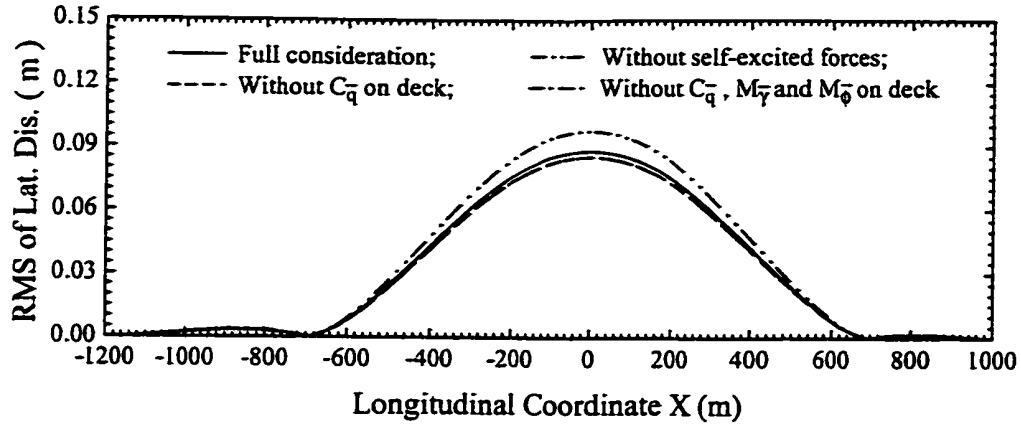

(a) Lateral

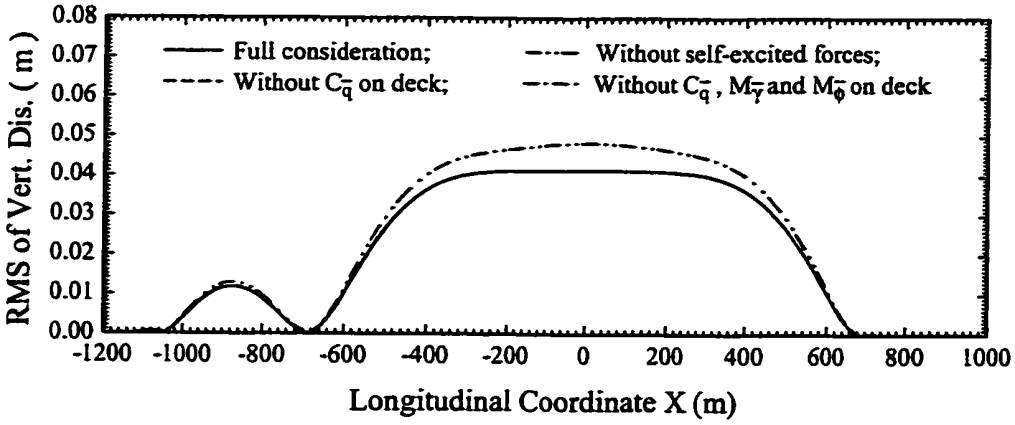

(b) Vertical

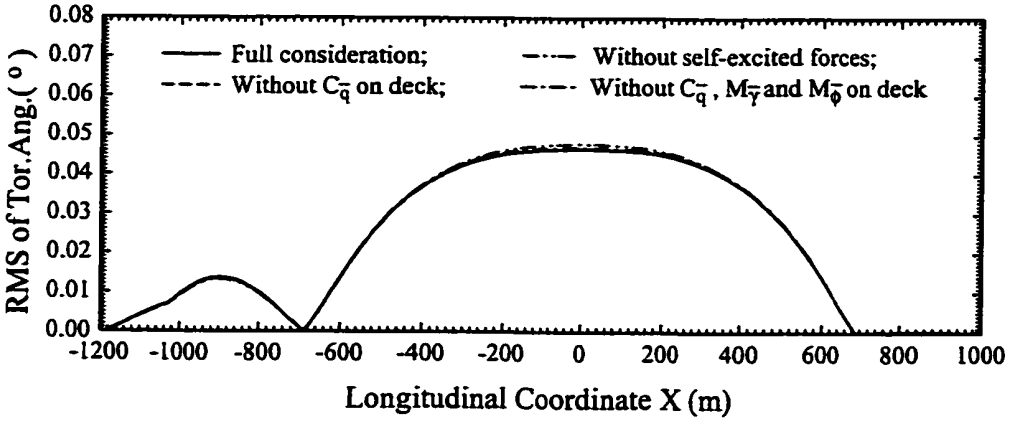

(c) Torsional

Figure 10-11 Effects of Self-excited Forces, Crosswind Force, Rolling and Yawing Moments on Buffeting Responses of Bridge Deck ($\theta_0 = -2°, \beta_0 = 12°$)

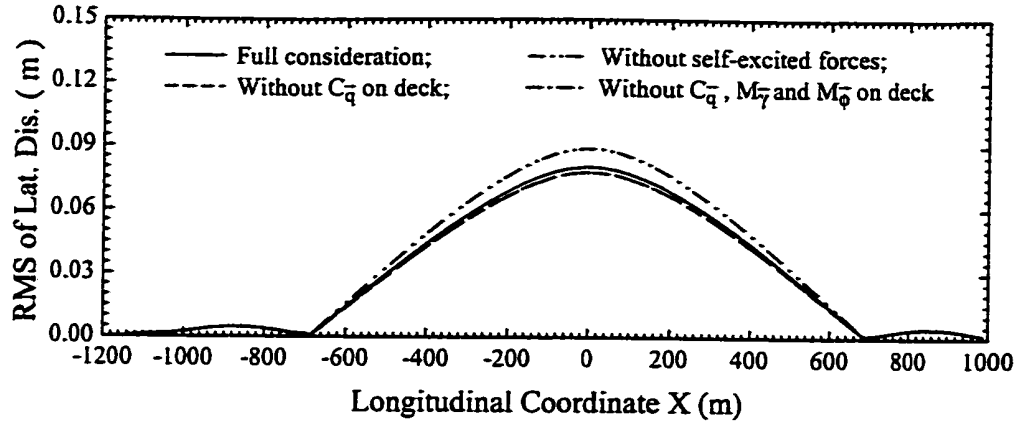

(a) Lateral

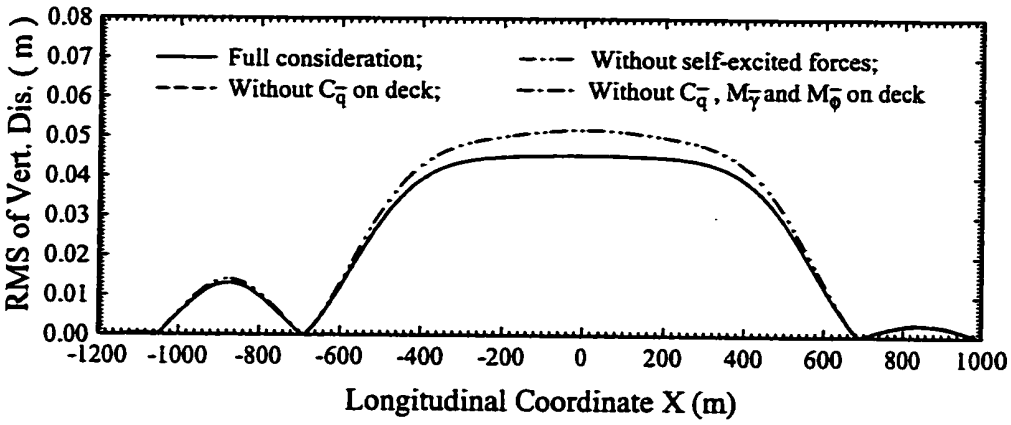

(b) Vertical

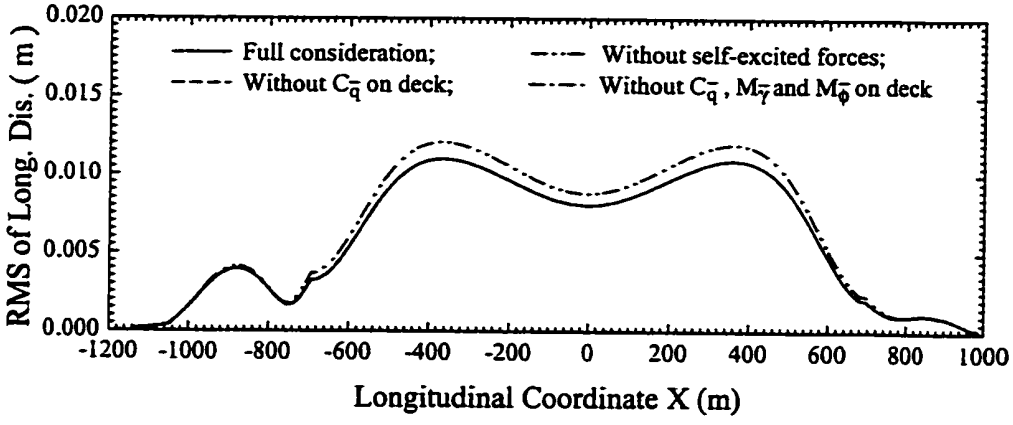

(c) Longitudinal

Figure 10-12 Effects of Self-excited Forces, Crosswind Force, Rolling and Yawing Moments on Buffeting Responses of Bridge Cables ($\theta_0 = -2°, \beta_0 = 12°$)

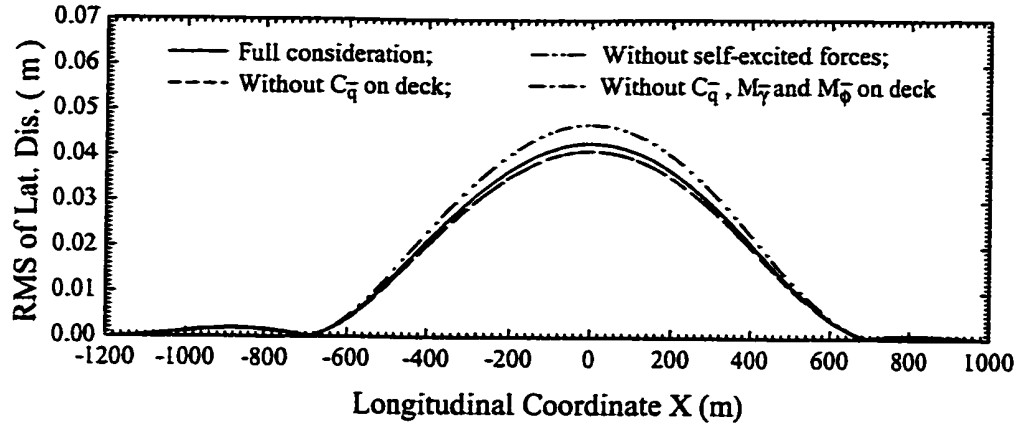

(a) Lateral

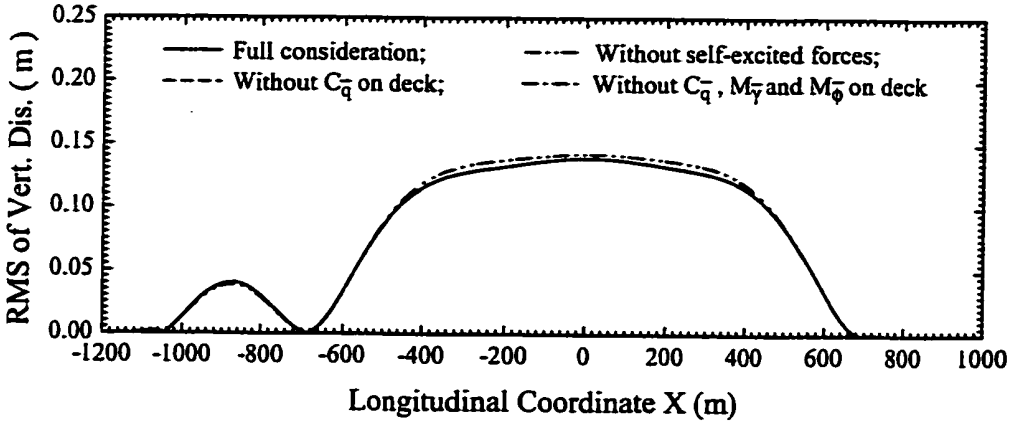

(b) Vertical

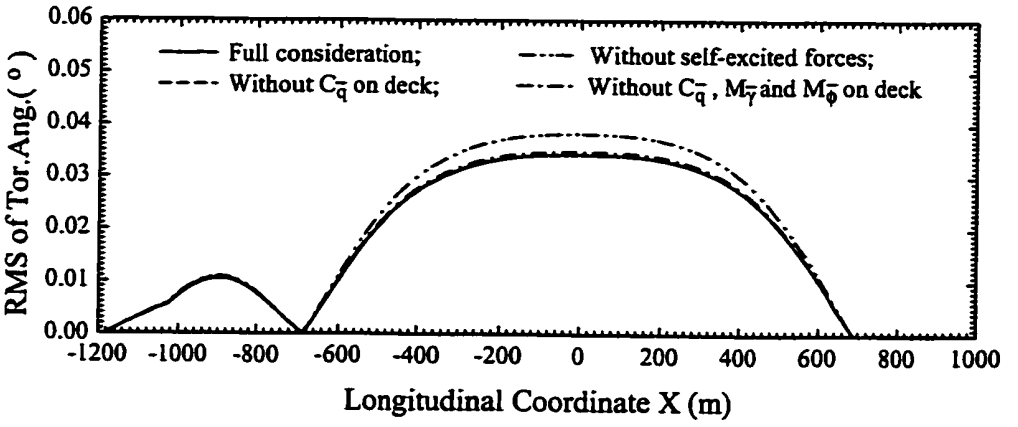

(c) Torsional

Figure 10-13 Effects of Self-excited Forces, Crosswind Force, Rolling and Yawing Moments on Buffeting Responses of Bridge Deck ($\theta_0 = 4°, \beta_0 = 12°$)

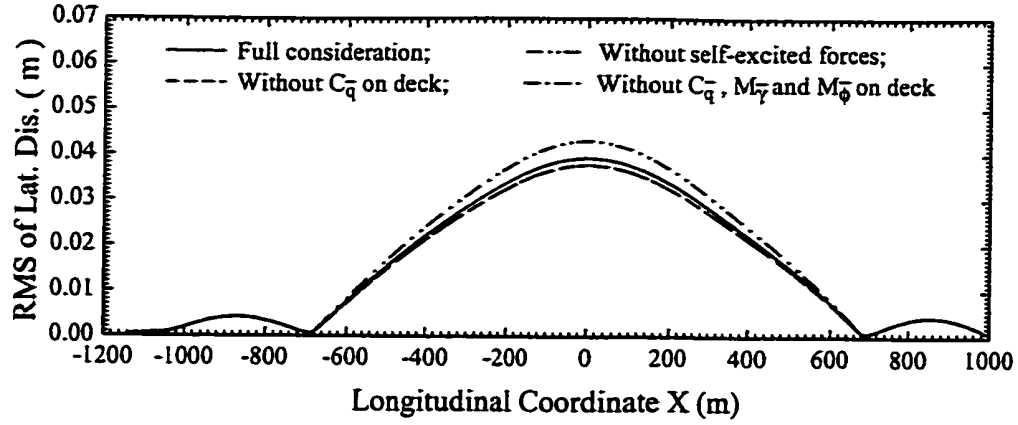

(a) Lateral

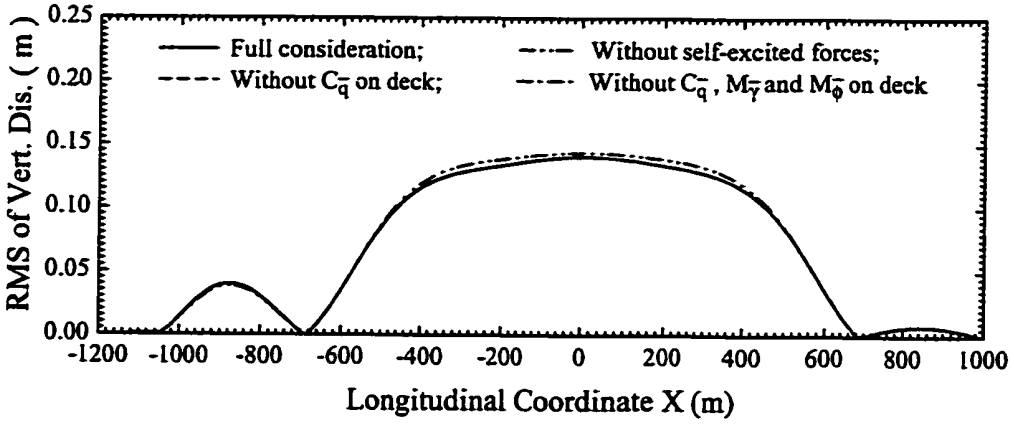

(b) Vertical

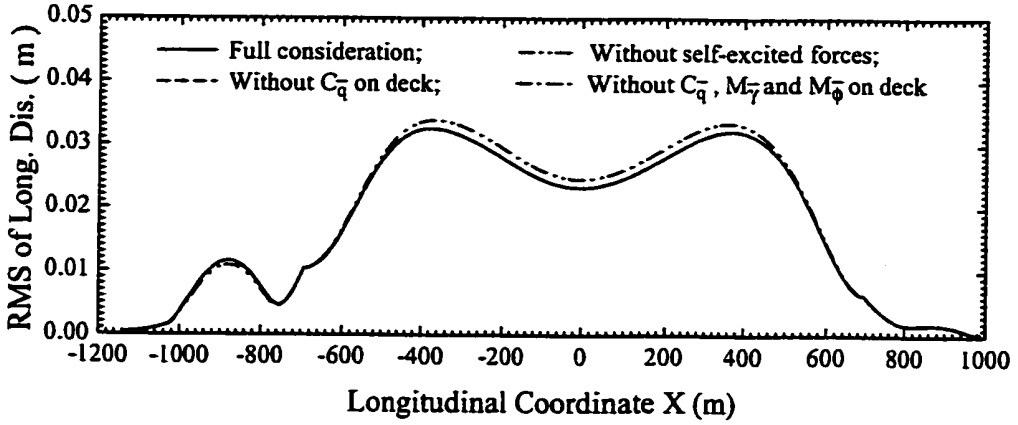

(c) Longitudinal

Figure 10-14 Effects of Self-excited Forces, Crosswind Force, Rolling and Yawing Moments on Buffeting Responses of Bridge Cables ($\theta_0 = 4°, \beta_0 = 12°$)

Chapter 11

CONCLUSIONS AND RECOMMENDATIONS

11.1 CONCLUSIONS

In this dissertation, wind structures and structural responses measured by the Wind And Structural Health Monitoring System (WASHMS) installed on the Tsing Ma suspension Bridge during Typhoons Victor and Sam have been analyzed in detail. A modified frequency-domain method for buffeting analysis of long-span cable-supported bridges under skew winds has been developed based on the quasi-steady theory and the oblique strip theory. A series of wind tunnel tests have been performed to measure the aerodynamic coefficients and flutter derivatives of bridge deck and towers under skew winds using innovative test rigs developed in this study. The comparison of buffeting response of the Tsing Ma Bridge has been carried out between the computed results using the modified method and those measured on the bridge to verify the modified method. Parametric studies have also been conducted for investigating the effects of skew winds, aeroelastic self-excited forces, aerodynamic crosswind force and rolling and yawing moments on the buffeting response of the Tsing Ma Bridge. The main contributions and conclusions made in this dissertation can be summarized as follows:

1. The field measurement results of wind characteristics clearly showed that during typhoons, both mean and turbulent characteristics varied considerably due to the change of wind direction and the heterogeneous upwind terrain. Turbulence intensities measured during typhoons were higher than those due to seasonal trade winds. The decreasing rate of turbulence intensities with height under the complex and heterogeneous terrain and typhoon conditions would be significantly lower than that under the smooth terrain and seasonal trade wind conditions. Furthermore, for a long suspension bridge located in a complex and heterogeneous topography and attacked by a typhoon, field measurement demonstrated that wind direction often deviated from the normal of the bridge

span. Wind characteristics along bridge span, such as the friction velocity, roughness length, mean wind profile, spectra of wind turbulence, etc. also varied along the bridge span. Thus, to consider the observed behaviours of the natural wind, it is necessary to modify current analytical methods for predicting the buffeting response of long suspension bridges located in complicated terrain and typhoon prone regions.

2. In the modified frequency-domain method developed for buffeting analysis of long span bridges under skew winds, a set of universal expressions for six component buffeting forces acting on the oblique strip have been derived. These expressions include all the contributions of three orthogonal components of wind turbulence and are adequate for all the bridge components including deck, towers and cables. A general expression for the cross-spectral matrix of buffeting forces has been presented after considering turbulence spatial correlation and aerodynamic admittance. Self-excited aeroelastic forces have been also taken into consideration in the modified method by including 18 flutter derivatives of an oblique strip under skew winds.

3. The modified method has been established under the frame of finite element technique. The modified method and the associated computer program are capable of handling the skew winds with varying wind characteristics along bridge span, such as the friction velocity, roughness length, mean wind profile, and spectra of wind turbulence. Moreover, the effects of multi-modes, spatial modes, inter-mode couplings, aerodynamic couplings, interaction between different bridge components such as bridge deck, towers and cables, can also be naturally taken into account in the buffeting analysis of long span bridges. By employing the pseudo excitation method in conjunction with an optimal process of the wind excitation sequence, the developed modified method and computer program can efficiently perform a full-coupled buffeting analysis of a long span cable-supported bridge with acceptable computational efforts.

4. A wind tunnel test technique for measuring the aerodynamic coefficients of bridge deck under skew winds has been developed in this study in order to perform a reasonable comparison between measured and computed bridge buffeting responses. This test technique included the design of sectional model,

the development of test rig and measurement system, and the analysis of test results. A typical oblique sectional model of the Tsing Ma Bridge deck was manufactured and tested in a wind tunnel under a series of combination of mean wind inclination and yaw angle. The measured data were fitted to obtain the six aerodynamic coefficient curves as functions of wind inclination and yaw angle for the use of comparison between field measurement and analysis and parameter studies. It was found that the drag force, lift force, and pitching moment coefficients were much larger than the crosswind force, rolling moment, and yawing moment coefficients even for a large yaw angle of 31°. The variation of lift coefficient with yaw angle was small for the angle of inclination less than 5°. The value of drag force coefficient, however, decreased with increasing yaw angle for all the concerned angles of inclination whereas the value of pitching moment increased with increasing yaw angle for the angle of inclination less than 10°. The effects of model end angle distortion on lift force, drag force, and pitching moment coefficients were very small. However, there were moderate effects on crosswind force coefficients, and significant effects on rolling moment and yawing moment coefficients. Furthermore, the obtained six aerodynamic coefficient curves were also used to examine the cosine rule currently used in the buffeting analysis of long span bridges under yaw winds. It was found that the traditional cosine rule may significantly underestimate buffeting forces, in particular at large yaw angles.

5. To include the effect of aeroelastic self-excited forces on the buffeting response of long span bridges to skew winds, a wind tunnel test technique has been developed in this study for measuring the flutter derivatives of bridge deck under skew wind condition. This test technique included the design of oblique sectional model, the development of a dynamic test rig, and the application of unifying least-square (ULS) method for identification. The flutter derivatives of a typical oblique strip of the Tsing Ma bridge deck under skew winds were measured. The measured data were fitted and analyzed to find the relationship between flutter derivatives, reduced frequency, wind inclination, and wind yaw angle. The results were also used to examine the approximate formulae derived from the skew wind theory proposed by Scanlan. In general, significant discrepancies existed except for lower reduced velocities, where the approximate formulae may

give an acceptable estimation of flutter derivatives of a bridge deck under skew winds. Furthermore, the effects of wind yaw angle on the critical wind speed of the Tsing Ma Bridge were also investigated based on the SDOF torsional flutter theory. It was found that critical wind speed may not increase with increasing wind yaw angle.

6. A 3D stiff model comprised of a whole bridge tower and a segment of bridge deck was designed and tested. The averaged aerodynamic coefficients of the upper and lower segments of both windward and leeward tower legs and those of tower transverse beams under yaw winds were obtained. With additional comparative tests, the interference effects between the tower legs, the tower transverse beams, and the bridge deck were investigated. It was found that the effect of windward tower leg on the aerodynamic coefficients of leeward tower leg was remarkable. The aerodynamic coefficients of lower tower leg segment were significantly larger than those of upper tower leg segment. It is thus appropriate to use the separate aerodynamic coefficients for the upper and lower segments of either the windward or leeward tower leg rather than taking a tower as a whole. The measured aerodynamic coefficients were used in the comparison of buffeting response of the Tsing Ma Bridge between field measurement and analysis and also in the parameter study of buffeting response of the Tsing Ma Bridge.

7. Approximate expressions for the aerodynamic drag and lift coefficients of cables under skew winds were presented based on the experimental data provided by Sachs (1978). To perform a parametric study, the approximated formulae were derived for estimating all 18 flutter derivatives under skew winds from those measured under normal wind in the light of approximate skew wind flutter theory proposed by Scanlan. The theoretical formulae for the flutter derivatives of flat plate under normal wind condition were also extended to the yaw wind condition based on the Scanlan skew wind flutter theory. The quasi-steady expressions of flutter derivatives were also derived for skew wind condition. Two simplified expressions were suggested, respectively, for the real and imaginary parts of aerodynamic admittance function of flat plate, which fitted the Sear admittance function quite well for both the real and imaginary parts. The module function of

the proposed expression was more close to that of the original Sears function than the Liepmann expression. Apart from the parametric study performed in this thesis, all the above empirical or approximate expressions may be useful in buffeting prediction of long span bridges at preliminary design stage when the experimental data of aerodynamic and aeroelastic coefficients are not available.

8. The computed buffeting acceleration responses of both the Tsing Ma bridge deck and cables were compared with those measured by the WASHMS during Typhoon Sam. The field-measured modal damping ratios and wind characteristics including the mean wind speed, wind inclination, wind yaw angle, auto and cross spectra of wind turbulence, friction velocity and others were used as input data in the computation. The aerodynamic coefficients and flutter derivatives of the bridge deck and the aerodynamic coefficients of the bridge tower members obtained from the wind tunnel tests for specified wind yaw angle and inclination were also taken as input data in the computation. Meanwhile, some empirical formulae were adopted in the computation for the drag and lift coefficients of the main cables for the identified skew wind, for some flutter derivatives not measured in the wind tunnel tests of 2D sectional model, and for the coherence of wind turbulence. The comparison was found to be satisfactory in general for the RMS responses and response spectra of both the bridge deck and cables. The discrepancies of RMS acceleration response were, respectively, less than 24%, 17% and 17% in the lateral, vertical and torsional vibrations of the main span of the bridge deck. The differences of RMS acceleration response of the main span cables were not more than 20%, 5% and 6% in the lateral, vertical and longitudinal directions, respectively.

9. Parametric studies were finally carried out in this thesis. The parametric studies mainly focused on the effects of wind inclination and yaw angle on the buffeting response of the Tsing Ma Bridge. The results revealed that the variation of buffeting response of the bridge was not monotonous with wind yaw angle and inclination. The maximum bridge response might not occur at zero of wind yaw as indicated by the traditional cosine rule. For the Tsing Ma Bridge within the ranges of wind yaw angle (±30°) and wind inclination (±5°), the maximum displacement response of bridge deck occurred at about ±12° (yaw angle) and 4°

(inclination) in the vertical direction, about 5° (yaw angle) and –2.5° (inclination) in the lateral direction, and about 0° (yaw angle) and -2° (inclination) in the torsional direction. The lateral and vertical RMS displacement responses of the bridge deck were found to be much more sensitive to wind inclination than wind yaw. In particular, the lateral RMS displacement response of the bridge deck remained almost constant within a wind yaw angle range of ±15° for all wind inclination concerned. It was also found that the variation patterns of the RMS responses of the bridge deck with wind yaw angle and inclination depended mainly on the variations of the corresponding effective coefficients of buffeting forces or moment on the bridge deck with wind yaw angle and inclination.

10. The effects of aeroelastic self-excited forces, aerodynamic crosswind force and rolling and yawing moments on the buffeting response of the Tsing Ma Bridge were also investigated through parametric studies. The aeroelastic self-excited forces on the bridge deck were found to exert a fairly significant effect on the buffeting analysis of long span bridges. If the self-excited forces were neglected, the RMS response of the Tsing Ma Bridge under wind speed of 17.1m/s would be overestimated by up to 17% for the deck vertical response and by up to 11% for the deck lateral and torsional responses and the cable lateral and longitudinal responses. The aerodynamic coefficients of crosswind force and rolling and yawing moments of the bridge deck and their derivatives about wind yaw angle and inclination had very small effects on the RMS vertical, lateral, and longitudinal displacement responses of the Tsing Ma Bridge.

11.2 RECOMMENDATIONS

Although a progress has been made in this dissertation in the buffeting analysis of long span cable-supported bridges under skew winds and the comparison of bridge buffeting response between computational results and field measurement data, there remain some important issues deserving further study to enhance our understanding of buffeting behavior of super long span cable-supported bridges.

1. The variations of wind parameters along the bridge deck such as mean wind speed, turbulence intensity, and wind auto and cross spectra can be taken into

account in the modified method and the associated computer program developed in this study. However, due to the limitation of the instrumentation in the WASHMS during Typhoon Sam, variations of wind parameters along the bridge deck were not included in the computation and comparison. It is desirable to carry out more comparisons between field measured and computed buffeting responses in the future with variations of wind parameters included. Furthermore, the comparison between the computed and wind tunnel test results of buffeting responses of long span bridges also needs to be performed in the future.

2. At the present stage, the modified method focuses on the prediction of the response spectra and RMS responses of bridge displacements, velocities and accelerations at different positions in different directions. However, the prediction of buffeting internal forces or stresses in bridge members is also needed in wind-resistant design and fatigue analysis of bridges. Currently, the response spectra of internal forces are often computed using the computed spectral matrix of generalized displacements based on the modal superposition method in conjunction with the associated differential equations of structural deformation. In the modified method using the pseudo-excitation method, the response spectra of internal forces can be directly computed by summing all the pseudo responses caused by the pseudo excitations without using differential equations. The formulation and implementation of the spectra analysis of internal force using the pseudo excitation method will be carried out in the near future.

3. The high-frequency components of wind turbulence are caused by eddies with small length scales. Thus, they cannot be regarded as spatially smooth around the bridge members. As a conventional approach in bridge aerodynamics, aerodynamic admittance is introduced to consider the contributions of the high-frequency turbulence components (Davenport, 1962a, 1962b). The aerodynamic admittance measures the departures of the aerodynamic forces in fluctuating flow to the steady flow values, which can be easily obtained by means of wind tunnel model test in smooth flow (Davenport, 1962b). However, most of previous studies on aerodynamic admittance functions were for the normal wind condition. The aerodynamic admittance functions of the Tsing Ma Bridge deck, tower legs and cables under both normal and skew winds are not available at the present

stage. Thus, some empirical and approximated formulas are employed in the comparison and parameter studies of buffeting response of the Tsing Ma Bridge under skew winds. It is desirable to carry out the measurement of aerodynamic admittance functions of the Tsing Ma Bridge under both normal and skew winds to improve our understanding of aerodynamic admittance functions and achieve a more realistic comparison between computed and measured bridge buffeting responses.

4. Conventionally, flutter derivatives are identified through sectional model test in wind tunnel under smooth flow condition. However, turbulence may affect the flutter derivatives in some subtle ways. The effect of turbulence on flutter derivatives has been studied by some researchers by comparing the flutter derivatives measured under turbulent flow condition with their smooth-flow counterparts. Nevertheless, the available comments on the turbulence effect on the flutter derivatives are different from researcher to researcher due to the different model aspects and the different scales of turbulence simulated in wind tunnel. Thus, this issue deserves further investigation in the future.

5. The geometric non-linear effects of a bridge under static wind loads on buffeting response can be considered in this modified method to some extent by taking the static nodal displacements and element torsional angles as initial deformations. However, due to the time limitation, the static nonlinear analysis of the Tsing Ma Bridge under mean wind is not carried out in this dissertation. The geometric non-linear effect on the buffeting response of the Tsing Ma Bridge due to mean wind loads will be investigated in the future.

6. When mean wind speed approaches either the critical wind speed of flutter instability or the wind speed at which vortex-induced resonant vibration is significant, wind-induced dynamic responses of long span bridges will be significantly large. The geometric non-linearity of structure and the non-linearity of aerodynamic coefficients and flutter derivatives due to large bridge motions should be taken into account. Furthermore, as pointed in Bocciolone et al. (1990), the variation of the instantaneous inclination between wind and bridge deck due to fluctuating wind components can reach $\pm 10°$ with a usual turbulence intensity around 10%. This indicates that the non-linearity of aerodynamic coefficients and

flutter derivatives may exert a great influence on the buffeting response of long span bridges because they are sensitive to wind inclination in general. To include the above non-linear effects, a time-domain method for the buffeting analysis of long span bridges under skew winds needs to be introduced in the future in parallel to the modified frequency-domain method developed in this dissertation.

7. Although a quite good comparison has been attained in this study, the analysis of the confidence of the comparison result has not been carried out in this dissertation. To further validate the modified buffeting analysis method, this confidence analysis is required, which involves many aspects, such as, the reliability analyses of the field measurement results of both wind characteristics and structural response, wind tunnel test results including the stability of measurement instruments, the accuracy of model manufacture, flow simulation, and others. To carry out such a confidence or reliability analysis, more applications of the modified method should be made and proper probability models of errors of field measurement and wind tunnel test should be established.

Appendix A

COMPUTED NATURAL MODES OF TSING MA BRIDGE

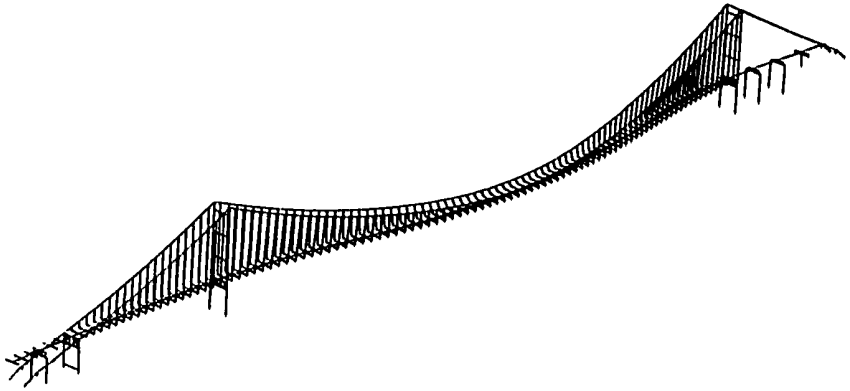

Mode No. 1 **f = 0.0681 Hz**

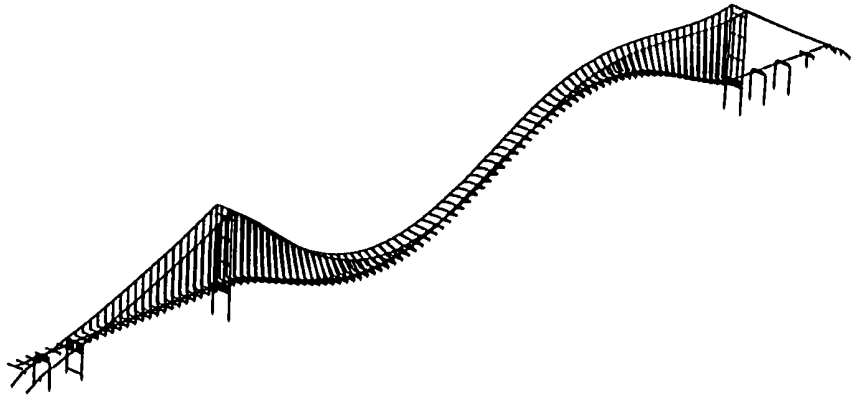

Mode No. 2 **f = 0.1166 Hz**

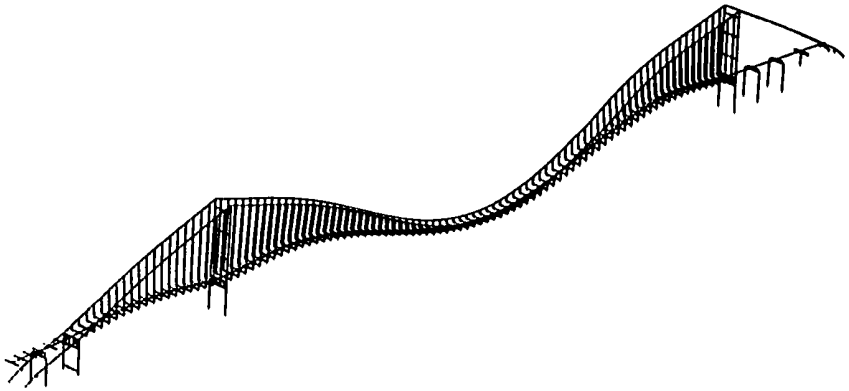

Mode No. 3 ***f*** **= 0.1367 Hz**

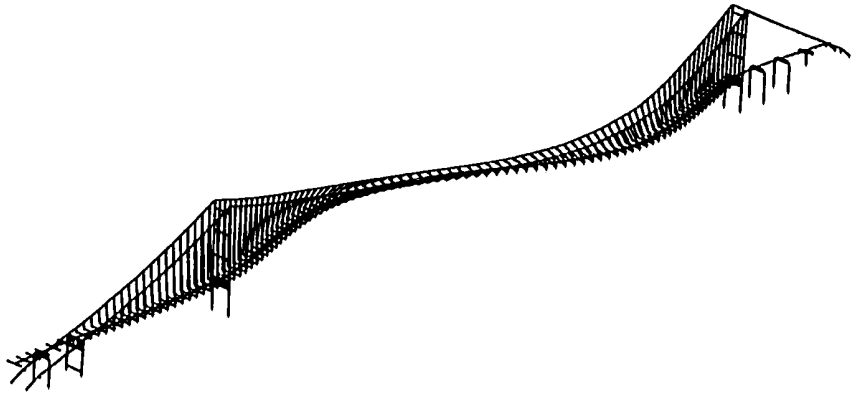

Mode No. 4 ***f*** **= 0.1578 Hz**

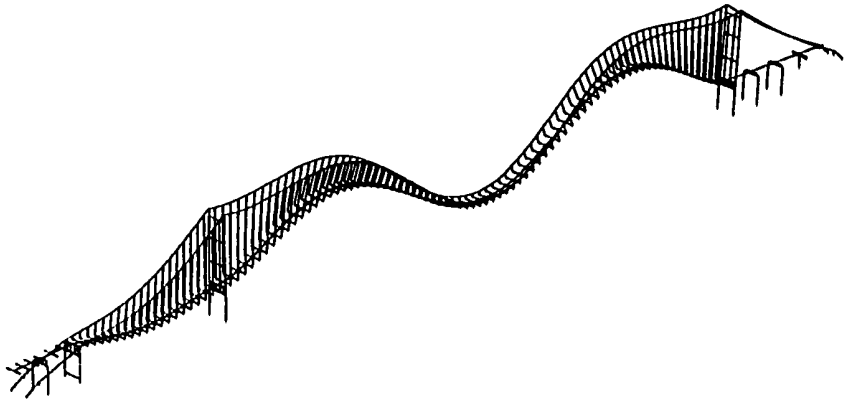

Mode No. 5 **f = 0.1890 Hz**

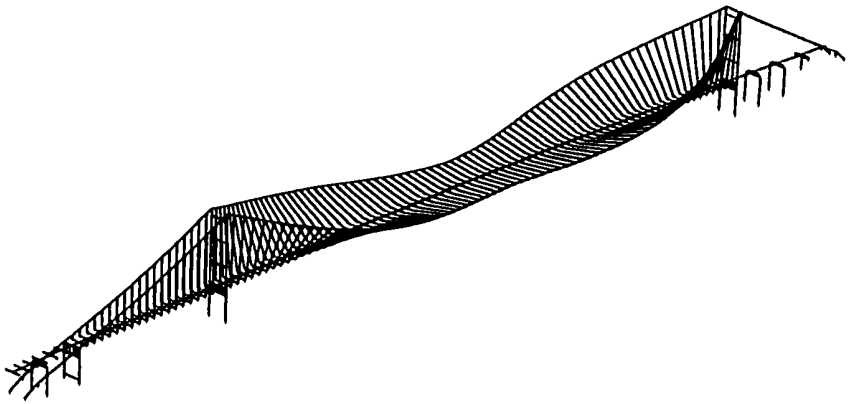

Mode No. 6 **f = 0.2104 Hz**

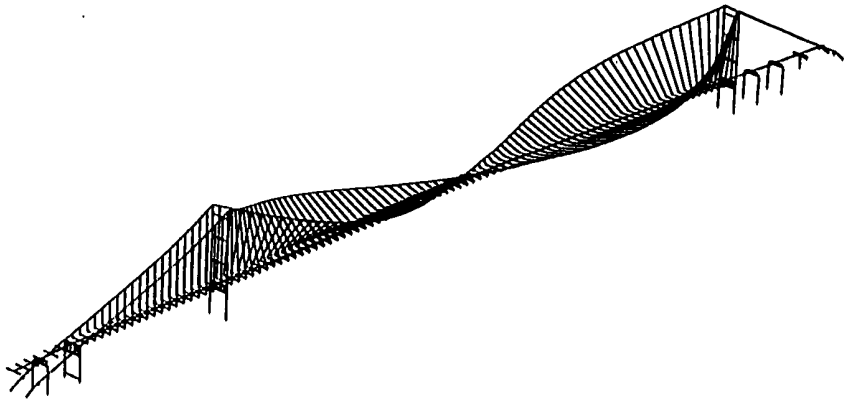

Mode No. 7 ***f*** **= 0.2305 Hz**

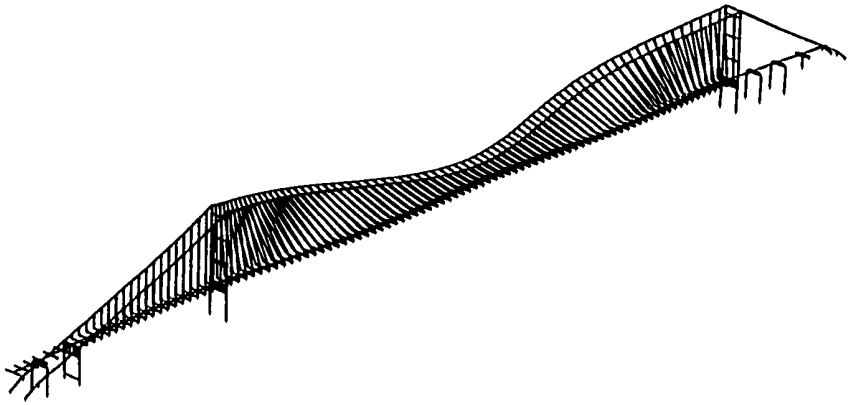

Mode No. 8 ***f*** **= 0.2324 Hz**

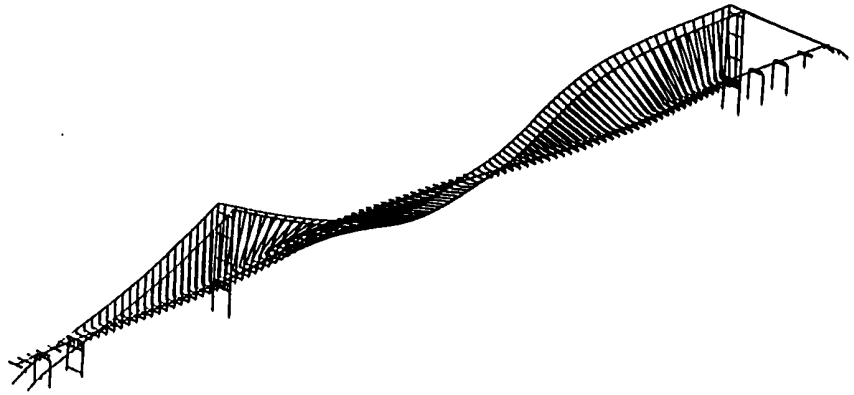

Mode No. 9 **f = 0.2401 Hz**

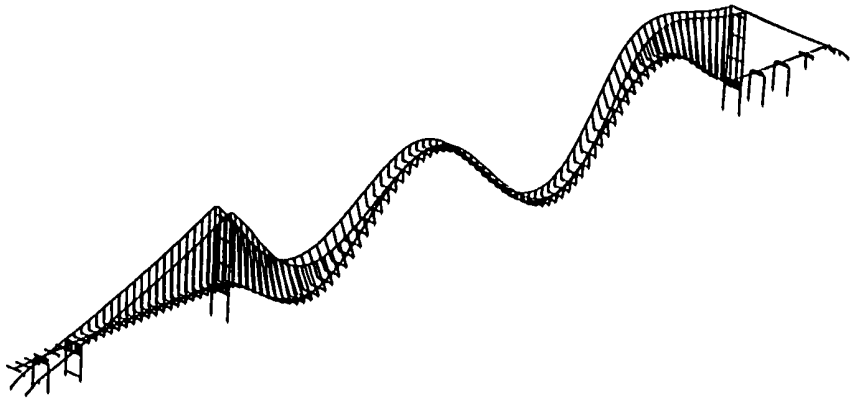

Mode No. 10 **f = 0.2448 Hz**

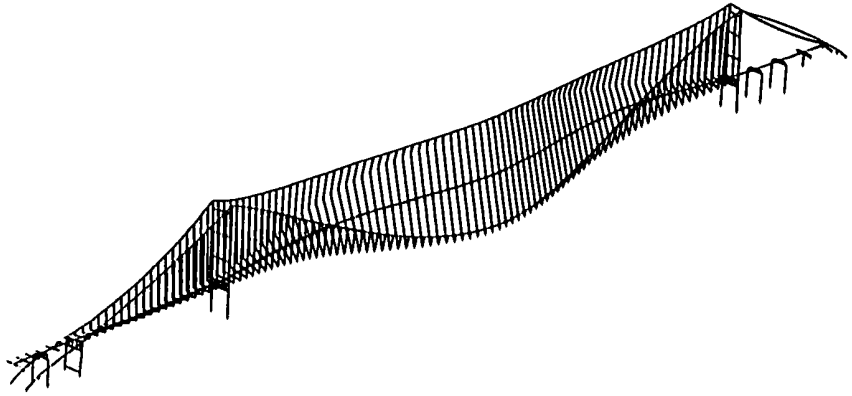

Mode No. 11 ***f*** **= 0.2713 Hz**

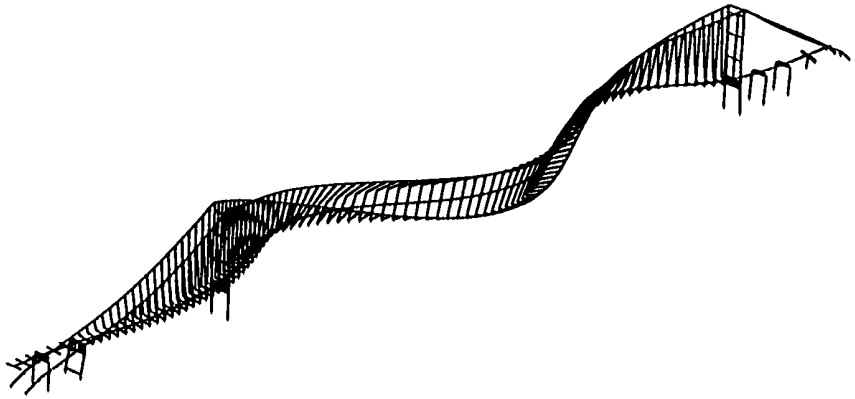

Mode No. 12 ***f*** **= 0.2851 Hz**

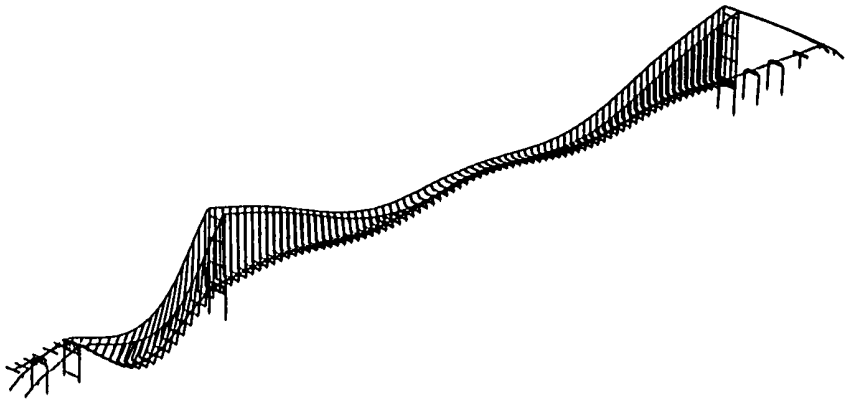

Mode No. 13 **f = 0.2945 Hz**

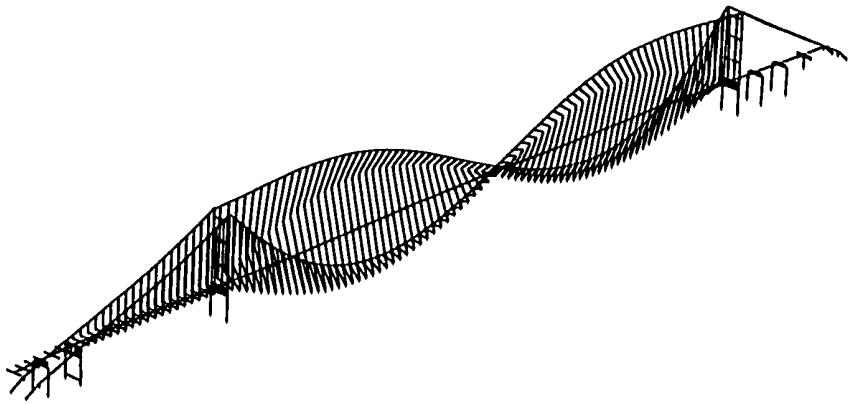

Mode No. 14 **f = 0.3106 Hz**

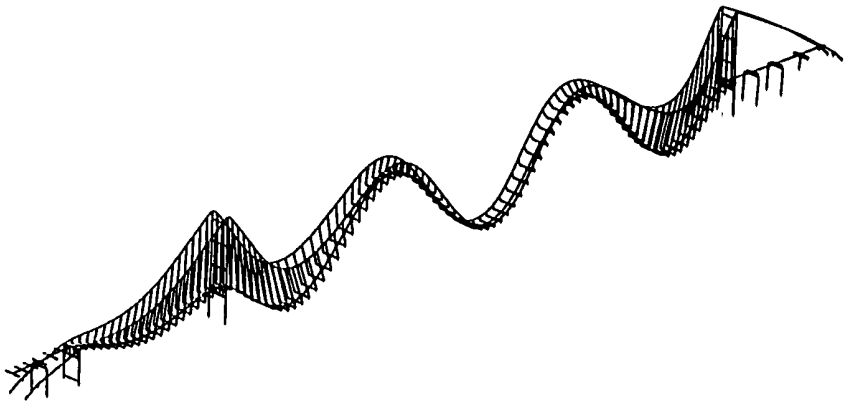

Mode No. 15 ***f*** **= 0.3246 Hz**

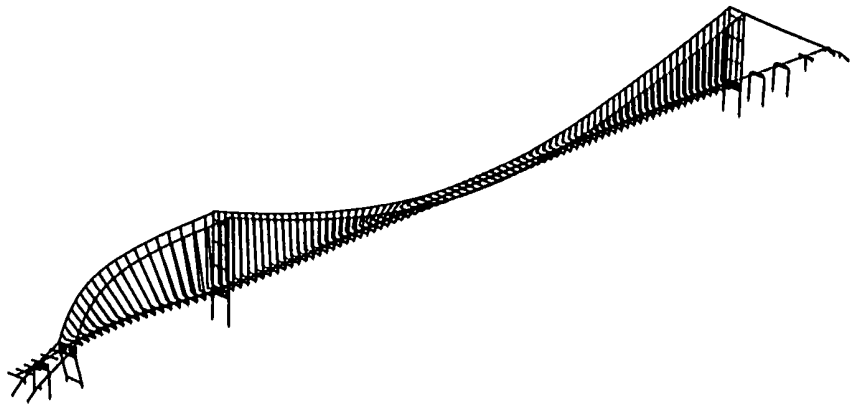

Mode No. 16 ***f*** **= 0.3331 Hz**

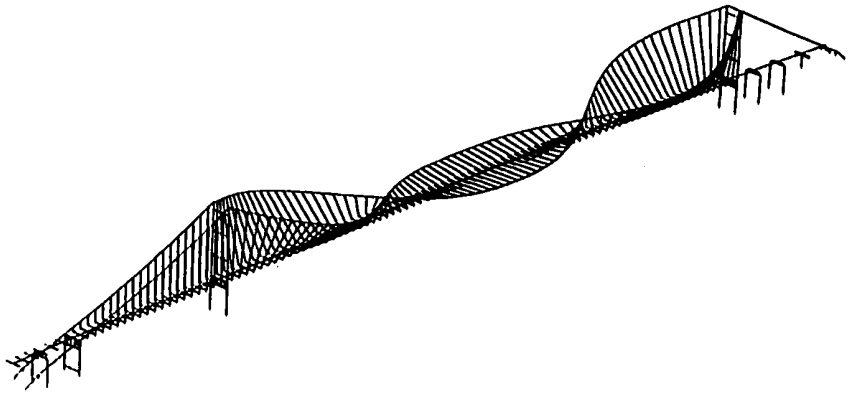

Mode No. 17 **f = 0.3404 Hz**

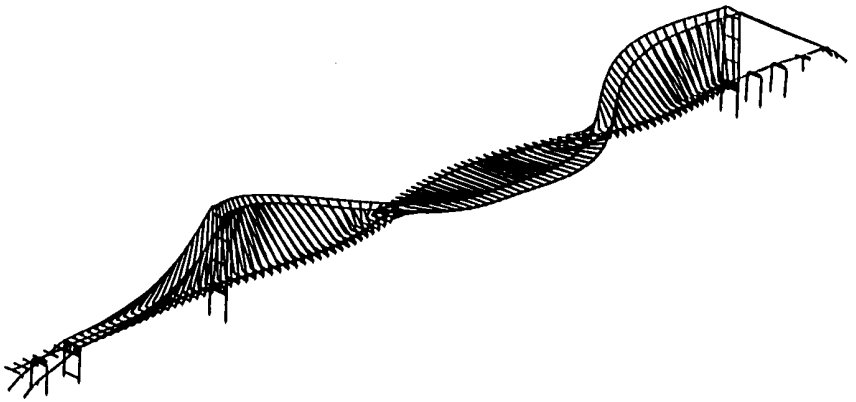

Mode No. 18 **f = 0.3651 Hz**

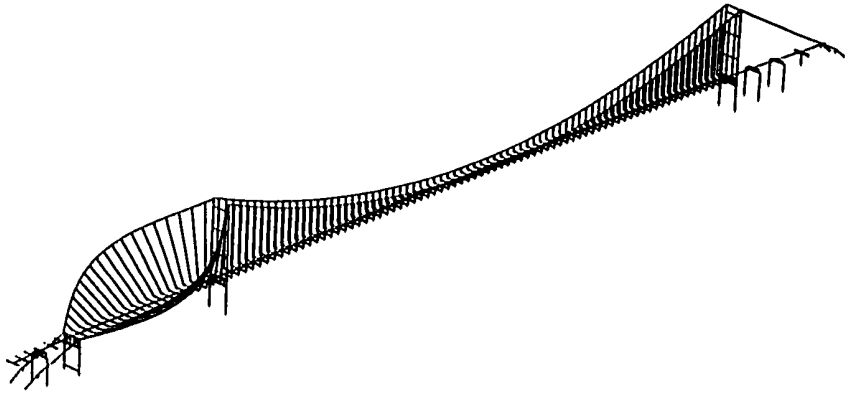

Mode No. 19 ***f*** **= 0.3671 Hz**

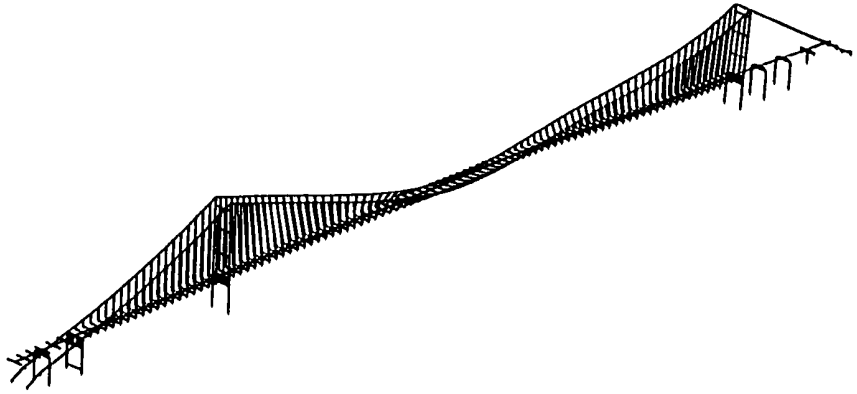

Mode No. 20 ***f*** **= 0.3800 Hz**

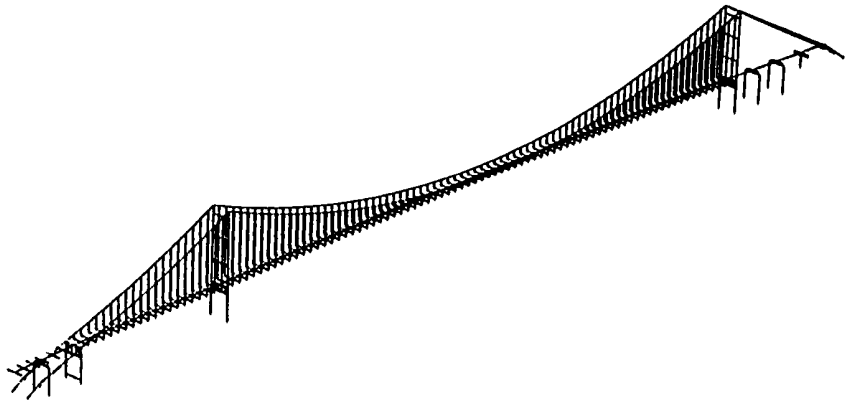

Mode No. 21 **f = 0.3933 Hz**

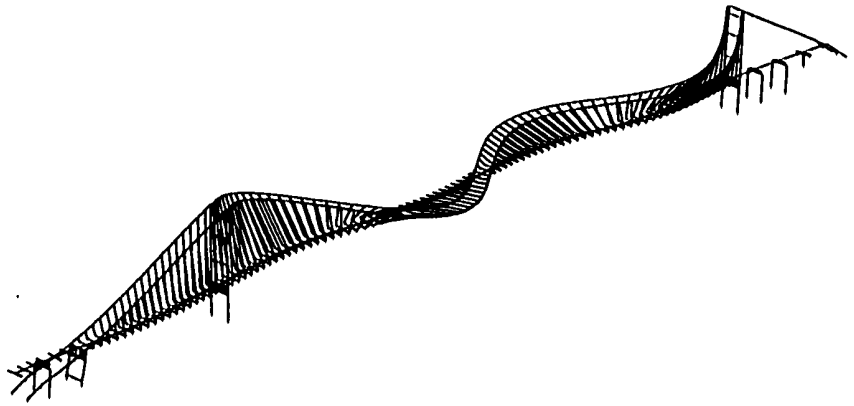

Mode No. 22 **f = 0.3960 Hz**

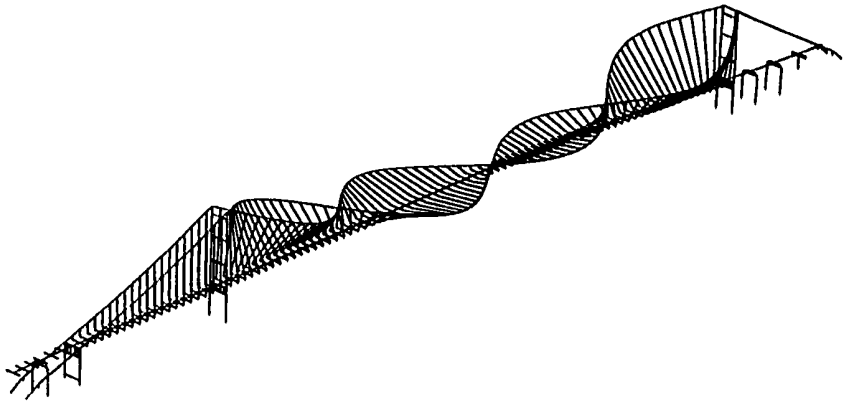

Mode No. 23 ***f*** **= 0.4040 Hz**

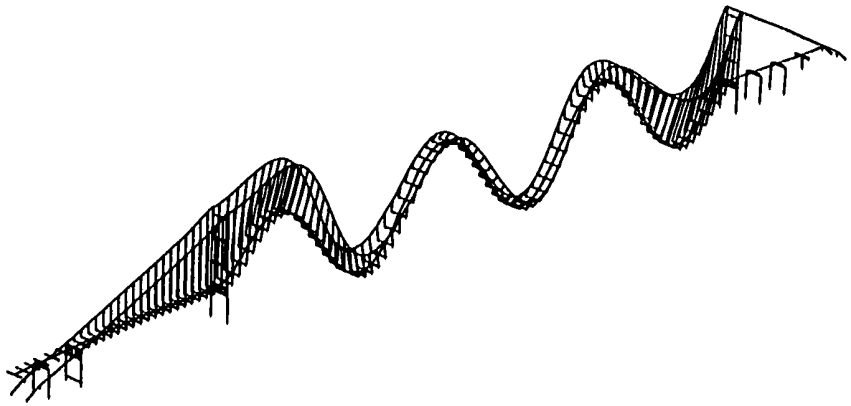

Mode No. 24 ***f*** **= 0.4060 Hz**

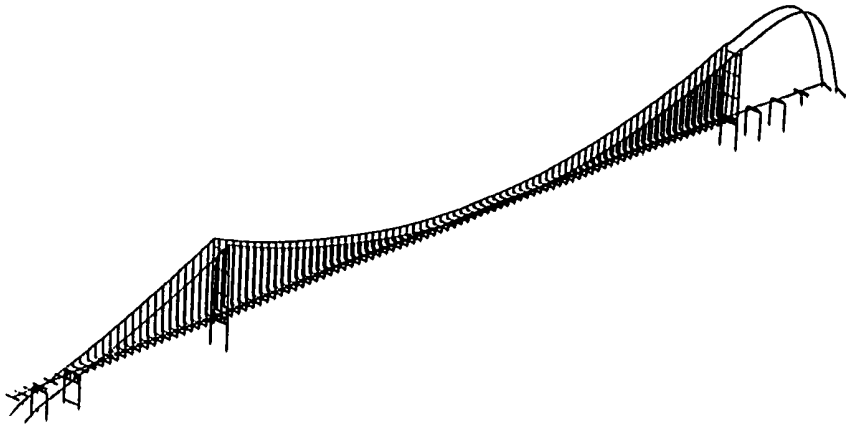

Mode No. 25 f = 0.4334 Hz

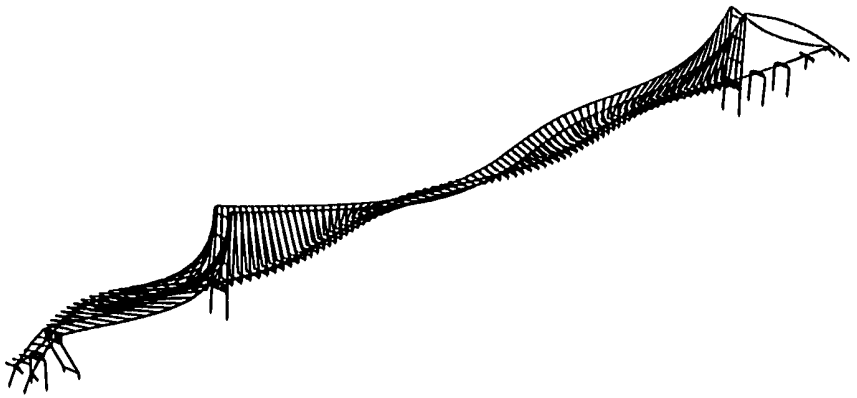

Mode No. 26 f = 0.4344 Hz

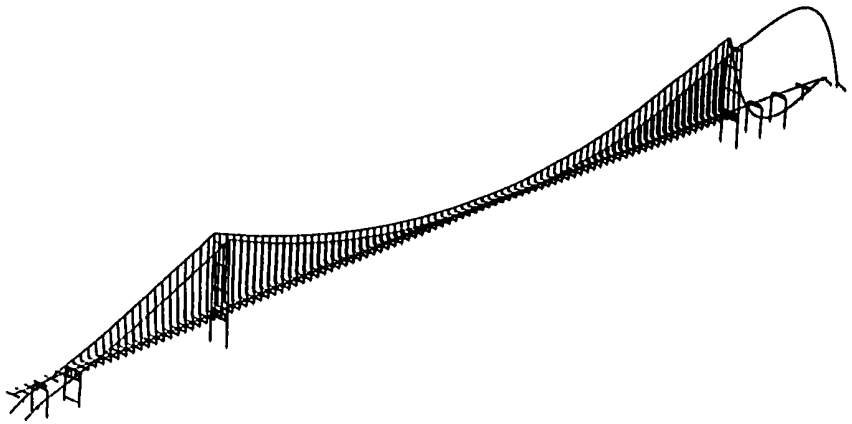

Mode No. 27 *f* = 0.4358 Hz

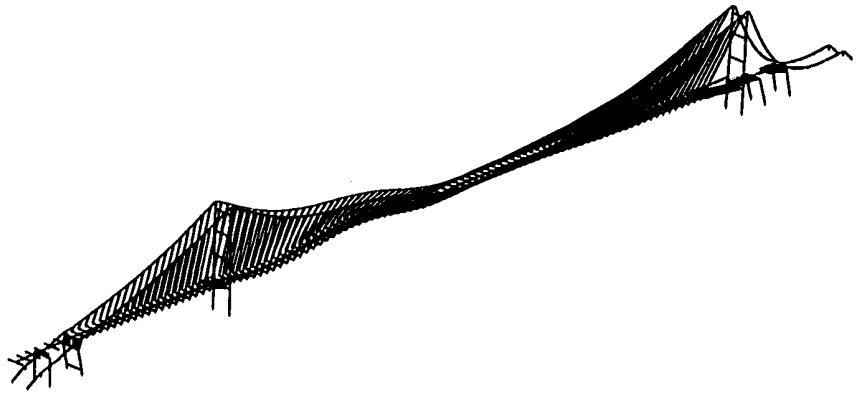

Mode No. 28 *f* = 0.4431 Hz

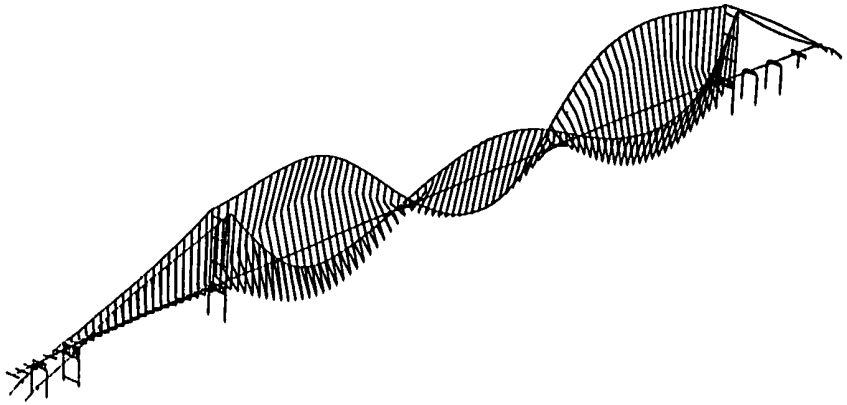

Mode No. 29 **f = 0.4755 Hz**

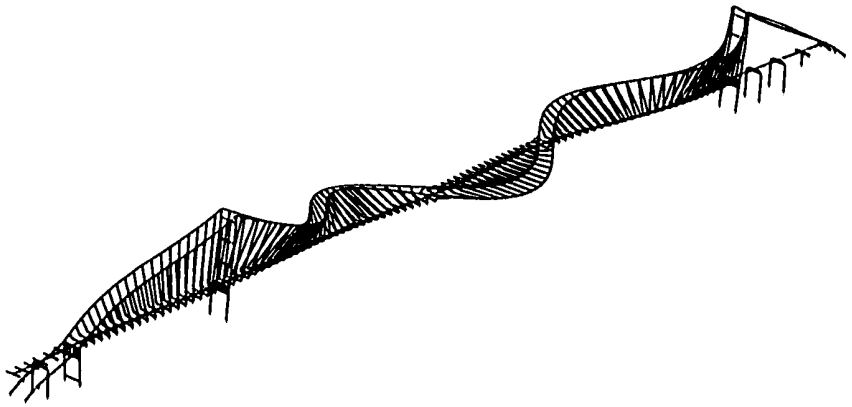

Mode No. 30 **f = 0.4832 Hz**

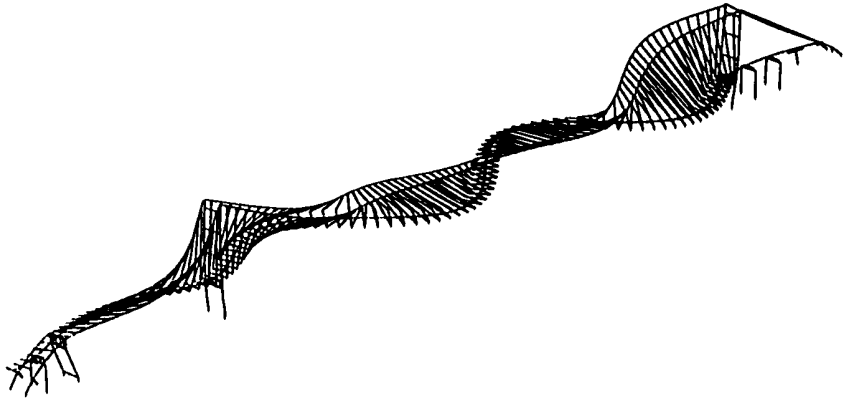

Mode No. 31 ***f*** **= 0.4892 Hz**

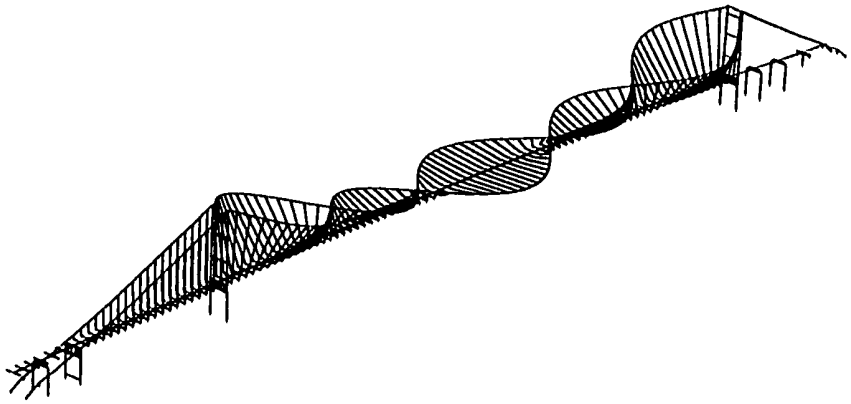

Mode No. 32 ***f*** **= 0.4964 Hz**

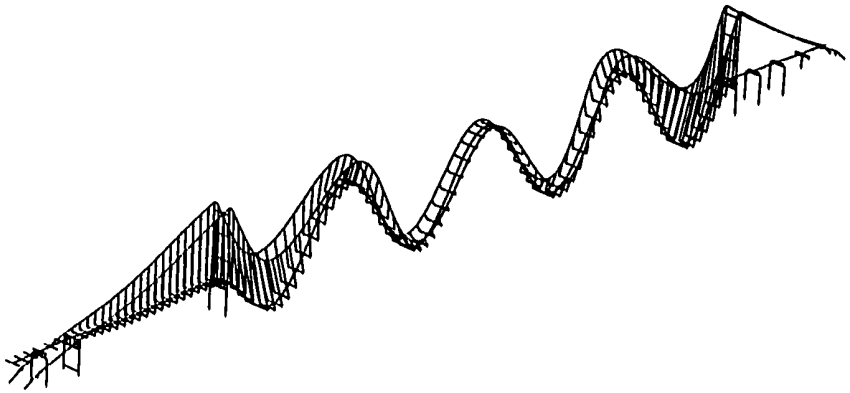

Mode No. 33 f = 0.4991 Hz

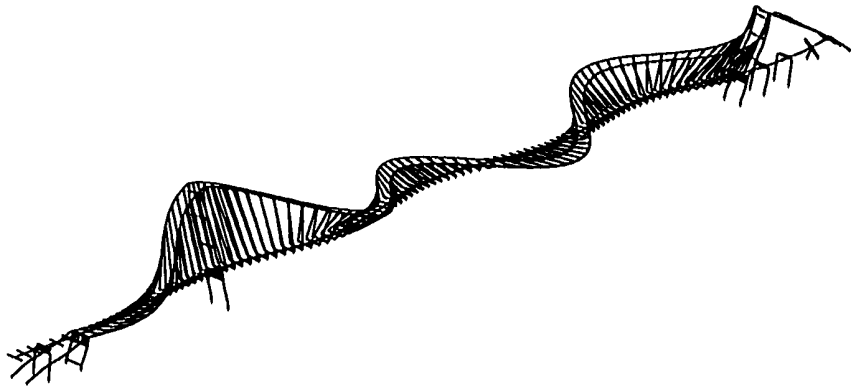

Mode No. 34 f = 0.5260 Hz

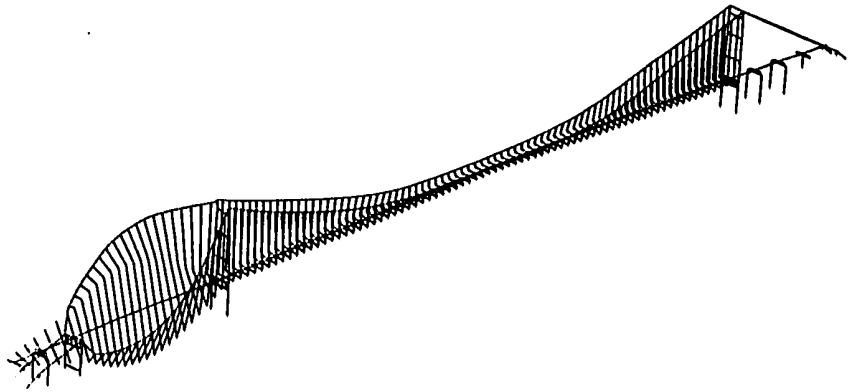

Mode No. 35 *f* = 0.5392 Hz

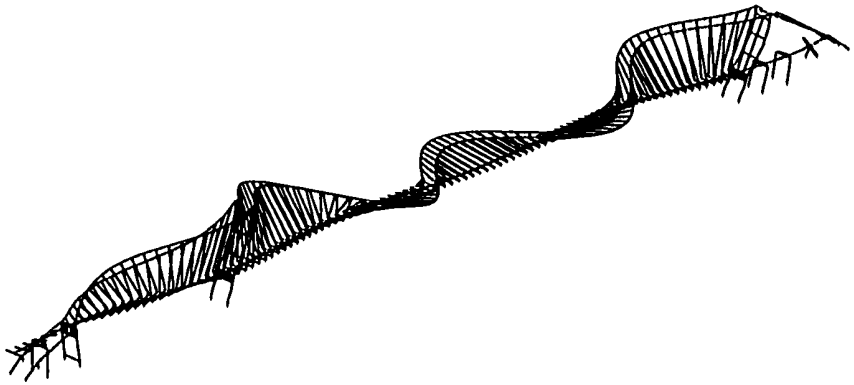

Mode No. 36 *f* = 0.5461 Hz

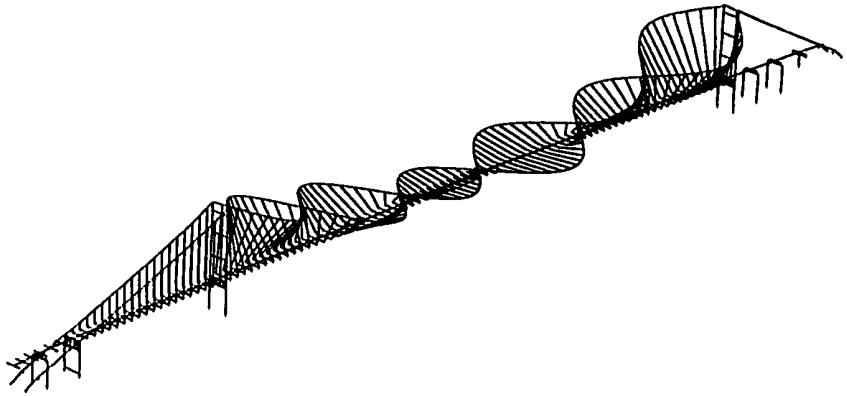

Mode No. 37 **f = 0.5798 Hz**

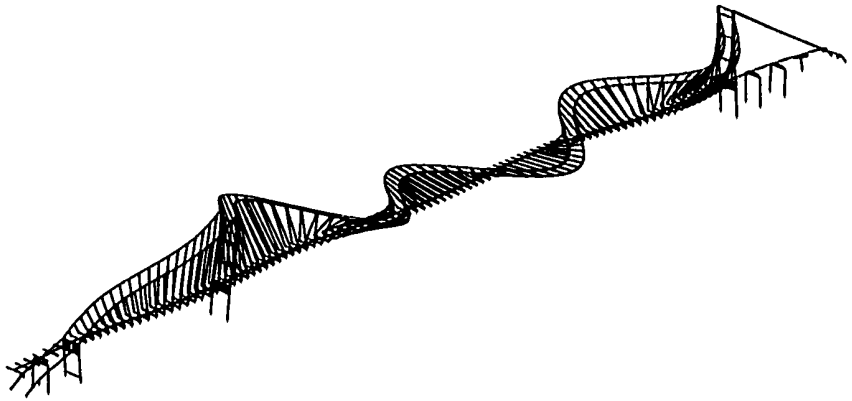

Mode No. 38 **f = 0.5943 Hz**

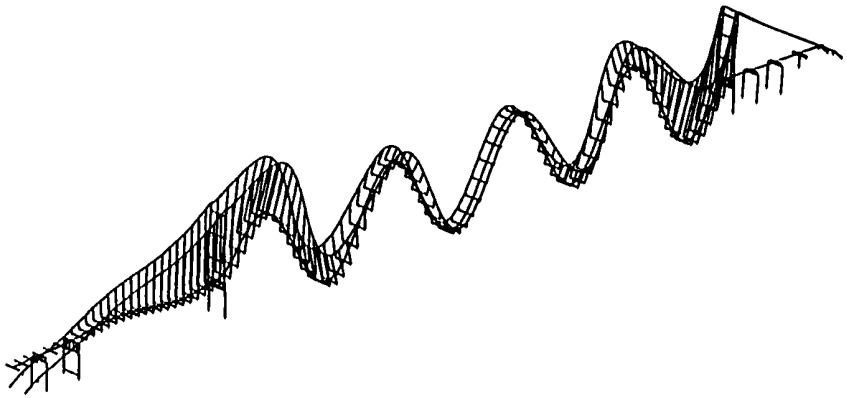

Mode No. 39 ***f*** **= 0.5989 Hz**

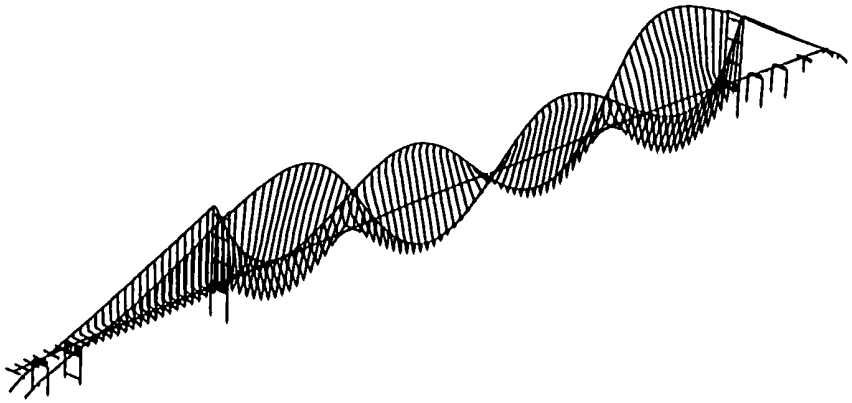

Mode No. 40 ***f*** **= 0.6162 Hz**

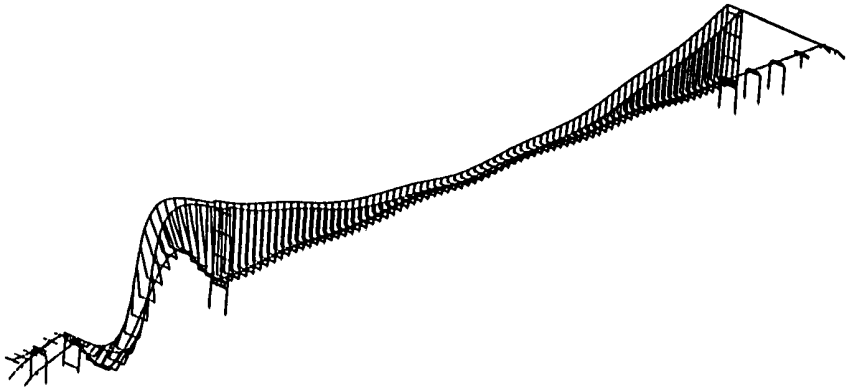

Mode No. 41 **f = 0.6480 Hz**

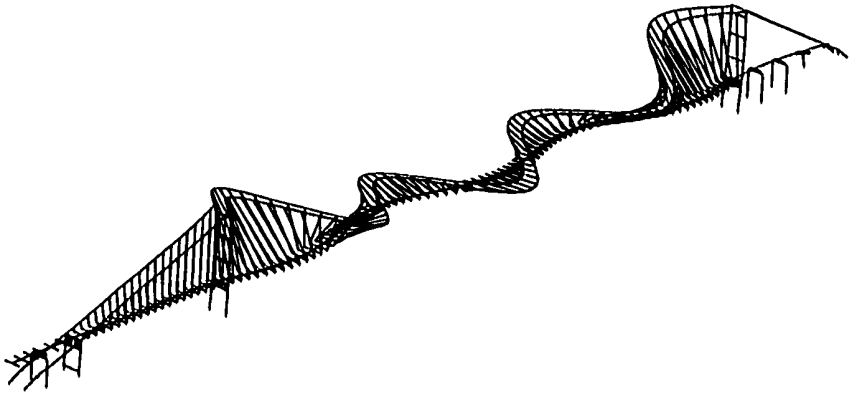

Mode No. 42 **f = 0.6686 Hz**

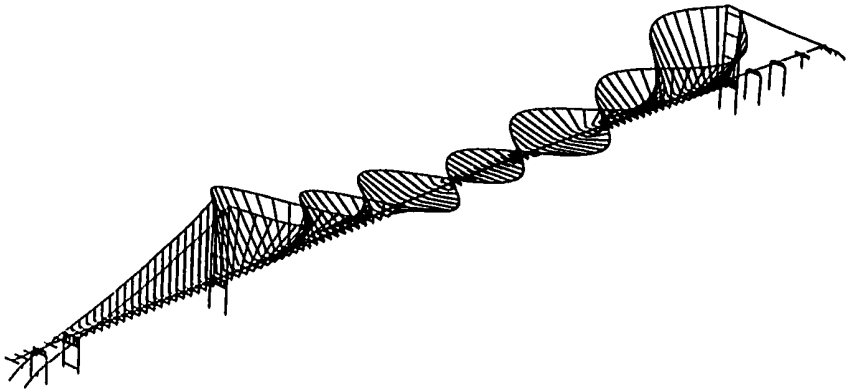

Mode No. 43 ***f*** **= 0.6698 Hz**

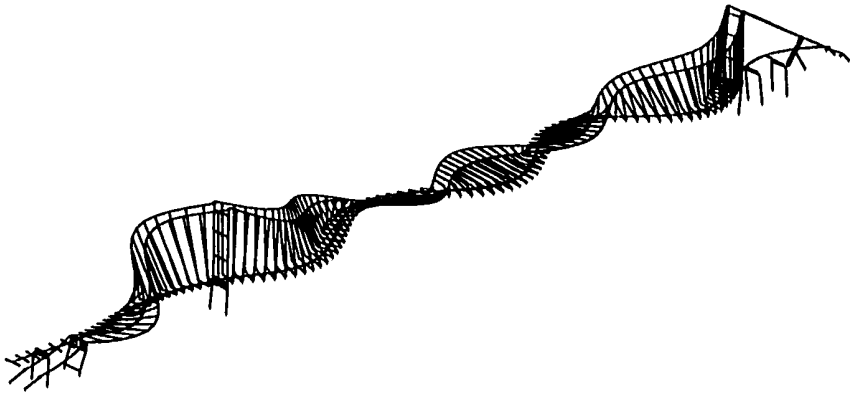

Mode No. 44 ***f*** **= 0.6954 Hz**

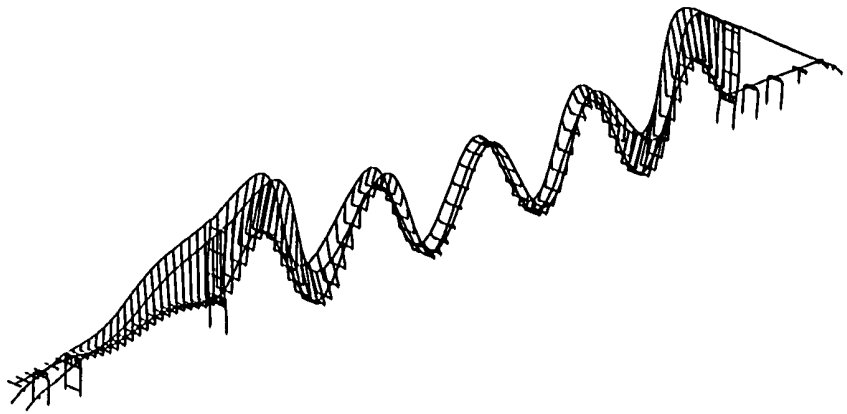

Mode No. 45 f = 0.7062 Hz

Appendix B

ELEMENTAL AEROELASTIC STIFFNESS AND DAMPING MATRICES

As shown in Figures 5-4a to 5-4h, there are totally eight types of the combination between the local reference coordinate *qph*-system and the local structural coordinate *xyz*-system. Thus, correspondingly, there are also eight types of the elemental aeroelastic stiffness matrix as Eqs.B-1a to B-1h, and eight types of the elemental aeroelastic damping matrix as Eqs.B-2a to B-2h, which are with respect to the local *xyz*-system.

$$
\mathbf{K}'^{se}_{e,k} = \left[\begin{array}{c|c|c|c|c|c|c|c|c|c|c|c}
0 & 0 & 0 & 0 & 0 & 0 & 0 & 0 & 0 & 0 & 0 & 0 \\
\hline
0 & -\frac{13}{35}k_{10} & \frac{13}{35}k_{9} & -\frac{7}{20}k_{11} & -\frac{11}{210}k_{12} & -\frac{11}{210}k_{13} & 0 & -\frac{9}{70}k_{10} & \frac{9}{70}k_{9} & -\frac{3}{20}k_{11} & \frac{13}{420}k_{12} & \frac{13}{420}k_{13} \\
\hline
0 & \frac{13}{35}k_{2} & -\frac{13}{35}k_{1} & \frac{7}{20}k_{3} & \frac{11}{210}k_{4} & \frac{11}{210}k_{5} & 0 & \frac{9}{70}k_{2} & -\frac{9}{70}k_{1} & \frac{3}{20}k_{3} & -\frac{13}{420}k_{4} & -\frac{13}{420}k_{5} \\
\hline
0 & -\frac{7}{20}k_{18} & \frac{7}{20}k_{17} & -\frac{1}{3}k_{19} & -\frac{1}{20}k_{20} & -\frac{1}{20}k_{21} & 0 & -\frac{3}{20}k_{18} & \frac{3}{20}k_{17} & -\frac{1}{6}k_{19} & \frac{1}{30}k_{20} & \frac{1}{30}k_{21} \\
\hline
0 & -\frac{11}{210}k_{5} & \frac{11}{210}k_{4} & -\frac{1}{20}k_{6} & -\frac{1}{105}k_{7} & -\frac{1}{105}k_{8} & 0 & -\frac{13}{420}k_{5} & \frac{13}{420}k_{4} & -\frac{1}{30}k_{6} & \frac{1}{140}k_{7} & \frac{1}{140}k_{8} \\
\hline
0 & -\frac{11}{210}k_{13} & \frac{11}{210}k_{12} & -\frac{1}{20}k_{14} & -\frac{1}{105}k_{15} & -\frac{1}{105}k_{16} & 0 & -\frac{13}{420}k_{13} & \frac{13}{420}k_{12} & -\frac{1}{30}k_{14} & \frac{1}{140}k_{15} & \frac{1}{140}k_{16} \\
\hline
0 & 0 & 0 & 0 & 0 & 0 & 0 & 0 & 0 & 0 & 0 & 0 \\
\hline
0 & -\frac{9}{70}k_{10} & \frac{9}{70}k_{9} & -\frac{3}{20}k_{11} & -\frac{13}{420}k_{12} & -\frac{13}{420}k_{13} & 0 & -\frac{13}{35}k_{10} & \frac{13}{35}k_{9} & -\frac{7}{20}k_{11} & \frac{11}{210}k_{12} & \frac{11}{210}k_{13} \\
\hline
0 & \frac{9}{70}k_{2} & -\frac{9}{70}k_{1} & \frac{3}{20}k_{3} & \frac{13}{420}k_{4} & \frac{13}{420}k_{5} & 0 & \frac{13}{35}k_{2} & -\frac{13}{35}k_{1} & \frac{7}{20}k_{3} & -\frac{11}{210}k_{4} & -\frac{11}{210}k_{5} \\
\hline
0 & -\frac{3}{20}k_{18} & \frac{3}{20}k_{17} & -\frac{1}{6}k_{19} & -\frac{1}{30}k_{20} & -\frac{1}{30}k_{21} & 0 & -\frac{7}{20}k_{18} & \frac{7}{20}k_{17} & -\frac{1}{3}k_{19} & \frac{1}{20}k_{20} & \frac{1}{20}k_{21} \\
\hline
0 & \frac{13}{420}k_{5} & -\frac{13}{420}k_{4} & \frac{1}{30}k_{6} & \frac{1}{140}k_{7} & \frac{1}{140}k_{8} & 0 & \frac{11}{210}k_{5} & -\frac{11}{210}k_{4} & \frac{1}{20}k_{6} & -\frac{1}{105}k_{7} & -\frac{1}{105}k_{8} \\
\hline
0 & \frac{13}{420}k_{13} & -\frac{13}{420}k_{12} & \frac{1}{30}k_{14} & \frac{1}{140}k_{15} & \frac{1}{140}k_{16} & 0 & \frac{11}{210}k_{13} & -\frac{11}{210}k_{12} & \frac{1}{20}k_{14} & -\frac{1}{105}k_{15} & -\frac{1}{105}k_{16}
\end{array}\right]_k \qquad \text{(B-1a)}
$$

$$
\mathbf{K}_{e,k}^{\prime se} = \left[\begin{array}{c|c|c|c|c|c|c|c|c|c|c|c}
0 & 0 & 0 & 0 & 0 & 0 & 0 & 0 & 0 & 0 & 0 & 0 \\
0 & -\frac{13}{35}k_{10} & \frac{13}{35}k_{9} & \frac{7}{20}k_{11} & -\frac{11}{210}k_{12} & -\frac{11}{210}k_{13} & 0 & -\frac{9}{70}k_{10} & \frac{9}{70}k_{9} & \frac{3}{20}k_{11} & \frac{13}{420}k_{12} & \frac{13}{420}k_{13} \\
0 & \frac{13}{35}k_{2} & -\frac{13}{35}k_{1} & -\frac{7}{20}k_{3} & \frac{11}{210}k_{4} & \frac{11}{210}k_{5} & 0 & \frac{9}{70}k_{2} & -\frac{9}{70}k_{1} & -\frac{3}{20}k_{3} & -\frac{13}{420}k_{4} & -\frac{13}{420}k_{5} \\
0 & \frac{7}{20}k_{18} & -\frac{7}{20}k_{17} & -\frac{1}{3}k_{19} & \frac{1}{20}k_{20} & \frac{1}{20}k_{21} & 0 & \frac{3}{20}k_{18} & -\frac{3}{20}k_{17} & -\frac{1}{6}k_{19} & -\frac{1}{30}k_{20} & -\frac{1}{30}k_{21} \\
0 & -\frac{11}{210}k_{5} & \frac{11}{210}k_{4} & \frac{1}{20}k_{6} & -\frac{1}{105}k_{7} & -\frac{1}{105}k_{8} & 0 & -\frac{13}{420}k_{5} & \frac{13}{420}k_{4} & \frac{1}{30}k_{6} & \frac{1}{140}k_{7} & \frac{1}{140}k_{8} \\
0 & -\frac{11}{210}k_{13} & \frac{11}{210}k_{12} & \frac{1}{20}k_{14} & -\frac{1}{105}k_{15} & -\frac{1}{105}k_{16} & 0 & -\frac{13}{420}k_{13} & \frac{13}{420}k_{12} & \frac{1}{30}k_{14} & \frac{1}{140}k_{15} & \frac{1}{140}k_{16} \\
0 & 0 & 0 & 0 & 0 & 0 & 0 & 0 & 0 & 0 & 0 & 0 \\
0 & -\frac{9}{70}k_{10} & \frac{9}{70}k_{9} & \frac{3}{20}k_{11} & -\frac{13}{420}k_{12} & -\frac{13}{420}k_{13} & 0 & -\frac{13}{35}k_{10} & \frac{13}{35}k_{9} & \frac{7}{20}k_{11} & \frac{11}{210}k_{12} & \frac{11}{210}k_{13} \\
0 & \frac{9}{70}k_{2} & -\frac{9}{70}k_{1} & -\frac{3}{20}k_{3} & \frac{13}{420}k_{4} & \frac{13}{420}k_{5} & 0 & \frac{13}{35}k_{2} & -\frac{13}{35}k_{1} & -\frac{7}{20}k_{3} & -\frac{11}{210}k_{4} & -\frac{11}{210}k_{5} \\
0 & \frac{3}{20}k_{18} & -\frac{3}{20}k_{17} & -\frac{1}{6}k_{19} & \frac{1}{30}k_{20} & \frac{1}{30}k_{21} & 0 & \frac{7}{20}k_{18} & -\frac{7}{20}k_{17} & -\frac{1}{3}k_{19} & -\frac{1}{20}k_{20} & -\frac{1}{20}k_{21} \\
0 & \frac{13}{420}k_{5} & -\frac{13}{420}k_{4} & -\frac{1}{30}k_{6} & \frac{1}{140}k_{7} & \frac{1}{140}k_{8} & 0 & \frac{11}{210}k_{5} & -\frac{11}{210}k_{4} & -\frac{1}{20}k_{6} & -\frac{1}{105}k_{7} & -\frac{1}{105}k_{8} \\
0 & \frac{13}{420}k_{13} & -\frac{13}{420}k_{12} & -\frac{1}{30}k_{14} & \frac{1}{140}k_{15} & \frac{1}{140}k_{16} & 0 & \frac{11}{210}k_{13} & -\frac{11}{210}k_{12} & -\frac{1}{20}k_{14} & -\frac{1}{105}k_{15} & -\frac{1}{105}k_{16}
\end{array}\right]_k \qquad \text{(B-1b)}
$$

$$
\mathbf{K}^{ne}_{e,k} = \begin{bmatrix}
0 & 0 & 0 & 0 & 0 & 0 & 0 & 0 & 0 & 0 & 0 & 0 \\
0 & -\frac{13}{35}k_{10} & -\frac{13}{35}k_{9} & \frac{7}{20}k_{11} & \frac{11}{210}k_{12} & -\frac{11}{210}k_{13} & 0 & -\frac{9}{70}k_{10} & -\frac{9}{70}k_{9} & \frac{3}{20}k_{11} & -\frac{13}{420}k_{12} & \frac{13}{420}k_{13} \\
0 & -\frac{13}{35}k_{2} & -\frac{13}{35}k_{1} & \frac{7}{20}k_{3} & \frac{11}{210}k_{4} & -\frac{11}{210}k_{5} & 0 & -\frac{9}{70}k_{2} & -\frac{9}{70}k_{1} & \frac{3}{20}k_{3} & -\frac{13}{420}k_{4} & \frac{13}{420}k_{5} \\
0 & \frac{7}{20}k_{18} & \frac{7}{20}k_{17} & -\frac{1}{3}k_{19} & -\frac{1}{20}k_{20} & \frac{1}{20}k_{21} & 0 & \frac{3}{20}k_{18} & \frac{3}{20}k_{17} & -\frac{1}{6}k_{19} & \frac{1}{30}k_{20} & -\frac{1}{30}k_{21} \\
0 & \frac{11}{210}k_{5} & \frac{11}{210}k_{4} & -\frac{1}{20}k_{6} & -\frac{1}{105}k_{7} & \frac{1}{105}k_{8} & 0 & \frac{13}{420}k_{5} & \frac{13}{420}k_{4} & -\frac{1}{30}k_{6} & \frac{1}{140}k_{7} & -\frac{1}{140}k_{8} \\
0 & -\frac{11}{210}k_{13} & -\frac{11}{210}k_{12} & \frac{1}{20}k_{14} & \frac{1}{105}k_{15} & -\frac{1}{105}k_{16} & 0 & -\frac{13}{420}k_{13} & -\frac{13}{420}k_{12} & \frac{1}{30}k_{14} & -\frac{1}{140}k_{15} & \frac{1}{140}k_{16} \\
0 & 0 & 0 & 0 & 0 & 0 & 0 & 0 & 0 & 0 & 0 & 0 \\
0 & -\frac{9}{70}k_{10} & -\frac{9}{70}k_{9} & \frac{3}{20}k_{11} & \frac{13}{420}k_{12} & -\frac{13}{420}k_{13} & 0 & -\frac{13}{35}k_{10} & -\frac{13}{35}k_{9} & \frac{7}{20}k_{11} & -\frac{11}{210}k_{12} & \frac{11}{210}k_{13} \\
0 & -\frac{9}{70}k_{2} & -\frac{9}{70}k_{1} & \frac{3}{20}k_{3} & \frac{13}{420}k_{4} & -\frac{13}{420}k_{5} & 0 & -\frac{13}{35}k_{2} & -\frac{13}{35}k_{1} & \frac{7}{20}k_{3} & -\frac{11}{210}k_{4} & \frac{11}{210}k_{5} \\
0 & \frac{3}{20}k_{18} & \frac{3}{20}k_{17} & -\frac{1}{6}k_{19} & -\frac{1}{30}k_{20} & \frac{1}{30}k_{21} & 0 & \frac{7}{20}k_{18} & \frac{7}{20}k_{17} & -\frac{1}{3}k_{19} & \frac{1}{20}k_{20} & -\frac{1}{20}k_{21} \\
0 & -\frac{13}{420}k_{5} & -\frac{13}{420}k_{4} & \frac{1}{30}k_{6} & \frac{1}{140}k_{7} & -\frac{1}{140}k_{8} & 0 & -\frac{11}{210}k_{5} & -\frac{11}{210}k_{4} & \frac{1}{20}k_{6} & -\frac{1}{105}k_{7} & \frac{1}{105}k_{8} \\
0 & \frac{13}{420}k_{13} & \frac{13}{420}k_{12} & -\frac{1}{30}k_{14} & -\frac{1}{140}k_{15} & \frac{1}{140}k_{16} & 0 & \frac{11}{210}k_{13} & \frac{11}{210}k_{12} & -\frac{1}{20}k_{14} & \frac{1}{105}k_{15} & -\frac{1}{105}k_{16}
\end{bmatrix}_{k} \qquad \text{(B-1c)}
$$

$$
\mathbf{K}_{e,k}^{\prime se} = \left[\begin{array}{c|c|c|c|c|c|c|c|c|c|c|c}
0 & 0 & 0 & 0 & 0 & 0 & 0 & 0 & 0 & 0 & 0 & 0 \\
0 & -\frac{13}{35}k_{10} & -\frac{13}{35}k_{9} & -\frac{7}{20}k_{11} & \frac{11}{210}k_{12} & -\frac{11}{210}k_{13} & 0 & -\frac{9}{70}k_{10} & -\frac{9}{70}k_{9} & -\frac{3}{20}k_{11} & -\frac{13}{420}k_{12} & \frac{13}{420}k_{13} \\
0 & -\frac{13}{35}k_{2} & -\frac{13}{35}k_{1} & -\frac{7}{20}k_{3} & \frac{11}{210}k_{4} & -\frac{11}{210}k_{5} & 0 & -\frac{9}{70}k_{2} & -\frac{9}{70}k_{1} & -\frac{3}{20}k_{3} & -\frac{13}{420}k_{4} & \frac{13}{420}k_{5} \\
0 & -\frac{7}{20}k_{18} & -\frac{7}{20}k_{17} & -\frac{1}{3}k_{19} & \frac{1}{20}k_{20} & -\frac{1}{20}k_{21} & 0 & -\frac{3}{20}k_{18} & -\frac{3}{20}k_{17} & -\frac{1}{6}k_{19} & -\frac{1}{30}k_{20} & \frac{1}{30}k_{21} \\
0 & \frac{11}{210}k_{5} & \frac{11}{210}k_{4} & \frac{1}{20}k_{6} & -\frac{1}{105}k_{7} & \frac{1}{105}k_{8} & 0 & \frac{13}{420}k_{5} & \frac{13}{420}k_{4} & \frac{1}{30}k_{6} & \frac{1}{140}k_{7} & -\frac{1}{140}k_{8} \\
0 & -\frac{11}{210}k_{13} & -\frac{11}{210}k_{12} & -\frac{1}{20}k_{14} & \frac{1}{105}k_{15} & -\frac{1}{105}k_{16} & 0 & -\frac{13}{420}k_{13} & -\frac{13}{420}k_{12} & -\frac{1}{30}k_{14} & -\frac{1}{140}k_{15} & \frac{1}{140}k_{16} \\
0 & 0 & 0 & 0 & 0 & 0 & 0 & 0 & 0 & 0 & 0 & 0 \\
0 & -\frac{9}{70}k_{10} & -\frac{9}{70}k_{9} & -\frac{3}{20}k_{11} & \frac{13}{420}k_{12} & -\frac{13}{420}k_{13} & 0 & -\frac{13}{35}k_{10} & -\frac{13}{35}k_{9} & -\frac{7}{20}k_{11} & -\frac{11}{210}k_{12} & \frac{11}{210}k_{13} \\
0 & -\frac{9}{70}k_{2} & -\frac{9}{70}k_{1} & -\frac{3}{20}k_{3} & \frac{13}{420}k_{4} & -\frac{13}{420}k_{5} & 0 & -\frac{13}{35}k_{2} & -\frac{13}{35}k_{1} & -\frac{7}{20}k_{3} & -\frac{11}{210}k_{4} & \frac{11}{210}k_{5} \\
0 & -\frac{3}{20}k_{18} & -\frac{3}{20}k_{17} & -\frac{1}{6}k_{19} & \frac{1}{30}k_{20} & -\frac{1}{30}k_{21} & 0 & -\frac{7}{20}k_{18} & -\frac{7}{20}k_{17} & -\frac{1}{3}k_{19} & -\frac{1}{20}k_{20} & \frac{1}{20}k_{21} \\
0 & -\frac{13}{420}k_{5} & -\frac{13}{420}k_{4} & -\frac{1}{30}k_{6} & \frac{1}{140}k_{7} & -\frac{1}{140}k_{8} & 0 & -\frac{11}{210}k_{5} & -\frac{11}{210}k_{4} & -\frac{1}{20}k_{6} & -\frac{1}{105}k_{7} & \frac{1}{105}k_{8} \\
0 & \frac{13}{420}k_{13} & \frac{13}{420}k_{12} & \frac{1}{30}k_{14} & -\frac{1}{140}k_{15} & \frac{1}{140}k_{16} & 0 & \frac{11}{210}k_{13} & \frac{11}{210}k_{12} & \frac{1}{20}k_{14} & \frac{1}{105}k_{15} & -\frac{1}{105}k_{16}
\end{array}\right]_k \qquad \text{(B-1d)}
$$

$$
\mathbf{K}'^{ve}_{e,k} = \left[\begin{array}{c|c|c|c|c|c|c|c|c|c|c|c}
0 & 0 & 0 & 0 & 0 & 0 & 0 & 0 & 0 & 0 & 0 & 0 \\
0 & -\frac{13}{35}k_1 & -\frac{13}{35}k_2 & -\frac{7}{20}k_3 & \frac{11}{210}k_5 & -\frac{11}{210}k_4 & 0 & -\frac{9}{70}k_1 & -\frac{9}{70}k_2 & -\frac{3}{20}k_3 & -\frac{13}{420}k_5 & \frac{13}{420}k_4 \\
0 & -\frac{13}{35}k_9 & -\frac{13}{35}k_{10} & -\frac{7}{20}k_{11} & \frac{11}{210}k_{13} & -\frac{11}{210}k_{12} & 0 & -\frac{9}{70}k_9 & -\frac{9}{70}k_{10} & -\frac{3}{20}k_{11} & -\frac{13}{420}k_{13} & \frac{13}{420}k_{12} \\
0 & -\frac{7}{20}k_{17} & -\frac{7}{20}k_{18} & -\frac{1}{3}k_{19} & \frac{1}{20}k_{21} & -\frac{1}{20}k_{20} & 0 & -\frac{3}{20}k_{17} & -\frac{3}{20}k_{18} & -\frac{1}{6}k_{19} & -\frac{1}{30}k_{21} & \frac{1}{30}k_{20} \\
0 & \frac{11}{210}k_{12} & \frac{11}{210}k_{13} & \frac{1}{20}k_{14} & -\frac{1}{105}k_{16} & \frac{1}{105}k_{15} & 0 & \frac{13}{420}k_{12} & \frac{13}{420}k_{13} & \frac{1}{30}k_{14} & \frac{1}{140}k_{16} & -\frac{1}{140}k_{15} \\
0 & -\frac{11}{210}k_4 & -\frac{11}{210}k_5 & -\frac{1}{20}k_6 & \frac{1}{105}k_8 & -\frac{1}{105}k_7 & 0 & -\frac{13}{420}k_4 & -\frac{13}{420}k_5 & -\frac{1}{30}k_6 & -\frac{1}{140}k_8 & \frac{1}{140}k_7 \\
0 & 0 & 0 & 0 & 0 & 0 & 0 & 0 & 0 & 0 & 0 & 0 \\
0 & -\frac{9}{70}k_1 & -\frac{9}{70}k_2 & -\frac{3}{20}k_3 & \frac{13}{420}k_5 & -\frac{13}{420}k_4 & 0 & -\frac{13}{35}k_1 & -\frac{13}{35}k_2 & -\frac{7}{20}k_3 & -\frac{11}{210}k_5 & \frac{11}{210}k_4 \\
0 & -\frac{9}{70}k_9 & -\frac{9}{70}k_{10} & -\frac{3}{20}k_{11} & \frac{13}{420}k_{13} & -\frac{13}{420}k_{12} & 0 & -\frac{13}{35}k_9 & -\frac{13}{35}k_{10} & -\frac{7}{20}k_{11} & -\frac{11}{210}k_{13} & \frac{11}{210}k_{12} \\
0 & -\frac{3}{20}k_{17} & -\frac{3}{20}k_{18} & -\frac{1}{6}k_{19} & \frac{1}{30}k_{21} & -\frac{1}{30}k_{20} & 0 & -\frac{7}{20}k_{17} & -\frac{7}{20}k_{18} & -\frac{1}{3}k_{19} & -\frac{1}{20}k_{21} & \frac{1}{20}k_{20} \\
0 & -\frac{13}{420}k_{12} & -\frac{13}{420}k_{13} & -\frac{1}{30}k_{14} & \frac{1}{140}k_{16} & -\frac{1}{140}k_{15} & 0 & -\frac{11}{210}k_{12} & -\frac{11}{210}k_{13} & -\frac{1}{20}k_{14} & -\frac{1}{105}k_{16} & \frac{1}{105}k_{15} \\
0 & \frac{13}{420}k_4 & \frac{13}{420}k_5 & \frac{1}{30}k_6 & -\frac{1}{140}k_8 & \frac{1}{140}k_7 & 0 & \frac{11}{210}k_4 & \frac{11}{210}k_5 & \frac{1}{20}k_6 & \frac{1}{105}k_8 & -\frac{1}{105}k_7
\end{array}\right]_k \qquad \text{(B-1e)}
$$

$$
\mathbf{K}_{e,k}^{\prime se} = \left[\begin{array}{c|c|c|c|c|c|c|c|c|c|c|c}
0 & 0 & 0 & 0 & 0 & 0 & 0 & 0 & 0 & 0 & 0 & 0 \\
0 & -\frac{13}{35}k_1 & -\frac{13}{35}k_2 & \frac{7}{20}k_3 & \frac{11}{210}k_5 & -\frac{11}{210}k_4 & 0 & -\frac{9}{70}k_1 & -\frac{9}{70}k_2 & \frac{3}{20}k_3 & -\frac{13}{420}k_5 & \frac{13}{420}k_4 \\
0 & -\frac{13}{35}k_9 & -\frac{13}{35}k_{10} & \frac{7}{20}k_{11} & \frac{11}{210}k_{13} & -\frac{11}{210}k_{12} & 0 & -\frac{9}{70}k_9 & -\frac{9}{70}k_{10} & \frac{3}{20}k_{11} & -\frac{13}{420}k_{13} & \frac{13}{420}k_{12} \\
0 & \frac{7}{20}k_{17} & \frac{7}{20}k_{18} & -\frac{1}{3}k_{19} & -\frac{1}{20}k_{21} & \frac{1}{20}k_{20} & 0 & \frac{3}{20}k_{17} & \frac{3}{20}k_{18} & -\frac{1}{6}k_{19} & \frac{1}{30}k_{21} & -\frac{1}{30}k_{20} \\
0 & \frac{11}{210}k_{12} & \frac{11}{210}k_{13} & -\frac{1}{20}k_{14} & -\frac{1}{105}k_{16} & \frac{1}{105}k_{15} & 0 & \frac{13}{420}k_{12} & \frac{13}{420}k_{13} & -\frac{1}{30}k_{14} & \frac{1}{140}k_{16} & -\frac{1}{140}k_{15} \\
0 & -\frac{11}{210}k_4 & -\frac{11}{210}k_5 & \frac{1}{20}k_6 & \frac{1}{105}k_8 & -\frac{1}{105}k_7 & 0 & -\frac{13}{420}k_4 & -\frac{13}{420}k_5 & \frac{1}{30}k_6 & -\frac{1}{140}k_8 & \frac{1}{140}k_7 \\
0 & 0 & 0 & 0 & 0 & 0 & 0 & 0 & 0 & 0 & 0 & 0 \\
0 & -\frac{9}{70}k_1 & -\frac{9}{70}k_2 & \frac{3}{20}k_3 & \frac{13}{420}k_5 & -\frac{13}{420}k_4 & 0 & -\frac{13}{35}k_1 & -\frac{13}{35}k_2 & \frac{7}{20}k_3 & -\frac{11}{210}k_5 & \frac{11}{210}k_4 \\
0 & -\frac{9}{70}k_9 & -\frac{9}{70}k_{10} & \frac{3}{20}k_{11} & \frac{13}{420}k_{13} & -\frac{13}{420}k_{12} & 0 & -\frac{13}{35}k_9 & -\frac{13}{35}k_{10} & \frac{7}{20}k_{11} & -\frac{11}{210}k_{13} & \frac{11}{210}k_{12} \\
0 & \frac{3}{20}k_{17} & \frac{3}{20}k_{18} & -\frac{1}{6}k_{19} & -\frac{1}{30}k_{21} & \frac{1}{30}k_{20} & 0 & \frac{7}{20}k_{17} & \frac{7}{20}k_{18} & -\frac{1}{3}k_{19} & \frac{1}{20}k_{21} & -\frac{1}{20}k_{20} \\
0 & -\frac{13}{420}k_{12} & -\frac{13}{420}k_{13} & \frac{1}{30}k_{14} & \frac{1}{140}k_{16} & -\frac{1}{140}k_{15} & 0 & -\frac{11}{210}k_{12} & -\frac{11}{210}k_{13} & \frac{1}{20}k_{14} & -\frac{1}{105}k_{16} & \frac{1}{105}k_{15} \\
0 & \frac{13}{420}k_4 & \frac{13}{420}k_5 & -\frac{1}{30}k_6 & -\frac{1}{140}k_8 & \frac{1}{140}k_7 & 0 & \frac{11}{210}k_4 & \frac{11}{210}k_5 & -\frac{1}{20}k_6 & \frac{1}{105}k_8 & -\frac{1}{105}k_7
\end{array}\right]_k \qquad \text{(B-1f)}
$$

$$
\mathbf{K}_{e,k}^{\prime se} = \left[\begin{array}{c|c|c|c|c|c|c|c|c|c|c|c}
0 & 0 & 0 & 0 & 0 & 0 & 0 & 0 & 0 & 0 & 0 & 0 \\
0 & -\frac{13}{35}k_1 & \frac{13}{35}k_2 & -\frac{7}{20}k_3 & -\frac{11}{210}k_5 & -\frac{11}{210}k_4 & 0 & -\frac{9}{70}k_1 & \frac{9}{70}k_2 & -\frac{3}{20}k_3 & \frac{13}{420}k_5 & \frac{13}{420}k_4 \\
0 & \frac{13}{35}k_9 & -\frac{13}{35}k_{10} & \frac{7}{20}k_{11} & \frac{11}{210}k_{13} & \frac{11}{210}k_{12} & 0 & \frac{9}{70}k_9 & -\frac{9}{70}k_{10} & \frac{3}{20}k_{11} & -\frac{13}{420}k_{13} & -\frac{13}{420}k_{12} \\
0 & -\frac{7}{20}k_{17} & \frac{7}{20}k_{18} & -\frac{1}{3}k_{19} & -\frac{1}{20}k_{21} & -\frac{1}{20}k_{20} & 0 & -\frac{3}{20}k_{17} & \frac{3}{20}k_{18} & -\frac{1}{6}k_{19} & \frac{1}{30}k_{21} & \frac{1}{30}k_{20} \\
0 & -\frac{11}{210}k_{12} & \frac{11}{210}k_{13} & -\frac{1}{20}k_{14} & -\frac{1}{105}k_{16} & -\frac{1}{105}k_{15} & 0 & -\frac{13}{420}k_{12} & \frac{13}{420}k_{13} & -\frac{1}{30}k_{14} & \frac{1}{140}k_{16} & \frac{1}{140}k_{15} \\
0 & -\frac{11}{210}k_4 & \frac{11}{210}k_5 & -\frac{1}{20}k_6 & -\frac{1}{105}k_8 & -\frac{1}{105}k_7 & 0 & -\frac{13}{420}k_4 & \frac{13}{420}k_5 & -\frac{1}{30}k_6 & \frac{1}{140}k_8 & \frac{1}{140}k_7 \\
0 & 0 & 0 & 0 & 0 & 0 & 0 & 0 & 0 & 0 & 0 & 0 \\
0 & -\frac{9}{70}k_1 & \frac{9}{70}k_2 & -\frac{3}{20}k_3 & -\frac{13}{420}k_5 & -\frac{13}{420}k_4 & 0 & -\frac{13}{35}k_1 & \frac{13}{35}k_2 & -\frac{7}{20}k_3 & \frac{11}{210}k_5 & \frac{11}{210}k_4 \\
0 & \frac{9}{70}k_9 & -\frac{9}{70}k_{10} & \frac{3}{20}k_{11} & \frac{13}{420}k_{13} & \frac{13}{420}k_{12} & 0 & \frac{13}{35}k_9 & -\frac{13}{35}k_{10} & \frac{7}{20}k_{11} & -\frac{11}{210}k_{13} & -\frac{11}{210}k_{12} \\
0 & -\frac{3}{20}k_{17} & \frac{3}{20}k_{18} & -\frac{1}{6}k_{19} & -\frac{1}{30}k_{21} & -\frac{1}{30}k_{20} & 0 & -\frac{7}{20}k_{17} & \frac{7}{20}k_{18} & -\frac{1}{3}k_{19} & \frac{1}{20}k_{21} & \frac{1}{20}k_{20} \\
0 & \frac{13}{420}k_{12} & -\frac{13}{420}k_{13} & \frac{1}{30}k_{14} & \frac{1}{140}k_{16} & \frac{1}{140}k_{15} & 0 & \frac{11}{210}k_{12} & -\frac{11}{210}k_{13} & \frac{1}{20}k_{14} & -\frac{1}{105}k_{16} & -\frac{1}{105}k_{15} \\
0 & \frac{13}{420}k_4 & -\frac{13}{420}k_5 & \frac{1}{30}k_6 & \frac{1}{140}k_8 & \frac{1}{140}k_7 & 0 & \frac{11}{210}k_4 & -\frac{11}{210}k_5 & \frac{1}{20}k_6 & -\frac{1}{105}k_8 & -\frac{1}{105}k_7
\end{array}\right]_k \qquad \text{(B-1g)}
$$

$$
\mathbf{K}^{esc}_{e,k} = \begin{bmatrix}
0 & 0 & 0 & 0 & 0 & 0 & 0 & 0 & 0 & 0 & 0 & 0 \\
0 & -\frac{13}{35}k_1 & \frac{13}{35}k_2 & \frac{7}{20}k_3 & -\frac{11}{210}k_5 & -\frac{11}{210}k_4 & 0 & -\frac{9}{70}k_1 & \frac{9}{70}k_2 & \frac{3}{20}k_3 & \frac{13}{420}k_5 & \frac{13}{420}k_4 \\
0 & \frac{13}{35}k_9 & -\frac{13}{35}k_{10} & -\frac{7}{20}k_{11} & \frac{11}{210}k_{13} & \frac{11}{210}k_{12} & 0 & \frac{9}{70}k_9 & -\frac{9}{70}k_{10} & -\frac{3}{20}k_{11} & -\frac{13}{420}k_{13} & -\frac{13}{420}k_{12} \\
0 & \frac{7}{20}k_{17} & -\frac{7}{20}k_{18} & -\frac{1}{3}k_{19} & \frac{1}{20}k_{21} & \frac{1}{20}k_{20} & 0 & \frac{3}{20}k_{17} & -\frac{3}{20}k_{18} & -\frac{1}{6}k_{19} & -\frac{1}{30}k_{21} & -\frac{1}{30}k_{20} \\
0 & -\frac{11}{210}k_{12} & \frac{11}{210}k_{13} & \frac{1}{20}k_{14} & -\frac{1}{105}k_{16} & -\frac{1}{105}k_{15} & 0 & -\frac{13}{420}k_{12} & \frac{13}{420}k_{13} & \frac{1}{30}k_{14} & \frac{1}{140}k_{16} & \frac{1}{140}k_{15} \\
0 & -\frac{11}{210}k_4 & \frac{11}{210}k_5 & \frac{1}{20}k_6 & -\frac{1}{105}k_8 & -\frac{1}{105}k_7 & 0 & -\frac{13}{420}k_4 & \frac{13}{420}k_5 & \frac{1}{30}k_6 & \frac{1}{140}k_8 & \frac{1}{140}k_7 \\
0 & 0 & 0 & 0 & 0 & 0 & 0 & 0 & 0 & 0 & 0 & 0 \\
0 & -\frac{9}{70}k_1 & \frac{9}{70}k_2 & \frac{3}{20}k_3 & -\frac{13}{420}k_5 & -\frac{13}{420}k_4 & 0 & -\frac{13}{35}k_1 & \frac{13}{35}k_2 & \frac{7}{20}k_3 & \frac{11}{210}k_5 & \frac{11}{210}k_4 \\
0 & \frac{9}{70}k_9 & -\frac{9}{70}k_{10} & -\frac{3}{20}k_{11} & \frac{13}{420}k_{13} & \frac{13}{420}k_{12} & 0 & \frac{13}{35}k_9 & -\frac{13}{35}k_{10} & -\frac{7}{20}k_{11} & -\frac{11}{210}k_{13} & -\frac{11}{210}k_{12} \\
0 & \frac{3}{20}k_{17} & -\frac{3}{20}k_{18} & -\frac{1}{6}k_{19} & \frac{1}{30}k_{21} & \frac{1}{30}k_{20} & 0 & \frac{7}{20}k_{17} & -\frac{7}{20}k_{18} & -\frac{1}{3}k_{19} & -\frac{1}{20}k_{21} & -\frac{1}{20}k_{20} \\
0 & \frac{13}{420}k_{12} & -\frac{13}{420}k_{13} & -\frac{1}{30}k_{14} & \frac{1}{140}k_{16} & \frac{1}{140}k_{15} & 0 & \frac{11}{210}k_{12} & -\frac{11}{210}k_{13} & -\frac{1}{20}k_{14} & -\frac{1}{105}k_{16} & -\frac{1}{105}k_{15} \\
0 & \frac{13}{420}k_4 & -\frac{13}{420}k_5 & -\frac{1}{30}k_6 & \frac{1}{140}k_8 & \frac{1}{140}k_7 & 0 & \frac{11}{210}k_4 & -\frac{11}{210}k_5 & -\frac{1}{20}k_6 & -\frac{1}{105}k_8 & -\frac{1}{105}k_7
\end{bmatrix}_k \qquad \text{(B-1h)}
$$

$$
\mathbf{C}^{rsc}_{e,k} = \left[\begin{array}{c|c|c|c|c|c|c|c|c|c|c|c}
0 & 0 & 0 & 0 & 0 & 0 & 0 & 0 & 0 & 0 & 0 & 0 \\
0 & -\frac{13}{35}c_{10} & \frac{13}{35}c_{9} & -\frac{7}{20}c_{11} & -\frac{11}{210}c_{12} & -\frac{11}{210}c_{13} & 0 & -\frac{9}{70}c_{10} & \frac{9}{70}c_{9} & -\frac{3}{20}c_{11} & \frac{13}{420}c_{12} & \frac{13}{420}c_{13} \\
0 & \frac{13}{35}c_{2} & -\frac{13}{35}c_{1} & \frac{7}{20}c_{3} & \frac{11}{210}c_{4} & \frac{11}{210}c_{5} & 0 & \frac{9}{70}c_{2} & -\frac{9}{70}c_{1} & \frac{3}{20}c_{3} & -\frac{13}{420}c_{4} & -\frac{13}{420}c_{5} \\
0 & -\frac{7}{20}c_{18} & \frac{7}{20}c_{17} & -\frac{1}{3}c_{19} & -\frac{1}{20}c_{20} & -\frac{1}{20}c_{21} & 0 & -\frac{3}{20}c_{18} & \frac{3}{20}c_{17} & -\frac{1}{6}c_{19} & \frac{1}{30}c_{20} & \frac{1}{30}c_{21} \\
0 & -\frac{11}{210}c_{5} & \frac{11}{210}c_{4} & -\frac{1}{20}c_{6} & -\frac{1}{105}c_{7} & -\frac{1}{105}c_{8} & 0 & -\frac{13}{420}c_{5} & \frac{13}{420}c_{4} & -\frac{1}{30}c_{6} & \frac{1}{140}c_{7} & \frac{1}{140}c_{8} \\
0 & -\frac{11}{210}c_{13} & \frac{11}{210}c_{12} & -\frac{1}{20}c_{14} & -\frac{1}{105}c_{15} & -\frac{1}{105}c_{16} & 0 & -\frac{13}{420}c_{13} & \frac{13}{420}c_{12} & -\frac{1}{30}c_{14} & \frac{1}{140}c_{15} & \frac{1}{140}c_{16} \\
0 & 0 & 0 & 0 & 0 & 0 & 0 & 0 & 0 & 0 & 0 & 0 \\
0 & -\frac{9}{70}c_{10} & \frac{9}{70}c_{9} & -\frac{3}{20}c_{11} & -\frac{13}{420}c_{12} & -\frac{13}{420}c_{13} & 0 & -\frac{13}{35}c_{10} & \frac{13}{35}c_{9} & -\frac{7}{20}c_{11} & \frac{11}{210}c_{12} & \frac{11}{210}c_{13} \\
0 & \frac{9}{70}c_{2} & -\frac{9}{70}c_{1} & \frac{3}{20}c_{3} & \frac{13}{420}c_{4} & \frac{13}{420}c_{5} & 0 & \frac{13}{35}c_{2} & -\frac{13}{35}c_{1} & \frac{7}{20}c_{3} & -\frac{11}{210}c_{4} & -\frac{11}{210}c_{5} \\
0 & -\frac{3}{20}c_{18} & \frac{3}{20}c_{17} & -\frac{1}{6}c_{19} & -\frac{1}{30}c_{20} & -\frac{1}{30}c_{21} & 0 & -\frac{7}{20}c_{18} & \frac{7}{20}c_{17} & -\frac{1}{3}c_{19} & \frac{1}{20}c_{20} & \frac{1}{20}c_{21} \\
0 & \frac{13}{420}c_{5} & -\frac{13}{420}c_{4} & \frac{1}{30}c_{6} & \frac{1}{140}c_{7} & \frac{1}{140}c_{8} & 0 & \frac{11}{210}c_{5} & -\frac{11}{210}c_{4} & \frac{1}{20}c_{6} & -\frac{1}{105}c_{7} & -\frac{1}{105}c_{8} \\
0 & \frac{13}{420}c_{13} & -\frac{13}{420}c_{12} & \frac{1}{30}c_{14} & \frac{1}{140}c_{15} & \frac{1}{140}c_{16} & 0 & \frac{11}{210}c_{13} & -\frac{11}{210}c_{12} & \frac{1}{20}c_{14} & -\frac{1}{105}c_{15} & -\frac{1}{105}c_{16}
\end{array}\right]_k \qquad \text{(B-2a)}
$$

$$
\mathbf{C}^{tse}_{ck} = \left[\begin{array}{c|c|c|c|c|c|c|c|c|c|c|c}
0 & 0 & 0 & 0 & 0 & 0 & 0 & 0 & 0 & 0 & 0 & 0 \\
0 & -\frac{13}{35}c_{10} & \frac{13}{35}c_{9} & \frac{7}{20}c_{11} & -\frac{11}{210}c_{12} & -\frac{11}{210}c_{13} & 0 & -\frac{9}{70}c_{10} & \frac{9}{70}c_{9} & \frac{3}{20}c_{11} & \frac{13}{420}c_{12} & \frac{13}{420}c_{13} \\
0 & \frac{13}{35}c_{2} & -\frac{13}{35}c_{1} & -\frac{7}{20}c_{3} & \frac{11}{210}c_{4} & \frac{11}{210}c_{5} & 0 & \frac{9}{70}c_{2} & -\frac{9}{70}c_{1} & -\frac{3}{20}c_{3} & -\frac{13}{420}c_{4} & -\frac{13}{420}c_{5} \\
0 & \frac{7}{20}c_{18} & -\frac{7}{20}c_{17} & -\frac{1}{3}c_{19} & \frac{1}{20}c_{20} & \frac{1}{20}c_{21} & 0 & \frac{3}{20}c_{18} & -\frac{3}{20}c_{17} & -\frac{1}{6}c_{19} & -\frac{1}{30}c_{20} & -\frac{1}{30}c_{21} \\
0 & -\frac{11}{210}c_{5} & \frac{11}{210}c_{4} & \frac{1}{20}c_{6} & -\frac{1}{105}c_{7} & -\frac{1}{105}c_{8} & 0 & -\frac{13}{420}c_{5} & \frac{13}{420}c_{4} & \frac{1}{30}c_{6} & \frac{1}{140}c_{7} & \frac{1}{140}c_{8} \\
0 & -\frac{11}{210}c_{13} & \frac{11}{210}c_{12} & \frac{1}{20}c_{14} & -\frac{1}{105}c_{15} & -\frac{1}{105}c_{16} & 0 & -\frac{13}{420}c_{13} & \frac{13}{420}c_{12} & \frac{1}{30}c_{14} & \frac{1}{140}c_{15} & \frac{1}{140}c_{16} \\
0 & 0 & 0 & 0 & 0 & 0 & 0 & 0 & 0 & 0 & 0 & 0 \\
0 & -\frac{9}{70}c_{10} & \frac{9}{70}c_{9} & \frac{3}{20}c_{11} & -\frac{13}{420}c_{12} & -\frac{13}{420}c_{13} & 0 & -\frac{13}{35}c_{10} & \frac{13}{35}c_{9} & \frac{7}{20}c_{11} & \frac{11}{210}c_{12} & \frac{11}{210}c_{13} \\
0 & \frac{9}{70}c_{2} & -\frac{9}{70}c_{1} & -\frac{3}{20}c_{3} & \frac{13}{420}c_{4} & \frac{13}{420}c_{5} & 0 & \frac{13}{35}c_{2} & -\frac{13}{35}c_{1} & -\frac{7}{20}c_{3} & -\frac{11}{210}c_{4} & -\frac{11}{210}c_{5} \\
0 & \frac{3}{20}c_{18} & -\frac{3}{20}c_{17} & -\frac{1}{6}c_{19} & \frac{1}{30}c_{20} & \frac{1}{30}c_{21} & 0 & \frac{7}{20}c_{18} & -\frac{7}{20}c_{17} & -\frac{1}{3}c_{19} & -\frac{1}{20}c_{20} & -\frac{1}{20}c_{21} \\
0 & \frac{13}{420}c_{5} & -\frac{13}{420}c_{4} & -\frac{1}{30}c_{6} & \frac{1}{140}c_{7} & \frac{1}{140}c_{8} & 0 & \frac{11}{210}c_{5} & -\frac{11}{210}c_{4} & -\frac{1}{20}c_{6} & -\frac{1}{105}c_{7} & -\frac{1}{105}c_{8} \\
0 & \frac{13}{420}c_{13} & -\frac{13}{420}c_{12} & -\frac{1}{30}c_{14} & \frac{1}{140}c_{15} & \frac{1}{140}c_{16} & 0 & \frac{11}{210}c_{13} & -\frac{11}{210}c_{12} & -\frac{1}{20}c_{14} & -\frac{1}{105}c_{15} & -\frac{1}{105}c_{16}
\end{array}\right]_k \qquad \text{(B-2b)}
$$

$$
\mathbf{C}'^{se}_{e,k} = \left[\begin{array}{c|c|c|c|c|c|c|c|c|c|c|c}
0 & 0 & 0 & 0 & 0 & 0 & 0 & 0 & 0 & 0 & 0 & 0 \\
0 & -\frac{13}{35}c_{10} & -\frac{13}{35}c_{9} & \frac{7}{20}c_{11} & \frac{11}{210}c_{12} & -\frac{11}{210}c_{13} & 0 & -\frac{9}{70}c_{10} & -\frac{9}{70}c_{9} & \frac{3}{20}c_{11} & -\frac{13}{420}c_{12} & \frac{13}{420}c_{13} \\
0 & -\frac{13}{35}c_{2} & -\frac{13}{35}c_{1} & \frac{7}{20}c_{3} & \frac{11}{210}c_{4} & -\frac{11}{210}c_{5} & 0 & -\frac{9}{70}c_{2} & -\frac{9}{70}c_{1} & \frac{3}{20}c_{3} & -\frac{13}{420}c_{4} & \frac{13}{420}c_{5} \\
0 & \frac{7}{20}c_{18} & \frac{7}{20}c_{17} & -\frac{1}{3}c_{19} & -\frac{1}{20}c_{20} & \frac{1}{20}c_{21} & 0 & \frac{3}{20}c_{18} & \frac{3}{20}c_{17} & -\frac{1}{6}c_{19} & \frac{1}{30}c_{20} & -\frac{1}{30}c_{21} \\
0 & \frac{11}{210}c_{5} & \frac{11}{210}c_{4} & -\frac{1}{20}c_{6} & -\frac{1}{105}c_{7} & \frac{1}{105}c_{8} & 0 & \frac{13}{420}c_{5} & \frac{13}{420}c_{4} & -\frac{1}{30}c_{6} & \frac{1}{140}c_{7} & -\frac{1}{140}c_{8} \\
0 & -\frac{11}{210}c_{13} & -\frac{11}{210}c_{12} & \frac{1}{20}c_{14} & \frac{1}{105}c_{15} & -\frac{1}{105}c_{16} & 0 & -\frac{13}{420}c_{13} & -\frac{13}{420}c_{12} & \frac{1}{30}c_{14} & -\frac{1}{140}c_{15} & \frac{1}{140}c_{16} \\
0 & 0 & 0 & 0 & 0 & 0 & 0 & 0 & 0 & 0 & 0 & 0 \\
0 & -\frac{9}{70}c_{10} & -\frac{9}{70}c_{9} & \frac{3}{20}c_{11} & \frac{13}{420}c_{12} & -\frac{13}{420}c_{13} & 0 & -\frac{13}{35}c_{10} & -\frac{13}{35}c_{9} & \frac{7}{20}c_{11} & -\frac{11}{210}c_{12} & \frac{11}{210}c_{13} \\
0 & -\frac{9}{70}c_{2} & -\frac{9}{70}c_{1} & \frac{3}{20}c_{3} & \frac{13}{420}c_{4} & -\frac{13}{420}c_{5} & 0 & -\frac{13}{35}c_{2} & -\frac{13}{35}c_{1} & \frac{7}{20}c_{3} & -\frac{11}{210}c_{4} & \frac{11}{210}c_{5} \\
0 & \frac{3}{20}c_{18} & \frac{3}{20}c_{17} & -\frac{1}{6}c_{19} & -\frac{1}{30}c_{20} & \frac{1}{30}c_{21} & 0 & \frac{7}{20}c_{18} & \frac{7}{20}c_{17} & -\frac{1}{3}c_{19} & \frac{1}{20}c_{20} & -\frac{1}{20}c_{21} \\
0 & -\frac{13}{420}c_{5} & -\frac{13}{420}c_{4} & \frac{1}{30}c_{6} & \frac{1}{140}c_{7} & -\frac{1}{140}c_{8} & 0 & -\frac{11}{210}c_{5} & -\frac{11}{210}c_{4} & \frac{1}{20}c_{6} & -\frac{1}{105}c_{7} & \frac{1}{105}c_{8} \\
0 & \frac{13}{420}c_{13} & \frac{13}{420}c_{12} & -\frac{1}{30}c_{14} & -\frac{1}{140}c_{15} & \frac{1}{140}c_{16} & 0 & \frac{11}{210}c_{13} & \frac{11}{210}c_{12} & -\frac{1}{20}c_{14} & \frac{1}{105}c_{15} & -\frac{1}{105}c_{16}
\end{array}\right]_k \qquad \text{(B-2c)}
$$

$$
\mathbf{C}'^{sc}_{e,k} = \begin{bmatrix}
0 & 0 & 0 & 0 & 0 & 0 & 0 & 0 & 0 & 0 & 0 & 0 \\
0 & -\frac{13}{35}c_{10} & -\frac{13}{35}c_{9} & -\frac{7}{20}c_{11} & \frac{11}{210}c_{12} & -\frac{11}{210}c_{13} & 0 & -\frac{9}{70}c_{10} & -\frac{9}{70}c_{9} & -\frac{3}{20}c_{11} & -\frac{13}{420}c_{12} & \frac{13}{420}c_{13} \\
0 & -\frac{13}{35}c_{2} & -\frac{13}{35}c_{1} & -\frac{7}{20}c_{3} & \frac{11}{210}c_{4} & -\frac{11}{210}c_{5} & 0 & -\frac{9}{70}c_{2} & -\frac{9}{70}c_{1} & -\frac{3}{20}c_{3} & -\frac{13}{420}c_{4} & \frac{13}{420}c_{5} \\
0 & -\frac{7}{20}c_{18} & -\frac{7}{20}c_{17} & -\frac{1}{3}c_{19} & \frac{1}{20}c_{20} & -\frac{1}{20}c_{21} & 0 & -\frac{3}{20}c_{18} & -\frac{3}{20}c_{17} & -\frac{1}{6}c_{19} & -\frac{1}{30}c_{20} & \frac{1}{30}c_{21} \\
0 & \frac{11}{210}c_{5} & \frac{11}{210}c_{4} & \frac{1}{20}c_{6} & -\frac{1}{105}c_{7} & \frac{1}{105}c_{8} & 0 & \frac{13}{420}c_{5} & \frac{13}{420}c_{4} & \frac{1}{30}c_{6} & \frac{1}{140}c_{7} & -\frac{1}{140}c_{8} \\
0 & -\frac{11}{210}c_{13} & -\frac{11}{210}c_{12} & -\frac{1}{20}c_{14} & \frac{1}{105}c_{15} & -\frac{1}{105}c_{16} & 0 & -\frac{13}{420}c_{13} & -\frac{13}{420}c_{12} & -\frac{1}{30}c_{14} & -\frac{1}{140}c_{15} & \frac{1}{140}c_{16} \\
0 & 0 & 0 & 0 & 0 & 0 & 0 & 0 & 0 & 0 & 0 & 0 \\
0 & -\frac{9}{70}c_{10} & -\frac{9}{70}c_{9} & -\frac{3}{20}c_{11} & \frac{13}{420}c_{12} & -\frac{13}{420}c_{13} & 0 & -\frac{13}{35}c_{10} & -\frac{13}{35}c_{9} & -\frac{7}{20}c_{11} & -\frac{11}{210}c_{12} & \frac{11}{210}c_{13} \\
0 & -\frac{9}{70}c_{2} & -\frac{9}{70}c_{1} & -\frac{3}{20}c_{3} & \frac{13}{420}c_{4} & -\frac{13}{420}c_{5} & 0 & -\frac{13}{35}c_{2} & -\frac{13}{35}c_{1} & -\frac{7}{20}c_{3} & -\frac{11}{210}c_{4} & \frac{11}{210}c_{5} \\
0 & -\frac{3}{20}c_{18} & -\frac{3}{20}c_{17} & -\frac{1}{6}c_{19} & \frac{1}{30}c_{20} & -\frac{1}{30}c_{21} & 0 & -\frac{7}{20}c_{18} & -\frac{7}{20}c_{17} & -\frac{1}{3}c_{19} & -\frac{1}{20}c_{20} & \frac{1}{20}c_{21} \\
0 & -\frac{13}{420}c_{5} & -\frac{13}{420}c_{4} & -\frac{1}{30}c_{6} & \frac{1}{140}c_{7} & -\frac{1}{140}c_{8} & 0 & -\frac{11}{210}c_{5} & -\frac{11}{210}c_{4} & -\frac{1}{20}c_{6} & -\frac{1}{105}c_{7} & \frac{1}{105}c_{8} \\
0 & \frac{13}{420}c_{13} & \frac{13}{420}c_{12} & \frac{1}{30}c_{14} & -\frac{1}{140}c_{15} & \frac{1}{140}c_{16} & 0 & \frac{11}{210}c_{13} & \frac{11}{210}c_{12} & \frac{1}{20}c_{14} & \frac{1}{105}c_{15} & -\frac{1}{105}c_{16}
\end{bmatrix}_k \qquad \text{(B-2d)}
$$

$$
C'^{w}_{e,k} = \begin{bmatrix}
0 & 0 & 0 & 0 & 0 & 0 & 0 & 0 & 0 & 0 & 0 & 0 \\
0 & -\frac{13}{35}c_1 & -\frac{13}{35}c_2 & -\frac{7}{20}c_3 & \frac{11}{210}c_5 & -\frac{11}{210}c_4 & 0 & -\frac{9}{70}c_1 & -\frac{9}{70}c_2 & -\frac{3}{20}c_3 & -\frac{13}{420}c_5 & \frac{13}{420}c_4 \\
0 & -\frac{13}{35}c_9 & -\frac{13}{35}c_{10} & -\frac{7}{20}c_{11} & \frac{11}{210}c_{13} & -\frac{11}{210}c_{12} & 0 & -\frac{9}{70}c_9 & -\frac{9}{70}c_{10} & -\frac{3}{20}c_{11} & -\frac{13}{420}c_{13} & \frac{13}{420}c_{12} \\
0 & -\frac{7}{20}c_{17} & -\frac{7}{20}c_{18} & -\frac{1}{3}c_{19} & \frac{1}{20}c_{21} & -\frac{1}{20}c_{20} & 0 & -\frac{3}{20}c_{17} & -\frac{3}{20}c_{18} & -\frac{1}{6}c_{19} & -\frac{1}{30}c_{21} & \frac{1}{30}c_{20} \\
0 & \frac{11}{210}c_{12} & \frac{11}{210}c_{13} & \frac{1}{20}c_{14} & -\frac{1}{105}c_{16} & \frac{1}{105}c_{15} & 0 & \frac{13}{420}c_{12} & \frac{13}{420}c_{13} & \frac{1}{30}c_{14} & \frac{1}{140}c_{16} & -\frac{1}{140}c_{15} \\
0 & -\frac{11}{210}c_4 & -\frac{11}{210}c_5 & -\frac{1}{20}c_6 & \frac{1}{105}c_8 & -\frac{1}{105}c_7 & 0 & -\frac{13}{420}c_4 & -\frac{13}{420}c_5 & -\frac{1}{30}c_6 & -\frac{1}{140}c_8 & \frac{1}{140}c_7 \\
0 & 0 & 0 & 0 & 0 & 0 & 0 & 0 & 0 & 0 & 0 & 0 \\
0 & -\frac{9}{70}c_1 & -\frac{9}{70}c_2 & -\frac{3}{20}c_3 & \frac{13}{420}c_5 & -\frac{13}{420}c_4 & 0 & -\frac{13}{35}c_1 & -\frac{13}{35}c_2 & -\frac{7}{20}c_3 & -\frac{11}{210}c_5 & \frac{11}{210}c_4 \\
0 & -\frac{9}{70}c_9 & -\frac{9}{70}c_{10} & -\frac{3}{20}c_{11} & \frac{13}{420}c_{13} & -\frac{13}{420}c_{12} & 0 & -\frac{13}{35}c_9 & -\frac{13}{35}c_{10} & -\frac{7}{20}c_{11} & -\frac{11}{210}c_{13} & \frac{11}{210}c_{12} \\
0 & -\frac{3}{20}c_{17} & -\frac{3}{20}c_{18} & -\frac{1}{6}c_{19} & \frac{1}{30}c_{21} & -\frac{1}{30}c_{20} & 0 & -\frac{7}{20}c_{17} & -\frac{7}{20}c_{18} & -\frac{1}{3}c_{19} & -\frac{1}{20}c_{21} & \frac{1}{20}c_{20} \\
0 & -\frac{13}{420}c_{12} & -\frac{13}{420}c_{13} & -\frac{1}{30}c_{14} & \frac{1}{140}c_{16} & -\frac{1}{140}c_{15} & 0 & -\frac{11}{210}c_{12} & -\frac{11}{210}c_{13} & -\frac{1}{20}c_{14} & -\frac{1}{105}c_{16} & \frac{1}{105}c_{15} \\
0 & \frac{13}{420}c_4 & \frac{13}{420}c_5 & \frac{1}{30}c_6 & -\frac{1}{140}c_8 & \frac{1}{140}c_7 & 0 & \frac{11}{210}c_4 & \frac{11}{210}c_5 & \frac{1}{20}c_6 & \frac{1}{105}c_8 & -\frac{1}{105}c_7
\end{bmatrix}_k \qquad \text{(B-2e)}
$$

$$
\mathbf{C}^{tw}_{e,k} = \begin{bmatrix}
0 & 0 & 0 & 0 & 0 & 0 & 0 & 0 & 0 & 0 & 0 & 0 \\
0 & -\frac{13}{35}c_1 & -\frac{13}{35}c_2 & \frac{7}{20}c_3 & \frac{11}{210}c_5 & -\frac{11}{210}c_4 & 0 & -\frac{9}{70}c_1 & -\frac{9}{70}c_2 & \frac{3}{20}c_3 & -\frac{13}{420}c_5 & \frac{13}{420}c_4 \\
0 & -\frac{13}{35}c_9 & -\frac{13}{35}c_{10} & \frac{7}{20}c_{11} & \frac{11}{210}c_{13} & -\frac{11}{210}c_{12} & 0 & -\frac{9}{70}c_9 & -\frac{9}{70}c_{10} & \frac{3}{20}c_{11} & -\frac{13}{420}c_{13} & \frac{13}{420}c_{12} \\
0 & \frac{7}{20}c_{17} & \frac{7}{20}c_{18} & -\frac{1}{3}c_{19} & -\frac{1}{20}c_{21} & \frac{1}{20}c_{20} & 0 & \frac{3}{20}c_{17} & \frac{3}{20}c_{18} & -\frac{1}{6}c_{19} & \frac{1}{30}c_{21} & -\frac{1}{30}c_{20} \\
0 & \frac{11}{210}c_{12} & \frac{11}{210}c_{13} & -\frac{1}{20}c_{14} & -\frac{1}{105}c_{16} & \frac{1}{105}c_{15} & 0 & \frac{13}{420}c_{12} & \frac{13}{420}c_{13} & -\frac{1}{30}c_{14} & \frac{1}{140}c_{16} & -\frac{1}{140}c_{15} \\
0 & -\frac{11}{210}c_4 & -\frac{11}{210}c_5 & \frac{1}{20}c_6 & \frac{1}{105}c_8 & -\frac{1}{105}c_7 & 0 & -\frac{13}{420}c_4 & -\frac{13}{420}c_5 & \frac{1}{30}c_6 & -\frac{1}{140}c_8 & \frac{1}{140}c_7 \\
0 & 0 & 0 & 0 & 0 & 0 & 0 & 0 & 0 & 0 & 0 & 0 \\
0 & -\frac{9}{70}c_1 & -\frac{9}{70}c_2 & \frac{3}{20}c_3 & \frac{13}{420}c_5 & -\frac{13}{420}c_4 & 0 & -\frac{13}{35}c_1 & -\frac{13}{35}c_2 & \frac{7}{20}c_3 & -\frac{11}{210}c_5 & \frac{11}{210}c_4 \\
0 & -\frac{9}{70}c_9 & -\frac{9}{70}c_{10} & \frac{3}{20}c_{11} & \frac{13}{420}c_{13} & -\frac{13}{420}c_{12} & 0 & -\frac{13}{35}c_9 & -\frac{13}{35}c_{10} & \frac{7}{20}c_{11} & -\frac{11}{210}c_{13} & \frac{11}{210}c_{12} \\
0 & \frac{3}{20}c_{17} & \frac{3}{20}c_{18} & -\frac{1}{6}c_{19} & -\frac{1}{30}c_{21} & \frac{1}{30}c_{20} & 0 & \frac{7}{20}c_{17} & \frac{7}{20}c_{18} & -\frac{1}{3}c_{19} & \frac{1}{20}c_{21} & -\frac{1}{20}c_{20} \\
0 & -\frac{13}{420}c_{12} & -\frac{13}{420}c_{13} & \frac{1}{30}c_{14} & \frac{1}{140}c_{16} & -\frac{1}{140}c_{15} & 0 & -\frac{11}{210}c_{12} & -\frac{11}{210}c_{13} & \frac{1}{20}c_{14} & -\frac{1}{105}c_{16} & \frac{1}{105}c_{15} \\
0 & \frac{13}{420}c_4 & \frac{13}{420}c_5 & -\frac{1}{30}c_6 & -\frac{1}{140}c_8 & \frac{1}{140}c_7 & 0 & \frac{11}{210}c_4 & \frac{11}{210}c_5 & -\frac{1}{20}c_6 & \frac{1}{105}c_8 & -\frac{1}{105}c_7
\end{bmatrix}_k \qquad \text{(B-2f)}
$$

$$
\mathbf{C}^{inc}_{e,k} = \begin{bmatrix}
0 & 0 & 0 & 0 & 0 & 0 & 0 & 0 & 0 & 0 & 0 & 0 \\
0 & -\frac{13}{35}c_1 & \frac{13}{35}c_2 & -\frac{7}{20}c_3 & -\frac{11}{210}c_5 & -\frac{11}{210}c_4 & 0 & -\frac{9}{70}c_1 & \frac{9}{70}c_2 & -\frac{3}{20}c_3 & \frac{13}{420}c_5 & \frac{13}{420}c_4 \\
0 & \frac{13}{35}c_9 & -\frac{13}{35}c_{10} & \frac{7}{20}c_{11} & \frac{11}{210}c_{13} & \frac{11}{210}c_{12} & 0 & \frac{9}{70}c_9 & -\frac{9}{70}c_{10} & \frac{3}{20}c_{11} & -\frac{13}{420}c_{13} & -\frac{13}{420}c_{12} \\
0 & -\frac{7}{20}c_{17} & \frac{7}{20}c_{18} & -\frac{1}{3}c_{19} & -\frac{1}{20}c_{21} & -\frac{1}{20}c_{20} & 0 & -\frac{3}{20}c_{17} & \frac{3}{20}c_{18} & -\frac{1}{6}c_{19} & \frac{1}{30}c_{21} & \frac{1}{30}c_{20} \\
0 & -\frac{11}{210}c_{12} & \frac{11}{210}c_{13} & -\frac{1}{20}c_{14} & -\frac{1}{105}c_{16} & -\frac{1}{105}c_{15} & 0 & -\frac{13}{420}c_{12} & \frac{13}{420}c_{13} & -\frac{1}{30}c_{14} & \frac{1}{140}c_{16} & \frac{1}{140}c_{15} \\
0 & -\frac{11}{210}c_4 & \frac{11}{210}c_5 & -\frac{1}{20}c_6 & -\frac{1}{105}c_8 & -\frac{1}{105}c_7 & 0 & -\frac{13}{420}c_4 & \frac{13}{420}c_5 & -\frac{1}{30}c_6 & \frac{1}{140}c_8 & \frac{1}{140}c_7 \\
0 & 0 & 0 & 0 & 0 & 0 & 0 & 0 & 0 & 0 & 0 & 0 \\
0 & -\frac{9}{70}c_1 & \frac{9}{70}c_2 & -\frac{3}{20}c_3 & -\frac{13}{420}c_5 & -\frac{13}{420}c_4 & 0 & -\frac{13}{35}c_1 & \frac{13}{35}c_2 & -\frac{7}{20}c_3 & \frac{11}{210}c_5 & \frac{11}{210}c_4 \\
0 & \frac{9}{70}c_9 & -\frac{9}{70}c_{10} & \frac{3}{20}c_{11} & \frac{13}{420}c_{13} & \frac{13}{420}c_{12} & 0 & \frac{13}{35}c_9 & -\frac{13}{35}c_{10} & \frac{7}{20}c_{11} & -\frac{11}{210}c_{13} & -\frac{11}{210}c_{12} \\
0 & -\frac{3}{20}c_{17} & \frac{3}{20}c_{18} & -\frac{1}{6}c_{19} & -\frac{1}{30}c_{21} & -\frac{1}{30}c_{20} & 0 & -\frac{7}{20}c_{17} & \frac{7}{20}c_{18} & -\frac{1}{3}c_{19} & \frac{1}{20}c_{21} & \frac{1}{20}c_{20} \\
0 & \frac{13}{420}c_{12} & -\frac{13}{420}c_{13} & \frac{1}{30}c_{14} & \frac{1}{140}c_{16} & \frac{1}{140}c_{15} & 0 & \frac{11}{210}c_{12} & -\frac{11}{210}c_{13} & \frac{1}{20}c_{14} & -\frac{1}{105}c_{16} & -\frac{1}{105}c_{15} \\
0 & \frac{13}{420}c_4 & -\frac{13}{420}c_5 & \frac{1}{30}c_6 & \frac{1}{140}c_8 & \frac{1}{140}c_7 & 0 & \frac{11}{210}c_4 & -\frac{11}{210}c_5 & \frac{1}{20}c_6 & -\frac{1}{105}c_8 & -\frac{1}{105}c_7
\end{bmatrix}_k \qquad \text{(B-2g)}
$$

$$
\mathbf{C}'^{sc}_{e,k} = \left[\begin{array}{c|c|c|c|c|c|c|c|c|c|c|c}
0 & 0 & 0 & 0 & 0 & 0 & 0 & 0 & 0 & 0 & 0 & 0 \\
0 & -\frac{13}{35}c_1 & \frac{13}{35}c_2 & \frac{7}{20}c_3 & -\frac{11}{210}c_5 & -\frac{11}{210}c_4 & 0 & -\frac{9}{70}c_1 & \frac{9}{70}c_2 & \frac{3}{20}c_3 & \frac{13}{420}c_5 & \frac{13}{420}c_4 \\
0 & \frac{13}{35}c_9 & -\frac{13}{35}c_{10} & -\frac{7}{20}c_{11} & \frac{11}{210}c_{13} & \frac{11}{210}c_{12} & 0 & \frac{9}{70}c_9 & -\frac{9}{70}c_{10} & -\frac{3}{20}c_{11} & -\frac{13}{420}c_{13} & -\frac{13}{420}c_{12} \\
0 & \frac{7}{20}c_{17} & -\frac{7}{20}c_{18} & -\frac{1}{3}c_{19} & \frac{1}{20}c_{21} & \frac{1}{20}c_{20} & 0 & \frac{3}{20}c_{17} & -\frac{3}{20}c_{18} & -\frac{1}{6}c_{19} & -\frac{1}{30}c_{21} & -\frac{1}{30}c_{20} \\
0 & -\frac{11}{210}c_{12} & \frac{11}{210}c_{13} & \frac{1}{20}c_{14} & -\frac{1}{105}c_{16} & -\frac{1}{105}c_{15} & 0 & -\frac{13}{420}c_{12} & \frac{13}{420}c_{13} & \frac{1}{30}c_{14} & \frac{1}{140}c_{16} & \frac{1}{140}c_{15} \\
0 & -\frac{11}{210}c_4 & \frac{11}{210}c_5 & \frac{1}{20}c_6 & -\frac{1}{105}c_8 & -\frac{1}{105}c_7 & 0 & -\frac{13}{420}c_4 & \frac{13}{420}c_5 & \frac{1}{30}c_6 & \frac{1}{140}c_8 & \frac{1}{140}c_7 \\
0 & 0 & 0 & 0 & 0 & 0 & 0 & 0 & 0 & 0 & 0 & 0 \\
0 & -\frac{9}{70}c_1 & \frac{9}{70}c_2 & \frac{3}{20}c_3 & -\frac{13}{420}c_5 & -\frac{13}{420}c_4 & 0 & -\frac{13}{35}c_1 & \frac{13}{35}c_2 & \frac{7}{20}c_3 & \frac{11}{210}c_5 & \frac{11}{210}c_4 \\
0 & \frac{9}{70}c_9 & -\frac{9}{70}c_{10} & -\frac{3}{20}c_{11} & \frac{13}{420}c_{13} & \frac{13}{420}c_{12} & 0 & \frac{13}{35}c_9 & -\frac{13}{35}c_{10} & -\frac{7}{20}c_{11} & -\frac{11}{210}c_{13} & -\frac{11}{210}c_{12} \\
0 & \frac{3}{20}c_{17} & -\frac{3}{20}c_{18} & -\frac{1}{6}c_{19} & \frac{1}{30}c_{21} & \frac{1}{30}c_{20} & 0 & \frac{7}{20}c_{17} & -\frac{7}{20}c_{18} & -\frac{1}{3}c_{19} & -\frac{1}{20}c_{21} & -\frac{1}{20}c_{20} \\
0 & \frac{13}{420}c_{12} & -\frac{13}{420}c_{13} & -\frac{1}{30}c_{14} & \frac{1}{140}c_{16} & \frac{1}{140}c_{15} & 0 & \frac{11}{210}c_{12} & -\frac{11}{210}c_{13} & -\frac{1}{20}c_{14} & -\frac{1}{105}c_{16} & -\frac{1}{105}c_{15} \\
0 & \frac{13}{420}c_4 & -\frac{13}{420}c_5 & -\frac{1}{30}c_6 & \frac{1}{140}c_8 & \frac{1}{140}c_7 & 0 & \frac{11}{210}c_4 & -\frac{11}{210}c_5 & -\frac{1}{20}c_6 & -\frac{1}{105}c_8 & -\frac{1}{105}c_7
\end{array}\right]_k \qquad \text{(B-2h)}
$$

where, k_i and c_i ($i = 1, \ldots, 21$) are as follows

$$k_1 = \frac{1}{2}\rho\bar{U}^2K^2LP_4^*; \qquad k_2 = \frac{1}{2}\rho\bar{U}^2K^2LP_6^*;$$

$$k_3 = \frac{1}{2}\rho\bar{U}^2K^2BLP_3^*; \qquad k_4 = \frac{1}{2}\rho\bar{U}^2K^2L^2P_4^* = Lk_1$$

$$k_5 = \frac{1}{2}\rho\bar{U}^2K^2L^2P_6^* = Lk_2; \qquad k_6 = \frac{1}{2}\rho\bar{U}^2K^2BL^2P_3^* = Lk_3$$

$$k_7 = \frac{1}{2}\rho\bar{U}^2K^2L^3P_4^* = Lk_4; \qquad k_8 = \frac{1}{2}\rho\bar{U}^2K^2L^3P_6^* = Lk_5$$

$$k_9 = \frac{1}{2}\rho\bar{U}^2K^2LH_6^*; \qquad k_{10} = \frac{1}{2}\rho\bar{U}^2K^2LH_4^*$$

$$k_{11} = \frac{1}{2}\rho\bar{U}^2K^2BLH_3^*; \qquad k_{12} = \frac{1}{2}\rho\bar{U}^2K^2L^2H_6^* = Lk_9$$

$$k_{13} = \frac{1}{2}\rho\bar{U}^2K^2L^2H_4^* = Lk_{10}; \qquad k_{14} = \frac{1}{2}\rho\bar{U}^2K^2BL^2H_3^* = Lk_{11}$$

$$k_{15} = \frac{1}{2}\rho\bar{U}^2K^2L^3H_6^* = Lk_{12}; \qquad k_{16} = \frac{1}{2}\rho\bar{U}^2K^2L^3H_4^* = Lk_{13}$$

$$k_{17} = \frac{1}{2}\rho\bar{U}^2K^2BLA_6^*; \qquad k_{18} = \frac{1}{2}\rho\bar{U}^2K^2BLA_4^*$$

$$k_{19} = \frac{1}{2}\rho\bar{U}^2K^2B^2LA_3^*; \qquad k_{20} = \frac{1}{2}\rho\bar{U}^2K^2BL^2A_6^* = Lk_{17}$$

$$k_{21} = \frac{1}{2}\rho\bar{U}^2K^2BL^2A_4^* = Lk_{18}$$

$$c_1 = \frac{1}{2}\rho\bar{U}KBLP_1^*; \qquad c_2 = \frac{1}{2}\rho\bar{U}KBLP_5^*$$

$$c_3 = \frac{1}{2}\rho\bar{U}KB^2LP_2^*; \qquad c_4 = \frac{1}{2}\rho\bar{U}KBL^2P_1^* = Lc_1$$

$$c_5 = \frac{1}{2}\rho\bar{U}KBL^2P_5^* = Lc_2; \qquad c_6 = \frac{1}{2}\rho\bar{U}KB^2L^2P_2^* = Lc_3$$

$$c_7 = \frac{1}{2}\rho\bar{U}KBL^3P_1^* = Lc_4; \qquad c_8 = \frac{1}{2}\rho\bar{U}KBL^3P_5^* = Lc_5$$

$$c_9 = \frac{1}{2}\rho\bar{U}KBLH_5^*; \qquad c_{10} = \frac{1}{2}\rho\bar{U}KBLH_1^*$$

$$c_{11} = \frac{1}{2}\rho\bar{U}KB^2LH_2^*; \qquad c_{12} = \frac{1}{2}\rho\bar{U}KBL^2H_5^* = Lc_9$$

$$c_{13}=\frac{1}{2}\rho\bar{U}KBL^2H_1^*=Lc_{10};\qquad c_{14}=\frac{1}{2}\rho\bar{U}KB^2L^2H_2^*=Lc_{11}$$

$$c_{15}=\frac{1}{2}\rho\bar{U}KBL^3H_5^*=Lc_{12};\qquad c_{16}=\frac{1}{2}\rho\bar{U}KBL^3H_1^*=Lc_{13}$$

$$c_{17}=\frac{1}{2}\rho\bar{U}KB^2LA_5^*;\qquad c_{18}=\frac{1}{2}\rho\bar{U}KB^2LA_1^*$$

$$c_{19}=\frac{1}{2}\rho\bar{U}KB^3LA_2^*;\qquad c_{20}=\frac{1}{2}\rho\bar{U}KB^2L^2A_5^*=Lc_{17}$$

$$c_{21}=\frac{1}{2}\rho\bar{U}KB^2L^2A_1^*=Lc_{18}$$

where, L is the length of the element; B is the characteristic width of the element; ρ is air density; $\bar{U}$ is the mean wind speed at the element center; $K=\omega B/\bar{U}$ is reduced frequency; ω is circular frequency; P_i^*, H_i^* and A_i^* (i = 1, ..., 6) are the flutter derivatives of the element cross section, respectively, associated with the element "lateral", "vertical" and torsional motions in the sense of the local reference coordinate *qph*-system. The flutter derivatives are functions of not only the reduced frequency but the local wind yaw and the local wind inclination as well.

REFERENCES

Agar, T.J.A. (1989), Aerodynamic flutter analysis of suspension bridges by a modal technique, *Engineering Structures,* **11**, 75-82.

Agar, T.J.A. (1991), Dynamic instability of suspension bridges, *Computers & Structures*, **41:6**, 1321-1328.

Astiz, M.A. (1998), Flutter stability of very long suspension bridges, *J. Bridge Engineering,* **3:3**, 132-139.

Batchelor, G.K. (1953), *The Theory of Homogeneous Turbulence*, Cambridge University Press, London.

Beard, A.S., and Young, J.S. (1995), Aspect of the design of the Tsing Ma Bridge, *Proc., International Conference on Bridge into 21st Century,* Impressions Design & Print Ltd., Hong Kong, 93-100.

Beard, A.S., Norie, E.H., and Lau, C.K. (1995), The planning and implementation of the Lantau Fixed Crossing, *Proc., International Conference on Bridge into 21st Century,* Impressions Design & Print Ltd., Hong Kong, 85-92.

Beliveau, J.G. (1973), *Suspension Bridge Aeroelasticity Nonlinear Least Squares Technique for System Identification*, PhD. Dissertation, Princeton University.

Beliveau, J.G., Vaicaitis, R., and Shinozuka, M. (1977), Motion of suspension bridge subject to wind loads, *J. Structural Division,* ASCE, **103:ST6**, 1189-1205

Bietry J., Delaunay D., and Conti E. (1994), Comparison of full-scale measurement and computation of wind effects on a cable-stayed bridge, *Proc. Cable-stayed and Suspension Bridges,* Deaucille, 12-15 Oct., 1994, Vol.2, 109-116.

Bietry, J., Sacre, C., and Simiu E. (1978), Mean wind profiles and Changes of terrain roughness, *J. Structural Division, ASCE*, **104**, 1585-1593.

Blackadar, A.K., Panofsky, H.A., and Fiedler, F. (1974), *Investigation of the Turbulent Wind Field below 500 Feet Altitude at the Eastern Test Range, Florida*, NASA CR-2438, National Aeronautics and Space Administration, Washington, DC.

Bleich, F. (1949), Dynamic instability of truss-stiffened suspension bridges under wind action, *Tansactions of ASCE,* **114,** 1177-1222.

Bocciolone, M., Cheli, F., Curami, A., and Zasso, A. (1992), Wind measurements on the Humber Bridge and numerical simulations, *J. wind Engineering and Industrial Aerodynamics,* 41-44, 1393-1404, *Proc. 8th International Conference on Wind Engineering,* ICWE, London, Ont. Canada.

Boonyapinyo, V., Miyata, T., and Yamada H. (1999), Advanced Aerodynamic analysis of suspension bridges by state-space approach, *Journal of Structural Engineering, ASCE,* **125:12,** 1357-1366.

Bowen, A.J. (1980), Full scale measurement of the atmospheric turbulence over two escarpments, *Proceedings of Fifth International Conference on Wind Engineering,* Fort Collins, Colorado, USA, July 1979, Cermak J.E. (Ed.), Pergamon Press, Oxford, **1,** 161-172

Bucher, G.C., and Wall, F.J. (1992a), Probabilistic description of buffeting response of long span bridges, Part I: basic concepts, *J. Engineering Mechanics,* ASCE, **118:12,** 2401-2420.

Bucher, G.C., and Wall, F.J. (1992b), Probabilistic description of buffeting response of long span bridges, Part II: extended analysis, *J. Engineering Mechanics,* ASCE, **118:12,** 2421-2441.

Busch, N.E., and Panofskey, H.A. (1968), Recent Spectra of Atmospheric Turbulence, *J. Royal Meteorological Society,* 94, 132-148.

Cai, C.S, Albrecht, P., and Bosch, H.R. (1997), Flutter and buffeting analysis. I: Finite-element and RPE solution, *J. Bridge Engineering, ASCE,* **4:3,** 174-180

Cermak, J.E., and Cochran, S.L. (1992), Physical Modeling of the atmospheric surface layer, *J. Wind Engineering and Industrial Aerodynamics,* **41-44,** 935-946.

Chamberlain, A.C. (1983), Roughness length of sea, sand and snow, *Boundary Layer Meteorology,* **25,** 405-409.

Chen W. (1993), *The study on the buffeting response spectrum of long-span bridges,* PhD Thesis, Tongji University, Shanghai China (in Chinese)

Chen, W., and Xiang, H.F. (1993), Lateral buffeting of long span bridges and measurement of lateral flutter derivative, *New Advances and Applications in Structural Wind Engineering,* Publishing House of Tongji University, (in Chinese).

Chen, X.Z., Kareem, A., and Matsumoto, M. (1999), Coupled flutter and buffeting response of bridges, *Proc. of the Tenth International Conference on Wind Engineering: Wind Engineering into 21st Century,* 21-24, June, 1999, Copenhagen, Denmark, Edited by Larsen A., Larose G.L., and Livesey, F.M., 845-850

Chen, X.Z., Kareem, A., and Matsumoto, M. (2001), Multimode coupled flutter and buffeting analysis of long span bridges, *J. Wind Engineering and Industrial Aerodynamics,* **89**, 649-664.

Chen, X.Z., Matsumoto, M., and Kareem, A. (2000a), Time domain flutter and buffeting response analysis of bridges, *J. Engineering Mechanics, ASCE,* **126:1**, 7-16.

Chen, X.Z., Matsumoto, M., and Kareem, A. (2000b), Aerodynamic coupled effects on flutter and buffeting of bridges, *J. Engineering Mechanics, ASCE,* **126:1**, 17-26.

Clough, R.W., and Penzien, J. (1975), *Dynamics of Structures*, McGraw-Hill Inc., New York, USA.

Cobo del Arco, D., and Aparico, A.C. (1999), Improving suspension bridge wind stability with aerodynamic appendages, *J. Structural Engineering, ASCE,* **125:12**, 1367-1375.

Code of practice on wind effects Hong Kong-1983, Building Development Department, Hong Kong

Counihan, J. (1975), Adiabatic atmospheric boundary layers: a review and analysis of data from the period 1880-1972, *Atmospheric Environment,* **9**, 871-905.

Curami, A., and Zasso, A. (1993), Extensive identification of bridge deck aeroelastic coefficients, average angle of attack, Reynolds number and other parameter effects, *Proc., 3th Asia-Pacific Symposium on Wind Engineering,* Hong Kong.

Damsgaard, A., and Jensen, A.G. (1990), The use of section model wind tunnel tests in the design of the Storebelt East Bridge in Denmark, *Proc. The 2nd Symponsium on Strait Crossings*, Trondheim, Norway, 10-13, June, 281-287.

Davenport, A.G. (1961a), *A statistical approach to the treatment of wind loading on tall masts and suspension bridges*, Ph.D Thesis, University of Bristol

Davenport, A.G. (1961b), The application of statistical concepts to the wind loading of structures, *Proc. the Institute of Civil Engineers,* London, UK, **19**, 449-472.

Davenport, A.G. (1961c), The spectrum of horizontal gustiness near the ground in high winds, *J. Royal Meteorological. Society*, **87**, 194-211.

Davenport, A.G. (1962a), The response of slender, line-like structures to a gusty wind, *Proc. Institution of Civil Engineers*, London, **23**, 389-407.

Davenport, A.G. (1962b), Buffeting of a suspension bridge by storm winds, *J. Structural Division*, ASCE, **88:ST3**, 233-268.

Davenport, A.G. (1963), Buffeting of structures by gusts, *Proc. 1963 International Symposium on the Effects of Wind on Structures*, London, England.

Davenport, A.G. (1964), The distribution of largest values of a random function with application to gust loading, *Proc. Institution of Civil Engineers*, London, **28**, 187-196.

Davenport, A.G. (1966), The action of wind on suspension bridges, *Proc. International Symposium on Suspension Bridges*, National Civil Engineering Laboratory, Libon, Prtugal, 79-100

Davenport, A.G. (1967), Gust loading factors, *J. the Structural Division, ASCE*, **93**, 11-34.

Davenport, A.G. (1968), The dependence of wind load upon meteorological parameters, *Proc. The International Research Seminar on Wind Effects on Buildings and Structures*, University of Toronto Press, Toronto, 19-82.

Davenport, A.G. (1977), The prediction of risk under wind loading, *Proc. 2nd International Conference on Structural Safety and Reliability*, Munich, Germany, 511-538.

Davenport, A.G., and Tanaka, H, (1974), *Aerodynamic study of Taut Strip Models in turbulent boundary layer*, BLWT Report, University of Western Ontario, London, Canada, 1-74.

Davenport, A.G., Isyumov, N., and Miyata, T. (1971), The experimental determination of the response of suspension bridges to turbulent wind/flow, *Proc. 3rd International Conference on Wind Effects on Buildings and Structures*, Tokyo, 1207-1220.

Davenport, A.G., Isyumov, N., Fader, D.J., and Bowen, C.E.P. (1969), *A study of wind action on a suspension bridge during erection and on completion: The Narrows Bridge, Halifax, Canada*, Eng. Sci. Res. Rept., BLWT-3-69, University of Western Ontario, Canada

Davenport, A.G., Isyumov, N., Rothman, H., and Tanaka, H. (1979), Wind induced response of suspension bridges – wind tunnel model and full scale observations, *Proc. Fifth International Conference on Wind Engineering,* Fort Collins, Colorado, USA, July 1979, Cermak J.E. (Ed.), Pergamon Press, Oxford, **2**, 807-824.

Davenport, A.G., King, J.P.C., and Larose, G.L. (1992), Taut strip model tests, *Aerodynamics of Large Bridges*, Larsen, A. (ed.), Balkema, Rotterdam, 113-124.

Diana, G., Bruni, S., Cigada, A., and Collina, A. (1993), Turbulence effect on flutter velocity in long span suspension bridges, *J. Wind Engineering and Industrial Aerodynamics,* **48**, 329-342.

Diana, G., Bruni, S., Collina, A., and Zasso, A. (1998), Aerodynamic challenges in super long bridges design, *Bridge Aerodynamics,* Larsen & Esdahl (eds.), Balkema, Rotterdam, *Proc. of International Symposium on Advances in Bridge Aerodynamics*, 10-13 May, 1998, Copenhagen, Denmark, 131-143.

Diana, G., Cheli, F., Zasso, A., and Bocciolone M. (1999a), Suspension bridge response to turbulent wind: Comparison of a new numerical simulation method results with full scale data, *Proc. of the Tenth International Conference on Wind Engineering: Wind Engineering into 21st Century,* 21-24, June, 1999, Copenhagen, Denmark, Edited by Larsen A., Larose G.L. and Livesey, F.M., 871-878.

Diana, G., Cheli, F., Zasso, A., Collina, A., and Brownjohn, J. (1992), Suspension bridge parameter identification in full scal test, *J. Wind Engineering and Industrial Aerodynamics*, **41-44**, 165-176.

Diana, G., Falco, M., Bruni, S., Cigada, A., Larose, G.L., Damsgaard, A., and Collina, A. (1995), Comparison between wind tunnel tests on a full aeroelastic model of the proposed bridge over Stretto di Messina and numerical results, *J. Wind Engineering and Industrial Aerodynamics,* **54/55**, 101-113.

Diana, G., Falco, M., Cheli, F., and Cigada, A. (1999b), Experience gained in the Messina Bridge aeroelastic project, *Long-Span Bridges and Aerodynamics*, Edited by Miyata, T., Fujisawa, N. and Yamada, H., Springer-Verlag Tokyo, 155-180.

Dowell, E.H., Curtiss, H.C., Scanlan, R.H., and Sisto, F. (1989), *A modern Course in Aeroelasticity*, 2n edition, Kluwer Academic Publishers, Dordrecht, The Netherlands.

Duch ne-Marullaz, Ph. (1980), Effect of high roughness on the characteristics of turbulence in cases of strong winds, *Proc. Fifth International Conference on Wind Engineering,* Fort Collins, Colorado, USA, July 1979, Cermak J.E. (Ed.), Pergamon Press, Oxford, **1**, 179-193.

Dyrbye, C., and Hansen, S.O. (1996), *Wind Loads on Structures*, John Wiley & Sons Ltd, Chichester, England, UK.

ESDU 72026 (1972), *Characteristics of wind speed in the lower layers of atmosphere near ground: Strong winds (Neutral atmosphere)*, Engineering Sciences Data Unit, 1972.

ESDU 85020 (1985), *Characteristics of atmospheric turbulence near the ground, Part II: single point data for strong winds neutral atmosphere)*, Engineering Sciences Data Unit, 1985.

Facchini, L. (1996), The numerical simulation of Gaussian cross-correlated wind velocity fluctuations by means of a hybrid model, *J. Wind Engineering and Industrial Aerodynamics,* **64**, 187-202.

Falco, M., Curami, A., and Zasso, A. (1992), Nonlinear effects in sectional model aeroelastic parameter identification, *J. Wind Engineering and Industrial Aerodynamics,* **41-44**, 1321-1332.

Farell, C., and Iyengar, A.K.S.(1999), Experiments on the wind tunnel simulation of atmouspheric boundary layers. *J. Wind Engineering and Industrial Aerodynamics,* **79**, 11-35.

Ferraro, V., and Irwin, A. (1990), Wind tunnel model studies of the Skarnsund cable-stayed bridge, *Proc. The 2nd Symposium on Strait Crossings*, Trondheim, Norway, 10-13, June, 273-280.

Gade, R.H, Bosch, H.R., and Podolny, W. (1976), Recent aerodynamic studies of long-span bridges, *J. Structural Division, ASCE,* **102:ST7**, 1299-1315.

Garg, R.K., Lou, J.X., and Kasperski, M. (1997), Some features of modeling spectral characteristics of flow in boundary layer wind tunnels. *J. Wind Engineering and Industrial Aerodynamics,* **72**, 1-12.

Ge, Y.J., and Tanaka, H. (2000a), Aerodynamic flutter analysis of cable-supported bridges by multi-mode and full-mode approaches, *J. Wind Engineering and Industrial Aerodynamics,* **86**, 123-153.

Ge, Y.J., and Tanaka, H. (2000b), Aerodynamic stability of long-span suspension bridges under erection, *J. Structural Engineering, ASCE,* **126:12**, 1404-1412.

Gu. M., and Xiang, H.F. (1992), Optimization of TMD for suppressing buffeting response of long-span bridges, *J. Wind Engineering and Industrial Aerodynamics*, **41-44**, 1382-1392

Gu, M., Zhang, R.X., and Xiang, H.F. (2000), Identification of flutter derivatives of bridge decks, *J. Wind Engineering and Industrial Aerodynamics,* **84**, 151-162.

Güven, O., Farell, C., and Patel, V.C. (1980), Surface-roughness effects on the mean flow past circular cylinders, *J. Fluid Mechanics*, **98**, 673-701.

Harris, R.I. (1971), The nature of the wind, in *Seminar on Modern Design of Wind-Sensitive Structures,* Construction Industry Research & Information, CIRIA, London, UK, 29-55.

Harris, R.I. (1990), Some Further thoughts on spectrum of gustiness in strong winds, *J. Wind Engineering & Industrial Aerodynamics,* **33**, 461-477.

Harris, R.I., and Deaves, D.M. (1980), The structure of strong winds, *Wind Engineering in the Eighties: Proceedings of the CIRIA Conference*, held on 12-13 November 1980, London, Construction Industry Research and Information Association Paper 4.

Helliwell, N.C. (1972), Wind over London, *Proceedings of the Third International Conference on Wind Effects on Buildings and Structures*, Tokyo, 1971, Saikon, 1972, 23-32.

Holmes, J.D. (1975), Prediction of the response of a cable-stayed bridge to turbulence, *Proc. 4th International Conference on Wind Effects on Buildings and Structures*, Healthrow, U.K., Cambridge University Press, 1977, pp187-197.

Hong Kong Observatory (1998), *Tropical Cyclones in 1997*, Prepare and Published by Hong Kong Observatory, 134A Nathan Road, Kowloon, Hong Kong.

Hong Kong Observatory (2000), *Tropical Cyclones in 1999*, Prepare and Published by Hong Kong Observatory, 134A Nathan Road, Kowloon, Hong Kong.

Hoshiya, M., and Saito, E. (1984), Structural identification by extended Kalman filter, *J. Engineering Mechanics, ASCE,* **110:12.**

Hoxey, R.P., and Richards, P.J. (1992), Spectral characteristics of the atmospheric boundary layer near the ground, *Proceedings of UK Wind Engineering Conference,* Cambridge.

Huang, N.E., Shen, Z., and Long, S.R. (1999), A new view of nonlinear water waves: the Hilbert Spectrum, *Annual Review on Fluid Mechanics,* **31,** 417-457.

Huang, N.E., Shen, Z., Long, S.R., Wu, M. J.C., Shih, H.H., Zheng, Q.No., Yen, N.C., Tung, C.C., and Liu, H.H. (1998), The Empirical Mode Decomposition and the Hilbert Spectrum for Nonlinear and Non-Stationary Time Series Analysis, *Proc. Royal Society, Lond. A,* **Vol. 454,** 903-995.

Huston, D.R. (1987), Flutter derivatives from 14 generic deck sections, *Proc. ASCE Structure Congress,* Orlando, 281-292.

Huston, D.R., Bosch, H.R., and Scanlan, R.H. (1988), The effects of fairings and of turbulence on the flutter derivatives of a notably unstable bridge deck, *J. Wind Engineering and Industrial Aerodynamics,* **29,** 339-349.

Ibrahim, S.R. (1978), Modal confidence factor in vibration testing, *J. Spacecraft and Rockets,* **15:5.**

Ibrahim, S.R., and Mikulcik, E.C. (1973), A time-domain model vibration test technique, *The Shock and Vibration Bulletin,* **43:4,** 21-37.

Ibrahim, S.R., and Mikulcik, E.C. (1976), The experimental determination of vibration parameters from time responses, *The Shock and Vibration Bulletin,* **46:5,** 187-196.

Ibrahim, S.R., and Mikulcik, E.C. (1977), A method for the direct identification of vibration parameters from the free response, *The Shock and Vibration Bulletin,* **47:4,** 196-200.

Imai, H., Yun, C.B., Maruyama, O., and Shinozuka, M. (1989), Fundamentals of system identification in structural dynamics, *Prob. Engineering Mechanics,* **4:4,** 211-220.

Irwin, H.P.A.H (1977a), *Experiments on a full aerodynamic model of Lions' Gate Bridge in smooth and turbulent flow,* National Research Council of Canada, N.A.E.Report, LTR-LA-206, Ottawa, Canada.

Irwin, H.P.A.H (1977b), *Wind tunnel and analytical investigations of the response of Lions' Gate Bridge to a turbulent wind,* National Research Council of Canada, N.A.E. Report, LTR-LA-210, Ottawa, Canada.

Irwin, H.P.A.H (1978), Full aeroelastic model of Lions' Gate Bridge, *Proc. 3rd U.S. National Conference on Wind Engineering Research,* Gainesville, Florida, pp.355-358.

Irwin, P.A., and Gamble, S.L. (1985), *Wind tunnel tests for the Annacis Island Bridge, Vancouver, British Columbia,* Report No. 48515031 submitted to CBA Buckland and Taylor, Morrison Hershfield Ltd.

Iwamot, M., and Fujino, Y. (1993), Identification of flutter derivatives for bridge deck from free vibration data, *3rd Asia-Pacific Syumposium on Wind Engineering, APSOWE-3,* Hong Kong, **2**, 125-130.

Jackson, P.S. (1981), On the displacement height in the logarithmic velocity profile, *J. Fluid Mechanics,* **111**, 15-25.

Jain, A., Jones, N.P., and Scanlan, R.H. (1996a), Coupled aeroelastic and aerodynamic response analysis of long-span bridge, *J. Wind Engineering and Industrial Aerodynamics,* **60**, 69-80.

Jain, A., Jones, N.P., and Scanlan, R.H. (1996b), Coupled flutter and buffeting analysis of long-span bridge, *J. Structural Engineering, ASCE,* **122:7**, 716-725.

Jakobsen, J.B. (1995), Estimation of motion induced wind forces by a system identification method, *Proc., 9th International Conference on Wind Engineering,* New Delhi, India, 815-826.

Jakobsen, J.B., and Hjorth-Hansen, E. (1993), Determination of aerodynamic derivatives by a system identification method, *Proc., 1st IAWE European & African Reg. Conference, Guernsey,* 367-377.

Jakobsen, J.B., and Hjorth-Hansen, E. (1995), Determination of the aerodynamic derivatives by a system identification method, *J. Wind Engineering and Industrial Aerodynamics,* **57**, 295-305.

Jakobsen, J.B., and Larose, G.L. (1999), Estimation of aerodynamic derivatives from ambient vibration data, *Proc. of the Tenth International Conference on Wind Engineering: Wind Engineering into 21st Century,* 21-24, June, 1999, Copenhagen, Denmark, Larsen A., Larose G.L., and Livesey, F.M. (eds.), 837-844.

Jennings, A., and McKeown, J.J. (1992), *Matrix Computation*, 2nd Edition, John Wiley & Sons Ltd, Chichester, England, UK.

Johns, N.P., Singh, L., Scanlan, R.H., and Lorendeaux, O. (1995), A force balance for measurement of 3-D aeroelastic parameters, *Proc., Structures Congress, ASCE.*

Jones, N.P., and Scalan, R.H. (1998), Advances (and challenges) in the prediction of long-span bridge response to wind, *Bridge Aerodynamics,* Larsen & Esdahl (eds), Balkema, Rotterdam, *Proc. of International Symposium on Advances in Bridge Aerodynamics*, 10-13 May, 1998, Copenhagen, Denmark, 131-143.

Jones, R.T. (1940), *The unsteady lift on a wing of finite aspect ratio*, NACA Report 681, U.S. National Adversory Committee for Aeronaustics, Langley, Va.

Jones, W.P. (1945), *Aerodynamic forces on wings in non-uniform motion*, British Aeonautical Research Concil, R & M. 2117.

Kaimal, J.C., Wyngaard, J.C., Izumi, Y., and Cote, O.R. (1972), Spectral characteristics of surface-layer turbulence, *J. Royal Meteorological Society*, **98**, 132-148.

Kanda, J., and Royles, R. (1978), Further consideration of the height dependence of the root-coherence in the natural wind, *Building and Environment*, **13**, 175-184

Katsuchi H., Jones N.P., and Scanlan R.H. (1999), Multimode coupled flutter and buffeting analysis of the Akashi-Kaikyo bridge, *J. Structural Engineering*, **125:1**, 60-70.

Katsuchi, H., Saeki, S., Miyata, T., and Sato, H. (1998), Analytical assessment in wind-resistant design of long-span bridge in Japan, *Bridge Aerodynamics,* Larsen & Esdahl (eds), Balkema, Rotterdam, *Proc. of International Symposium on Advances in Bridge Aerodynamics*, 10-13 May, 1998, Copenhagen, Denmark, 87-98.

Kawatai, and Kim, H. (1992), Evaluation of aerodynamic admittance for buffeting analysis, *J. Wind Engineering and Industrial Aerodynamics,* **41-44**, 613-625.

Kimura, K., and Ohara, T. (1999), Lateral sway buffeting of bridge decks due to yawed wind, *Proc. of the Tenth International Conference on Wind Engineering: Wind Engineering into 21st Century,* 21-24, June, 1999, Copenhagen, Denmark, Edited by Larsen A., Larose G.L. and Livesey, F.M, **2**, 919-927.

Kimura, K., and Tanaka, H. (1992), Bridge buffeting due to wind with yaw angles, *J. Wind Engineering and Industrial Aerodynamics,* **41-44**, 1309-1320.

Kimura, K., Nakamura, S., and Tanaka, H. (1994), Buffeting analysis for cable-stayed bridges during construction in yawed wind, *Proc. Symposium on Cable-stayed and Suspension Bridges,* Deauville, France, 12-15,1994, **2**, 109-116.

King, J.P.C., Davenport, A.G., and Larose, G.L. (1991), *A Study of Wind Effects for the Storeb/lt Bridge Tender Design, Denmark,* BLWT-SS31-1991, the University of Western Ontario..

Krenk, S. (1995), Wind field coherence and dynamic wind forces, *symposium on the Advances in Nonlinear Stochastic Mechanics*, Naess and Krenk (eds.), Kluwer, Dordrecht.

Kristensen, L. (1978), On longitudinal spectral coherence, *Boundary Layer Meteorology*, **16**, 145-153.

Kristensen, L., and Jensen, N.O. (1979), Lateral coherence in isotropic turbulence and in the natural wind, *Boundary Layer Meteorology*, **17**, 353-373.

Kristensen, L., Panofsky, H.A., and Smith, S.D. Jensen, N.O. (1979), Lateral coherence of longitudinal wind components in strong winds, *Boundary Layer Meteorology*, **21**, 199-205.

Kukharets, V.P., and Tsvang, L.R. (1969), Spectra of turbulent heat flux in the atmospheric boundary layer, *Izv. Atmospheric Oceanic Physics*, **5**, 1132-1142.

Kumarasena, T. (1989), *Wind Response Prediction of Long-Span Bridges*, PhD. Dissertation, The Johns Hopkins University, USA.

Larose, G., Zasso, A., Melelli, S., and Casanova, D. (1997), Field measurements of the wind-induced response of a 254m high free-standing bridge pylon, *Proc. the 1997 2nd European & African Conference on Wind Engineering,2nd EACWE*, June 22-26, 1997, Genova, Italy, 1553-1560. *J. Wind Engineering and Industrial Aerodynamics*, **74-76**, 891-902.

Larose, G. L., Tanaka, H., Gimsing, N.J., and Dyrbye, C. (1997), Direct measurement of buffeting wind forces on bridge decks, *Proc. the 1997 2nd European & African Conference on Wind Engineering, 2nd EACWE,* June 22-26, 1997, Genova, Italy, 1425-1432. *J. Wind Engineering and Industrial Aerodynamics*, **74-76**, 809-818.

Larose, G. L., Damsgaard A., Diana G., and Falco, M., (1993), Wind-tunnel investigations of the tower for the Stretto di Messina Bridge, *J. Wind Engineering and Industrial Aerodynamics*, 48, 379-393.

Larose, G.L., Falco, M., and Cigada, A. (1995), Aeroelastic response of the towers for the proposed bridge over Stretto di Messina, *Journal of Wind Engineering & Industrial Aerodynamics*, 57, 363-373

Lau, C.K., and Wong, K.Y. (1997), Aerodynamic stability of Tsing Ma Bridge, *Structures in the New Millennium, Proc. The Fourth International Kerensky Conference*, September 3-5, 1997, Hong Kong, Lee, P.K.K.(ed.), Balkema, Rotterdam, 131-138.

Lau, C.K., Mak, W.P., Wong, K.Y., Chan, W.Y., Man, K.L., and Wong, K.F. (1999), Structural performance measurements and design parameter validation for Tsing Ma Suspension Bridge, *ICASS'99, Advances in Steel Structures*, Edited by S.L. Chan and J.G. Teng, Amsterdam, Elsevier Science Ltd., Netherlands, **Vol. I**, 487-496.

Lau, C.K., Wong K.Y., and Chan K.W.Y. (1998), Preliminary monitoring results of Tsing Ma Bridge, *The 14th National Conference on Bridge Engineering*, Shanghai, Vol.2:730-740

Lau, D.T., Cheung, M.S., and Cheng, S.H. (2000), 3D flutter analysis of bridges by spline finite-strip method, *J. Structural Engineering, ASCE*, **126:10**, 1246-1354.

Li, P.W., Poon, H.T., and Lai, S.T. (1998), Observational study of Typhoon Victor (9712) during its passage over Hong Kong, *12th Guangdong-HongKong-Macau Seminar on Hazardous Weather*, Hong Kong (in Chinese).

Li, M., and Dexin, H. (1997), Aerodynamic admittance of bridge deck section, *Proc. 2nd EACWE International Conference*, Genova, Italy.

Li, Q.C. (1995), Measuring flutter derivatives for bridge sectional models in water channel, *J. Engineering Mechanics*, **121:1**, 90-101.

Liepmann, H.W. (1952), On the application of statistical concepts to the buffeting problem, *J. the Aeronautical Sciences*, **19**, 793-800.

Lin, J.H. (1985), A deterministic algorithm of stochastic seismic responses. *Chinese J. Earthquake Engineering and Vibration*, **5**, 89-94.

Lin, J.H. (1985), A deterministic algorithm of stochastic seismic responses. *Chinese J. Earthquake Engineering and Vibration*, **5**, 89-94.

Lin, J.H. (1992), A Fast CQC Algorithm of PSD Matrices for Random Seismic Response, *Computer & Structures*, **44:3**, 683-687

Lin, J.H., and Sun, D.K. (1995), Wind-excited Random Vibration of Irregular Structures, *Education Practice and Promotion of Computer Methods in Engineering Using Small Computers*, Macau, 839-844.

Lin, J.H., Williams, F.W., and Zhang, W.S. (1993), A New Approach to Multi-excitation Stochastic Seismis Response, *Microcomputers in Civil Engineering*, **8:4**, 283-290.

Lin, J.H., Zhang, W.S., and Li, J. (1994), Structural Responses to Arbitrarily Coherent Stationary Random Excitations, *Computer & Structures*, **50:5**, 629-633.

Lin, Y.K. (1979a), Stochastic analysis of bridge motion in large-scale turbulent winds, *Proc. Fifth International Conference on Wind Engineering*, Fort Collins, Colorado, USA, July 1979, Cermak J.E. (Ed.), Pergamon Press, Oxford, **2**, 887-897.

Lin, Y.K. (1979b), Motion of suspension bridges in turbulent winds, *J. Engineering Mechanics Division*, ASCE, **105:EM6**, 921-932

Lin, Y.K., and Ariaratnam, S.T. (1978), Self-excited bridge motion in turbulent winds, *Proc. Third US National Conference on Wind Engineering Research*, Gainesville, Florida, 367-370.

Lin, Y.K., and Ariaratnam, S.T. (1980), Stability of bridge motion in turbulent winds, *J. Structural Mechanics*, **8:1**, 1-15.

Lin, Y.K., and Ariaratnam, S.T. (1980), Stability of bridge motion in turbulent winds, *J. Structural Mechanics*, **8:1**, 1-15.

Lin, Y.K., and Yang, J.N (1983), Multimode bridge response to wind excitation, *J. Engineering Mechanics, ASCE*, **109:2**, 586-603.

Lumley, J.L., and Panofsky, H.A. (1962), *The Structure of Atmospheric Turbulence*, Wiley, New York

MacDonald, A.J. (1975), *Wind Loading on Buildings*, Wiley, New York, USA.

Matsumoto, M. (1994), On flutter of bluff bodies, *Proc., 80th Brithday Symposium in honor of Prof. R.H. Scanlan,* The Johns Hopkins University, 285-294.

Matsumoto, M., Shiraishi, N, Shirato, H., Shigetaka, K., and Niihara, Y. (1993), Aerodynamic derivatives of coupled/hybrid flutter of fundamental structural sections, *J. Wind Engineering and Industrial Aerodynamics*, **49**, 575-584.

McBean, G.A. (1970), *The Turbulent Transfer Mechanisms In The Atmospheric Aurface Layer*, PhD thesis, University of British Columbia, Canada.

Melbourne, W. H. (1979), Model and full scale response to wind action of the cable stayed box girder West Gate Bridge. *IAHR/IUTAM Symposium on Practical Experience with Flow-Induced Vibration,* Karlsruhe Germany

Miyata, T. (1999), Comprehensive discussions on aero-elastic-coupled flutter control for very long span suspension bridges, *Lon-span Bridges and Aerodynamics,* Miyata, T., Fujisawa, N., and Yamada, H. (eds.), Springer-Verlag, Tokyo, Japan, 181-200.

Miyata, T., and Ito, M. (1972), Evaluation of gusts on flexible structures, *Proc. 9th Congress of IABSE*, Amsterdam, Netherlands.

Miyata, T., and Yamada, H. (1998), New idea on aero-elastic-coupled flutter control for very long span bridges, *Bridge Aerodynamics,* Larsen & Esdahl(eds), Balkema, Rotterdam, *Proc. of International Symposium on Advances in Bridge Aerodynamics*, 10-13 May, 1998, Copenhagen, Denmark,153-163.

Miyata, T., Yamada, H., and Kazama, K. (1995), On application of the direct flutter FEM analysis for long span bridge, *Proc., 9th International Conference on Wind Engineering*, New Delhi, India, 1030-1041.

Miyata, T., Yamada, H., Boonyapingyo, V., and Santos, J. (1995), Analytical investigation on the response of a very long suspension bridge under gusty wind, *Proc. 9th International Conference on Wind Engineering,* ICWE, New Delhi, India, 1006-1017

Morfiadakis, E.E., Glinou, G.L., and Koulouvari, M.J. (1996), The suitability of the von Karman spectrum for the structure of turbulence in a complex terrain wind farm, *J. Wind Engineering & Industrial Aerodynamics,* **62**, 237-257.

Namini, A., Albrecht, P., and Bosch, H. (1992), Finite element-based flutter analysis of cable-suspended bridges, *J. Structural Engineering, ASCE*, **118:6,** 1509-1526

Newland, D.E. (1975), *An Introduction to Random Vibrations, Spectral & Wavelet Analysis*, Third Edition, Longman Singarpore Publishers Pte Ltd, Sigapore.

Okubo, T., Narita, N., Yokoyama, K., and Sato, H. (1979), Field observation of aerodynamic behaviour of long-span bridges, *Proc. Fifth International Conference on Wind Engineering,* Fort Collins, Colorado, USA, Cermak J.E.

(Ed.), Fort Collins, Colorado, USA, July 1979, Cermak J.E. (Ed.), Pergamon Press, Oxford, **2**, 825-839.

Otsuki, Y., Washizu, K., Tomizawa, H., and Ohya, A. (1974), A note on the aeroelastic instability of a prismatic bar with square section, *J. Sound and Vibration*, **34:2**, 233-248.

Panofsky, H.A. et al. (1974), Two-points velocity statistics over Lake Ontario, *Boundary Layer Meteorology*, **7**, 309-321.

Panofsky, H.A., and Dutton, J.A. (1984), *Atmospheric turbulence: Models and methods for engineering applications*, John Willey & Sons Inc., New York, USA

Panofsky, H.A., and Mares, E. (1968), Recent measurements of cospectra for heat flux and stress, *Quart. J. Royal Meterological Society*, **94**, 581-584.

Panofsky, H.A., and McCormik, R.A. (1959), The spectrum of vertical velocity near the surface, *Collection of Mineral Industries*, Pennsylvenia Univ., University Park.

Panofsky, H.A., and Mizuno, T. (1975), Horizontal coherence and Pasquill's Beta, *Boundary Layer Meteorology*, **9**, 247-256.

Panofsky, H.A., Vilardo, M., and Lipschutz, R. (1980), Terrain effects on wind fluctuations, *Proc. Fifth International Conference on Wind Engineering*, Cermak J.E. (Ed.), Fort Collins, Colorado, USA, July 1979, Cermak J.E. (Ed.), Pergamon Press, Oxford, **1**, 173-177

Pappa, R.S. (1983), Close-mode identification performance of the ITD algorithm, *AIAA/ASME/ASCE/ASH 24th Structures, Structural Dynamics and Materials Conference*, Lake Tahoe, Nevada, USA, 193-205.

Pasquil, F. (1972), Some aspects of boundary layer description, *J. Royal Meteorological Society*, 98, 469-494.

Pfeil, M.S., and Batista, R.C. (1995), Aerodynamic stability analysis of cable-stayed bridges, *J. Structural Engineering, ASCE*, **121:12**,1784-1788.

Poulsen, N.K., Damsgaard, A., and Reinhold, T.A. (1991), Determination of flutter derivatives for the Great Belt Bridge, *Proc., 8th International Conference on Wind Engineeing, ICWE*, Longdon, Ontario, Canada, **1**, 1991; *J. Wind Engineering and Industrial Aerodynamics*, **41-44**, 1992; 153-164.

Ricciardelli, F., and Vickery, B.J. (1994), Wind loads on a pair of long prisms of square cross-section, *IN-VENTO-94, Proc. 3rd Nat. Italian Conf. Wind Engng., Roma, October,* 101-120.

Ricciardelli, F., and Vickery, B.J. (1998), The aerodynamic characteristics of twin column, high rise bridge towers, *Wind and Structures,* 1(3), 225-241.

Richards, P.J., Fong, S., and Hoxey, R.P. (1997), Anisotropic turbulence in the atmospheric surface layer, *J. Wind Eng. Ind. Aerodyn.,* **.69-71,** 903-913

Roberts, J.B., and Surry, D. (1973), Coherence of grid-generated turbulence, *J. Engineering Mechanics Division, ASCE,* **99:6,** 1227-1245.

Ropelewski, C.F., Tennekes, H., and Panofsky, H.A. (1972), Horizontal coherence of wind fluctuations, *Boundary Layer Meteorology,* **5,** 353-363.

Sachs, P. (1978), *Wind Forces in Engineering,* Second Edition, Pergmon Press, Oxford, England.

Sarkar, P.P. (1992), *New Identification Method Applied to the Response of Flexible Bridges to Wind,* PhD. Thesis, Department of Civil Engineering, Johns Hopkins University, Baltimore, MD, USA.

Sarkar, P.P., Jones, N.P., and Scanlan, R.H. (1991), System identification for estimation of flutter derivatives, *Proc., 8th International Conference on Wind Engineeing, ICWE,* Longdon, Ontario, Canada, **2,** 1991; *J. Wind Engineering & Industrial Aerodynamics,* **41-44,** 1992; 1243-1254

Sarkar, P.P., Jones, N.P., and Scanlan, R.H. (1993), A comparative study of the aeroelastic behaviour of three flexible bridges and a thin airfoil, *Proc., 7th US National Wind Engineering Conference,* UCLA, 595-604.

Sarkar, P.P., Jones, N.P., and Scanlan, R.H. (1994), Identification of aeroelastic parameters of flexible bridges, *J. Engineering Mechanics, ASCE,* **120:8,** 1718-1741.

Scanlan, R.H. (1978a), The action of flexible bridge under wind, I: flutter theory, *J. Sound and Vibration,* **60:2,** 187-199.

Scanlan, R.H. (1978b), The action of flexible bridge under wind, II: buffeting theory, *J. Sound and Vibration,* **60:2,** 201-211.

Scanlan, R.H. (1981), *State-of-the-art Methods for Caculating Flutter, Vortex-induced, and Buffeting Response of Bridge Structures,* Federal Highway Administration, Offices of Research & Development, Report No. FHWA/RD 80/050.

Scanlan, R.H. (1984), Role of indicial functions in buffeting analysis of bridges, *J. Structural Engineering,* **110:7,** pp.1433-1446.

Scanlan, R.H. (1987a), Aspects of wind and earthquake dynamics of cable-stayed bridges, *Bridges and Transmission Line Structures,* ASCE, L. Tall (ed.), 329-340.

Scanlan, R.H. (1987b), Interpreting aeroelastic models of cable-stayed bridges, *J. Engineering Mechanics, ASCE,* **113:4,** 555-575.

Scanlan, R.H. (1988), On flutter and buffeting mechanism in long-span bridges, *Probabilistic Engineering Mechanics,* **3:1,** 22-27.

Scanlan, R.H. (1992), Wind dynamics of long-span bridges, *Aerodynamics of Large Bridges,* A. Larsen (ed.), Balkema, Rotterdam, 47-57.

Scanlan, R.H. (1993a), Bridge buffeting by skew winds in erection stages, *J. Engineering Mechanics,* ASCE, **119:2,** 251-269.

Scanlan, R.H. (1993b), Problematics in formulation of wind-force models for bridge decks, *J. Engineering Mechanics,* ASCE, **119,** 1353-1375.

Scanlan, R.H. (1996), Aerodynamics of cable-supported bridges, *J. Constructional Steel Research,* **39:1,** 51-68.

Scanlan, R.H. (1997), Amplitude and turbulence effects on bridge flutter derivatives, *J. Structural Engineering, ASCE,* **123:2,** 232-236.

Scanlan, R.H. (1999a), Developments in aeroelasticity for the design of long-span bridges, *Lon-span Bridges and Aerodynamics,* Miyata, T., Fujisawa, N., and Yamada, H. (eds.), Springer-Verlag, Tokyo, Japan, 139-149.

Scanlan, R.H. (1999b), Estimates of skew wind speeds for bridge flutter, *J. Bridge Engineering,* **4:2,** 95-98.

Scanlan, R.H., and Budlong, K.S. (1972), Flutter and aerodynamic response considerations for bluff objects in a smooth flow, *Proc. IUTAM-IAHR Symposium on Flow-induced Structural Vibrations,* Karsruhe, Germany, 14-16, Aug. 1972, edited by Naudascher, E., Springer-Verlag, Berlin, 1974, 339-354

Scanlan, R.H., and Gade, R.H. (1977), Motion of suspension bridge spans under gusty wind, *J. The Structural Division, ASCE,* **103:ST9,** 1867-1883.

Scanlan, R.H., and Jones, N.P. (1990), Aeroelastic analysis of Cable-stayed bridges, *J. Structural Engineering,* ASCE, **116:2,** 1279-297.

Scanlan, R.H., and Lin, W.H. (1978), Effects of turbulence on bridge flutter derivatives, *Journal of the Engineering Mechanics Division*, ASCE, **104:EM4**, Proc. Paper 13939, 719-733.

Scanlan, R.H., and Sabzevari, A. (1967), A suspension bridge flutter revisited, *ASCE National Meeting on Structural Engineering*, Seattle, Pre-print No.468, 1967

Scanlan, R.H., and Tomko, J.J. (1971), Airfoil and bridge deck flutter derivatives, *J. Engineering Mechanics, ASCE*, **97:6**, 1717-1737.

Scanlan, R.H., Beliveau, J. G., and Budlong, K.S. (1974), Indicial aerodynamic functions for bridge decks, *J. Engineering Mechanics Division*, ASCE, **100:EM4**, 657-672.

Scanlan, R.H., Jones, N.P., and Singh, L. (1997), Inter-relations among flutter derivatives, *J. Wind Engineering and Industrial Aerodynamics*, **69-71, 829-837.**

Sears, W.R. (1941), Aspects of non-stationary airfoil theory and its practical application, *J. the Aeronautical Sciences*, **8**, 104-108.

Shinozuka, M., Yun, C.B., and Imai, H. (1982), Identification of linear structural dynamic system, *J. Engineering Mechanics, ASCE*, **108:6**, 1371-1390.

Shiraishi, A., and Ogawa, K. (1979), An investigation of wind instability of long-span bridge based on the concept of aeroelastic modes, *Wind Engineering—Proc. Fifth International Conference*, Fort Collins, Colorado, USA, July 1979, Cermak J.E. (Ed.), Pergamon Press, Oxford, **2**, 853-864.

Simiu, E (1974), Wind spectra and dynamic alongwind response, *J. Structural Division, ASCE*, **100:ST9**, 1897-1910.

Simiu, E., and Leigh, S.D. (1983), *Turbulent Wind Effects on Tension Leg Platform Surge*, Building Science Series BSS 151, National Bureau of Standards, Washington, DC, March.

Simiu, E., and Scanlan, R.H. (1996), *Wind Effects on Structures: Fundamentals and Applications to Design*, 3rd Edition, John Wiley & Sons, INC., New York, USA.

Singh, L. (1997), *Experimental Determination of Aeroelastic and Aerodynamic Parameters of Long-span Bridges*, PhD Thesis, Department of Civil Engineering, Johns Hopkins University, Baltimore, MD, USA.

Singh, L., Jones, N.P., Scanlan, R.H., and Lorendeaux, O. (1995), Simultaneous identification of 3-D aeroelastic parameters, *Proc. 9th International Conference on Wind Engineering,* New Delhi, India, 972-978.

Singh, L., Jones, N.P., Scanlan, R.H., and Lorendeaux, O. (1996), Identification of lateral flutter derivatives of bridge decks, *J. Wind Engineering and Industrial Aerodynamics*, **60**, 81-89

Solari, G. (1993a), Gust buffeting I: peak wind velocity and equivalent pressure, *J. Structural Engineering, ASCE,* **119**, 365-382.

Solari, G. (1993b), Gust buffeting II: dynamic alongwind response, *J. Structural Engineering, ASCE,* **119**, 383-398.

Strømmen, E., and Hjorth-Hasen, E. (1995), The buffeting wind loading of the structural members at an arbitrary attitude in the flow, *J. Wind Engineering and Industrial Aerodynamics*, **56**, 267-290.

Sun, D.K. (1999), *Three Dimensional Wind-induced Vibration Analysis of Long-span Bridges*, PhD Thesis, Dalian University of Technology, China, (in Chinese).

Tanaka, H. (1971), Vibrations of bluff-sectional structures under wind action, *Proc., 3rd International Conference on Wind Effects on Buildings and Structures,* Tokyo, 889-910.

Tanaka, H., and Davenport, A.G. (1982), Response of taut strip models to turbulent wind, *J. Engineering Mechanics Division,* ASCE, **108:EM1**, 33-49

Tennekes, H., and Lumley, J.L. (1972), *A First Course in Turbulence*, MIT Press, Cambridge, USA.

Teunissen, H.W. (1970), Characteristics of the mean wind and turbulence in the planetary boundary layer, *Review No. 32, Institute for aerospace studies*, University of Toronto

Theodorsen, T. (1935), *General theory of aerodynamic instability and the mechamism of flutter*, NACA Report, No.496.

Thorbek, L.T., and Hansen, S.O. (1998), Coupled buffeting response of suspension bridges, *J. Wind Engineering and Industrial Aerodynamics,* **74-76**, 839-847

Tieleman, H.W. (1992), Wind characteristics in the surface layer over heterogeneous terrain, *J. Wind Engineering & Industrial Aerodynamics,* **41-44**, 329-340.

Tieleman, H.W., and Mullins, S.E. (1980), The structure of moderately strong winds at a Mid-Atlantic coastal site (below 75m), *Proceedings of Fifth International Conference on Wind Engineering,* Pergamon Press, Oxford, Vol. 1, 145-159

Ukeguchi, N., Sakata, H., and Nishitani, H. (1966), An investigation of aeroelastic instability of suspension bridges, *Proc., International Symposium on Suspension Bridges,* Lisbon, 273-284.

Vicent, G.S. (1953), *Investigation of wind forces on highway bridges,* Highawy Research Board, Special Report 10, presented at the 32nd Annual Meeting, 13-16 Jan, Washington, D.C., USA.

Vickery, B.J. (1965), *On the Flow behind a Coarse Grid and its Use as a Model of Atmospheric Turbulence in Studies Related to Wind Loads on Buildings,* National Physical Laboratory, Aero Report 1143.

Vickery, B.J. (1966), Fluctuating lift and drag on a long cylinder of square cross-section in a smooth and in a turbulent stream, *J. Fluid Mechanics,* **25,** Part 3, 481-494.

Virlogeux, M. (1992), Wind design and analysis for the Normandy Bridges, Aerodynamics of Large *Bridge,* A. Larsen (ed), Balkema, Rotterdam, 183-216.

Von Karman, T. (1948), Progress in the statistical theory of turbulence, *Proc. National Academic Society,* Washington, DC, 530-539

Wall, F.J., and Bucher, G.C. (1992a), Probabilistic description of buffeting response of long-span bridges. I: basic concepts, *J. Engineering Mechanics,* ASCE, **118:12,** 2401-2420.

Wall, F.J., and Bucher, G.C. (1992b), Probabilistic description of buffeting response of long-span bridges. II: extended analysis, *J. Engineering Mechanics,* ASCE, **118:12,** 2421-2441.

Walshe, D.E, and Wyatt, T.E. (1983), Measurement and application of the aerodynamic admittance function for a box-girder bridge, *J. Wind Engineering and Industrial Aerodynamics,* **14,** 211-222.

Wang, Z.H. (1994), Simulation of Wind Loading, *J. Building Structures,* **15:1,** 44-52, in Chinese.

Webster, I.T., and Burling, R.W. (1981), A test of isotropy and Tayloer's Hypothsis in the atmospheric boundary layer, *Boundary Layer Metheorology,* **20,** 429-443.

Wilson, E.L., Der Kiureghian, A., and Bayo, E.P. (1981), A Replacement for the SRSS Method in Seismic Analysis, *Earthquake Engineering and Structural Dynamics*, **9:2**, 187-192.

Wooton, L.R., and Scruton, C. (1971), Aerodynamic Stability, *The Modern Design of Wind-Sensitive Structures*, Construction Industry Research and Information Association, London, 65-81.

Wyngaard, J.C., and Coté, O.R. (1972), Cospectral similarity in the atmospheric surface layer, *Quart. J. Royal Meterological Society*, **98**, 590-603.

Xiang, H.F., and Chen, A.R. (1998), 21st century long-span bridges in China, *Bridge Aerodynamics, Proc. The International Symposium on Advances in Bridge Aerodynamics,* Copenhagen, Denmark, 10-13 May, 1998, Larsen A. and Eshahl, S. (eds.), 175-186.

Xiang, H.F., Lin, Z.X., Bao., W.G., Chen, A.R., and Gu., M. (1996), *Wind-resistant Design Guideline for Highway Bridges*, People's Communication Press, China, (in Chinese).

Xie, J., et al. (1989), Identification of the aerodynamic admittance functions for bridge road decks, *Proc. 2nd APSOWE*, Beijing, China, 618-628.

Xie, J., and Tanaka, H. (1991), Buffeting analysis of long span bridges to turbulent wind with yaw angle, *J. Wind Engineering and Industrial Aerodynamics*, **37:1**, 65-77.

Xie, J.M. (1984), *Theory ofFlutter for Bridge Structures & Study of Flutter Behaviours of Cable-stayed Bridges*, PhD thesis, Tongji University, China, (in Chinese).

Xie, J.M. (1986), Method of coupled vibration under initial impulse for identification of non-steady aerodynamic model, *J. Aerodynamics,* No.3, 258-267, (in Chinese).

Xie, J.M. (1987), CVR method for identification of nonsteady aerodynamic model, *Advances In Wind Engineering, Proc., 7th International Congress on Wind Engineering,* Aachen, F.R.G, July, 1987, Kramer, C., and Gerhardt, H.J.(eds.); *J. Wind Engineering and Industrial Aerodynamics*, **29**, 1988, 389-397.

Xie, J.M., and Xiang, H.F. (1985), State-space method for 3D flutter analysis of bridge structures, *Proc., Asia Pacific Symposium on Wind Engineering,* India, 269-276.

Xu, Y.L. (1999), Buffeting of Tsing Ma suspension bridge: Analysis and comparison, *Proc. of the Tenth International Conference on Wind Engineering: Wind Engineering into 21st Century,* 1075-1080, June, 1999, Copenhagen, Denmark, Edited by Larsen A., Larose G.L. and Livesey, F.M.

Xu, Y.L., Ko, J.M., and Zhang, W.S. (1997), Vibration studies of Tsing Ma Suspension Bridge, *J. Bridge Eng. ASCE,* 2:4, 149-156.

Xu, Y.L., Sun, D.K., Ko, J.M., and Lin, J.H. (1998), Buffeting analysis of long span bridges: a new algorithm, *Computers & Structures*, **68**, 303-313.

Xu, Y.L., Sun, D.K., Ko, J.M., and Lin, J.H. (2000a), Fully coupled buffeting analysis of Tsing Ma suspension bridge, *J. Wind Engineering and Industrial Aerodynamics*, **85:1**, 97-117.

Xu, Y.L., Zhu, L.D., Wong, K.Y., and Chan K.W.Y. (2000b), Field measurement results of Tsing Ma suspension bridge during Typhoon Victor, *Structural Engineering Mechanics*, **10:6**, 454-559.

Yamada, H., and Miyata, T. (1997), Introduction of a modal decomposition and reassemblage method for the multi-dimensional unsteady aerodynamic force measurement, *J. Wind Engineering and Industrial Aerodynamics*, **69-71**, 769-775.

Yamada, H., Miyata, T., and Ichikawa, H. (1991), Measurement of aerodynamic coefficients by system identification methods, *Proc., 8th International Conference on Wind Engineeing, ICWE,* Longdon, Ontario, Canada, **2**, 1991; *J. Wind Engineering and Industrial Aerodynamics*, **41-44**, 1992; 1255-1263.

Yamada, H., Miyata, T., Minh, N.N., and Katsuchi, H. (1999), Complex flutter-mode analysis for coulpled gust response of Akashi Kaikyo Bridge model, *Proc. of the Tenth International Conference on Wind Engineering: Wind Engineering into 21st Century,* 21-24, June, 1999, Copenhagen, Denmark, Edited by Larsen A., Larose G.L., and Livesey, F.M., 1081-1088.

Zan, S.J. (1987), *The effect of mass, wind angle, and erection technique on the aeroelastic behaviour of a cable-stayed bridge model*, Aeronautical Note, NAE-AN-46, NRC No. 28207, National Aeronautical Establishment, National Research Council Canada, Ottawa, Canada

Zasso, A. (1996), Flutter derivatives: Advantages of a new representation convention, *J. Wind Engineering and Industrial Aerodynamics,* **60**, 35-47.

Zasso, A., and Curami, A. (1993), Extensive Identification of bridge deck aeroelastic coefficients: average angle of attack, Reynolds number and other parameter effects, *Proc. 3rd Asian-Pacific Symposium on Wind Engineering,* Hong Kong, 143-148.

Zasso, A., Cigada, A., and Negri, S. (1996), Flutter derivatives identification through full bridge aeroelastic model transfer function analysis, *J. Wind Engineering and Industrial Aerodynamics*, **60**, 17-33.

Zhang, R.X (1998), *Theoretical and Experimental Study on Identification of Aerodynamic Parameters of Bridge Decks*, PhD Thesis, Tongji University, China, (in Chinese).

Zhu, L.D., and Xiang, H.F. (1989), A numerical method for flutter analysis — A improvement of Scanlan's method, *Proc., 4th National Academic Conference on Wind Effects on Structures*, Shunde, Guangdong, China, 350-356, (in Chinese).

Zhu, L.D., and Xiang, H.F. (1995), Mass-system simulation of sectional model for bridge flutter, *Structural Engineers*, **35:4**, 39-45, 38(cont.), (in Chinese).

Zhu, L.D., Xu, Y.L., Wong, K.Y., and Chan, K.W.Y. (1999), Wind characteristics and response of Tsing Ma Bridge during Typhoon Victor, *ICASS'99, Advances in Steel Structures*, Edited by S.L. Chan and J.G. Teng, Amsterdam, Elsevier Science Ltd., Netherlands, **Vol. I**, 497-504.

Zhu, L.D., Xu. Y.L., and Xiang, H.F. (2000), Buffeting analysis of a long suspension bridge under inclined wind, *Advances in Structural Dynamics*, J.M., Ko and Y.L., Xu (eds.), *Proc. The International Conference on Advances in Structural Dynamics*, 13-15 December 2000, Hong Kong, China, 1535-1542.